PARTICLE TRANSPORT IN FLOW THROUGH POROUS MEDIA: ADVECTION, LONGITUDINAL DISPERSION, AND FILTRATION

Thesis by

Russell Edgar Mau

In Partial Fulfillment of the Requirements

for the Degree of

Doctor of Philosophy

California Institute of Technology

Pasadena, California

1992

(Submitted February 18, 1992)

Notice

The research on which this report is based was financed in part by the United States Department of the Interior, Geological Survey, through the State Water Resources Research Institute, Project No. 14-08-0001-G1550, and by the University of California Water Resources Center, Projects UCAL-WRC-W-22605-89(03) and -W-773. Contents of this publication do not necessarily reflect the views and policies of the U.S. Department of the Interior, nor does mention of trade names or commercial products constitute their endorsement or recommendation for use by the U.S. Government.

Dedicated to my wife

I would like to acknowledge the financial support of both the Andrew W. Mellon Foundation and the United States Department of the Interior, Geological Survey, through the State Water Resources Research Institute, Project No. 14-08-0001-G1550, and by the University of California Water Resources Center, Projects UCAL-WRC-W-22605-89(03) and -W-773.

Acknowledgments

I wish to express my appreciation in verse,
I am no Robert Frost, but this could have been much worse.

I am my Father, my father, and my mother, all three.
If it were not for them, I would not be me.

To my sisters, Barbara and Roberta, goes much blame.
How could I allow them to be doctors and never receive my own fame?

Mike Surace and Mark Schlautman as roommates, colleagues, and friends were first-rate.
Our times together will only be thought of as great.
Of these times which I will remember
When all is said and done, they were probably the best ever.

I think fondly of librarian Rayma Harrison; secretaries: Joan Matthews, Fran Matzen, Elaine Granger, Karen Hodge; and Gunilla Hastrup, also a librarian.
They always were helpful and considerate even when I looked and acted as a barbarian.

Others who more than deserve thanks are Mike and Wendy Scott, Marco and Jane Rasi, Sandy and Annabel Elliot, Kit Ng, Talal Balaa, E. Carraway, and Jerry Ramsden and Denise his wife.
Without these people, I would not have had a social life.

In the dungeon of the subbasement, Joe Fontana, Rich Eastvedt, and Hai Vu must receive mention,
Without them, my work would never have begun.

I thank my committee, John List, James Morgan, and Fred Raichlen for their diligence in assuring my thesis success.
I am so glad they found the facts buried in all of the b.s.

To Norman Brooks I will always feel as a debtor.
As an advisor and friend there are none better.

Finally, to those of you who do not fear ghosts, goblins, and ghouls,
Keep in mind, they are now using tools.

Abstract

A theoretical and experimental investigation of the transport parameters of particles flowing through porous media has been made. These parameters are the particle advective velocity, longitudinal dispersion coefficient, and filter coefficient. Both theoretical and experimental results are limited to flows with low Reynolds number (linear, laminar flow) and high Peclet number (advection dominates diffusion). The theoretical development used dimensionless numbers to define the transport parameters and incorporated them into an advective-dispersion equation describing particle transport. A relationship for unfavorable filtration due to repulsive double layer interactions is proposed.

A solution to the complete advective-dispersion equation for particle transport was derived for the case of a constant filter coefficient. This solution when compared to a similar solution previously derived for solute transport, showed that for small filtration the solutions were identical except for the exponential decay factor due to filtration. A numerical model was developed for the case of a variable filter coefficient.

Flow experiments were conducted in a 1.5 m vertical column with sand (geo. mean diameter = 381 micron), with suspensions of polystyrene latex particles (three cases, mean diameter = 0.1, 1.0, and 2.8 micron), and with NaCl as the electrolyte (0.4 mM < Ionic strength < 2.1 mM). The range of Peclet number studied was 1.26×10^4 to 2.00×10^6. The measurement of the particle

concentrations during passage of a displacement front provided the necessary data to determine the particle transport parameters.

The particle advective velocities for the three different sized particles was found to range approximately from 0 to 5.4% greater than the solute velocity, and these values were within a few percent of predictions based on particle and pore radii.

The longitudinal dispersion coefficient for the three different sized particles was found to be a function of only the advective velocity of the particles and grain diameter of the porous bed which confirmed the dimensional analysis argument and closely matched previous solute work.

A dimensional analysis argument for the relationship between the favorable and unfavorable filter coefficient was proposed to be a function of the ratio of the particle diffusion length of an advecting particle and the double layer thickness (which in turn depends on the ionic strength of the water). A wide range of filtration data (Brownian to advective particles) was empirically fitted using this dimensionless number.

The effects of ionic strength on particle transport were found to be either minimal or separable from the hydraulic variables. For advection, effects of changing ionic strength were analyzed as changes in the effective particle radius and calculations made using this apparent particle radius matched experimental results. For dispersion, an increase of a factor of 6 in the ionic strength increased the longitudinal dispersion by a factor of 1.2.

Table of Contents

Notation

A = column cross-sectional area (L^2)

A_e = area of electrode (L^2)

A_s = dimensionless flow model parameter (-)

a_p = radius of particle (L)

C = particle concentration ($M\ L^{-3}$)

C_b = breakthrough particle concentration in column ($M\ L^{-3}$)

C_B = background particle concentration in spectrophotometer ($M\ L^{-3}$)

C_i = initial (background) particle concentration in column ($M\ L^{-3}$)

C_{pl} = plateau particle concentration in column ($M\ L^{-3}$)

$C_r = C_0$ = reservoir particle concentration for column ($M\ L^{-3}$)

C_T = total CO_2 concentration (M)

C_0 = particle concentration at x=0 in column ($M\ L^{-3}$)

$C^* = C/C_0$ = particle relative concentration including filtration reduction (-)

C^*_a = approximate particle relative concentration including filtration reduction (-)

C^*_e = exact particle relative concentration including filtration reduction (-)

C'^* = solute concentration or particle concentration scaled by filtration reduction (-)

D = free fluid Brownian diffusion coefficient ($L^2\ T^{-1}$)

D_k = dark current

D_L = longitudinal dispersion coefficient for solute ($L^2\ T^{-1}$)

D_{Lp} = longitudinal dispersion coefficient for particles ($L^2\ T^{-1}$)

D_m = porous medium Brownian diffusion coefficient ($L^2\ T^{-1}$)

D_p = free fluid particle Brownian diffusion coefficient ($L^2\ T^{-1}$)

d = distance between electrodes (L)

d_g = diameter of the grain of the medium (L)

d_p = diameter of particle (L)

F = Faraday constant ($C\ mol^{-1}$)

F_t = tortuosity (-)

g = gravitational acceleration ($L\ T^{-2}$)

H = Hamaker constant (ergs)

h = piezometric head (L)

I = ionic strength (Molar)

K = hydraulic conductivity ($L\ T^{-1}$)

K_c = cell constant (L^{-1})

K_H = Henry's law constant ($M\ atm^{-1}$)

k = specific conductance ($mho\ cm^{-1}$)

L = coordinate of sample position (L)

P = dynamic pressure ($ML\ T^{-2}L^{-2}$)

P_{CO2} = partial pressure of CO_2 (atm)

$Pe = V_s d_g/D$ = fluid Peclet number (-)

Pe_D = fluid dynamic Peclet number (-)

Pe_{Dp} = particle dynamic Peclet number (-)

$Pe_p = V_s d_g/D_p$ = particle Peclet number (-)

Pe_{pu} = upper limit of particle Peclet number for linear, laminar flow (-)

Pe_u = upper limit of Peclet number for linear, laminar flow (-)

pH_{zpc} = pH of zero point of charge (mol liter^{-1})

Q = volume flow rate (L^3 T^{-1})

R = gas constant (J $mol^{-1}K^{-1}$)

$1/R_c$ = observed conductance reading (mhos)

$Re = V_s d_g/\nu$ = Reynolds number (-)

r = radial position (L)

r_0 = capillary radius (L)

S = molecule radius of gyration (L)

T = transmittance (-)

T_e = temperature (K)

t = time (T)

t_{50} = time to 50% breakthrough (T)

$t^* = V_p t/d_g$ = dimensionless time for particles (-)

$t'^* = V_s t/d_g = t^*(V_s/V_p)$ = dimensionless time for solute (-)

$U_p(r)$ = particle velocity distribution in pore (L T^{-1})

$U_s(r)$ = fluid velocity distribution in pore (L T^{-1})

U_0 = fluid centerline velocity (L T^{-1})

V_D = specific discharge (Darcy velocity) (L T^{-1})

V_p = interstitial velocity of particle (L T^{-1})

V_s = interstitial velocity of fluid (L T^{-1})

w_s = particle settling velocity ($L\ T^{-1}$)

V^* = enhanced velocity ratio (-)

x = longitudinal position (L)

$x^* = x/d_g$ = dimensionless longitudinal coordinate for particles (-)

$x'^* = x'/d_g$ = dimensionless longitudinal coordinate for solute (-)

α = full solution filter coefficient (L^{-1})

α_c = collision efficiency factor (-)

$\alpha^* = \alpha d_g$ = dimensionless filter coefficient (-)

β_{CT} = buffer intensity of two-protic acid for C_T = constant (equivalents $liter^{-1}$)

β_{PCO2} = buffer intensity of two-protic acid for P_{CO2} = constant (equivalents $liter^{-1}$)

$\beta_{P,B,T}$ = extinction coefficients for particles, background, and total

ΔC^* = error between exact and approximate particle concentrations (-)

Δt = time step (T)

$\Delta t^* = V_s \Delta t/d_g$ = dimensionless time step for particles (-)

$\Delta t'^* = \Delta t^*(V_s/V_p)$ = dimensionless time step for solute (-)

Δx = length step (L)

$\Delta x^* = \Delta x/d_g$ = dimensionless length step for particles (-)

$\Delta x'^* = \Delta x'/d_g$ = dimensionless length step for solute (-)

ΔV = enhanced velocity fraction (-)

δ_{DB} = thickness of diffusion boundary layer for a moving particle (L)

δ_{HB} = thickness of the hydrodynamic boundary layer (L)

$\delta_\kappa \sim \kappa^{-1}$ = diffuse double layer thickness (L)

ϵ = dielectric constant multiplier for water (-)

ϵ_0 = dielectric constant for vacuum ($C^2\ L^{-1}J^{-1}$)

κ^{-1} = diffuse double layer thickness (L)

η = single collector efficiency (-)

θ_e = effective porosity (-)

θ_T = total porosity (-)

λ = approximate solution filter coefficient (L^{-1})

λ_f = favorable filter coefficient (L^{-1})

$\lambda^* = \lambda d_g$ = dimensionless filter coefficient (-)

μ = dynamic fluid viscosity ($M\ L^{-1}T^{-1}$)

ν = kinematic viscosity of the fluid ($L^2\ T^{-1}$)

ρ_f = fluid density ($M\ L^{-3}$)

ρ_p = particle density ($M\ L^{-3}$)

σ_x = single standard deviation of the width of the breakthrough (L)

σ_t = single standard deviation of the elapsed time for passage of the breakthrough (T)

$\Omega = \Omega(L)$ = light intensity for measured sample

Ω_B = light intensity for reference sample

Ω_i = incident light intensity

$\Omega(x)$ = light intensity at position x

List of Tables

Chapter 2

Chapter 5

List of Figures

Chapter 1

Chapter 2

Chapter 3

Chapter 4

Chapter 5

1. INTRODUCTION

The transport of particles in water flowing through a saturated porous medium is investigated in a laboratory column under well-controlled physical and chemical conditions. The results include the characterization of the advective velocity, longitudinal dispersion, and filtration of colloidal particles.

The polystyrene latex particles, with diameters of 0.1, 1.0, and 2.8 micron, which are studied in this work are considered to be colloids, which are defined in this work as particles whose sizes range from Brownian particles ($d_p < 10^{-6}$ meter) to advective particles (10^{-6} m $< d_p < 10^{-5}$ m). With their low gravitational settling velocities ($< 10^{-4}$ cm/second), these particles may be suspended in groundwater and, consequently, transported long distances. In this work, the term "particles" refers to the transporting colloidal material while the terms "medium" or "media grains" refer to the porous medium through which the particle suspension flow. In this work, a uniform sand is used which has a mean diameter of 381 microns.

1.1 Motivation

Colloidal particles have been shown to exhibit significant movement in aquifers. Bacterial migration up to 830 meters and virus migration up to 400 meters from their sources have been reported (Gerba et al. 1975; Keswick and Gerba 1980; Gerba and Goyal 1985). Colloidal clay particles from surface soils were responsible for turbidity observed in wells several hundred meters from a recharge site (Nightingale and Bianchi 1977). Asbestos fibers were detected in an aquifer which was recharged from a reservoir containing high levels of fibers

(Hayward 1984). Organic macromolecules similar to natural humic substances have been reported to migrate with little retardation in some aquifers. Tannin and lignin in the colloidal size range from a waste pulp liquor transported as fast as a plume of sodium ions through a sand aquifer (Robertson et al. 1984).

Naturally occurring particles have been shown to consist of both organic macromolecules and inorganic particles. These colloids have been shown to be capable of associating with groundwater contaminants considered to be highly retarded due to strong interactions with the immobile aquifer medium.

For organic colloidal particles, humic substances extracted from soil have been shown to bind hydrophobic organic contaminants (Carter and Suffet 1982; Landrum et al. 1984; McCarthy and Jimenez 1985), to enhance the pollutant's apparent solubility in water (Chiou et al. 1983 and 1986), and to reduce the chemical's apparent affinity for binding to sediment particles (Hassett and Anderson 1982; Gschwend and Wu 1985; McCarthy and Black 1987). This association with mobile humic macromolecules could enhance the transport of hydrophobic contaminants. This may be true for DDT which has been reported to move much further under field conditions than predicted by computer models (Enfield et al. 1982).

For inorganic colloidal particles, actinides formed complexes with organic and inorganic colloids in groundwater samples and associated with iron oxide colloids in test solutions (Nakayama et al. 1986). Actinides in borosilicate glass leached with organic-free water eluted as colloidal particles that were retained by

soil columns (Avogadro et al. 1982). The introduction of low-conductivity recharge water dispersed clay colloids from surface soil and resulted in high turbidity in wells several hundred meters away from the recharge site (Nightingale and Bianchi 1977). Treatment of the recharge area with gypsum relieved the turbidity by destabilizing the colloids. At a nuclear detonation cavity at the Nevada Test Site, radionuclides were found to be associated with colloidal mineral particles outside the detonation zone (Buddemeier 1986; Buddemeier and Isherwood 1985). The presence of these colloid-associated nuclides outside of the detonation cavity suggests that they are moving by particle transport.

These observations in the literature may be summarized as:

1) Colloidal particles occur in some aquifers.

2) They have been observed to move through aquifers.

3) Contaminants may be adsorbed on the colloids.

To solve groundwater contamination problems which have come into the forefront of public awareness in recent years, a better understanding of particle transport is necessary. The relevance of this work may be realized through the modification of existing contaminant transport models. Previously, contaminant transport has been conceptualized as only the partitioning of a pollutant between an immobile adsorbed phase and a mobile aqueous phase, and models based on this concept can greatly underestimate the amount of contaminant transport. Findings suggest that colloids can alter the mobility of adsorbed contaminants by transporting otherwise immobile pollutants through porous media systems. By

developing a better fundamental understanding of particle transport, the ability to predict mass transport in these porous media systems will be greatly improved.

1.2 Objectives

The DOE in report DOE/ER-0384 (1988) has outlined a specific five year program which is intended to analyze colloid and colloid-facilitated contaminant transport. This program is intended to address major questions concerning subsurface colloids, and the following question is quoted directly from this report:

"2. Do colloids move through aquifers? Can the chemical and hydrologic factors controlling the stabilization, transport, and deposition of colloidal particles be described and incorporated within predictive transport models?"

The objective of this research is to answer the colloid transport component of this question. In this work, a particle mass transport equation is developed which includes the transport parameters advective velocity, longitudinal dispersion coefficient, and filter coefficient, and the individual parameters are analyzed according to dimensional analysis arguments. The applicability of this equation is verified by carefully controlled experiments, and the experimentally determined parameters are compared to the respective dimensionless groups.

This research investigated key physical and chemical variables which are associated with particle transport. The key physical variables which were studied or measured are:

1) Particle size.

2) Interstitial velocity.

3) Medium grain size distribution.

4) Temperature.

The key chemical variables which were studied and controlled are:

1) Solution ionic strength.

2) Solution pH.

3) Solution buffer intensity.

The laboratory program has one principal component which was the measurement of one-dimensional particle breakthrough curves. In these experiments, steady flow of input water or particles displaces resident particles or water. During the breakthroughs, particle concentrations are measured at various longitudinal distances and times. Also, salt tracer breakthroughs are measured in order to have a direct comparison of solute and particle transport behavior. Salt tracer breakthrough experiments are similar to particle breakthrough experiments in that changing salt concentrations are measured at various longitudinal distances and times.

1.3 Basic Concepts of Particle Transport through Porous Media

In order to develop the theories and experiments of this work, an understanding of the basics of flow in porous media is needed.

1.3.1 Advective Fluid Velocity

For an incompressible Newtonian fluid, the recognized relationship between flow rate and hydraulic gradient for one dimension is the Darcy equation:

$$V_D = -K\frac{\partial h}{\partial x} \tag{1.1}$$

where: V_D = *specific discharge (Darcy velocity)* ($L\ T^{-1}$);
K = *hydraulic conductivity* ($L\ T^{-1}$);
h = *piezometric head* (L); *and*
x = *longitudinal position* (L).

The specific discharge is defined as Q/A where Q = volume flux and A = column cross section. For transport analysis, consider the interstitial velocity, V_s, in the direction of flow given by:

$$V_s = \frac{V_D}{\theta_e} \tag{1.2}$$

where: V_s = *interstitial velocity* ($L\ T^{-1}$); *and*
θ_e = *effective porosity* (–)
= *interconnected void volume/total volume.*

The interstitial velocity is the pore-averaged fluid velocity or the speed of an immiscible displacement front. Darcy's law (Eq. (1.1)) is limited to low Reynolds number flows, Re < 4 (Bear, 1972). For porous media, the Reynolds number is given by:

$$Re = \frac{V_s d_g}{\nu}$$

where: d_g = *diameter of the grain of the medium* (L); *and*
ν = *kinematic viscosity of the fluid* ($L^2\ T^{-1}$).

In the above discussion, the interstitial velocity refers to a pore-averaged velocity which is the average velocity inside individual pores averaged for all

pores. In order to discuss particle transport and determine the average velocity of a particle suspension, the velocity distribution at the scale of the each pore must be considered. By approximating each pore as a capillary tube (a rough analogy), the velocity distribution for the fluid will be parabolic with a no slip condition at the walls. A particle will not be able to travel the same pathways as a solute, because the particle center of mass will be excluded from the immediate region of the wall. They will also be excluded from pores smaller than the particle. The result of this exclusion based upon size is that the particles will take on an average velocity which is greater than that of the carrier fluid. A particle flowing through a capillary tube and subsequent size exclusion is shown in Fig. 1.1.

1.3.2 Longitudinal Dispersion of Solutes

If one fluid placed in porous media displaces another with both fluids being miscible, a transition zone develops across an initial sharp interface. This developing transition zone can be viewed as a leveling of the differences between the fluids with time and a tendency towards a uniform chemical composition. Dispersion is the general term which describes all physical phenomena governing the evolution of this transition zone. Longitudinal dispersion is the dispersion which occurs parallel to the main direction of flow. In this work, it is expected that the particles will show the same characteristics as that of solutes, and all statements which are presented in the following sections to summarize solute dispersion are assumed to apply to particle dispersion.

Several mechanisms have been proposed as the causes of dispersion in

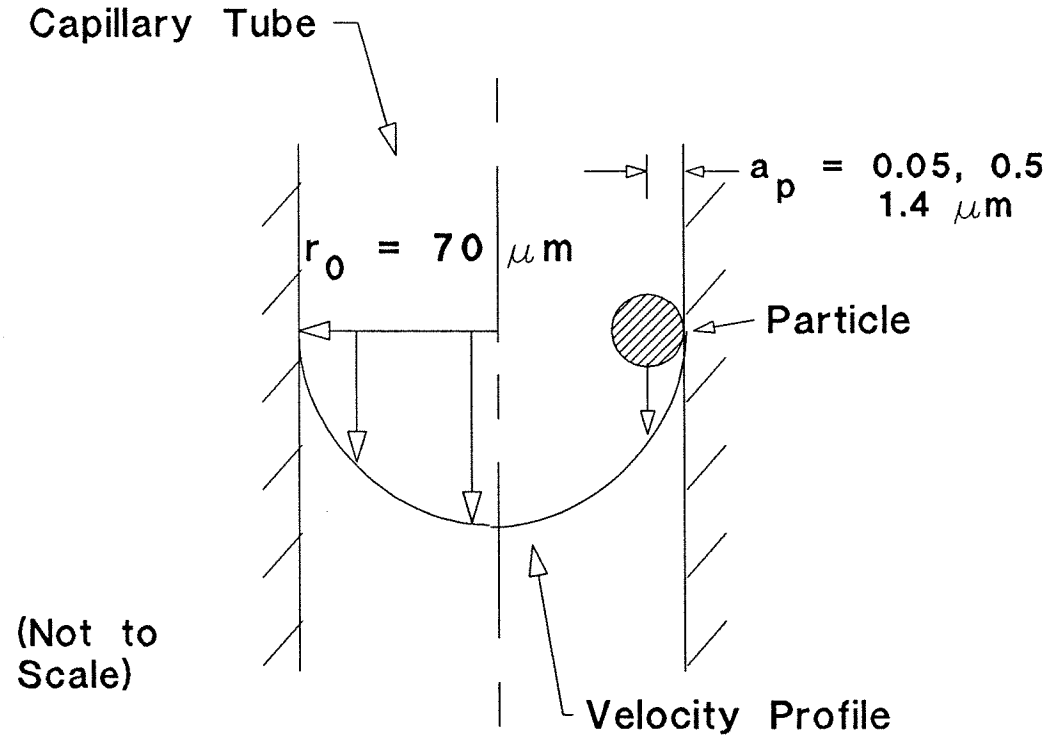

(Given values are
taken from this work.)

Fig. 1.1: Graphic representation of the size exclusion principle for a particle flowing through a capillary tube.

porous media (Greenkorn 1981; Fried and Combarnous 1971). Of these, the underlying physical mechanisms responsible for dispersion of a conservative tracer can be reduced to three microscopic causes:

1) Brownian diffusion.

2) Tortuosity.

3) Differential advection.

For solutes flowing through porous media, these mechanisms result in different instantaneous velocities for different solute molecules. This shows that the interstitial velocity is an average of a complicated velocity distribution. A brief mention of these mechanisms which includes their relevance is given here; whereas, in Houseworth (1984) a detailed discussion is presented.

1.3.2.1 Brownian Diffusion

In stagnant or slowly flowing fluids, Brownian diffusion is the main dispersive mechanism. The rate of macroscopic Brownian diffusion in a porous medium is related to the rate of diffusion in a free fluid by:

$$D_m = \frac{\theta_T D}{F_t}$$

where: D_m = *porous medium diffusion coefficient* ($L^2\ T^{-1}$);
D = *free fluid diffusion coefficient* ($L^2\ T^{-1}$);
F_t = *tortuosity* (-); *and*
θ_T = *total volumetric porosity* (-).

The Brownian diffusion coefficient in porous media is seen to be smaller than in a free fluid because of the constrictions placed on free movement by the media

grains.

For higher velocity fluids (Pe > 10), mechanical or hydrodynamic dispersion is of more importance relative to Brownian dispersion; although, diffusion into and out of stagnant pores when combined with advective transport can be seen as tailing in breakthrough curves.

1.3.2.2 Tortuosity

The tortuosity refers to the tortuous or twisted path a fluid follows while flowing through a porous medium. This twistedness can increase the path length for some of the fluid. The randomness of the tortuosity due to the structure of the porous bed results in different fluid streamlines travelling various random paths of differing lengths which results in longitudinal dispersion. Various methods exist for measuring or quantifying tortuosity, and these are given in Bear (1972), Winsauer et al. (1952), and Oliphant and Tice (1985).

1.3.2.3 Differential Advection

Although the interstitial velocity of a solute is averaged across all pores, the instantaneous advective velocity of a solute which is responsible for dispersion is defined as the tangential speed of a solute molecule along a streamline. Dispersion due to differential advection occurs on two scales in a porous medium:

1) Advective speed varies within a pore due to viscous velocity profile.
2) Advective speed varies between different pores due to the differing pore sizes.

1.3.3 Filter Coefficient

An understanding of filtration is needed to develop particle transport theories. In general, deep bed filtration studies have been conducted to analyze the mechanisms involved in the processes of capturing and retaining particles in porous media. In deep bed filtration, retention of particles occurs throughout the entire depth of the filter and not just on the filter surface. As such, particle filtration can be separated into two distinct processes which are characterized by separate mechanisms (Amirtharajah 1982; Cleasby 1981; Ghosh et al. 1975; Grutsch and Mallatt 1977; Herzig et al. 1970; Jordan et al. 1974; O'Melia 1985; Tien and Payatakes 1979; Tobiason and O'Melia 1988; Wang et al. 1986; Yao et al. 1971; Rajagopalan and Tien 1976 and 1977; Elimelech and O'Melia 1990):

1) Transport which is basically physical.

2) Attachment which is basically chemical.

In this work, the mass transport equation for solutes is to be modified for particle transport by including a sink term describing particle filtration.

Adequate theories (Rajagopalan and Tien 1976; Tien and Payatakes 1979) exist for describing favorable filtration, but no reasonable theory has been developed to describe unfavorable filtration. Favorable filtration refers to filtration which occurs when the chemical conditions are favorable. For favorable filtration, no repulsive energy barrier due to surface forces exists, and as such, the problem is transport limited. In unfavorable filtration, the chemical conditions are unfavorable. For unfavorable filtration, the surface forces exhibit repulsive

energy barriers which must be overcome before any particle-media grain contact can occur, and as such, the problem is chemically limited.

1.4 Scope of Study

A mass transport equation has been developed for analyzing particle transport during flow through uniform porous media. The parameters which are advective velocity, longitudinal dispersion coefficient, and filter coefficient in this transport equation are analyzed by using dimensional analysis arguments. These particles are chemically nonreactive and dynamically passive in that their presence does not create significant density or viscosity deviations from the pure fluid state. In addition, the flow is saturated and is in the Darcy range for laminar, linear flow.

A laboratory investigation of particle transport in a uniform porous medium has been conducted. Currently, very little data exists for measuring particle velocity compared to solute velocity, no data exists for particle longitudinal dispersion, and little data exists for unfavorable filter coefficients especially for the Brownian case. The laboratory data characterizing these parameters is compared to the models.

Chapter 2 is a review of relevant literature associated with particle transport and filtration. In Chapter 3, dimensional analysis arguments are used to define the transport parameters which are the advective velocity, the longitudinal dispersion coefficient, and the filter coefficient for particles, and these are included in mass transport equations. Solutions are derived for these equations.

Chapter 4 presents a summary of the experimental program. Chapter 5 is a summary and discussion of the experimental results. The main results and conclusions of this work are listed in Chapter 6, and this chapter also includes a discussion of possible future work.

2. LITERATURE REVIEW

The study of colloid transport through porous media is quite diverse, incorporating ideas from the following areas of study:

1) Chemistry of particle-particle interactions.

2) Macroscopic particle transport.

3) Transport equations and parameters.

In the first part, which is the microscopic view of this study, a general review of surface chemistry as related to particle-particle interactions will be presented. This section will review the effects of variable system chemistry on particle-particle interactions. Such a review will provide the necessary theoretical insight for both choosing the appropriate particles and media and the system pH and ionic strength needed to properly define the experimental system for this work and analyzing the experimental results and theoretical models.

In the second part, which is the macroscopic perspective of this study, qualitative or empirical studies of particle transport are reviewed in order to develop a general working framework for the experimental program and transport models. This review shows the trends in the amount of transport for changing hydraulic and chemical variables which will aid in the prediction of system behavior as related to system properties. This will complement the section on the chemistry of particle-particle interactions when developing both the experimental program and theory and when analyzing results.

In the third part, which is the link between the macroscopic and

microscopic views, the results of both experimental and theoretical work are reviewed which will aid in the development of both an equation and transport parameters which will describe fully the transport, mixing, and filtration of particles in porous media. In this equation, the transport, mixing, and filtration of particles will be defined by the following parameters: particle advective velocity, particle longitudinal dispersion coefficient, and filter coefficient. Such an equation will be similar to the advective-dispersion equation which has been used extensively for conservative and reactive solutes.

These three separate parts may be summarized as follows. Part 1 provides both the necessary insight for developing and explaining experimental results for this experimental program and the theoretical basis for formulating the models for the parameters of this work. Part 2 provides the general framework for these experiments by reviewing previous experimental work which was specifically focused on systems which were designed to test for optimum particle transport. Part 3 provides the existing models and application of the theories reviewed in part 1 for the specific parameters of this study.

2.1 Chemistry of Particle-particle Interactions

The close interaction and possible subsequent attachment of the particles to the medium is dominated by the surface forces resulting from the chemical makeup of the system. The chemistry of the system can be altered by changing either the ionic strength or pH of the interstitial fluid. In this work, special interest is being focused on unfavorable filtration due to the ionic strength rather

than pH of the system.

Particle capture and retention can be analyzed according to the surface chemistry of particle-particle interactions as well as hydraulic transport variables. Complete filtration theory should account for both macroscopic hydraulic transport processes and surface interactions between suspension particles and media grains. The general importance of particle chemistry studies may be summarized as follows, and Table 2.1 lists these same points along with the corresponding references:

1) Chemical aspects of particle-particle interactions include the origins of particle stability, the structure of the solid-liquid interface, and the chemical interactions between such interfacial regions.
2) DLVO (Derjaguin and Landau 1941; Verwey and Overbeek 1948) theory in which London-van der Waals attraction and electrostatic interactions are considered as the quantitative basis used to explain stability of particle suspensions and the chemistry of particle-particle interactions.
3) Calculation of double layer forces may be made using either of two extremes, constant surface potential or constant surface charge, and calculations based on these are used to predict respective lower and upper limits for the double layer repulsion.
4) For Brownian encounters and short duration particle-media interactions typically encountered in filtration, the constant surface charge

Table 2.1: Summary of the Chemistry of Particle-Particle Interactions

CHEMISTRY RESULTS	REFERENCES
1) Particle stability depends upon interactions between interfacial regions.	O'Melia 1987; Stumm & Morgan 1981
2) DLVO theory is used to explain interactions.	Hull & Kitchener 1969; Spielman & Cukor 1973; Spielman 1977; Gregory & Wishart 1980; Spielman & Friedlander 1974; Ruckenstein & Prieve 1980; Tobiason & O'Melia 1988; Ottewill & Shaw 1966; Lyklema 1980; Gregory 1981; Chan & Mitchell 1983; Dukhin & Lyklema 1987; O'Melia 1987; Liang 1988; Ruckenstein & Prieve 1973; Rajagopalan & Tien 1977; Ghosh et al. 1975; Elimelech & O'Melia 1990
3) Calculation of double layer forces can be made using either of two extremes.	Spielman & Cukor 1973; Gregory & Wishart 1980; Gregory 1975; Lyklema 1980; Chan & Mitchell 1983; Dukhin & Lyklema 1987; O'Melia 1987
4) For filtration, use constant surface charge condition.	Lyklema 1980; Gregory & Wishart 1980
5) Theory predicts favorable attachment, but underpredicts unfavorable attachment.	O'Melia 1987; Bowen & Epstein 1979; Gregory & Wishart 1980; Hull & Kitchener 1969; Liang 1988; Tobiason & O'Melia 1988; Rajagopalan & Tien 1977; Onorato & Tien 1980; Yoshimura et al. 1980; Wang et al. 1986; Yao et al. 1971; Tien & Payatakes 1979; O'Melia 1985
6) Surface forces are short range forces.	Cerda 1987; Chan and Mitchell 1983; Gregory 1975, 1981; Hamaker 1937; Hogg et al. 1965; Ives & Gregory 1966; Liang 1988; Verwey & Overbeek 1948; Stumm & Morgan 1981; Derjaguin & Landau 1941

condition can be used to calculate colloid stability.

5) For favorable interactions, experimental results are generally quantitatively similar to theory, but, for unfavorable interactions, actual attachment is found to be substantially more than the theory predicts.

6) Surface forces act only over very short distances with a possible maximum of 500 nanometers in distilled water, but more likely to be less than 200 nm.

This review shows that the major forces involved in attachment are chemical in nature. Also, unfavorable interactions are currently not well-understood.

2.1.1 Surface Chemistry

The medium to be used in this work is a quartz sand which has an SiO_2 structure. Such an oxide exhibits similar surface chemistry properties as those of Al and Fe oxides which have been extensively studied (Stumm and Morgan 1981). The particles used in this work are polystyrene latexes which have surface carboxyl groups. In the presence of water, the sand and latex particles form pH-dependent surface groups.

2.1.1.1 Oxide Particle

In the presence of water, the oxides are generally covered with surface hydroxyl groups where the specific adsorption of H^+ and OH^- can be treated in terms of surface coordination reactions at the oxide-water interface. The proton transfers at the amphoteric surface which result in a pH-dependent surface charge for the oxide can be formalized in the following system of equations (Stumm and

Morgan 1981):

$$>SOH_2^+ = >SOH + H^+ \qquad K_{a1}^s = \frac{\{>SOH\}[H^+]}{\{>SOH_2^+\}}$$
$$>SOH = >SO^- + H^+ \qquad K_{a2}^s = \frac{\{>SO^-\}[H^+]}{\{>SOH\}} \qquad (2.1)$$

where: [ ] = *aqueous phase species concentration* (*mol* ℓ^{-1});
{ } = *surface species concentration* (*mol* kg^{-1}); *and*
$>S$ = *surface species.*

The pH of zero point of charge, pH_{zpc}, corresponds to the pH at which the surface of the oxide on the average is uncharged:

$$\{>SOH_2^+\} = \{>SO^-\} \qquad (2.2)$$

The pH_{zpc} is independent of the system ionic strength, and in the absence of specifically adsorbable ions other than H^+ and OH^-, the pH_{zpc} is identical with the isoelectric point. For a pH $\leq$ pH_{zpc}, the surface becomes positively charged and, conversely, negatively charged for pH $\geq$ pH_{zpc}. This pH is expected to occur around pH = 2 for sand (Stumm and Morgan 1981).

2.1.1.2 Carboxylated Polystyrene Particles

In the presence of water, the carboxylated latexes are generally covered with surface hydroxyl groups where the specific adsorption of H^+ and OH^- can be treated in terms of surface coordination reactions at the latex-water interface. The proton transfers at the amphoteric surface which result in a pH-dependent surface charge for the latex can be formalized in the following equation:

$$>SCOOH = >SCOO^- + H^+ \qquad K_{a2}^s = \frac{\{>SCOO^-\}[H^+]}{\{>SCOOH\}} \tag{2.3}$$

The carboxyl surface complex does not form a third, positively charged surface group. At the pH of this acidity constant (pK_{a2}^s), the surface is 50% uncharged and 50% negatively charge. For a pH > pK_{a2}^s, the surface becomes more negatively charged. This pK_{a2}^s is expected to occur for pH << 7 (Elimelech and O'Melia 1990; Fitzpatrick and Spielman 1973; Ghosh et al. 1975; Jordan et al. 1974; Tobiason and O'Melia 1988; Yoshimura et al. 1980; Gregory and Wishart 1980; Ottewill and Shaw 1972) with approximately 100% surface saturation of negative charges at pH ≥ 7.

2.1.1.3 Ionic Strength Effects

As shown above, colloidal particles and media grains will develop electrical charges on their surfaces when in contact with water. The surrounding water will develop an equivalent charge of opposite sign in order to preserve electroneutrality. An electrical double layer is formed with a layer of fixed charges on the solid surfaces and a diffuse layer develops with an excess of oppositely charged ions extending into the aqueous phase. The approximate thickness of this diffuse layer is given by the Debye-Huckel length, κ^{-1}. This thickness is inversely dependent upon the square root of the ionic strength of the solution and is given by (Stumm and Morgan 1981):

$$\kappa^2 = \frac{F^2\Sigma(n_i z_i^2)}{\epsilon\epsilon_0 RT_e} \tag{2.4}$$

where: F = *Faraday constant* ($C\ mol^{-1}$);
$\Sigma n_i z_i^2 = I$
= *ionic strength* (M);
ϵ = *dielectric constant multiplier for water*;
ϵ_0 = *dielectric constant for vacuum* ($C^2 m^{-1} J^{-1}$);
R = *gas constant* ($J\ mol^{-1} K^{-1}$); *and*
T_e = *temperature* (K).

For fresh water ($I \approx 10^{-4}$ M), the double layer thickness is of the order of 10 nm. For saline water ($I \approx 10^{-1}$ M), the double layer thickness is of the order of 1 nm. In this work, I ranged from 4.0×10^{-4} to 2.1×10^{-3} M, and the double layer thickness approximately ranged from 12.5 to 8.5 nm.

The electrostatic interaction energy can be either repulsive or attractive depending upon the signs of the zeta potentials of both the interacting particle and media grain. The distance over which this energy extends is directly dependent upon the thickness of the diffuse layers of both particles. The effect of increasing the ionic strength is to compress the diffuse layer which limits the extent of the electrostatic repulsion or attraction.

2.2 Macroscopic Particle Transport

A review of macroscopic particle transport studies was completed in order to determine qualitative transport properties. A summary of the key points of these studies is given here, and Table 2.2 lists these same points along with the corresponding references:

1) Transport of colloids through a porous medium occurs under appropriate conditions.

Table 2.2: Summary of Results of Macroscopic Particle Transport Studies.

MACROSCOPIC PARTICLE TRANSPORT RESULTS	REFERENCES
1) Colloid transport does occur.	Curry & Beasley 1962; Curry et al. 1965; Scharpenseel & Kerpen 1967; Coutts et al. 1968; Mel'Nikova & Kovenya 1971; Kovenya et al. 1972; Small 1974; Arulanandan et al. 1975; Erle et al. 1977; Donaldson et al. 1977; Muecke 1979; Gruesbeck & Collins 1982; Pilgrim & Huff 1983; Khilar & Fogler 1983
2) Colloid transport can be altered.	Curry & Beasley 1962; Curry et al. 1965; Scharpenseel & Kerpen 1967; Mel'Nikova & Kovenya 1971; Kovenya et al. 1972; Small 1974; Donaldson et al. 1977; Muecke 1979; Gruesbeck & Collins 1982; Khilar & Fogler 1983
3) For large particles, surface cake deposition occurs.	Curry et al. 1965; Donaldson et al. 1977
4) For smaller particles, deposition occurs within the porous bed.	Curry et al. 1965; Donaldson et al. 1977; Muecke 1979; Gruesbeck & Collins 1982
5) Origins of colloids varies.	Scharpenseel & Kerpen 1967; Muecke 1979; Gruesbeck & Collins 1982; Pilgrim & Huff 1983; Khilar & Fogler 1983

2) By changing the physical and chemical factors which represent the transport and attachment mechanisms of particle motion, the balance between particle transport and filtration can be altered significantly.

3) For large particles, filtration occurs in the form of a cake at the surface of the porous bed.

4) Particle filtration within the medium occurs as either pore

clogging or surface coating of media grains which are referred to as straining and physical-chemical filtration, respectively.

5) The origins of colloids include entrainment of original media grains, re-entrainment of previously retained particles, and external sources.

The review presented here provides the framework for this experimental study including an evaluation of the experimental apparatus, methods and materials, and analyses of experimental results. Most of this literature review relates to oil or water pumping where the emphasis was placed on maximizing transport by reducing filtration and subsequent pore clogging.

2.3 Transport Parameter Models

Particle transport is expected to be similar to that of solutes; therefore, this can be expressed as an advective-dispersion equation. In this equation, the three key parameters to be measured or predicted are particle advective velocity, particle longitudinal dispersion coefficient, and filter coefficient. In this work, these parameters are modelled according to dimensional analysis with the functional relationships being determined empirically by experimental results. In this literature review, an emphasis is placed on previous work which has used this same type of approach.

2.4 Advective Velocity

In porous media, the average velocity of a particle has been found by experiments to be either the same or slightly higher than that of the carrier fluid (Small 1974; Goldsmith and Mason 1962; Enfield and Bengtsson 1988). This

deviation is caused by the particle's size. The expected difference can be determined theoretically by analyzing the velocity profiles of both the fluid and the particles in a pore (DiMarzio and Guttmann 1969 and 1970).

In the formulation of the DiMarzio and Guttmann (1969, 1970) model for determining particle velocity, several assumptions are needed. First, the existing model has been formulated for a capillary tube which has a constant radius. In this tube, there are assumed to be no interactions between the particles and the wall, the suspension is well-mixed with a constant concentration across the cross-section, and there is no transverse flow.

In general, consider small particles of radius a_p traveling through capillary tubes. If this fluid flow is assumed to be laminar Poiseuille flow, the velocity profile will be parabolic with a no-slip condition at the tube wall; furthermore, the effect of the particles at dilute concentrations on the fluid velocity is neglected. The velocity of a spherical particle has been found to be that of the fluid carrier streamline velocity at the particle's center of mass minus a constant quantity dependent on the shear field of the fluid (Happel and Byrne 1954):

$$\left(\frac{U_s - U_p}{U_s}\right)_{r=0} = \gamma\left(\frac{S}{r_0}\right)^2 = \frac{2}{3}\left(\frac{S}{r_0}\right)^2 \qquad (2.5)$$

where: $U_s(r)$ = *fluid velocity;*
$U_p(r)$ = *particle velocity;*
r_0 = *capillary radius;*
a_p = *particle radius; and*
S = a_p *or*
= *molecule radius of gyration.*

DiMarzio and Guttman (1969, 1970) derived the same expression for oddly shaped polymers in which S equals the radius of gyration of the polymer molecule.

In this equation, the velocity profiles for the fluid carrier and particle can be expressed as parabolas in terms of the radius of the tube. In the following equations for these velocities, the radius is measured from the capillary tube centerline out to the tube wall:

$$U_s = U_0\left(1 - \left\{\frac{r}{r_0}\right\}^2\right) \qquad (0 < r < r_0)$$
$$U_p = U_0\left(1 - \left\{\frac{r}{r_0}\right\}^2 - \gamma\left\{\frac{a_p}{r_0}\right\}^2\right) \qquad (0 < r < r_0 - a_p) \qquad (2.6)$$

where: $U_0 = -\frac{\partial P}{\partial x}\frac{r_0^2}{4\mu}$;
= *fluid centerline velocity;*
r = *radial distance;*
P = *dynamic pressure; and*
x = *longitudinal distance.*

As the particle travels through a tube, Brownian motion and shear action will cause the particle to travel across the entire cross-section of the tube except that the center-line of the particle will be excluded from the immediate region of the wall due to its radial dimension (Fig. 1.1). After the particle has traveled far

enough longitudinally through the tube, the particle will have spent equal amounts of time in all radial positions across the capillary tube. Integration of the velocity profiles of Eq. (2.6) over the range of possible radii shown in Eq. (2.6) for both the particle and fluid yields a higher average velocity for the particles than that for the carrier fluid. These integrations have been completed here for the case of spherical particles and cylindrical capillary tubes as previously discussed, and the results of these integrations are the average velocities of the fluid and particles in a tube. These average velocities are expected to apply also to flow in a porous bed where the average pore radius is substituted for the capillary radius. The average fluid velocity, V_s, in a capillary tube is:

$$V_s = \frac{U_o}{2} \tag{2.7}$$

The average velocity of a particle, V_p, in a capillary tube is:

$$V_p = U_0\left(1 - \frac{1}{2}\left\{1 - \frac{a_p}{r_0}\right\}^2 - \gamma\left\{\frac{a_p}{r_0}\right\}^2\right) \tag{2.8}$$

By inspecting Eqs. (2.7) and (2.8), the particles are expected to have a larger average velocity than the carrier fluid velocity. This enhanced velocity of the particles can be expressed as a fractional difference between the two average velocities:

$$\Delta V = \frac{V_p - V_s}{V_s} = 2\frac{a_p}{r_0} - \frac{7}{3}\left(\frac{a_p}{r_0}\right)^2 \tag{2.9}$$

This equation shows that as the radius of the particle increases, the difference between the average particle velocity and the average fluid interstitial velocity also increases. This increase is not unbounded but reaches a maximum ΔV value for $a_p/r_0 = 3/7$. As $a_p/r_0 > 3/7$, the velocity difference decreases. In an application of this model, an upper limit on the size of a particle capable of transporting through a porous bed must be determined.

In a physical sense, the pore radius can be estimated to be approximately equal to one-fifth of the media grain diameter ($r_0 = 1/5\ d_g$); therefore, the largest possible particle to be able to fit through the porous bed has a radius equal to this pore radius ($a_p = r_0$). For a particle with $a_p \approx r_0$, the particles have been shown to collect on the bed surface in a cake (Willis and Tosun 1980; McDowell-Boyer et al. 1986; Sakthivadivel 1969; Herzig et al. 1970; Sherard et al. 1984). These references show that the onset of straining (deep bed) filtration occurs for a particle radius a_p less than one-twentieth of the media grain diameter ($a_p < 1/20\ d_g$). Particles with radii larger than this will not transport into the bed, but will collect on the surface. By letting $d_g = 5r_0$, the largest particle which will transport has a radius equal to one-fourth of the pore radius ($a_p \leq 1/4\ r_0$).

This enhanced velocity was experimentally tested in three studies (Small 1974; Goldsmith and Mason 1962; Enfield and Bengtsson 1988). In two cases, some pertinent data were missing, pore size in one case (Small 1974) and both particle and pore size in the other (Enfield and Bengtsson 1988), so that a positive comparison could not be made. Even with these limitations and using the

assumptions listed in the following, the results qualitatively (Enfield and Bengtsson 1988) and quantitatively (Small 1974) support this theory. Figs. 2.1 and 2.2 show the results of one work (Small 1974). In Fig. 2.1, the plotted data was collected in experiments in which the variables were particle and media grain size. In Fig. 2.2, the plotted data was collected in experiments in which the variables were particle size and ionic strength. For Fig. 2.1, the theoretical line is calculated using Eq. (2.9). Also, the y-axis in this figure is $1 + \Delta V$ ($V^* = 1 + \Delta V$, $V^* = V_p/V_s$). In part (a), the pore radius is assumed to be one-fifth of the media grain diameter. As can be seen, the data for the smaller medium show a good correlation, while a large deviation is shown for the other media. In part (b), the two larger media diameters are divided by 4 while the smaller is still divided by 5. A better comparison cannot be made without knowing the actual pore sizes. This confirms the importance of knowing the pore size as well as the particle size.

In the analysis of the data for Fig. 2.2, the grain size of the medium was not mentioned by Small (1974). In order to analyze the data according to the model developed here, incremental increases in velocity due to the ionic strength changes are considered. The changing ionic strength on particle transport results in changes in double layer thickness for the particles and media grains. In the work of Small (1974), the media grains and particles had surfaces which had charges of the same sign; therefore, the double layer interaction of the particles and media was repulsive. In this analysis, the effect of the changing ionic strength

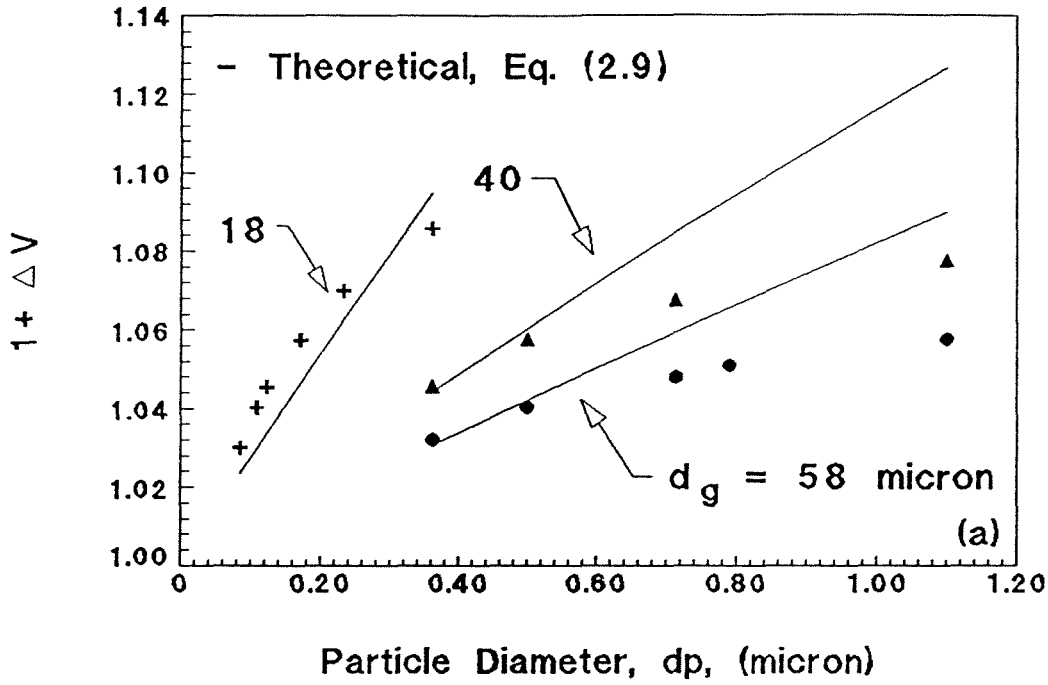

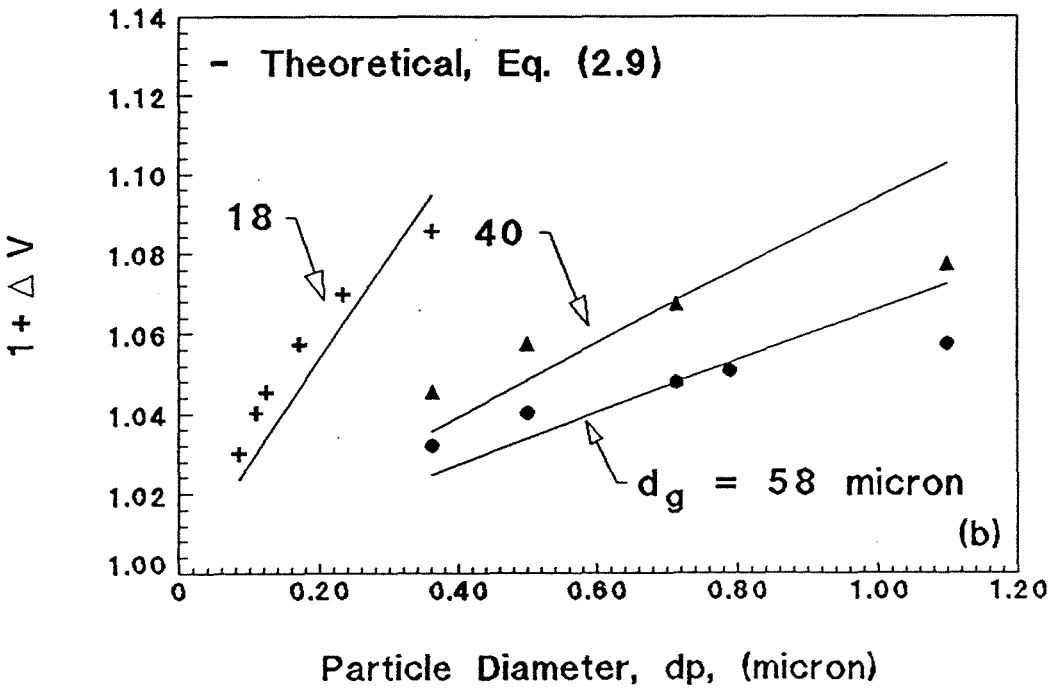

Fig. 2.1: Comparison of experimentally measured enhanced velocities (Small 1974) to theory (DiMarzio and Guttmann 1970; Happel and Byrne 1954) for changing particle and pore size.

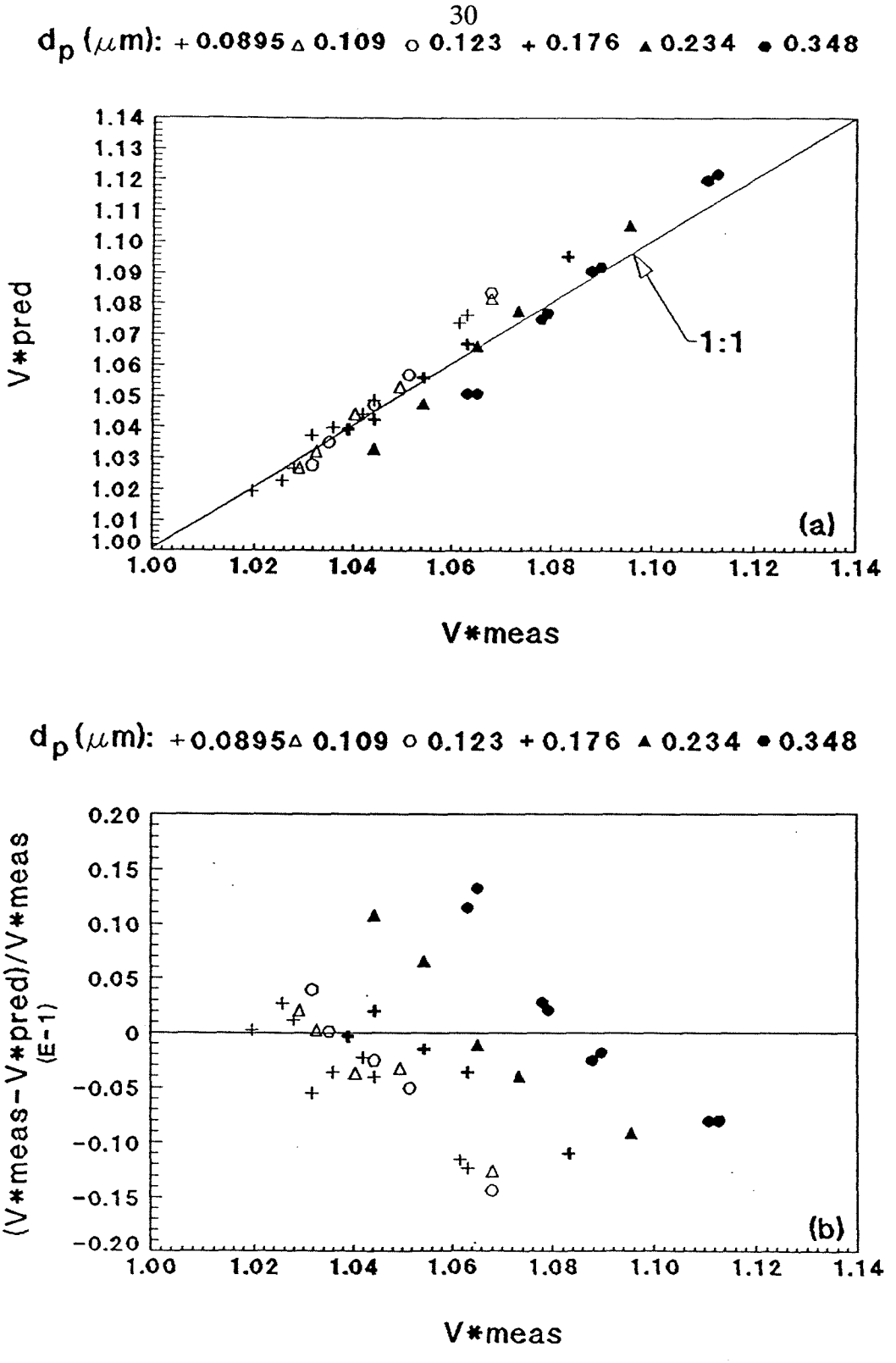

Fig. 2.2: Comparison of experimentally measured enhanced velocities (Small 1974) to theory (DiMarzio and Guttmann 1970; Happel and Byrne 1954) for changing particle size and ionic strength.

on particle transport is the modification of the distance from the media grain where the particle is influenced by the media grain. This can be visualized as an apparent particle radius with the actual radius of the particle being increased by the double layer thickness. The velocity of the particle will then change as its apparent radius is modified by the changing ionic strength of the fluid. This is shown in the following:

$$V*' = V* + \Delta V* \tag{2.10}$$

$$\Delta V* = \Delta(\Delta V) \tag{2.11}$$

where: $V*'$ = *enhanced velocity ratio due to incremental change*;
$\Delta V*$ = *incremental change in enhanced velocity ratio*; *and*
$\Delta V \approx 2\left(\frac{a_p}{r_0}\right)$ (*first term of Eq.* (2.9) *only*).

The incremental change in the enhanced velocity ratio can be rewritten as:

$$\textit{where: } \Delta(\Delta V) \approx \Delta\left(2\frac{a_p}{r_0}\right) \approx 2\left(\frac{a_p + \delta}{r_0}\right) - 2\left(\frac{a_p}{r_0}\right) = 2\left(\frac{\delta}{r_0}\right) \tag{2.12}$$

In this equation (Eq. (2.12)), the effect of ionic strength is assumed to be felt only by the particle and not by the pore radius. Eq. (2.12) is simplified in order to be useful to this analysis:

$$\Delta(\Delta V) \propto \delta \tag{2.13}$$

As stated above, the ionic strength is expected to influence the particle through the double layer thickness, and the apparent radius of the particle should be changed by twice the double layer thickness to account for the two interacting

double layers of the particle and medium grain. Therefore, δ in Eq. (2.13) is twice the change in the double layer thickness which is shown in the following:

$$\delta = 2\Delta(\kappa^{-1}) \tag{2.14}$$

Substituting this approximation into Eq. (2.13) yields:

$$V*' = V* + 2\Delta(\kappa^{-1}) \tag{2.15}$$

This equation (Eq. (2.15)) is used to calculate the predicted enhanced velocity ratio due to incremental changes in ionic strength for a given particle size for the data of Small (1974). In part (a) of Fig. 2.2, the predicted velocities are plotted versus the measured velocities, and the line labeled as 1:1 represents a line of perfect agreement between theory and experiment. Part (b) of this figure shows the error between the predicted and measured velocities. This analysis shows that the effect of ionic strength on particle advective velocity can be analyzed as changes in the size of the particle giving the particle an apparent size due to the extent of the double layer surrounding the particle.

2.5 Longitudinal Dispersion Coefficient

An important element of any dispersion model is the representation of the geometry of the porous medium. Previous theoretical investigations into the nature of solute dispersion in porous media have incorporated a variety of geometrical models. Houseworth (1984) has thoroughly reviewed such longitudinal dispersion models for solute tracers. Instead of modelling the internal structure of a porous medium, dimensional analysis is used to analyze the

problem (Bear 1972; Pfannkuch 1962; Greenkorn 1981). In this case, the actual mechanisms of dispersion are not specifically modelled or included; instead, the effect of these mechanisms is expected to scale with the pertinent transport variables. The pertinent variables for solute dispersion are:

D_L = *longitudinal dispersion coefficient* ($L^2\ T^{-1}$);
D = *free fluid molecular diffusion coefficient of solute* ($L^2\ T^{-1}$);
V_s = *fluid interstitial velocity* ($L\ T^{-1}$); *and*
d_g = *media grain diameter* (L).

From the Buckingham pi theorem, the following pairs of groups are formed:

$$1)\ \frac{D_L}{V_s d_g} = F\left[\frac{V_s d_g}{D}\right],\ \textit{or alternatively,}$$
$$2)\ \frac{D_L}{D} = F\left[\frac{V_s d_g}{D}\right] \qquad (2.16)$$

$$\textit{where: } Pe = \textit{Peclet number} = \frac{V_s d_g}{D}.$$

Experimental data for solute longitudinal dispersion in uniform media show good correlation with these dimensionless groups. This is shown in Fig. 2.3 which is taken from Houseworth (1984). When the Peclet number is greater than 1, the two groups can be reduced to one:

$$\frac{D_L}{V_s d_g} \approx \textit{Constant} \qquad (2.17)$$

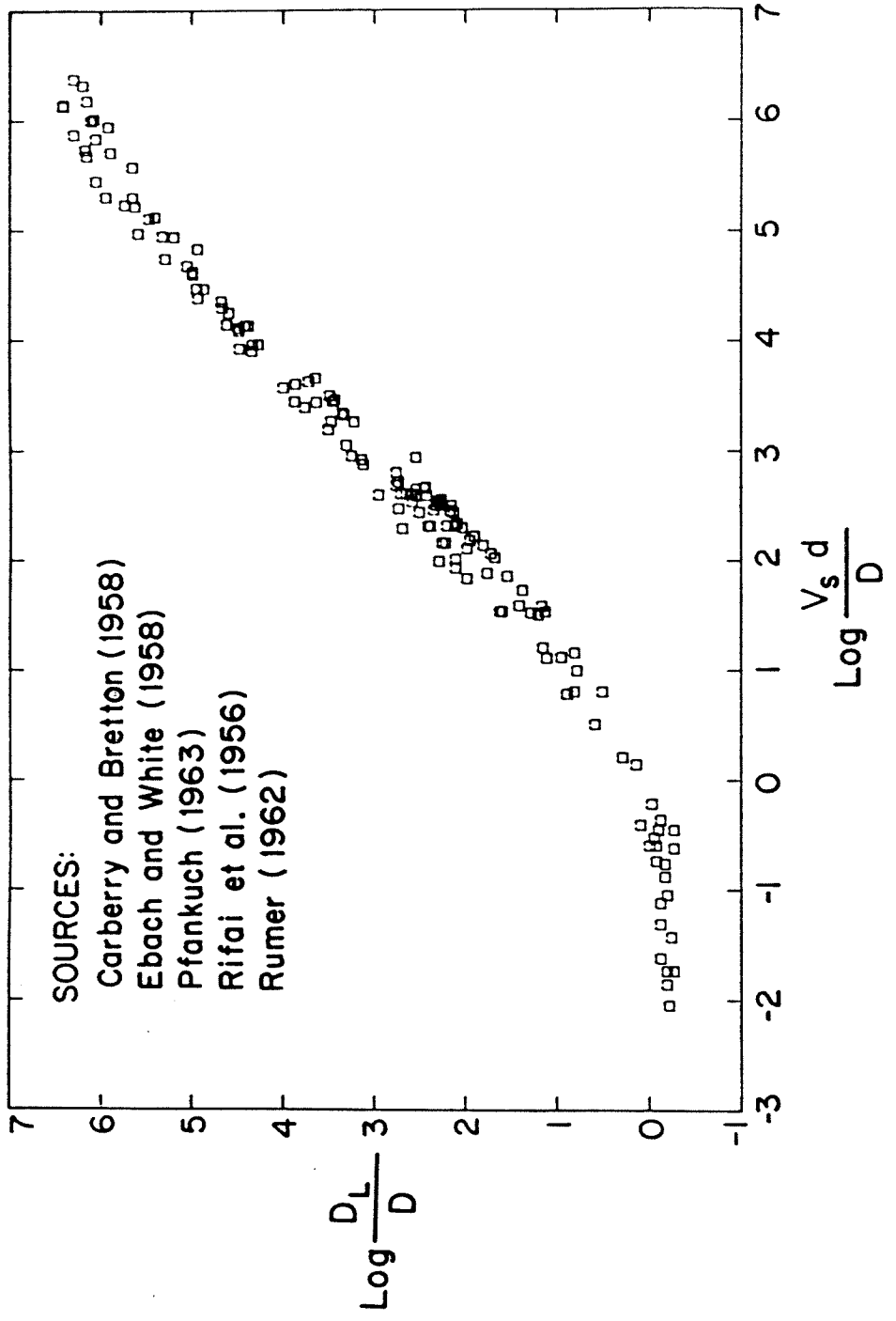

Fig. 2.3: Longitudinal dispersion versus the Peclet number for uniform porous media (Houseworth 1984).

$$\textit{where: } Pe_D = \textit{dynamic Peclet number} = \frac{V_s d_g}{D_L}.$$

An order of magnitude approximation for the longitudinal dispersion coefficient for solutes can be made with:

$$D_L \approx V_s d_g \tag{2.18}$$

Particle longitudinal dispersion is expected to be similar to that of solutes. Currently, no particle breakthroughs have been performed by others from which particle longitudinal dispersion coefficients could be determined.

2.6 Filter Coefficient

Two approaches exist for analyzing the filter coefficient. These are the macroscopic mass balance approach and the microscopic trajectory analysis approach. Deep bed filtration studies have been conducted to analyze both the system variables and the underlying mechanisms involved in the processes of capturing and retaining particles in porous media. These studies are listed in Tables 2.3, 2.4, 2.5, and 2.6. In deep bed filtration, retention of particles occurs throughout the entire depth of the column and not just on the bed surface.

The particle filtration process can be separated into two distinct steps as cited in Table 2.6 (Amirtharajah 1982; Cleasby 1981; Ghosh et al. 1975; Grutsch and Mallatt 1977; Herzig et al. 1970; Jordan et al. 1974; O'Melia 1985; Tien and Payatakes 1979; Tobiason and O'Melia 1988; Wang et al. 1986; Yao et al. 1971; Rajagopalan and Tien 1976 and 1977; Elimelech and O'Melia 1990):

1) Transport which is basically physical.

2) Attachment which is basically chemical.

These two steps are characterized by separate collection system variables and mechanisms responsible for particle capture and retention.

2.6.1 Macroscopic Approach

In this approach, the filter coefficient is determined by macroscopic, bulk system variables. A summary of experimental studies of filtration is given in Table 2.3 along with the corresponding references. The key points of the filtration studies may be summarized as follows, and Table 2.4 lists these same points along with the corresponding references:

1) The macroscopic process of filtration or change in suspension concentration over depth is a first-order decay with distance in steady flow.
2) The filter coefficient may be expressed as a function of a single collector efficiency.
3) The single collector efficiency may be related to microscopic filtration mechanisms.
4) The filtration process consists of transport and attachment mechanisms.
5) Derived and experimentally verified filter coefficients apply for initial conditions of filtration and must be re-evaluated as filtration progresses.
6) System chemistry can significantly affect the filtration process.
7) For favorable filtration, theoretical predictions generally match

Table 2.3: Summary of Filtration Experimental Studies.

MEDIA GRAINS		PARTICLES		
TYPE	SIZE (microns)	TYPE	SIZE (microns)	REFERENCES
Plastic planar surfaces	---	Polystrene Latexes	0.308	Hull & Kitchener 1969
Glass spheres	460, 548 658, 777	Kaolinite	2-10	Ison & Ives 1969
Sand	335, 714 1122	Vermiculite	10-100	Craft 1969
Glass spheres	397	Polystyrene & Styrenedivinylbenzene latexes	0.091-1.091; 7.6, 25.7	Yao et al. 1971
Glass spheres	720 100-4000 ---	Latexes	3.5-21.0; 0.7-21.0; ---	Fitzpatrick 1972; Fitzpatrick & Spielman 1973 Spielman & Cukor 1973
Sand	500	Monodisperse Polystyrene Latexes	0.091-15.2	Jordan et al. 1974
Sand	500	Monodisperse Polystyrene & Polystyrene Divinylbenzene Latexes	0.091-15.2	Ghosh et al. 1975
Glass spheres & polymethyl Methacrylate	12000	Polystyrene & Styrene Divinylbenzene Latexes	0.312 - 1.101;5.7 25.7	Rajagopalan & Tien 1977
Glass spheres	300	Salt Tracer	15 - 18	Pendse et al. 1978
Glass spheres	540	Polystyrene, Styrene Divinylbenzene & Polyvinyltoluene latexes	3.7,5.7; 5.7,11.3; 2.02	Yoshimura et al. 1980

(Continued)

Table 2.3 (cont.): Summary of Filtration Experimental Studies.

Alumina fibers	2.0	Polystyrene latexes	0.172	Gregory & Wishart 1980
Glass spheres & fibers	100000, 100	Polyvinyl toluene & polystrene divinylbenzene latexes	2.02,5.2, 9.8	Onorato & Tien 1980
Uniform & Graded Sand	548,437	Iron	---	Amirtharajah & Wetstein 1980
Uniform Sand	1000 - 10000	Sand	120-1600	Sherard et al. 1984
Uniform Sand	400 - 10000	Silt & Clay	10 - 580	Sherard et al. 1984
Glass spheres	---	Carboxyl latexes & Hematite	---	Wang et al. 1986
Glass spheres	---	Carboxyl latexes & Hematite	---	O'Melia 1987
Glass spheres	400;550	Latexes	4; 10.6	Tobiason & O'Melia 1988
Glass spheres	200,400; 200;200	Polystyrene latex	0.046; 0.378; 0.753	Elimelech & O'Melia 1990

experimental results, but for unfavorable filtration, theory underpredicts experimental results.

As stated in point 1), observed filtration results for steady flow, neglecting longitudinal dispersion, have led to the following (Iwasaki 1937):

$$\frac{\partial C}{\partial x} = -\lambda C \qquad (2.19)$$

Table 2.4: Summary of Results of Macroscopic Filtration Studies.

MACROSCOPIC FILTRATION RESULTS	REFERENCES
1) Macroscopic filtration is a first-order decay over distance.	Fitzpatrick & Spielman 1973; Yao et al. 1971; Tien & Payatakes 1979; O'Melia 1985; Jordan et al. 1974; Ghosh et al. 1975; Tobiason & O'Melia 1988; Spielman & Fitzpatrick 1973; Payatakes et al. 1974; Spielman 1979; Gregory & Wishart 1980; Yoshimura et al. 1980; Iwasaki 1937
2) Filter coefficient may be expressed as single collector efficiency.	Ghosh et al. 1975; Tobiason & O'Melia 1988; Spielman & Fitzpatrick 1973; Spielman 1977; Gregory & Wishart 1980; Yoshimura et al. 1980; Yao et al. 1971; O'Melia 1985; Rajagopalan & Tien 1976
3) Single collector efficiency can be related to microscopic deposition mechanisms.	See Table 2.2
4) Deposition process consists of transport and attachment mechanisms.	Jordan et al. 1974; Tien & Payatakes 1979; Ghosh et al. 1975; O'Melia 1985; Rajagopalan & Tien 1976, 1977; Yao et al. 1971; Amirtharajah 1982; Cleasby 1981; Grutsch & Mallatt 1977 Herzig et al. 1970; Tobiason & O'Melia 1988; Wang et al. 1986; Elimelech & O'Melia 1991
5) Filter coefficient applies for initial conditions during filtration.	Yao et al. 1971; Tien & Payatakes 1979; O'Melia 1985; Payatakes et al. 1974; Rajagopalan & Tien 1976, 1977; Gregory & Wishart 1980; Yoshimura et al. 1980; Jordan et al. 1974; Ghosh et al. 1975; Wang et al. 1986; Tobiason & O'Melia 1988; Pendse et al. 1978; Tien et al. 1979; Amirtharajah & Wetstein 1980; Saatci & Oulman 1980
6) Chemistry can affect deposition.	Yao et al. 1971; Tien & Payatakes 1979; Fitzpatrick & Spielman 1973; Hull & Kitchener 1969; Payatakes et

(Continued)

Table 2.4 (cont.): Summary of Results of Macroscopic Filtration Studies.

	al. 1974; Rajagopalan & Tien 1976, 1977; Gregory & Wishart 1980; Onorato & Tien 1980; Yoshimura et al. 1980; O'Melia 1985,1987; Jordan et al. 1974; Ghosh et al. 1975; Wang et al. 1986; Tobiason & O'Melia 1988; Elimelech & O'Melia 1990; Vaidyanathan & Tien 1986, 1988; Bowen & Epstein 1979
7) Theory predicts favorable filtration, but underpredicts unfavorable filtration.	Hull & Kitchener 1969; Rajagopalan & Tien 1977; Onorato & Tien 1980; Yoshimura et al. 1980; O'Melia 1987; Wang et al. 1986; Yao et al. 1971; Tien & Payatakes 1979; O'Melia 1985; Gregory & Wishart 1980; Bowen & Epstein 1979; Elimelech & O'Melia 1990; Tobiason & O'Melia 1988; Fitzpatrick & Spielman 1973; Ghosh et al. 1975; Jordan et al. 1974; Vaidyanathan & Tien 1986, 1988

with a solution:

$$C = C_0 exp[-\lambda x] \tag{2.20}$$

where: C = *particle concentration* ($M\ L^{-3}$);
C_0 = $C[x = 0]$;
x = *longitudinal position* (L); *and*
λ = *filter coefficient* (L^{-1}).

As stated in point 2), the filter coefficient theoretically may be expressed as a single collector efficiency as follows:

$$\lambda = \frac{3}{2}\frac{(1 - \theta_e)}{d_g}\alpha_c \eta_T \tag{2.21}$$

where: θ_e = *effective porosity* (-);
α_c = *collision efficiency factor* (-); *and*
η_T = *total single collector efficiency* (-).

$$\eta_T = \frac{\textit{number of particles striking medium grain}}{\textit{total approaching medium grain}}$$

$$\alpha_c = \frac{\textit{number of successful collisions}}{\textit{total collisions}}$$

For η_T, the particles under consideration are those contained in a cylinder of diameter d_g which is coincident with the vertical axis through the media grain collector. In these equations, λ can be found either experimentally or from the individual collector efficiency, η_T, and system variables using Eq. (2.21). η_T is determined by analyzing the microscopic interactions of a particle and collector. As proposed by Tobiason and O'Melia (1988), α_c is the factor which defines the difference between λ_f and λ when unfavorable chemical conditions are encountered. In this work, α_c is assumed to be equal to one, and the effects of unfavorable filtration are lumped into λ.

2.6.2 Trajectory Analysis

The microscopic study of particle motion near a collector is defined as trajectory analysis. The first step in this analysis is the definition of a geometric model for describing the medium. Several models have been proposed such as a sphere-in-cell or a constricted tube model (Brinkham 1947 and 1947; Happel 1958 and 1959; Kuwabara 1959). Regardless of the model chosen, the following discussion is consistent.

In porous media, particle paths far from media grains follow fluid

streamlines. As the particles approach a media grain, the motion deviates from the streamline because of various forces and torques acting on the particle. These forces and torques are represented by transport and attachment mechanisms (Ghosh et al. 1975; Jordan et al. 1974; O'Melia 1985; Rajagopalan and Tien 1976, 1977 and 1977; Tien and Payatakes 1979; Yao et al. 1971). The transport mechanisms are considered to be the following:

1) Gravity settling.

2) Interception.

3) Brownian diffusion.

4) Advection.

Attachment mechanisms are considered to be the following:

1) Gravity.

2) London-van der Waals attraction.

3) Double layer forces.

A particle path or trajectory can be obtained from the solution of particle equations of motion which incorporate the forces and torques acting on the particles which are responsible for the various filtration mechanisms.

The studies which have analyzed filtration according to particle trajectories are listed in Table 2.5. These studies may be summarized as follows, and Table 2.6 lists these same points along with the corresponding references:

1) In a region far from any collector, a particle's path follows that of a fluid streamline.

Table 2.5: Summary of Theoretical Trajectory Studies.

PARTICLE TYPE	COLLECTION MECHANISM	REFERENCES
Non-Brownian	Brownian Diffusion & Interception; Unretarded London & Hydrodynamic Forces	Spielman & Goren 1970
Brownian & Non-Brownian	Gravity Settling, Brownian Diffusion & Interception	Yao et al. 1971
Non-Brownian	Gravity Settling; Unretarded London, Negligible Double Layer & Hydrodynamic Forces	Spielman & Fitzpatrick 1973
Non-Brownian	Unretarded London & Finite Double Layer Forces	Spielman & Cukor 1973
Brownian	Brownian Diffusion; Unretarded London & Double Layer Forces	Ruckenstein & Prieve 1973
Non-Brownian	Gravity Settling & Interception; Retarded London, Double Layer & Hydrodynamic Forces	Payatakes et al. 1974
Brownian & Non-Brownian	Gravity Settling & Brownian Diffusion; Unretarded London & Hydrodynamic Forces	Prieve & Ruckenstein 1974
Non-Brownian	Brownian Diffusion & Interception; Unretarded London, Negligible Double Layer & Hydrodynamic Forces	Jordan et al. 1974
Brownian	Brownian Diffusion; Unretarded London & Double Layer Forces	Spielman & Friedlander 1974
Brownian & Non-Brownian	Gravity Settling, Brownian Diffusion & Interception; Unretarded London, Negligible Double Layer & Hydrodynamic Forces	Ghosh et al. 1975
Non-Brownian	Gravity Settling, Brownian Diffusion & Interception; Retarded London, Double Layer & Hydrodynamic Forces	Rajagopalan & Tien 1976, 1977
Brownian &	Gravity Settling, Brownian Diffusion	Spielman

(Continued)

Table 2.5 (Cont.): Summary of Theoretical Trajectory Studies.

Non-Brownian	& Interception; Unretarded London & Double Layer & Forces	1977
Brownian	Brownian Diffusion; Retarded London & Double Layer Forces	Gregory & Wishart 1980
Non-Brownian	Gravity Settling & Interception; Retarded London & Double Layer Forces	Onorato & Tien 1980
Non-Brownian	Gravity Settling, Brownian Diffusion & Interception; Retarded London & Hydrodynamic Forces	Yoshimura et al. 1980
Brownian	Unretarded London & Double Layer Forces	Ruckenstein & Prieve 1980
Non-Brownian	Gravity Settling, Brownian Diffusion & Interception; Retarded London Forces	Tobiason & O'Melia 1988
Brownian	Retarded Brownian Diffusion; Double Layer Forces	Elimelech & O'Melia 1990

2) As a particle comes in close proximity to a collector, its path deviates from that of a fluid streamline according to the various forces and torques acting on the particle.

3) Hydrodynamic retardation is defined as the slow drainage of fluid from between two closely interacting particles which occurs before contact of the particles.

4) In the analysis of trajectories, the various forces and other factors which affect particle motion and interactions may be organized into dimensionless groups.

5) The solved trajectories, represented by these groups, are expressed as collector efficiencies.

Table 2.6: Summary of Results of Trajectory Studies.

TRAJECTORY RESULTS	REFERENCES
1) Far from a collector, a particle's path follows fluid streamlines.	See Table 2.5; O'Melia 1987
2) As particle approaches a collector, its path deviates from a fluid streamline.	See Table 2.5
3) Hydrodynamic retardation occurs as particle comes very close to collector.	See Table 2.5; Spielman & Goren 1970; Payatakes et al. 1974; Rajagopalan & Tien 1976, 1977; Spielman 1977; Gregory & Wishart 1980; Onorato & Tien 1980; Yoshimura et al. 1980; Ruckenstein & Prieve 1980; Tobiason & O'Melia 1988; O'Melia 1987; Elimelech & O'Melia 1990
4) Various forces affecting particle motion can be organized into dimensionless groups.	See Table 2.5
5) Solved trajectories can be expressed as collector efficiencies.	See Table 2.5
6) Collector efficiencies can be expressed as filter coefficients.	See Table 2.5

6) As stated previously, these collector efficiencies can be expressed as filter coefficients.

From a combination of trajectory analysis and dimensional analysis, the three major contributors to filtration can be formulated. These are collection due

to Brownian diffusion, interception, and settling. In the formulation of the equations for the collection due to these mechanisms, it is assumed that double layer repulsive forces and hydrodynamic retardation are negligible. The equations for these collection efficiencies are given in the following (Yao et al. 1971; Tien and Payatakes 1979; O'Melia 1985; McDowell-Boyer et al. 1986; Rajagopalan and Tien 1976, 1977, and 1979; Cookson 1972; Payatakes et al. 1974; Levich 1962; Gregory and Wishart 1980; Yao et al. 1971; Elimelech and O'Melia 1990).

Consider collection due to Brownian diffusion, η_D (originally Levich 1962; Cookson 1972):

$$\eta_D = 4A_s^{1/3} Pe_p^{-2/3} \tag{2.22}$$

where: A_s = *dimensionless flow model parameter*;

$$= \frac{2(1 - \gamma^5)}{2 - 3\gamma + 3\gamma^5 - 2\gamma^6}; \text{ and}$$

$$\gamma^3 = 1 - \theta_e.$$

In this equation, $4A_s^{1/3}$ is relatively constant, within a factor of three, for expected porous bed cases. With this in mind, either the particle Peclet number can be allowed to reach a minimum value of approximately 1, or as $Pe_p < 1$ the efficiency reaches an asymptotic value of 1.

Consider collection due to interception, η_I:

$$\eta_I = 1.5\gamma^2 A_s N_R^2 \tag{2.23}$$

$$\textit{where: } N_R = \frac{d_p}{d_g}$$

In this equation, $1.5\gamma^2 A_s$ is relatively constant, within a factor of five, for expected porous bed cases. With this in mind, the relative size group (N_R) can be allowed to reach a minimum value of approximately 1 in order for the efficiency to remain less than or equal to 1. From the previous discussion, the size of the largest particles which are able to penetrate and transport through a porous bed is one-twentieth of the media grain diameter ($a_p < 1/20\ d_g$) or one-fourth of the pore radius ($a_p < 1/4\ r_0$).

Consider collection due to settling, η_G:

$$\eta_G = \frac{w_s}{V_s} = \frac{2(\rho_p - \rho_f) g a_p^2}{9\mu V_s} \qquad (2.24)$$

where: w_s = *particle settling velocity*;
V_s = *fluid interstitial velocity*;
ρ_{pf} = *densities of particle and fluid, respectively*;
μ = *fluid viscosity; and*
g = *gravitational acceleration.*

In this equation, the best possible collection occurs for the settling velocity equaling the interstitial velocity. This is the limit for collection efficiency. As the settling velocity becomes greater than the interstitial velocity, the efficiency remains at a value of 1.

These separate effects are expected to be additive and an equation for total collection efficiency, η_T, is (Payatakes et al. 1974; Rajagopalan and Tien

1976 and 1977; Yao et al. 1971; Spielman and Fitzpatrick 1973; Tien and Payatakes 1979; Prieve and Ruckenstein 1974; Cookson 1972; Fitzpatrick 1972; Payatakes et al. 1974):

$$\eta_T = \eta_D + \eta_I + \eta_G \tag{2.25}$$

In the case of total collection efficiency, η_T has an asymptotic maximum value of 1.

The comparison of experimental results to this theory can be summarized in the following. For Brownian particles (d_p < 1.0 micron), there is good agreement between experimental results and theoretical predictions using these groups. Conversely, for advective particles (d_p > 1.0 microns), the experimental results do not agree well with the theory.

This discrepancy is the result of neglecting hydrodynamic retardation and London-van der Waals attraction during the formulation of these separate collection efficiencies. No exact analytical solution has been developed from trajectory analysis when including these processes. However, a single collector efficiency has been obtained by numerical integration of the equations of particle motion when hydrodynamic retardation, London-van der Waals attraction, diffusion, interception, and gravity are considered (Rajagopalan and Tien 1976; Tien and Payatakes 1979):

$$\eta_T = 4A_s^{1/3}Pe_p^{-2/3} + 0.72A_s N_{Lo}^{1/8} N_R^{15/8} + 2.4E\text{-}3A_s N_G^{1.2} N_R^{-0.4} \tag{2.26}$$

$$\textit{where: } N_{Lo} = \textit{London group;}$$
$$= \frac{H}{9\pi\mu a_p^2 V_s};$$
$$H = \textit{Hamaker constant (ergs); and}$$
$$N_G = \textit{gravitational group}$$
$$= \eta_G.$$

An inspection of Eq. (2.26) yields several important points which are stated in the following. First, the first term represents filtration due to Brownian diffusion. This term was previously found to accurately describe Brownian particle filtration, and as expected, this term has not been modified by the inclusion of any effects of retardation or London-van der Waals attraction. Next, the second and third terms represent the combined effects of interception and gravity, respectively, when retardation and London-van der Waals attraction are included. The final point is that in this analysis the effects of surface double layer forces are ignored. As such, this equation describes favorable filtration in the sense that a system featuring favorable, attractive surface double layer forces is controlled by transport processes and not dependent on surface chemistry. However, this equation must be modified or reformulated in order to describe the effects of unfavorable, repulsive surface forces.

These results show that particle transport includes physical and chemical factors, and the relative importance of these varies as both the particle approaches a collector and system chemistry ranges from favorable to unfavorable. Also, the numerical equation formulated from the numerical analysis is only good for favorable filtration and becomes less and less accurate as

the system becomes less and less favorable (Elimelech and O'Melia 1990; Fitzpatrick and Spielman 1973; Ghosh et al. 1975; Jordan et al. 1974; Tobiason and O'Melia 1988; Yoshimura et al. 1980; Gregory and Wishart 1980; Hull and Kitchener 1969; Rajagopalan and Tien 1976 and 1977; Onorato and Tien 1980; O'Melia 1985 and 1987; Bowen and Epstein 1979; Payatakes et al. 1974; Wang et al. 1986; Yao et al. 1971; Tien and Payatakes 1979).

2.6.3 Unfavorable Filter Coefficient

Several models have been formulated using trajectory analysis which attempt to include the effects of unfavorable surface forces (Payatakes et al. 1974; Tien and Payatakes 1979; Spielman and Cukor 1973; Ruckstein and Prieve 1973; Spielman 1977; Elimelech and O'Melia 1990). The predominant feature of these theories is a catastrophic decline in the filter coefficient at the transition point between favorable and unfavorable filtration. In practice, experimental results show a more gradual decline in the filter coefficient across this transition region (Elimelech and O'Melia 1990; Fitzpatrick and Spielman 1973; Ghosh et al. 1975; Jordan et al. 1974; Tobiason and O'Melia 1988; Yoshimura et al. 1980; Gregory and Wishart 1980). The filter coefficient is observed to be asymptotic to the value of the favorable filter coefficient while crossing a transition region. This result is shown in Fig. 2.4 with parts (a) - (f) being data from separate studies. Part (a) shows data for Brownian particles, and parts (b) - (f) show data for advective particles. Table 2.7 lists the electrolyte and surface groups/particle type used by these investigators. Other data for these studies are listed in Table 2.3.

Table 2.7: Chemical Data for Experiments Which Measure Unfavorable Filtration.

ELECTROLYTE	SURFACE GROUPS/ PARTICLE TYPE	REFERENCES
KCl	Sulfate	Elimelech & O'Melia 1990
HNO_3	latex	Fitzpatrick & Spielman 1973
$CaCl_2$	latex	Ghosh et al. 1975
$CaCl_2$	latex	Jordan et al. 1974
$Ca(NO_3)_2$	Sulfate	Tobiason & O'Melia 1988
NaCl	latex	Yoshimura et al. 1980
NaCl	Carboxyl	This work

This figure (Fig. 2.4) shows both the gradual decline in filter coefficient with decreasing ionic strength of the liquid, instead of a catastrophic decline. For data in Fig. 2.4, there appears to be an asymptotic value of λ at high ionic strength. As seen in parts (b) - (f), this gradual decline begins at an ionic strength of approximately 10^{-2} for the advective particles; whereas, as seen in part (a) the decline begins at an ionic strength of approximately 10^{-1}.

Vaidyanathan (1986) and Vaidyanathan and Tien (1988) observed and empirically fitted the following equation using advective particle data which describes both the transition region from favorable to unfavorable filtration and the asymptotic value for favorable filtration for the filter coefficient:

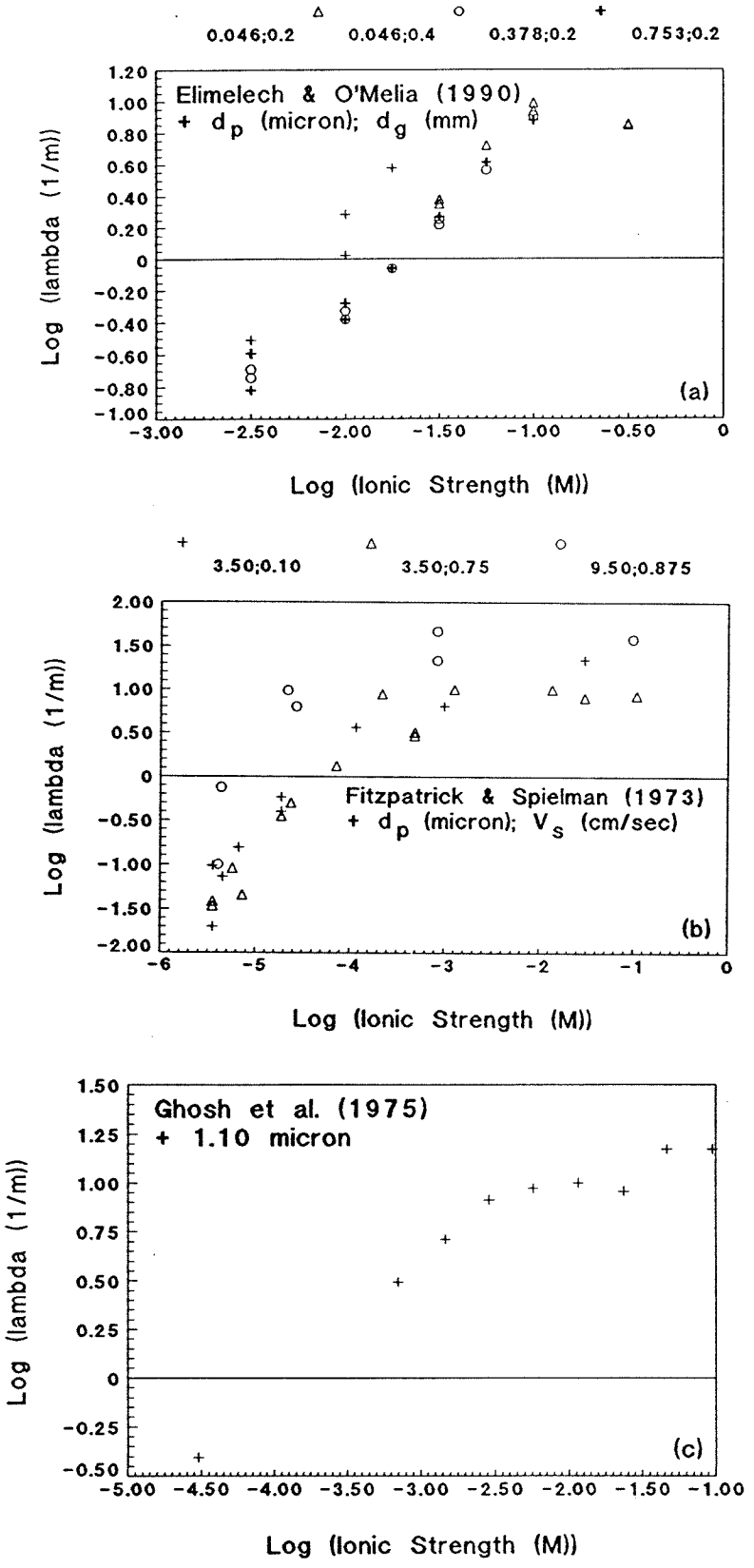

Fig. 2.4: Relationship between measured filter coefficients (λ) and ionic strength (I).

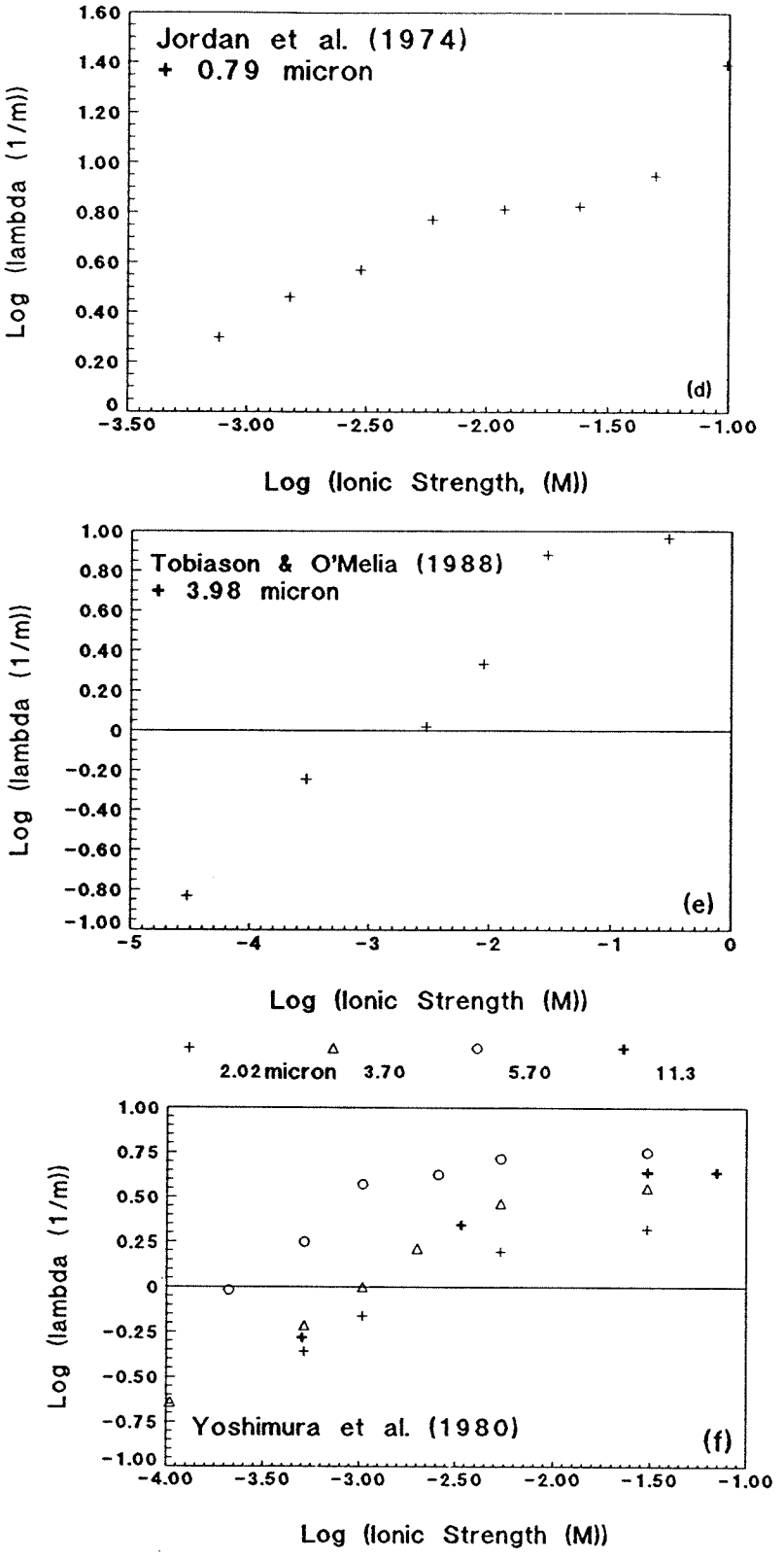

Fig. 2.4(cont.): Relationship between measured filter coefficients (λ) and ionic strength (I).

$$Y = -0.1597 - 0.2813X - 0.1239X^2 \qquad X < -1.1355$$
$$= 0 \qquad X \geq -1.1355 \qquad (2.27)$$

where: $Y = Log\left[\frac{\lambda}{\lambda_f}\right]$;
λ = *measured filter coefficient*;
λ_f = *favorable filter coefficient*;
X = *Log[I]*; *and*
I = *ionic strength.*

This equation applies only for the region $X < X_{tr} = -1.1355$. X_{tr} is defined as the starting point of the transition region at which the best-fit parabola meets the line $\lambda = \lambda_f$. For $X > X_{tr}$, Y assumes the value of 0 ($\lambda = \lambda_f$). Eq. (2.27) is plotted versus various data of Fig. 2.4 in Fig. 2.5. In this figure, λ_f is calculated using Eqs. (2.26) and (2.21). In part (a), only the advective particle data are shown. In part (b), all data including Brownian particle work are shown. This data refutes the trajectory theories, because, as X becomes less than X_{tr}, λ as calculated from trajectory theory should become a value several orders of magnitude less than λ_f which is not shown by the experimental results.

2.7 Summary

This literature review has provided the necessary information for developing and analyzing the experimental program and theoretical models. Different models for particle advective velocity, solute longitudinal dispersion coefficient, and filter coefficient have been reviewed and compared to published experimental data. The objectives of this work can be expressed in the following paragraphs.

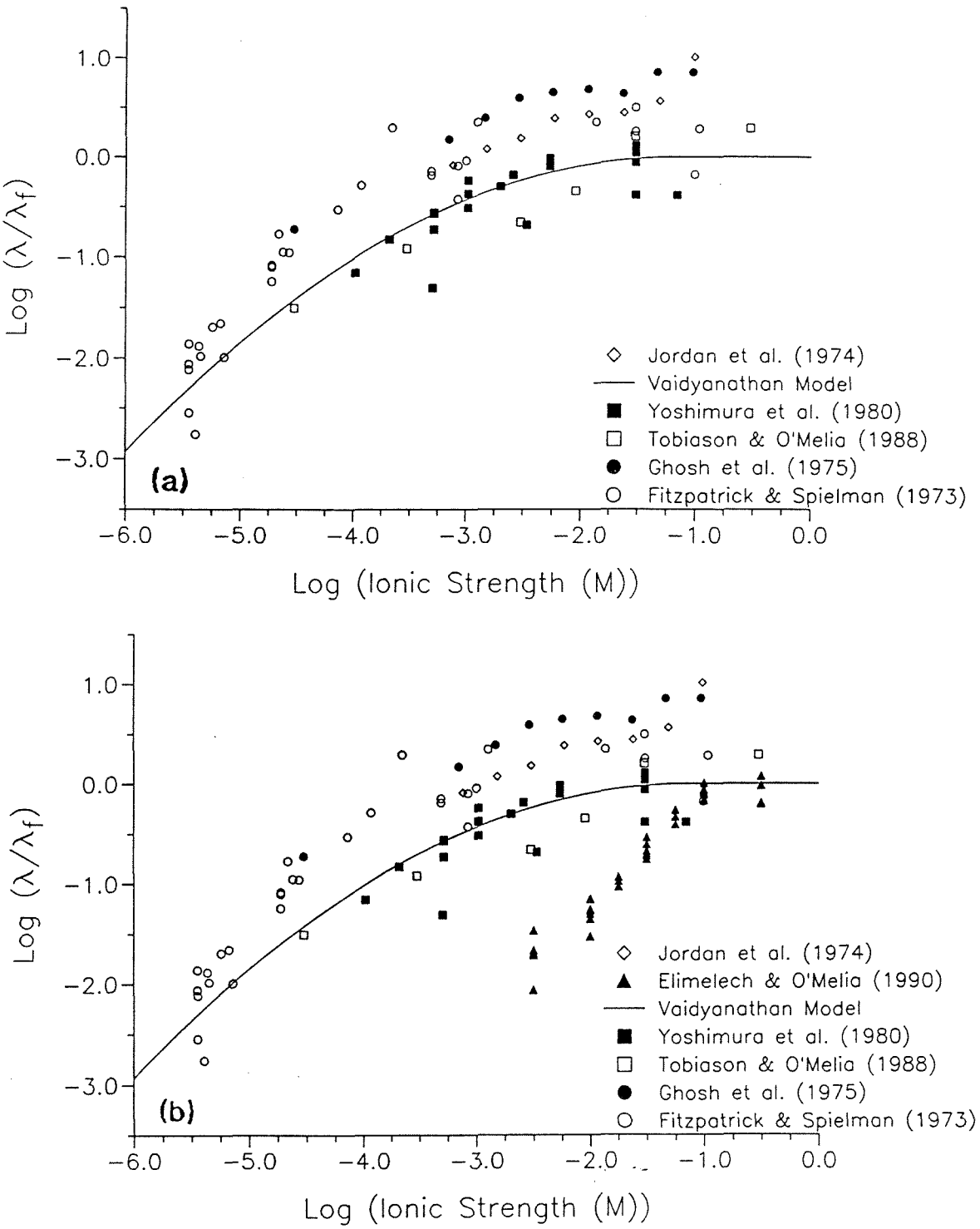

Fig. 2.5: Comparison of experimental data versus Vaidyanathan (1986) and Vaidyanathan and Tien (1988) model.

The experimental program is designed to provide the necessary data for determining experimental values of the longitudinal dispersion coefficient for particles, the particle velocity, and filter coefficient. Currently, no particle dispersion data appears in the literature. The experimental data for particle velocity as compared to fluid interstitial velocity is sparse and usually poorly presented. For the filter coefficient, current theories for unfavorable filtration are not adequate and little experimental data is available to define the transition region.

The three transport parameters have been included in an advective-dispersion equation for which a solution has been determined for the case of constant filter coefficient. A numerical model has been developed for the case of transient filter coefficient.

These objectives are attained by the modelling of Chapter 3, with a description of the apparatus and experimental methods of Chapter 4, showing the results of experiments in Chapter 5, and a discussion of conclusions of Chapter 6.

3. MODELLING OF PARTICLE TRANSPORT AND FILTRATION

In this chapter, new models are presented for the transport parameters and these parameters are included in transport equations for which solutions have been derived by this work.

3.1 Introduction

Models for the transport parameters are presented first. For the advective velocity of particles, the previously reviewed model is given. For the particle longitudinal dispersion coefficient, modification of the dimensional analysis model for solute dispersion is presented to account for particles. For the filter coefficient, a new model based on dimensional analysis is presented to define unfavorable filtration due to ionic strength changes.

These transport parameters are included in both steady and unsteady one-dimensional advective-dispersion equations. These equations have been expanded to include a sink term representing filtration. Exact and approximate analytical solutions are derived for the steady and unsteady cases. Calculated distributions of concentration in both time and position in dimensionless form for various cases are shown in order to illustrate limiting cases and sensitivity to various variables.

The results of this section are used to analyze the experimental data collected in this work, and this analysis is presented in Chapter 5.

3.2 Chemistry

The close interaction and possible subsequent attachment of the media and particles is dominated by the surface forces resulting from the chemical makeup

of the system. The chemistry of the system can be altered by changing either the ionic strength or pH of the interstitial fluid. In this work, special interest is being focused on unfavorable filtration due to ionic strength variation.

The specific information regarding the chemistry of the system used in this work is presented in Chapter 2. No new models are presented to describe the chemistry of particle-particle interaction. The main role of chemistry in this work is the effect of ionic strength on the filter coefficient. As stated in Chapter 2, the ionic strength in this work is varied between 4.0×10^{-4} to 2.1×10^{-3} M using NaCl as the electrolyte.

3.3 Particle Transport Modelling

As stated above, the hydrodynamic transport parameters are expected to be independent of system chemistry. The system chemistry in this work generally has been chosen in order to maximize transport to insure that a detectable concentration of particles moves through the porous medium. The system chemistry, namely the ionic strength, is varied in order to determine if the hydrodynamic transport parameters are independent of the chemistry.

The individual parameters are determined according to dimensional analysis arguments. These parameters then are incorporated into transport equations, and solutions are derived and presented.

3.3.1 Transport Parameters

The parameters necessary to formulate a complete advective-dispersion equation for particle transport and filtration are the particle advective velocity,

particle longitudinal dispersion coefficient, and filter coefficient. An existing model has been used to define an enhanced particle advective velocity. As shown previously, this general model has been modified to simulate Poiesuille flow in a capillary tube. The result of this review is given here. An existing dimensional analysis model for solute longitudinal dispersion is modified by using the particle's enhanced advective velocity and particle Brownian diffusion coefficient to account for the transport effects of a particle versus those of a solute. A new model based on dimensional analysis for the filter coefficient is presented to account for unfavorable filtration due to ionic strength variations.

3.3.1.1 Particle Advective Velocity

The result of the size exclusion principal for particles flowing in a capillary tube can be summarized in the following.

The average velocity of a particle, V_p, in a capillary tube is:

$$V_p = U_0\left[1 - \frac{1}{2}\left(1 - \frac{a_p}{r_0}\right)^2 - \gamma\left(\frac{a_p}{r_0}\right)^2\right] \qquad (2.8)$$

where: U_0 = *fluid centerline velocity* (*L*/*T*);
r_0 = *capillary radius* (*L*);
a_p = *particle radius* (*L*); *and*
γ = 2/3.

The average fluid velocity, V_s, in a capillary tube is:

$$V_s = \frac{U_0}{2} \qquad (2.7)$$

From the two expressions for average velocities, the following difference equation

can be written:

$$\Delta V = \frac{V_p - V_s}{V_s} = 2\frac{a_p}{r_0} - \frac{7}{3}\left(\frac{a_p}{r_0}\right)^2 \qquad (2.9)$$

$$V* = 1 + \Delta V \qquad (3.1)$$

$$\textit{where: } V* = \frac{V_p}{V_s} \qquad (3.2)$$

This result shows that as the particle size increases, the difference between particle velocity and fluid velocity increases.

3.3.1.2 Particle Longitudinal Dispersion Coefficient

A simple method of analyzing the problem of particle longitudinal dispersion is by using a similar dimensional analysis argument as shown previously in the literature review for solutes. This model uses a single velocity and length scale and does not model the internal structure of a porous medium. In modelling particle dispersion, the following variable substitutions are used:

$$D \rightarrow D_p$$
$$V \rightarrow V_p$$
$$D_L \rightarrow D_{Lp}$$

The pertinent variables for particle longitudinal dispersion are:

D_{Lp} = *particle longitudinal dispersion coefficient* ($L^2\ T^{-1}$);
D_p = *particle molecular diffusion coefficient in a free fluid* ($L^2\ T^{-1}$);
V_p = *particle velocity* ($L\ T^{-1}$);
d_g = *media grain diameter* (L); *and*
d_p = *particle diameter* (L).

The particle size variable, d_p, can be removed by using the particle properties as shown, provided $d_p/d_g << 1$. Also, the effect of particle size is included in the enhanced advective velocity for the particles.

This dimensional analysis shows that particle and solute longitudinal dispersion are similar. When the particle Peclet number ($Pe_p = V_p d_g/D_p$) is greater than 10, it can be hypothesized that the two groups can be reduced to one (based on similarity to data for solute dispersion which is shown in Fig. 2.3):

$$\frac{D_{Lp}}{V_p d_g} = Constant \tag{3.3}$$

where: Pe_{Dp} = *particle dynamic Peclet number*

$$= \frac{V_p d_g}{D_{Lp}}.$$

An order of magnitude approximation for the longitudinal dispersion coefficient for particles can be made with:

$$D_{Lp} \approx V_p d_g \tag{3.4}$$

The final result of this analysis is that the same dimensionless groups which are used to correlate the data for solute longitudinal dispersion can be used to correlate the data for particles by making the substitution listed above (see Fig.

2.3).

As mentioned previously in this section, the dimensional argument for defining the longitudinal dispersion coefficient is only valid when $Pe_p >> 1$. For uniform media, this restriction is seen to be $Pe_p > 10$ in Fig. 2.3. Flow conditions are simultaneously limited to the linear, laminar regime for which the Reynolds number must be less than 10 (Bear 1972). For solutes, Houseworth (1984) showed an approximate range on Pe of $10 < Pe < Pe_u = 10^4$. For particle work, the upper limit on Pe_p must be scaled according to the ratio of the molecular diffusion coefficient of a solute to the Brownian diffusion coefficient of the particles. This can be expressed as the following:

$$Pe_{pu} = Pe_u\left(\frac{D}{D_p}\right)$$

For the 1.0 micron particles, Pe_{pu} becomes $10^{7.4}$.

3.3.1.3 Filter Coefficient

As discussed previously in the literature review, models do exist for calculating the filter coefficient for favorable and unfavorable filtration. In the favorable case, the model is widely accepted (Rajagopalan and Tien 1976 and 1979; McDowell-Boyer et al. 1986; Tien and Payatakes 1979; O'Melia 1985; Vaidyanathan and Tien 1986 and 1988; Amiratharajah 1988; Tobiason and O'Melia 1988); whereas, in the unfavorable case, data exists which can not be predicted by this or any other model.

For the formulation of the unfavorable filter coefficient model, a few

comments should be mentioned in order to form a framework for the analysis. First, this work is limited to unfavorable filtration due to ionic strength effects only. Second, the effects of unfavorable filtration can be expressed as a function of favorable filtration. In this form, as conditions become more favorable, this function should become asymptotic to the favorable case. Finally, the effects of ionic strength on filtration can be expressed as a comparison of the pertinent length scales.

Three length scales exist for a transporting particle in a porous medium: 1) diffusion length; 2) hydrodynamic boundary layer thickness; and 3) double layer thickness. A comparison of the size scale of these three lengths is shown in Fig. 3.1. The first two length scales are hydraulic length scales, and the third is a chemical length scale. By showing these in dimensionless form, a comparison of their contributions to particle transport and attachment can be completed.

According to Levich (1962), the diffusion length scale, δ_{DB}, for an advecting particle can be expressed as follows:

$$\delta_{DB} \sim a_p\left(\frac{D_p}{V_p d_g}\right)^{\frac{1}{3}} = a_p(Pe_p)^{-\frac{1}{3}}$$

$$\therefore \delta_{DB} \sim a_p(Pe_p)^{-\frac{1}{3}} \qquad (3.5)$$

In this equation, δ_{DB} is the distance a moving (advecting) particle will deviate (diffuse) from a streamline in a porous medium. This equation applies for large Peclet numbers which are encountered in this work.

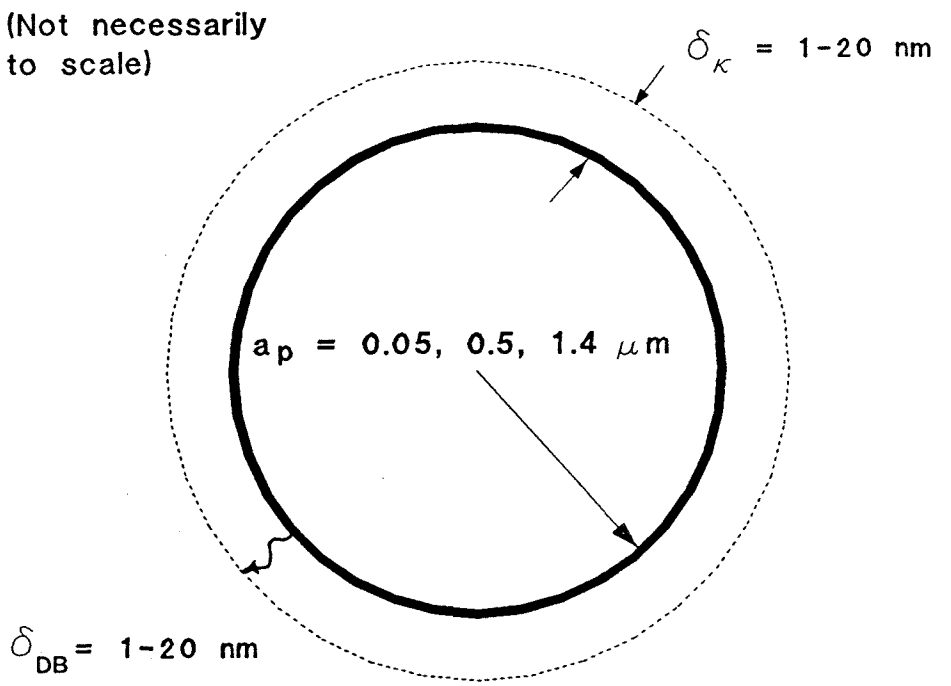

Fig. 3.1: Size comparison of the three length scales encountered in particle-media interactions which account for λ versus λ_f.

According to Levich (1962), the thickness of the hydrodynamic (shear) boundary layer, δ_{HB}, is:

$$\delta_{HB} \sim \delta_{DB}(Pr)^{\frac{1}{3}} = \delta_{DB}\left(\frac{\nu}{D_p}\right)^{\frac{1}{3}}$$

where: Pr = *Prandtl number.*

For small particles in the colloidal range, the shear layer thickness is several orders of magnitude larger than the diffusion length. Also, a developed shear layer thickness is expected to be so large as to be irrelevant in the context of a pore radius or the other length scales mentioned here.

The chemical length scale of interest is the double layer thickness, δ_κ (Stumm and Morgan 1981; Spielman and Friedlander 1973):

$$\delta_\kappa \sim \kappa^{-1} \tag{3.6}$$

where: κ^{-1} = *double layer thickness* (L).

This distance is only a few nanometers and depends upon I (Stumm and Morgan 1981) and is also much smaller than the hydrodynamic shear layer thickness. For fresh water, ($I = 10^{-4}$ M) the double layer thickness is 30 nm; whereas, for saline water, ($I = 10^{-2}$ M) the double layer thickness is 3 nm.

For colloidal particles, both the diffusion length and double layer thickness are much smaller than the hydrodynamic boundary layer thickness. Thus, the forces of attachment in filtration occur over much smaller length scales than the

transport forces.

For unfavorable filtration due to ionic strength variations, both the diffusion length and double layer thickness are assumed to be similar. These two length scales can be compared by their ratio, which is completed by dividing Eq. (3.5) by Eq. (3.6):

$$\delta_{DB}/\delta_{\kappa} = \kappa a_p (Pe_p)^{-1/3} \tag{3.7}$$

This dimensionless group is expected to measure the increasing effectiveness of filtration due to increasing ionic strength. As the ionic strength is increased to a certain critical value, the increasingly compressed double layer will allow a particle to diffuse unrepulsed to the surface leading to a condition of favorable filtration. This tendency will be expressed by an increased ratio of the diffusion length to the double layer thickness (Eq. (3.7)). A functional representation of this can be expressed as:

$$\frac{\lambda}{\lambda_f} = F\left[\kappa a_p (Pe_p)^{-\frac{1}{3}}\right] \tag{3.8}$$

where: λ = *actual filter coefficient* (L^{-1}); *and*
λ_f = *favorable filter coefficient.*

This proposed relationship will be explored in Chapter 5, Section 5.3 using experimental data collected from this and others work.

3.3.2 Steady-state Transport Equation and Solutions

Particle removal or filtration occurs as a particle suspension flows through

a porous medium due to the interaction of the advecting particles and grains of the medium (with median diameter d_g). As discussed previously in the literature review, Iwasaki (1937) is credited with being the first to express filtration as a first-order decay of particle concentration with distance (determined from observed results):

$$\frac{\partial C}{\partial x} = -\lambda C \tag{3.9}$$

where: C = *particle concentration* ($M\ L^{-3}$); *and*
x = *longitudinal position* (L).

with the following boundary condition:

$$1)\ C(x=0) = C_0. \tag{3.9.1}$$

and a solution in dimensional terms:

$$C = C_0 exp[-\lambda x] \tag{3.10}$$

or, in dimensionless terms:

$$C* = exp[-\lambda * x*] \tag{3.11}$$

where: $C* = \frac{C}{C_0}$;
$C_0 = C(x=0)$;
$\lambda * = \lambda d_g$; *and*
$x* = \frac{x}{d_g}$.

A complete equation of steady-state filtration can be formulated by using

the general steady-state advective-dispersion equation of transport for particle concentration with a sink term to describe particle removal due to filtration:

$$0 = D_{Lp}\frac{\partial^2 C}{\partial x^2} - V_p\frac{\partial C}{\partial x} - V_p\lambda C \tag{3.12}$$

The following semi-infinite medium boundary conditions are:

$$\begin{aligned} &1)\ C(x=0) = C_0;\ \textit{and} \\ &2)\ \lim_{x\to+\infty} C(x) = 0. \end{aligned} \tag{3.12.1}$$

A solution which is shown in dimensional terms is derived in Appendix A:

$$C(x) = C_0 exp[\alpha x] \tag{3.13}$$

$$\textit{where: } \alpha = \frac{1}{2}\frac{V_p}{D_{Lp}}\left(1 - \sqrt{1 + 4\lambda\frac{D_{Lp}}{V_p}}\right).$$

In dimensionless terms the transport equation becomes:

$$0 = \frac{\partial^2 C*}{\partial x*^2} - Pe_{Dp}\frac{\partial C*}{\partial x*} - Pe_{Dp}\lambda* C* \tag{3.14}$$

with the same boundary conditions:

$$\begin{aligned} &1)\ C*(x*=0) = 1;\ \textit{and} \\ &2)\ \lim_{x*\to+\infty} C*(x*) = 0. \end{aligned} \tag{3.14.1}$$

and a solution in dimensionless terms:

$$C* = exp[\alpha* x*] \tag{3.15}$$

$$where:\ \alpha* = \alpha d_g = \frac{1}{2} Pe_{Dp}\left(1 - \sqrt{1 + \frac{4\lambda*}{Pe_{Dp}}}\right). \qquad (3.16)$$

3.3.2.1 Approximate Versus Exact Solution

In the complete steady-state advective-dispersion equation (Eq. (3.14)), the effects of longitudinal dispersion and advection are grouped together into the dynamic Peclet number, Pe_{Dp}. As shown in the previous section, the order of Pe_{Dp} is unity for this work. From this result, the effects of the second-order derivative on concentration for this steady-state solution can be assumed to be small compared to the effects of both the concentration gradient and removal terms on concentration. This assumption can be shown to be accurate for this work by completing a Taylor series analysis of α^* (Eq. (3.16)).

This analysis is completed in Appendix A. A first-order Taylor series expansion has been performed on the radical portion of α^* and yields: $\alpha^* = -\lambda^*$. This approximation for α^* shows that the exact, complete filtration equation (Eq. (3.15)) can be approximated by the classical filtration equation (Eq. (3.11)). In this form, particle suspension concentrations are independent of the longitudinal dispersion during steady-state filtration.

The error due to using the approximate solution which omits the dispersion term in steady-state filtration can be determined from the relative error of the two solutions, Eqs. (3.11) and (3.15):

$$\frac{C^*_a - C^*_e}{C^*_e} = \Delta C^* = \frac{exp[-\lambda^* x^*] - exp[\alpha^* x^*]}{exp[\alpha^* x^*]} \tag{3.17}$$

where: C^*_a = *approximate solution; and*
C^*_e = *exact solution.*

This analysis is completed in Appendix A. The result of this analysis is the determination of the absolute error ΔC^*:

$$|error| = |\Delta C^*| \leq \frac{\lambda^{*2} x^*}{Pe_{Dp}} \tag{3.18}$$

In this work, an absolute error of 5% was deemed acceptable, because such an error is expected to be similar to the experimental error. Rearranging Eq. (3.18) yields (assume an equal sign in Eq. (3.18)):

$$\lambda^* = \left(\frac{|error| Pe_{Dp}}{x^*} \right)^{1/2} \tag{3.19}$$

In this form, Eq. (3.19) can be plotted as error contours for given Pe_{Dp} as x^* and λ^* are varied. Such contours of 5% error have been plotted for various Pe_{Dp} values in Fig. 3.2. In the region below the contour lines in this figure, the error is less than 5% for the listed Pe_{Dp} value. In part (a) of this figure, the contours are plotted for the maximum possible range of λ^* and a large range of x^*. In part (b), both λ^* and x^* are limited to the range of values encountered in this work. As can be seen in this figure, the error is more than 5% only for extremely large values of λ^*. Also, the lines of Fig. 3.2 represent contours of error for constant values of $|error| * Pe_{Dp}$ which is evident from an inspection of Eq. (3.19); e.g., the

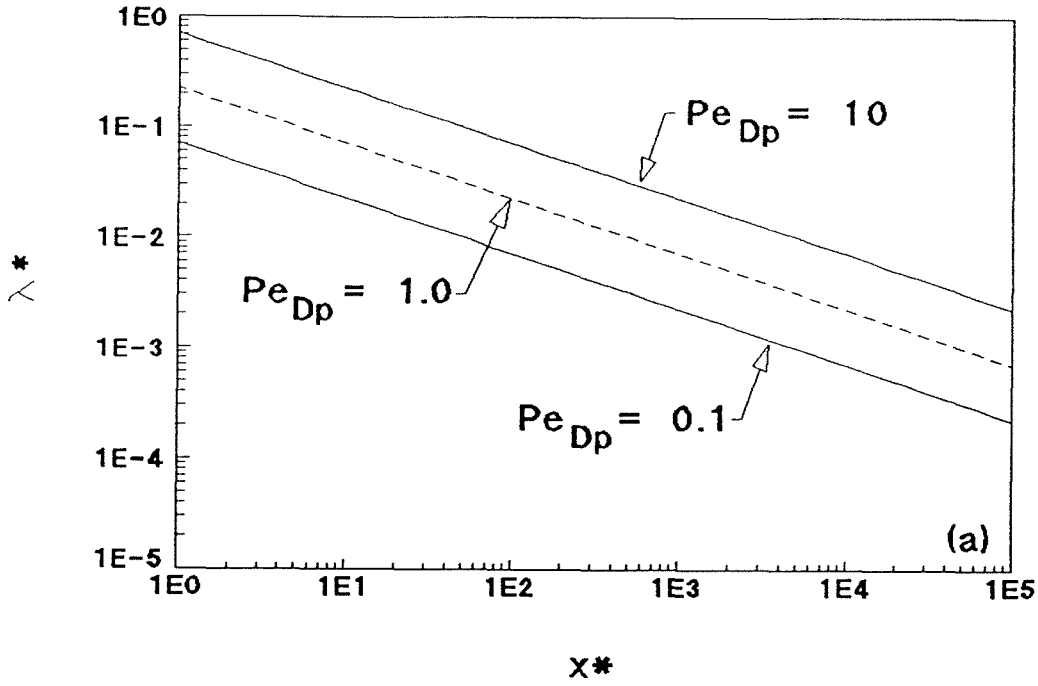

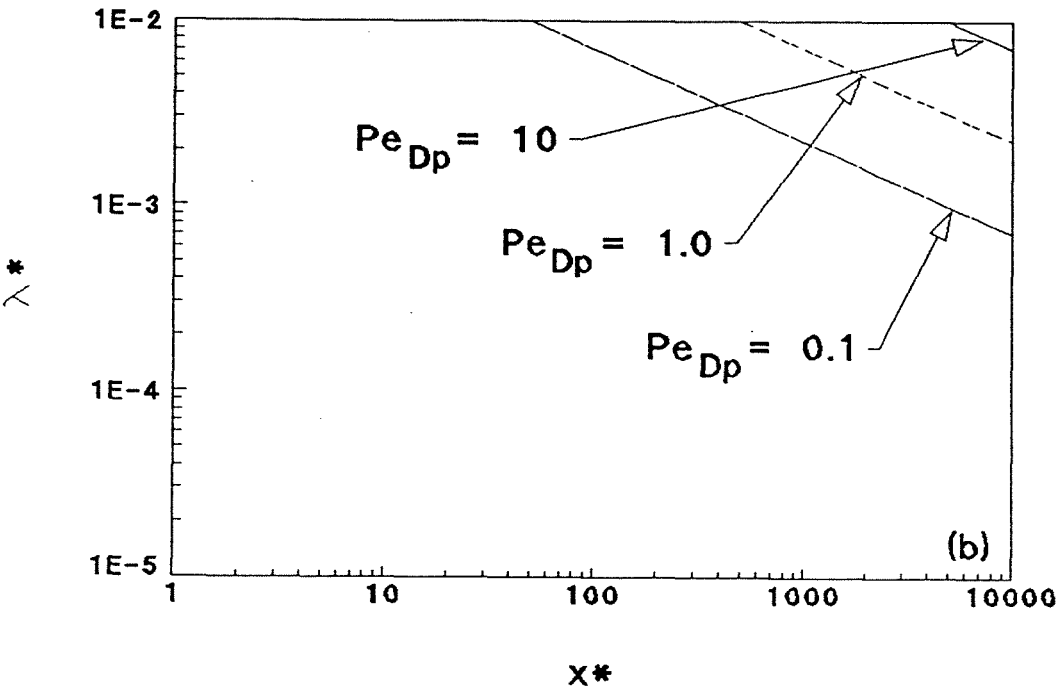

Fig. 3.2: 5% error contours for steady-state solutions for various Pe_{Dp}.

contour labeled as 5% error for Pe_{Dp}=0.1 is also the 0.05% error contour for Pe_{Dp} = 1.0.

3.3.3 Unsteady Transport Equation and Solutions

In order to account for the effects of particle removal during transient transport, a complete equation can be formulated by using the general transient advective-dispersion equation which includes effects of dispersion and advection and then incorporates a sink term to describe particle removal due to filtration:

$$\frac{\partial C}{\partial t} = D_{Lp}\frac{\partial^2 C}{\partial x^2} - V_p\frac{\partial C}{\partial x} - V_p\lambda C \qquad (3.20)$$

where: t = *time* (T).

with the following conditions for an infinite medium:

boundary condition:

$$1) \lim_{x\to+\infty} C(x,t) = 0. \qquad (3.20.1)$$

initial conditions:

$$\begin{aligned} &1)\ C(x,0) = C_0 exp[\alpha x] && x<0;\ and \\ &2)\ C(x,0) = 0 && x>0. \end{aligned} \qquad (3.20.2)$$

The solution which is shown in dimensional terms is derived in Appendix B for an infinite medium:

$$C(x,t) = \frac{1}{2}C_0\ exp[\alpha x]\ erfc\left[\frac{x - (V_p - 2\alpha D_{Lp})t}{2\sqrt{D_{Lp}t}}\right] \qquad (3.21)$$

In dimensionless terms the transport equation becomes:

$$\frac{\partial C*}{\partial t*} = \frac{1}{Pe_{Dp}}\frac{\partial^2 C*}{\partial x*^2} - \frac{\partial C*}{\partial x*} - \lambda* C* \qquad (3.22)$$

$$where:\ t* = \frac{V_p t}{d_g}.$$

with the same conditions:

boundary condition:

$$1)\ \lim_{x*\to+\infty} C*(x*,t*) = 0. \qquad (3.22.1)$$

initial conditions:

$$\begin{array}{lll} 1)\ C*(x*,0) = exp[\alpha* x*] & & x*<0;\ and \\ 2)\ C*(x*,0) = 0 & & x*>0. \end{array} \qquad (3.22.2)$$

and the solution in dimensionless terms:

$$C* = \frac{1}{2}\, exp[\alpha* x*]\ erfc\left[\sqrt{Pe_{Dp}}\left(\frac{x* - \{t*\}\left\{1 - \frac{2\alpha*}{Pe_{Dp}}\right\}}{2\sqrt{t*}}\right)\right] \qquad (3.23)$$

3.3.3.1 Approximate Versus Exact Solution

In order to evaluate experimental data so as to extract the desired parameters (Pe_{Dp},V_p,$\lambda*$), a simpler form of the unsteady solution is needed. As has been shown for a conservative tracer, the dynamic Peclet number term can be determined directly from experimental values of C*, t*, and x* by inverting the erfc. In the present form, recursive calculations would be required to determine

this term and also any of the other parameters.

In the complete transient advective-dispersion equation (Eq. (3.22)), no simple assumptions about the order of the terms can be made due to the characteristics of a transient breakthrough. In order to make any assumptions about the contributions of α^* in Eq. (3.23), the problem should be separated into two parts. The first part will consider the steady-state factor and the second part only the transient factor. In both cases, Taylor series expansions of α^* will be performed.

In the first part, the analysis for the steady-state approximation has been completed in Appendix A and is referred to in Appendix B. This is also discussed in the previous section with the result being a first-order Taylor series expansion for α^* which yields: $\alpha^* = -\lambda^*$. The resulting equation for approximating steady-state transport is: $C^*(x^*) = \exp[-\lambda^* x^*]$. As previously shown, the error due to this approximation has been estimated by the truncated term in a Taylor series expansion, and the relative error between the approximate and exact solutions has been calculated by the ΔC^* equation.

In the second part, the analysis for the transient approximation has been completed in Appendix B. In the erfc term in Eq. (3.23), α^* is divided by Pe_{Dp}. Assuming Pe_{Dp} is of order unity which is expected, this quantity may be expected to be small. This assumption can be shown to be accurate for this work by completing a Taylor series analysis of α^* (Eq. (3.16)). A zeroth-order Taylor series expansion has been performed on the radical portion of α^* and yields: 1 -

$2\alpha^*/Pe_{Dp} = 1$ in Eq. (3.23). The resulting solution for approximating the transient factor is similar to the classical advective-dispersion equation solution, and this solution is (including the steady-state approximation):

$$C'^*(x^*,t^*) = \frac{C^*(x^*,t^*)}{exp[-\lambda^* x^*]} = \frac{1}{2} erfc\left[\sqrt{Pe_{Dp}}\left(\frac{x^* - t^*}{2\sqrt{t^*}}\right)\right] \qquad (3.24)$$

In this form, C'* is simply the solution to conservative tracer breakthrough if D_{Lp} is replaced by D_L in the dynamic Peclet number. Without using any approximation for α^*, the solution to the transient transport equation is:

$$C'^*(x^*,t^*) = \frac{C^*(x^*,t^*)}{exp[\alpha^* x^*]} = \frac{1}{2} erfc\left[\sqrt{Pe_{Dp}}\left(\frac{x^* - \{t^*\}\left\{1 - \frac{2\alpha^*}{Pe_{Dp}}\right\}}{2\sqrt{t^*}}\right)\right] \qquad (3.25)$$

By coupling the two approximations for α^* into the same solution, particle suspension concentrations during transient transport are given by the product of the transient conservative tracer transport and the steady-state transport. Using the above approximations in the steady-state and transient factors of Eq. (3.23), the result (which is a rewritten form of Eq. (3.24)) is:

$$C^*(x^*,t^*) = \frac{1}{2} exp[-\lambda^* x^*] \; erfc\left[\sqrt{Pe_{Dp}}\left(\frac{x^* - t^*}{2\sqrt{t^*}}\right)\right] \qquad (3.26)$$

Physically, we neglect the effect of dispersion on the steady-state factor, and the effect of filtration on the transient factor.

The error due to using the approximate solution can be determined from the relative error of the two solutions, Eqs. (3.26) and (3.23):

$$\frac{C^*_a - C^*_e}{C^*_e} = \Delta C^* = \frac{exp[-\lambda^* x^*]erfc_a - exp[\alpha^* x^*]erfc_e}{exp[\alpha^* x^*]erfc_e} \qquad (3.27)$$

where: $erfc_a$ = *approximate solution erfc; and*
$erfc_e$ = *exact solution erfc.*

This analysis is completed in Appendix B. In this relative error analysis, the error at 50% breakthrough is determined, because the error is expected to be the largest at this point of maximum slope in erfx for small x. The result of this analysis is the determination of the absolute error, ΔC^*, which is:

$$|error| = |\Delta C^*| \le \frac{\frac{\lambda^{*2} x^*}{Pe_{Dp}} + 2x^* \sqrt{\frac{Pe_{Dp}}{\pi x^*}} \left(\frac{\lambda^*}{Pe_{Dp}} - \left\{ \frac{\lambda^*}{Pe_{Dp}} \right\}^2 \right)}{1 + 2x^* \sqrt{\frac{Pe_{Dp}}{\pi x^*}} \left(\frac{\lambda^*}{Pe_{Dp}} - \left\{ \frac{\lambda^*}{Pe_{Dp}} \right\}^2 \right)} \qquad (3.28)$$

As stated previously, an error of 5% is acceptable. Rearranging Eq. (3.28) in terms of λ^* yields a second-order polynomial (with an equal sign in Eq. (3.28)):

$$0 = \left(\frac{x^*}{Pe_{Dp}} - \frac{2x^*}{Pe_{Dp}^2} \sqrt{\frac{Pe_{Dp}}{\pi x^*}} \{1 - |error|\} \right) \lambda^{*2} + \left(\frac{2x^*}{Pe_{Dp}} \sqrt{\frac{Pe_{Dp}}{\pi x^*}} \{1 - |error|\} \right) \lambda^* - |error| \qquad (3.29)$$

When the polynomial of Eq. (3.29) is solved for the positive root, error contours can be plotted for given Pe_{Dp} values as x^* and λ^* are varied. Contours of 5% error have been plotted for various Pe_{Dp} values in Fig. 3.3. In the region below the contour lines in this figure, the errors are less than 5%. In part (a) of this

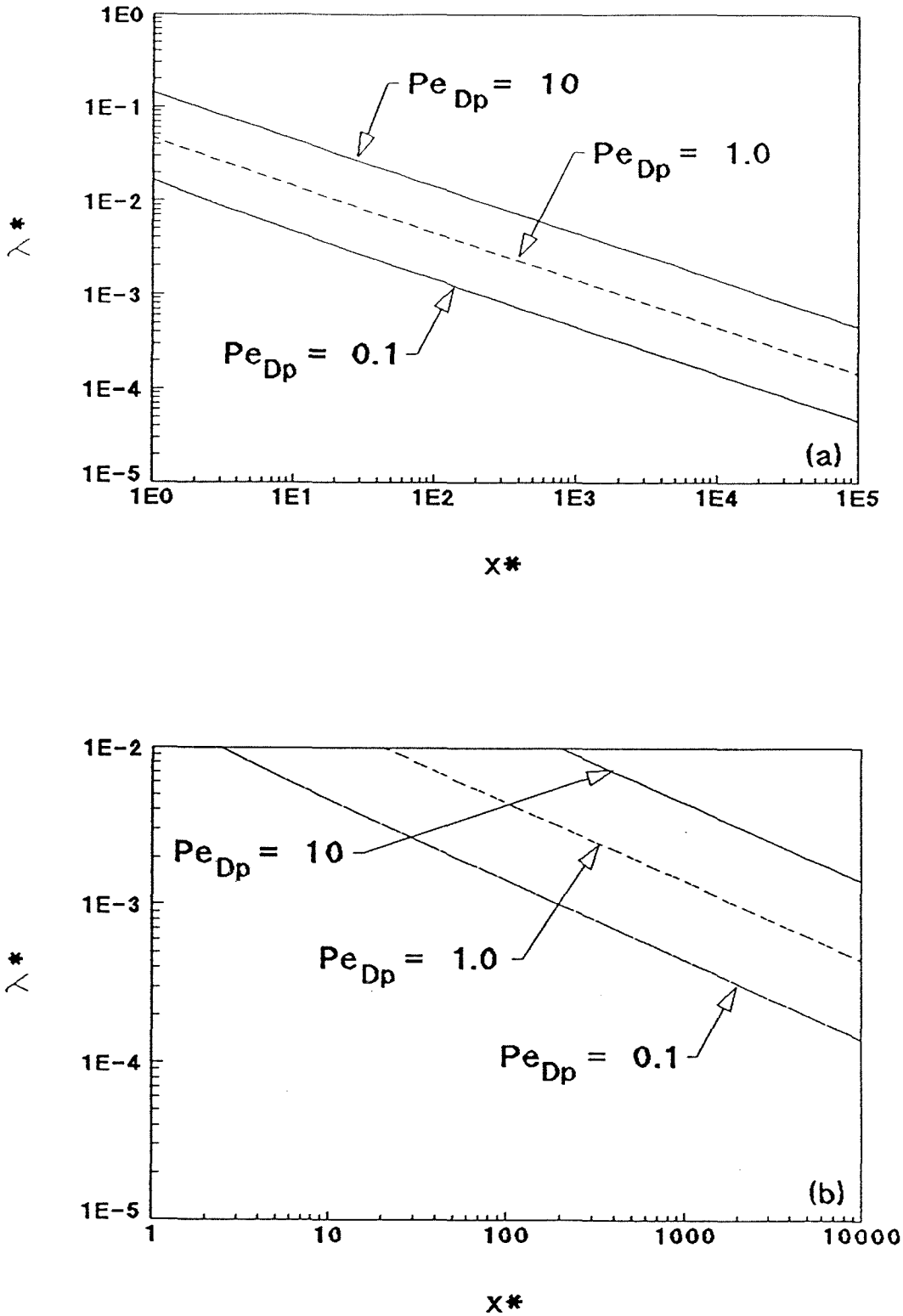

Fig. 3.3: 5% error contours for unsteady solutions for various Pe_{Dp}.

figure, the contours are plotted for the maximum possible range of λ^* and a large range of x^*. In part (b), both x^* and λ^* are limited to the range of values encountered in this work. As can be seen in this figure, only for extremely large λ^* is the error more than 5%. A comparison of Figs. 3.2 and 3.3 reveals that the error contours in Fig. 3.3 are shifted toward the lower left. This translation shows that the error for 50% breakthrough is greater than for steady-state for any given set of conditions. Therefore, the greater contribution of error comes from the erfc term and not from the exponential term. However, the error due to the erfc term is asymptotic to zero at both plus and minus infinity. This result of a larger error for 50% breakthrough also supports the assumption that the largest error of the breakthrough occurs at the 50% breakthrough point, and the error in either direction is asymptotic to the steady-state value.

For a second method of measuring the overall error due to the approximation, the two equations describing transient transport are compared by plotting the two equations. These two equations are:

approximate:

$$C'^*(x^*,t^*) = \frac{C^*}{exp[-\lambda^* x^*]} = \frac{1}{2}\, erfc\left[\sqrt{Pe_{Dp}}\left(\frac{x^* - t^*}{2\sqrt{t^*}}\right)\right] \qquad (3.24)$$

exact:

$$C'^* = \frac{C^*}{exp[\alpha^* x^*]} = \frac{1}{2}\, erfc\left[\sqrt{Pe_{Dp}}\left(\frac{x^* - \{t^*\}\left\{1 - \frac{2\alpha^*}{Pe_{Dp}}\right\}}{2\sqrt{t^*}}\right)\right] \qquad (3.25)$$

$$where:\ \alpha* = \frac{1}{2}Pe_{Dp}\left(1 - \sqrt{1 + \frac{4\lambda*}{Pe_{Dp}}}\right). \qquad (3.16)$$

The first set of figures shows the actual shape of the breakthroughs. Figs. 3.4 and 3.5 show forward breakthroughs from the perspective of fixed t* and x*. In these figures, the approximate breakthrough solution (Eq. (3.26)) is compared to the conservative tracer breakthrough solution, which is either Eq. (3.24) or Eq. (3.26) with $\lambda^* = 0$. This shows that for the approximate solution, particle transport is conservative if the concentration at any time or distance is scaled by the expected steady-state concentration at the given distance. In Fig. 3.6, progressive approximate breakthroughs are compared to the approximate steady-state solution for several values of t*. Figs. 3.7 - 3.10 show comparisons of the approximate versus exact unsteady filtration breakthrough solutions for fixed x* or t*. In these figures, parts (a,b,c) show different values of λ^*. Figs. 3.7 and 3.9 show forward breakthroughs, while Figs. 3.8 and 3.10 show reverse breakthroughs. These figures show that the difference between the two solutions only becomes important when the concentration is extremely small (λ^* is large).

The main results of this analysis are as follows. First, the approximate equation (Eq. (3.26)) can be inverted in order to directly determine Pe_{Dp} from experimental data. Second, for the range of variables encountered in this work, the error from using the approximate equation is small (Error < 5%) and is less than the experimental error. Third, the relative error between the approximate and exact equations only becomes important at extremely small concentration

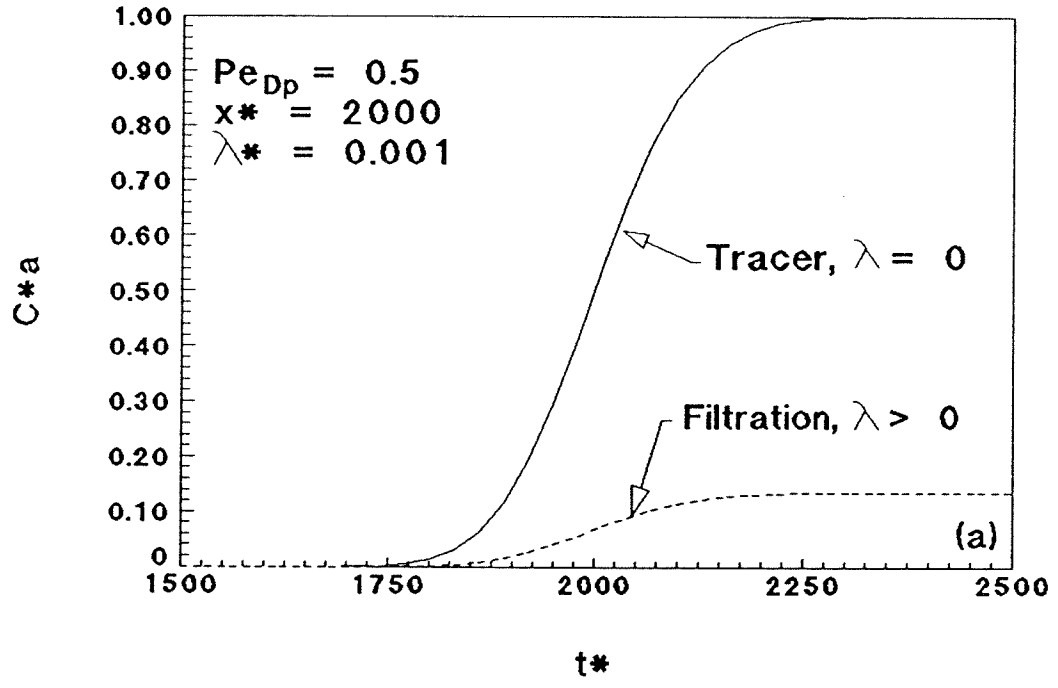

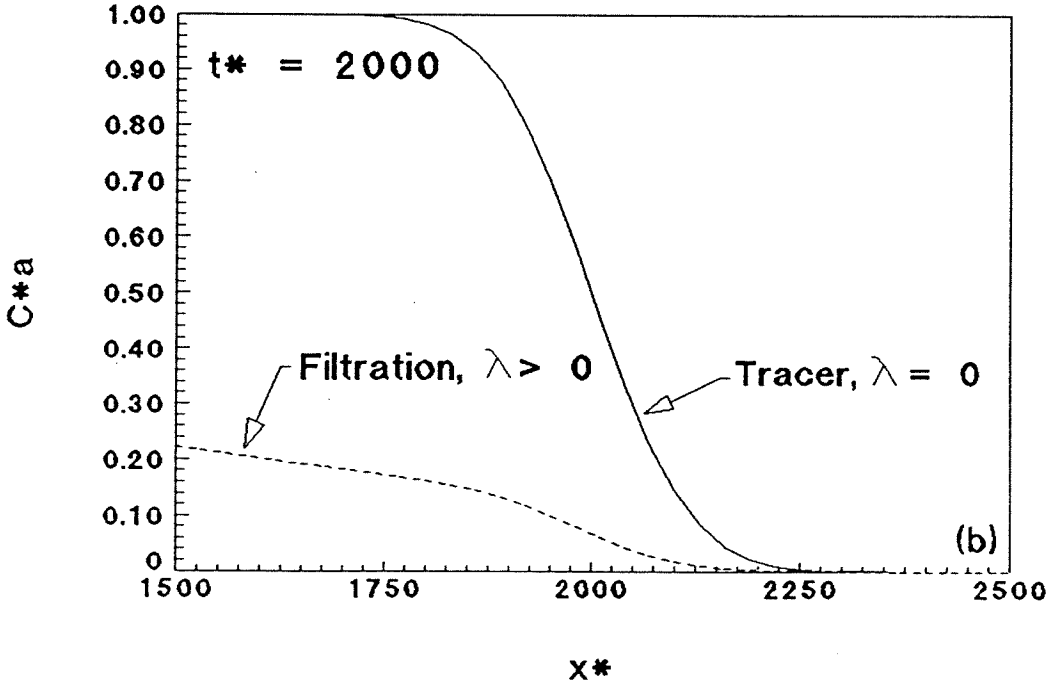

Fig. 3.4: Comparison of unsteady conservative tracer breakthroughs versus approximate unsteady filtration, forward breakthroughs ($\lambda^* = 0.001$).

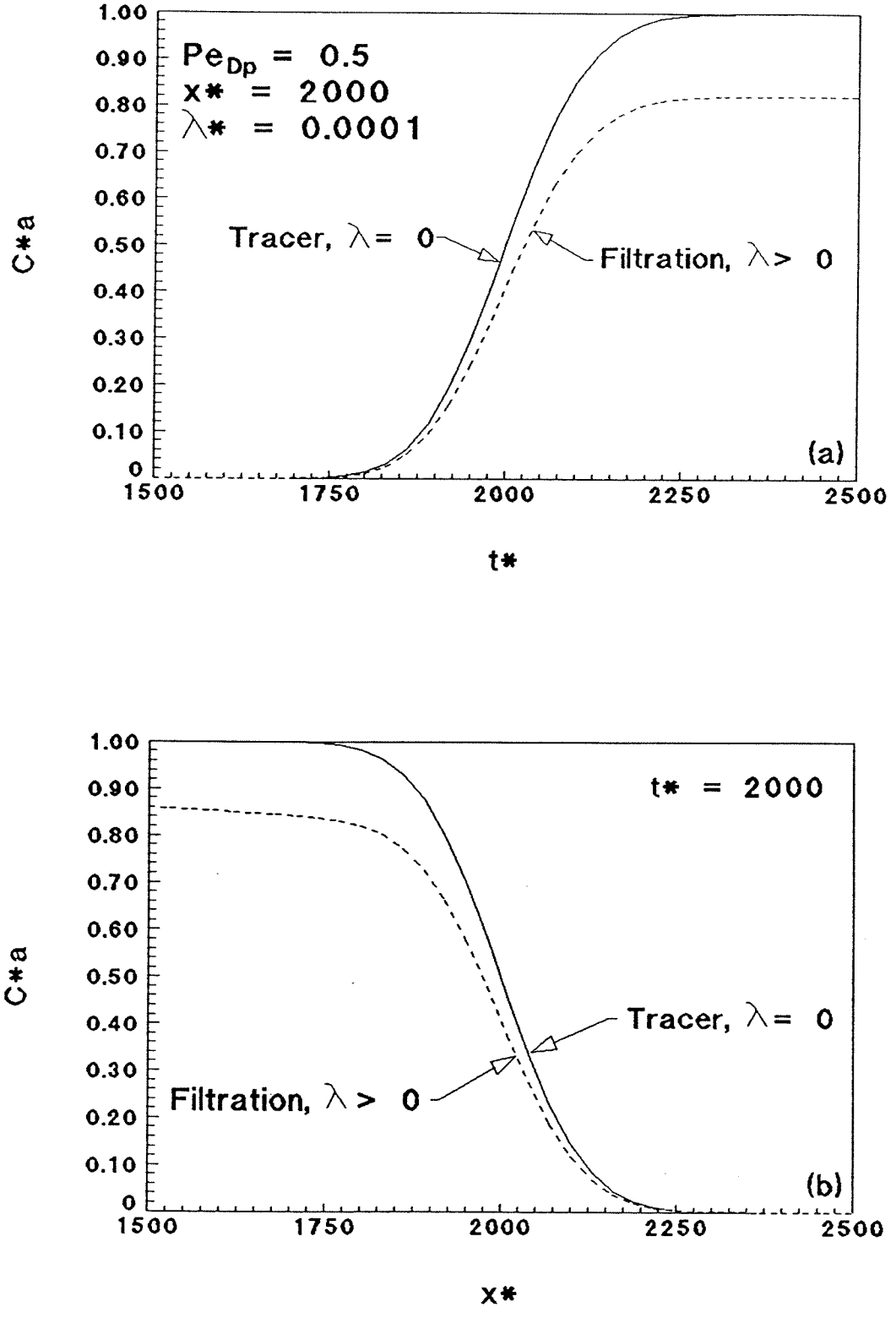

Fig. 3.5: Comparison of unsteady conservative tracer breakthroughs versus approximate unsteady filtration, forward breakthroughs ($\lambda^* = 0.0001$).

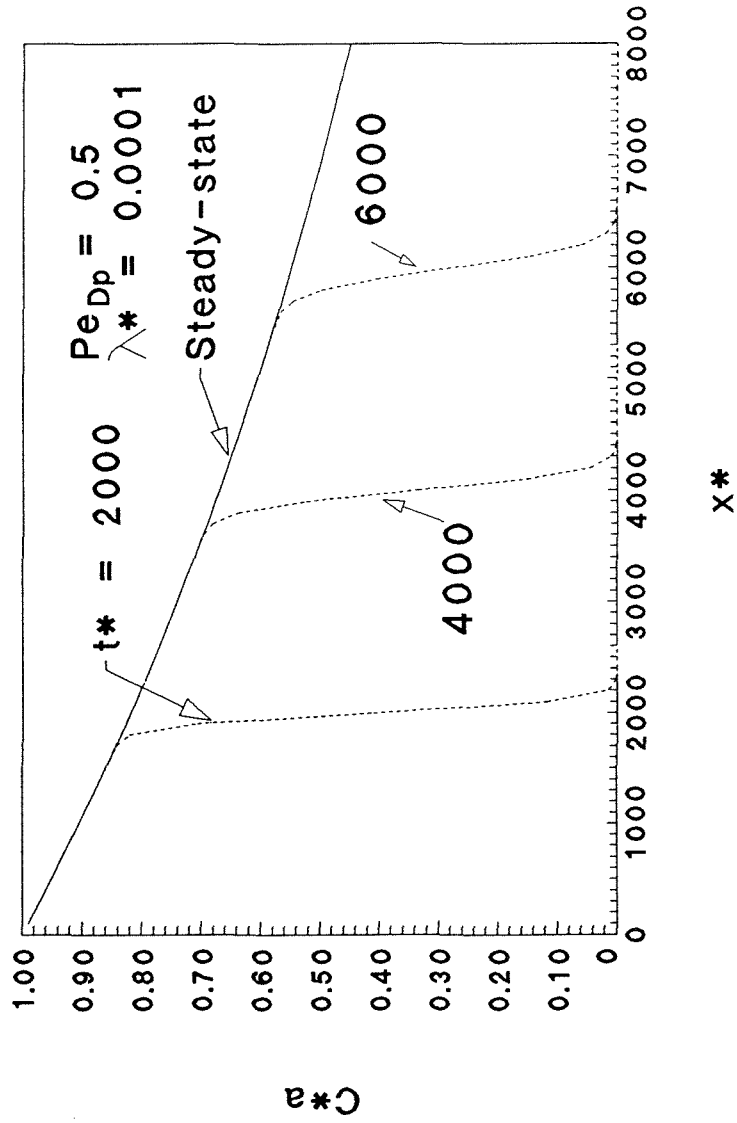

Fig. 3.6: Comparison of progressive approximate unsteady filtration forward breakthroughs for various values of t* compared to the approximate steady-state solution.

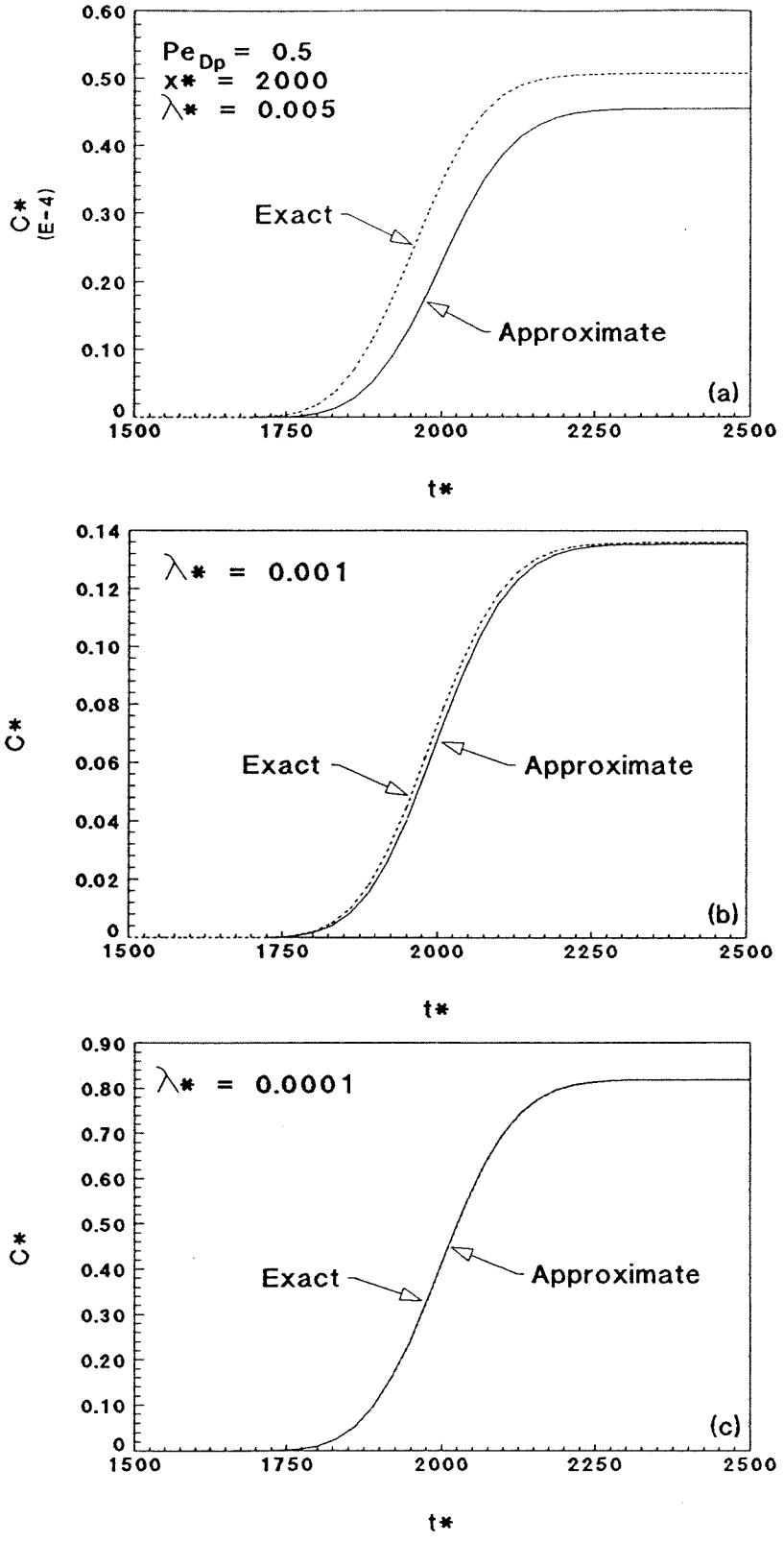

Fig. 3.7: Comparison of the approximate versus exact unsteady filtration forward breakthroughs for fixed x*.

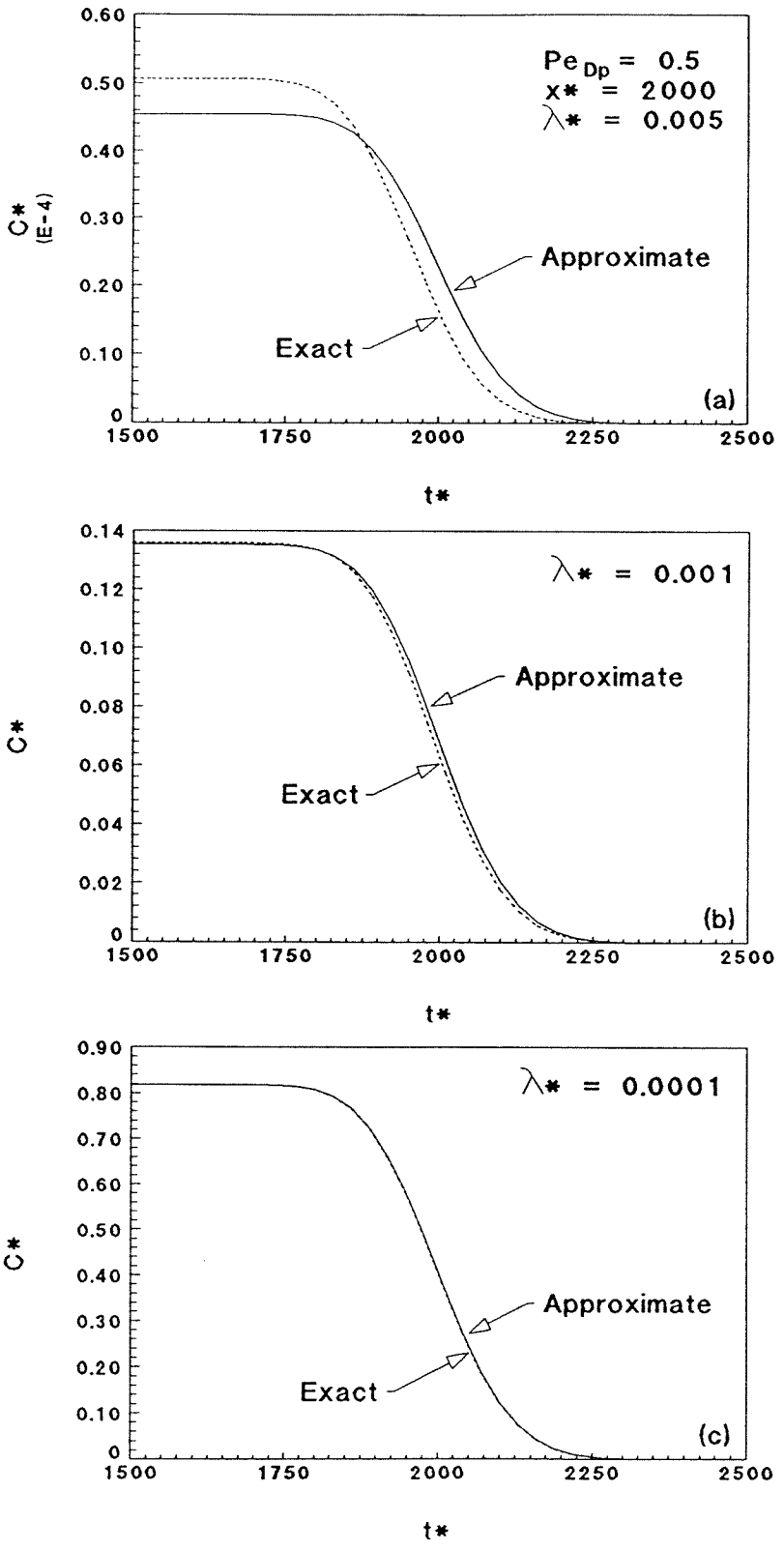

Fig. 3.8: Comparison of the approximate versus exact unsteady filtration reverse breakthroughs for fixed x*.

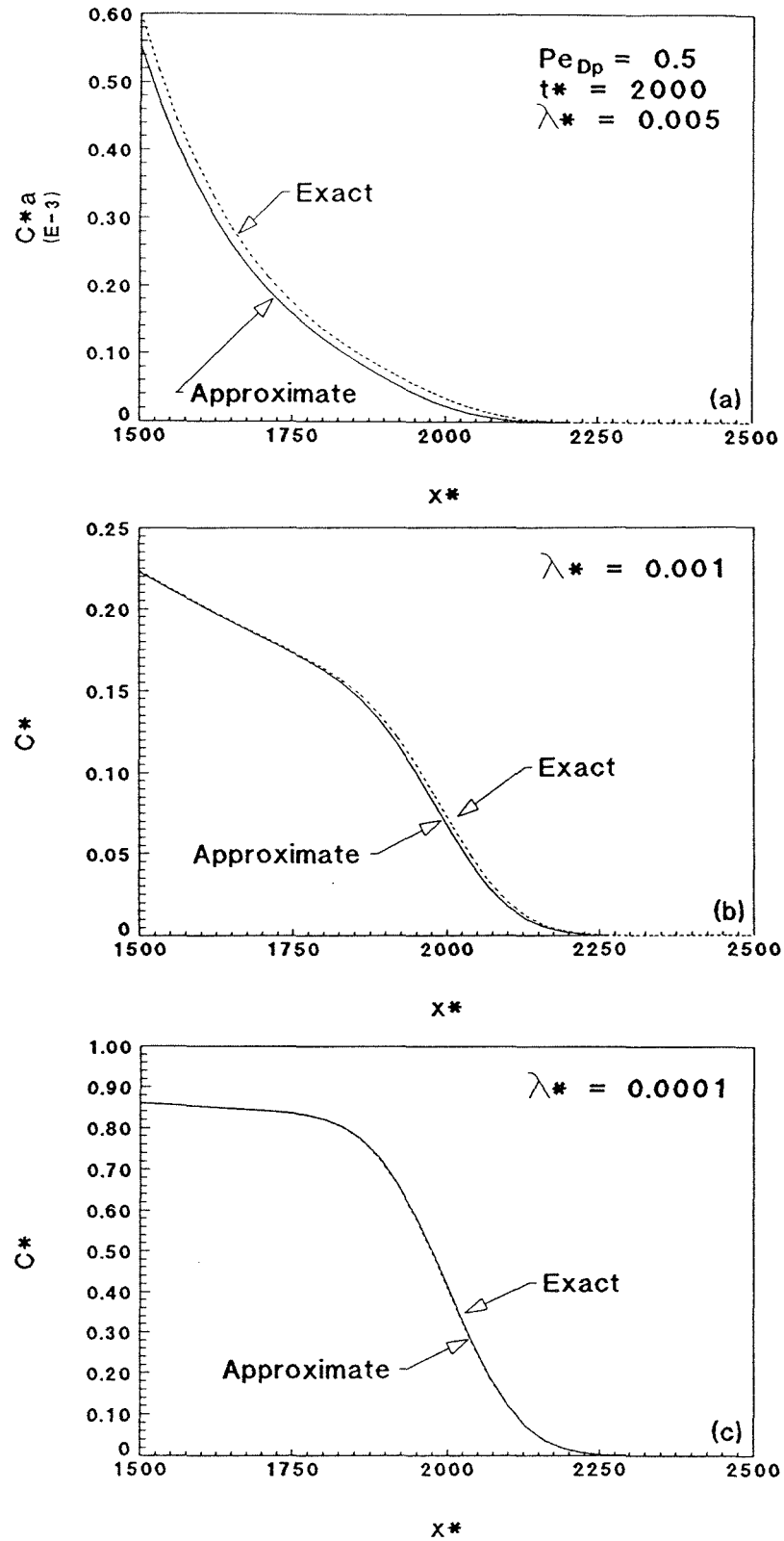

Fig. 3.9: Comparison of the approximate versus exact unsteady filtration forward breakthroughs for fixed t*.

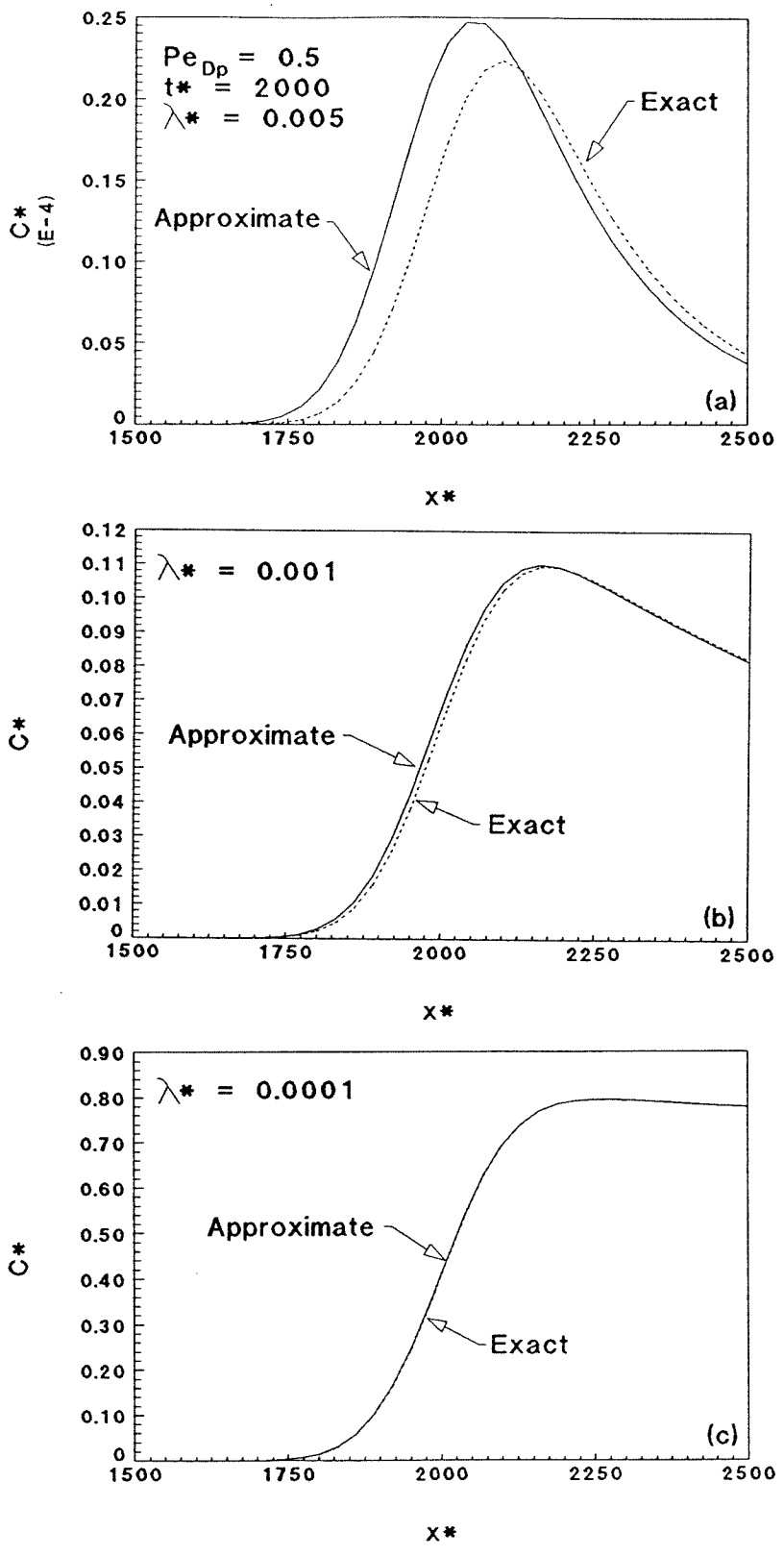

Fig. 3.10: Comparison of the approximate versus exact unsteady filtration reverse breakthroughs for fixed t*.

values. These concentration values are only of importance in a mathematical sense, because they are far too small to be distinguishable in a practical application.

3.3.4 Unsteady Transport With Unsteady Filter Coefficient

Up to this point, all analyses have been performed assuming the filter coefficient is constant in time and space. This condition will not be true for coupled breakthroughs in which particles and solutes are simultaneously transporting. In such a system with a saline solute, the particle breakthrough region would be experiencing differing ionic strength effects and subsequent transient filter coefficients. The filter coefficients would be variable over time and space according to the breakthrough profile of the saline tracers.

This system can be modelled by completing a finite central difference numerical analysis on the applicable equation and boundary conditions (Anderson et al. 1984; Gerald and Wheatley 1984; Golub and Van Loan 1983; Bear and Verruijt 1987; Hornbeck 1975). The proper advective-dispersion equation in dimensionless form with all possible time- and space-dependent variables is:

$$\frac{\partial C*[x*,t*]}{\partial t*} = \frac{1}{Pe_{Dp}} \frac{\partial^2 C*[x*,t*]}{\partial x*^2} - \frac{\partial C*[x*,t*]}{\partial x*} - \lambda*[x*,t*]C*[x*,t*] \tag{3.22}$$

with previous boundary and initial conditions for an infinite medium. The following is a description of this finite central difference numerical analysis.

Perform a Crank-Nicholson central difference scheme on the transport equation (Eq. (3.22)):

$$\frac{1}{2}\left(\frac{1}{Pe_{Dp}}\right)\left(\frac{C*_{j+1,k+1}-2C*_{j+1,k}+C*_{j+1,k-1}}{(\Delta x*)^2}+\frac{C*_{j,k+1}-2C*_{j,k}+C*_{j,k-1}}{(\Delta x*)^2}\right) - \frac{C*_{j,k+1}-C*_{j,k-1}}{2(\Delta x*)} - \lambda*_{j+1,k}C*_{j+1,k} = \frac{C*_{j+1,k}-C*_{j,k}}{\Delta t*} \tag{3.30}$$

Solve for $C^*_{j+1,m}$ (the unknowns) on the left-hand side and $C^*_{j,m}$ (the knowns) on the right-hand side of Eq. (3.30). Such a solution can be put in matrix form:

$$\begin{bmatrix} \gamma & 1 & 0 & \cdots & 0 \\ 1 & \gamma & 1 & \cdots & 0 \\ \ddots & \ddots & \ddots & \ddots & \ddots \\ 0 & \cdots & 1 & \gamma & 1 \\ 0 & \cdots & 0 & 1 & \gamma \end{bmatrix} \times \begin{Bmatrix} C^*_{j+1,1} \\ C^*_{j+1,2} \\ \vdots \\ C^*_{j+1,n-1} \\ C^*_{j+1,n} \end{Bmatrix} = \begin{Bmatrix} \phi_1 - 1 \\ \phi_2 \\ \vdots \\ \phi_{n-1} \\ \phi_n \end{Bmatrix} \tag{3.31}$$

$$\textit{where: } \gamma = -2 - 2Pe_{Dp}(\Delta x*)^2\lambda*_{j+1,k} - 2Pe_{Dp}\left(\frac{(\Delta x*)^2}{\Delta t*}\right)$$

$$\phi_k = \{-1 - Pe_{Dp}(\Delta x*)\}C*_{j,k-1} + \left\{2 - 2Pe_{Dp}\left(\frac{(\Delta x*)^2}{\Delta t*}\right)\right\}C*_{j,k} + \{-1 + Pe_{Dp}(\Delta x*)\}C*_{j,k+1}$$

In this form, the solution process will develop an error referred to as numerical dispersion (Bear and Verruijt 1987). This is due to the forward difference scheme used to calculate the $\partial/\partial t^*$ - term. In this forward difference, the errors are of first order with respect to both Δx^* and Δt^*; whereas, the errors for the $\partial/\partial x^*$ and $\partial^2/\partial x^{*2}$ are of order $(\Delta x^*)^2$. This error associated with the $\partial/\partial t^*$ - term can be reduced by including the second-order derivative in the finite difference equation:

$$\frac{\partial C*}{\partial t*} = \frac{C*_{j+1,k} - C*_{j,k}}{\Delta t*} - \frac{1}{2}\Delta t* \frac{\partial^2 C*}{\partial x*^2} \tag{3.32}$$

By including this term in the transport equation when performing a Crank-Nicholson central difference scheme, Eq. (3.30) becomes:

$$\frac{1}{2}\left(\frac{1+\omega}{Pe_{Dp}}\right)\left(\frac{C*_{j+1,k+1}-2C*_{j+1,k}+C*_{j+1,k-1}}{(\Delta x*)^2}+\frac{C*_{j,k+1}-2C*_{j,k}+C*_{j,k-1}}{(\Delta x*)^2}\right) \tag{3.33}$$
$$- \frac{C*_{j,k+1}-C*_{j,k-1}}{2(\Delta x*)} - \lambda*_{j+1,k}C*_{j+1,k} = \frac{C*_{j+1,k}-C*_{j,k}}{\Delta t*}$$

$$\textit{where: } \omega = \frac{1}{2}\Delta t* Pe_{Dp} \quad \textit{for } 2^{nd}\textit{-order}$$
$$= 0 \quad \textit{for } 1^{st}\textit{-order}$$

The matrix of this solution looks the same except for the values of γ and Φ:

$$\textit{where: } \gamma = -2 - 2\frac{Pe_{Dp}}{1+\omega}(\Delta x*)^2\lambda*_{j+1,k} - 2\frac{Pe_{Dp}}{1+\omega}\left(\frac{(\Delta x*)^2}{\Delta t*}\right)$$

$$\phi_k = \left\{-1 - \frac{Pe_{Dp}}{1+\omega}(\Delta x*)\right\}C*_{j,k-1} + \left\{2 - 2\frac{Pe_{Dp}}{1+\omega}\left(\frac{(\Delta x*)^2}{\Delta t*}\right)\right\}C*_{j,k}$$
$$+ \left\{-1 + \frac{Pe_{Dp}}{1+\omega}(\Delta x*)\right\}C*_{j,k+1}$$

A second method of countering the numerical dispersion is to incorporate the error into the velocity term. For this method, a solution is first found for the case which uses the first-order forward differences for the time derivative. The input velocity can then be modified by considering the velocity calculated numerically. The results of this numerical analysis are shown in Figs. 3.11 - 3.14 which are discussed in the next section.

In these equations, a functional representation for $\lambda^*_{m,n}$ ($\lambda^*_{m,n}$ = F[I]) is needed as input to the matrix. The first step in determining λ^* is to calculate the transient ionic strength values. The equation for transient ionic strength breakthrough is the equation of conservative solute tracer transport:

$$\frac{\partial I*}{\partial t'*} = \frac{1}{Pe_D}\frac{\partial^2 I*}{\partial x*^2} - \frac{\partial I*}{\partial x*} \tag{3.34}$$

$$\textit{where: } I* = \frac{I - I_b}{I_e - I_b};$$
$$e \Rightarrow \textit{end, } b \Rightarrow \textit{beginning;}$$
$$t'* = \frac{V_s t}{d_g}; \textit{ and}$$
$$Pe_D = \frac{V_s d_g}{D_L}.$$

with infinite medium conditions:

boundary conditions:

$$\begin{aligned} &1)\ \lim_{x*\to-\infty} I*(x*,t'*) = 1; \textit{ and} \\ &2)\ \lim_{x*\to+\infty} I*(x*,t'*) = 0. \end{aligned} \tag{3.34.1}$$

initial conditions:

$$\begin{aligned} &1)\ I*(x*,0) = 1 \qquad x*<0; \textit{ and} \\ &2)\ I*(x*,0) = 0 \qquad x*>0. \end{aligned} \tag{3.34.2}$$

and a solution in dimensionless terms:

$$I* = \frac{1}{2}\, erfc\left[\sqrt{Pe_D}\left(\frac{x* - t'*}{2\sqrt{t'*}}\right)\right] \tag{3.35}$$

This erfc equation describes the salt concentration for all times and positions. As mentioned previously, the filter coefficient is known to be a function of the ionic strength of the system:

$$\frac{\lambda}{\lambda_f} = F\left[\kappa a_p (Pe_p)^{-\frac{1}{3}}\right] \tag{3.8}$$

By coupling Eqs. (3.35) and (3.8) and by knowing the functional relationships of Eq. (3.8), the transient filter coefficient caused by the saline breakthrough can be determined.

In this finite difference scheme, the criterion for stability is:

$$\beta = \frac{1}{Pe_{Dp}}\left(\frac{\Delta t*}{\Delta x*^2}\right) \leq \frac{1}{2} \tag{3.36}$$

In order to implement this numerical model, the relationship between dimensionless times and distances (t*,x*) needs to be determined. This analysis is performed by scaling between fluid terms and particle terms. Such a scaling is needed because the velocities for the particles and fluid are not necessarily equal. If not corrected, the full effect of variant velocities will not be seen, and the model will not correctly match experimental results.

First consider the variables responsible for completing the difference, the time and space variables:

$$x* = \frac{x}{d_g} \; , \; x'* = \frac{x}{d_g}; \; and$$
$$t* = \frac{V_p t}{d_g} \; , \; t'* = \frac{V_s t}{d_g}.$$

Regardless of the reference considered (fluid or particles), the variables real space and real time (x,t) are the same. When choosing $(x^*,t^*) \rightrightarrows (\Delta x^*,\Delta t^*)$, corresponding $(x'^*,t'^*) \rightrightarrows (\Delta x'^*,\Delta t'^*)$ are needed to keep the same (x,t). As can be seen, $x^* = x'^*$, but the following show the necessary transformations for t^* and t'^* and Δt^* and $\Delta t'^*$:

$$t* = \frac{V_p t}{d_g} \; ; \; t'* = \frac{V_s t}{d_g}$$
$$t = \frac{t* d_g}{V_p} \Rightarrow t = \frac{t'* d_g}{V_s}$$

by letting t = t:

$$t'* = t*\left(\frac{V_s}{V_p}\right) \tag{3.37}$$

also:

$$\Delta t* = t*_2 - t*_1 \; , \; \Delta t'* = t'*_2 - t'*_1$$

substituting for t'^* in this equation:

$$\Delta t'* = \Delta t*\left(\frac{V_s}{V_p}\right) \tag{3.38}$$

These scale changes can now be incorporated into both Eq. (3.35) and the finite difference model for t'^* and $\Delta t'^*$ (Eq. (3.31)) to complete the numerical

analysis.

3.3.4.1 Numerical Model Implementation and Comparison to Analytical

The accuracy of this numerical model as compared to analytical solutions was checked by performing several simulations in which the filter coefficient remained constant. The results of such runs are shown in Figs. 3.11 - 3.14. In each of these figures, part (a) shows the actual shape of breakthroughs and part (b) shows the difference between the analytical solution and the numerical simulation. These figures show the four possible combinations of constant filter coefficient. These are forward and reverse breakthroughs with either zero or positive filtration.

These figures show the difference between simulations using a first-order and a second-order time derivative. The errors of using a simple first-order time derivative are reduced using a second-order time derivative. The second-order time derivative is used for all of the rest of this work including Chapter 5.

These figures show that the numerical model can accurately match the analytical solutions for conservative and filtration-influenced breakthroughs. Model calculations for cases with variable I and λ will be shown in comparison with experiments in Chapter 5.

3.4 Conclusions

In this chapter, a mass-balance particle transport equation which includes filtration has been developed and an analytical solution was derived for the case of a constant filter coefficient. This model includes transport parameters which

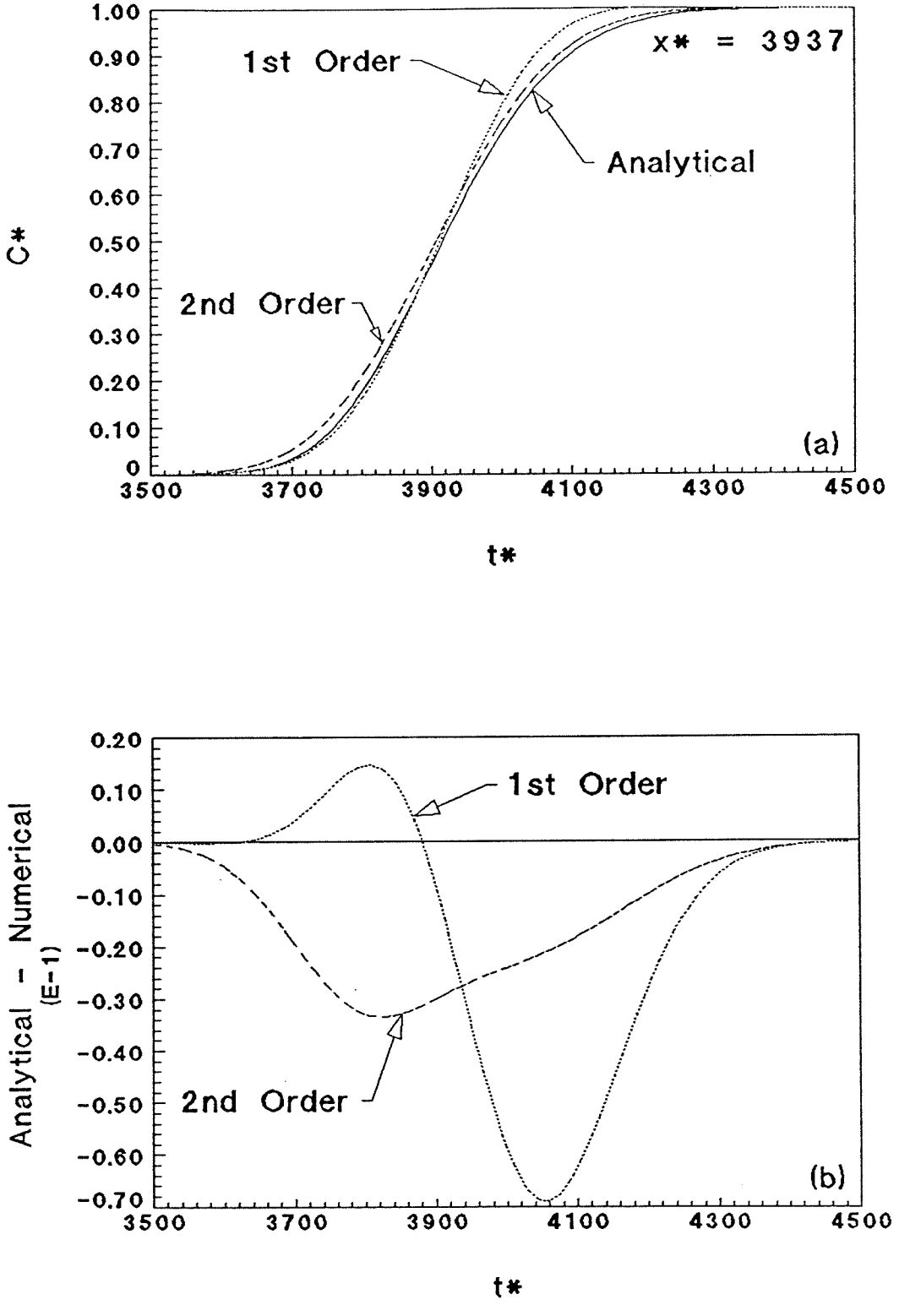

Fig. 3.11: Comparison of numerical and analytical forward breakthroughs for $\lambda^* = 0$.

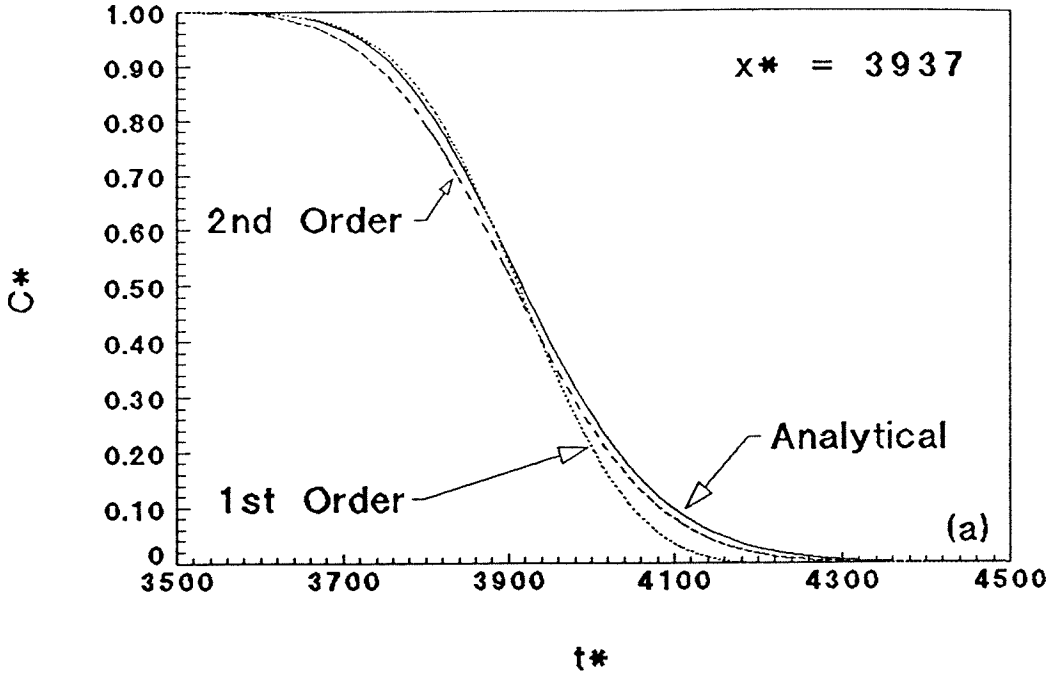

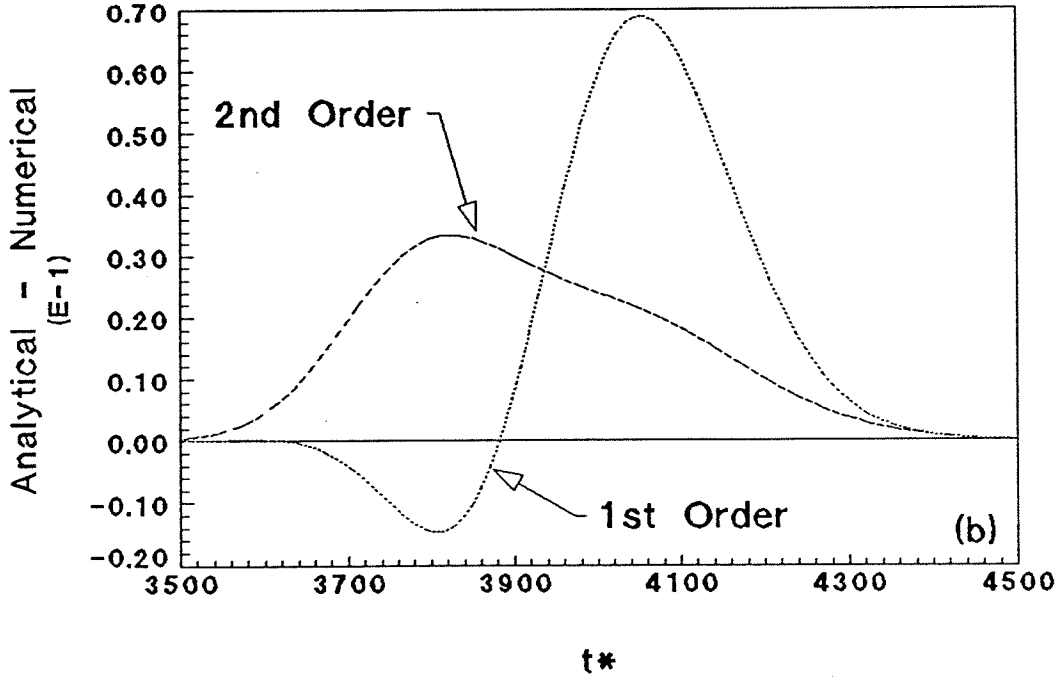

Fig. 3.12: Comparison of numerical and analytical reverse breakthroughs for $\lambda^* = 0$.

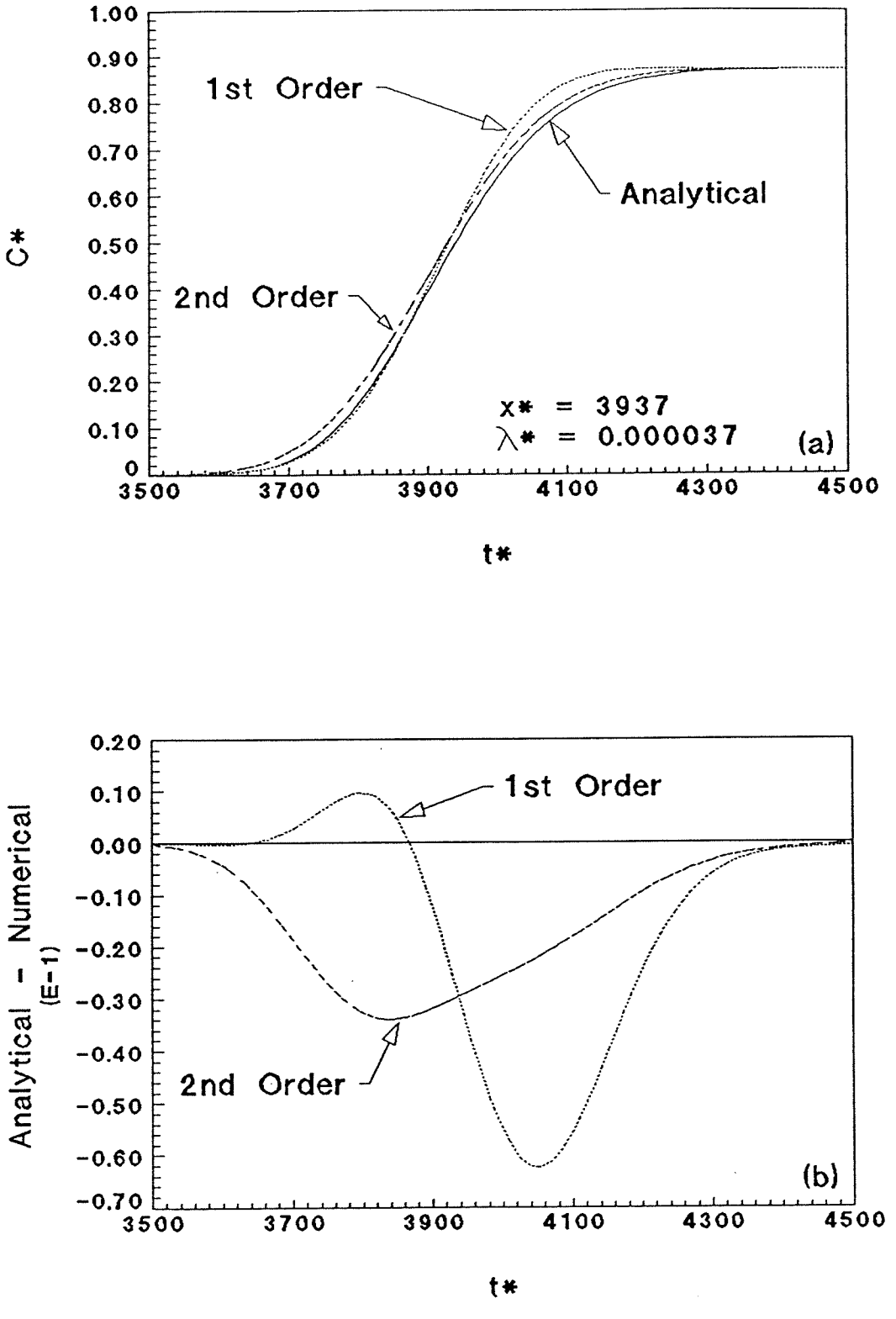

Fig. 3.13: Comparison of numerical and analytical forward breakthroughs for $\lambda^* > 0$.

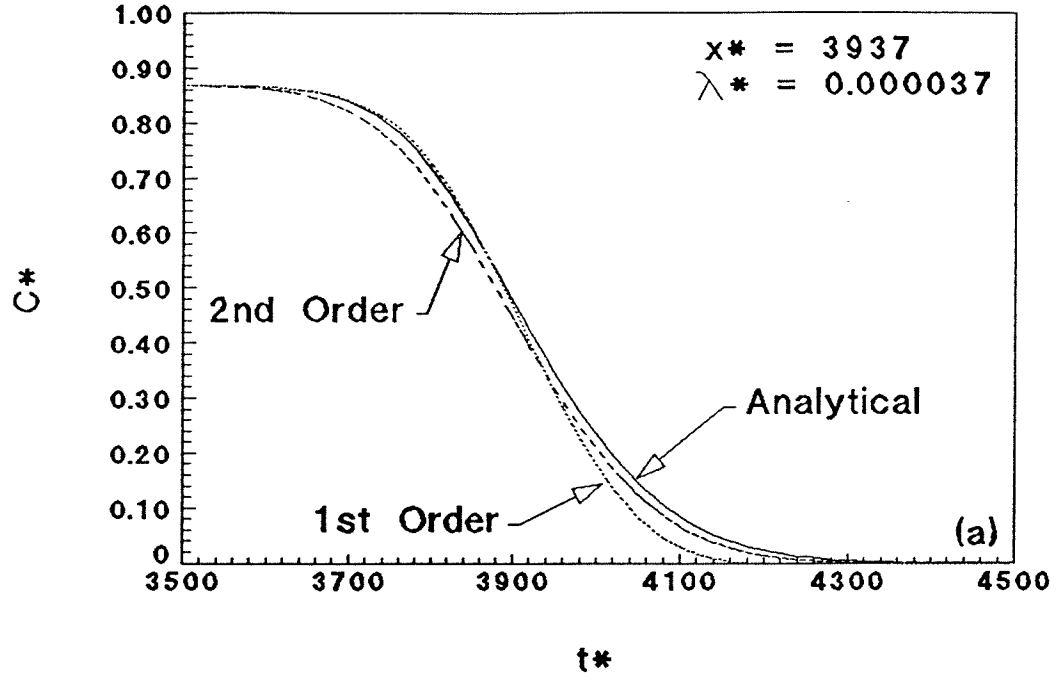

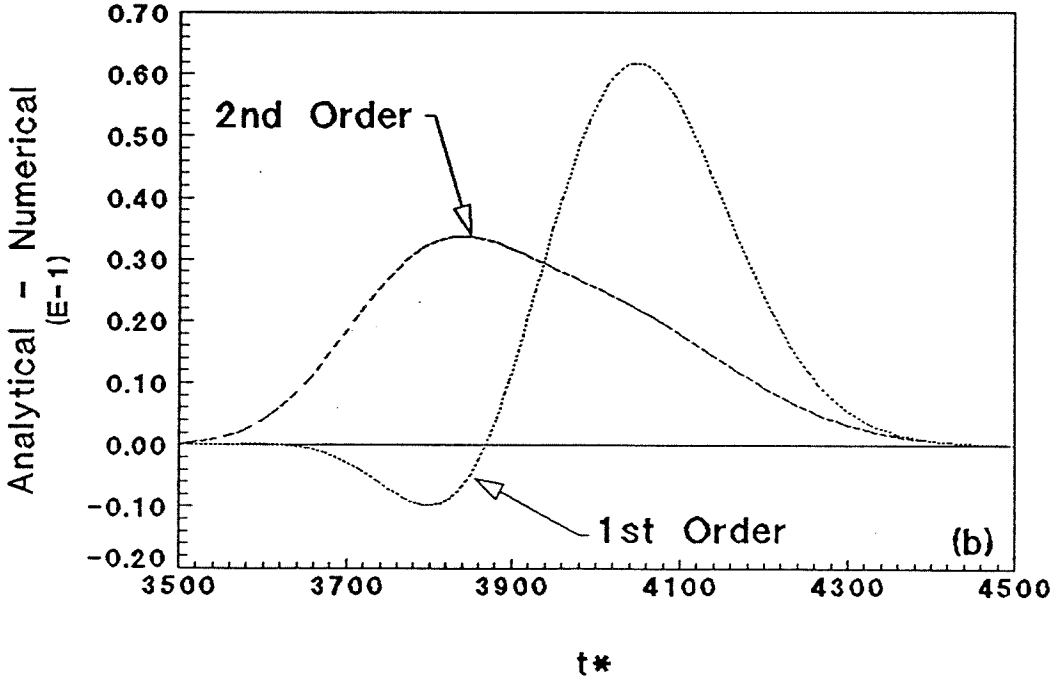

Fig. 3.14: Comparison of numerical and analytical reverse breakthroughs for $\lambda^* > 0$.

are particle advective velocity, particle longitudinal dispersion coefficient, and filter coefficient. These parameters have been defined by dimensional analysis using the pertinent variables of this porous media system. The transport equation has been approximated so that the particle longitudinal dispersion coefficient can be calculated directly from experimental data, and the accuracy of this approximation for the range of variables used in this work was checked and found to be acceptable (error $<<$ 10%). Finally, a numerical model was developed for the general case of a transient filter coefficient. The accuracy of this model for the cases of conservative transport and constant filter coefficient was checked by comparing the results to that of the analytical solutions and found to be acceptable (error $<<$ 10%).

4. APPARATUS AND METHODS

To test the theories developed in Chapter 3, a laboratory investigation was undertaken to measure particle advective velocity, particle longitudinal dispersion, and filter coefficient on one uniform granular medium. No known experimental study has provided measurements of particle dispersion. In this work, the effects of both physical and chemical variables on particle advection, particle longitudinal dispersion, and filtration were studied. In these experiments, the physical variables (particle and grain diameters and flow rate) and the chemical variables (pH and ionic strength) were well-known and -controlled.

The dispersion experiments were carried out in a packed column which is shown in Fig. 4.1. Three different sets of breakthrough experiments were performed. These are salt tracer breakthroughs using NaCl, simple particle breakthroughs, and coupled breakthroughs. These experiments consist of a breakthrough water displacing an existing water from the column. As the displacing water transports through the column, the initially sharp interface between the two waters mixes. This mixing transforms the sharp interface into a zone of intermediate concentration of either particles or salt. The mixed zone continuously increases in length as the waters continue to transport downstream.

For forward salt tracer breakthroughs, the existing column water was non-saline clean water, and the experimental breakthrough water was saline clean water. For reverse salt tracer breakthroughs, the existing column water was saline clean water, and the experimental breakthrough water was non-saline clean water.

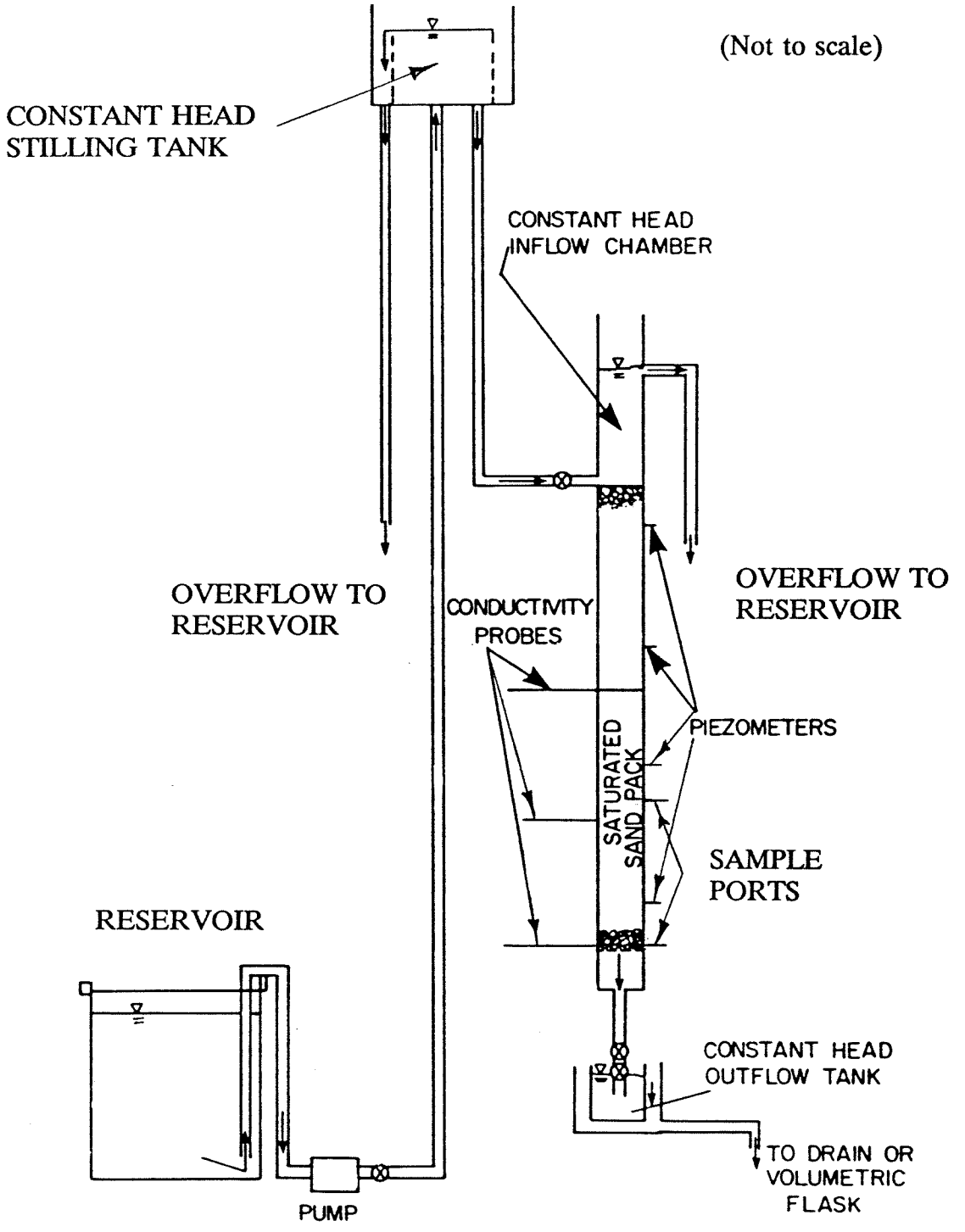

Fig. 4.1: Packed column apparatus showing flow system (modified from Houseworth (1984)).

For the simple particle breakthrough experiments, the salt concentrations in both the particle breakthrough water and the existing column clean water were kept constant. In these simple particle breakthrough experiments for forward particle breakthroughs, the existing column water was clean water, and the experimental breakthrough water was the particle suspension. For reverse particle breakthroughs, the existing column water was particles, and the experimental breakthrough water was clean water. A final set of dispersion experiments consisted of coupling particle and salt tracer breakthroughs. In these experiments as the particle and saline fronts concurrently transport through the column, the mixing zone of the salt results in a variable filter coefficient which produces variable filtration of the transporting particles.

Measurements of either particle or salt concentrations at a given position during the passage of the mixed zone comprise a breakthrough curve. Salt concentrations are measured by using conductivity probes placed in the column, and particle concentrations are measured by extracting water samples from the column using syringes and needles. From the measured concentration history, a longitudinal dispersion coefficient can be obtained. The advective velocity is determined from the time for 50% breakthrough. The filter coefficient is measured from the particle concentration plateau in the dispersion experiments.

In these experiments, special attention was focused on maintaining a constant chemical system. In this work, the operating pH for the breakthrough experiments was set at 8 as discussed previously, established by adding NaOH

base to the reservoir water, and then maintained by adding prescribed amounts of $NaHCO_3$ buffer to the reservoir water. The temperature was measured during each experiment and remained in the range of 23 to 25°C.

4.1 Packed Column

The dispersion experiments are carried out in a packed column, in which a one-dimensional flow proceeds from top to bottom. This arrangement is similar to one used by Rumer (1962) and Houseworth (1984), and the column is the same one used by Houseworth (1984) but has been modified for particle sampling. The column is a clear lucite tube with an inside diameter of 89 mm. The sand occupies a 1.539 m long section of the column, and is held in by an end screen at the bottom. This column is shown in Fig. 4.1.

The size of the column has been chosen, so that both the boundary effects at the inlet, outlet, and the wall are negligible, and a natural system is more closely simulated. Theoretical and experimental work for uniform media presented by Cohen and Metzner (1981) suggest that a ratio of the column diameter to the grain diameter greater than 30 is necessary to avoid significant wall boundary effects. For the uniform medium of this work, this ratio using the geometric mean grain diameter is 233. Houseworth (1984) showed that by 48 grain diameters downstream, inlet and outlet boundary effects are negligible. Using infinite medium boundary conditions versus some type of finite length conditions produces less than 1% maximum error. For this work, the length of the column is almost 4000 grain diameters. The real constraint on the length of

the column is the length needed for an adequate breakthrough width from which to sample. The breakthrough widths need to be large enough to provide ample sampling time in order to be able to collect data at distinct points on the breakthrough. A more detailed discussion concerning sampling protocol is discussed in section 4.7.

Piezometer tubes are connected along the column at four locations as measured down from the sand surface: 7.1 cm, 42.7 cm, 78.5 cm, and 131.7 cm. Valves are placed in all of the piezometer lines, so that the column may be made air tight when a vacuum is applied to draw water into the column during the saturation process. This is shown in Fig. 4.2.

Changes in salinity within the column are detected by conductivity probes placed inside the column at three locations as measured down from the sand surface: 60.5 cm, 105 cm, and 149.4 cm. These are shown in Fig. 4.2. The probes are inserted into the column such that the probe's conducting plates are located along the column axis. The probes which were constructed in the Keck Lab. machine shop are held and sealed by swagelock fittings attached to the column. The probe design is described in detail by Houseworth (1984). The probes are connected directly to a Ysi conductance meter. This meter in turn is connected to a PC for analog-to-digital (A/D) data translation.

Changes in particle concentrations within the column are measured by withdrawing samples from within the column through sample ports. The sample ports which were used in this work are placed along the column at two locations

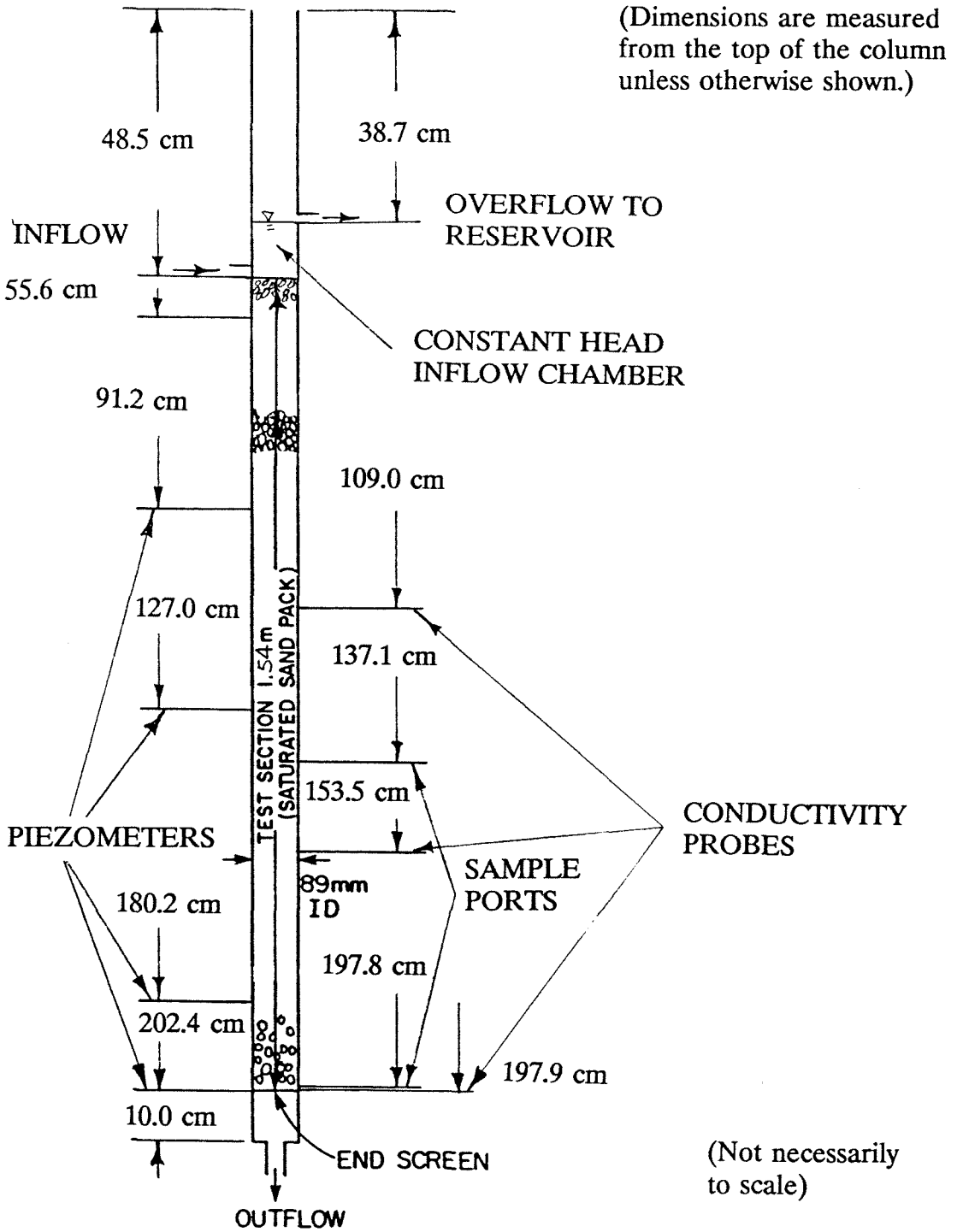

Fig. 4.2: Packed column for miscible displacement experiments showing conductivity probes, piezometers, and sample ports (modified from Houseworth (1984)).

as measured down from the sand surface: 88.6 cm and 149.3 cm. These ports consist of swagelock fittings which have been closed on rubber-silicon membranes. The samples are withdrawn at a distance of approximately 1.2 cm from the inside edge of the column wall by using syringes and hypodermic needles. This distance is approximately 30 grain diameters for which wall effects should be negligible (Cohen and Metzner 1981). The syringes were Hamilton 1000 series with leur tips and had a 0.25 ml volume. The needles were Hamilton stainless steel in Kel-F hub and were 28 gage with a 0.006 inch inside diameter. Particle concentrations are measured using an HP spectrophotometer. A flowchart of the conductivity and particle sample data acquisition system is shown in Fig. 4.3.

The flow system for the experiments is shown in Fig. 4.1 and described in this paragraph. Water is supplied to the column through three separate supply reservoir systems for fresh water, saline water, and particle suspensions. The water is pumped from the various reservoirs to a stilling tank mounted above the column. This water then flows into the constant head inlet chamber in the column just above the top of the packed sand. Constant head is maintained through an overflow port. Water flowing through the column passes through an end screen into the end chamber of the column. The water then passes through a flow control valve which maintains column saturation before flowing through a flowmeter. The water finally drains into a constant head outflow tank. The flow rate is controlled by the flow control valve, and this valve and the flowmeter are kept submerged by the constant head outflow tank.

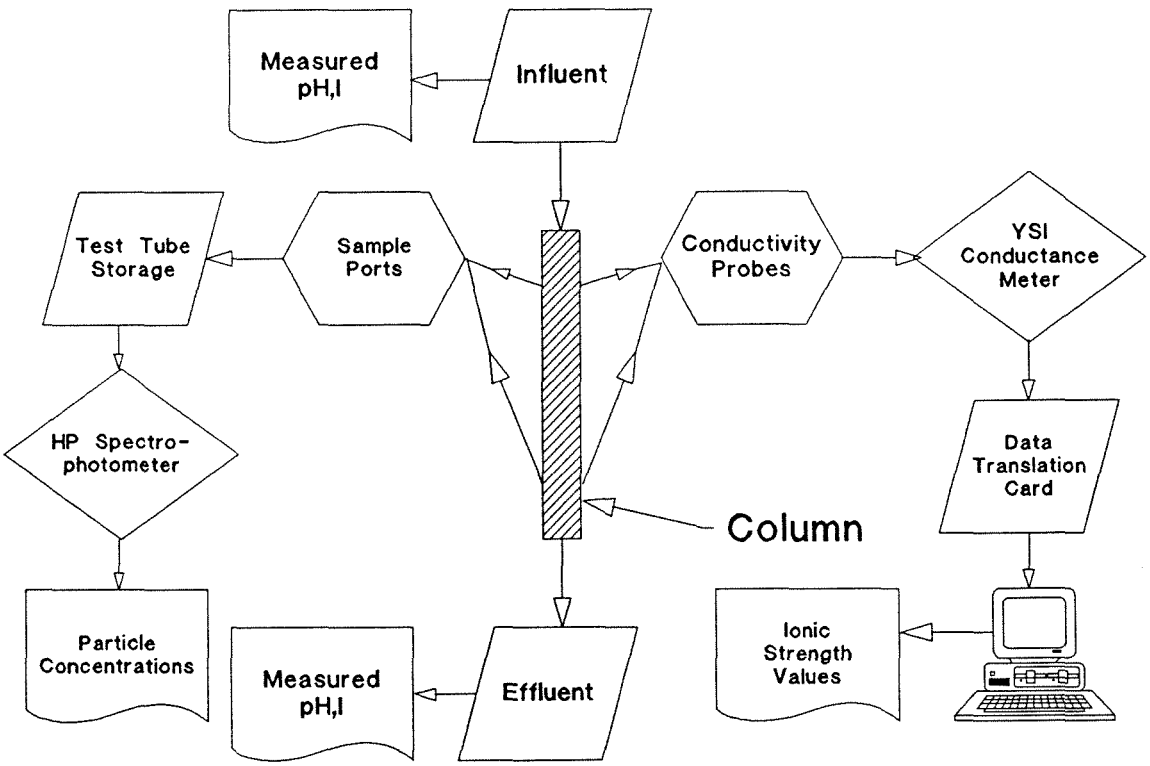

Fig. 4.3: Packed column apparatus showing flowchart of conductivity and particle sample data acquisition system.

All water used in the column is first de-aired under vacuum to remove most of the dissolved gases. The de-aired water will then dissolve any residual gas pockets in the packed column medium, and prevent bubble formation and collection in the medium. Any bubble formation in the medium would greatly affect the filtration and breakthrough results (Aonuma et al. 1981). The water is de-aired under a vacuum of 29 inches of mercury until bubble formation is observed to be minimal which was usually about an hour. A set of 5 gallon glass jugs are connected in parallel to a vacuum line for the de-airing process. The de-aired water is siphoned from the jugs into the supply reservoirs in order to minimize any air re-entrainment during the transfer process. After the de-airing process, the pH of the reservoir is raised to pH = 8, and the necessary amount of the $NaHCO_3$ buffer is added to stabilize this pH.

The column is packed by continuously pouring oven-dry sand into the top of the column. The conductivity probes and piezometer tubes but not the syringe needles are in place in the column before the sand is loaded. The column is overfilled to provide a small amount of extra initial compaction which minimizes additional subsequent compaction which could occur during experimentation due to the head of water in the constant head inlet chamber. No other methods of compacting (e.g., shaking, tapping, or vibrating) are used. All ports and openings are sealed and air is evacuated through a port on the bottom of the column with a vacuum pump. After starting the air evacuation, water is poured into the top of the column, and this inlet chamber is filled to provide extra head to force the

water through the column. This extra head and the vacuum pumping increases the head to saturate the column and causes the water to move quickly through the column with a sharp saturation front while pushing all of the air out in front. The vacuum pump is turned off after the entire packed column has been saturated, and no more air bubbles are observed to exit the media. This vacuum saturation further packs the column, and the excess sand is removed from the top of the column until the test section dimension is reached.

4.2 pH Stabilization

The water used in this work is initially saturated with atmospheric CO_2 and has a pH $\approx$ 5.7. Rather than remove this artifact, an HCO_3^- buffer is used to maintain a constant pH during experimentation. For this work, two possible limiting conditions exist which are an open system in continual equilibrium with the atmosphere and a closed system with a fixed total quantity of CO_2.

The total system will be operated on the open CO_2 system by adding the correct amount of $NaHCO_3$ buffer in order to reach the open CO_2 curve for the given operating pH. In this case, the equation (Stumm and Morgan 1981) for being on the equilibrium curve for the open CO_2 system is:

$$C_T = \frac{1}{\alpha_0} K_H P_{CO_2} \tag{4.1}$$

where: C_T = *total* CO_2 *concentration* (*M*);

$$\alpha_0 = \left(1 + \frac{K_1}{[H^+]} + \frac{K_1 K_2}{[H^+]^2}\right)^{-1};$$

K_1, K_2 = *acidity constants* (*M*);

$[H^+]$ = *concentration of hydrogen ions* (*M*);

K_H = *Henry's law constant* ($M\ atm^{-1}$); *and*

P_{CO_2} = *partial pressure of* CO_2 (*atm*).

For the aqueous CO_2 system open to the atmosphere, the constants in Eq. (4.1) have the following values (Stumm and Morgan 1981) for 25°C:

$$pK_1 = 6.3;$$
$$pK_2 = 10.25;$$
$$pK_H = 1.5;\ \textit{and}$$
$$P_{CO_2} = 10^{-3.5}.$$

In this work, the operating pH = 8. In this case, the total CO_2 needed for equilibrium is 5.14 x 10^{-4} Molar. The initial concentration of CO_2 (pH ≈ 5.7) in the water is 1 x 10^{-5} Molar. This is found from Eq. (4.1) with $\alpha_0 = 1$. The amount of $NaHCO_3$ to be added can be determined from a mass balance equation. The following is the mass balance for total CO_2:

$$V_T C_T = (VC)_{initial} + (VC)_{added} \qquad (4.2)$$

In this equation (Eq. (4.2)), let $V_T = V_{initial}$ (reservoir volume is much greater than volume of buffer added). With this approximation, Eq. (4.2) becomes:

$$(VC)_{added} = V_T(C_T - C_{initial}) \qquad (4.3)$$

In this equation, VC is the volume in liters multiplied by the concentration in moles/liter. For the amount of buffer added, the following is used:

$$(VC)_{added} = (X\ grams\ NaHCO_3)\left(\frac{1\ Mole\ NaHCO_3}{84\ grams\ NaHCO_3}\right)$$
$$= Moles\ of\ NaHCO_3\ buffer\ added.$$

Substituting for the values, Eq. (4.3) becomes:

$$X = V_T(C_T - C_{initial})(84)$$
$$= V_T(5.14 \times 10^{-4} - 1 \times 10^{-5})(84) \qquad (4.4)$$

The final form of Eq. (4.4) for pH = 8 is:

$$X = 4.2336 \times 10^{-2}(V_T) \qquad (4.5)$$

This equation is used to calculate the number of grams of $NaHCO_3$ buffer, X, to be added to a reservoir of volume V_T (liters).

The buffer intensity provided by this amount of CO_2 can be analyzed in two fashions, one for the open system (P_{CO_2} = constant) and a second for a closed system (C_T = constant) (Stumm and Morgan 1981). In this work, the open system best describes flow in the reservoir and constant head tanks, and the closed system best describes flow as soon as it enters the packed column. The buffer equation for the open system is:

$$\beta_{P_{CO_2}} = 2.3\{[H^+]+[OH^-]+C_T[\alpha_1(\alpha_0+\alpha_2)+4\alpha_0\alpha_2+(\alpha_1+2\alpha_2)^2]\} \qquad (4.6)$$

where: $\beta_{P_{CO_2}}$ = *buffer intensity of two-protic acid for* P_{CO_2} = *constant (eq* ℓ^{-1});

$$\alpha_1 = \left(\frac{[H^+]}{K_1} + 1 + \frac{K_2}{[H^+]} \right)^{-1}$$

$$\alpha_2 = \left(\frac{[H^+]^2}{K_1 K_2} + \frac{[H^+]}{K_2} + 1 \right)^{-1}$$

For the open system at pH = 8, the buffer intensity is 5.135×10^{-4} equivalents/liter. The buffer equation for the closed system is:

$$\beta_{C_T} = 2.3\left\{[H^+]+[OH^-]+C_T[\alpha_1(\alpha_0+\alpha_2)+4\alpha_0\alpha_2]\right\} \qquad (4.7)$$

where: β_{C_T} = *buffer intensity of two-protic acid for* C_T = *constant (eq* ℓ^{-1}); *and*

$$C_T = \frac{1}{\alpha_0} K_H P_{CO_2} \ (M).$$

For the closed system at the same pH, the buffer intensity is 1.373×10^{-5} eq/l. These buffering equations are plotted in Fig. 4.4. As can be seen in these equations, C_T for the closed system is determined from the open system curve. These buffer intensities may appear to be small, but measurements of pH for the flow before and after passing through the column showed the pH remained at 8.

4.3 Media Properties and Preparation

The medium used in this work is a uniform, silica sand, was taken from the sand storage in Keck Lab., and is referred to as "Houseworth" sand, because this is the uniform sand used by Houseworth (1984). The characterization of this SiO_2 sand for grain and pore diameters has been completed by Houseworth (1984).

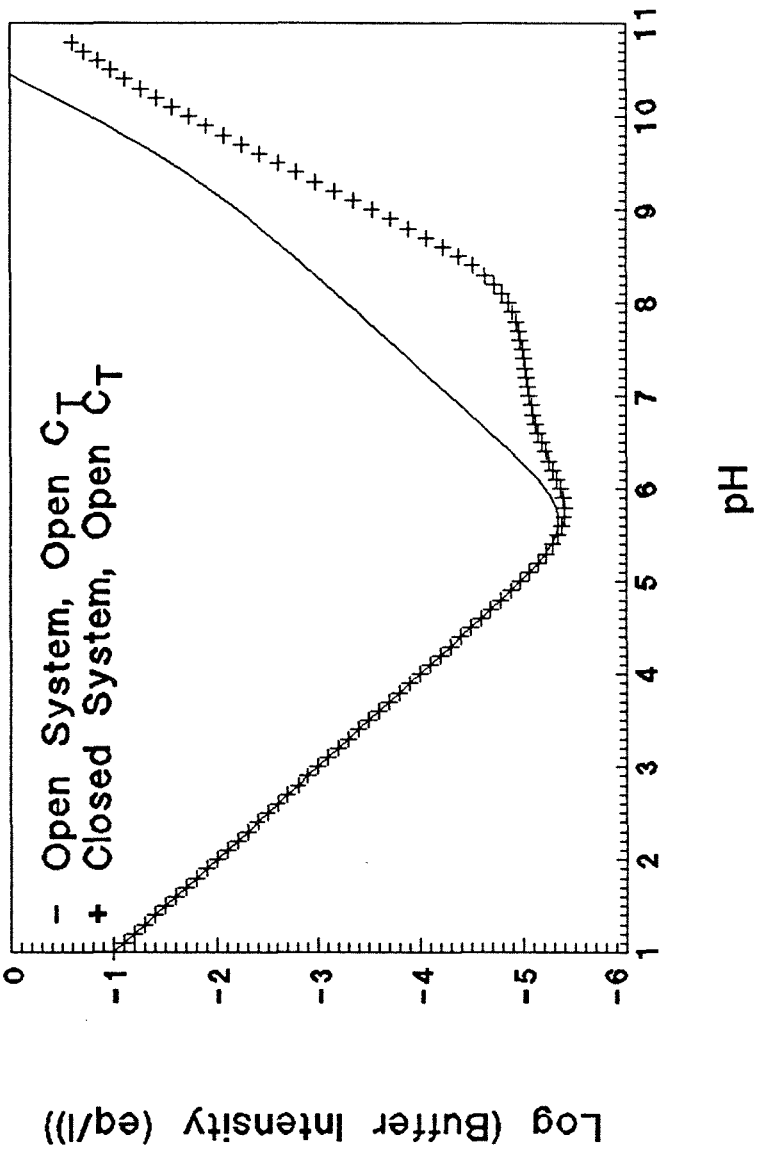

Fig. 4.4: Buffer capacity curve.

The geometric means and standard deviations for volume-weighted and area-weighted distributions for the grain diameter are: d_g = 0.382 mm, σ_g = 1.15; d_g = 0.380 mm, σ_g = 1.16; and the same for volume-weighted and number frequency distributions for the pore radius are: r_a = 0.0679 mm, σ_a = 1.14; r_a = 0.0635 mm, σ_a = 1.27. In this work, the permeability was measured and ranged between 5.5 x 10^{-5} to 7.5 x 10^{-5} mm^2, and the effective porosity also was measured and ranged between 0.25 to 0.33.

The surface chemical structure in terms of surface speciation as a function of pH of an oxide particle has been reviewed in Chapter 2 of this work according to the model given in Stumm and Morgan (1981). For both pure silicon oxide sands and the sand used in this work, the pH_{zpc} is expected to be approximately 2. The Houseworth sand can be seen to have some type of iron impurities leading to a reddish color. A simple surface titration was performed on the sand, and the result was pH_{zpc} = 1.6. The results of this titration are shown in Fig. 4.5. Part (a) of this figure shows the actual titration curve, while part (b) shows the surface charge versus pH which was calculated from the titration data. This result is assuring in that this sand exhibits characteristics similar to those given in the literature. As the pH goes above the pH_{zpc}, the surface of the oxide becomes more and more negatively charged. The system pH for this work is chosen at pH = 8 in order to insure as large a percentage of negative surface charges on the sand and particles and also to remain in a naturally occurring pH range. Additionally, for pH values greater than nine, dissolution of the silicone oxide

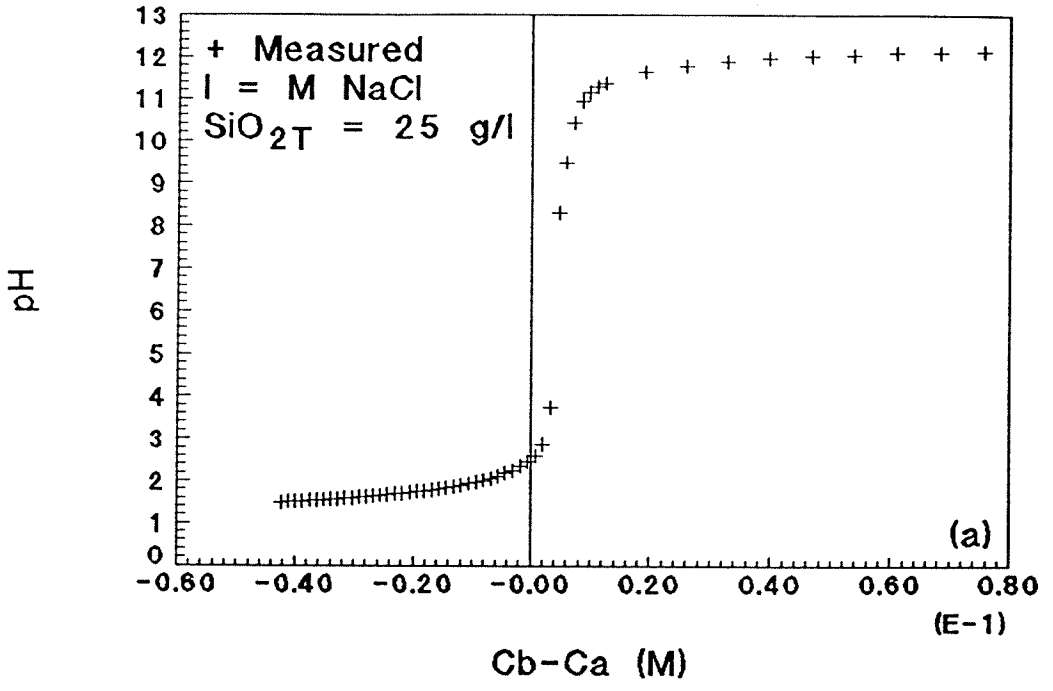

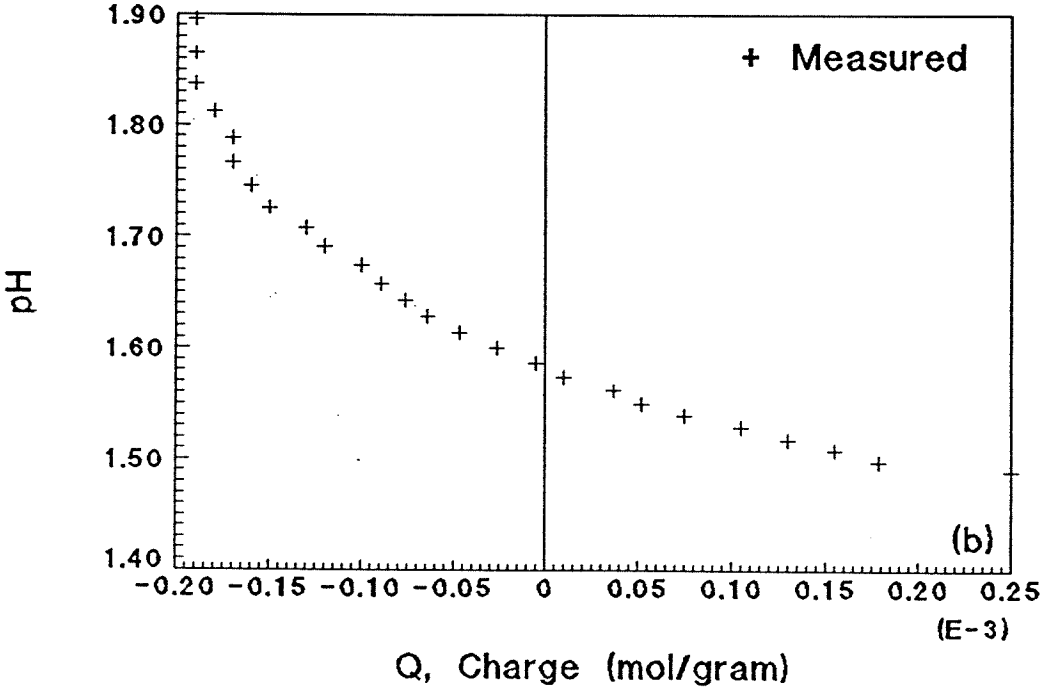

Fig. 4.5: Results of surface titration of sand medium: (a) titration results; (b) surface charge versus pH.

becomes significant (Stumm and Morgan 1981).

The sand was cleaned prior to use in order to remove both attached surface impurities and organic matter. All cleaning was performed in a separate, oversized column. A backwash cleaning method is used in a five part procedure as follows:

1. The sand is backwashed with recirculated clean water for one hour in order to saturate the particles and to break up any agglomerates through agitation. This process also would aid in loosening any attached particles, because the backwash water which was used is double deionized and at equilibrium with the atmosphere ($pH \approx 5.7$, $I \approx 10^{-4}$ M).

2. The sand is backwashed with an oxidant (sodium oxidase) suspension which was recirculated for one hour. The concentration of sodium oxidase which was used is approximately $10^{-3.13}$ M. This treatment of the sand is intended to oxidize any organics and assists in stripping the sand surface of any impurities. After recirculating, the sand is left to soak overnight in the oxidant suspension.

3. The sand is flushed (no recirculation) with the same initial clean water for one hour.

4. The sand is backwashed again with the sodium oxidase suspension which was recirculated for one hour. After recirculating, the sand is left to soak overnight in the oxidant suspension.

5. The sand is flushed with the same initial clean water for one hour. At this point, the effluent from the column is observed by eye for any turbidity. The

flushing is continued until the effluent is observed to be clear. After cleaning, the sand is oven-dried.

The column is packed with the dry sand and then saturated by pulling a vacuum off of the bottom as water is added to the top as described previously. A final cleaning step is performed with the sand packed in the column. This final step is intended to strip off any leftover surface contaminants by using charge reversal. The pH of the de-aired influent to the column is adjusted to 2 and then flowed through the column. This is continued for several pore volumes which lasted approximately an hour. Next, the column is titrated with the buffered, de-aired influent with pH = 8. This flushing is continued until the column is stabilized at pH = 8.

4.4 Particle Properties

The particles used in this work are made of polystyrene latex with carboxyl surface groups. These particles are manufactured by Polysciences, Inc. of Warrington, Pennsylvania, and the particles which were used are referred to as polybead carboxylate microspheres. The surface carboxyl groups are expected to become negatively charged for the range of pH from 2 to 4 (Ottewill and Shaw 1972). The particles which were used are in the colloidal size range and surround the transition region between Brownian and advective particles. For this work, the nominal diameters and standard deviations of the particles as reported by the manufacturer are: d_p = 0.1, 1.0, and 2.8 microns; s.d. = 0.003, 0.0055, and 0.023 micron, respectively. These sizes were given by the manufacturer and the

diameter of the 1.0 micron particles was verified once by a Coulter counter reading. This reading showed over 90% of the particles to be within a few percent of 1.0 micron. The density of the polystyrene latex composing the three particles is 1.05 g/cm^3.

4.5 Particle Concentration Measurement

The concentrations of particles are measured by a Hewlett Packard 8451A Diode Array Spectrophotometer. This spectrophotometer detects reductions in transmitted light due to the particles in suspension. A quick explanation of the operation of this instrument is given in the following:

1. A particle concentration sample is placed in a cuvette which is a sample holder designed for this instrument, and this is inserted in the holder of the instrument.
2. Light is then shone through the cuvette, and a detector on the far side of the cuvette measures decreases in light intensity due to scattering from particles in the sample.

In order to understand the readings given by the spectrophotometer, the general theory of light scattering needs to be examined. The measure of light scattering can be expressed by a first order decay of light intensity over distance traveled:

$$\frac{d\Omega(x)}{dx} = -(\beta_p + \beta_B)\Omega(x) = -B_T\Omega(x) \qquad (4.8)$$

where: $\beta_{P,B}$ = *extinction coefficient for particles and background, respectively;*

$\beta_P \propto C_p$

$= \gamma C_P$;

$\beta_B \propto C_B$

$= \gamma C_B$;

$\beta_T = \beta_P + \beta_B$;

$\beta_T \propto C$;

$= \gamma C$;

C_p = *particle only concentration*;

C_B = *background concentration*;

C = *total concentration*

$= C_P + C_B$; *and*

$\Omega(x)$ = *light intensity at position x.*

with a solution to Eq. (4.8):

$$\ln\left[\frac{\Omega(x)}{\Omega_i}\right] = -\beta_T x \tag{4.9}$$

where: Ω_i = *incident light intensity.*

For this work, a distance L is fixed and is the distance through a cuvette. Using this distance L, the concentration will become constant with position, and Eq. (4.9) becomes:

$$\beta_T = -\frac{1}{L}\ln\left[\frac{\Omega}{\Omega_i}\right] \tag{4.10}$$

where: $\Omega(x) = \Omega(L) = \Omega$

Substituting for β_T in Eq. (4.10), the concentration can be expressed as:

$$\gamma C = \gamma(C_P + C_B) = -\frac{1}{L}\ln\left[\frac{\Omega}{\Omega_i}\right] \tag{4.11}$$

In this form, the concentration is expected to be proportional to the natural logarithm of the ratio of the light intensity at position L and the incident light intensity. The proportionality constant will depend on the size and nature of the particles. This is only the general theory for light scattering, and this equation needs to be tailored to the machine used in this work.

For the HP system used in this work, a sample concentration is given a transmittance value (as the readout) based on the light intensity passing through the sample, light intensity passing through a reference sample, and an internal system dark current. The dark current refers to a constant excitation of the diode. This excitation can arise from two possible sources which are stray light waves and thermal currents due to the natural operation of the diode. An internal equation which accounts for this background diode excitation is used to determine the light transmittance, and this equation is:

$$T = \frac{\Omega - D_k}{\Omega_B - D_k} \tag{4.12}$$

where: T = *light transmittance for measured sample*;
Ω_B = *light intensity for reference sample*;
Ω = *light intensity for measured sample; and*
D_k = *dark current.*

The reference light intensity is defined as the light intensity which passes through a baseline sample. An example of a reference sample would be a clean water

sample, so that any turbidity increases can be directly measured as increases in concentration. In Eq. (4.12), only transmittance (T) is a direct reading of the instrument, and all other variables are internal to the spectrophotometer. The above equation, Eq. (4.12), can be rearranged and manipulated as follows:

$$\frac{\Omega}{\Omega_B} = T\left(1 - \frac{D_k}{\Omega_B}\right) + \frac{D_k}{\Omega_B}$$

$$\frac{\Omega/\Omega_i}{\Omega_B/\Omega_i} = T\left(1 - \frac{D_k}{\Omega_B}\right) + \frac{D_k}{\Omega_B}$$

Taking the natural logarithms of both sides yields:

$$\ln\left[\frac{\Omega/\Omega_i}{\Omega_B/\Omega_i}\right] = \ln\left[T\left(1 - \frac{D_k}{\Omega_B}\right) + \frac{D_k}{\Omega_B}\right]$$

$$\ln\left[\frac{\Omega/\Omega_i}{\Omega_B/\Omega_i}\right] = \ln[T\ (1 - a) + a] \qquad (4.13)$$

$$\textit{where: } a = \frac{D_k}{\Omega_B}.$$

The natural logarithm on the left-hand side of Eq. (4.13) can be split as follows:

$$\ln\left[\frac{\Omega}{\Omega_i}\right] - \ln\left[\frac{\Omega_B}{\Omega_i}\right] = \ln[T(1 - a) + a] \qquad (4.14)$$

Now, using the identities previously determined:

$$\beta_T = \gamma C = -\frac{1}{L}\ln\left[\frac{\Omega}{\Omega_i}\right] \qquad (4.10)$$

$$\beta_B = \gamma C_B = -\frac{1}{L}\ln\left[\frac{\Omega_B}{\Omega_i}\right] \tag{4.15}$$

Using these relationships yields:

$$\begin{aligned} C &\propto \ln\left[\frac{\Omega}{\Omega_i}\right] \\ C_B &\propto \ln\left[\frac{\Omega_B}{\Omega_i}\right] \end{aligned} \tag{4.16}$$

Substituting Eqs. (4.16) into Eq. (4.14) yields:

$$C - C_B \propto \ln[T(1 - a) + a]$$

Substituting for the total concentration yields:

$$C_P + C_B - C_B \propto \ln[T(1 - a) + a]$$

$$C_p \propto \ln[T(1 - a) + a] \tag{4.17}$$

An experimental solution to Eq. (4.17) can be found by a least-squares analysis using:

$$C_j = A \ln[T_j(1 - a) + a] \tag{4.18}$$

where: C_j = *sample "j" concentration; and*
T_j = *sample "j" transmittance value.*

In this equation, C_{pj} has been replaced by C_j in order to simplify the expression. A simple rearrangement linearizes Eq. (4.18):

$$C_j = A \ln\left[T_j + \frac{a}{1 - a}\right] + A \ln[1 - a] \tag{4.19}$$

This equation is of the form:

$$y = mx + b$$

where: $y = C_j$;
$m = A$;
$x = \ln\left[T_j + \frac{a}{1 - a}\right]$; *and*
$b = A \ln[1 - a]$.

Several sample concentrations were made and measured and the results were fitted by this equation. These measured data are shown in part (a) of Fig. 4.6. The least-squares, best-fit equation using concentrations ranging from 0 to 40 mg/l for the 1 micron particles is:

$$C = -24.11 \ln[T - 0.0244] - 0.5955 \tag{4.20}$$

$$C = -55.51 Log[T - 0.0244] - 0.5955 \tag{4.21}$$

where: $a = -0.025$;
R^2 = *correlation coefficient*; *and*
= 0.9999.

Eqs. (4.20) and (4.21) have similar forms to Eq. (4.11) which was found using the general theory in that it is a logarithm function and are different due to the dark current of the instrument.

These results are shown in Figs. 4.6 and 4.7. In Fig. 4.6, part (a) shows measured concentrations versus transmittance readings. This figure is plotted in

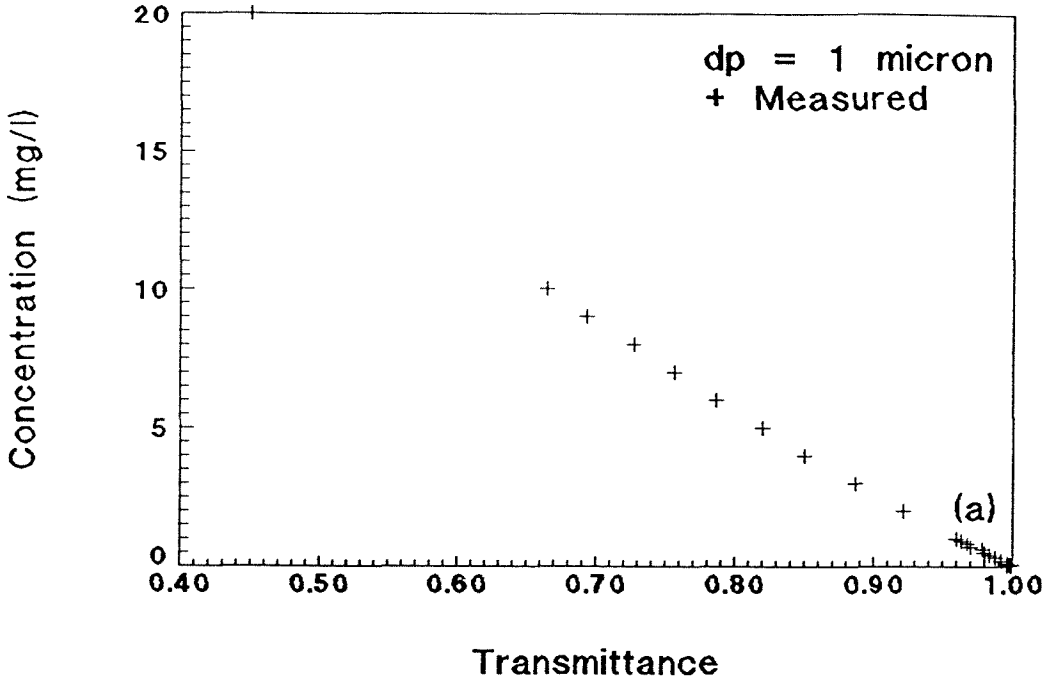

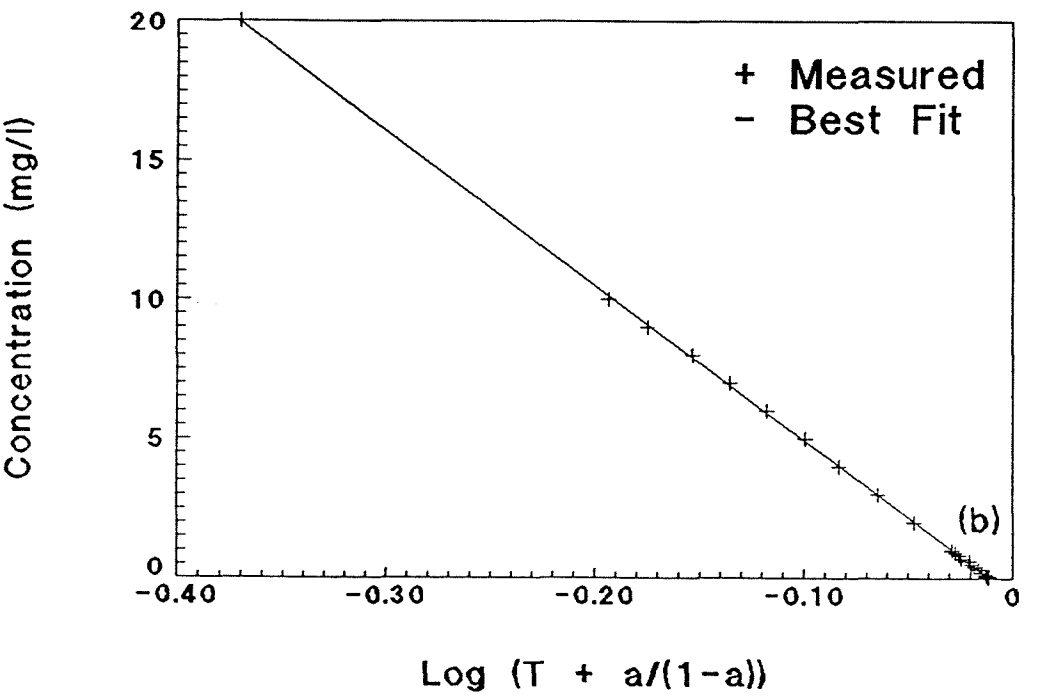

Fig. 4.6: Calibration of concentration versus transmittance for 1.0 micron particles: (a) arithmetic plot; (b) semilog plot with regression line.

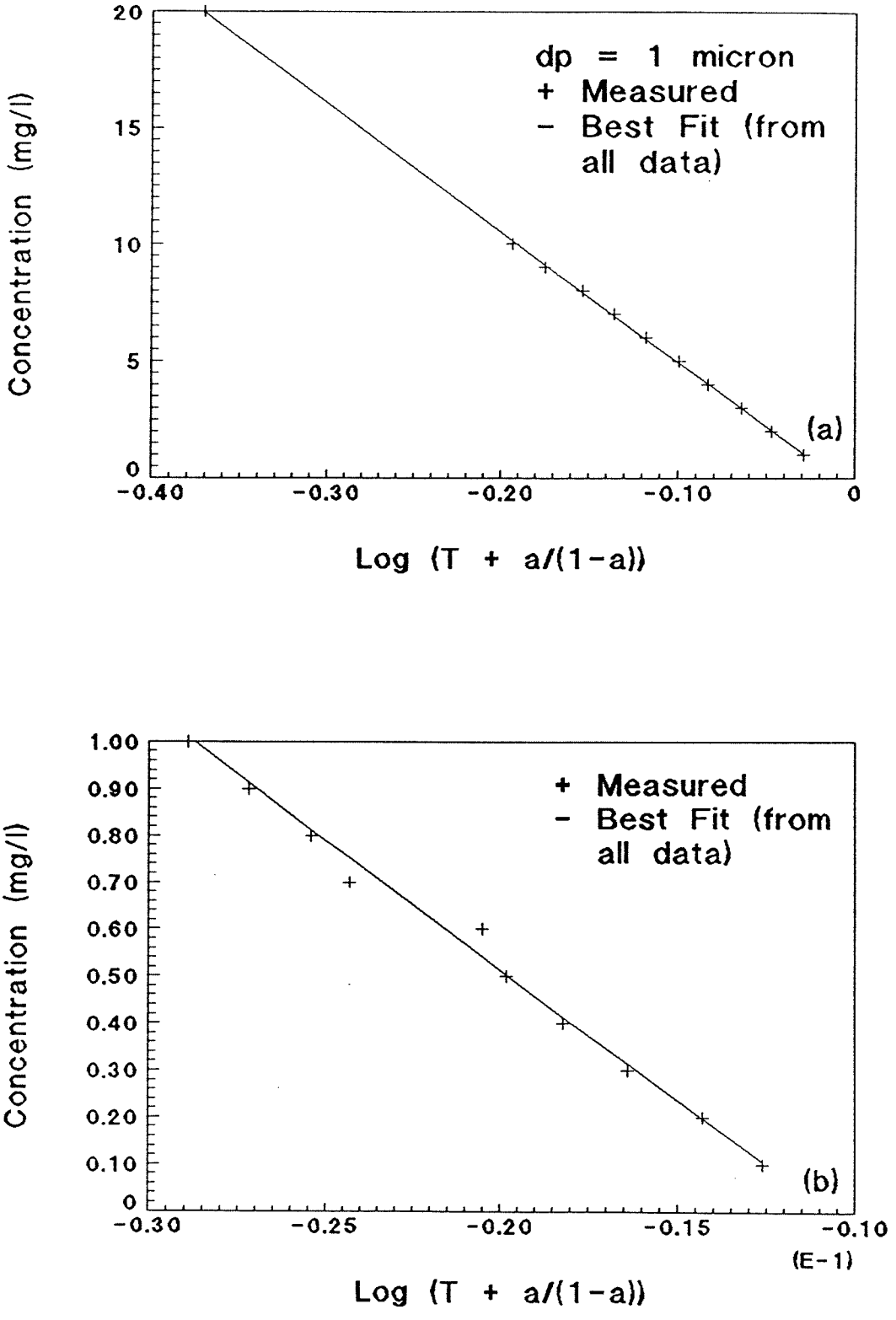

Fig. 4.7: Comparison of regression line and measurements for different concentration ranges for 1.0 micron particles.

this inverted order, because in practice transmittance will be the known value; whereas, concentration will be the desired quantity. Part (b) shows both the best-fit curve developed in the theory section and the measured concentrations versus Log[T + a/(1-a)] for the range of concentration used in this work. Fig. 4.7 shows both the best-fit curve and the measured concentrations for the two orders of concentration of interest in this work. Theoretically, a single best-fit curve can be used to determine concentrations versus transmittance readings for all particle sizes. In order to complete this analysis, two assumptions are needed. First, the particles are spherical; and, second, the decrease in light transmittance is due to the cross-sectional area of the spheres. In order to have the transmittance between two particle sets be the same, the area blocked by spheres must be the same:

$$\frac{A_1}{A_2} = 1 = \frac{\#_1 \pi a_{p1}^2}{\#_2 \pi a_{p2}^2} = \frac{\#_1 a_{p1}^2}{\#_2 a_{p2}^2} \tag{4.22}$$

where: 1,2 = *first and second particles, respectively*;
a_p = *particle radius*; *and*
\# = *number of particles.*

Now, to find the relationship between concentrations of the two particle sets, the concentrations of both are:

$$\frac{C_2}{C_1} = \frac{\#_2 (4/3)\pi a_{p2}^3 \rho_{p2}/V_T}{\#_1 (4/3)\pi a_{p1}^3 \rho_{p1}/V_T} = \frac{\#_2 a_{p2}^3 \rho_{p2}}{\#_1 a_{p1}^3 \rho_{p1}} \tag{4.23}$$

where: V_T = *total volume of particles and fluid* (ℓ); *and*
ρ_p = *particle density* ($g\ \ell^{-1}$).

Substituting the identity shown in Eq. (4.22) into Eq. (4.23) yields:

$$C_2 = \left(\frac{a_{p2}}{a_{p1}}\right)\left(\frac{\rho_{p2}}{\rho_{p1}}\right)C_1 \tag{4.24}$$

This analysis shows that only one calibration curve is needed. In order to determine other particle concentrations from transmittance readings, the scaling shown in Eq. (4.24) can be used. No other calibrations are needed. The accuracy of this derivation was tested by preparing known reservoir concentrations of different particles, measuring transmittance values, and then comparing the calculated concentration given by Eq. (4.24) to the known reservoir concentration. This comparison was shown to be accurate to within a few percent.

The HP spectrophotometer has two measures of accuracy. The first is the baseline flatness of the reading which refers to the significant digits of accuracy of the reading, and the second is the stability of the readings over time which refers to the drift over time of the readings relative to the reference value. The baseline flatness = T ± 0.00299, and the stability = T ± 0.00643/hour. The stability can be improved by periodically re-referencing the instrument which was done in this work.

4.6 Ionic Strength Measurement

In this work, the effect of suspension ionic strength due to an NaCl electrolyte on advective velocity, longitudinal dispersion, and filter coefficient of

particles was investigated. The conductance of the experimental water is measured using a YSI Model 35 Conductance Meter manufactured by the Yellow Springs Instrument Co., Inc. of Yellow Springs, Ohio. Instead of using a manufactured conductivity probe, several probes were made in the Keck lab, and three were inserted into the column (see Fig. 4.2). The probe design is described in detail by Houseworth (1984). A cross-sectional sketch of a probe is shown in Fig. 4.8. The geometry of this probe needs to be analyzed in order to insure its proper use. Such an analysis is reviewed in the YSI Model 35 Conductance Meter Instruction Manual, and this manual provided the information for this discussion. This can be checked by considering the equation of conductivity for the meter:

$$\frac{1}{R_c} = k\left(\frac{A_e}{d}\right) = k\left(\frac{1}{K_c}\right)$$

where: $\frac{1}{R_c}$ = *observed conductance reading (mhos)*;
k = *specific conductance (mho/cm)*;
A_e = *area of electrode* (cm^2);
d = *distance between electrodes (cm); and*
K_c = *cell constant* (cm^{-1})
$= \frac{d}{A_e}$.

In this work, d = 1.0 mm, A_e = 20.1 mm^2, and K_c = 0.50 cm^{-1}. For the best results when using this meter in water, the following rules apply:

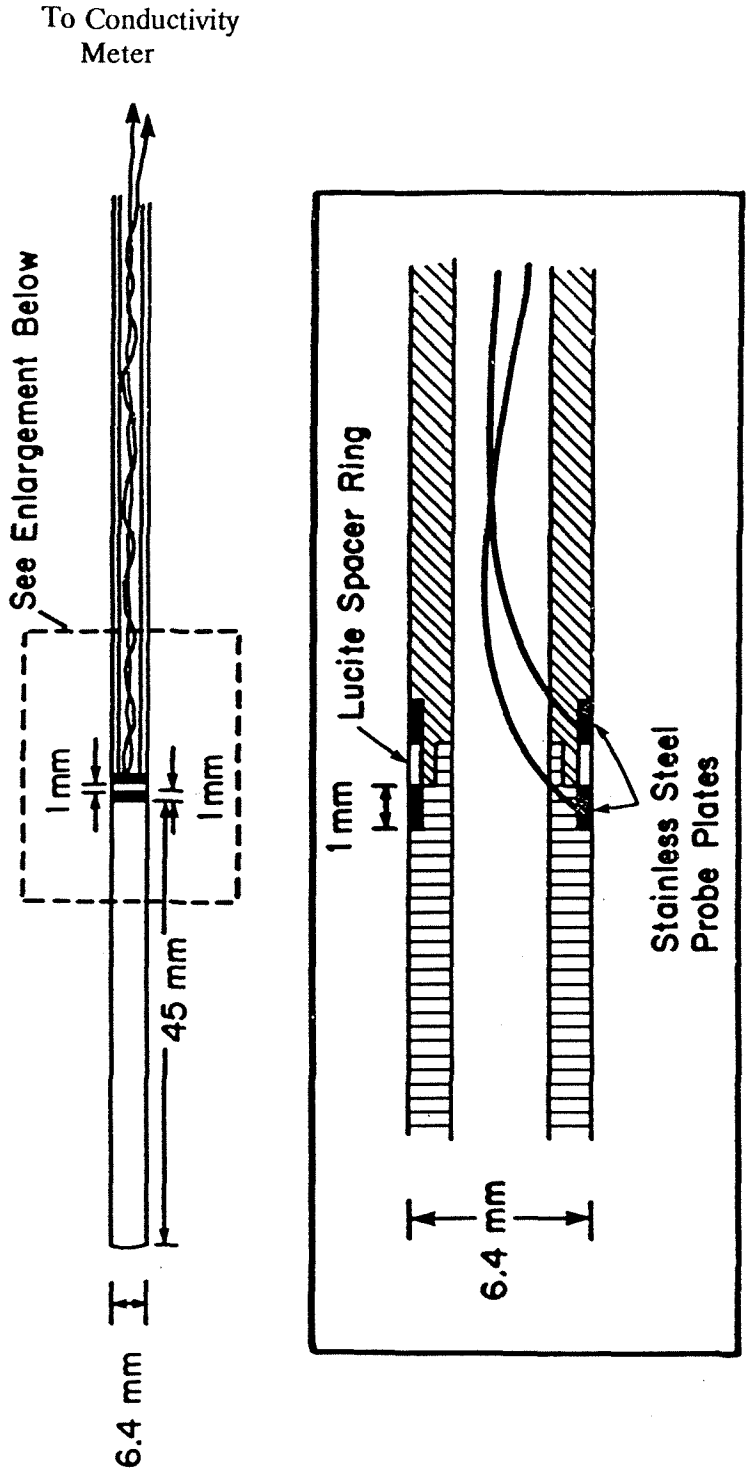

Fig. 4.8: Cross-sectional sketch of conductivity probe with detail of probe plates (from Houseworth (1984)).

Cell Constant, K_c	*Used For*
0.1 cm^{-1}	< 20 *micromhos*
1.0 cm^{-1}	20 - 20,000 *micromhos*
10.0 cm^{-1}	> 20,000 *micromhos*

In this list, the cell constants are only order of magnitude. In this work, the range of micromhos is from 5 to 2000 micromhos. An inspection of the list shows that the conductivity probes made for this work will be adequate.

For the readings given by the conductance meter, a calibration must be made for ionic strength versus conductance reading. As done for the particle concentration calibration, specific sample concentrations of an NaCl salt were made and measured, and the results were fitted by a least-squares analysis. These results are shown in Fig. 4.9. This figure shows the measured data and the least-squares, best-fit curve plotted versus the conductance meter reading for the two scales of the conductance meter which were used in this work. The two equations of best-fit are:

for the scale reading 200 x 10^{-6}:

$$Log[I] = 1.19 Log[Cond] - 5.59 \qquad (4.25)$$

where: I = *ionic strength* (M);
$Cond$ = *conductance* (*micromho*); *and*
R^2 = 0.999.

and for the scale reading 2000 x 10^{-6}:

$$Log[I] = 1.15 Log[Cond] - 5.57 \qquad (4.26)$$

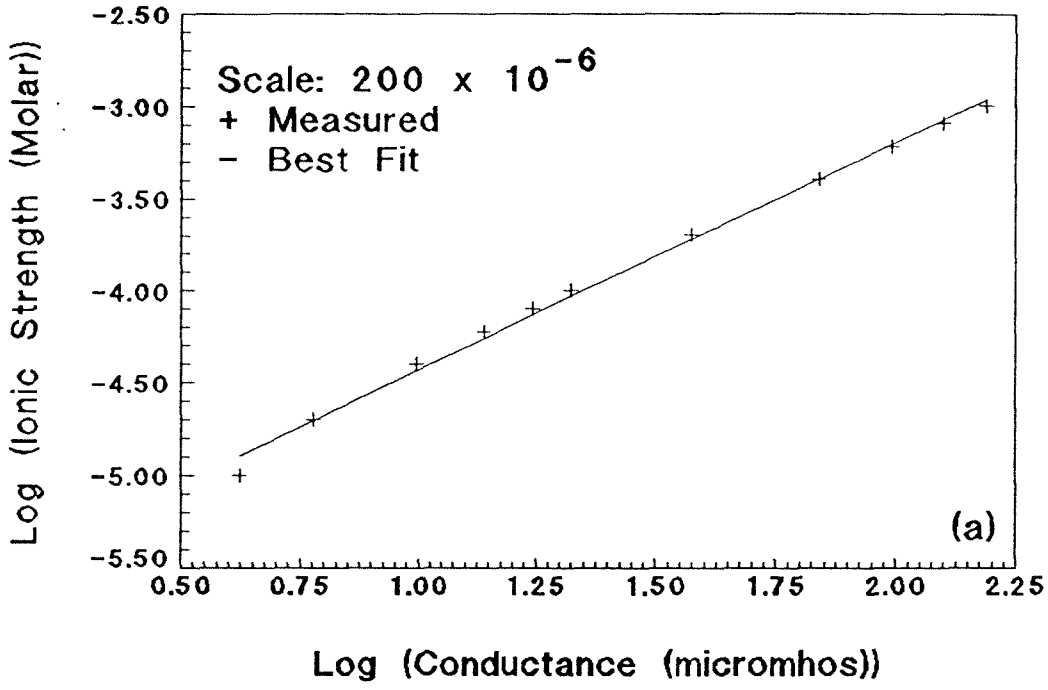

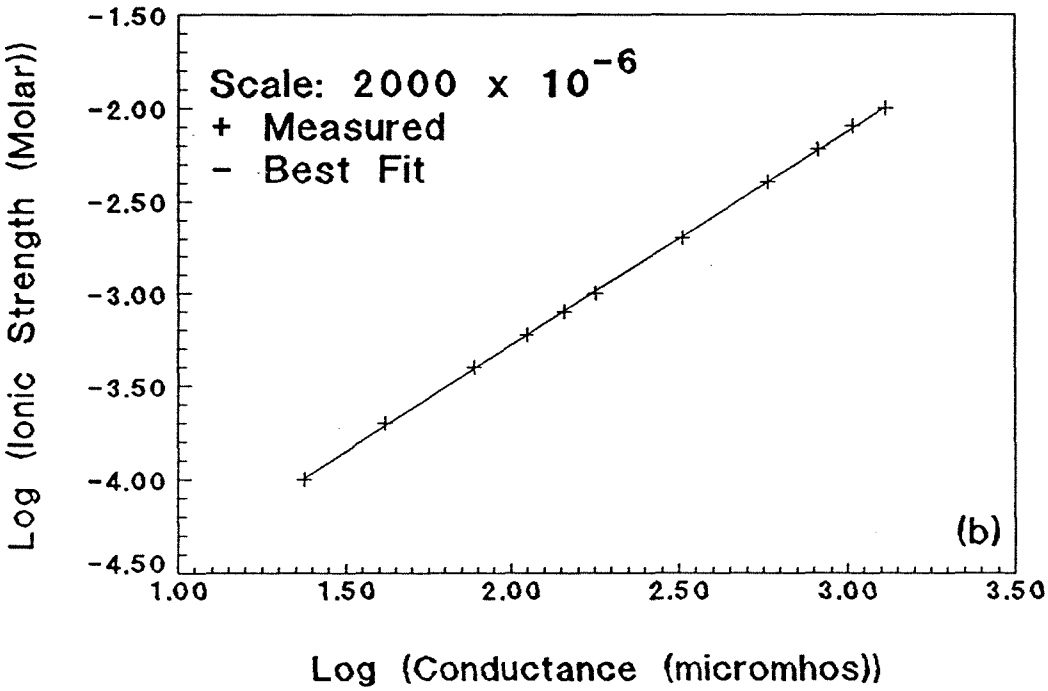

Fig. 4.9: Calibration curve for ionic strength versus conductance for two meter scales: (a) scale setting of 200 x 10^{-6}, (b) scale setting of 2000 x 10^{-6}.

where: $R^2 = 0.9998$

This figure shows that a linear relationship exists between the logarithm of conductance and the logarithm of ionic strength.

For this work, the conductance meter is interfaced with an IBM PC computer for purposes of measuring salt tracer breakthroughs by continuously reading and recording ionic strengths in the column using an analog-to-digital board. The board which was used is the Data Translation, Inc. Analog and Digital I/O Board manufactured by Data Acquisition, Inc. for IBM PC's. A schematic diagram of the ionic strength data acquisition system is shown in Fig. 4.3. The YSI conductance meter output port is connected directly to a channel box which in turn is connected to the A/D board. The analog signal from the conductance meter is translated into digital voltage readings by the board. These voltage readings then are saved onto disk by the computer. For this data acquisition, the readings given by the conductance meter must be calibrated to the A/D conversion voltage readings of the PC. A similar procedure as described for the ionic strength versus conductance readings was completed. In this process, various concentrations of saline water were made and both the meter conductance readings and the corresponding A/D voltage readings of the PC were recorded. The measured conductance readings versus A/D voltage readings were fitted by a least-squares analysis. Fig. 4.10 shows the results for this analysis. This figure shows the measured A/D voltage reading data and the least-squares, best-fit curve plotted versus the conductance meter reading for the two scales of the

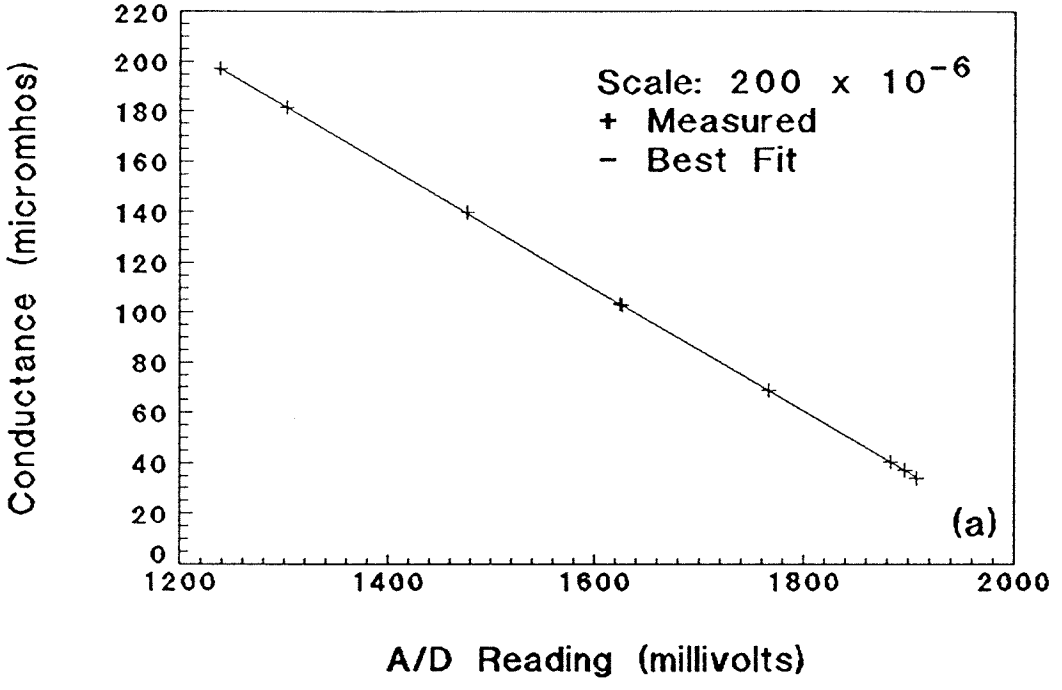

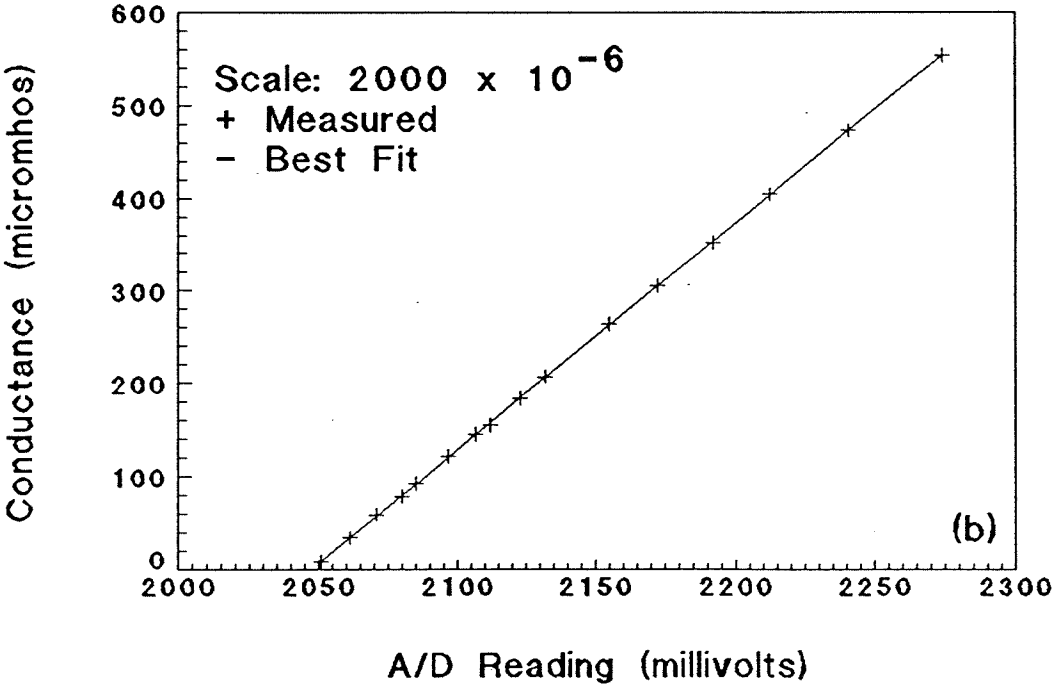

Fig. 4.10: Calibration curve for conductance versus A/D reading for two meter scales: (a) scale setting of 200 x 10^{-6}, (b) scale setting of 2000 x 10^{-6}.

conductance meter which are used in this work. The two equations of best-fit are: for the scale reading 200 x 10^{-6}:

$$Cond = -0.24A/D + 499.12 \tag{4.27}$$

where: $Cond$ = *conductance* (*micromhos*);
A/D = *analog-to-digital reading* (*millivolts*); *and*
R^2 = 1.0000.

and for the scale reading 2000 x 10^{-6}:

$$Cond = 2.44A/D - 5005.45 \tag{4.28}$$

where: R^2 = 0.9999

This figure shows that a linear relationship exists between A/D voltage reading and conductance, but the slopes for the two curves are opposite of each other.

In this work, the conductance readings given by the in-situ (closed, constricted system) conductivity probes need to be calibrated to the conductance readings given by a batch (open, unconstricted reservoir system) conductivity probe. (Note that the effect of a porous medium on measured ionic strength in a free fluid versus a constricted system is similar to the effect on Brownian diffusion in a free fluid versus a constricted system). A similar calibrating procedure as described above was completed in which readings given by the in-situ probes for water flowing through the column were compared to readings given by batch probes for the same water, and the results were fitted by a least-squares analysis. Fig. 4.11 shows the results of this analysis. The equation of this best-fit line is:

$$I_{batch} = 2.85 I_{column} + 0.000061 \quad (4.29)$$

where: I_{batch} = *actual ionic strength measured in batch* (M);
I_{column} = *apparent ionic strength measured in column* (M); *and*
R^2 = 0.992.

This figure shows that a linear relationship exists between column ionic strength and batch ionic strength. The slope of this best-fit line is 2.85 which is an approximate measure of both the tortuosity (Oliphant and Tice 1985; Winsauer et al. 1952) and the reciprocal of the porosity of the medium and is in the range of packed sand. The slope value shows that the flux path lengths between the probe rings in the packed column are longer than they are in the batch measurements, but not all of the 2.85 factor can be attributed to tortuosity because the electrical field flux depends on the effective area which is proportional to the porosity. The reciprocal of the slope value (1/2.85) is 0.35 which is approximately equal to the effective porosity measured for the column. In either case, both the tortuosity and the effective porosity are within the expected ranges for uniform, packed sand.

4.7 Breakthrough Experiment Protocol

Each breakthrough experiment is composed of a two-part process. The forward particle breakthrough has the particle suspension displacing resident, clean water, and the reverse particle breakthrough has clean water displacing the particle suspension. Similar terminology is used for salt breakthroughs except saline water replaces the particle suspension. In the simple breakthrough experiments, the clean water and particle suspension have the same ionic strength,

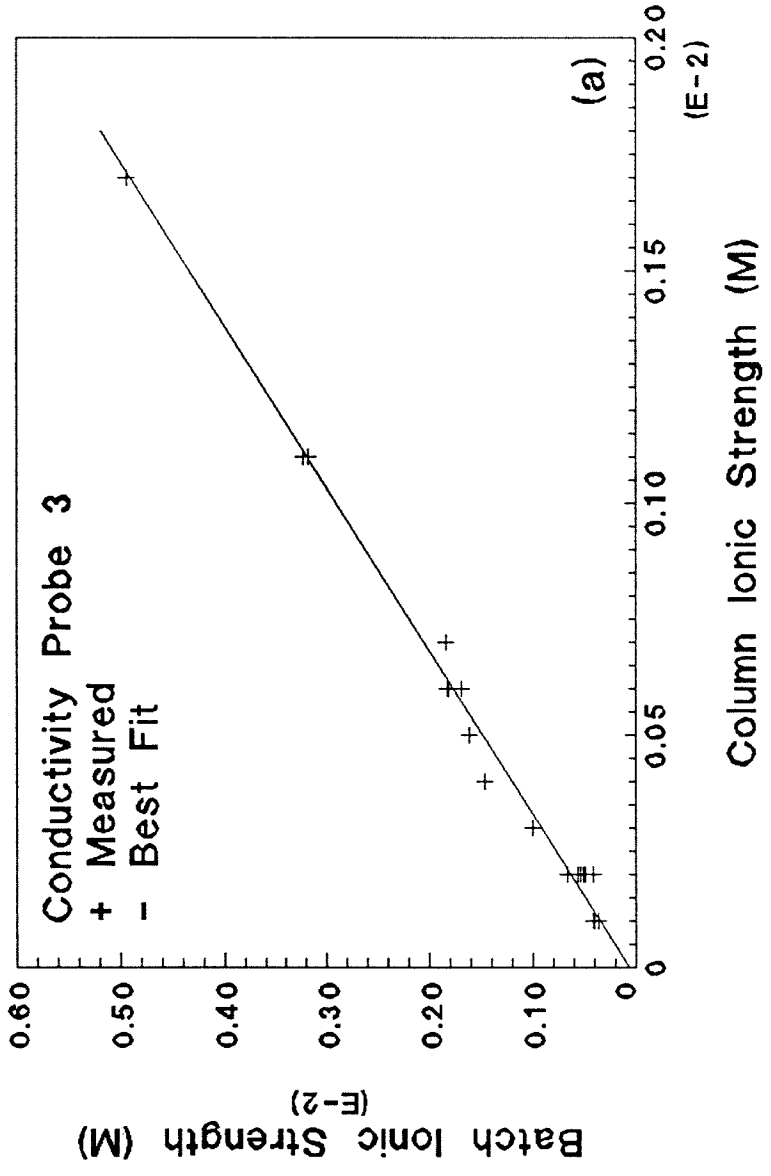

Fig. 4.11: Calibration curve for batch (actual) ionic strength versus column (apparent) ionic strength for packed column system.

but the ionic strength for these waters differs from each other for the coupled experiments. In general, the two sample ports which were described previously (see Figs. 4.1 and 4.2) are also used in order to measure two sets of breakthroughs for each experiments. Also, for each experiment the flow rate and ionic strength are established first with the flow rate kept constant during all experiments.

Preliminary to any particle breakthrough experiment, a salt tracer experiment is performed in order to determine the effective porosity of the packed sand column. For this, the Darcy velocity (V_D) is measured by timing the collection of the effluent in volumetric flasks:

$$V_D = \frac{Q}{A} \tag{4.30}$$

where: Q = *volume flow rate* ($L^3\ T^{-1}$); *and*
A = *column cross-sectional area* (L^2).

The interstitial velocity is determined by the time for 50% breakthrough to occur at a given longitudinal position:

$$V_p = \frac{L}{t_{50}} \tag{4.31}$$

where: L = *longitudinal distance to sample port from top of sand column* (L).

In porous media, flow only takes place in interconnecting pores. The effective porosity, θ_e, for the media is:

$$\theta_e = \frac{V_D}{V_p} \tag{4.32}$$

In order to outline the sampling schedule, the expected interstitial velocity which was chosen for the given experiment is used to determine the needed parameters of the breakthrough. These parameters are the breakthrough width ($4\sigma_x$) and time ($4\sigma_t$), and these are found from the seepage velocity (V_p), grain diameter (d_g) of medium, and longitudinal distance to breakthrough (L). First, the time to 50% breakthrough, t_{50}, is found by rewriting Eq. (4.31):

$$t_{50} = \frac{L}{V_p} \tag{4.33}$$

One standard deviation of the width of the breakthrough, σ_x, is found by assuming the longitudinal dispersion coefficient can be approximated as the interstitial velocity multiplied by the grain size:

$$\begin{aligned} \sigma_x^2 &= 2D_L t_{50} \\ &\approx 2V_p d_g t_{50} = 2Ld_g \end{aligned} \tag{4.34}$$

One standard deviation of the elapsed time for the passage of a breakthrough, σ_t, can be found from σ_x:

$$\sigma_t = \frac{\sigma_x}{V_p} \tag{4.35}$$

The expected time for the entire breakthrough to occur can be estimated as four times the single standard deviation, σ_t.

For this work, an attempt was made to take at least five samples during a

breakthrough. In order to insure that enough samples would be taken, sampling is begun at least 10% before the time of the start of the expected breakthrough (10% before $4\sigma_t$) and is continued until at least 10% after the time of the end of the expected breakthrough (10% after $4\sigma_t$). The sample size and length of time to extract one sample are discussed later.

A description for a general breakthrough experiment follows. The column is given a final flushing with existing column water while establishing the wanted flow rate. The existing column water has the same chemical properties as the water which is to be displaced during the breakthrough experiment. This existing column water influent then is turned off, and the inlet lines are rinsed with the breakthrough water to be used in the experiment. The column shut-off valve is left open to allow the water level in the constant head inlet chamber to drain down to the top of the medium. At this time, the shut-off valve is closed. The breakthrough water then is flowed into the inlet chamber and allowed to overflow to establish the constant head for the experiment. In order to begin the experiment, the column shut-off valve is opened, and the experimental clock is started. Samples are then extracted at prescribed times in order to measure the initial and final concentrations and the actual breakthrough. The breakthrough experiment ended after at least 1.5 pore volumes has flowed through the column. The Darcy flow rate is measured by timing the collection of effluent in volumetric flasks. In order to verify that the system chemistry remained constant, 100 ml samples are taken from the input reservoirs and the end chamber at prescribed

intervals, and the ionic strength and pH of these samples are measured. The particle reservoir is sampled at the beginning and ending of the forward breakthrough experiment, and the clean water reservoir is sampled at the half-way point of the reverse breakthrough experiment. The end chamber is sampled before the beginning of and at the ending of the forward breakthrough experiment, and this is also sampled at the ending of the reverse breakthrough experiment.

For forward particle breakthroughs, the existing column water is clean water, and the experimental breakthrough water is the particle suspension. For reverse particle breakthroughs, the existing column water is particles, and the experimental breakthrough water is clean water. For both the forward and reverse particle breakthroughs, the ionic strength of the particle suspension and the clean water is the same. For forward salt tracer breakthroughs, the existing column water is nonsaline clean water, and the experimental breakthrough water is saline clean water. For reverse salt tracer breakthroughs, the existing column water is saline clean water, and the experimental breakthrough water is nonsaline clean water. For the salt tracer breakthroughs, the clean water has a baseline ionic strength, and the saline clean water has an incrementally larger ionic strength which provides the measured breakthrough. For coupled breakthroughs or salt breakthroughs, an additional step is the turning on of the computer in order to measure the salt breakthrough.

For the HP spectrophotometer, a one ml sample is needed as input, and

for proper breakthrough analysis, approximately five distinct samples are desired. In order to be distinct, the time to extract one sample should be as small as possible. In this sampling protocol, each sample is expected to be an average of the concentrations withdrawn during the extraction period, and this average concentration is expected to be centered around the midpoint of the extraction period. For this to be true, any variation of concentration is assumed to be linear. This assumption will be true for very short times regardless of the position on the breakthrough curve. If the extraction period is too large, this averaging procedure will smother the actual breakthrough value.

In this sampling protocol, rapid sampling is proposed for each sampling period while maintaining the constraint of removing only 5% of the total flow for the entire sampling period. In this, the sampling period refers to the time from the start of a given sample extraction to the start of the next sample extraction. The use of rapid sampling can be explained by visualizing the column, the sampling system, and the one-dimensional flow in the column as a potential flow problem. In this potential flow problem, the needle is a point sink, and the column is uniform flow. A separation streamline will occur, and the size of this is governed by the ratio of the strengths of both the sink and the flow field. A rapid sample extraction results in a larger spread in the separation streamline due to a large sink strength which results in a narrower sample strip (smaller Δx) within the column. As this strip becomes smaller, the sample more closely reflects an average particle concentration at the sample port for the given sample time. By

maintaining a removal of only 5% of the total flow, the disturbance in the flow pattern due to this sampling event will have ample time to transport past the sampling region before the next sampling event commences. Also, as the strip is made smaller, less time is required for the disturbance to flow past the sampling region.

In order to have a one ml sample, two methods can be employed. The first is to extract one ml sample volumes for each sample period, and the second is to extract smaller volumes and then add clean water to this sample to reach a total of one ml. The fastest manual sampling rate employed in this work using these syringes and needles is 1 ml over 30 seconds. The sampling rate and volume must fit two constraints. First, to maintain accuracy, only a very small fraction of the column flow rate should be removed (5% for a given sampling period was used as a limit), and the second is that the sample size must not be so small that subsequent dilution reduces the concentration below the level of detection (instrument capability) or distinction (distinguish from background concentration). These constraints place both a maximum and a minimum on the flow rate. For the maximum flow rate, the time for breakthrough is so small that in order to take enough samples the sampling period and the subsequent size become too small to provide a distinct sample after dilution. For the minimum flow rate, the one ml sample is easily collected because of the large breakthrough time, but increased filtration due to the low velocity (a smaller velocity results in a larger filter coefficient) causes the concentration to become too small to provide

a distinguishable sample. The collected samples are placed in test tubes which are sealed with parafilm in order to minimize evaporation prior to concentration measurements.

This chapter has presented the various procedures of the experimental work, has shown their inter-relationships, and discussed their associated errors. The experimental conditions, results, and analysis are presented in the next chapter along with an estimate of the overall error of the experiments.

5. RESULTS AND DISCUSSION

The equations describing particle transport developed in Chapter 3 can be defined as mass balance equations whose parameters are determined by dimensional analysis. In this form, the equations are based on macroscopic, average values and are predictive only in an order of magnitude sense. Experimentation was needed in order to determine the functional relationship between the developed dimensionless groups defining the transport parameters.

A single surface titration experiment was performed on the sand in order to determine surface speciation, and the 1.0 micron particles were sized once in a Coulter Counter. These two experiments were only performed in order to verify literature or manufacturer values. A series of 16 salt tracer breakthroughs were performed in order to verify the results of Houseworth (1984), confirm the column performance, and have a direct comparison of salt tracer and particle longitudinal dispersion coefficients. Also, this provided a chance to become familiar with the operation of the column and experimental data analysis.

A set of 105 particle breakthrough experiments were performed. The variables which were altered during this set of experiments were the particle diameter, interstitial velocity, and NaCl concentration. For these experiments, the suspension ionic strength was kept constant for both the particles and the clean water in order to have a constant filter coefficient which is required of the analytical equation derived in Chapter 3. Other breakthrough experiments, referred to as coupled breakthroughs, were performed in which the particle

suspension and clean water had differing ionic strengths. In these experiments, the particle breakthrough was coupled to the ionic strength breakthrough and the filter coefficient was variable during the ionic strength breakthrough. A series of 18 coupled breakthrough experiments were performed.

5.1 Surface Chemistry

The only experiment performed was a surface titration of the sand medium. The sand medium was titrated from which the zero point of charge was found to be 1.6 (pH_{zpc} = 1.6). This pH_{zpc} matches literature values, and all other constants for determining the surface speciation (acidity constants) are taken from the literature (Stumm and Morgan 1981). A comparison of these acidity constants with the chosen operating pH (pH = 8) shows that the sand surface is expected to be significantly (> 50% of available surface sites) negatively charged.

No surface chemistry measurements were made on the particles; instead, literature values for surface speciation were used (Ottewill and Shaw 1972). Using these values, the polystyrene particles are expected to be significantly (≈ 100% of available surface sites) negatively charged at the operating pH.

5.2 Particle Sizing

The size of the 1.0 micron particles was checked once by Coulter counting. From this measurement, approximately 90% of the particles were shown to be within ±10% percent of the size listed by the manufacturer.

5.3 Salt Tracer Experiments

A series of 16 salt tracer breakthrough experiments were performed. Both

salt water displacing fresh water (forward breakthrough) and fresh water displacing salt water (reverse breakthrough) experiments were completed. There are no distinguishable differences in the calculated values for longitudinal dispersion coefficient for the forward or reverse breakthroughs. Tests for differences in longitudinal dispersion coefficient values at the three different longitudinal positions in the column (x = 60.5 cm, x = 105.0 cm, and x = 149.4 cm) shows no distinguishable differences in the dispersion coefficient. No differences are expected, because the distance to all three conductivity probes is much greater than necessary to avoid inlet boundary effects. For the salt tracer, the experimental results begin to deviate (tail) from the theoretical results for relative concentrations greater than approximately 80% for forward breakthroughs and less than approximately 20% for reverse breakthroughs.

The longitudinal dispersion coefficient was determined for each experiment by inverting the classical erfc solution for conservative tracer breakthrough. In the classical equation, the dispersion coefficient only appears once and can be calculated directly. The procedure for calculating the coefficient is described below. As given in Chapter 3, the classical erfc solution for a step input of a conservative tracer in an infinite medium is:

$$C^* = \frac{1}{2} erfc\left[\sqrt{Pe_D}\left(\frac{x^* - t^*}{2\sqrt{t^*}}\right)\right] \qquad (3.24)$$

In this equation, D_L and D_{Lp} are interchangeable in the dynamic Peclet number. Using a mathematical identity, the erfc is proportional to the Gaussian probability

integral, F(x), as follows:

$$erfx = \frac{2}{\sqrt{\pi}}\int_0^x exp[-t^2]dt = 2F[\sqrt{2}x] - 1 \tag{5.1}$$

This identity is substituted into Eq. (3.24):

$$C'* = 1 - F\left[\sqrt{Pe_D}\left(\frac{x* - t*}{\sqrt{2t*}}\right)\right] \tag{5.2}$$

The inverse of the Gaussian probability integral in Eq. (5.2) is completed as follows:

$$F^{-1}[1 - C'*] = \sqrt{Pe_D}\left(\frac{x* - t*}{\sqrt{2t*}}\right) \tag{5.3}$$

Eq. (5.3) is linear as follows:

$$y = mx + b \tag{5.4}$$

$$\begin{aligned} \textit{where: } y &= F^{-1}[1 - C'*]; \\ m &= \sqrt{Pe_D}; \textit{ and} \\ x &= \frac{x* - t*}{\sqrt{2t*}}. \end{aligned}$$

The slope of the line can be found by completing a least squares analysis on the experimental data when plotted according to the x- and y- variables of Eq. (5.4). In this least squares analysis, only the points of the breakthrough which are linear are used in this calculation. The longitudinal dispersion coefficient is calculated from the slope value by using the dynamic Peclet number identity:

$$m = \sqrt{Pe_D} = \sqrt{\frac{V_s d_g}{D_L}}$$

$$D_L = \frac{V_s d_g}{m^2}$$

After the longitudinal dispersion coefficient is determined, this value is substituted into the erfc solution (Eq. (3.24)) in order to calculate the best-fit breakthrough curve for the experimental data.

In the application of Eqs. (5.2) and (5.4), the following power series approximations are used (National Bureau of Standards Applied Mathematics Series 1970):

for erfx:

$$erfx = 1 - (a_1 t + a_2 t^2 + a_3 t^3) exp[-x^2] + \epsilon(x) \qquad (5.5)$$

$$\begin{aligned} \textit{where: } 0 \le x < \infty; \\ t &= \frac{1}{1 + px}; \\ p &= 0.47047; \\ a_1 &= 0.3480242; \\ a_2 &= -0.0958798; \\ a_3 &= 0.7478556; \textit{ and} \\ |\epsilon(x)| &\le 2.5\times10^{-5}. \end{aligned}$$

for x_p where $F^{-1}[P] = x_p$:

$$x_p = t - \frac{c_0 + c_1 t + c_2 t^2}{1 + d_1 t + d_2 t^2 + d_3 t^3} + \epsilon(P) \qquad (5.6)$$

$$\textit{where: } 0 < P \le 0.5;$$

$$t = \sqrt{\ln\left[\frac{1}{P^2}\right]};$$

$$P = \textit{Probability} = 1 - C^{*};$$

$$c_0 = 2.515517;$$

$$c_1 = 0.802853;$$

$$c_2 = 0.010328;$$

$$d_1 = 1.432788;$$

$$d_2 = 0.189269;$$

$$d_3 = 0.001308; \textit{ and}$$

$$|\epsilon(P)| < 4.5\times10^{-4}.$$

Figs. 5.1 and 5.2 show experimental breakthrough curves for salt. All salt-only breakthrough experimental results are shown in Appendix C; whereas, the salt portion of the coupled breakthroughs are shown in both section 5.4 of this chapter and in Appendix C. Part (a) shows the measured data for the entire experiment. In part (b), the data of the breakthrough is plotted linearly as a function of the inverted Gaussian probability function according to the description given above in which the negative sign is used for convenience. In this plot, the solid line is the best-fit line found from a least-squares analysis of only the data which is linear and excludes the tails. In part (c), only the immediate breakthrough data is shown in dimensionless terms on an arithmetic plot. The solid line in this part is the best-fit solution of Eq. (3.24) using the longitudinal dispersion coefficient value found from the straight line slope of part (b).

The variation of D_L/D versus the Peclet number ($V_s d_g/D$) for the salt experiments is shown in Fig. 5.3. In this figure, the data for the longitudinal dispersion coefficients were calculated by completing the linearized breakthrough

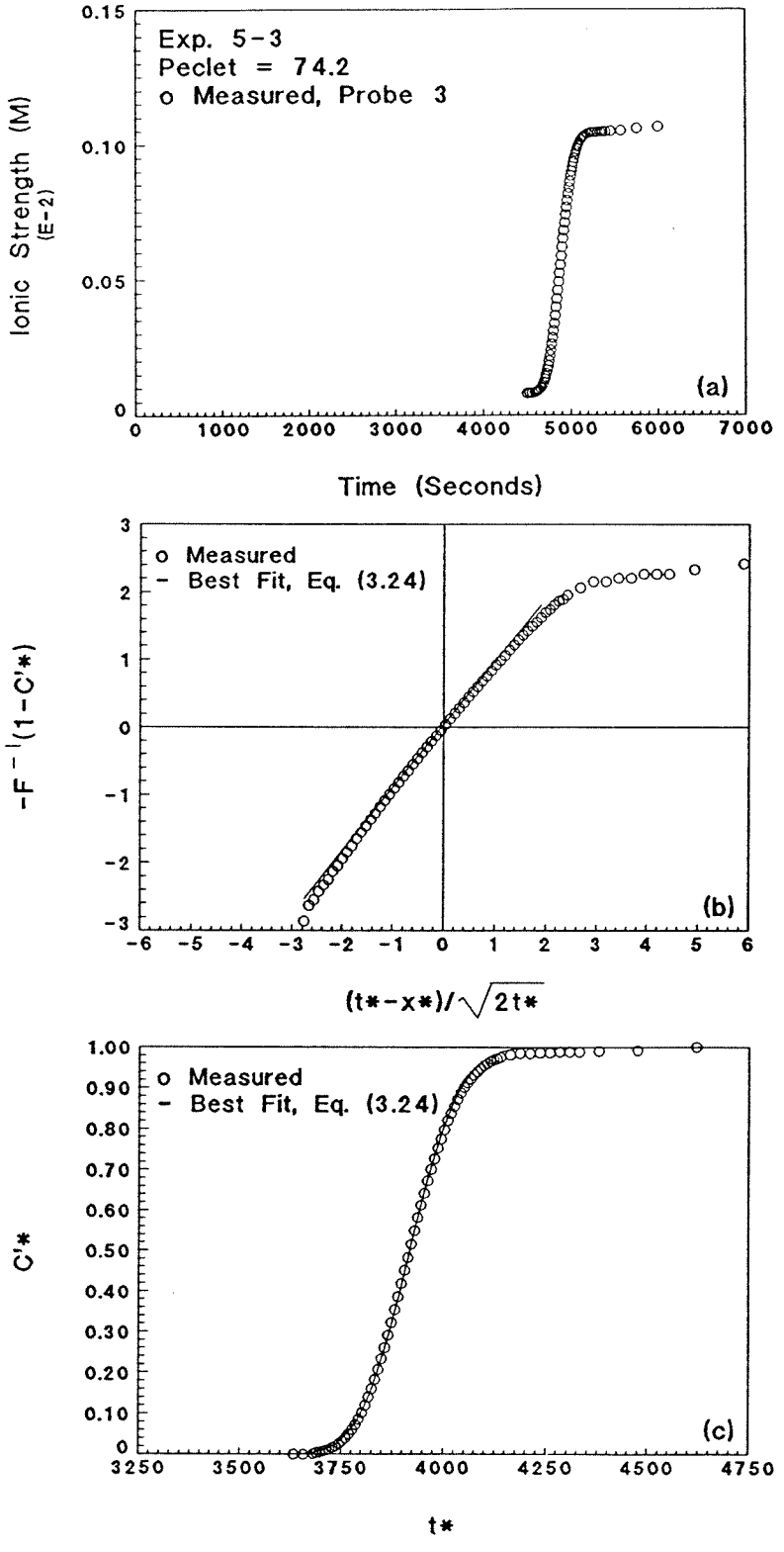

Fig. 5.1: Exp. 5-3 forward breakthrough curve, conductivity probe 3, Pe = 74.6: (a) complete experimental data; (b) linearization with least-squares fit; and (c) breakthrough only with best-fit, Eq. (3.24).

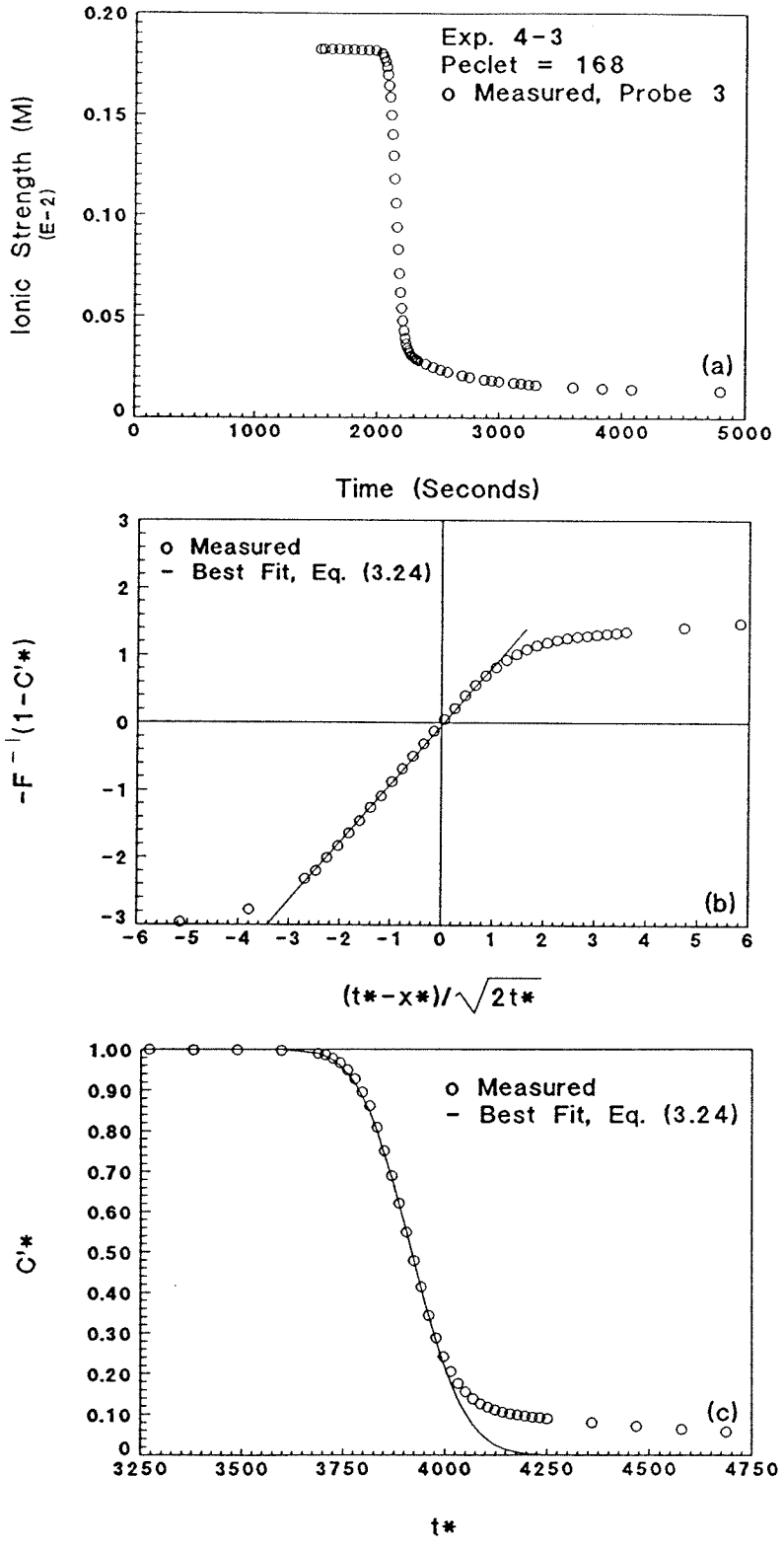

Fig. 5.2: Exp. 4-3 reverse breakthrough curve, conductivity probe 3, Pe = 167: (a) complete experimental data; (b) linearization with least-squares fit; and (c) breakthrough only with best-fit, Eq. (3.24).

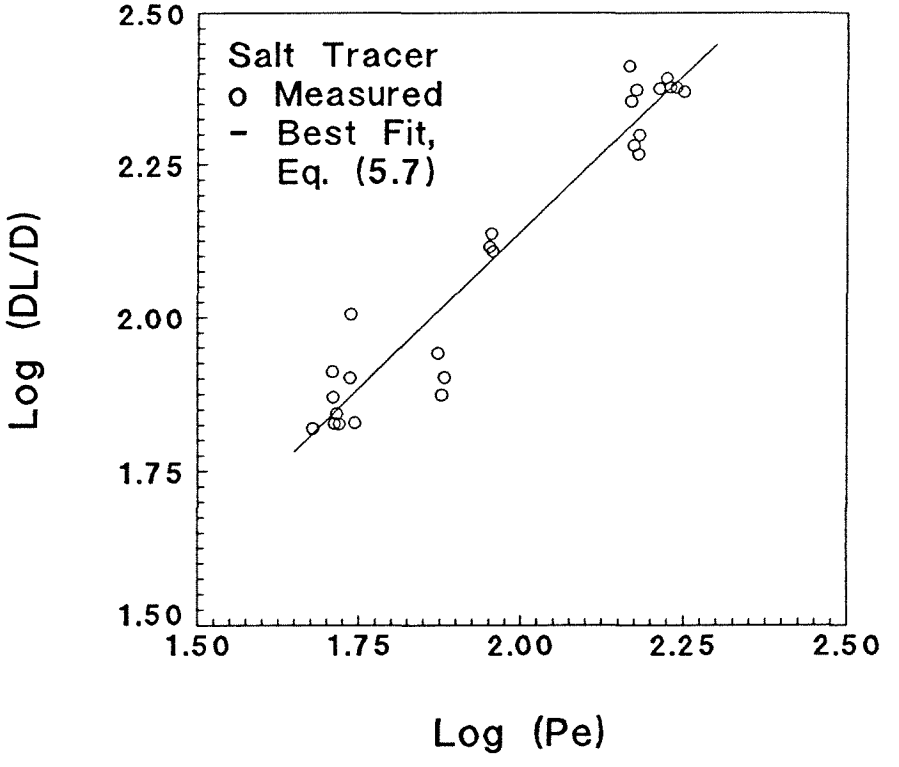

Fig. 5.3: Measured longitudinal dispersion coefficients and least-squares, best-fit of this data versus the Peclet number for salt tracers.

analysis discussed above. The best-fit line in this figure is determined by a least-squares analysis of the determined data regressing D_L/D on Pe. The equation of this best-fit line is:

$$Log\left[\frac{D_L}{D}\right] = 1.023Log[Pe] + 0.094 \qquad (5.7)$$

$$where:\ R^2 = correlation\ coefficient = 0.932.$$

Fig. 5.4 is similar to Fig. 5.3 but includes the work of Houseworth (1984) for the uniform medium. The variation of $D_L/V_s d_g$ versus the Peclet number for the salt experiments is shown in Fig. 5.5. Fig. 5.6 is similar to Fig. 5.5 but includes the work of Houseworth (1984) for both the uniform and nonuniform medium. These figures show that for this work, D_L is 0.2 order of magnitude greater than that of Houseworth (1984) for the same medium, but is still less than D_L found for the nonuniform medium. Experimental data for the salt experiments are listed in Table 5.1.

5.4 Particle Experiments

A series of 105 particle breakthrough experiments were performed. In these experiments, both the particle suspension and the clean water had the same ionic strength. Both particles displacing clean water (forward breakthrough) and clean water displacing particles (reverse breakthrough) experiments were completed. The major variables were the flow rate, ionic strength, and particle diameter. For the breakthrough experiments, the samples were taken from the

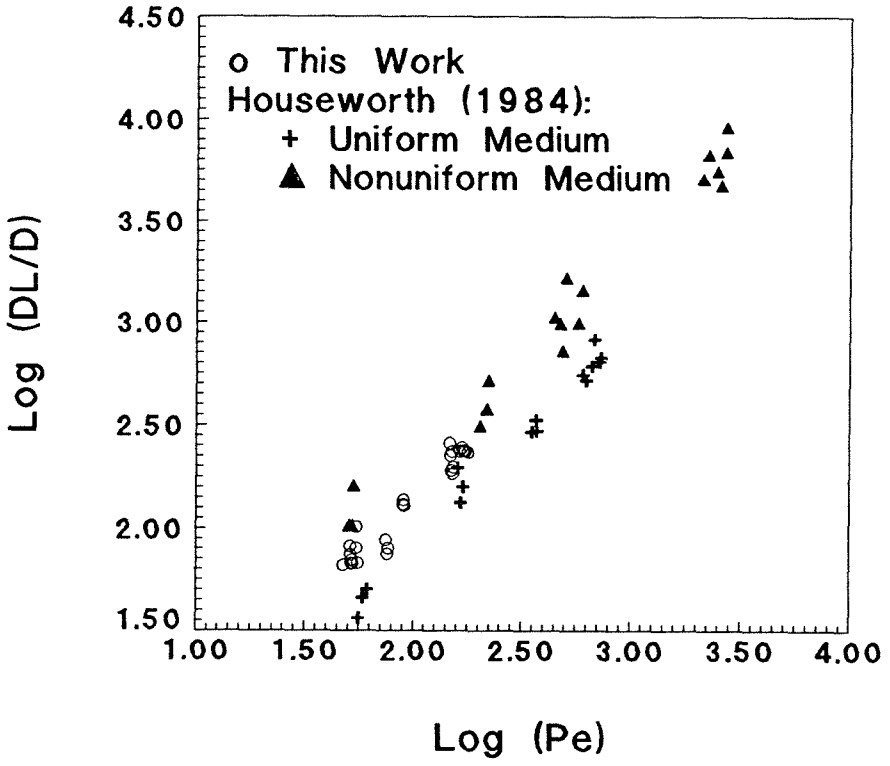

Fig. 5.4: Measured longitudinal dispersion coefficients versus the Peclet number for salt tracer breakthroughs of this work and Houseworth (1984).

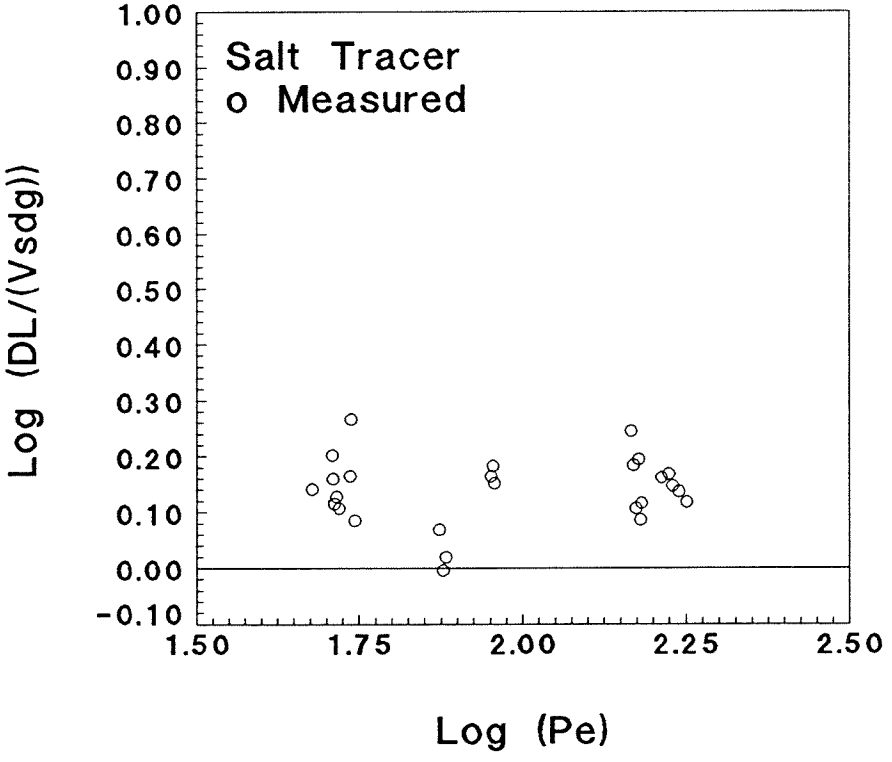

Fig. 5.5: $D_L/V_s d_g$ versus the Peclet number for salt.

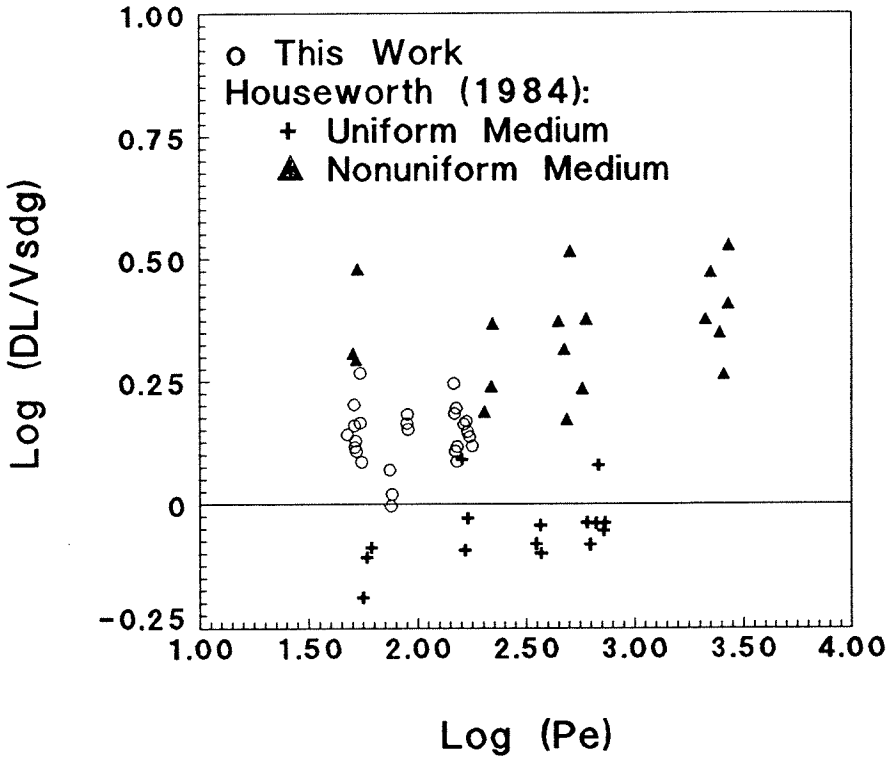

Fig. 5.6: $D_L/V_s d_g$ versus the Peclet number for salt for this work and Houseworth (1984).

Table 5.1: Experimental Variables and Measured Parameters for Salt

Experiment	V_s (cm/s)	D_L (cm^2/s)	Pe
CPB1P1S1	0.0373	0.002015	90.5
RCPB1P1S1	0.0371	0.002153	90.0
CPB2P1S1	0.0368	0.002049	89.4
CPB3P1S1	0.0616	0.003002	149.4
RCPB3P1S1	0.0627	0.003123	152.2
CPB4P1S1	0.0625	0.002904	151.6
RCPB4P1S1	0.0621	0.003706	150.7
CPB5P1S1	0.0196	0.001036	47.7
CPB7P1S1	0.0214	0.001095	51.9
RCPB7P1S1	0.0216	0.001054	52.4
CPB8P1S1	0.0211	0.001281	51.2
RCPB8P1S1	0.0211	0.001164	51.3
CPB1P3S1	0.0610	0.00355	148.0
RCPB1P3S1	0.0605	0.004057	146.7
CPB2P3S1	0.0228	0.001058	55.4
RCPB2P3S1	0.0225	0.001251	54.5
CPB3P3S1	0.0225	0.001588	54.7
RCPB1P4S1	0.0212	0.001055	51.6
1-3	0.0716	0.003736	173.7
2-3	0.0673	0.003723	163.3
3-3	0.0700	0.003741	169.8
4-1	0.0735	0.003676	178.4
4-3	0.0690	0.003875	167.5
5-1	0.0311	0.001174	75.5
5-2	0.0314	0.001254	76.3
5-3	0.0307	0.001372	74.6

third and fifth sample ports (x = 89.4 cm and x = 149.3 cm) as shown in Figs. 4.1 and 4.2. The velocity scale used for all analyses is the average particle velocity and not the fluid interstitial velocity. These velocities differ by a few percent as explained in Chapter 3 and shown in the next section.

5.4.1 Advective Velocity

Two analyses are made in this section. First, the effect of particle radius on particle velocity is explored by comparing measured values found in this work of particle velocity, V_p, to fluid velocity, V_s. This comparison can be expressed mathematically as shown in Chapter 2 and referred to in Chapter 3 as:

$$V^* = 1 + \Delta V = 1 + \frac{V_p - V_s}{V_s} = \frac{V_p}{V_s} \qquad (5.8)$$

Second, the measured values of V* are compared to the values given by the theoretical model developed in Chapter 2 for ΔV (Happel and Byrne 1954; DiMarzio and Guttman 1969 and 1970).

The key definitions for completing the first analysis follow. For each dispersion experiment, an average interstitial particle velocity is calculated by dividing the distance x, L, of the sample port from the beginning of the column by the elapsed time required for 50% particle breakthrough, t_{50}:

$$V_p = \frac{L}{t_{50}} \qquad (5.9)$$

The average interstitial fluid velocity is calculated by dividing the volume flow rate, Q, by the product of the cross-sectional area of the column, A, and the effective porosity of the packed column, θ_e:

$$V_s = \frac{Q}{A\theta_e} \qquad (5.10)$$

The determination of the effective porosity was discussed in Chapter 4 and is determined from salt tracer breakthroughs as follows:

$$\theta_e = \frac{V_s}{V_D} \qquad (5.11)$$

$$\textit{where: } V_D = \textit{Specific discharge} = Q/A$$

For this equation, the fluid velocity, V_s, is calculated from a salt tracer

breakthrough in a similar fashion as that of the particle velocity in which L and t_{50} are the distance to the conductivity port from the beginning of the column and the time required for 50% salt breakthrough, respectively.

The comparison of particle velocity to fluid velocity shows that the particles have a velocity which is a few percent greater than that of the fluid itself as seen in Figs. 5.7 - 5.9, but the magnitude of the difference depends on the particle radius. Fig. 5.7 is for the 1.0 micron particles, and Figs. 5.8 and 5.9 are for the 2.8 and 0.1 micron particles, respectively. Each of these figures is comprised of three separate plots and within each plot the measured enhanced velocities found at either sample port 3 or 5 (x = 89.4 cm and x = 149.3 cm) are plotted so as to be distinct from each other. The enhanced velocities measured at either port are shown in this fashion in order to ascertain any possible inlet boundary effects which would be more pronounced at the beginning of the column and then become less apparent as the distance traveled through the column becomes greater. In part (a) of these figures, V* is plotted versus V_p. This is shown in order to see if the enhanced velocity is influenced by the order of the velocity itself. This was not expected to show a correlation, because all of these velocities are within the framework of Poiseuille flow. In part (b), V* is plotted versus the filter coefficient. This is shown in order to see if the combined effects of particle removal (manifested in the filter coefficient) have an effect on the enhanced velocity. This was not expected to show any correlation, because the length scale of interaction (limiting trajectory) between the particles and the grains of the

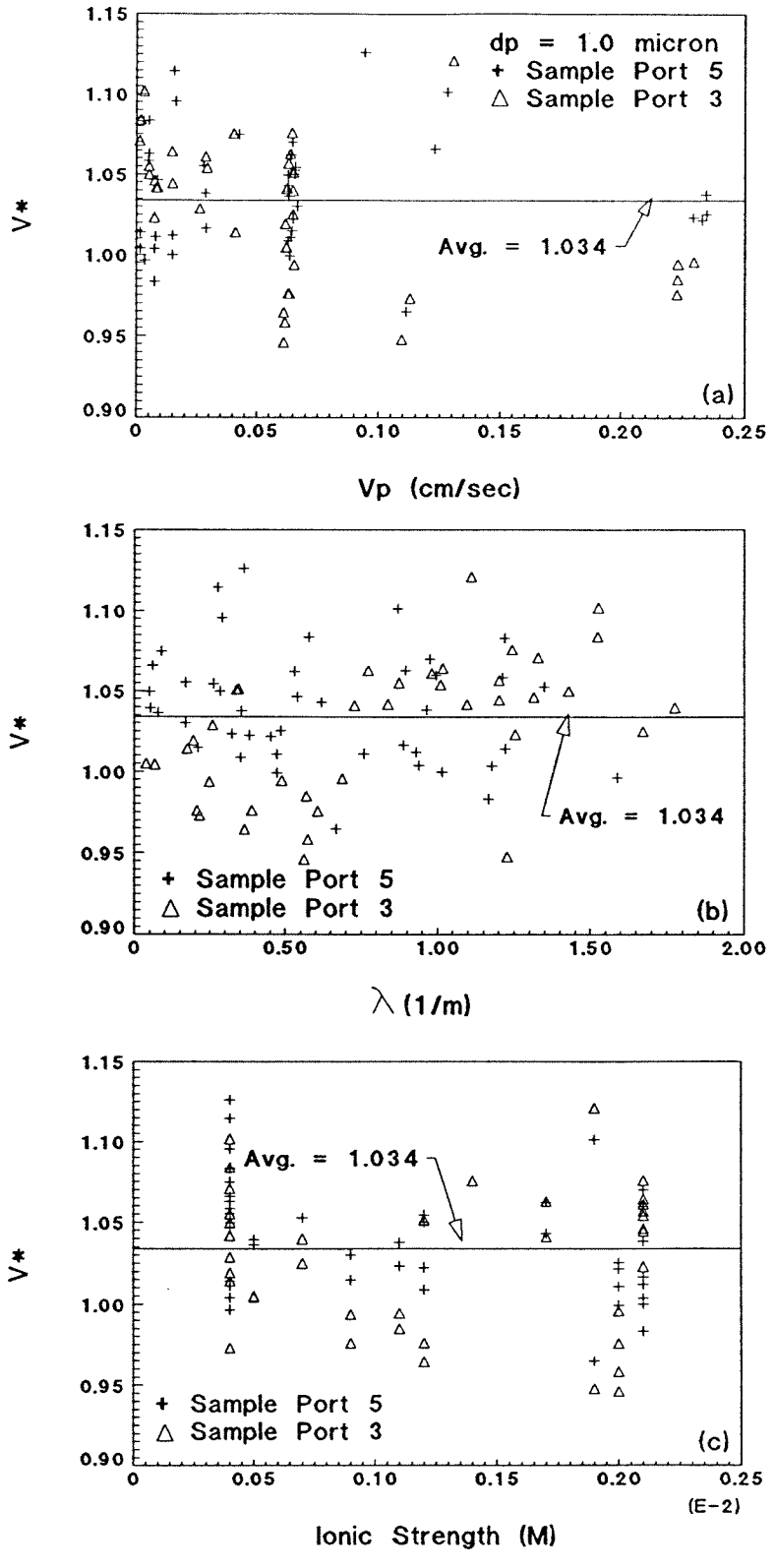

Fig. 5.7: Measured enhanced velocity ratios for both sample ports for the 1.0 micron particles versus: (a) V_p; (b) λ; and (c) I.

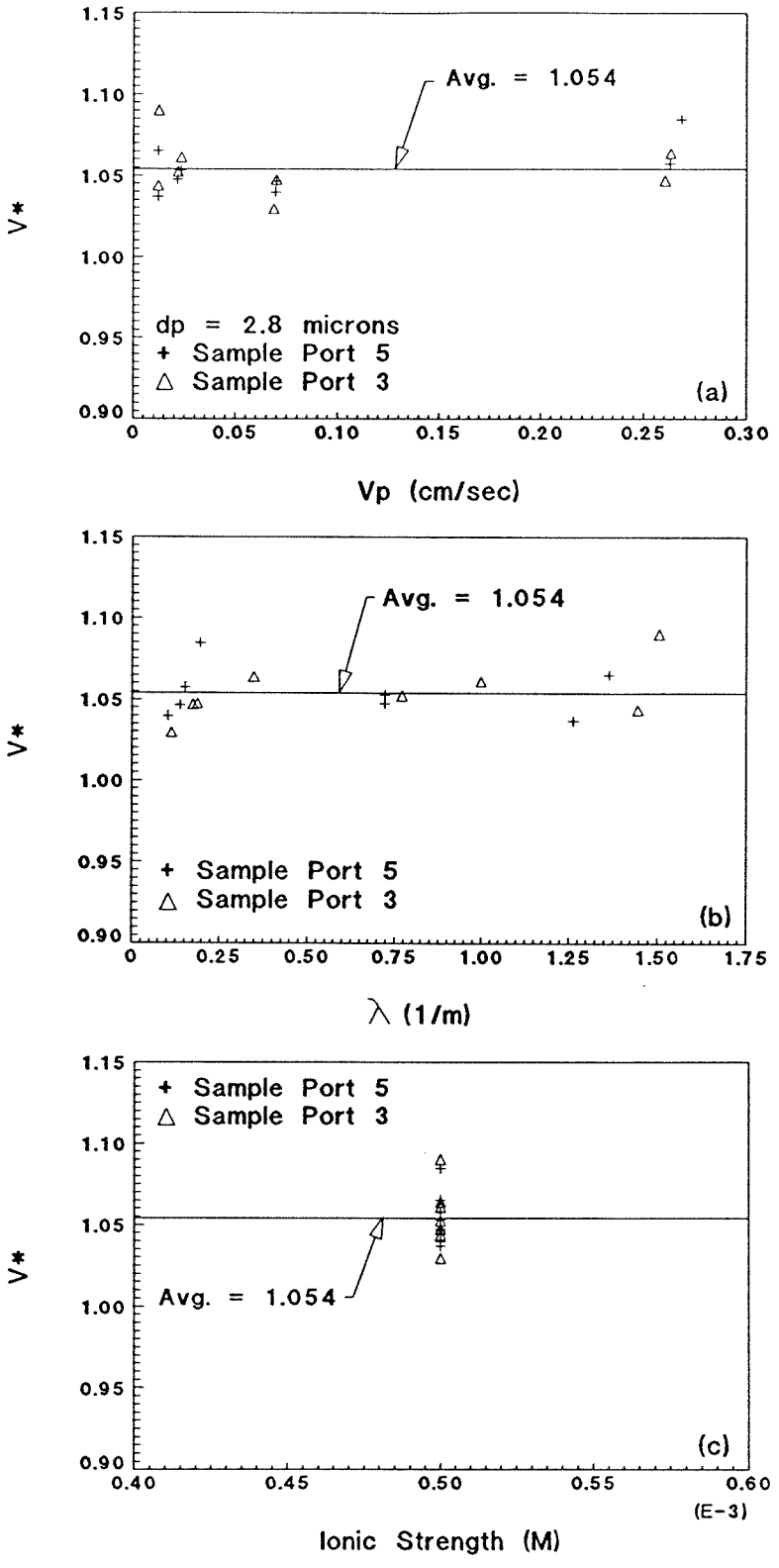

Fig. 5.8: Measured enhanced velocity ratios for both sample ports for the 2.8 micron particles versus: (a) V_p; (b) λ; and (c) I.

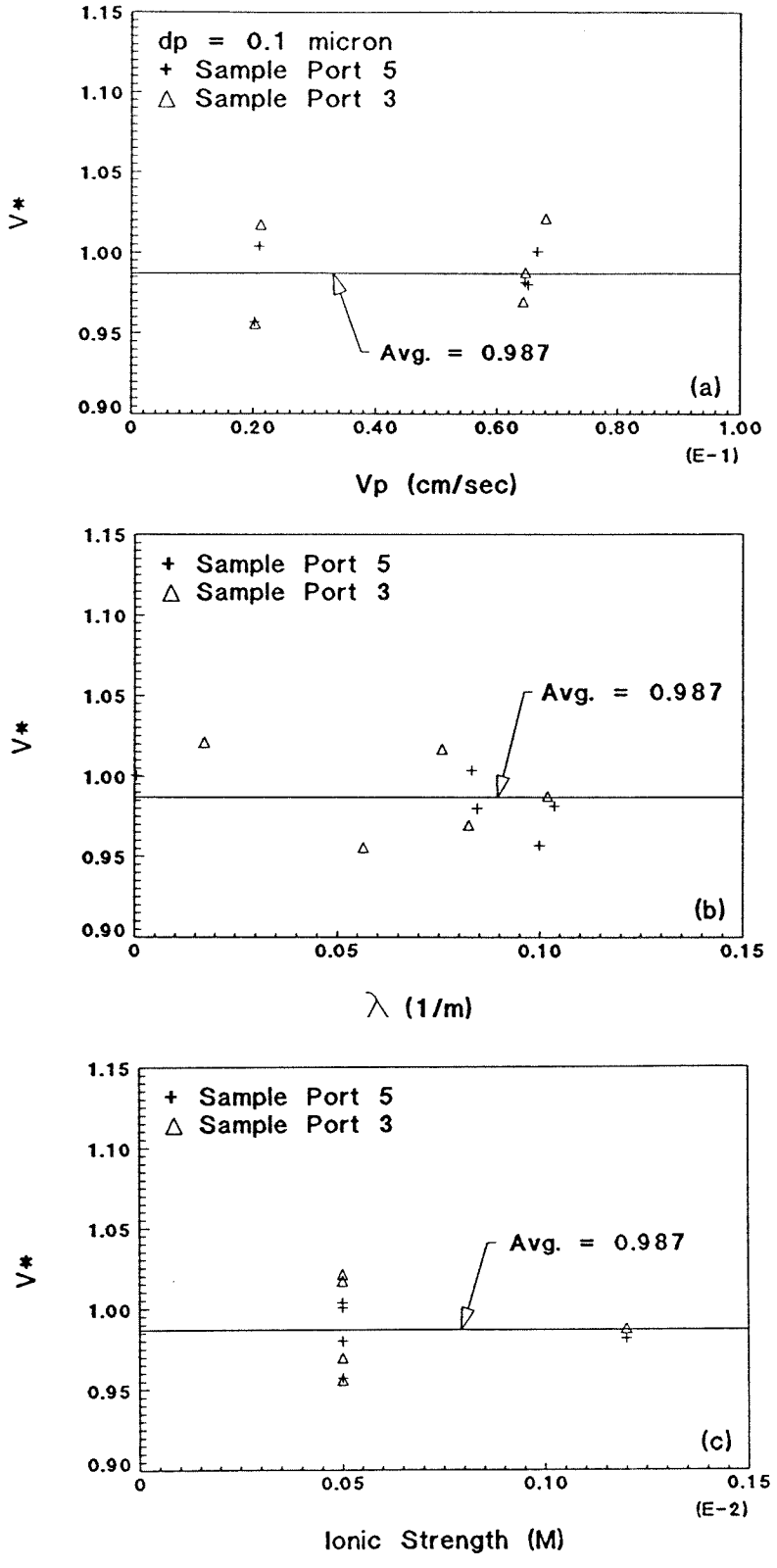

Fig. 5.9: Measured enhanced velocity ratios for both sample ports for the 0.1 micron particles versus: (a) V_p; (b) λ; and (c) I.

medium in this work is small compared to the radius of the pore (< 5%). For very large filter coefficients, the limiting trajectories for particles may become several times larger than the particle radius. Such a case was not encountered in this work. In part (c), V* is plotted versus the ionic strength of the fluid. This is shown in order to verify the assumption made in Chapter 2 that the only effect of the ionic strength on advection is to modify the particle radius. This was not expected to show any correlation, because the length scale of the ionic strength (double layer thickness, κ^{-1}) is small compared to the particle radius for this work (< 7%). If the particle radius is assumed to be increased by twice this double layer thickness as demonstrated in Chapter 2 using the work of Small (1974), the increase in V* will be very slight (< 0.4%).

As can be seen in these figures, as the particle radius ranged from larger to smaller, the velocity discrepancy also ranged from larger to smaller. These results are shown in Table 5.2 and are discussed in the following. For the 2.8 micron particles, the average particle velocity determined from the experiments is approximately 1.054 (± 0.016) times the velocity of the interstitial fluid, and that calculated from the theory developed in Chapter 3 (Eq. (3.1)) is expected to be approximately 1.04. For the 1.0 micron particles, the average particle velocity is approximately 1.034 (± 0.039) times the velocity of the interstitial fluid, and that calculated from the theory is expected to be approximately 1.015. For the 0.1 micron particles, the average particle velocity is approximately 0.987 (± 0.022) times the velocity of the interstitial fluid velocity, and that calculated from the

Table 5.2: Enhanced Velocity Ratios: Measured Means and Predictions (Eq. (3.1)).

Particle Diameter (micron)	V*	
	Measured	Predicted
0.1	0.987	1.001
1.0	1.034	1.015
2.8	1.054	1.040

theory is expected to be approximately 1.001. For the theoretical values, the pore radius is taken to be the median pore radius found by Houseworth (1984) for this sand medium which is approximately 70 microns. Even though the average values for enhanced velocity are similar to the predicted values, there is considerable spread of data around the average as seen in Figs. 5.7 - 5.9.

The results of this analysis as determined from an inspection of these figures are stated in the following:

1) The measured velocities of the particles which differed from the fluid velocity are not artifacts of the inlet boundary condition, but are actual enhanced velocities.

2) The enhanced velocities of the particles in this work are not significantly influenced by chemistry or removal. The largest the length scales of these two interactions became in this work as measured by the double layer thicknesses and limiting trajectories are not significant when compared to the pore radius (< 5%).

3) The overall range of velocities in this work is in the linear, laminar range, and,

at this magnitude, increases in velocity result in similar increases in enhanced velocity.

Fig. 5.10 shows the combined results of both this work and Small (1974). In part (a) of this figure, the pore radius to be used for calculating theoretical V* ratios is taken directly from Houseworth (1984) (r_0 ≈ 70 microns). In part (b), the pore radius which was used is the pore radius of Houseworth (1984) reduced by the ratio of the effective porosity measured in this work to the effective porosity measured by Houseworth (1984). These results verify the predictions of enhanced transport of particles, but the actual velocity enhancement could not be explained totally by the size exclusion principal. This discrepancy could be explained by the fact that the actual pore radius was not found for either the packed column of this work or the work of Small (1974).

5.4.2 Longitudinal Dispersion Coefficient

As shown previously by completing a dimensional analysis argument in Chapter 3, the longitudinal dispersion coefficient is assumed to scale with the velocity, media grain diameter, and particle diffusion coefficient but not with the system chemistry:

$$\frac{D_{Lp}}{D_p} = F[Pe_p] = F[\frac{V_p d_g}{D_p}] \qquad (5.12)$$

In order to experimentally verify this, a set of breakthrough experiments have been performed while varying the velocity, particle size, and ionic strength.

The longitudinal dispersion coefficient was determined for each experiment

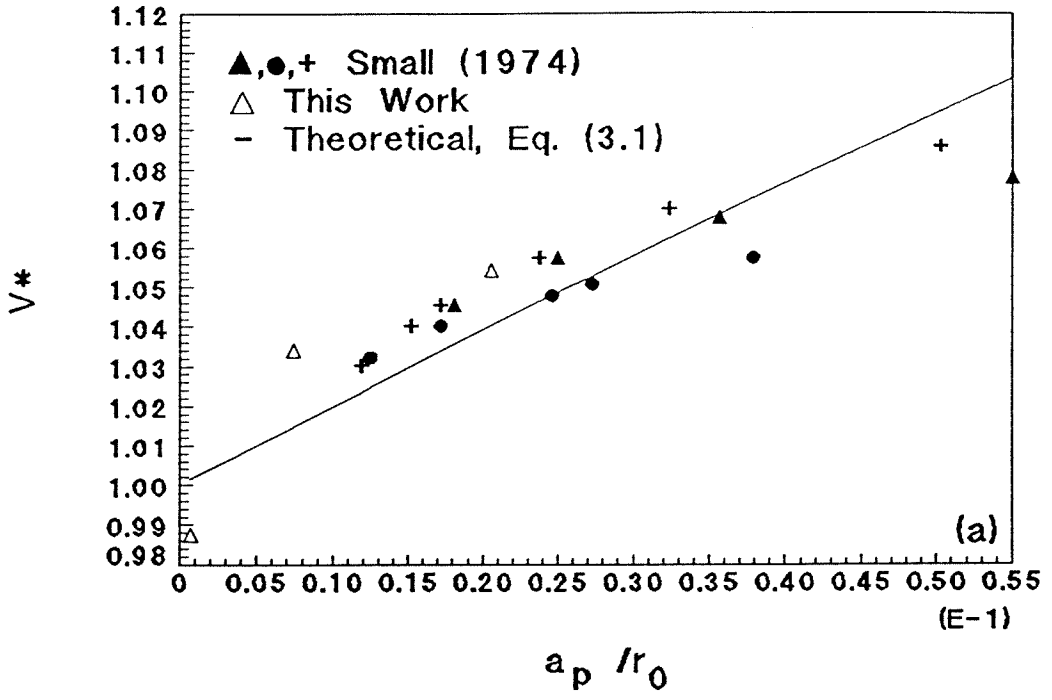

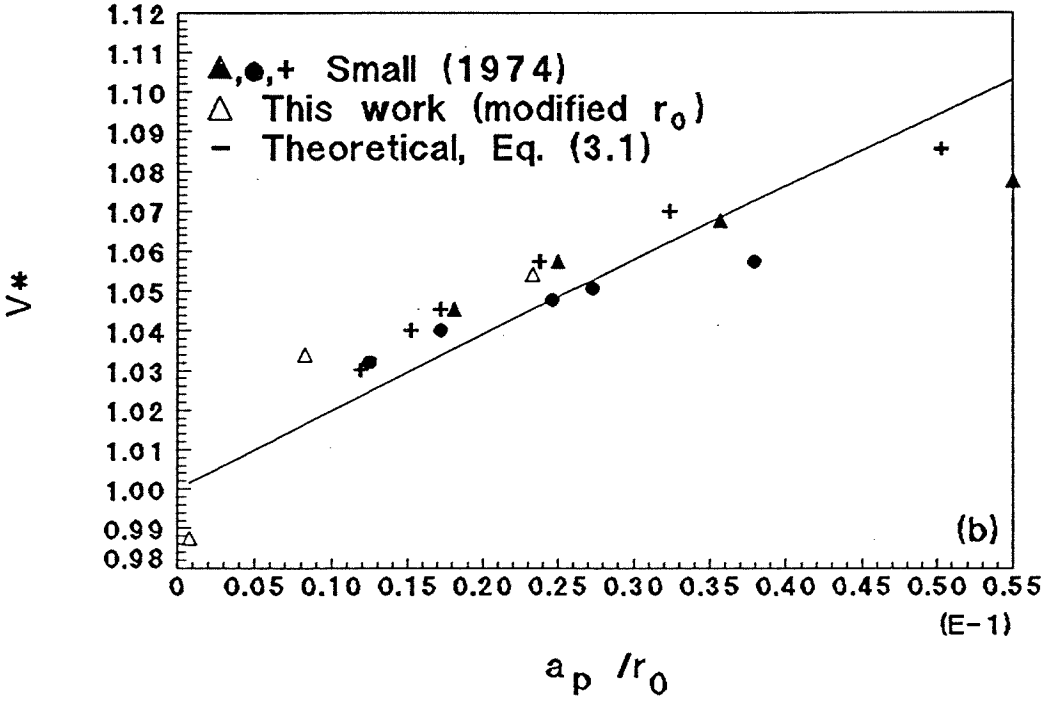

Fig. 5.10: Measured enhanced velocity ratios versus ratio of particle radius to pore radius for comparing experiment to theory: (a) Houseworth (1984) pore radius; (b) modified Houseworth (1984) pore radius.

from the inverted, simplified erfc (Eq. (3.24)). In the simplified form, the dispersion coefficient only appears once and can be calculated directly. This simplification can only be performed if the filter coefficient is small enough as shown in Chapter 3 and Appendices A and B. For each experiment, the maximum error associated with approximating the complete transient solution has been calculated and is shown in Fig. 5.11 versus the dimensionless filter coefficient. As explained in Chapter 3, this error is the maximum error for the measurable portion of the breakthrough. This figure shows that the maximum error for all except one of the experiments is less than 6%. The simplified erfc solution to be used in the particle breakthrough analysis which was determined previously in Chapter 3 is:

$$C* = exp[-\lambda *x*]\frac{1}{2}erfc\left[\sqrt{Pe_{Dp}}\left(\frac{x* - t*}{2\sqrt{t*}}\right)\right] \qquad (3.26)$$

This equation can be rewritten as shown in Chapter 3 to be the same as Eq. (3.24). The procedure for calculating the dispersion coefficient was described above in the section which discussed salt tracer breakthroughs. The only difference is that the fluid variables are replaced by particle variables at this point. The longitudinal dispersion coefficient is calculated from the slope value by using the dynamic Peclet number identity:

$$m = \sqrt{Pe_{Dp}} = \sqrt{\frac{V_p d_g}{D_{Lp}}}$$

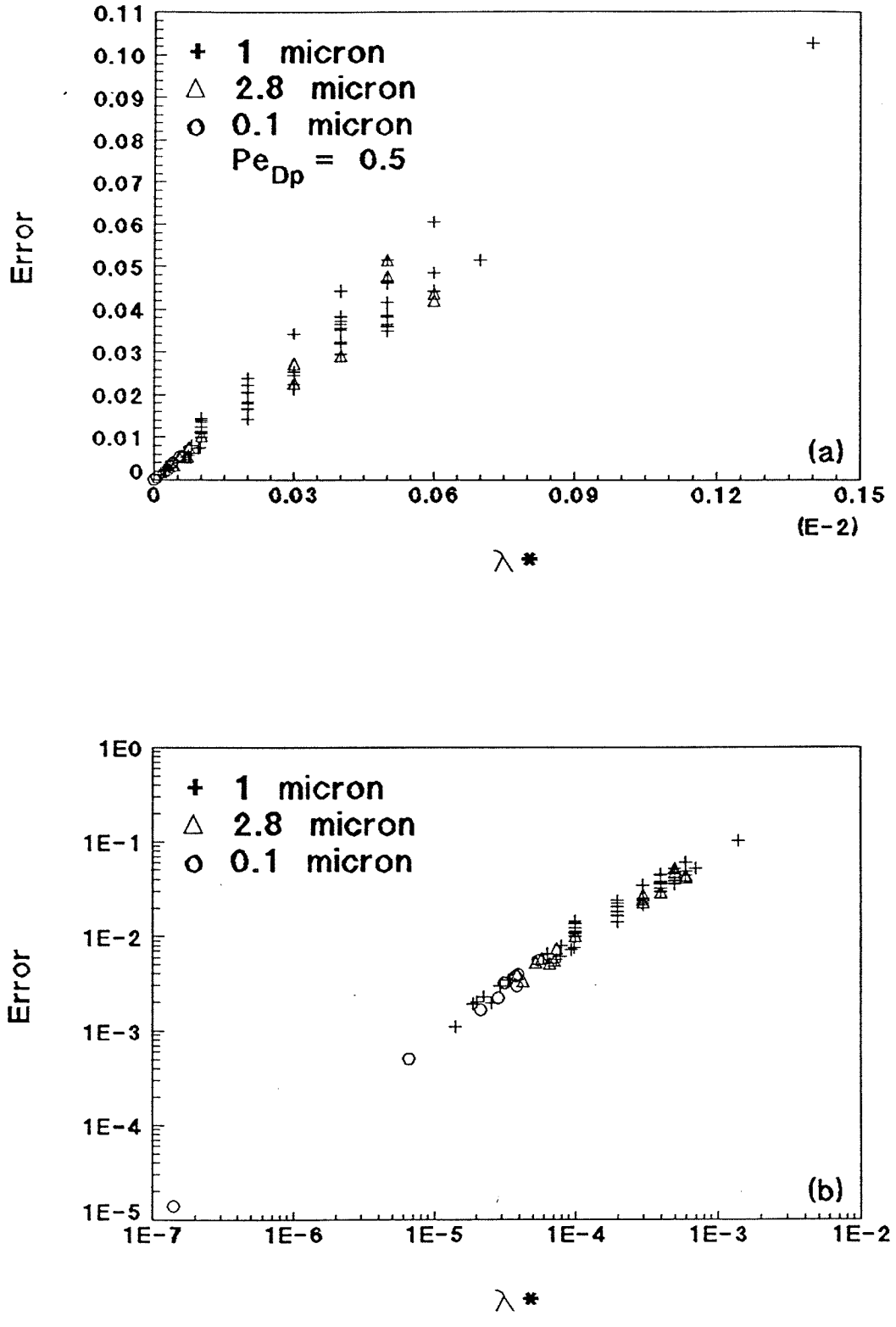

Fig. 5.11: Maximum error in concentration at 50% breakthrough of particle breakthrough experiments using approximate versus exact solution.

$$D_{Lp} = \frac{V_p d_g}{m^2}$$

As in the case of salt breakthroughs, the tails are ignored, and only the linear points are used in the least-squares analysis. After the longitudinal dispersion coefficient is determined, this value is substituted into the erfc solution, Eq. (3.24), in order to calculate the best-fit breakthrough curve for the experimental data.

Figs. 5.12 - 5.17 show representative experimental breakthrough curves for 1.0 micron particles. These figures are comprised of three separate plots which are described in the following. In part (a), the measured data are shown for the entire experiment. In part (b), the data of the breakthrough is plotted linearly as a function of the inverted Gaussian probability function according to the description given above and in section 5.3. In this part, the solid line is the best-fit line found from a least-squares analysis on only the data which is linear and excludes tails. In part (c), the breakthrough data is shown in dimensionless terms on an arithmetic plot. The solid line in this part is the best-fit solution of Eq. (3.24) using the longitudinal dispersion coefficient value found from the straight line slope of part (b). Experimental breakthrough curves for all experiments are shown in Appendix C, and these are comprised of the same three plots as described above.

These curves show that the experimental breakthrough curves start deviating from the theoretical solution for relative concentrations greater than approximately 60 to 90% for forward breakthroughs and less than approximately

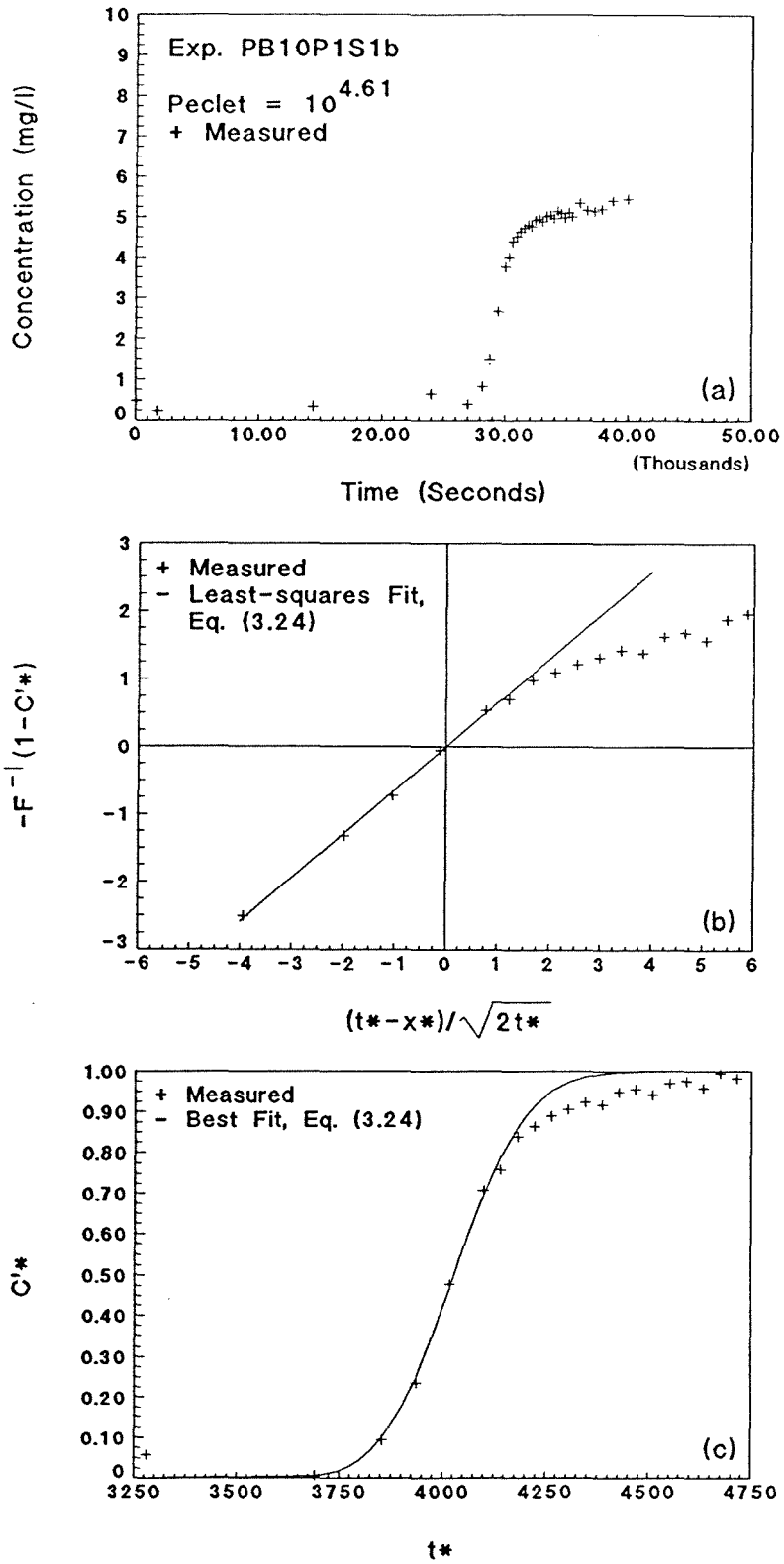

Fig. 5.12: Exp. PB10P1S1b forward breakthrough, sample port 5, $Pe_p = 10^{4.61}$: (a) complete experimental data; (b) linearization with least-squares fit; and (c) breakthrough only with best-fit, Eq. (3.24).

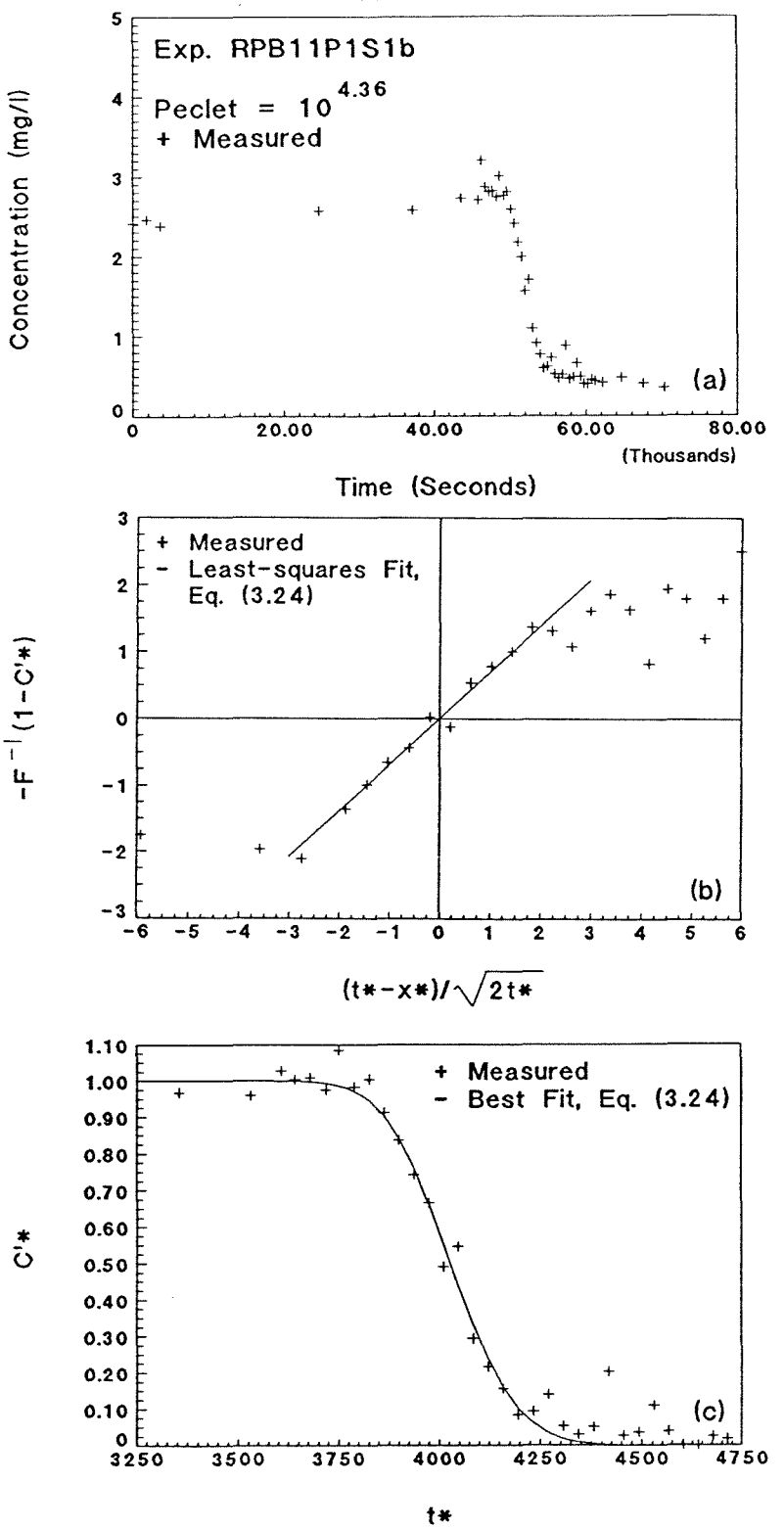

Fig. 5.13: Exp. RPB11P1S1b reverse breakthrough, sample port 5, $Pe_p = 10^{4.36}$: (a) complete experimental data; (b) linearization with least-squares fit; and (c) breakthrough only with best-fit, Eq. (3.24).

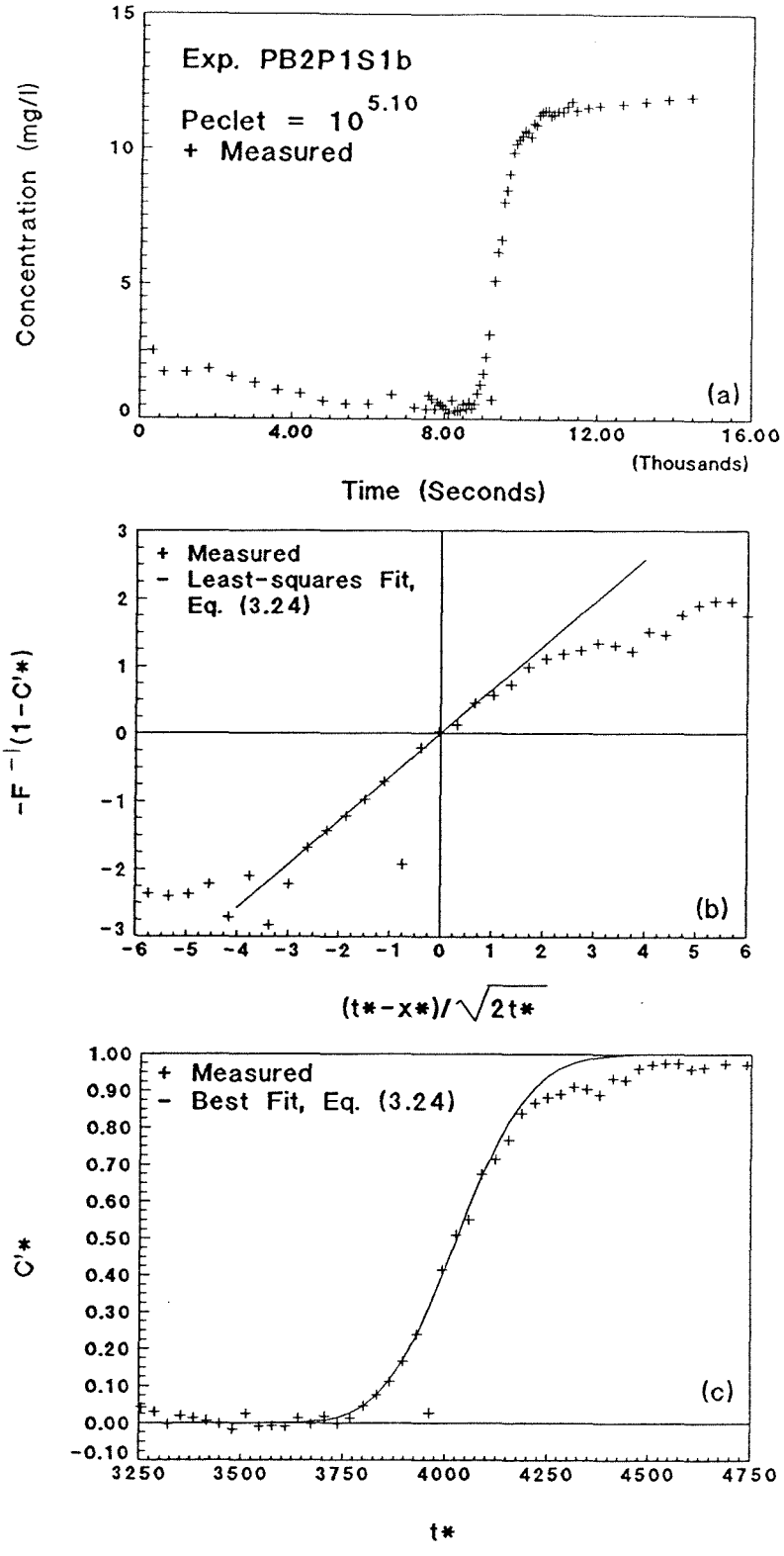

Fig. 5.14: Exp. PB2P1S1b forward breakthrough, sample port 5, $Pe_p = 10^{5.10}$: (a) complete experimental data; (b) linearization with least-squares fit; and (c) breakthrough only with best-fit, Eq. (3.24).

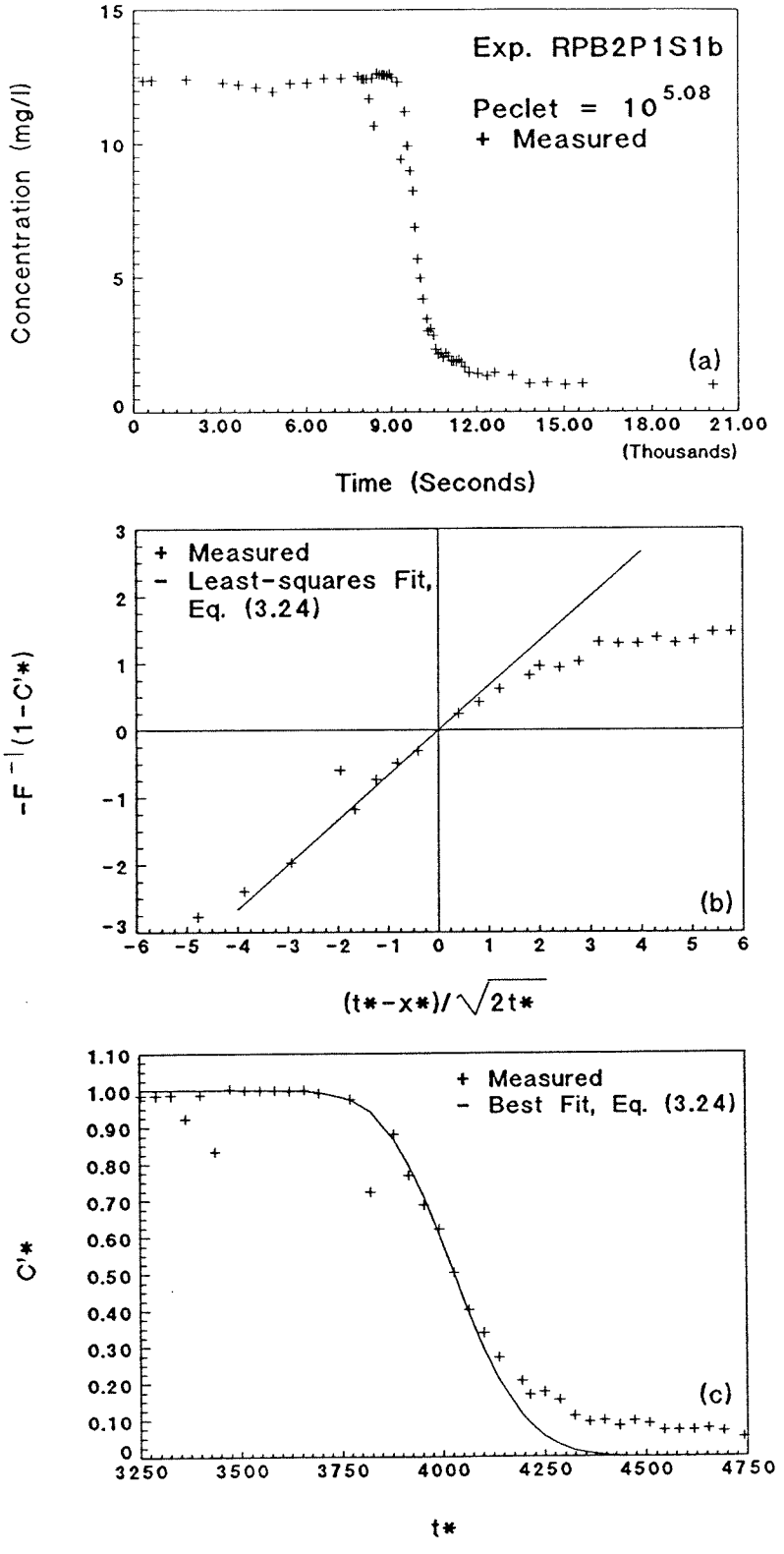

Fig. 5.15: Exp. RPB2P1S1b reverse breakthrough, sample port 5, $Pe_p = 10^{5.08}$: (a) complete experimental data; (b) linearization with least-squares fit; and (c) breakthrough only with best-fit, Eq. (3.24).

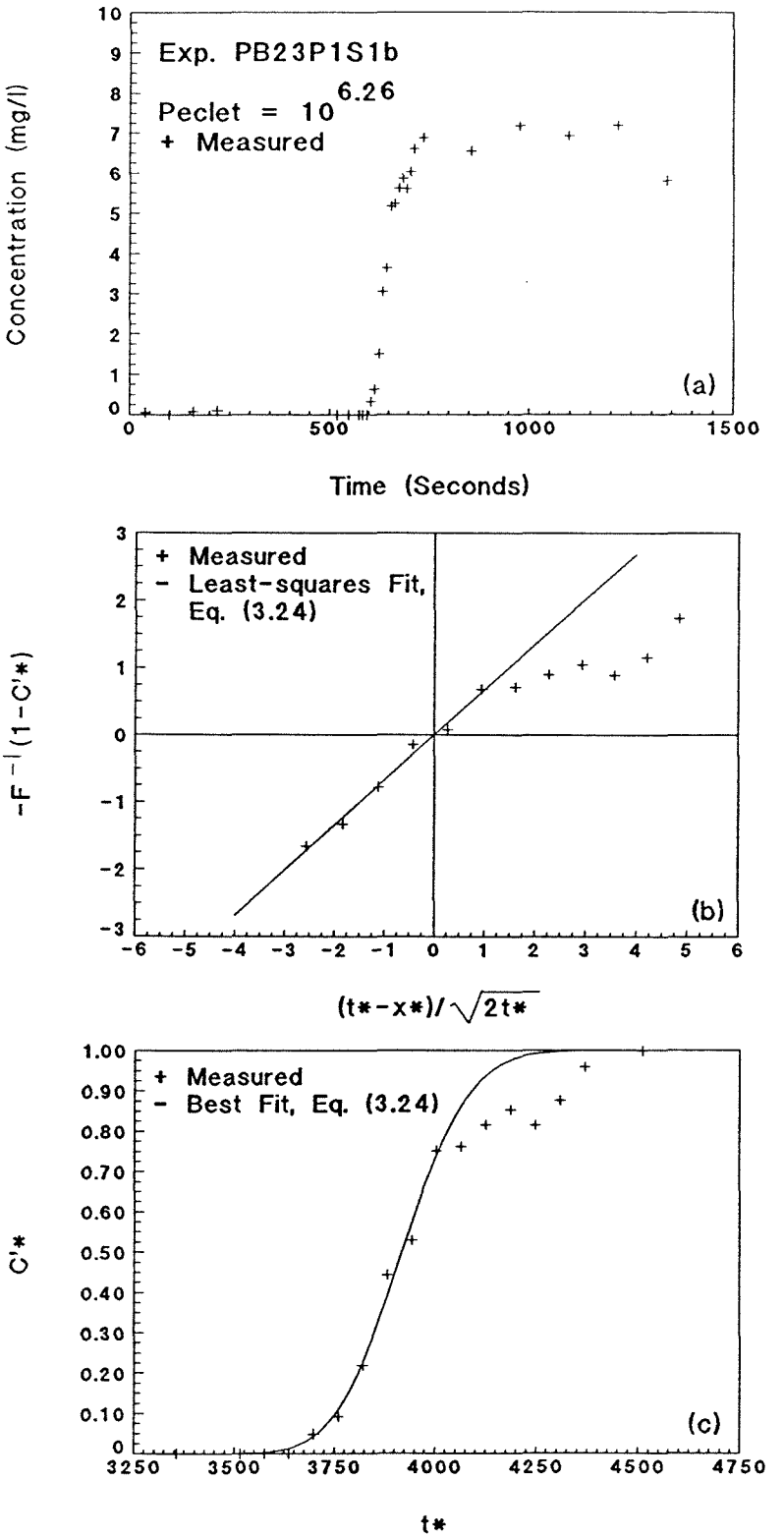

Fig. 5.16: Exp. PB23P1S1b forward breakthrough, sample port 5, $Pe_p = 10^{6.26}$: (a) complete experimental data; (b) linearization with least-squares fit; and (c) breakthrough only with best-fit, Eq. (3.24).

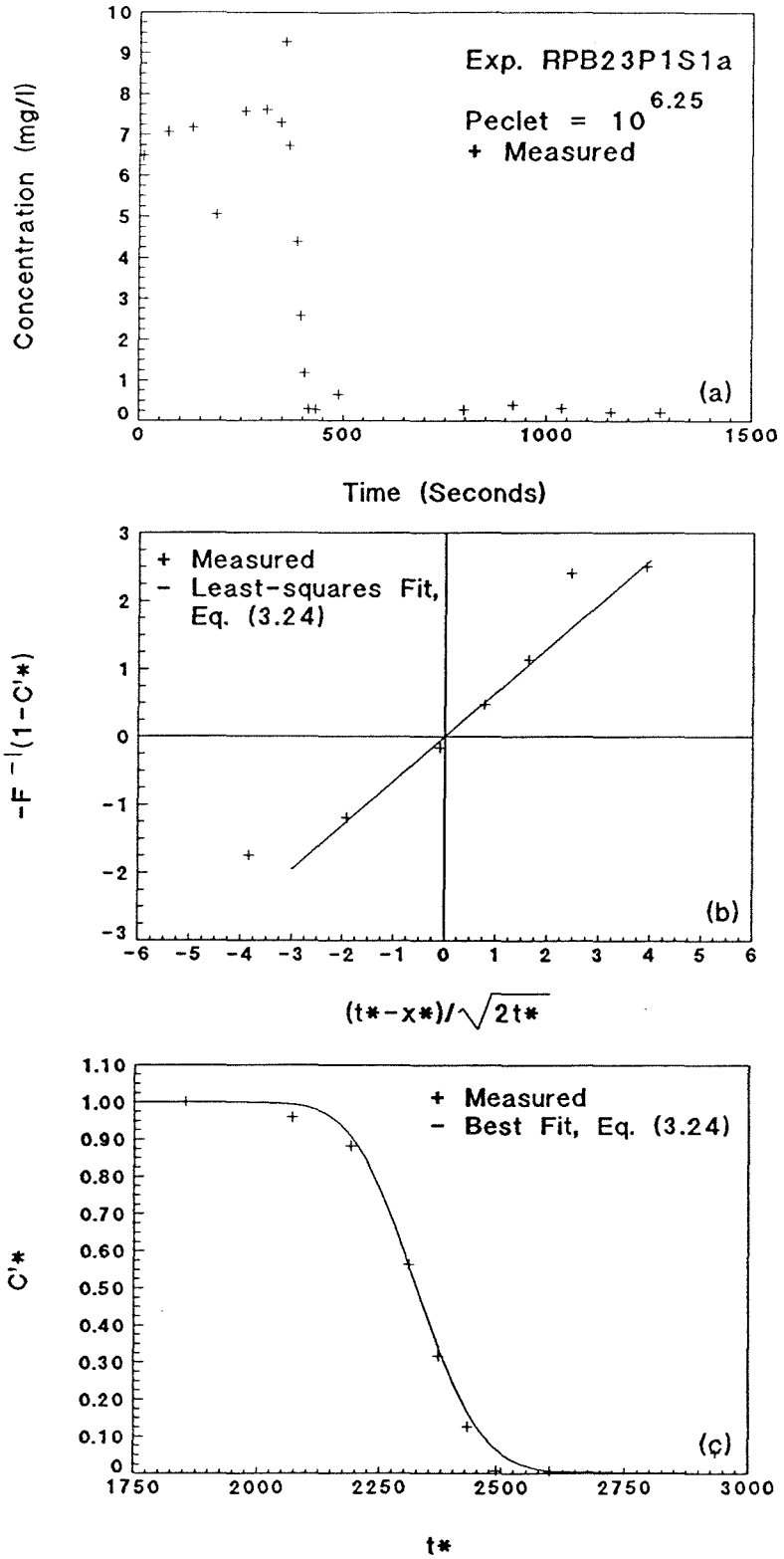

Fig. 5.17: Exp. RPB23P1S1a reverse breakthrough, sample port 3, $Pe_p = 10^{6.25}$: (a) complete experimental data; (b) linearization with least-squares fit; and (c) breakthrough only with best-fit, Eq. (3.24).

20 to 40% for reverse breakthroughs. This deviation depends upon the Peclet number and filter coefficient. This deviation of the experimental breakthrough curve from the theoretical curve is called "tailing". This tailing behavior for particle breakthroughs was generally more pronounced than for saline tracers. As shown by Houseworth (1984), the tailing is greater for large Peclet flows and is not as great for low Peclet flows. As the filter coefficient became larger, the breakthrough became less distinct which resulted in fewer linear points on the breakthrough. This may be more of an indication of difficulty in breakthrough detection rather than in increased tailing. Because of this behavior, the theoretical equation can only be applied to the leading portion of the experimental breakthrough curves, and when calculating dispersion coefficients, the least-squares analysis was only completed for the leading data which were linear. A significant point to note is that the leading portion does follow the theory. Even though tailing may become significant after 60% for forward breakthrough or 40% for reverse breakthrough, the theory as presented earlier for particle transport which includes filtration appears to be correct and is similar to solute tracer transport.

The 1.0 micron particle was studied first and more extensively than either the 2.8 or 0.1 micron particles. The range of the particle Peclet number for the 1.0 micron particles which was tested is 1.26×10^4 to 2.00×10^6 which are the limits of this experimental system; i.e., excessive filtration and breakthrough period too short. The variation of D_{Lp}/D_p versus the particle Peclet number for

1.0 micron particles is shown in Fig. 5.18. In this figure, the data for the longitudinal dispersion coefficient was calculated by completing the linearized breakthrough analysis listed above. The best-fit line in this figure is determined by a least-squares analysis of the determined data regressing D_{Lp}/D_p on Pe_p. The equation of this best-fit line is:

$$Log\left[\frac{D_{Lp}}{D_p}\right] = 1.0095 Log[Pe_p] + 0.294 \qquad (5.13)$$

$$where: R^2 = 0.993.$$

This can be rewritten as:

$$Log\left[\frac{D_{Lp}}{V_p d_g}\right] = 0.0095 Log[Pe_p] + 0.294 \qquad (5.14)$$

This equation shows that there is a very small effect of particle Brownian diffusion on longitudinal dispersion.

Fig. 5.19 shows the errors incurred during the analysis for the dispersion coefficient for experiments with 1.0 micron particles. These errors refer to the nonlinearity of the straight line portion of the linearized breakthrough as shown in Figs. 5.12b - 5.17b. Part (a) shows the standard error of the slope coefficient ($m^2 = V_p d_g/D_{Lp}$) which was calculated from the least-squares analysis of the linearized breakthrough for each experiment. Part (b) shows the correlation coefficient between the x- and y-variables for the same least-squares analysis of the linearized breakthrough. Both of these error terms were determined from least-squares analysis values of the linearized breakthrough data. This figure shows that the

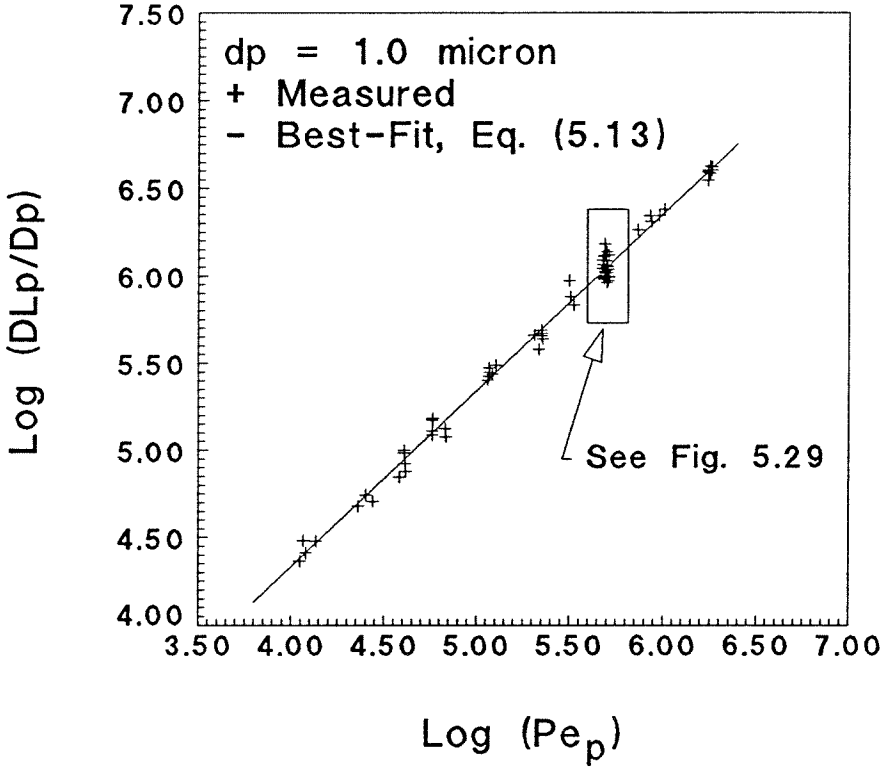

Fig. 5.18: Measured longitudinal dispersion coefficients and least-squares, best-fit of this data versus the particle Peclet number for 1.0 micron particles.

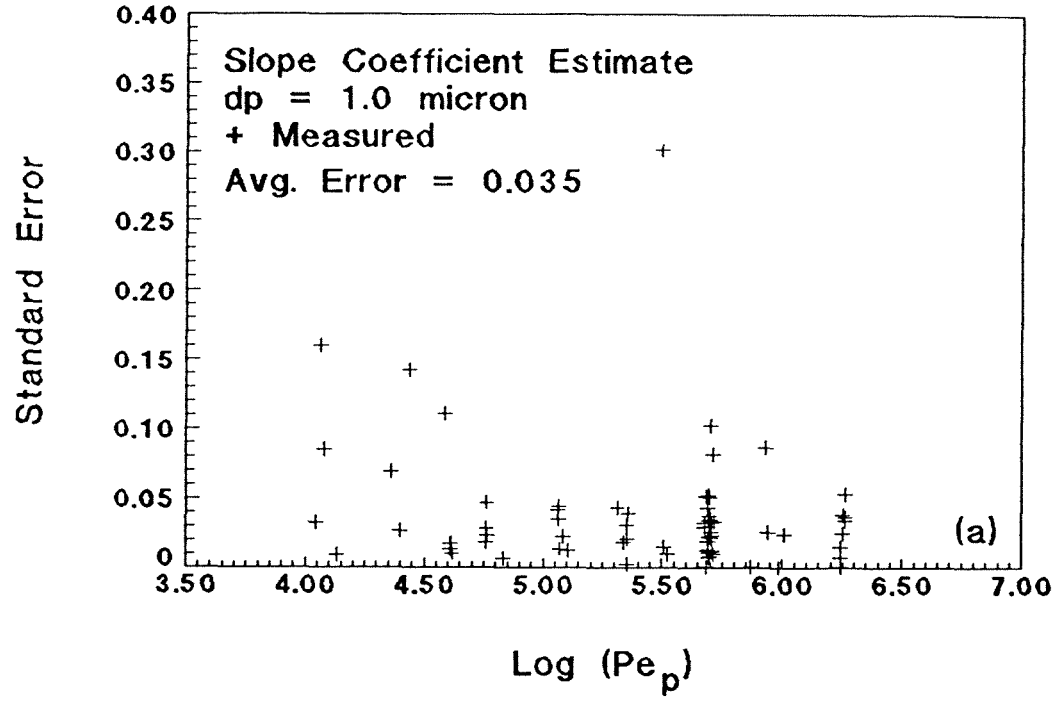

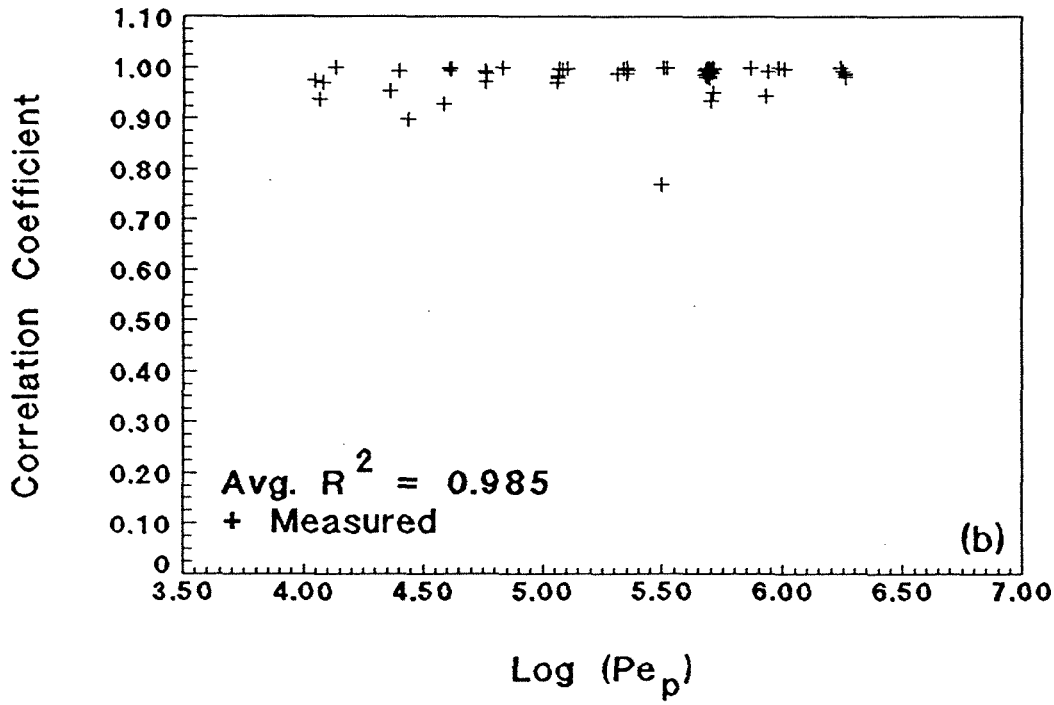

Fig. 5.19: Errors in D_{Lp} for 1.0 micron particles due to nonlinearity of experimental data as calculated from the least-squares, best-fit analysis of the linearized breakthrough data plotted versus the particle Peclet number.

standard errors due to the nonlinearity of the data as manifested in the slope coefficient are generally less than 0.05, and the correlation coefficients between the x- and y-variables are generally greater than 0.95.

In order to verify the scaling arguments for the longitudinal dispersion coefficient, experiments were performed on two other particle sizes, namely, 2.8 and 0.1 micron. Figs. 5.20 and 5.22 show the variation of D_{Lp}/D_p versus the particle Peclet number for the 2.8 and 0.1 micron particles, respectively. The range of the particle Peclet number which was studied for the 2.8 micron particles is 3.16×10^5 to 5.62×10^6 and for the 0.1 micron particles is 1.58×10^4 to 6.3×10^4. The best-fit line in these figures is determined by a least-squares analysis of the determined data. The equation of the best-fit line for 2.8 microns is:

$$Log\left[\frac{D_{Lp}}{D_p}\right] = 1.018 Log[Pe_p] + 0.263 \qquad (5.15)$$

$$where: R^2 = 0.990.$$

The equation of the best-fit line for 0.1 micron is:

$$Log\left[\frac{D_{Lp}}{D_p}\right] = 1.036 Log[Pe_p] + 0.216 \qquad (5.16)$$

$$where: R^2 = 0.985.$$

These equations can be rewritten as:

for 2.8 micron particles:

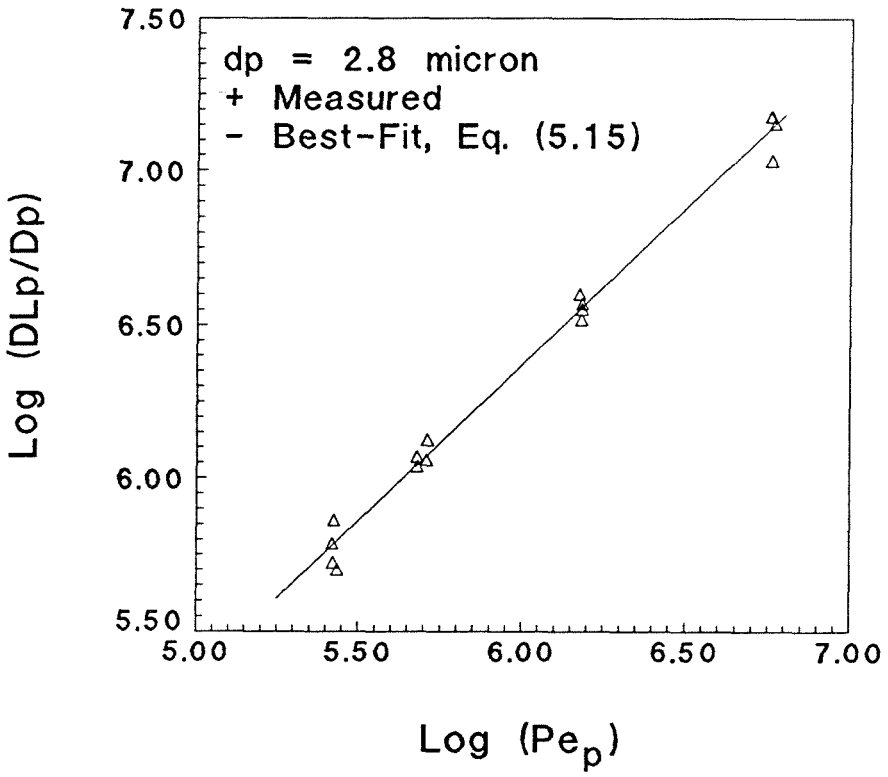

Fig. 5.20: Measured longitudinal dispersion coefficients and least-squares, best-fit of this data versus the particle Peclet number for 2.8 micron particles.

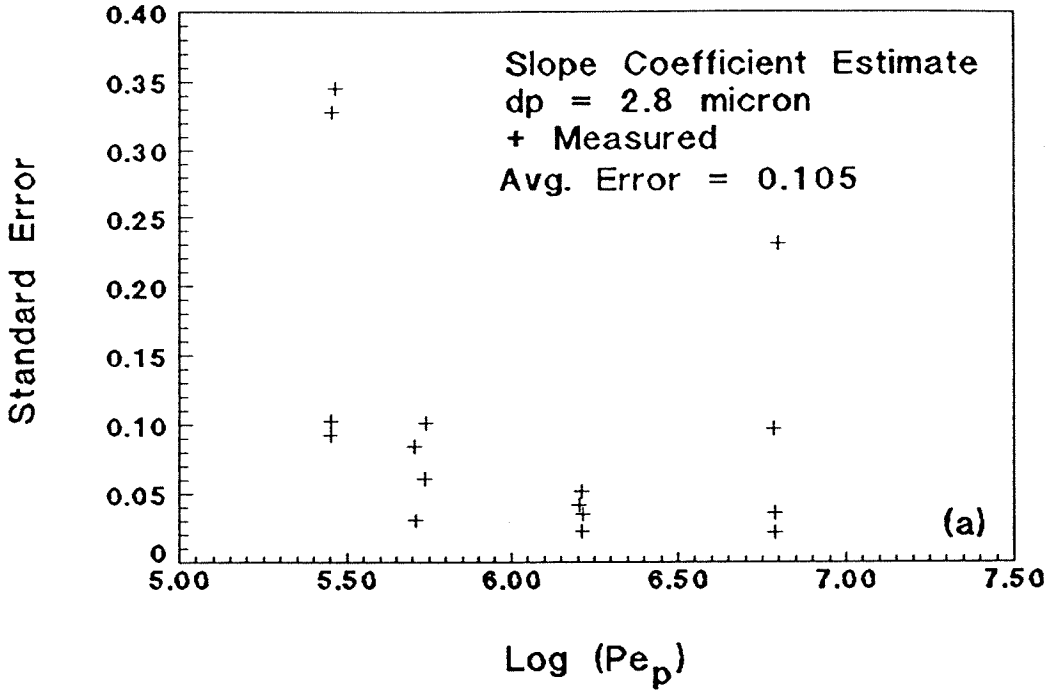

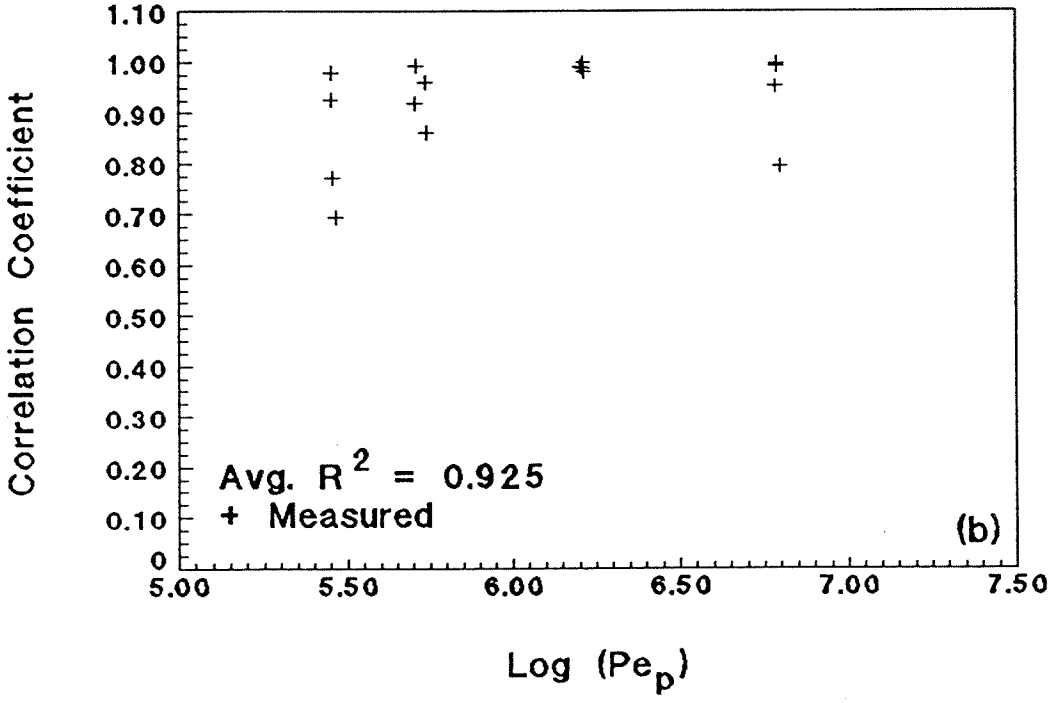

Fig. 5.21: Errors in D_{Lp} for 2.8 micron particles due to nonlinearity of experimental data as calculated from the least-squares, best-fit analysis of the linearized breakthrough data plotted versus the particle Peclet number.

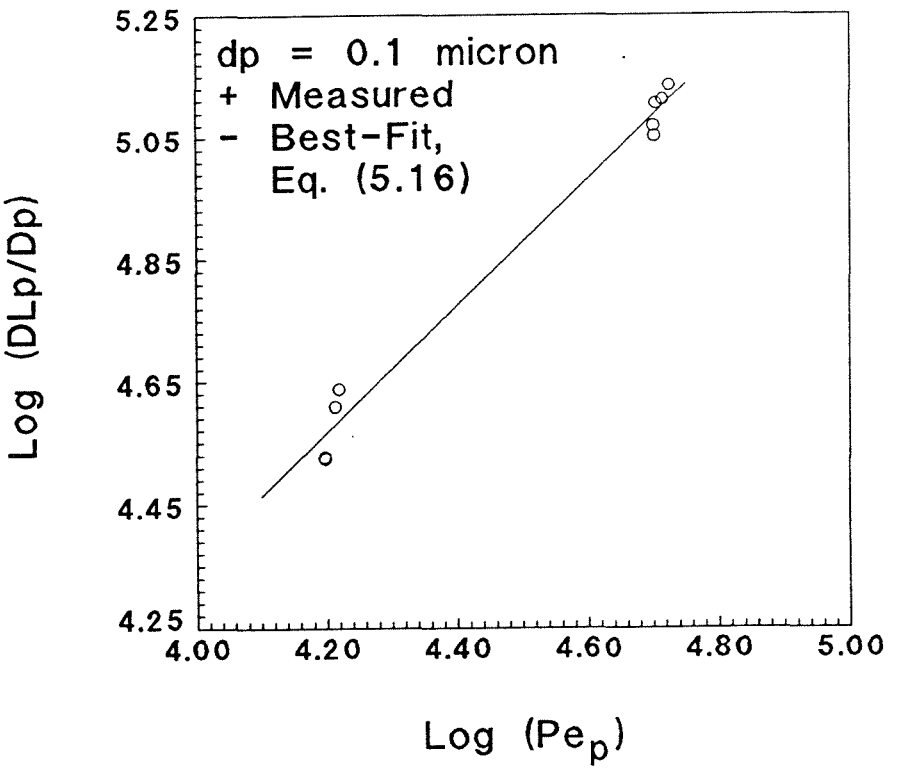

Fig. 5.22: Measured longitudinal dispersion coefficients and least-squares, best-fit of this data versus the particle Peclet number for 0.1 micron particles.

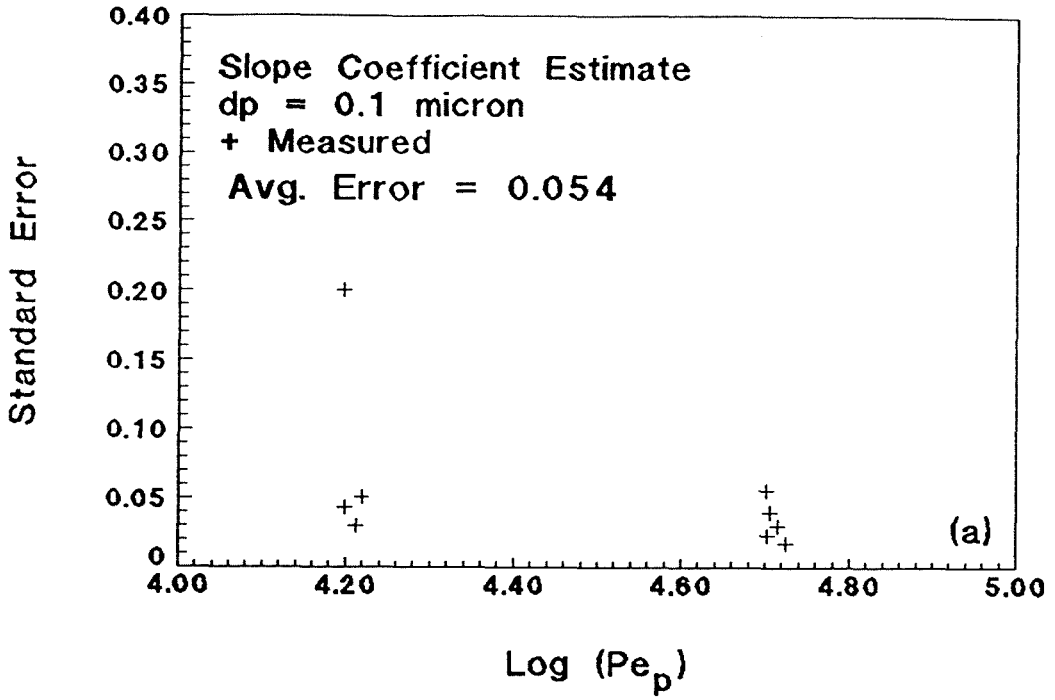

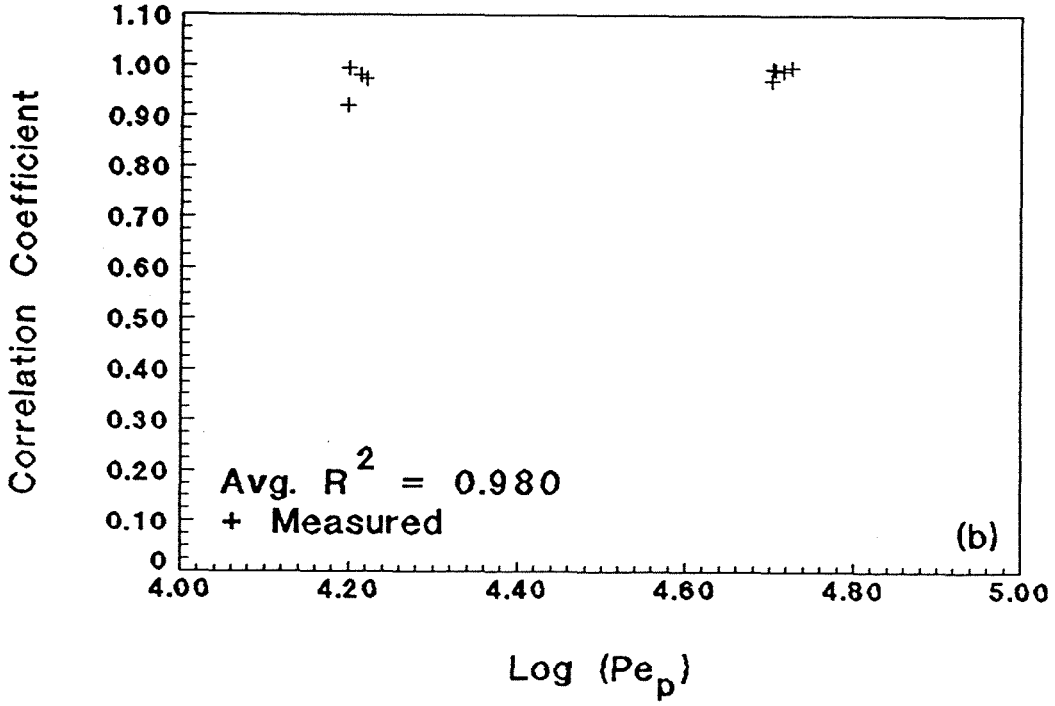

Fig. 5.23: Errors in D_{Lp} for 0.1 micron particles due to nonlinearity of experimental data as calculated from the least-squares, best-fit analysis of the linearized breakthrough data plotted versus the particle Peclet number.

$$Log\left[\frac{D_{Lp}}{V_p d_g}\right] = 0.018 Log[Pe_p] + 0.263 \qquad (5.17)$$

for 0.1 micron particles:

$$Log\left[\frac{D_{Lp}}{V_p d_g}\right] = 0.036 Log[Pe_p] + 0.216 \qquad (5.18)$$

These equations show that there is a very small effect of Brownian diffusion on longitudinal dispersion. Figs. 5.21 and 5.23 show the errors incurred during the analysis of the dispersion coefficients for the 2.8 and 0.1 micron particles. These errors as described above refer to the nonlinearity of the linearized portion of the individual breakthrough curves as shown in Figs. 5.12b - 5.17b. As described above, part (a) shows the standard error of the slope coefficient estimate for each experiment. Part (b) shows the correlation coefficient for the x- and y-variables of the linearized breakthroughs. As seen in these figures, the larger particle displays a larger error (less than 0.10) and a smaller correlation coefficient (greater than 0.85) while the 0.1 particle shows the same accuracy as that of the 1.0 micron particle.

Fig. 5.24 shows the combined results of the three particles. The best-fit line in this figure is determined by completing a single least-squares analysis on all of the determined data for all particles. The equation of the best-fit line for all data is:

$$Log\left[\frac{D_{Lp}}{D_p}\right] = 1.007 Log[Pe_p] + 0.313 \qquad (5.19)$$

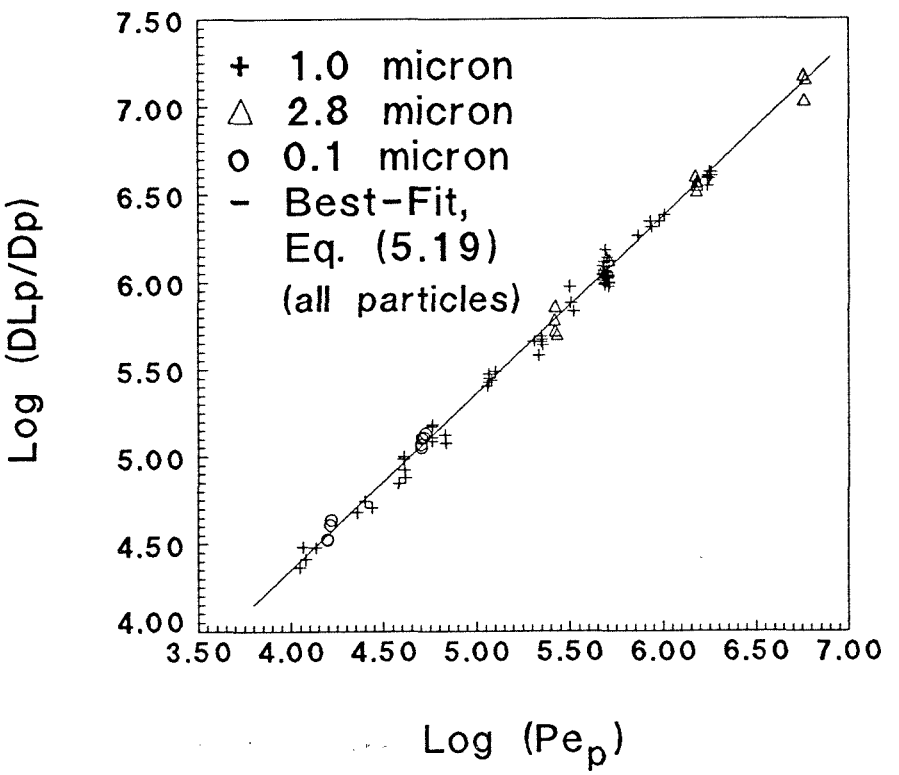

Fig. 5.24: Measured longitudinal dispersion coefficients and least-squares, best-fit of all data versus the particle Peclet number for all particles.

where: $R^2 = 0.994$.

This equation can be rewritten as:

$$Log\left[\frac{D_{Lp}}{V_p d_g}\right] = 0.007 Log[Pe_p] + 0.313 \qquad (5.20)$$

This figure shows that the dimensional analysis argument given previously for the longitudinal dispersion coefficient leads to the proper groups for any particle. A significant point in this analysis is that the particle velocity is used rather than the fluid velocity for all velocity scales. Figs. 5.25 and 5.26 show a comparison of this particle work to that of solutes by showing an envelope of solute data taken from Fig. 2.3 (from Houseworth 1984). The particle data is seen to be of the same order as the solute.

As can be seen in the best-fit equations for the individual particles and combined results, each has different values for the slopes and intercepts. Even though a difference exists between the intercepts, these differences are not very significant especially over the range of the particle Peclet number studied in this work (< 1%). These results are shown in Fig. 5.27. In part (a), the actual best-fit lines for all cases are plotted versus each other over the range of the particle Peclet number encountered in this work. In part (b), the differences between the individual particle best-fit lines and the combined best-fit lines are plotted over the same range of Pe_p. In this figure, the difference refers to the ratio of the individual to the combined best-fit lines. As can be seen, the difference between the different individual best-fit lines and the combined best-fit lines for the

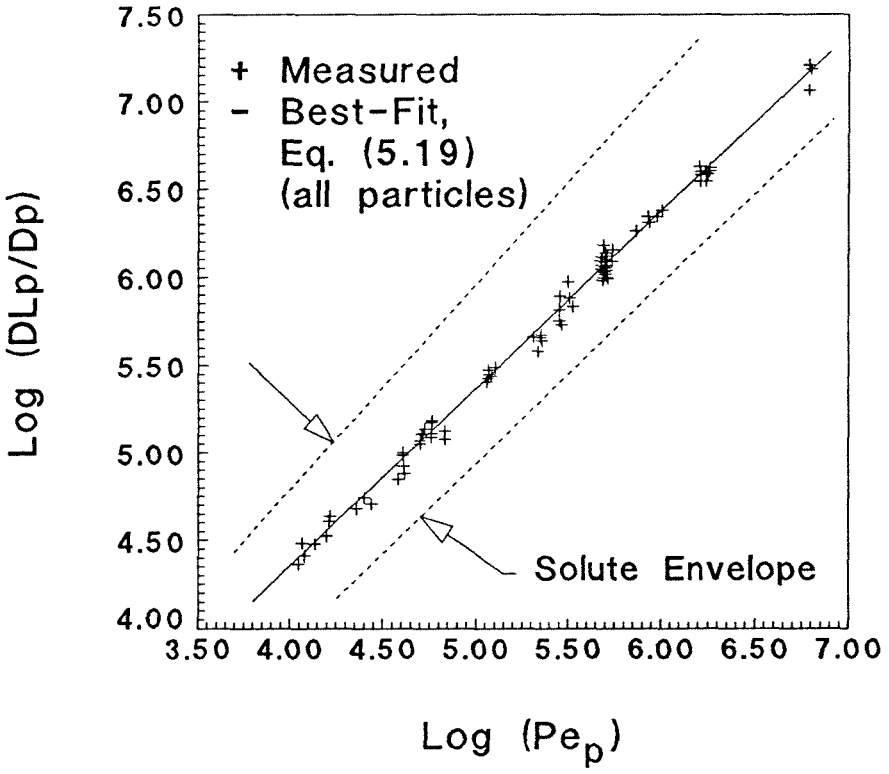

Fig. 5.25: Comparison of particle dispersion to solute dispersion (from Fig. 2.3) for the range of the Peclet number encountered in this work.

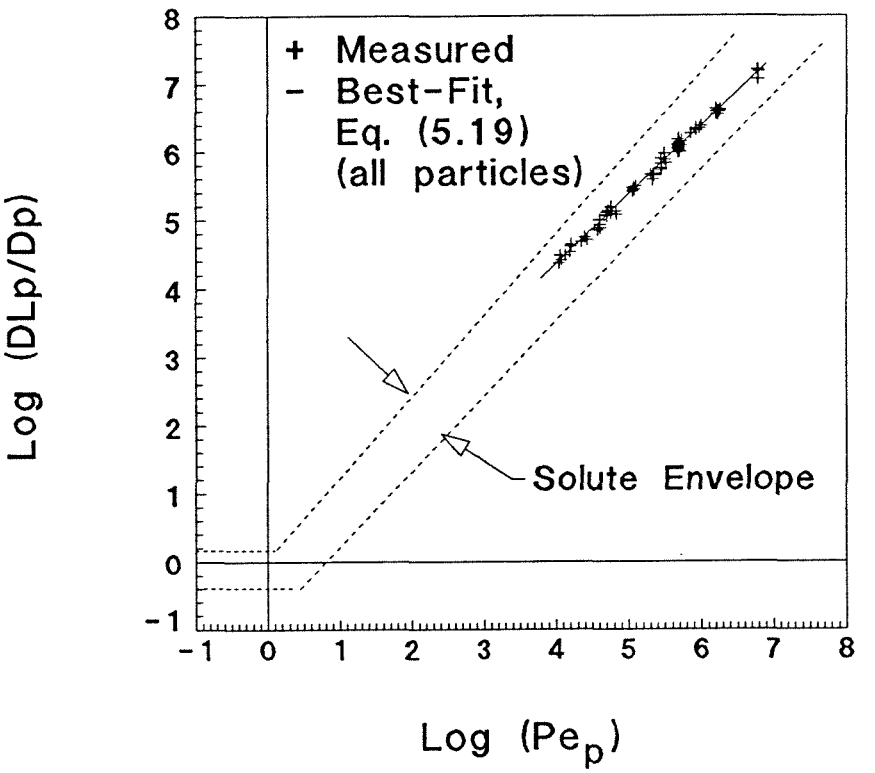

Fig. 5.26: Comparison of particle dispersion to solute dispersion (from Fig. 2.3) for the complete range of the Peclet number encountered in solute work.

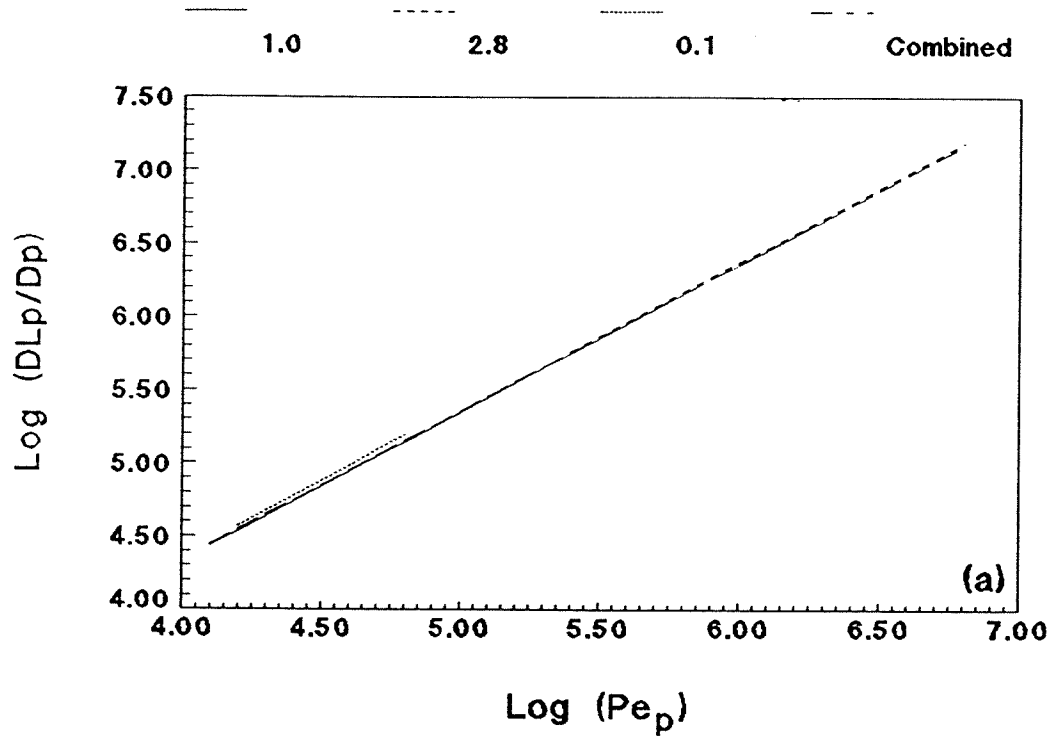

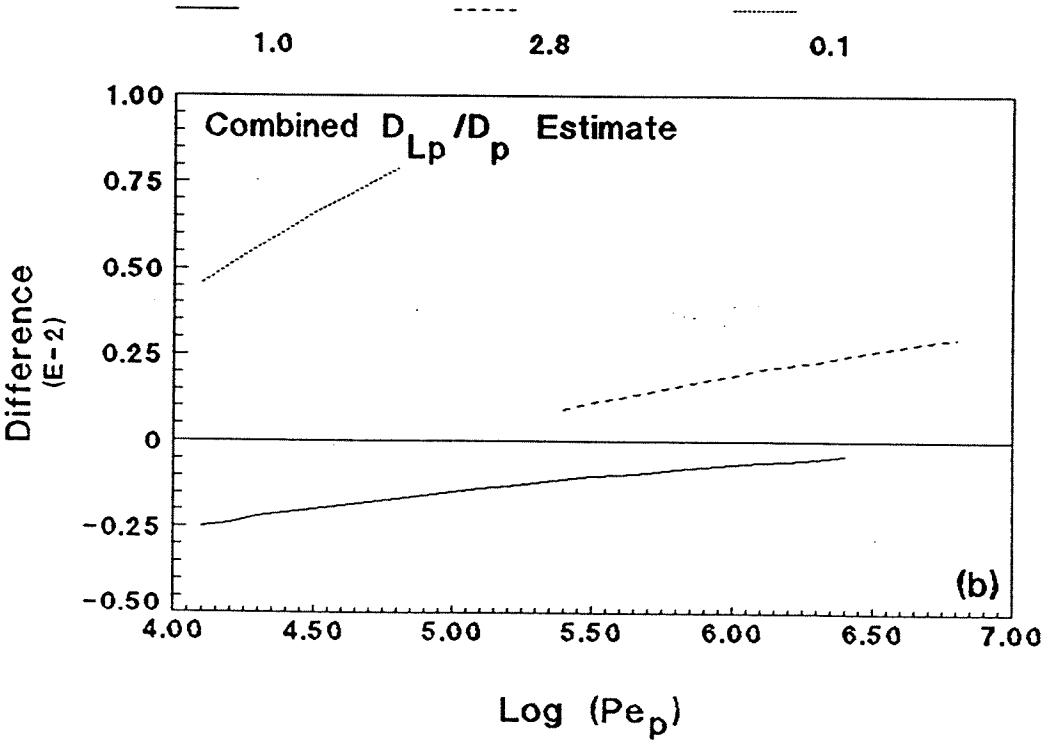

Fig. 5.27: Comparison of the best-fit curves of D_{Lp}/D_p versus Pe_p found from least-squares analysis for the individual and combined particle data.

studied range is less than 0.8% for the regions of applicability.

As shown empirically in the above analysis, the longitudinal dispersion coefficient has been shown to be fairly independent of the particle molecular diffusion coefficient. In light of this, $D_{Lp}/V_p d_g$ has been plotted versus the particle Peclet number in Fig. 5.28. A comparison of this figure to the salt data shown in Fig. 5.6 shows that the particles have larger longitudinal dispersion coefficients than salt for either the uniform medium or the nonuniform medium. The comparison of particle and salt longitudinal dispersion coefficients is shown more clearly in the coupled breakthrough section of this chapter. The data analysis of this section shows that the transport models presented in Chapter 3 have been verified by experimental work for a significant range of particle radii and velocities.

The next consideration is the effect of system chemistry on the longitudinal dispersion coefficient of particles. When completing the dimensional argument for the longitudinal dispersion coefficient in Chapter 3, only transport and not chemistry variables were included in this analysis. The expectation was that chemistry will only affect the rate of filtration of particles but will not affect the dispersion coefficient of the particles. This was tested by performing a group of experiments using the 1.0 micron particles in which the particle Peclet number was kept relatively constant while varying the system ionic strength. The chosen particle Peclet number was approximately $10^{5.7}$ and the ionic strengths ranged from 0.4 to 2.11 milliMolar (NaCl) which are the limits of this work due to

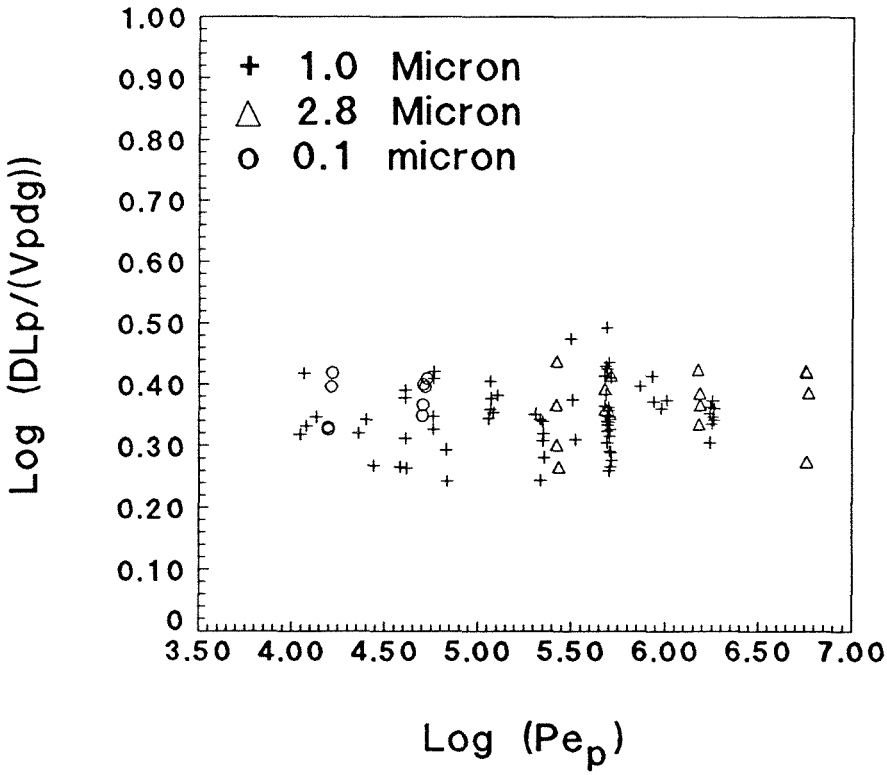

Fig. 5.28: $D_{Lp}/V_p d_g$ versus the particle Peclet number for all particle data.

excessive filtration (for a column of this length) at higher ionic strengths. The results of this work can be seen in Figs. 5.18 and 5.29 and Fig. 5.30. In Fig. 5.18, this group of data is plotted with all other 1.0 micron particle data and can be seen as a bundle of points around the chosen particle Peclet number. For all the other 1 micron particle data, the ionic strength is approximately 0.4 milliMolar (NaCl). In Fig. 5.29, this bundle of points is plotted at an expanded scale, and the values for the ionic strengths corresponding to each data point are shown. This figure shows a very small (if any) relationship between longitudinal dispersion coefficient and ionic strength. Also, in Fig. 5.18, the vertical range (error from the best-fit line) of the bundle of points appears to be the same as that for other data points. In order to investigate further the relationship of ionic strength to dispersion, the data in Fig. 5.29 was plotted as both D_{Lp}/D_p and $D_{Lp}/V_p d_g$ versus ionic strength in Fig. 5.30. This figure shows a slight dependence of particle longitudinal dispersion on ionic strength. A second set of variant ionic strength breakthrough experiments were performed using the 0.1 micron particles. In this case, the different values for ionic strength ranged from 0.4 to 1.2 mM. As shown in Fig. 5.22, the longitudinal dispersion coefficients plot as expected. These results validate the proposal that the contribution of system chemistry to the mixing process of a breakthrough front is very small when compared to the contribution of the transport properties. All data from the particle experiments are listed in Tables 5.3 and 5.4.

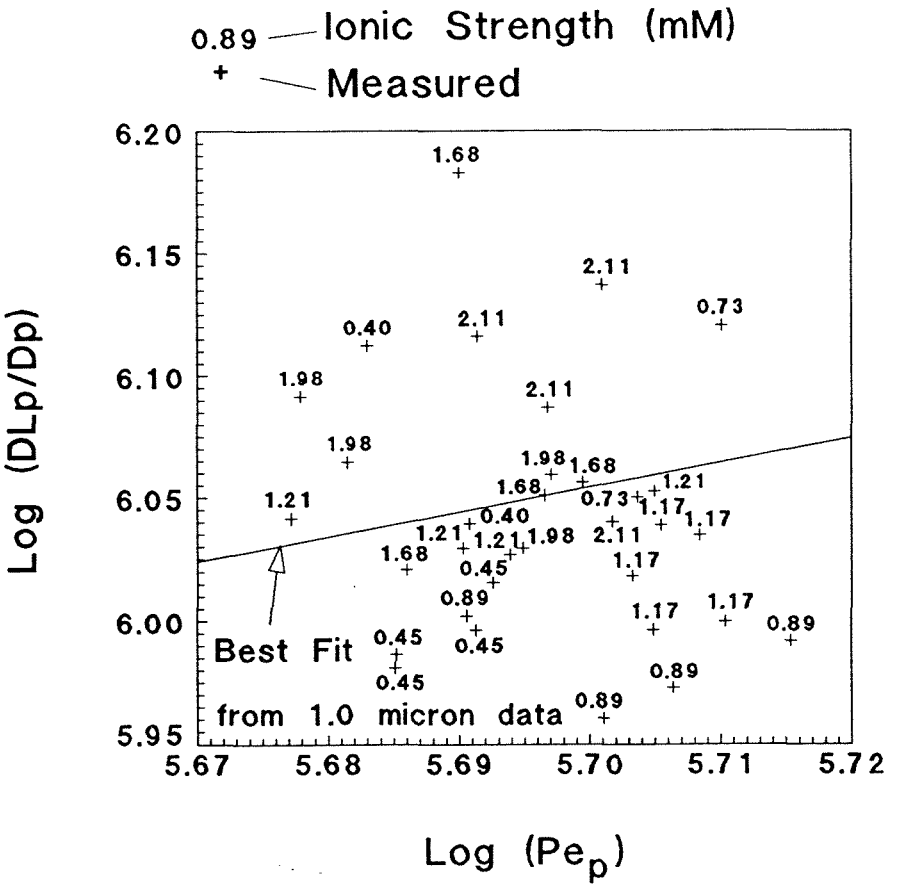

Fig. 5.29: Measured longitudinal dispersion coefficients and least-squares, best-fit for all 1.0 micron particle data versus Pe_p (from Fig. 5.18) with corresponding ionic strength values.

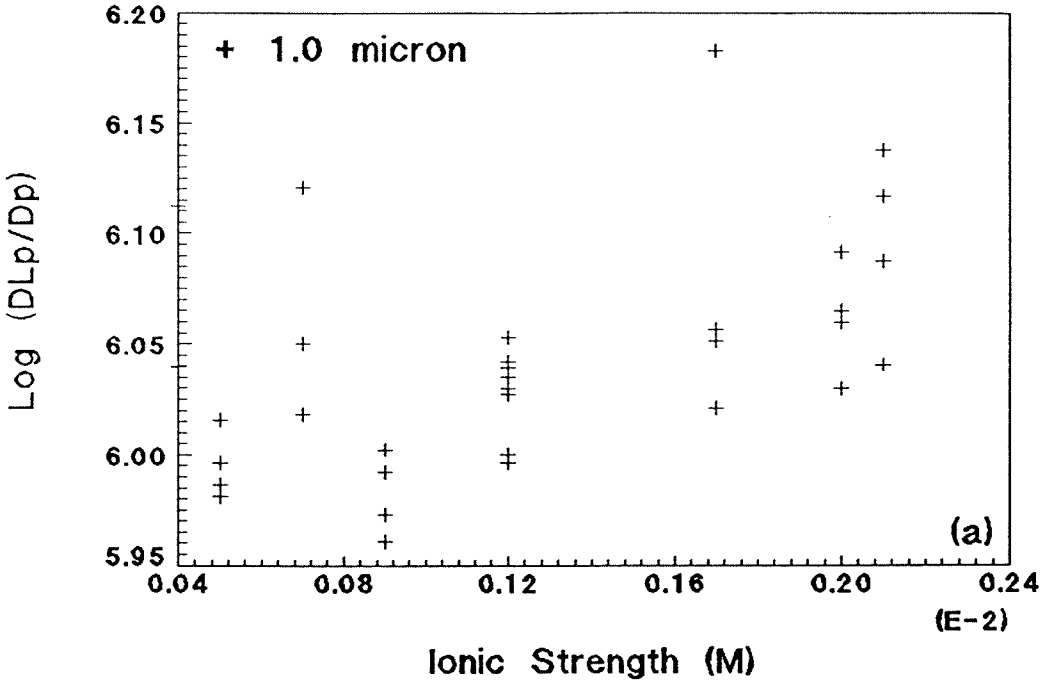

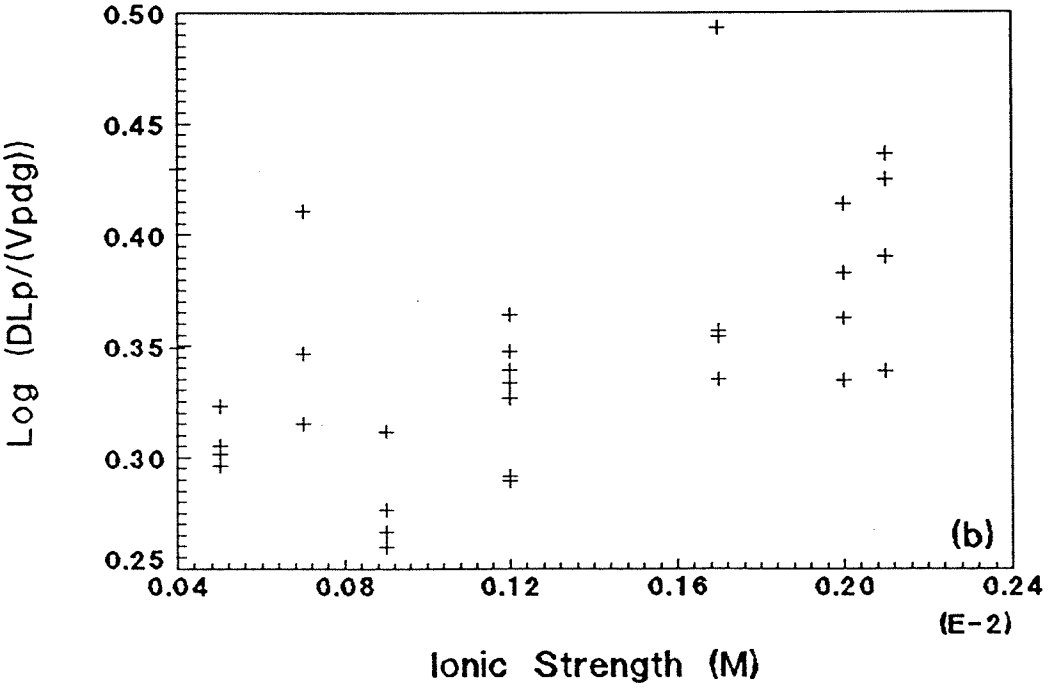

Fig. 5.30: Determination of relationship between D_{Lp} and ionic strength: (a) D_{Lp}/D_p versus I; and (b) $D_{Lp}/V_p d_g$ versus I.

Table 5.3: Experimental Variables and Measured Parameters for 1.0 micron Particles

Experiment	Ionic Strength (M)	V_p (cm/s)	V*	Pe_p	D_{Lp} (cm^2/s)	λ (1/m)
PB2P1S1b	4.00e-04	0.0163	1.0954	1.27e+05	0.00150	0.2908
RPB2P1S1b	4.00e-04	0.0156	1.1146	1.22e+05	0.00134	0.2762
PB3P1S1b	4.00e-04	0.0049	1.0583	3.83e+04	0.00034	1.2118
RPB3P1S1b	4.00e-04	0.0944	1.1262	7.36e+05	0.00897	0.3627
RPB4P1S1a	4.00e-04	0.0405	1.0754	3.16e+05	0.00461	3.5786
RPB5P1S1b	4.00e-04	0.1231	1.0659	9.60e+05	0.01077	0.0595
PB6P1S1a	4.00e-04	0.0618	1.0193	4.82e+05	0.00633	0.1938
RPB6P1S1b	4.00e-04	0.0629	1.0496	4.91e+05	0.00535	0.0496
PB7P1S1a	4.00e-04	0.0412	1.0143	3.21e+05	0.00372	0.1739
RPB7P1S1b	4.00e-04	0.0428	1.0749	3.34e+05	0.00333	0.0888
PB8P1S1a	4.00e-04	0.0263	1.0287	2.05e+05	0.00225	0.2586
RPB8P1S1b	4.00e-04	0.0278	1.0552	2.17e+05	0.00186	0.1689
PB9P1S1a	4.00e-04	0.0082	1.0417	6.42e+04	0.00069	1.0956
RPB9P1S1a	4.00e-04	0.0088	1.0419	6.83e+04	0.00058	0.8375
RPB9P1S1b	4.00e-04	0.0087	1.0463	6.78e+04	0.00065	0.5382
PB10P1S1a	4.00e-04	0.0052	1.0500	4.07e+04	0.00049	1.4282
PB10P1S1b	4.00e-04	0.0052	1.0628	4.05e+04	0.00047	0.8957
RPB10P1S1a	4.00e-04	0.0052	1.0552	4.09e+04	0.00041	0.8741
RPB10P1S1b	4.00e-04	0.0053	1.0835	4.13e+04	0.00037	0.5771
PB11P1S1b	4.00e-04	0.0035	0.9966	2.75e+04	0.00025	1.5889
RPB11P1S1a	4.00e-04	0.0032	1.1018	2.52e+04	0.00027	1.5258
RPB11P1S1b	4.00e-04	0.0029	1.0829	2.29e+04	0.00023	1.2188
PB14P1S1a	7.30e-04	0.0648	1.0250	5.05e+05	0.00510	1.6718
PB14P1S1b	7.30e-04	0.0658	1.0525	5.13e+05	0.00645	1.3474
RPB14P1S1a	7.30e-04	0.0648	1.0399	5.05e+05	0.00549	1.7755
PB15P1S1a	1.17e-03	0.0650	1.0514	5.07e+05	0.00485	0.3458
PB15P1S1b	1.17e-03	0.0656	1.0499	5.11e+05	0.00530	0.2834
RPB15P1S1a	1.17e-03	0.0651	1.0510	5.08e+05	0.00535	0.3387
RPB15P1S1b	1.17e-03	0.0659	1.0545	5.13e+05	0.00489	0.2620
PB16P1S1a	1.68e-03	0.0623	1.0410	4.85e+05	0.00513	0.7278
PB16P1S1b	1.68e-03	0.0628	1.0430	4.90e+05	0.00745	0.6188
RPB16P1S1a	1.68e-03	0.0638	1.0628	4.97e+05	0.00550	0.7723
RPB16P1S1b	1.68e-03	0.0642	1.0623	5.01e+05	0.00557	0.5301
PB17P1S1a	2.11e-03	0.0630	1.0566	4.91e+05	0.00639	1.2016
PB17P1S1b	2.11e-03	0.0638	1.0598	4.98e+05	0.00597	0.9952
RPB17P1S1a	2.11e-03	0.0644	1.0758	5.02e+05	0.00670	1.2431
RPB17P1S1b	2.11e-03	0.0646	1.0700	5.03e+05	0.00536	0.9745
PB18P1S1a	4.51e-04	0.0621	1.0044	4.84e+05	0.00468	0.0671
PB18P1S1b	4.51e-04	0.0632	1.0365	4.93e+05	0.00507	0.0780
RPB18P1S1a	4.51e-04	0.0621	1.0050	4.84e+05	0.00474	0.0376
RPB18P1S1b	4.51e-04	0.0630	1.0393	4.91e+05	0.00485	0.0529
PB19P1S1a	8.91e-04	0.0629	0.9762	4.90e+05	0.00491	0.2071
PB19P1S1b	8.91e-04	0.0645	1.0148	5.02e+05	0.00446	0.2103
RPB19P1S1a	8.91e-04	0.0653	0.9937	5.09e+05	0.00459	0.2472
RPB19P1S1b	8.91e-04	0.0666	1.0302	5.19e+05	0.00480	0.1676

(Continued)

Table 5.3 (cont.): Experimental Variables and Measured Parameters for 1.0 micron Particles

PB20P1S1a	1.21e-03	0.0610	0.9644	4.76e+05	0.00538	0.3648
PB20P1S1b	1.21e-03	0.0629	1.0087	4.90e+05	0.00523	0.3523
RPB20P1S1a	1.21e-03	0.0634	0.9760	4.94e+05	0.00520	0.3897
RPB20P1S1b	1.21e-03	0.0650	1.0224	5.07e+05	0.00552	0.3811
PB21P1S1a	1.98e-03	0.0611	0.9461	4.76e+05	0.00604	0.5607
PB21P1S1b	1.98e-03	0.0636	0.9992	4.95e+05	0.00523	0.4729
RPB21P1S1a	1.98e-03	0.0616	0.9582	4.80e+05	0.00567	0.5740
RPB21P1S1b	1.98e-03	0.0639	1.0107	4.98e+05	0.00561	0.4717
PB22P1S1a	1.14e-03	0.2231	0.9943	1.74e+06	0.01960	0.4876
PB22P1S1b	1.14e-03	0.2294	1.0235	1.79e+06	0.01891	0.3234
RPB22P1S1a	1.14e-03	0.2230	0.9848	1.74e+06	0.01716	0.5687
RPB22P1S1b	1.14e-03	0.2344	1.0376	1.83e+06	0.02047	0.3553
PB23P1S1a	1.95e-03	0.2228	0.9757	1.74e+06	0.01908	0.6062
PB23P1S1b	1.95e-03	0.2329	1.0216	1.82e+06	0.01970	0.4515
RPB23P1S1a	1.95e-03	0.2295	0.9958	1.79e+06	0.02062	0.6868
RPB23P1S1b	1.95e-03	0.2347	1.0252	1.83e+06	0.01963	0.4853
PB24P1S1a	1.94e-03	0.1094	0.9478	8.53e+05	0.01080	1.2272
PB24P1S1b	1.94e-03	0.1112	0.9648	8.67e+05	0.00998	0.6677
RPB24P1S1a	1.94e-03	0.1307	1.1211	1.02e+06	0.01177	1.1110
PB25P1S1a	2.12e-03	0.0293	1.0541	2.28e+05	0.00213	1.0097
PB25P1S1b	2.12e-03	0.0287	1.0383	2.24e+05	0.00223	0.9642
RPB25P1S1a	2.12e-03	0.0288	1.0611	2.24e+05	0.00239	0.9811
RPB25P1S1b	2.12e-03	0.0289	1.0164	2.25e+05	0.00230	0.8886
PB26P1S1a	2.10e-03	0.0150	1.0444	1.17e+05	0.00137	1.2015
PB26P1S1b	2.10e-03	0.0149	0.9998	1.17e+05	0.00145	1.0145
RPB26P1S1a	2.10e-03	0.0148	1.0642	1.15e+05	0.00124	1.0169
RPB26P1S1b	2.10e-03	0.0150	1.0121	1.17e+05	0.00130	0.9291
PB27P1S1a	2.05e-03	0.0074	1.0232	5.78e+04	0.00063	1.2532
PB27P1S1b	2.05e-03	0.0074	0.9834	5.77e+04	0.00073	1.1673
RPB27P1S1a	2.05e-03	0.0074	1.0462	5.78e+04	0.00060	1.3139
RPB27P1S1b	2.05e-03	0.0074	1.0035	5.80e+04	0.00075	1.1780
PB28P1S1a	4.26e-04	0.0017	1.0838	1.36e+04	0.00015	1.5225
PB28P1S1b	4.26e-04	0.0015	1.0040	1.20e+04	0.00013	0.9396
RPB28P1S1a	4.26e-04	0.0014	1.0708	1.11e+04	0.00011	1.3281
RPB28P1S1b	4.26e-04	0.0015	1.0143	1.16e+04	0.00015	1.2213

5.4.3 Filter Coefficient

The experiments which have been described in the previous sections of this chapter have been specifically designed to yield values for the advective velocity and longitudinal dispersion coefficient of the particles and were not initially intended to yield filter coefficients. This is an important point when analyzing the data for filtration results. For most filtration work, several column pore volumes

Table 5.4: Experimental Variables and Measured Parameters for 2.8 and 0.1 micron Particles

2.8 micron Particles

Experiment	Ionic Strength (M)	V_p (cm/s)	V*	Pe_p	D_{Lp} (cm^2/s)	λ (1/m)
PB1P3S1a	4.61e-04	0.0699	1.0475	1.53e+06	0.00647	0.1868
PB1P3S1b	4.61e-04	0.0700	1.0466	1.53e+06	0.00621	0.1382
RPB1P3S1a	4.61e-04	0.0687	1.0294	1.50e+06	0.00695	0.1130
RPB1P3S1b	4.61e-04	0.0696	1.0398	1.52e+06	0.00574	0.1030
PB2P3S1a	4.88e-04	0.0219	1.0524	4.78e+05	0.00191	0.7710
PB2P3S1b	4.88e-04	0.0218	1.0475	4.75e+05	0.00205	0.7222
RPB2P3S1a	4.88e-04	0.0235	1.0612	5.13e+05	0.00233	0.9989
RPB2P3S1b	4.88e-04	0.0234	1.0531	5.10e+05	0.00200	0.7218
PB3P3S1a	5.08e-04	0.0121	1.0439	2.65e+05	0.00093	1.4456
PB3P3S1b	5.08e-04	0.0121	1.0370	2.63e+05	0.00107	1.2634
RPB3P3S1a	5.08e-04	0.0125	1.0902	2.72e+05	0.00088	1.5049
RPB3P3S1b	5.08e-04	0.0122	1.0653	2.66e+05	0.00127	1.3646
PB4P3S1a	4.86e-04	0.2629	1.0638	5.74e+06	0.01883	0.3474
PB4P3S1b	4.86e-04	0.2683	1.0848	5.86e+06	0.02489	0.1953
RPB4P3S1a	4.86e-04	0.2604	1.0470	5.68e+06	0.02622	0.1743
RPB4P3S1b	4.86e-04	0.2626	1.0575	5.73e+06	0.02633	0.1516

0.1 micron Particles

Experiment	Ionic Strength (M)	V_p (cm/s)	V*	Pe_p	D_{Lp} (cm^2/s)	λ (1/m)
PB1P4S1a	5.08e-04	0.0202	0.9558	1.58e+04	0.00164	0.0564
PB1P4S1b	5.08e-04	0.0202	0.9571	1.57e+04	0.00165	0.0999
RPB1P4S1a	5.08e-04	0.0212	1.0170	1.66e+04	0.00212	0.0758
RPB1P4S1b	5.08e-04	0.0210	1.0037	1.63e+04	0.00199	0.0832
PB2P4S1b	4.91e-04	0.0651	0.9800	5.07e+04	0.00623	0.0845
RPB2P4S1a	4.91e-04	0.0681	1.0212	5.31e+04	0.00667	0.0173
RPB2P4S1b	4.91e-04	0.0667	1.0006	5.20e+04	0.00632	0.0004
RPB3P4S1a	1.18e-03	0.0647	0.9876	5.05e+04	0.00551	0.1019
RPB3P4S1b	1.18e-03	0.0646	0.9816	5.03e+04	0.00572	0.1036

are displaced before an analysis for the filter coefficient is conducted (Yoshimura et al. 1980; Jordan et al. 1974; Elimelech and O'Melia 1990). In this work, the total volume of flow was only 1.5 to 2 pore volumes of the column which is all that was necessary to determine a complete breakthrough. Also, the column in this work is 4 to 10 times longer than most columns used in filtration work. A

column of this size is needed in order to insure the existence of a large enough breakthrough for sampling. In a column of this dimension, even relatively small filter coefficients result in large particle removals over distance; therefore, not as large of a range of ionic strength or velocity could be tested as in shorter column studies.

As shown previously, the filter coefficient is expected to depend on the velocity, media grain diameter, particle diffusion coefficient, and ionic strength. The experiments which were performed to determine the longitudinal dispersion coefficients also yielded values for the filter coefficient. Figs. 5.12, 5.14, and 5.16 show forward breakthrough curves for 1.0 micron particles. In part (a), the raw data is shown for the entire experiment. From part (a), the initial concentration value and the final concentration plateau can be determined. The difference between these two values is the actual breakthrough concentration. The filter coefficient is determined from this concentration breakthrough value and the reservoir particle concentration value as follows:

$$\lambda = -\frac{\ln[C_b/C_r]}{L} \tag{5.21}$$

where: $C_b = C_{pl} - C_i$
$= $ *breakthrough concentration*;
$C_{pl} = $ *plateau concentration*;
$C_i = $ *initial background concentration in column*;
$C_r = $ *reservoir concentration*;
$= C_0$; *and*
$L = $ *distance to sample port.*

Extensive experiments were performed on the 1.0 micron particles. Representative measured values of λ determined from these experiments are shown in Figs. 5.31 and 5.32. In Fig. 5.31, the filter coefficient value is plotted versus velocity for various ionic strengths. In part (b), the same data is replotted but data for the 2.8 micron particles is included. This figure shows that for the various ionic strengths and particle sizes the expected qualitative result can be seen. In this case, the filter coefficient decreases as the velocity increases. As expected from filtration theory as presented in Chapter 2, the slope of this decrease is an approximate 1:1 relationship for each ionic strength shown. In Fig. 5.32, the filter coefficient value is plotted versus the ionic strength for various velocities. In part (b), the same data is replotted but data for the 0.1 micron particles is included. This figure shows that for the various velocities and particle sizes the expected qualitative result can be seen. In this case, the filter coefficient increases as the ionic strength increases.

The relationship between filter coefficient, ionic strength, and velocity has been examined further. The model for this theory has been presented previously in Section 3.3.1 with the result being:

$$\frac{\lambda}{\lambda_f} = F\left[\kappa a_p (Pe_p)^{-\frac{1}{3}}\right] \tag{3.8}$$

Two possible methods exist for using this equation. In the first case, the favorable filter coefficient, λ_f, can be determined experimentally by completing pilot studies in which ever increasing ionic strengths are used. The favorable

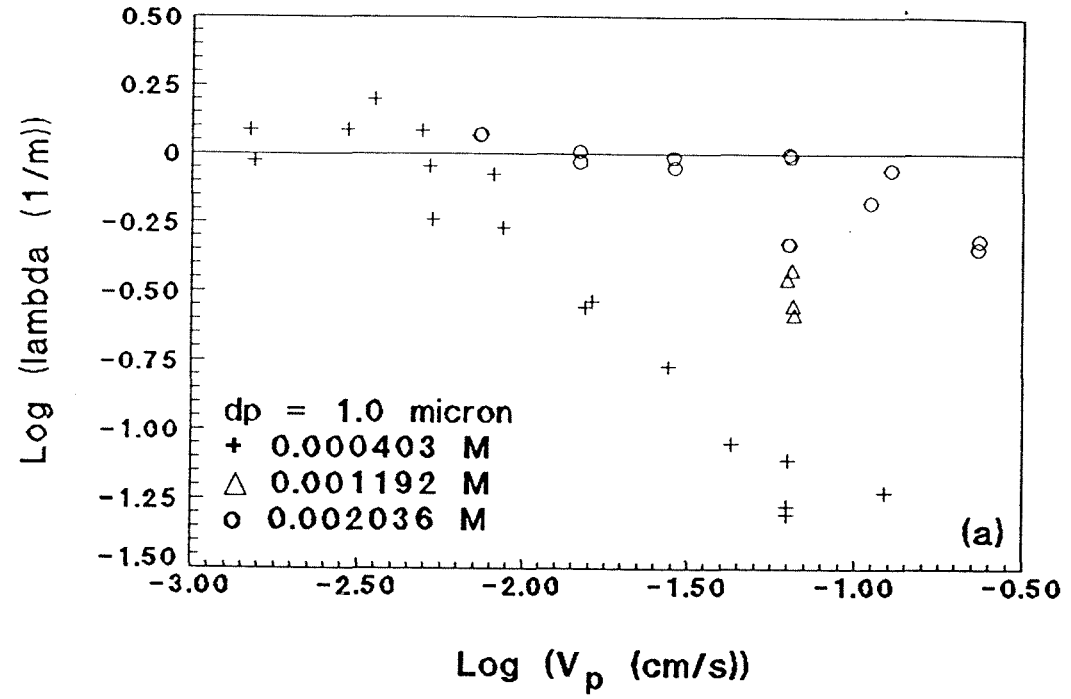

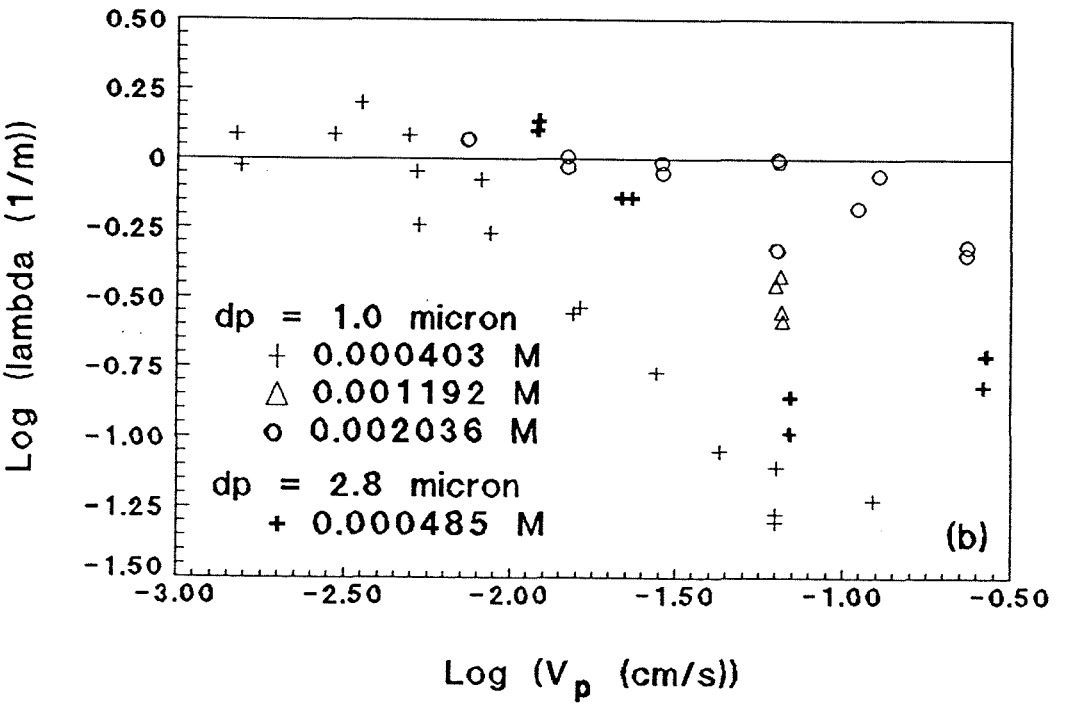

Fig. 5.31: Measured filter coefficients versus particle velocity for various ionic strengths for 1.0 and 2.8 micron particles.

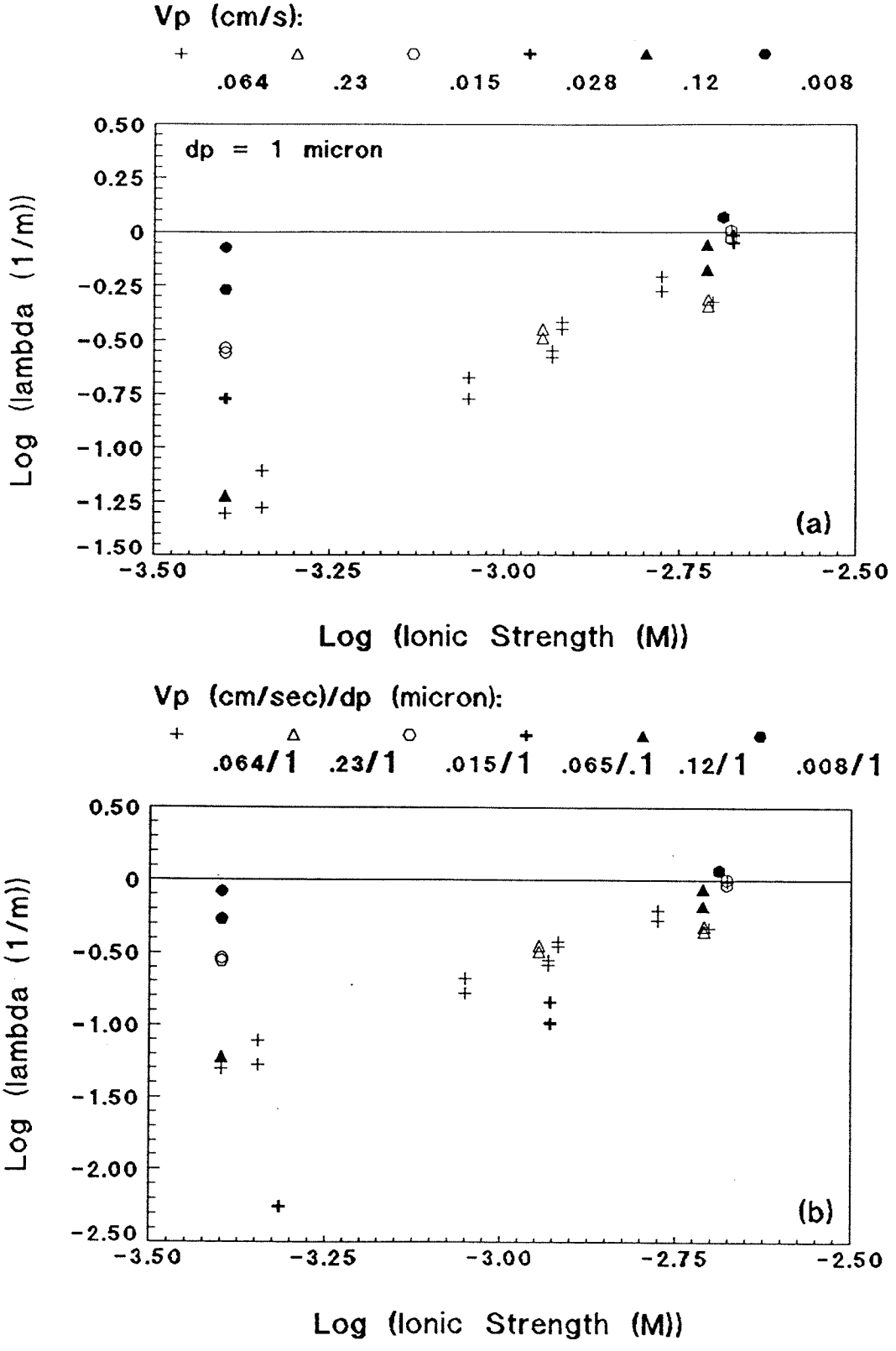

Fig. 5.32: Measured filter coefficients versus ionic strength for various particle velocities for 1.0 and 0.1 micron particles.

filter coefficient then becomes the average asymptotic filter coefficient value found at high ionic strengths. In the second case, the expected favorable filter coefficient can be calculated directly using the given experimental variables. The theoretical equation for the favorable single collector efficiency has been determined by Rajagopalan and Tien (1976) and Tien and Payatakes (1979), was given previously in Chapter 2, and is shown here:

$$\eta_T = 4A_s^{1/3}Pe_p^{-2/3} + 0.72A_sN_{Lo}^{1/8}N_R^{15/8} + 2.4E\text{-}3A_sN_G^{1.2}N_R^{-0.4} \qquad (2.26)$$

The relationship between the single collector efficiency and the filter coefficient was presented in Chapter 2 and is given here:

$$\lambda = \frac{3}{2}\frac{(1 - \theta_e)}{d_g}\alpha_c\eta_T \qquad (2.21)$$

In this equation, $\lambda = \lambda_f$ for $\alpha_c = 1$.

The choice of solution method is not arbitrary. The value for the favorable filter coefficient calculated by this theoretical equation may not match experimental results. For several experimental data sets considered by this work (Ghosh et al. 1975; Jordan et al. 1974; and Fitzpatrick and Spielman 1973), the favorable filter coefficients as calculated by the theoretical equation differ by a factor of up to approximately ± 10 from experimentally measured values of λ and λ_f. Also, for some of the experimental work which showed the measured filter coefficients approaching an asymptotic λ_f value, the calculated λ_f values differ from asymptotic experimental λ_f values by factors of 2 to 6 (Fitzpatrick and Spielman 1973; Ghosh et al. 1975; Jordan et al. 1974; Tobiason and O'Melia

1988; and Yoshimura et al. 1980).

The data from this work for 1.0 and 0.1 micron particles and the data from several others (Elimelech and O'Melia 1990; Fitzpatrick and Spielman 1973; Ghosh et al. 1975; Jordan et al. 1974; Tobiason and O'Melia 1988; and Yoshimura et al. 1980) which were shown individually in Chapter 2 are plotted collectively in Fig. 5.33 using the calculated values for λ_f. In part (a), the data are plotted versus the variables of the theory presented in this work, and, in part (b), the data are plotted versus the ionic strength as suggested by Vaidyanathan (1986) and Vaidyanathan and Tien (1988). Fig. 5.34 shows only the work for which the experimental data shows an asymptotic filter coefficient (Elimelech and O'Melia 1990; Fitzpatrick and Spielman 1973; Ghosh et al. 1975; Jordan et al. 1974; Tobiason and O'Melia 1988; and Yoshimura et al. 1980), and this data is plotted according to the two theories using the experimentally measured values for λ_f. This figure shows the same two parts as Fig. 5.33.

As stated above, Fig. 5.33 shows that the favorable filter coefficient as calculated by the theoretical equation (Eq. (2.26)) may be in error of up to plus or minus an order of magnitude. Part (a) of Fig. 5.33 shows a range of 2 to 2.5 orders of magnitude for the variables proposed in this work. Part (b) shows no real correlation when considering all of the data collectively; instead, part (b) shows separate branches of data which deviate from the asymptotic λ_f value for Brownian particles (d_p < 1.0 micron) and for advective particles (d_p > 1.0 micron). The larger particles are shown to filter more efficiently for a given ionic

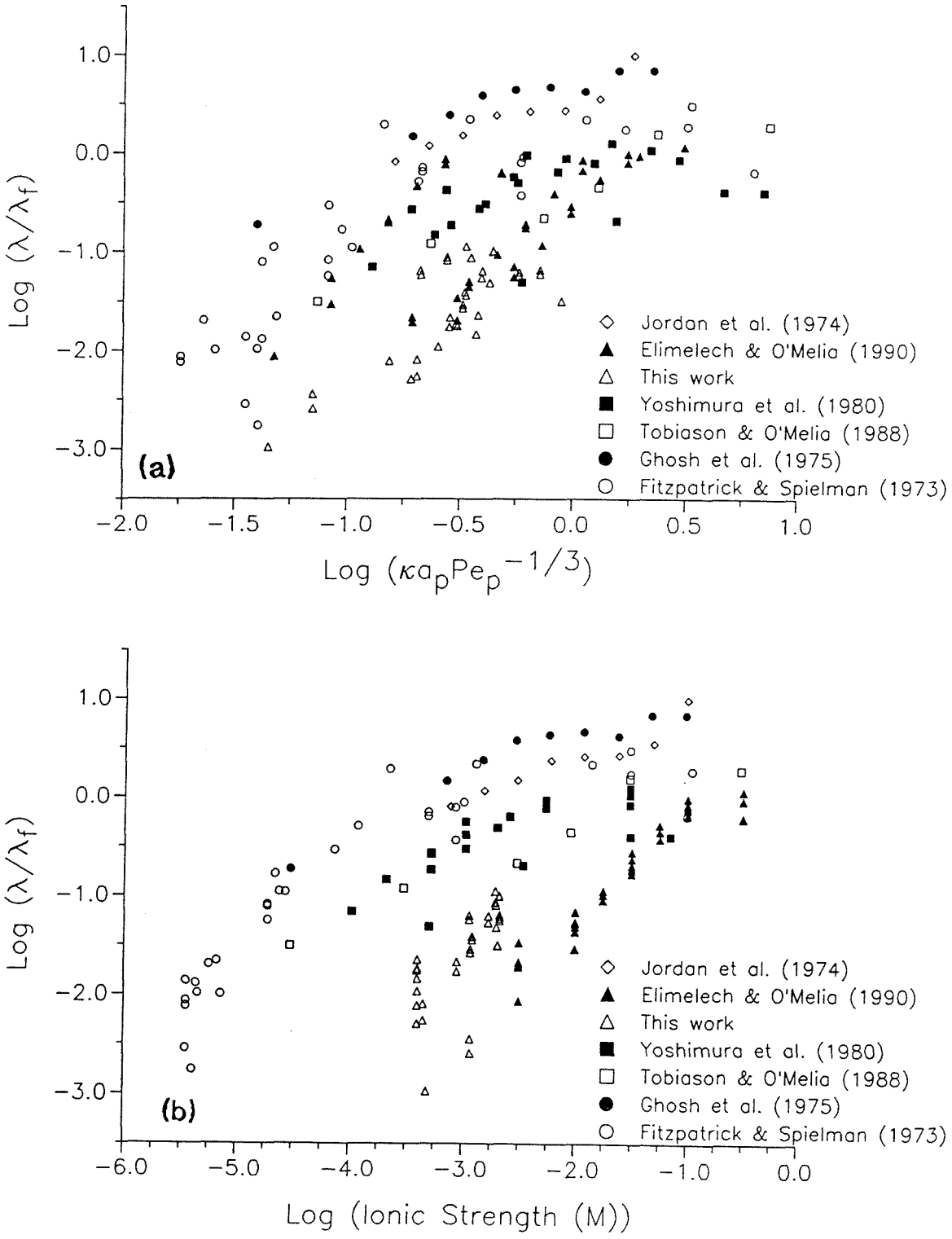

Fig. 5.33: Measured λ divided by calculated λ_f values versus: (a) variable proposed by this work; and (b) I.

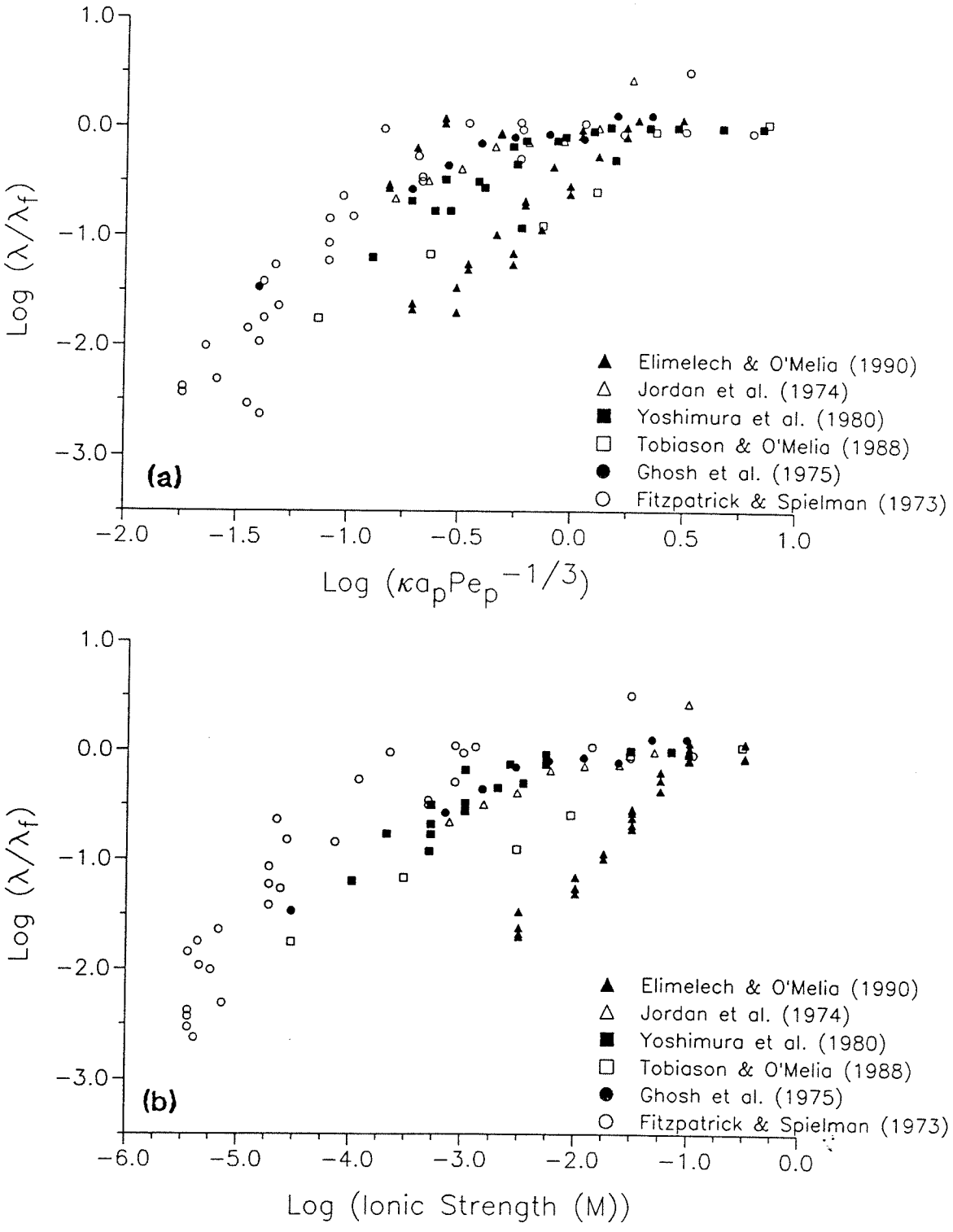

Fig. 5.34: Measured λ divided by measured asymptotic λ_f values (not all experiments allowed experimental measurement of asymptotic λ_f values) versus: (a) variable proposed by this work; and (b) I.

strength than the smaller particles. This result differs from that which was shown in Elimelech and O'Melia (1990). In the work of Elimelech and O'Melia (1990), predictive filtration curves which were calculated theoretically from a trajectory analysis are inverted from the results shown in Figs. 5.33 and 5.34 with the larger particles being filtered less efficiently than smaller particles. For the different sizes of particles, a different ionic strength value exists for which the experimental data intersect the asymptotic λ_f value.

Fig. 5.34 also shows distinct branches of data which deviate away from the asymptotic λ_f value. As in Fig. 5.33, the lower branch corresponds to Brownian particles and the upper branch corresponds to advective particles. In part (a) of Fig. 5.34, the data are plotted for the variables presented in this work. In part (b) of this figure, the data are plotted using the ionic strength as the independent variable. Part (a) shows the data to be more tightly grouped and the two branches less distinct than in part (b), but the variance is still 1.5 to 2 orders of magnitude. A key point is that in Fig. 5.34a the two branches of data appear to intersect the asymptotic λ_f value over a narrower range as compared to the plot shown in part (b) (note the difference in scales of the abscissas of the two graphs). The use of the independent variable defined in this work allows the setting of a single transition point between favorable and unfavorable filtration for all particles sizes. This illustrates the apparent shortcoming of using only ionic strength as the independent variable in this analysis. The ionic strength variable is not able to distinguish between particle sizes (advective or Brownian). Even

though different curves can be drawn for different particle sizes for the ionic strength variable in order to fit the measured data, this does not provide the key underlying physical and chemical basis for explaining this filtration phenomenon. In Fig. 5.34a, the single transition point defined by the variables of this work occurs near the origin which says the transition from favorable to unfavorable filtration occurs for similar particle diffusion length and double layer thickness. At the transition point, as the particle diffusion length becomes larger than the double layer thickness, the conditions become favorable and the filtration is diffusion or advection controlled; and, conversely, as the double layer thickness becomes larger than the particle diffusion length, the conditions become more unfavorable and the diffusion of particles to the surface becomes reduced by electrostatic interactions between particle and grain surface.

In order to show that the collective data plotted in Figs. 5.33 and 5.34 can be predicted when separated into different particle size groups, the experiments (Fitzpatrick and Spielman 1973; Ghosh et al. 1975; Jordan et al. 1974; Tobiason and O'Melia 1988; Yoshimura et al. 1980) with advective particles ($d_p > 1.0$ micron) which have an experimental value for λ_f are plotted in Fig. 5.35. In part (a), the experimental results are plotted according to the variables of this work, and, in part (b), they are plotted according to ionic strength only. This shows that there is little difference between these two methods in grouping the results for advective particles.

An important point to be made from the comparison of Fig. 5.33a to Fig.

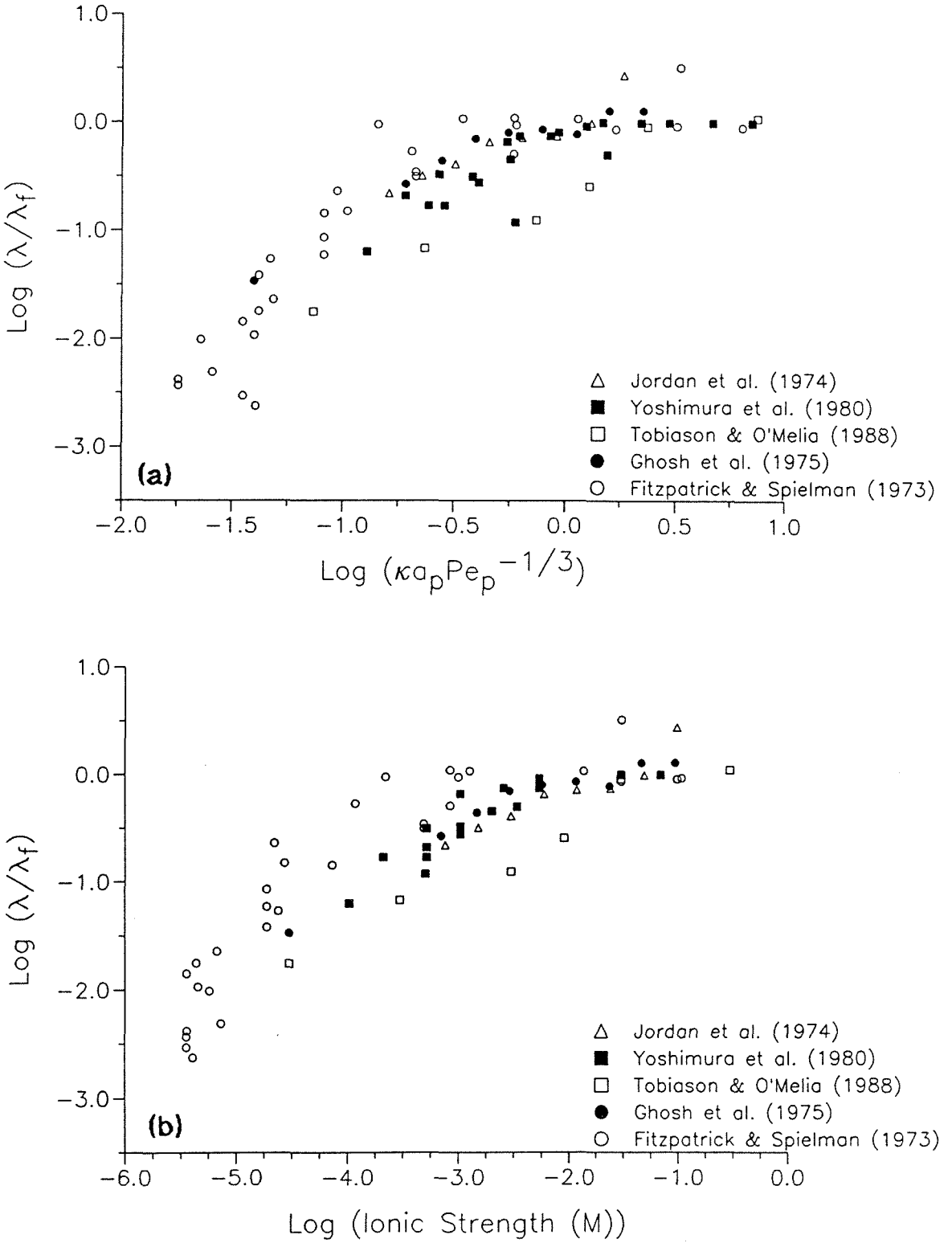

Fig. 5.35: Comparison of the two models for unfavorable filtration for only advective particles using data of others which have a measured asymptotic λ_f.

5.34a is that the correlation of the data is highly dependent upon the accuracy of λ_f. For the theory developed in this work, the range of experimental data is reduced from 2 - 2.5 orders of magnitude as seen in Fig. 5.33a to 1.5 - 2 orders of magnitude as seen in Fig. 5.34a. In this analysis, Fig. 5.34a is considered to be more reliable because the values of λ_f are measured for each experiment.

Part of the discrepancy shown in Figs. 5.33 and 5.34 when using the variable proposed by this work may be in knowing the actual particle size. Sulfonate surface groups have been shown to increase the actual particle size, and this apparent particle size would better represent the physical and chemical properties of the particle. For the work of Elimelech and O'Melia (1990), using a larger apparent particle size would result in a shift of their measured data to the left in Figs. 5.33 and 5.34 which would be closer to the other measured data. This same change in particle size would not affect the position of these measured data when using ionic strength as the independent variable.

5.5 Coupled Experiments

A set of eighteen coupled breakthrough experiments were performed. These experiments differ from the previously discussed particle breakthrough experiments, because the ionic strengths of the particle suspension and the resident, clean water are not the same. Similar breakthrough experiments were performed to test for the effects of variable ionic strength in which the breakthroughs of salt and particles are occurring simultaneously. The breakthrough of the particles is affected by the ionic strength breakthrough,

primarily in causing a variable filter coefficient. Such a coupled system can only be analyzed with a numerical model as discussed in Chapter 3. The major variables are the flow rate, ionic strength, and particle size. Four combinations of breakthroughs are possible, and they are described in the following and are listed in Table 5.5. The particle suspension or clean water breakthrough may be of either low or high ionic strengths. Conversely, the displaced clean water or particle suspension may be either high or low ionic strength. Several experiments for each type were performed. Regardless of the difference in ionic strength, a forward breakthrough refers to particles displacing clean water, and a reverse breakthrough is the opposite. For these experiments, the particle samples were taken from the fifth sample port (x = 149.3 cm), and the interstitial fluid ionic strength was continuously measured using conductivity probe number 3 (x = 149.4 cm).

At this point, a justification for completing the numerical model presented in Chapter 3 for determining coupled breakthroughs is given. Longitudinal dispersion coefficients for the particles are calculated from the experimental data collected from the coupled breakthroughs without considering a variable filter coefficient. These apparent dispersion values are plotted in Fig. 5.36. Also plotted are the salt tracer longitudinal dispersion coefficient values and the best-fit line for all particles (Eq. (5.19)). Two key points can be seen in this figure. The first is that the spread of these apparent dispersion values for some of the data is over a factor of five; whereas, Fig. 5.26 shows less scatter which is

Table 5.5: Four Possible Combinations of Coupled Breakthroughs.

Case	Resident Fluid		Displacing Fluid	
	I	Particles	I	Particles
I	High	0	Low	C_0
II	Low	C_0	High	0
III	Low	0	High	C_0
IV	High	C_0	Low	0

approximately a factor of two. The second is that in a direct comparison for the same velocity (within a few percent) the salt tracer shows a smaller longitudinal dispersion coefficient than the particles. This confirms both the point which was discussed earlier in this chapter that the salt has a smaller dispersion coefficient and the need to implement the numerical model to calculate coupled breakthroughs.

5.5.1 Completion Of Numerical Model

The numerical model developed in Chapter 3 now can be completed using the results of the previous section of this chapter.

For the numerical model, we use the particle longitudinal dispersion coefficient predicted by the best-fit equation of the previous section as follows:

$$Log\left[\frac{D_{Lp}}{D_p}\right] = 1.007 Log[Pe_p] + 0.313 \qquad (5.19)$$

The relationship between the filter coefficient and ionic strength which is

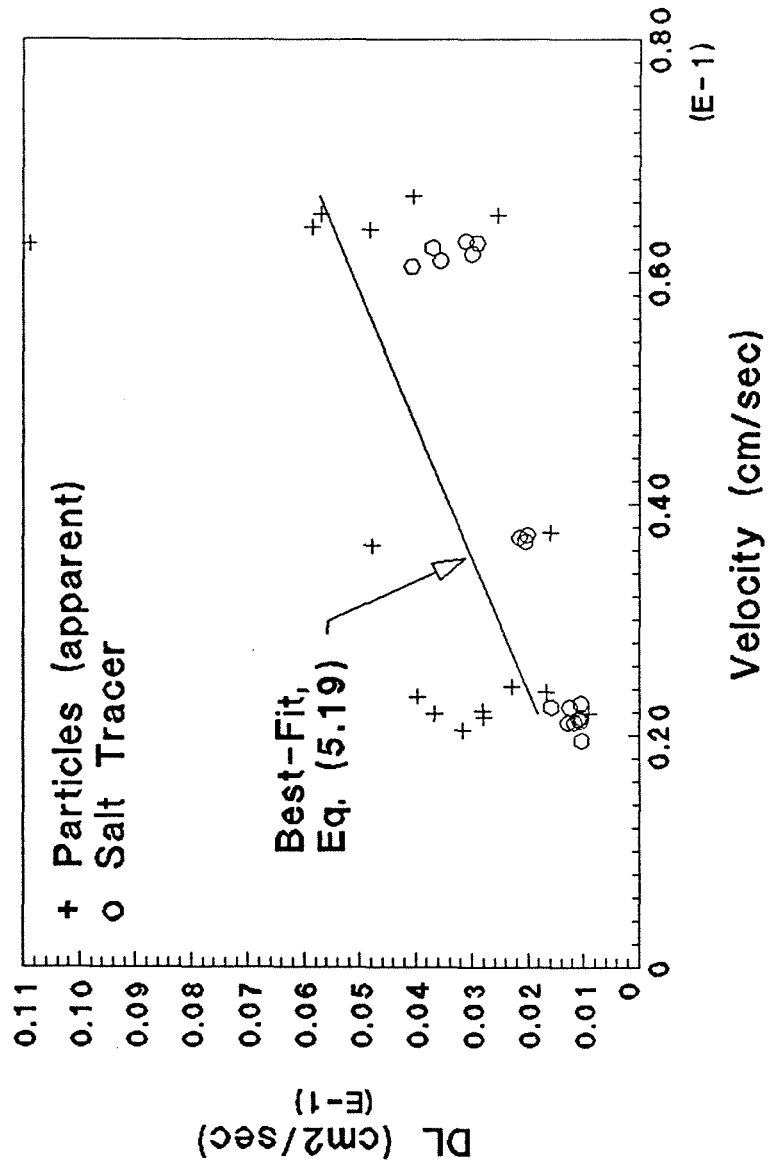

Fig. 5.36: Dispersion coefficients versus velocity for coupled breakthroughs.

needed to calculate the variable filter coefficient due to the ionic strength breakthrough is the best-fit of the data in Fig. 5.34a. This best-fit of the data was completed by evaluating a two-part fit in which the first part is an asymptotic constant section, and the second part is the second-order fit to the parabolic section. This analysis method is outlined in Vaidyanathan (1986). In the asymptotic section, the data is fitted with a constant line of value 0.0 where $\lambda/\lambda_f = 1.0$. For the parabolic section, a quadratic fit was tried, and the peak of the parabola is made to pass through the asymptotic line. This can be summarized by the following system of equations:

$$\begin{aligned} Y &= a_0 + a_1 X + a_2 X^2 && X < X_{tr} \\ &= 0 && X \geq X_{tr} \\ \frac{dY}{dX} &= 0 && X = X_{tr} \end{aligned} \qquad (5.22)$$

$$\textit{where: } Y = Log\left[\frac{\lambda}{\lambda_f}\right]; \textit{ and}$$
$$X = Log\left[\kappa a_p Pe_p^{-1/3}\right].$$

This equation can be simplified to:

$$\begin{aligned} Y &= a_2 X_{tr}^2 - (2a_2 X_{tr})X + a_2 X^2 && X < X_{tr} \\ &= 0 && X \geq X_{tr} \end{aligned} \qquad (5.23)$$

A two parameter search is completed by splining the system of equations of Eq. (5.23) at $X = X_{tr}$. This search is iterative in that a value for X_{tr} is chosen and all data for X less than or equal to this X_{tr} are used in the second-order, least-squares analysis. The peak of the parabola is then inspected for both its X- and

Y-values. If the X-value of the peak is not coincident with the chosen X_{tr}, then a new X_{tr} is chosen. The Y-value should be constrained by the system of equations to a value of 0.0 (λ/λ_f = 1.0), but it should be inspected to insure the value is proper. The equation of best-fit which was determined is:

$$\begin{aligned} Y &= -0.1887 + 0.6013X - 0.3687X^2 \qquad X < 0.7654 \\ &= 0 \qquad\qquad\qquad\qquad\qquad\qquad\quad X \geq 0.7654 \end{aligned} \tag{5.24}$$

$$\textit{where: } X_{tr} = 0.7654.$$

The ionic strength breakthrough can be modelled analytically and is simply the erfc solution of a conservative tracer.

This completes the numerical model by providing the necessary means of calculating the longitudinal dispersion coefficient and filter coefficient.

5.5.2 Comparison of Model to Experiments

As previously stated, four combinations of ionic strength, particles, and clean water breakthroughs are possible. Each of these has been tested, and these are discussed separately. In all cases, the numerical model matches the general shape of the breakthroughs. The best-fit criteria are the particle velocity and filter coefficient inputs to the model. For each experiment, the velocity is changed until the predicted breakthrough matches the experimental breakthrough at the midpoint, and the filter coefficient is changed until the predicted breakthrough matches the experimental breakthrough at the breakthrough plateau concentration. Of more interest is the comparison of the numerical model with the variable filter coefficient to the numerical model with a constant filter

coefficient. For the constant filter coefficient numerical model case, the chosen filter coefficient corresponds to the filter coefficient calculated from the ionic strength of the particles for both forward and reverse breakthroughs. For both cases of numerical model use, the same input values for particle velocity are used.

5.5.2.1 Forward Breakthroughs: Case I

In general, the variable filter coefficient model shows lower breakthrough concentrations than the constant filter coefficient model as can be seen in Figs. 5.37 and 5.38. This is a result of the initial particles being filtered at a greater rate due to the high ionic strength clean water than the final particles which are affected by the low ionic strength particle suspension. Also evident from these results is that the particles had an apparent velocity which is lower than expected. This is only a result of the initial concentration curve being shifted downward. In these figures, part (a) shows a direct comparison of saline breakthrough versus particle breakthrough. The actual concentrations are scaled for this direct comparison. Also, the salt tracer relative concentrations are inverted if necessary to match the shape of the particle breakthrough. Part (b) and part (c) show the true breakthroughs of the salt tracer and particles, respectively. Part (d) shows the comparison of the two numerical model cases versus the experimental data.

5.5.2.2 Reverse Breakthroughs: Case II

In general, the variable filter coefficient case shows lower breakthrough concentrations than the constant filter coefficient case as can be seen in Fig. 5.39 which has the same four parts as discussed previously. This is a result of the final

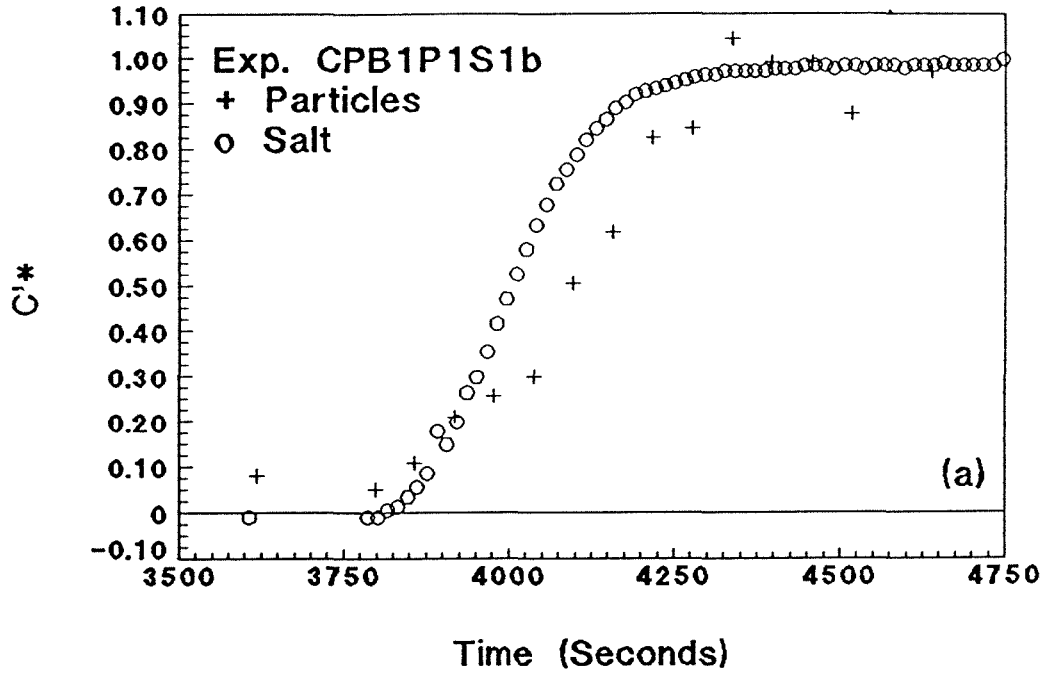

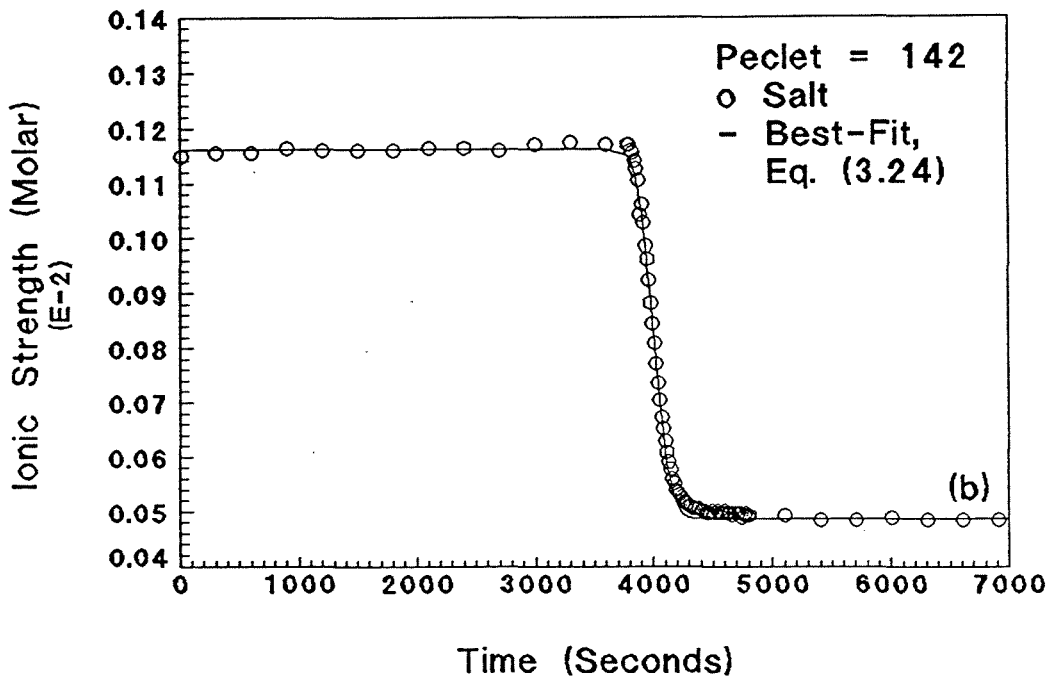

Fig. 5.37: Exp. CPB1P1S1b coupled breakthrough, $Pe_p = 10^{5.45}$, Pe = 142, 1.0 micron particles: (a) particles and salt relative breakthroughs and (b) salt experimental data with best-fit, Eq. (3.24).

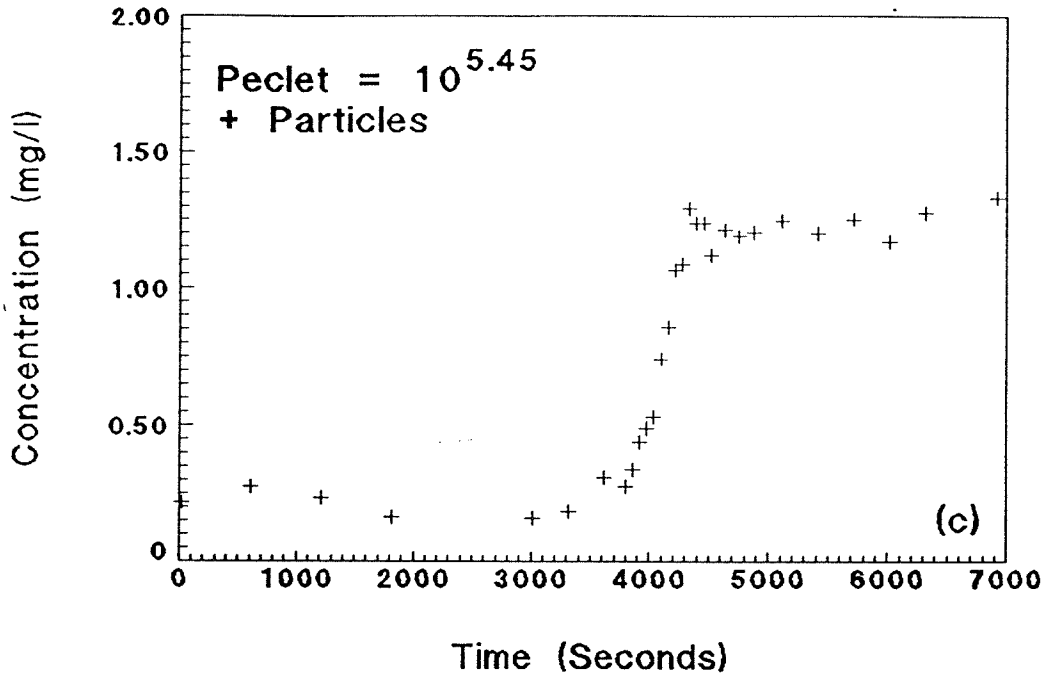

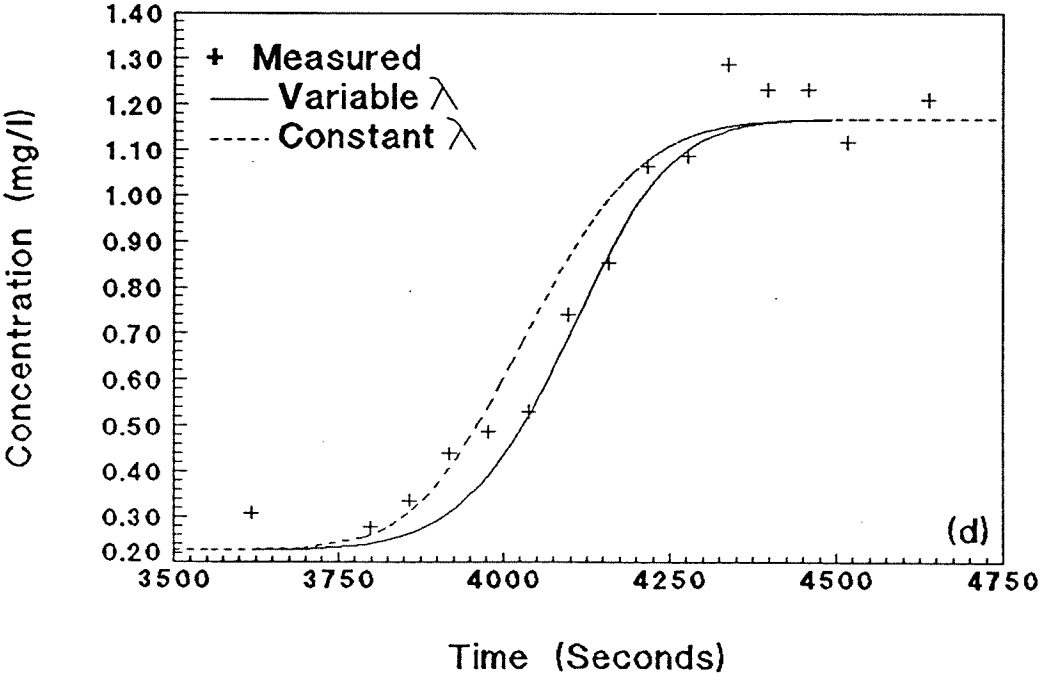

Fig. 5.37(cont.): Exp. CPB1P1S1b coupled breakthrough, $Pe_p = 10^{5.45}$, Pe = 142, 1.0 micron particles: (c) particle breakthrough and (d) particle experimental data with best-fit, numerical model.

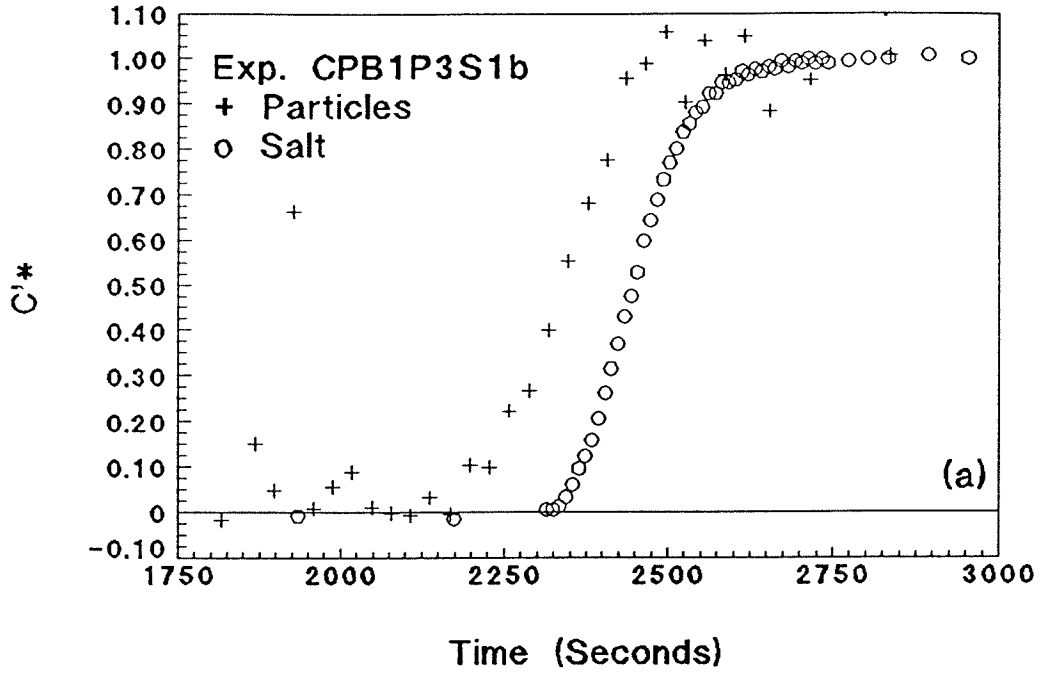

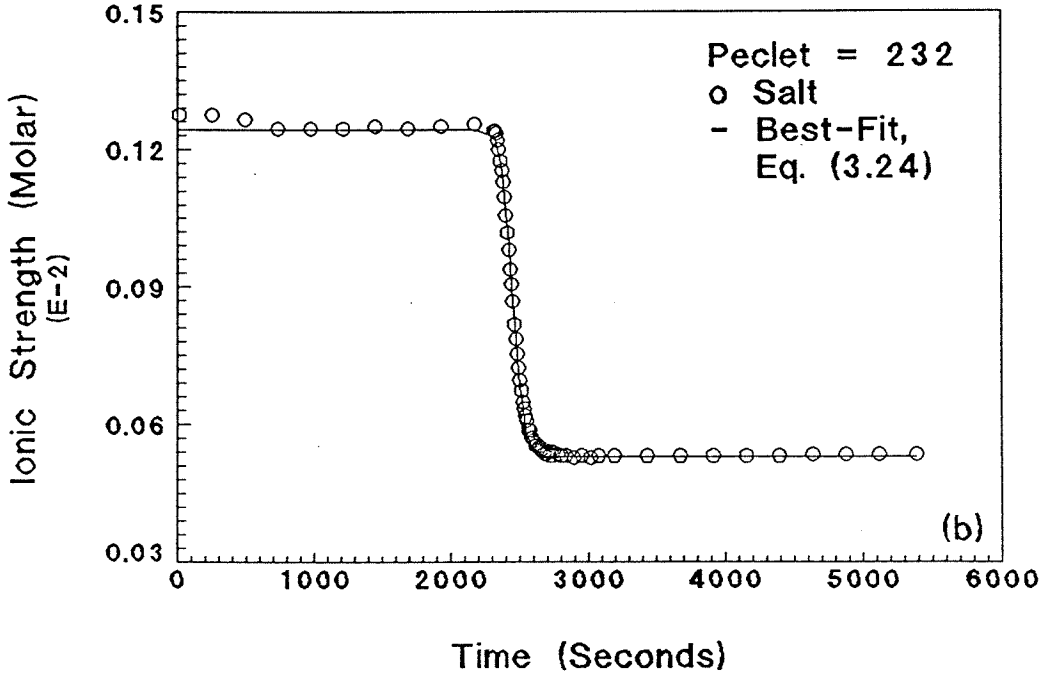

Fig. 5.38: Exp. CPB1P3S1b coupled breakthrough, $Pe_p = 10^{6.17}$, Pe = 232, 2.8 micron particles: (a) particle and salt relative breakthroughs; (b) salt experimental data with best-fit, Eq. (3.24).

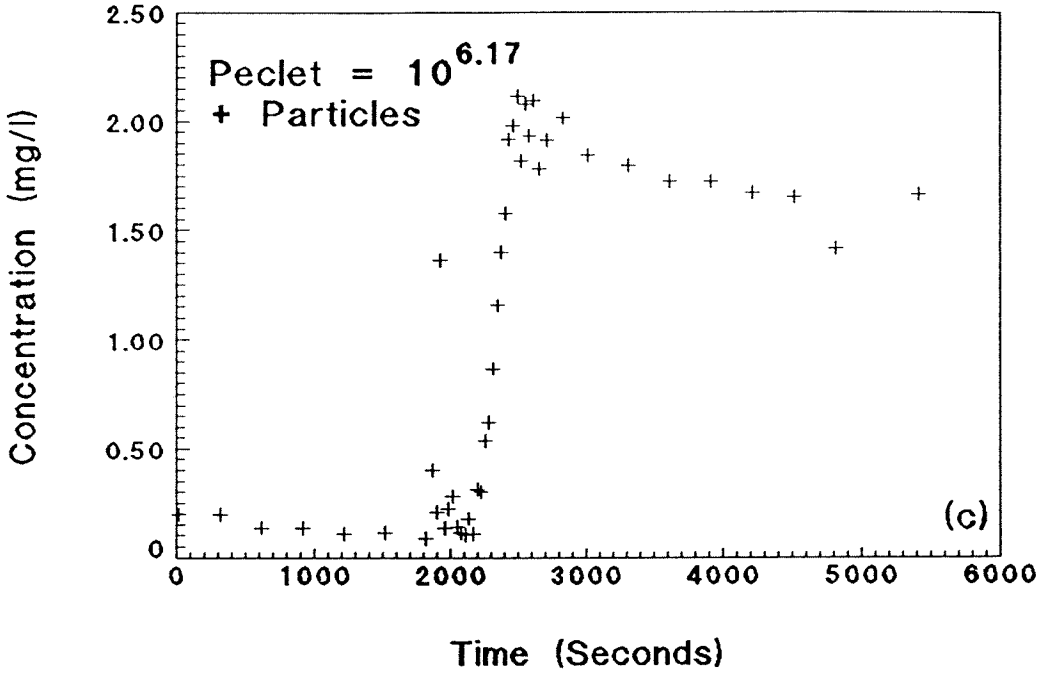

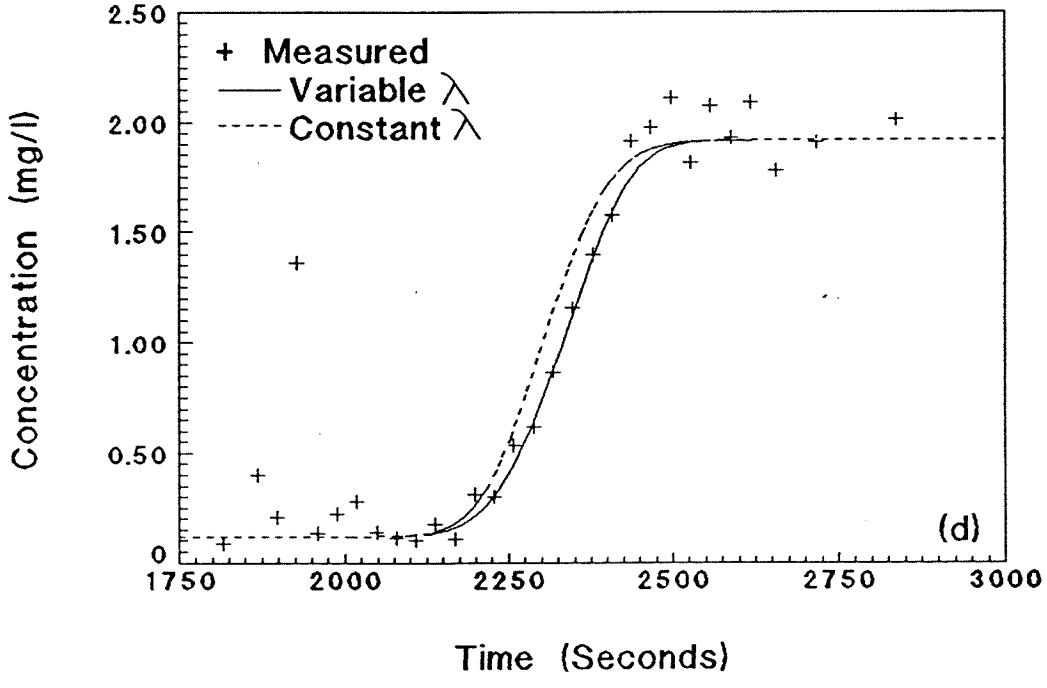

Fig. 5.38(cont.): Exp. CPB1P3S1b coupled breakthrough, $Pe_p = 10^{6.17}$, Pe = 232, 2.8 micron particles: (c) particle breakthrough and (d) particle experimental data with best-fit, numerical model.

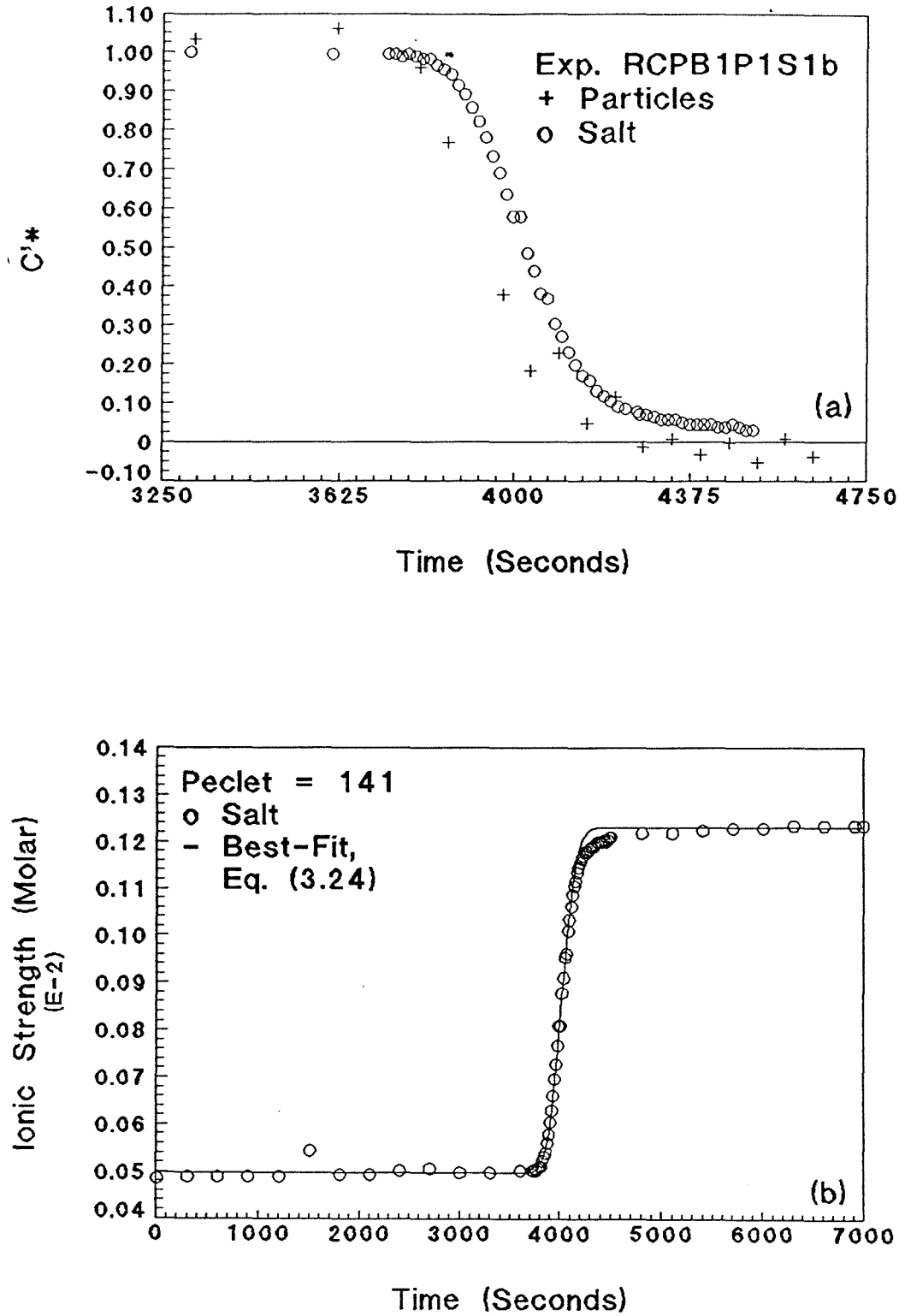

Fig. 5.39: Exp. RCPB1P1S1b coupled breakthrough, $Pe_p = 10^{5.47}$, Pe = 141, 1.0 micron particles: (a) particle and salt relative breakthroughs and (b) salt experimental data with best-fit, Eq. (3.24).

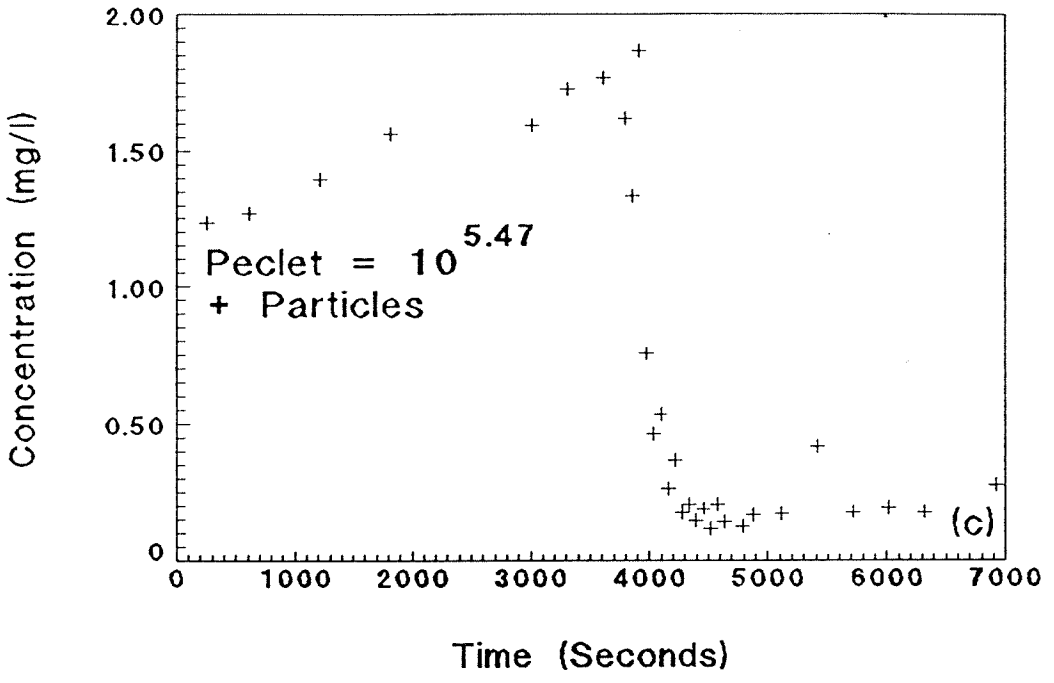

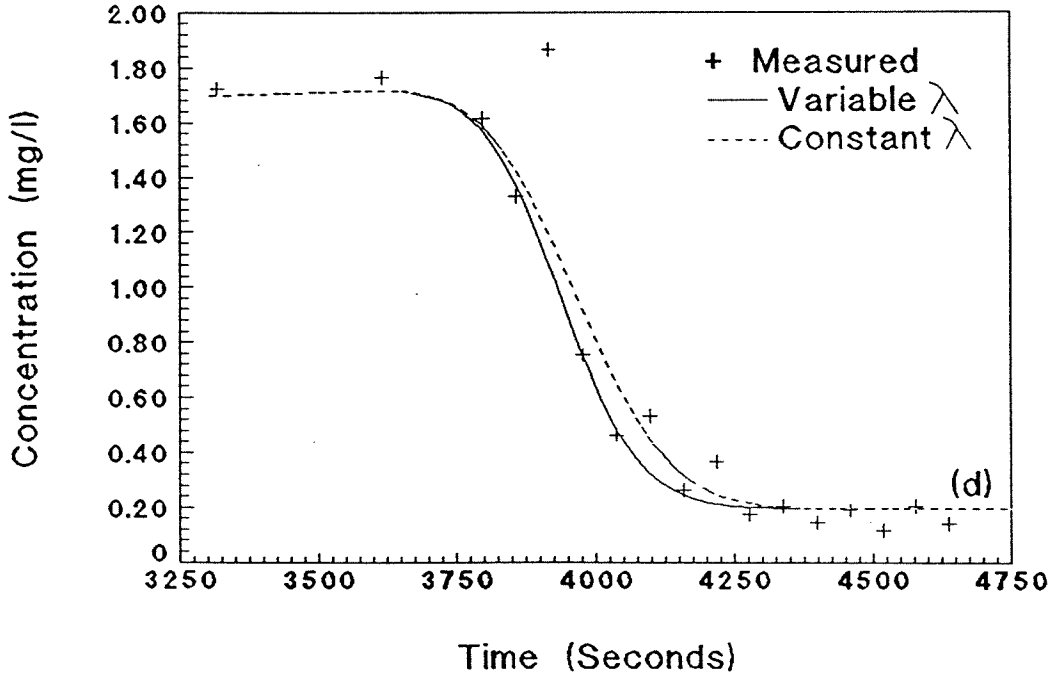

Fig. 5.39(cont.): Exp. RCPB1P1S1b coupled breakthrough, $Pe_p = 10^{5.47}$, Pe = 141, 1.0 micron particles: (c) particle breakthrough and (d) particle experimental data with best-fit, numerical model.

particles being filtered at a greater rate due to the high ionic strength clean water than the initial particles which are affected by the low ionic strength particle water. Also evident from these results is that the particles had an apparent velocity which is greater than expected. This is only a result of the final concentration curve being shifted downward. In addition, a comparison of the experimental data shows less tailing due to high filtration than for the constant ionic strength breakthroughs. The high ionic strength water increases the filtration rate and reduces any tailing effects due to re-entrainment or diffusion.

5.5.2.3 Forward Breakthroughs: Case III

The variable filter coefficient case shows higher breakthrough concentrations than the constant filter coefficient case as shown in Fig. 5.40. This is a result of the initial particles being filtered at a lower rate due to the low ionic strength clean water than the final particles which are affected by the high ionic strength particle water. Also evident from these results is that the particles had an apparent velocity which is greater than expected. This is only a result of the initial concentration curve being shifted upward. Fig. 5.40 has the same four parts as discussed previously.

5.5.2.4 Reverse Breakthroughs: Case IV

The variable filter coefficient case shows higher breakthrough concentrations than the constant filter coefficient case as shown in Figs. 5.41 and 5.42. This is a result of the final particles being filtered at a lower rate due to the low ionic strength clean water than the initial particles which are affected by the

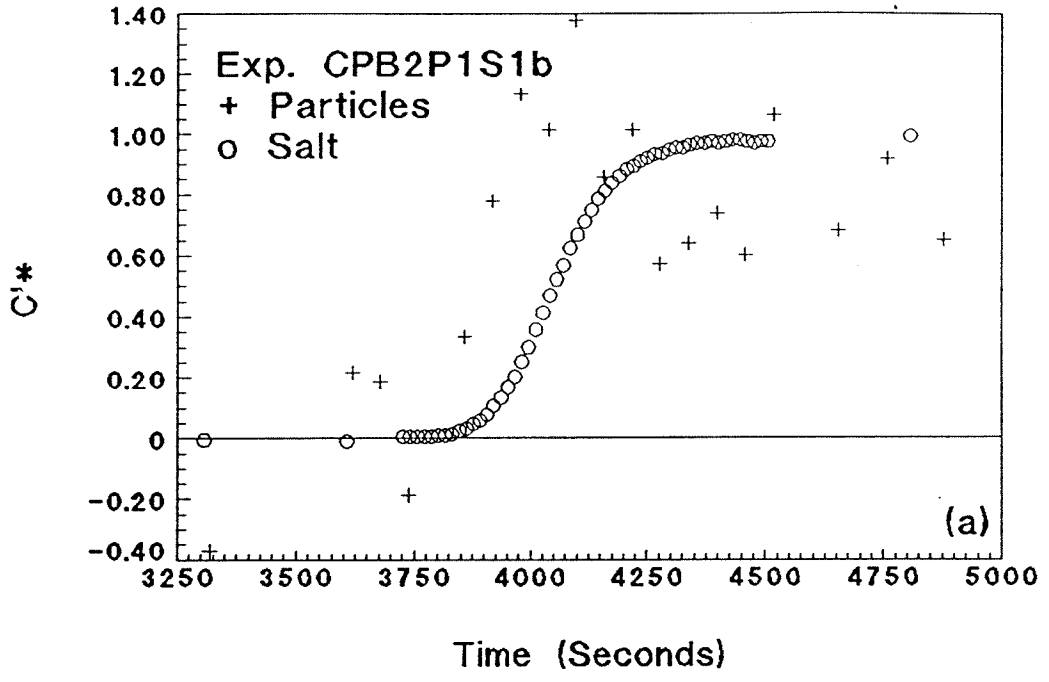

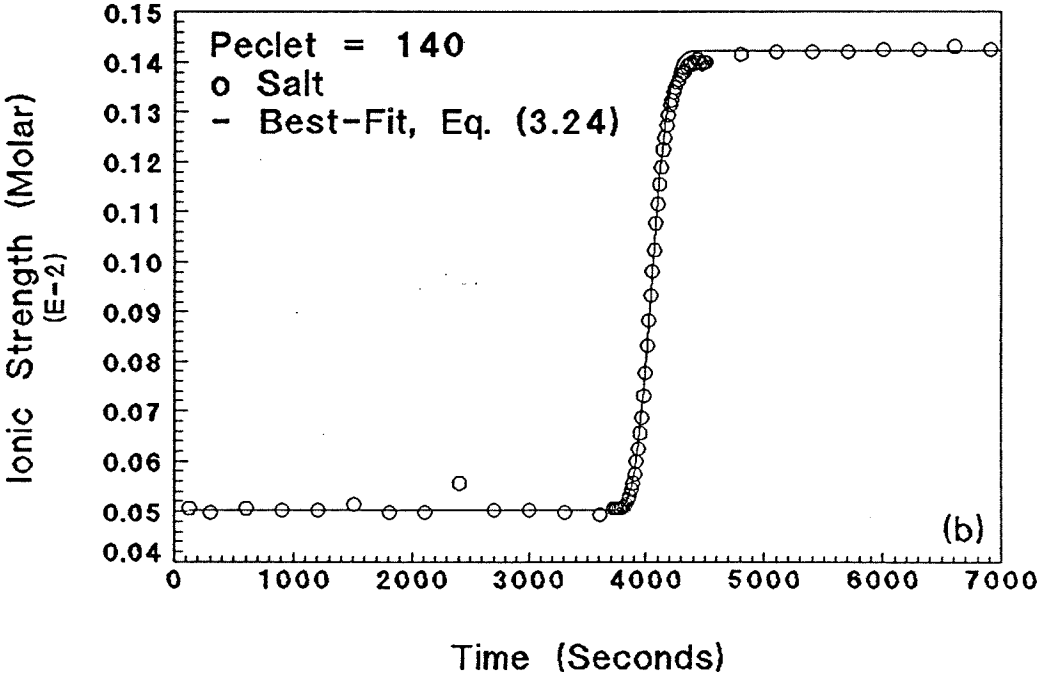

Fig. 5.40: Exp. CPB2P1S1b coupled breakthrough, $Pe_p = 10^{5.48}$, Pe = 140, 1.0 micron particles: (a) particles and salt relative breakthroughs; (b) salt experimental data with best-fit, Eq. (3.24).

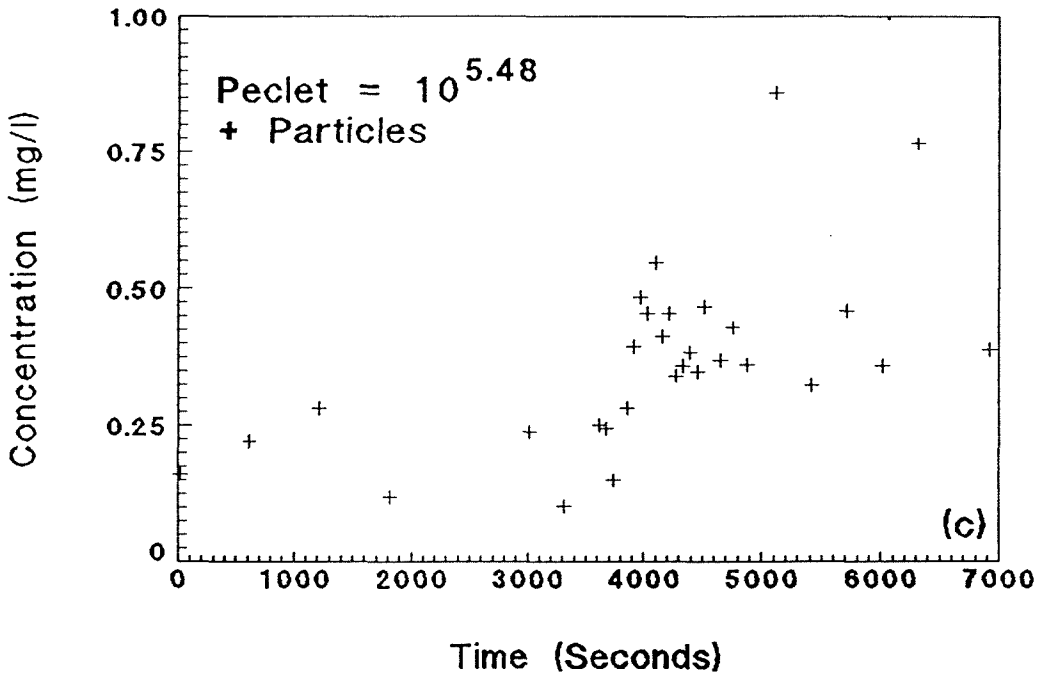

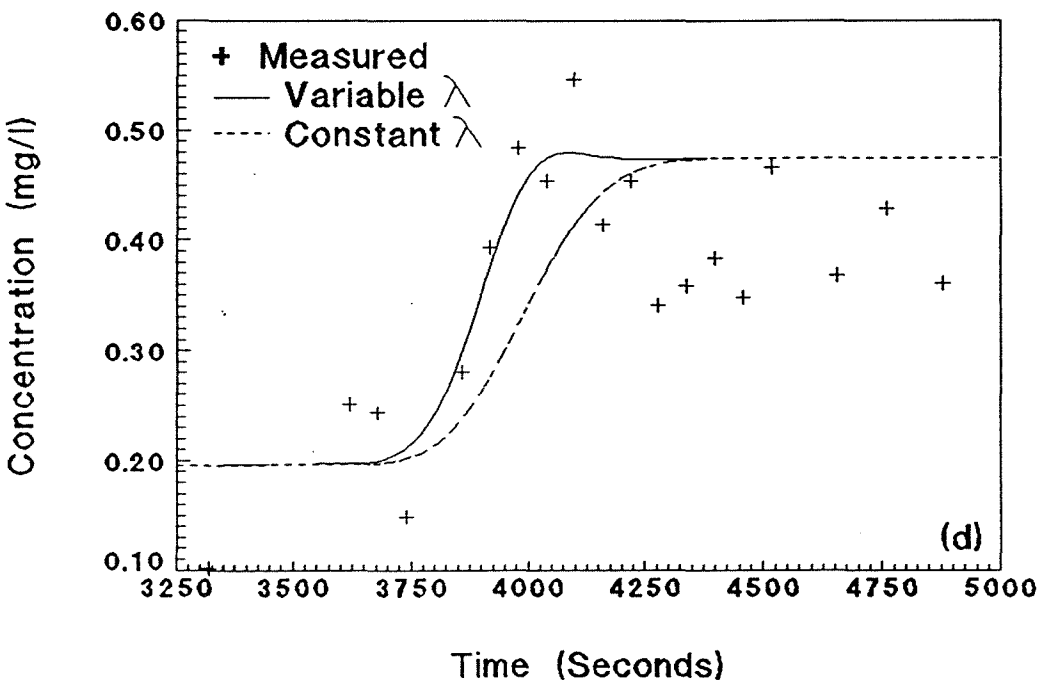

Fig. 5.40(cont.): Exp. CPB2P1S1b coupled breakthrough, $Pe_p = 10^{5.48}$, Pe = 140, 1.0 micron particles: (c) particle breakthrough and (d) particle experimental data with best-fit, numerical model.

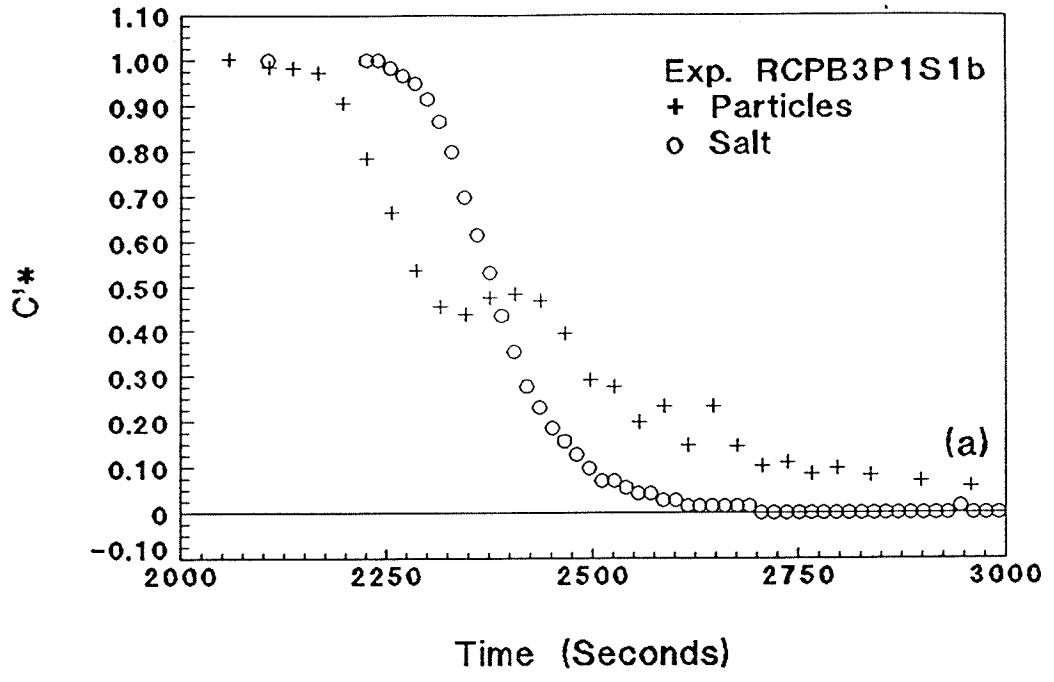

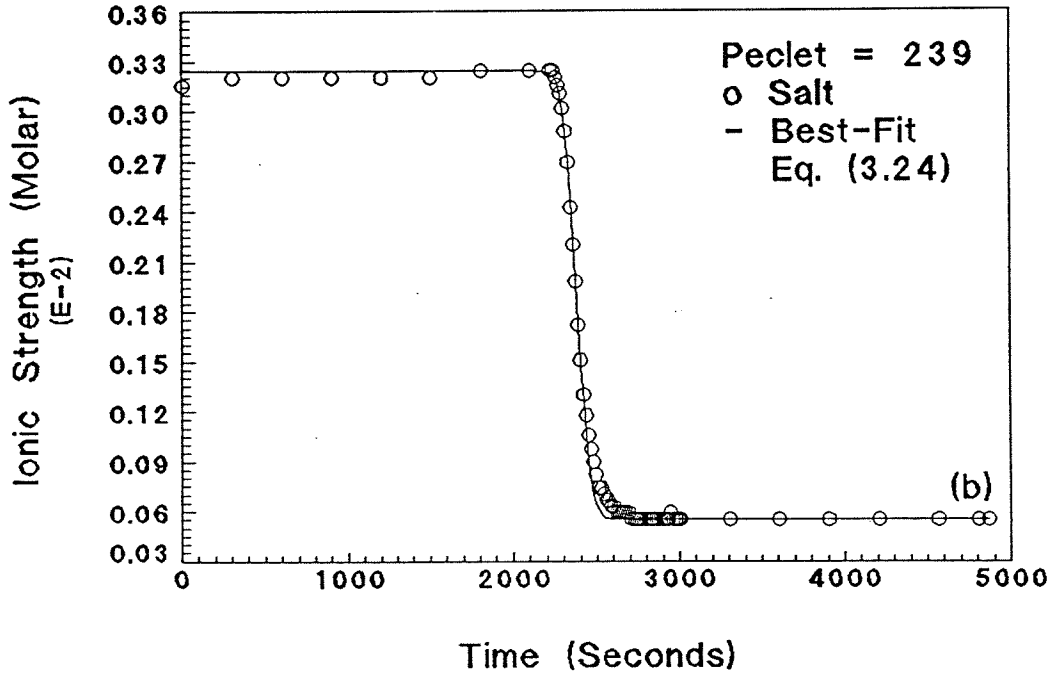

Fig. 5.41: Exp. RCPB3P1S1b coupled breakthrough, $Pe_p = 10^{5.70}$, Pe = 239, 1.0 micron particles: (a) particle and salt relative breakthroughs and (b) salt experimental data with best-fit, Eq. (3.24).

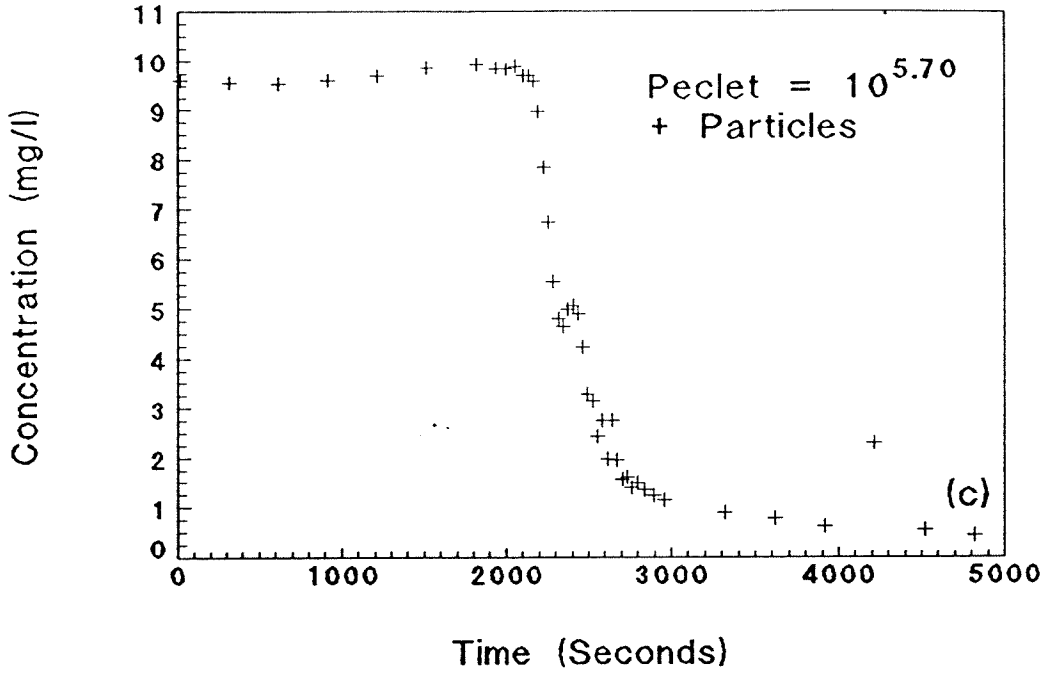

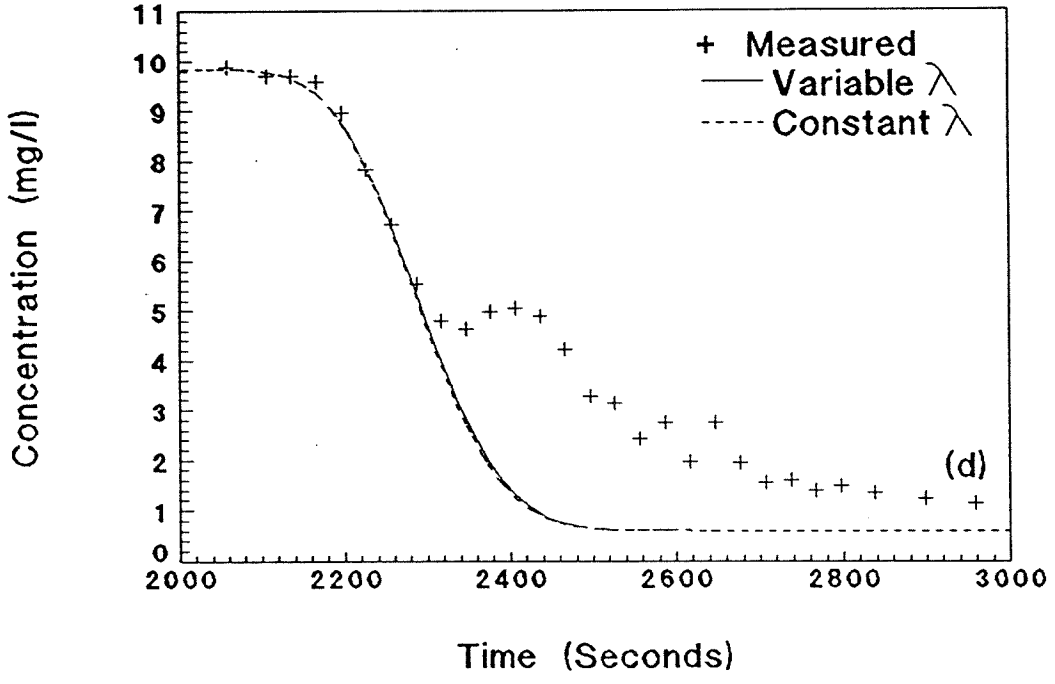

Fig. 5.41(cont.): Exp. RCPB3P1S1b coupled breakthrough, $Pe_p = 10^{5.70}$, Pe = 239, 1.0 micron particles: (c) particle breakthrough and (d) particle experimental data with best-fit, numerical model.

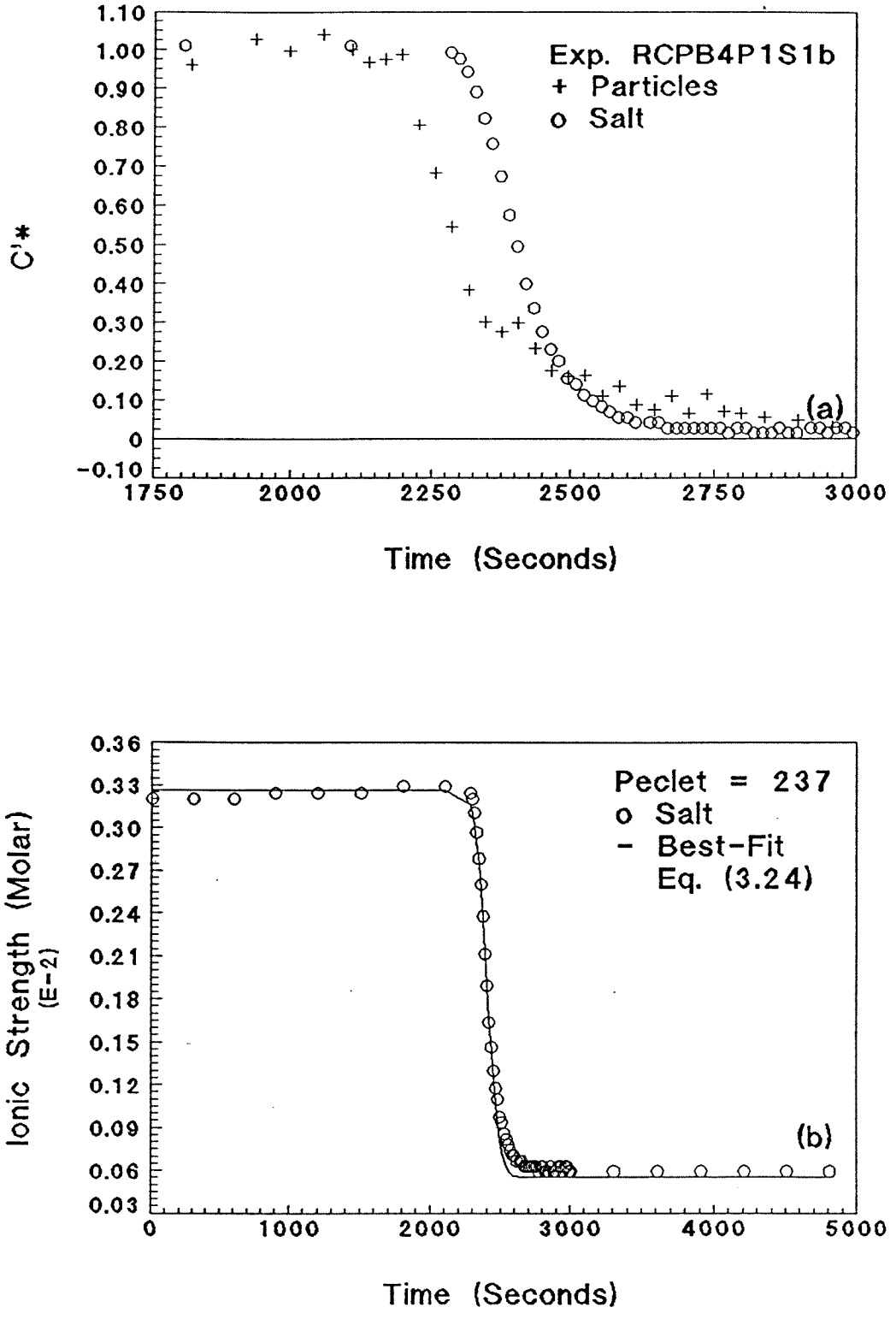

Fig. 5.42: Exp. RCPB4P1S1b coupled breakthrough, $Pe_p = 10^{5.70}$, Pe = 237, 1.0 micron particles: (a) particle and salt relative breakthroughs and (b) salt experimental data with best-fit, Eq. (3.24).

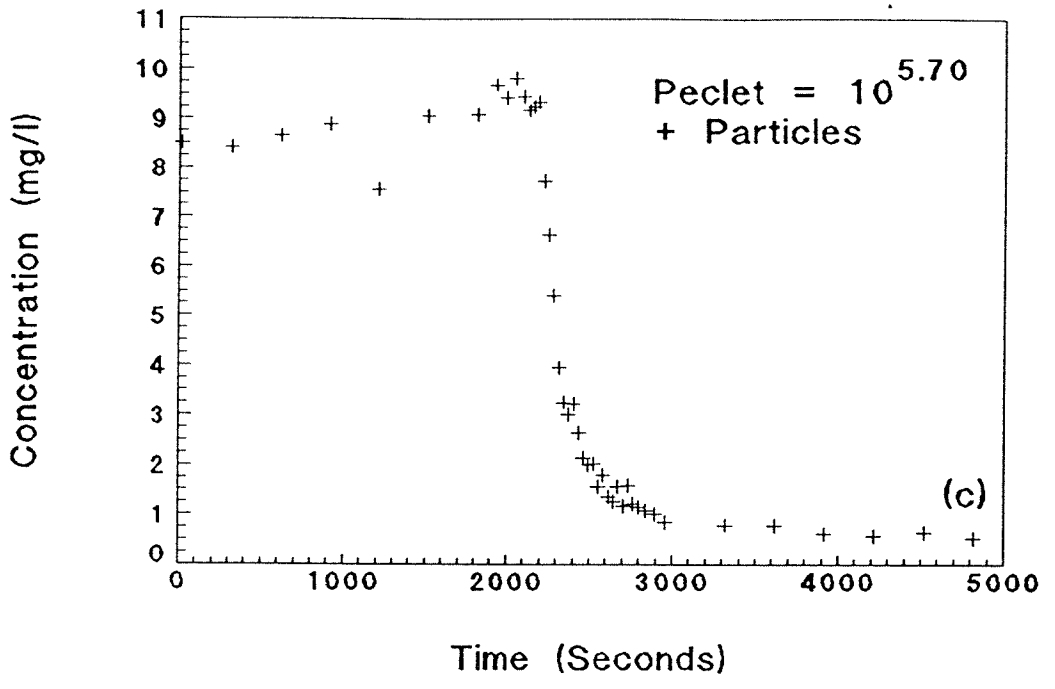

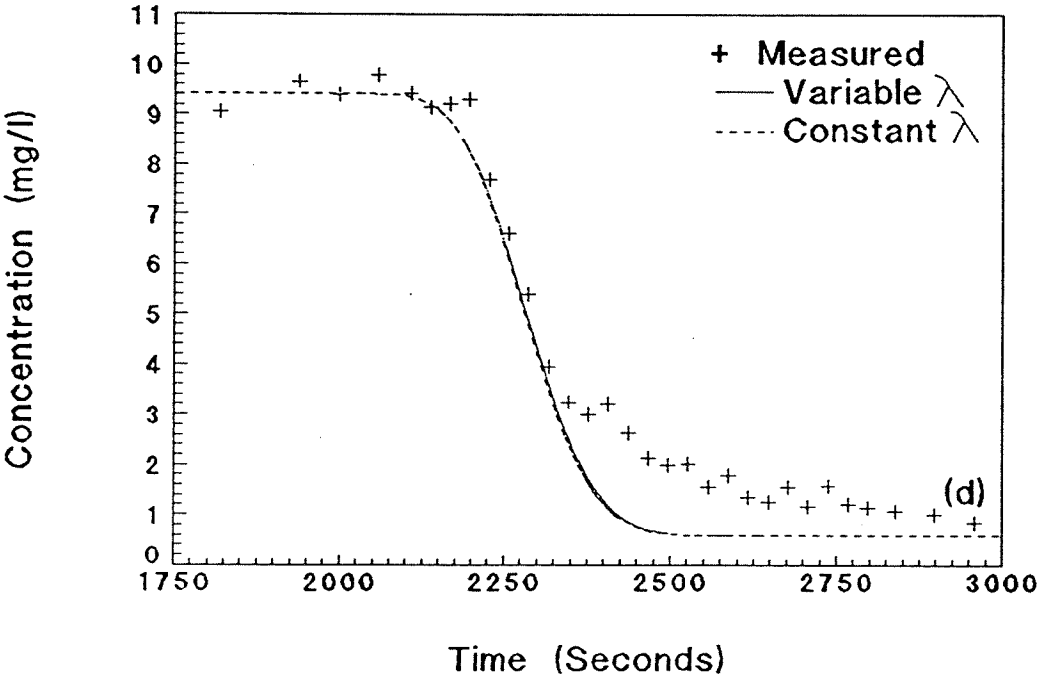

Fig. 5.42(cont.): Exp. RCPB4P1S1b coupled breakthrough, $Pe_p = 10^{5.70}$, Pe = 237, 1.0 micron particles: (c) particle breakthrough and (d) particle experimental data with best-fit, numerical model.

high ionic strength particle water. Also evident from these results is that the particles had an apparent velocity which is lower than expected. This is a result of the final concentration curve being shifted upward. In addition, the experimental data show a large tailing effect due to re-entrainment of particles resulting from the ionic strength change. The decrease in ionic strength results in a larger extent of surface repulsion; therefore, any loosely attached particles could have become dislodged and re-entrained into the flow. The figures show that as the ionic strength began to decrease an almost immediate release of particles occurred.

5.5.3 Coupled Breakthrough Conclusions

All data from the coupled breakthrough experiments are listed in Table 5.6. The coupled experiments show conclusively that the particles do transport at a rate greater than the interstitial fluid velocity. Although a best-fit analysis was not completed, the simulations completed using the numerical model show that the variable filter coefficient case produced significantly different results from those of a constant filter coefficient case. If the variable filter coefficient is not considered, major errors could be made when determining both the particle velocity and the longitudinal dispersion. These results both confirm the need for carefully controlled system chemistry when measuring any time-dependent coefficients (velocity, longitudinal dispersion) and reinforce the results of the constant ionic strength and pH breakthrough experiments.

Table 5.6: Experimental Variables and Measured Parameters for Coupled Breakthroughs

Experiment	V_p (cm/s)	V_s (cm/s)	D_L (cm^2/s)	Apparent D_{Lp} (cm^2/s)	Best-Fit D_{Lp} (cm^2/s)	Pe_p	Pe
CPB1P1S1	0.0364	0.0373	0.00201	0.00478	0.00312	2.84e+05	90.5
RCPB1P1S1	0.0376	0.0371	0.00215	0.00160	0.00322	2.93e+05	90.0
CPB2P1S1	0.0385	0.0368	0.00205	-----	0.00329	3.00e+05	89.4
CPB3P1S1	0.0637	0.0616	0.00300	0.00483	0.00547	4.96e+05	149.4
RCPB3P1S1	0.0649	0.0627	0.00312	0.00254	0.00558	5.06e+05	152.2
CPB4P1S1	0.0665	0.0625	0.00290	0.00404	0.00571	5.18e+05	151.6
RCPB4P1S1	0.0650	0.0621	0.00371	0.00570	0.00559	5.07e+05	150.7
CPB5P1S1	0.0205	0.0196	0.00104	0.00317	0.00175	1.60e+05	47.7
CPB7P1S1	0.0219	0.0214	0.00109	0.00367	0.00187	1.71e+05	51.9
RCPB7P1S1	0.0221	0.0216	0.00105	0.00282	0.00189	1.72e+05	52.4
CPB8P1S1	0.0219	0.0211	0.00128	-----	0.00187	1.71e+05	51.2
RCPB8P1S1	0.0216	0.0211	0.00116	0.00279	0.00184	1.68e+05	51.3
CPB1P3S1	0.0639	0.0610	0.00355	0.00586	0.00553	1.39e+06	148.0
RCPB1P3S1	0.0624	0.0605	0.00406	0.01091	0.00540	1.36e+06	146.7
CPB2P3S1	0.0238	0.0228	0.00106	0.00167	0.00204	5.19e+05	55.4
RCPB2P3S1	0.0234	0.0225	0.00125	0.00397	0.00201	5.11e+05	54.5
CPB3P3S1	0.0242	0.0225	0.00159	0.00229	0.00208	5.29e+05	54.7
RCPB1P4S1	0.0219	0.0212	0.00106	0.00090	0.00183	1.70e+04	51.6

5.6 Conclusions

The experimental program of this work supported the models developed in Chapter 3. The particle transport equation was able to be used to calculate longitudinal dispersion coefficients from experimental data, and the coefficient calculated from the data matched the model for this coefficient modelled from dimensional analysis. The other parameters of this model (V_p,λ) were also measured experimentally, and these results matched the models developed from both theoretical arguments and dimensional analysis. The coupled experiments confirmed both these results and the need for carefully controlled system chemistry. The significance of both these results and this work will be summarized in the next chapter.

6. SUMMARY AND CONCLUSIONS

Particle transport through uniform porous media has been studied theoretically and experimentally. This transport was described in two separate equations, steady-state and transient, for which solutions were given. The transport parameters in these equations which are the particle advective velocity, longitudinal dispersion coefficient, and filter coefficient have been experimentally measured and defined according to dimensional analysis arguments. Breakthrough experiments were carried out in a 1.5 m column of uniform sand with median grain diameter of 381 micron using carboxylated, polystyrene latex particles which have average diameters of 0.1, 1.0, and 2.8 micron in order to test the theoretical model.

This chapter includes a general summary including conclusions of the models developed and used in this study, the experimental apparatus and techniques, experimental results and model/experiment comparisons. The relevance of the studies to the transport of particles in either natural or filtration systems is discussed, and suggestions for future studies are also made.

In this work, the experimental procedures were developed specifically for measuring particle breakthroughs and not for measuring filtration. In most filtration work, several pore volumes are flowed until a steady-state concentration is reached. In this work, only 1.5 - 2 pore volumes were flowed, and the concentration plateau reached at this point was considered the steady-state concentration.

6.1 Summary of This Work

The following statements summarize the results of this work:

1) The average particle velocity was found by experiments performed in this work to be greater than the average fluid velocity by a range of approximately 0 to ~5.4%. A compilation of other experimental work (Small 1974) and this work showed that the particle velocity could be predicted by knowing only the particle and pore radii as detailed by DiMarzio and Guttman (1969, 1970) and extended to porous media in this work as shown in Eqs. (2.9) and (3.1).

2) The longitudinal dispersion coefficient for particles was defined by a dimensional analysis argument which is similar to the dimensional argument used to define solute longitudinal dispersion ($D_{Lp} \approx V_p d_g$), and this is shown in Eqs. (3.3) and (3.4). The particle longitudinal dispersion coefficient in uniform media was found to be approximately in the mid-range of solute longitudinal dispersion in uniform media when properly scaled using D_{Lp}/D_p versus Pe_p.

a) Salt tracer longitudinal dispersion coefficients measured in this work were found to be approximately 1.6 times greater than those of Houseworth (1984) for the same uniform medium. This difference was not investigated in this work.

b) The equations of the best-fit line (Eqs. (5.19) and (5.20)) of all particle longitudinal dispersion experimental data showed a smaller dependence on the Brownian diffusion coefficient than for solute dispersion in a uniform medium as determined in Houseworth (1984), but the Peclet numbers for the work of

Houseworth (1984) were considerably smaller than the Peclet numbers for this work.

3) The tailing of the breakthrough curves for the particle experiments was observed to occur for smaller relative concentrations (0.6 - 0.7) than for salt tracers (0.8 - 0.9) which may be attributed to the effect of high Peclet number on tailing. Houseworth (1984) showed in his work that as the solute Peclet numbers changed from 50.7 to 2480 the tailing increased. In this work, the Peclet numbers ranged from 1.26×10^4 to 2.00×10^6, and greater tailing was observed. The increased tailing was also linked to the filter coefficient of the given experiment. As the filter coefficient increased and less particles were observed to breakthrough, the breakthroughs became less distinct which led to lower reliability in determining which experimental data were part of the actual breakthrough.

4) The transition from favorable to unfavorable filtration was defined by a dimensional analysis argument in this work in which a comparison of the length scales of the interactions between particles and media grains were used as the independent variable. This dimensional argument variable differed from that of the model of Vaidyanathan (1986) and Vaidyanathan and Tien (1988) which used only the ionic strength as the independent variable. These length scales of interest were the double layer thickness (κ^{-1}) and the diffusion path length of an advecting particle ($a_p Pe_p^{-1/3}$) with the relationship shown in Eq. (3.8). The fit of experimental data using the model proposed by this work

was improved versus using only the ionic strength, but the scatter was still ± an order of magnitude.

a) The transition point at which the filter coefficient began to deviate from the favorable filter coefficient (onset of unfavorable conditions) was defined over a narrow range for all types of particles (Brownian or advective) for the dimensionless group developed in this work occurring at $\kappa a_p Pe_p^{-1/3} = 5.8$; whereas, the transition point occurred for different ionic strengths for different particle sizes ($I = 10^{-2}$ for advective particles and $I < 10^{-1}$ for Brownian particles).

5) The classical equation of filtration ($\partial C/\partial x = -\lambda x$, Eq. (3.9), Iwasaki 1937) has been corrected to include the effects of dispersion as shown in Eqs. (3.12) and (3.14). A Taylor series analysis showed that the complete solution (Eqs. (3.13) and (3.15)) could be approximated by the solution to the classical equation (Eqs. (3.10) and (3.11)) provided the dimensionless filter coefficient was relatively small. A review of filtration work has shown that in some cases this approximation was used when the dimensionless filter coefficient was too large. In these cases, the data may be misinterpreted due to the inaccuracy of using the approximation which would result in improper predictions for either concentration or the filter coefficient. For some of the data of Iwasaki (1937), an analysis of the data using only the approximation equation would lead to a predicted concentration which would differ by 44% from the actual concentration, and, for some of the data of Fitzpatrick (1972), a similar

analysis would lead to a predicted concentration which would differ by 72% from the actual concentration.

6) The classical advective-dispersion equation for transient solute transport has been modified by including a sink term to describe filtration as shown in Eqs. (3.20) and (3.22). An analytical solution (Eqs. (3.21) and (3.23)) was derived for the special case of a constant filter coefficient. A Taylor series analysis showed that the complete equation solution could be approximated by the solution to the transient advective-dispersion equation without filtration for the breakthrough of a conservative tracer multiplied by the solution to the steady-state equation without dispersion provided the dimensionless filter coefficient was relatively small as shown in Eq. (3.26). In this form, the particle breakthroughs are simply conservative breakthroughs whose breakthrough plateaus are reduced by multiplying by the steady-state filtration solution (see Fig. 3.5).

7) A general model developed for a variable filter coefficient has been solved numerically and compared with experimental results for coupled breakthrough experiments. Through a direct comparison of the salt and particle breakthroughs, these experiments proved conclusively that the particles have a larger advective velocity than a solute, and this difference became greater as the particle radius increased.

a) The variable filter coefficient significantly affected the particle experimental breakthroughs due to variable filtration but did not change either the particle

longitudinal dispersion coefficient or advective velocity. Depending on conditions, either the shape of the breakthrough or the apparent speed of the particle front was altered. Apparent longitudinal dispersion coefficients which were calculated directly (ignoring the coupled nature of the breakthroughs) from the experimental data showed wide discrepancies (up to a factor of 5) from the previous particle results in which the ionic strength (and the filter coefficient) was kept constant during the breakthrough. When making breakthrough predictions using the numerical model, an average particle longitudinal dispersion coefficient based on the results of the experimental work performed using constant filter coefficients (Eq. (5.19)) was used as independent input to the model, and such predictions closely matched the measured data. Also, particle advective velocities which were dependent input to the model and were varied until the predicted breakthroughs matched the experimental data matched the velocities observed in the constant ionic strength experiments. These results found in this investigation supported the claim that the changing chemical conditions in the coupled breakthroughs affected the particle breakthrough through changes in particle concentration due to particle removal (filtration) and not through changes in the hydraulics of the transport (particle longitudinal dispersion and advection).

8) The effect of chemistry on the hydraulics of particle transport are minimal or separable.

a) For the case of particle longitudinal dispersion in which the ionic strength was

kept constant throughout a given experiment but was varied between experiments, the longitudinal dispersion as shown in Fig. 5.30 varied slightly (increased for a given particle Peclet number) as the ionic strength increased. An increase of a factor of 6 in the ionic strength increased the longitudinal dispersion coefficient by a factor of 1.2.

b) As explained in the discussion of the coupled breakthrough experiments, the change in shape of the breakthroughs was a result of varying filtration due to the changing ionic strength. The hydraulics of the particle transport in these experiments (particle advection and longitudinal dispersion) were not noticeably affected by the changing ionic strength.

c) For the case of particle advection, changes in chemistry (e.g., ionic strength variations) which resulted in changes in particle apparent radius led to different particle velocities for fixed particle and pore radii as seen in Small (1974). This analysis showed that for media grains and particles which had surface charges of the same sign increases in the double layer size could be viewed as similar to increases in the particle radius due to the repulsive interactions of the surface double layers.

6.2 Relevance of This Work

The practical applications of this study include work in the fields of particle-facilitated contaminant transport, filtration, and hydrodynamic chromotagraphy.

For particle-facilitated contaminant transport models, this work has

provided the necessary quantitative framework for determining enhanced contaminant transport due to particle transport. Previous models of this type have chosen to neglect either particle dispersion, particle filtration, or both. Such models should be improved by including these processes.

For filtration, a new framework is proposed for analyzing unfavorable chemical conditions due to variant ionic strength. Also, an expression has been provided to estimate the error of using the approximate steady-state equation. The use of this error estimate expression has been shown to provide a better analysis of experimental work when attempting to verify theoretical models.

For hydrodynamic chromotagraphy for particle sizing, this work has provided experimental verification of a particle enhanced velocity model and has developed a model which is capable of describing particle transport in terms of dispersion and filtration. This is important for chromotagraphic work, because the mixing and advection of particles can be determined quantitatively in order to be able to distinguish between various sized particles more clearly.

6.3 Suggestions for Future Work

The completed work has provided the first step in developing a complete model for particle transport, mixing, and removal. Several key areas of study have arisen which will need attention in order to improve the models and results shown here. The suggestions for future work include:

1) Develop models based on both diffusion and entrainment to describe the particle tailing phenomenon. The coupled experiments in this work may have

provided a critical clue for developing a model to describe entrainment and/or re-entrainment of particles and its subsequent effect on tailing.

2) The results of this work have been obtained using on a uniform, homogeneous medium. Further work would include testing particle dispersion in a nonuniform, highly heterogeneous medium. Such work could also be conducted in a field test. Also, the network model developed by Houseworth (1984) for solutes could be applied to particle dispersion. In all of this work, salt tracer breakthroughs should also be performed in order to have a direct comparison of particle and salt breakthroughs.

3) The model describing particle enhanced velocity could be improved by using a network model which would account for randomly sized (in both length and cross-section) pores.

4) Both experimental and theoretical work on particle lateral dispersion is needed. It is expected that particle lateral dispersion will behave similarly to that of particle longitudinal dispersion as compared to solutes.

5) Develop a model based on the physics of particle-particle interactions which can describe unfavorable filtration due to variable ionic strength and matches the model developed in this work. Current predictive models which are based on physics of particle-particle interactions greatly underestimate the actual filtration by 2 or more orders of magnitude. These models describe filtration as being an abrupt jump from unfavorable to favorable filtration; whereas, this work has shown this to be a more gradual transition. A key insight provided

by the model in this work is that electrostatic surface force interactions which exist during particle-particle encounters depend on both the magnitude and the extent of these forces.

6) Investigate effects of particle surface groups on particle size. Such measurements may improve the fit of the filtration model developed in this work.

7) Incorporate particle advection, dispersion, and filtration into models describing contaminant transport. Current models ignore all particle interactions except advection.

REFERENCES

Adin, A. and M. Rebhun, "Components of Deep-Bed Filtration Mathematical Model," Proceedings of the International Symposium "Water Filtration," European Federation of Chemical Engineering, Antwerp, May 1982, pp. 1.15-1.21.

Amirtharajah, A. and D.P. Wetstein, "Initial Degradation of Effluent Quality During Filtration," Journal AWWA, Sept. 1980, pp. 518-524.

Amirtharajah, A., "Modeling Initial Degradation of Effluent Quality," Proceedings of the International Symposium "Water Filtration," European Federation of Chemical Engineering, Antwerp, May 1982, pp. 1.65-1.75.

Amirtharajah, A., "Some Theoretical and Conceptual Views of Filtration," Journal AWWA, Dec. 1988, pp. 36-46.

Anderson, D.A., et al., Computational Fluid Mechanics and Heat Transfer, Hemisphere Publishing Corp., Washington, 1984.

Anderson, J. and H. Keh, "Electrophoretic Transport of Colloids in Porous Media," Abstract No. 353, Electrochemical Society Extended Abstracts, Vol. 85-1, 1985, p. 505.

Aonuma, T., et al., "Effect of a Dissolved Gas on the Flow Rate of Water Through a Porous Medium," International Chemical Engineering, Vol. 21, No. 3, July 1981, pp. 459-464.

Arulanandan, K., et al., "Pore and Eroding Fluid Influences on Surface Erosion of Soil," Journal of the Geotechnical Engineering Division, GT1, Jan. 1975, pp. 51-66.

Avogadro, A., et al., "Env. Migration of Long-lived Radionuclides," International Atomic Energy Agency, Vienna, 1982, pp. 527-540.

Bales, R.C., "Surface Chemical and Physical Behavior of Chrysotile Asbestos in Natural Waters and Water Treatment," Ph.D. Thesis, Caltech, Pasadena, CA, Report No. AC-8-84, August 1984.

Bear, J., Dynamics of Fluids in Porous Media, American Elsevier, New York, New York, 1972, 764 pp.

Bear, J., Hydraulics of Groundwater, McGraw-Hill, New York, 1979.

Bear, J and A. Verruijt, Modeling Groundwater Flow and Pollution, D. Reidel Publishing Co., 1987, 408 pp.

Bowen, B.D. and M. Epstein, J. Colloid Interface Sci., 72, 81, 1979.

Brinkman, H.C., "A Calculation of the Viscous Force Exerted by a Flowing Fluid on a Dense Swarm of Particles," Appl. Sci. Res., Vol. A1, 1947, pp. 27-34.

Brinkman, H.C., "On the Permeability of Media Consisting of Closely Packed Porous Particles," Appl. Sci. Res., Vol. A1, 1947, pp. 81-86.

Buddemeier, R.W., Eos, Vol. 67, 1986, p. 955.

Buddemeier, R.W. and D. Isherwood, "Radionuclide Migration Project 1984 Progress Report," UCRL-53628, Lawrence Livermore National Laboratory, Livermore, CA, 1985, pp. 1-71.

Carter, C.W. and I.H. Suffet, Environmental Science Technology, Vol. 16, 1982, pp. 735-740.

Cerda, C., "Mobilization of Kaolinite Fines in Porous Media," Colloids and Surfaces, Vol. 27, Oct. 1987, No. 1-3, pp. 219-241.

Chan, D.Y.C., and D.J. Mitchell, "The Free Energy of an Electrical Double Layer," Journal of Colloid and Interface Science, Vol. 95, No. 1, Sept. 1983, pp. 193-197.

Chiou, C.T., et al., Environmental Science and Technology, Vol. 20, 1986, pp. 502-508.

Cleasby, J., "Filtration - Back to the Basics," Proceedings AWWA Seminar: Coagulation and Filtration - Back to the Basics, Denver, June 1981, pp. 59-84.

Cohen, Y. and A.B. Metzner, "Wall Effects in Laminar Flow of Fluids Through Packed Beds," AIChE Journal, Vol. 27, No. 5, Sept. 1981, pp. 705-715.

Cookson, J., "Removal of Submicron Particles in Packed Beds," Environmental Science and Technology, Vol. 4, No. 2, Feb. 1972, pp. 128-134.

Coutts, J.R.H., et al., "Use of Radioactive ^{59}Fe for Tracing Soil Particle Movement," Journal of Soil Science, Vol. 19, No. 2, 1968, pp. 325-343.

Craft, T.F., "Radiotracer Study of Rapid Sand Filtration," Ph.D. Thesis, 1969.

Curry, R.B. and R.P. Beasley, "Flow of Colloidal Suspension Through Porous Media as Related to Reservoir Sealing," Transactions of ASCE, Journal Series No. 2230, 1962, pp. 160-164.

Curry, R.B., et al., "Interrelation of Physical and Chemical Properties in Flow of Colloidal Suspensions in Porous Media," Transactions of ASCE, Journal Article No. 75-64, 1965, pp. 259-263.

Daily, J.W. and D.R.F. Hanleman, Fluid Dynamics, Addison-Wesley, Reading, Mass., 1966, pp. 454.

Department of Energy, "Transport of Contaminants in the Subsurface: The Role of Organic and Inorganic Colloidal Particles," Subsurface Transport Program Interactive Seminar Series, DOE/ER-0331, 1986, 70 pp.

Department of Energy, "Role of Colloidal Particles in the Subsurface Transport of Contaminants," Subsurface Transport Program Interactive Seminar Series, DOE/ER-0384, 1988, 48 pp.

Derjaguin, B.V. and L. Landau, "Theory of the Stability of Strongly Charged Lyophobic Sols and of the Adhesion of Strongly Charged Particles in Solutions of Electrolytes," Acta Physicochimica URSS, Vol. 14, 1941, pp. 633.

DiMarzio, E.A. and C.M. Guttman, "Separation By Flow," Polymer Letters, Vol. 7, 1969, pp. 267-272.

DiMarzio, E.A. and C.M. Guttman, "Separation By Flow," Macromolecules, Vol. 3, No. 2, 1970, pp. 131-146.

Donaldson, E.C., et al., "Particle Transport in Sandstones," SPE6905, 52nd Annual Fall Technical Conference and Exhibition of the Society of Petroleum Engineers, 1977, pp. 1-20.

Dukhin, S.S. and J. Lyklema, "Dynamics of Colloid Particle Interaction," Langmuir, Vol. 3, No. 1, 1987, pp. 94-98.

Elimelech, M. and C. O'Melia, "Effect of Particle Size on Collosion Efficiency in the Deposition of Brownian Particles with Electrostatic Energy Barriers," Langmuir, Vol. 6, No. 6, 1990, pp. 1153-1163.

Enfield, C.G., et al., Groundwater, Vol. 20, 1982, pp. 711-722.

Enfield, C.G., "Chemical Transport Facilitated by Multiphase Flow Systems," Water Science Technology, Vol. 17, 1985, pp. 1-12.

Enfield, C.G. and G. Bengtsson, "Macromolecular Transport of Hydrophobic Contaminants in Aqueous Environments," Ground Water, Vol. 26, No. 1, Jan. - Feb. 1988, pp. 64-70.

Fischer, H.B., et al., Mixing in Inland and Coastal Waters, Academic Press, Orlando, Florida, 1979, 483 pp.

Fitzpatrick, J.A., "Mechanisms of Particle Capture in Water Filtration," Ph.D. Thesis, Harvard University, Cambridge, Massachusetts, 1972.

Fitzpatrick, J.A. and L.A. Spielman, "Filtration of Aqueous Latex Suspensions Through Beds of Glass Spheres," Journal of Colloid and Interface Science, Vol. 43, No. 2, May 1973, pp. 350-369.

Fried, J.J. and M.A. Combarnous, "Dispersion in Porous Media," Advances in Hydroscience, Vol. 7, 1971, pp. 169-282.

Friedlander, S.K., "Particle Diffusion in Low-Speed Flows," Journal of Colloid and Interface Science, Vol. 23, 1967, pp. 157-164.

Gerald, C.F. and P.O. Wheatley, Applied Numerical Analysis, Addison-Wesley Publishing Co., Reading, Massachusetts, 1984.

Gerba, C.P. and S.M. Goyal, "Artificial Recharge of Groundwater," Asano, T., El., Butterworth, Boston, 1985, pp. 238-317.

Gerba, C.P., et al., American Society of Civil Engineering, Journal of Irrigation and Drainage Division, 1975, 101(IR3), pp. 157-174.

Ghosh, M.M., et al., "Physicochemical Approach to Water and Wastewater Filtration," Journal of the Environmental Engineering Division, EE1, Feb. 1975, pp. 71-86.

Gimbel, R., "Influence of the Filter Grain Surface Structure on the Transport and Adhesion Mechanisms in Deep-Bed Filters," Proceedings of the International Symposium "Water Filtration," Antwerp, May 1982, European Federation of Chemical Engineering, pp. 1.23-1.33.

Goldsmith, H.L. and S.G. Mason, Journal of Colloid Science, Vol. 17, 1962, p. 448.

Golub, G.H. and C.F. Van Loan, Matrix Computations, The Johns Hopkins University Press, Baltimore, Maryland, 1983.

Goren, S.L. and M. O'Neill, "On the Hydrodynamic Resistance to a Particle of a Dilute Suspension When in the Neighborhood of a Large Obstacle," Chemical Engineering Science, Vol. 26, 1971, pp. 325-338.

Greenkorn, R.A., "Steady Flow Through Porous Media," AIChE Journal, Vol. 27, No. 4, July 1981, pp. 529-545.

Gregory, J., "Interaction of Unequal Double Layers at Constant Charge," Journal of Colloid and Interface Science, Vol. 51, No. 1, April 1975, pp. 44-51.

Gregory, J., "Approximate Expressions for Retarded van der Waals Interaction," Journal of Colloid and Interface Science, Vol. 83, No. 1, Sept. 1981, pp. 138-145.

Gregory, J. and A.J. Wishart, "Deposition of Latex Particles on Alumina Fibers," Colloids and Surfaces, Vol. 1, 1980, pp. 313-334.

Gruesbeck, C. and R.E. Collins, "Entrainment and Deposition of Fine Particles in Porous Media," Society of Petroleum Engineers Journal, Dec. 1982, pp. 847-856.

Grutsch, J.F. and R. Mallatt, "Optimizing Granular Media Filtration," Chemical Engineering Progress, Vol. 73, No. 4, April 1977, pp. 57-66.

Gschwend, P.M. and S.C. Wu, Environmental Science and Technology, Vol. 19, 1985, p. 90.

Guzy, C.J., et al., "A Theory of Retention of Colloidal Fines During Drainage," Canadian Pulp and Paper Assoc., Technical Section, 1982, pp. 41-46.

Hamaker, H.C., "The London-van der Waals Attraction Between Spherical Particles," Physica IV, No. 10, 1937, pp. 1058-1072.

Happel, J., "Viscous Flow in Multiparticle Systems: Slow Motion of Fluids Relative to Beds of Spherical Particles," AIChE Journal, Vol. 4, No. 2, June 1958, pp. 197-201.

Happel, J., "Viscous Flow Relative to Arrays of Cylinders," AIChE Journal, Vol. 5, No. 2, June 1959, pp. 174-177.

Happel, J. and B.J. Byrne, Ind. Eng. Chem., Vol. 46, 1954, p. 1181.

Harvey, R.W., et al., "Transport of Microspheres and Indigenous Bacteria Through a Sandy Aquifer: Results of Natural- and Forced-Gradient Tracer Experiments," Environmental Science and Technology, Vol. 23, 1989, pp. 51-56.

Hassett, J.P. and M.A. Anderson, Water Res., Vol. 16, 1982, pp. 681-686.

Hayward, S.B., Journal AWWA, Vol. 76, 1984, pp. 66-73.

Herzig, J.P., et al., "Flow of Suspensions Through Porous Media - Application to Deep Filtration," Industrial and Engineering Chemistry, Vol. 62, No. 5, May 1970, pp. 8-35.

Hogg, R., et al., "Mutual Coagulation of Colloidal Dispersions," 1965, pp. 1638-1651.

Hornbeck, R.W., Numerical Methods, Prentice-Hall, Inc., Englewood Cliffs, New Jersey, 1975.

Houseworth, J.E., "Longitudinal Dispersion in Nonuniform Isotropic Porous Media," Ph.D. Thesis, Caltech, Pasadena, CA, Report No. KH-R-45, June 1984.

Hull, M. and J.A. Kitchener, "Interaction of Spherical Colloidal Particles with Planar Surfaces," Jan. 1969, pp. 3093-3104.

Ison, C.R. and K.J. Ives, "Removal Mechanisms in Deep Bed Filtration," Chemical Engineering Science, Vol. 15, 1969, pp. 717-729.

Ives, K.J. and J. Gregory, "Surface Forces in Filtration," Society for Water Treatment and Examination, Proceedings, Vol. 15, 1966, pp. 93-116.

Ives, K.J. and J. Gregory, "Surface Forces in Filtration," Society for Water Treatment and Examination, Proceedings, Vol. 16, 1967, pp. 147-169.

Ives, K., "Fundamentals of Filtration," Proceedings of the International Symposium "Water Filtration," European Federation of Chemical Engineering, Antwerp, May 1982, pp. 1-11.

Iwasaki, T., "Some Notes on Sand Filtration," Journal AWWA, Vol. 29, No. 10, 1937, pp. 1591-1602.

Janssens, J., et al., "Statistical Analysis of Variables Affecting Direct-Filtration," Proceedings of the International Symposium "Water Filtration," European Federation of Chemical Engineering, Antwerp, May 1982, pp. 4.65-4.80.

Jordan, T.A., et al., "Physico-chemical Aspects of Deep-Bed Filtration," Journal WPCF, Vol. 46, No. 12, Dec. 1974, pp. 2745-2754.

Karger, B.L., et al., An Introduction to Separation Science, Wiley Interscience, New York, New York, 1973, 586 pp.

Kavanaugh, M., et al., "Particulates and Tracer Pollution Removal by Depth Filtration," Progress in Water Technology, Vol. 10, Nos. 5/6, 1978, pp. 197-215.

Keswick, B.H. and C.P. Gerba, Environmental Science and Technology, Vol. 14, 1980, pp. 1290-1297.

Khilar, K.C. and H.S. Fogler, "Water Sensitivity of Sandstones," Society of Petroleum Engineers Journal, Feb. 1983, pp. 55-64.

Kovenya, S.V., et al., "Study of the Role of Mechanical Forces and Geometric Conditions in the Movement of Highly Dispersed Particles in Soil Columns," Soviet Soil Science, 1972, pp. 605-612.

Kuwabara, S., "The Forces Experienced by Randomly Distributed Parallel Circular Cylinders of Spheres in a Viscous Flow at Small Reynolds Numbers," Journal of the Physical Society of Japan, Vol. 14, No. 4, April 1959, pp. 527-532.

Landrum, P.F., et al., Environmental Science and Technology, Vol 18, 1984, pp. 187-192.

Lever, A. and R. Dawe, "Clay Migration and Entrapment in Synthetic Porous Media," Marine and Petroleum Geology, Vol. 4, No. 2, May 1987, pp. 112-118.

Levich, V.G., Physicochemical Hydrodynamics, Prentice-Hall, Englewood Cliffs, New Jersey, 1962.

Liang, L., "Effects of Surface Chemistry on Kinetics of Coagulation of Submicron Iron Oxide Particles in Water," Ph.D. Thesis, Caltech, Pasadena, CA, June 1988.

Logsdon, G., et al., "Alternative Filtration Methods for Removal of Giardia Cysts and Cyst Models," Journal AWWA, Feb. 1981, pp. 111-118.

Lyklema, J., "Colloid Stability as a Dynamic Phenomenon," Pure and Applied Chemistry, Vol. 52, 1980, pp. 1221-1227.

Mackrle, V., "Hydrodynamics of the Disposal of Low-level Liquid Radioactive Wastes in Soil," Research Contract No. 98, International Atomic Energy Agency, Vienna, 1965, pp. 4-7.

McCarthy, J.F. and B.D. Jimenez, Environmental Science and Technology, Vol. 19, 1985, pp. 1072-1076.

McCarthy, J.F. and M.C. Black, "Tenth Symposium on Aquatic Toxicology and Hazard Assessment," American Society for Testing and Materials, Philadelphia, PA, 1987.

McDowell-Boyer, L.M., et al., "Particle Transport Through Porous Media," Water Resources Research, Vol. 22, No. 13, Dec. 1986, pp. 1901-1921.

Mel'Nikova, M.K., et al., "Use of Radioactive Tracers for Simulating the Lessivage Process," Soviet Soil Science, 1971, pp. 611-618.

Muecke, T.W., "Formation Fines and Factors Controlling Their Movement in Porous Media," Journal of Petroleum Technology, Feb. 1979, pp. 144-150.

Nakayama, S., et al., Journal Nuc. Sci. Technology, Vol. 23, 1986, pp. 731-739.

Nightingale, H.L. and W.C. Bianchi, Groundwater, 1977, Vol. 15, pp. 146-152.

Oliphant, J. and A. Tice, "An Experimental Measurement of Channeling of Flow in Porous Media," Soil Science, Vol. 139, No. 5, May 1985, pp. 394-399.

O'Melia, C.R. and W. Ali, "The Role of Retained Particles in Deep Bed Filtration," Progress in Water Technology, Vol. 10, Nos. 5/6, 1978, pp. 167-182.

O'Melia, C.R., "Particles, Pretreatment, and Performance in Water Filtration," Journal of Environmental Engineering, Vol. 111, No. 6, Dec. 1985, pp. 874-890.

Onorato, F. and C. Tien, "Effect of Surface Interaction on Non-Brownian Particle Deposition - Single Collector Experiment," I. Chem. E. Symposium Series No. 59, 1980, pp. 5:2/1-5:2/21.

Ottewill, R.H. and J.N. Shaw, "Stability of Monodisperse Polystyrene Latex Dispersions of Various Sizes," 1966, pp. 154-163.

Ottewill, R.H. and J. Shaw, "Electrophoretic Studies on Polystyrene Latices," Electroanalytical Chemistry and Interfacial Electrochemistry, Vol. 37, 1972, pp. 133-142.

Payatakes, A.C., et al., "Trajectory Calculation of Particle Deposition in Deep Bed Filtration: Part I. Model Formulation," AIChE Journal, Vol. 20, No. 5, Sept. 1974, pp. 889-900.

Payatakes, A.C., et al., "Trajectory Calculation of Particle Deposition in Deep Bed Filtration: Part II. Case Study of the Effect of the Dimensional Groups and Comparison with Experimental Data," AIChE Journal, Vol. 20, No. 5, Sept. 1974, pp. 900-905.

Payatakes, A.C., et al., "Application of Porous Media Models to the Study of Deep Bed Filtration," The Canadian Journal of Chemical Engineering, Vol. 52, Dec. 1974, pp. 722-731.

Pendse, J., et al., "Dispersion Measurement in Clogged Filter Beds: A Diagnostic Study on the Morphology of Particle Deposits," AIChE Journal, Vol. 24, No. 3, May 1978, pp. 473-485.

Pfannkuch, H.O., "Contribution a'l'Etude des Deplacement de Fluides Miscible dans un Milieu Poreux," Rev. Inst. Fr. Petrol., 18, #2, 215, 1962.

Philip, J. and D. Smiles, "Macroscopic Analysis of the Behavior of Colloidal Suspensions," Advances in Colloid and Interface Science, Vol. 17, Aug. 1982, pp. 83-103.

Pilgrim, D.H. and D.D. Huff, "Suspended Sediment in Rapid Subsurface Stormflow on a Large Field Plot," Earth Surface Processes and Landforms, Vol. 8, 1983, pp. 451-463.

Priesing, C.P., "A Theory of Coagulation Useful for Design," Industrial and Engineering Chemistry, Vol. 54, No. 8, Aug. 1962, p. 38.

Prieve, D.C. and E. Ruckenstein, "Effect of London Forces upon the Rate of Deposition of Brownian Particles," AIChE Journal, Vol. 20, No. 6, Nov. 1974, pp. 1178-1187.

Rajagopalan, R. and C. Tien, "Trajectory Analysis of Deep-Bed Filtration with the Sphere-in-Cell Porous Media Model," AIChE Journal, Vol. 22, No. 3, May 1976, pp. 523-533.

Rajagopalan, R. and C. Tien, "Single Collector Analysis of Collection Mechanisms in Water Filtration," The Canadian Journal of Chemical Engineering, Vol. 55, June 1977, pp. 246-255.

Rajagopalan, R. and C. Tien, "Experimental Analysis of Particle Deposition on Single Collectors," The Canadian Journal of Chemical Engineering, Vol. 55, June 1977, pp. 256-264.

Rajagopalan, R. and C. Tien, The Theory of Deep Bed Filtration, Progress in Filtration and Separation, Elsevier Scientific Pub. Co., 1979, pp. 179-269.

Robertson, W.D., et al., Groundwater, Vol. 22, 1984, pp. 191-197.

Ruckenstein, E. and D.C. Prieve, "Rate of Deposition of Brownian Particles under the Action of London and Double-layer Forces," Apr. 1973, pp. 1522-1536.

Ruckenstein, E. and D.C. Prieve, "Role of Physico-chemical Properties in the Deposition of Hydrosols," Chapter 7, Testing and Characterization of Powders and Fine Particles, ed. by Beddow, J.K. and J.P. Meloy, Heyden, Philadelphia, 1980, pp. 107-137.

Rumer, R.R., "Longitudinal Dispersion in Steady and Unsteady Flow," Proceedings of the American Society of Civil Engineers, Hydraulics Division, Vol. 80, HY 4, July 1962, pp. 147-172.

Saatci, A.M. and C.S. Oulman, "The Bed Depth Service Time Design Method for Deep Bed Filtration," Journal AWWA, Sept. 1980, pp. 524-528.

Sakthivadivel, R., "Clogging of a granular porous medium by sediment," Rep. HEL 15-7, pp. 106, Hydraulic Eng. Lab., University of Calif., Berkeley, 1969.

Scharpenseel, J.W. and W. Kerpen, "Studies on Tagged Clay Migration Due to Water Movement," Symposium on the Use of Isotope and Radiation Techniques in Soil Physics and Irrigation Studies, International Atomic Energy Agency, 1967, pp. 279-287.

Sembi, S. and K. Ives, "Optimization of Size-Graded Filters," Proceedings of the International Symposium "Water Filtration," European Federation of Chemical Engineering, Antwerp, May 1982, pp. 5.1-5.11.

Sherard, J.L., et al., "Basic Properties of Sand and Gravel Filters," Journal of Geotechnical Engineering, Vol. 110, No. 6, June 1984, pp. 684-700.

Sherard, J.L., et al., "Filters for Silts and Clays," Journal of Geotechnical Engineering, Vol. 110, No. 6, June 1984, pp. 701-718.

Small, H., "Hydrodynamic Chromatography: A Technique for Size Analysis of Colloidal Particles," Journal of Colloid and Interface Science, Vol. 48, No. 1, 1974, pp. 147-161.

Spielman, L.A., "Particle Capture from Low-speed Laminar Flows," Annual Reviews of Fluid Mechanics, Vol. 9, 1977, pp. 297-319.

Spielman, L.A. and P.M. Cukor, "Deposition of Non-Brownian Particles under Colloidal Forces," Journal of Colloid and Interface Science, Vol. 43, No. 1, Apr. 1973.

Spielman, L.A. and J.A. Fitzpatrick, "Theory for Particle Collection Under London and Gravity Forces," Journal of Colloid and Interface Science, Vol. 42, No. 3, March 1973, pp. 607-623.

Spielman, L.A. and S.K. Friedlander, "Role of the Electrical Double Layer in Particle Deposition by Convective Diffusion," Journal of Colloid and Interface Science, Vol. 46, No. 1, Jan. 1974, pp. 22-31.

Spielman, L.A. and S.L. Goren, "Capture of Small Particles by London Forces from Low-speed Liquid Flows," Environmental Science and Technology, Vol. 4, No. 2, Feb. 1970, pp. 135-140.

Stumm, W. and J.J. Morgan, Aquatic Chemistry, Wiley Interscience, New York, New York, 1981, 780 pp.

Stumm, W., "Particle-Particle Interactions," Chapter 14, Aquatic Surface Chemistry, 1987, pp. 385-403.

Taylor, G.I., "Dispersion of Soluble Matter in Solvent Flowing Slowly Through a Tube," Proceedings of the Royal Society of London, Series A, Vol. 219, August 1953, pp. 186-203.

Tien, C. and A.C. Payatakes, "Advances in Deep Bed Filtration," AIChE Journal, Vol. 25, No. 5, Sept. 1979, pp. 737-759.

Tien, C., et al., "Simulation of the Dynamic Behavior of Deep Bed Filters," AIChE Journal, Vol. 25, No. 3, May 1979, pp. 385-395.

Tien, C. and R. Gimbel, "On the Development of a Comprehensive Model of Deep Bed Filtration," Proceedings of the International Symposium "Water Filtration," European Federation of Chemical Engineering, Antwerp, May 1982, pp. 1.1-1.13.

Tobiason, J.E. and C.R. O'Melia, "Physicochemical Aspects of Particle Removal in Depth Filtration," Journal AWWA, Dec. 1988, pp. 54-64.

Vaidyanathan, R., "Hydrosol Filtration in Granular Beds," Masters Thesis, Syracuse University, August 1986.

Vaidyanathan, R. and C. Tien, "Hydrosol Deposition in Granular Beds," Chemical Engineering Science, Vol. 43, No. 2, pp. 289-302, 1988.

Verwey, E. and J. Overbeek, Theory of the Stability of Lyophobic Colloids, Elsevier, Amsterdam, 1948.

Wang, Z., et al., "Chemical Aspects of Packed Bed Filtration in Water Treatment," World Filtration Congress, 4th, 1986, pp. 8.23-8.27.

Willis, M.S. and I. Tosun, "A Rigorous Cake Filtration Theory," Chem. Eng. Sci., 30(9), 1035-1047, 1975.

Winsauer, W., et al., "Resistivity of Brine-saturated Sands in Relation to Pore Geometry," Bulletin of the American Assoc. of Petroleum Geologists, Vol. 36, No. 2, Feb. 1952, pp. 253-277.

Yao, K., et al., "Water and Waste Water Filtration: Concepts and Applications," Environmental Science and Technology, Vol. 5, No. 11, 1971.

Yoshimura, Y., et al., "Initial Particle-Collection Mechanism in Clean, Deep-Bed Filtration," International Chemical Engineering, Vol. 20, No. 4, Oct. 1980, pp. 600-608.

APPENDIX A

Steady-state Particle Suspension Transport

A.1 Solution Derivation

Consider the complete one-dimensional steady-state particle advective-dispersion equation which includes a removal term to account for filtration effects:

$$0 = D_{Lp}\frac{\partial^2 C}{\partial x^2} - V_p\frac{\partial C}{\partial x} - \lambda V_p C \qquad \text{(A.1)}$$

where: C = *concentration* ($M\ L^{-3}$);
x = *longitudinal distance* (L);
D_{Lp} = *longitudinal dispersion coefficient for particles* ($L^2\ T^{-1}$);
V_p = *average particle interstitial velocity* ($L\ T^{-1}$); *and*
λ = *filter coefficient* (L^{-1}).

with the following boundary conditions:

$$\begin{aligned} &1)\ C(x=0) = C_0;\ \textit{and} \\ &2)\ \lim_{x\to+\infty} C(x) = 0. \end{aligned} \qquad \text{(A.1.1)}$$

For convenience, the x-variable is allowed to range from negative to positive infinity ($-\infty < x < +\infty$), although the equations are only applied for $x > 0$. This avoids difficulty at $x = 0$, because small dispersion is allowed. In dimensionless form, the transport equation becomes:

$$0 = \frac{\partial^2 C*}{\partial x*^2} - Pe_{Dp}\frac{\partial C*}{\partial x*} - \lambda* Pe_{Dp} C* \qquad \text{(A.2)}$$

$$\text{where: } C* = \frac{C}{C_0};$$
$$C_0 = C(x=0);$$
$$d_g = \text{media grain diameter } (L);$$
$$x* = \frac{x}{d_g};$$
$$Pe_{Dp} = \frac{V_p d_g}{D_{Lp}}; \text{ and}$$
$$\lambda* = \lambda d_g.$$

with the same boundary conditions:

$$\begin{aligned} &1)\ C*(x*=0) = 1; \text{ and} \\ &2)\ \lim_{x*\to+\infty} C*(x*) = 0. \end{aligned} \qquad \textbf{(A.2.1)}$$

In order to derive a solution, try the following as a solution:

$$C*(x*) = exp[\alpha* x*] \qquad \textbf{(A.3)}$$

Check Eq. (A.3) by substituting into Eq. (A.2):

$$\alpha*^2 exp[\alpha* x*] - Pe_{Dp}\alpha* exp[\alpha* x*] - \lambda* Pe_{Dp} exp[\alpha* x*] = 0$$
$$\alpha*^2 - Pe_{Dp}\alpha* - \lambda* Pe_{Dp} = 0$$

This results in a second-degree polynomial in terms of α^*, and the two roots of this polynomial are:

$$\alpha*_1 = \frac{1}{2}Pe_{Dp}\left(1 - \sqrt{1 + \frac{4\lambda*}{Pe_{Dp}}}\right) \quad ; \quad \alpha*_2 = \frac{1}{2}Pe_{Dp}\left(1 + \sqrt{1 + \frac{4\lambda*}{Pe_{Dp}}}\right)$$

Using these two roots, Eq. (A.3) becomes:

$$C*(x*) = Aexp[\alpha*_1 x*] + Bexp[\alpha*_2 x*] \qquad \textbf{(A.4)}$$

The constants of this equation can be determined by applying the boundary conditions:

$$1)\ C*(x*=0) = 1 = A + B;\ \textit{and}$$
$$2)\ C*(x*\Rightarrow+\infty) = 0 = (A)(0) + (B)(+\infty).$$
$$\therefore A = 1 \textit{ and } B = 0.$$

By substituting these constants into Eq. (A.4), the solution to Eq. (A.2) becomes:

$$C*(x*) = exp\left[\frac{1}{2}Pe_{Dp}\left(1 - \sqrt{1 + \frac{4\lambda*}{Pe_{Dp}}}\right)x*\right] \qquad \textbf{(A.5)}$$

A.2 Solution Approximation

Consider an approximation for Eq. (A.5) by simplifying α^*:

$$\alpha* = \frac{1}{2}Pe_{Dp}\left(1 - \sqrt{1 + \frac{4\lambda*}{Pe_{Dp}}}\right) \qquad \textbf{(A.6)}$$

Perform a Taylor series expansion of the radical portion of α^* of Eq. (A.6) by considering a function f(x):

$$f(x) = \sqrt{1 + x}$$
$$\textit{where: } x = \frac{4\lambda*}{Pe_{Dp}}.$$

The Taylor series approximation is:

$$\sqrt{1 + x} = 1 + \frac{1}{2}x - \frac{1}{8}x^2 + \frac{1}{16}x^3 - \frac{5}{128}x^4 \cdots$$

Since this series is an alternating series, the truncation error must be less than the first truncated term (absolute values). Substituting the first two terms of the

series into Eq. (A.6) for the radical portion of α^* yields:

$$\alpha* \approx \frac{1}{2}Pe_{Dp}\left(1 - \left\{1 + \frac{2\lambda*}{Pe_{Dp}}\right\}\right) = -\lambda* \tag{A.7}$$

Substitute the approximation for α^*, Eq. (A.7), into the exact steady-state equation, Eq. (A.5), in order to determine an approximate solution to the steady-state equation:

$$C* = exp[-\lambda*x*] \tag{A.8}$$

Using Eq. (A.8), λ^* can be directly calculated from concentration and position measurements. Also, Eq. (A.8) is the same result that would have been derived by ignoring the dispersion term originally.

A.3 Approximate Versus Exact Solution

The error using the approximate solution can be determined from the relative error of the two solutions, Eqs. (A.3) and (A.8):

$$\Delta C* = \frac{C*_a - C*_e}{C*_e} = \frac{exp[-\lambda*x*] - exp[\alpha*x*]}{exp[\alpha*x*]} \tag{A.9}$$

where: $C*_a$ = *approximate solution; and*
$C*_e$ = *exact solution.*

Eq. (A.9) can be simplified as follows:

$$\Delta C* = exp[-x*(\lambda* + \alpha*)] - 1 \tag{A.10}$$

The Taylor series expansion for the exponential portion of Eq. (A.10) is:

$$exp[-x*(\lambda* + \alpha*)] = 1 - x*(\lambda* + \alpha*) + \cdots \quad \textbf{(A.11)}$$

At this point, the approximate value for α^* can be determined using the Taylor series for α^* found in Section A.2:

$$\begin{aligned} \alpha* &= \frac{1}{2}Pe_{Dp}\left(1 - \sqrt{1 + x}\right) \\ &= -\frac{1}{2}Pe_{Dp}\left(\frac{1}{2}x - \frac{1}{8}x^2 \cdots\right) \\ &\leq -\frac{1}{4}Pe_{DP}x + \frac{1}{16}Pe_{Dp}x^2 \end{aligned}$$

Substitute for x:

$$\alpha* \leq -\lambda* + \frac{\lambda*^2}{Pe_{Dp}} \quad \textbf{(A.12)}$$

Now, add λ^* to Eq. (A.12) in order to determine the argument of the exponential term of Eq. (A.10) so that Eq. (A.11) can be evaluated:

$$\alpha* + \lambda* \leq \frac{\lambda*^2}{Pe_{Dp}} \quad \textbf{(A.13)}$$

Substitute this approximation into the series expansion expression, Eq. (A.11), of the exponential term in Eq. (A.10):

$$|\Delta C*| \leq |1 - x*(\lambda* + \alpha*) - 1| \leq \frac{\lambda*^2 x*}{Pe_{Dp}} \quad \textbf{(A.14)}$$

The absolute value of the error is the absolute value of ΔC^* of Eq. (A.14):

$$\therefore |Error| = |\Delta C*| \leq \frac{\lambda*^2 x*}{Pe_{Dp}} \quad \textbf{(A.15)}$$

APPENDIX B

Transient Particle Suspension Transport

B.1 Solution Derivation

Consider the complete one-dimensional transient particle advective-dispersion equation which includes a removal term to account for filtration effects:

$$\frac{\partial C}{\partial t} = D_{Lp}\frac{\partial^2 C}{\partial x^2} - V_p\frac{\partial C}{\partial x} - \lambda V_p C \qquad \text{(B.1)}$$

where: C = *concentration* ($M\ L^{-3}$);
t = *time* (T);
x = *longitudinal distance* (L);
D_{Lp} = *longitudinal dispersion coefficient for particles* ($L^2\ T^{-1}$);
V_p = *average particle interstitial velocity* ($L\ T^{-1}$); *and*
λ = *filter coefficient* (L^{-1}).

with the following conditions for an infinite medium:

boundary condition:

$$1)\ \lim_{x \to +\infty} C(x,t) = 0. \qquad \text{(B.1.1)}$$

initial conditions:

$$\begin{aligned} &1)\ C(x,0) = C_0 exp[\alpha x] && x < 0;\ \textit{and} \\ &2)\ C(x,0) = 0 && x > 0. \end{aligned} \qquad \text{(B.1.2)}$$

In this entire analysis, α is selected to be the solution to the steady-state equation which is the same α as found in Appendix A, and this is:

$$\alpha = \frac{Pe_{Dp}}{2d_g}\left(1 - \sqrt{1 + \frac{4\lambda d_g}{Pe_{Dp}}}\right)$$

For convenience, the x-variable is allowed to range from negative to positive infinity ($-\infty < x < +\infty$), although the equations are only applied for $x > 0$. This avoids difficulty at $x = 0$, because small dispersion is allowed. In dimensionless form, the transport equation becomes:

$$\frac{\partial C*}{\partial t*} = \frac{1}{Pe_{Dp}}\frac{\partial^2 C*}{\partial x*^2} - \frac{\partial C*}{\partial x*} - \lambda* C* \qquad \textbf{(B.2)}$$

where: $C* = \frac{C}{C_0}$;

$C_0 = C(x=0)$;

d_g = *media grain diameter* (*L*);

$x* = \frac{x}{d_g}$;

$t* = \frac{V_p t}{d_g}$;

$Pe_{Dp} = \frac{V_p d_g}{D_{Lp}}$; *and*

$\lambda* = \lambda d_g$.

with the same infinite medium conditions:

boundary condition:

$$1) \lim_{x* \to +\infty} C*(x*,t*) = 0. \qquad \textbf{(B.2.1)}$$

initial conditions:

$$\begin{aligned} &1)\ C*(x*,0) = exp[\alpha*x*] && x* < 0;\ and \\ &2)\ C*(x*,0) = 0 && x* > 0. \end{aligned} \qquad \textbf{(B.2.2)}$$

In order to derive a solution, try the following as a solution:

$$C*(x*,t*) = exp[\alpha*x*]\ f(x*,t*) \qquad \textbf{(B.3)}$$

In this equation, f(x*,t*) will be shown to be the solution for transient conservative tracer transport, and exp[α*x*] is the solution to steady-state transport which includes removal due to filtration.

This solution can be checked by substituting into the Eq. (B.2). First determine partial derivatives:

$$\begin{aligned} \frac{\partial C*}{\partial t*} &= exp[\alpha*x*]\frac{\partial f}{\partial t*}; \\ \frac{\partial C*}{\partial x*} &= exp[\alpha*x*]\alpha*f + exp[\alpha*x*]\frac{\partial f}{\partial x*};\ and \\ \frac{\partial^2 C*}{\partial x*^2} &= \alpha*^2 exp[\alpha*x*]f + 2\alpha*exp[\alpha*x*]\frac{\partial f}{\partial x*} + exp[\alpha*x*]\frac{\partial^2 f}{\partial x*^2}. \end{aligned}$$

Substitute these derivatives into the chosen solution, Eq. (B.3):

$$\begin{aligned} exp[\alpha*x*]\frac{\partial f}{\partial t*} = \frac{1}{Pe_{Dp}}&\left(\alpha*^2 exp[\alpha*x*]f + 2\alpha*exp[\alpha*x*]\frac{\partial f}{\partial x*} + exp[\alpha*x*]\frac{\partial^2 f}{\partial x*^2}\right) \\ &- \left(\alpha*exp[\alpha*x*]f + exp[\alpha*x*]\frac{\partial f}{\partial x*}\right) \\ &- \lambda*(exp[\alpha*x*]f) \end{aligned}$$

Simplifying:

$$\frac{\partial f}{\partial t*} = \frac{1}{Pe_{Dp}}\left(\alpha*^2 f + 2\alpha*\frac{\partial f}{\partial x*} + \frac{\partial^2 f}{\partial x*^2}\right) - \left(\alpha* f + \frac{\partial f}{\partial x*}\right) - \lambda*(f)$$

$$= \frac{1}{Pe_{Dp}}\frac{\partial^2 f}{\partial x*^2} - (1 - 2\alpha*)\frac{\partial f}{\partial x*} + \left(\frac{1}{Pe_{Dp}}\alpha*^2 - \alpha* - \lambda*\right) f$$

where: $\frac{1}{Pe_{Dp}}\alpha*^2 - \alpha* - \lambda* = 0$ ($\alpha*$ *was chosen to match steady-state eq.*).

This simplification shows that the complete solution, Eq. (B.3), to the total transient transport problem, Eq. (B.2), is a superpositioning of steady-state and transient equations. The transient portion of the total solution found from the simplification is:

$$\frac{\partial f}{\partial t*} = \frac{1}{Pe_{Dp}}\frac{\partial^2 f}{\partial x*^2} - \left(1 - \frac{2\alpha*}{Pe_{Dp}}\right)\frac{\partial f}{\partial x*} \qquad \textbf{(B.4)}$$

This transient equation in terms of f(x*,t*) and the boundary and initial conditions is similar in form to the equation describing conservative tracer transport in an infinite medium with a step input initial condition. In order to derive a solution to this equation, the following change of variables is used:

$$V_p'* = 1 - \frac{2\alpha*}{Pe_{Dp}};$$

$$\xi = x* - V_p'*t*; \text{ and}$$

$$\tau = t*.$$

Substituting this change of variables, Eq. (B.4) becomes:

$$\frac{\partial f}{\partial \tau} = \frac{1}{Pe_{Dp}}\frac{\partial^2 f}{\partial \xi^2} \qquad \textbf{(B.5)}$$

with the same infinite medium conditions:

boundary conditions:

$$\begin{aligned} &1) \lim_{x^* \to -\infty} f(\xi,\tau) = 1; \text{ and} \\ &2) \lim_{x^* \to +\infty} f(\xi,\tau) = 0. \end{aligned} \tag{B.5.1}$$

initial conditions:

$$\begin{aligned} &1)\ f(\xi,0) = 1 \qquad \xi < 0; \text{ and} \\ &2)\ f(\xi,0) = 0 \qquad \xi > 0. \end{aligned} \tag{B.5.2}$$

The derivation of the solution to this transient equation with these infinite medium conditions is similar to the solution to the classical conservative tracer transport equation. The solution to the transient equation, Eq. (B.5), in terms of $f(\xi,\tau)$ is:

$$f(\xi,\tau) = \frac{1}{2} erfc\left[\sqrt{Pe_{Dp}}\left(\frac{\xi}{2\sqrt{\tau}}\right)\right] \tag{B.6}$$

Now, the variables (ξ,τ) are transformed back to the original variables (x^*,t^*,α^*) in order to find $f(x^*,t^*)$:

$$f(x*,t*) = \frac{1}{2} erfc\left[\sqrt{Pe_{Dp}}\left(\frac{x* - V_p' * t*}{2\sqrt{t*}}\right)\right] = \frac{1}{2} erfc\left[\sqrt{Pe_{Dp}}\left(\frac{x* - \left\{1 - \frac{2\alpha*}{Pe_{Dp}}\right\} t*}{2\sqrt{t*}}\right)\right]$$

The full solution to the particle suspension transport equation, Eq. (B.2), becomes:

$$C*(x*,t*) = \frac{1}{2}\, exp[\alpha*x*]\; erfc\left[\sqrt{Pe_{Dp}}\left(\frac{x* - \left\{1 - \frac{2\alpha*}{Pe_{Dp}}\right\}t*}{2\sqrt{t*}}\right)\right] \qquad \textbf{(B.7)}$$

Which may be rewritten:

$$C*(x*,t*) = \frac{1}{2}\, exp[\alpha*x*]\; erfc\left[\sqrt{Pe_{Dp}}\left(\frac{x* - \sqrt{1 + \frac{4\lambda*}{Pe_{Dp}}}\, t*}{2\sqrt{t*}}\right)\right] \qquad \textbf{(B.8)}$$

B.2 Solution Approximation

Consider approximations for α^* in both the exponential term and in the erfc term in Eq. (B.7) where α^* is the following:

$$\alpha* = \frac{1}{2} Pe_{Dp}\left(1 - \sqrt{1 + \frac{4\lambda*}{Pe_{Dp}}}\right) \qquad \textbf{(B.9)}$$

The approximation for α^* in the exponential term has already been completed in Appendix A and is:

$$\alpha* \approx -\lambda* \qquad \textbf{(A.7)}$$

This approximation is substituted into the argument of the exponential term of Eq. (B.7).

The α^* term in the erfc term is approximated by considering approximations to the following:

$$1 - \frac{2\alpha*}{Pe_{Dp}} = \sqrt{1 + \frac{4\lambda*}{Pe_{Dp}}} \qquad \textbf{(B.10)}$$

Perform a Taylor series expansion of the radical portion of λ^* in this equation by considering a function g(x):

$$g(x) = \sqrt{1 + x}$$
$$\textit{where: } x = \frac{4\lambda^*}{Pe_{Dp}}.$$

The Taylor series approximation is:

$$\sqrt{1 + x} = 1 + \frac{1}{2}x - \frac{1}{8}x^2 + \frac{1}{16}x^3 - \frac{5}{128}x^4 \cdots$$

$$g_0(x) \approx g(x) = 1 + Err$$
$$\textit{where: } Err \le R_1(x) = \frac{1}{2}\left(\frac{4\lambda^*}{Pe_{Dp}}\right) = \frac{2\lambda^*}{Pe_{Dp}}.$$

Since this series is an alternating series, the truncation error must be less than the first truncated term (absolute values). Substituting the first term of the series into Eq. (B.10) for the radical portion of α^* yields:

$$1 - \frac{2\alpha^*}{Pe_{Dp}} = 1 + \frac{1}{2}\left(\frac{4\lambda^*}{Pe_{Dp}}\right) + \cdots = 1 + \frac{2\lambda^*}{Pe_{Dp}} + \cdots$$

$$\therefore 1 - \frac{2\alpha^*}{Pe_{Dp}} \approx 1 \qquad \textbf{(B.11)}$$

This approximation is substituted into the argument of the erfc term of Eq. (B7).

Using these approximations (Eqs. (B.10) and (A.7)) in Eq. (B.7) yields an approximate solution to the complete transient equation, Eq. (B.2):

$$C*(x*,t*) = \frac{1}{2}\, exp[-\lambda *x*]\; erfc\left[\sqrt{Pe_{Dp}}\left(\frac{x* - t*}{2\sqrt{t*}}\right)\right] \qquad \textbf{(B.12)}$$

Using Eq. (B.12), values for Pe_{Dp} can be directly computed from concentration, position, and time measurements.

B.3 Approximate Versus Exact Solution

The error when using the approximate solution can be determined from the relative error of the two solution, Eqs. (B.7) and (B.12):

$$\frac{C*_a - C*_e}{C*_e} = \Delta C* = \frac{exp[-\lambda *x*]erfc_a - exp[\alpha *x*]erfc_e}{exp[\alpha *x*]erfc_e} \qquad \textbf{(B.13)}$$

where: $erfc_a$ = *approximate solution erfc; and*
$erfc_e$ = *exact solution erfc.*

Eq. (B.13) can be simplified as follows:

$$\begin{aligned} \Delta C* = \frac{C*_a}{C*_e} - 1 &= \frac{exp[-\lambda *x*]erfc_a}{exp[\alpha *x*]erfc_e} - 1 \\ &= exp[-x*(\lambda * + \alpha *)]\frac{erfc_a}{erfc_e} - 1 \end{aligned} \qquad \textbf{(B.14)}$$

In this equation, the Taylor series expansion for the exponential factor has already been completed in Appendix A and the result is shown here:

$$exp[-x*(\lambda * + \alpha *)] \le 1 - \frac{\lambda *^2 x*}{Pe_{Dp}} \qquad \textbf{(B.15)}$$

For the erfc terms, the maximum error is expected to occur around the point where the arguments of the erfc terms are near zero. This is the point of maximum slope in the erfc; therefore, the maximum rate of change. Also, the

erfc is bounded in both the positive and negative directions, and the contribution of error from the erfc factor is expected to vanish with all the error coming from the steady-state approximation which was analyzed in Appendix A. At small values of η, the following approximation holds:

$$erfc[\eta] \approx 1 - \frac{2}{\sqrt{\pi}}\eta$$

Using this approximation, the following can be used for the erfc terms for small arguments:

$$\frac{erfc_a}{erfc_e} = \Delta erfc \approx \frac{1 - \frac{2}{\sqrt{\pi}}\sqrt{Pe_{Dp}}\left(\frac{x* - t*}{2\sqrt{t*}}\right)}{1 - \frac{2}{\sqrt{\pi}}\sqrt{Pe_{Dp}}\left(\frac{x* - t*\{1 - 2\alpha*/Pe_{Dp}\}}{2\sqrt{t*}}\right)} \approx \frac{1 - \sqrt{\frac{Pe_{Dp}}{\pi t*}}(x* - t*)}{1 - \sqrt{\frac{Pe_{Dp}}{\pi t*}}(x* - t*\{1 - 2\alpha*/Pe_{Dp}\})} \quad \textbf{(B.16)}$$

An approximate value for α^* which was found in Appendix A can be used in this equation, and this value is:

$$\alpha* \leq -\lambda* + \frac{\lambda*^2}{Pe_{Dp}} \quad \textbf{(A.12)}$$

Substituting this into Eq. (B.16) yields:

$$\Delta erfc \approx \frac{1 - \sqrt{\frac{Pe_{Dp}}{\pi t*}}(x* - t*)}{1 - \sqrt{\frac{Pe_{Dp}}{\pi t*}}\left(x* - t* + 2t*\left\{\left(\frac{\lambda*}{Pe_{Dp}}\right)^2 - \frac{\lambda*}{Pe_{Dp}}\right\}\right)} \qquad \textbf{(B.17)}$$

Using Eq. (B.17) with Eqs. (B.14) and (B.15) yields:

$$\frac{C*_a}{C*_e} = \frac{exp[-\lambda* x*]erfc_a}{exp[\alpha* x*]erfc_e} \leq \left(1 - \frac{\lambda*^2 x*}{Pe_{Dp}}\right)\Delta erfc \qquad \textbf{(B.18)}$$

Substituting this equation into Eq. (B.14) gives the expression for the total error:

$$\Delta C* \leq \left(1 - \frac{\lambda*^2 x*}{Pe_{Dp}}\right)\Delta erfc - 1 \qquad \textbf{(B.19)}$$

Substituting Eq. (B.17) into Eq. (B.19) yields:

$$\Delta C* \leq \frac{\left(1-\frac{\lambda*^2 x*}{Pe_{Dp}}\right)\left(1-\sqrt{\frac{Pe_{Dp}}{\pi t*}}(x*-t*)\right) - \left\{1-\sqrt{\frac{Pe_{Dp}}{\pi t*}}\left(x*-t*+2t*\left\{\left(\frac{\lambda*}{Pe_{Dp}}\right)^2-\frac{\lambda*}{Pe_{Dp}}\right\}\right)\right\}}{1-\sqrt{\frac{Pe_{Dp}}{\pi t*}}\left(x*-t*+2t*\left\{\left(\frac{\lambda*}{Pe_{Dp}}\right)^2-\frac{\lambda*}{Pe_{Dp}}\right\}\right)}$$

This can be simplified by cancelling like terms:

$$\Delta C* \leq \frac{-\frac{\lambda*^2 x*}{Pe_{Dp}} + \frac{\lambda*^2 x*}{Pe_{Dp}}\sqrt{\frac{Pe_{Dp}}{\pi t*}}(x* - t*) + 2t*\sqrt{\frac{Pe_{Dp}}{\pi t*}}\left\{\left(\frac{\lambda*}{Pe_{Dp}}\right)^2 - \frac{\lambda*}{Pe_{Dp}}\right\}}{1 - \sqrt{\frac{Pe_{Dp}}{\pi t*}}\left(x* - t* + 2t*\left\{\left(\frac{\lambda*}{Pe_{Dp}}\right)^2 - \frac{\lambda*}{Pe_{Dp}}\right\}\right)}$$

Rearranging this equation yields:

$$\Delta C* \le \frac{-\frac{\lambda*^2 x*}{Pe_{Dp}}\left(1-\sqrt{\frac{Pe_{Dp}}{\pi t*}}(x*-t*)\right)-2t*\sqrt{\frac{Pe_{Dp}}{\pi t*}\left(\frac{\lambda*}{Pe_{Dp}}-\left\{\frac{\lambda*}{Pe_{Dp}}\right\}^2\right)}}{1-\sqrt{\frac{Pe_{Dp}}{\pi t*}}(x*-t*)+2t*\sqrt{\frac{Pe_{Dp}}{\pi t*}\left(\frac{\lambda*}{Pe_{Dp}}-\left\{\frac{\lambda*}{Pe_{Dp}}\right\}^2\right)}} \qquad \textbf{(B.20)}$$

Taking the absolute values of Eqs. (B.13) and (B.20) yields:

$$\left|\frac{C*_a - C*_e}{C*_e}\right| = |\Delta C*| = |error| \qquad \textbf{(B.13a)}$$

$$|\Delta C*| \le \frac{\frac{\lambda*^2 x*}{Pe_{Dp}}\left(1-\sqrt{\frac{Pe_{Dp}}{\pi t*}}(x*-t*)\right)+2t*\sqrt{\frac{Pe_{Dp}}{\pi t*}\left(\frac{\lambda*}{Pe_{Dp}}-\left\{\frac{\lambda*}{Pe_{Dp}}\right\}^2\right)}}{1-\sqrt{\frac{Pe_{Dp}}{\pi t*}}(x*-t*)+2t*\sqrt{\frac{Pe_{Dp}}{\pi t*}\left(\frac{\lambda*}{Pe_{Dp}}-\left\{\frac{\lambda*}{Pe_{Dp}}\right\}^2\right)}} \qquad \textbf{(B.20a)}$$

As previously mentioned, the largest error will occur when x* = t* which coincides with the smallest values of the argument of the erfc. In order to determine the largest error, let x* = t* in Eq. (B.20a):

$$\therefore\ |error| = |\Delta C*| \le \frac{\frac{\lambda*^2 x*}{Pe_{Dp}} + 2x*\sqrt{\frac{Pe_{Dp}}{\pi x*}\left(\frac{\lambda*}{Pe_{Dp}}-\left\{\frac{\lambda*}{Pe_{Dp}}\right\}^2\right)}}{1+2x*\sqrt{\frac{Pe_{Dp}}{\pi x*}\left(\frac{\lambda*}{Pe_{Dp}}-\left\{\frac{\lambda*}{Pe_{Dp}}\right\}^2\right)}} \qquad \textbf{(B.21)}$$

In order to find error contours on a graph of (x*,λ*) as shown in Chapter 3, it is necessary to invert this equation in terms of λ* as follows (assume an equal sign in Eq. (B.21):

$$|error| + |error|2x*\sqrt{\frac{Pe_{Dp}}{\pi x*}}\left(\frac{\lambda*}{Pe_{Dp}} - \left\{\frac{\lambda*}{Pe_{Dp}}\right\}^2\right)$$
$$= \frac{\lambda*^2 x*}{Pe_{Dp}} + 2x*\sqrt{\frac{Pe_{Dp}}{\pi x*}}\left(\frac{\lambda*}{Pe_{Dp}} - \left\{\frac{\lambda*}{Pe_{Dp}}\right\}^2\right)$$

$$0 = \left(\frac{x*}{Pe_{Dp}} - \frac{2x*}{Pe_{Dp}^2}\sqrt{\frac{Pe_{Dp}}{\pi x*}}\{1-|error|\}\right)\lambda*^2 + \left(\frac{2x*}{Pe_{Dp}}\sqrt{\frac{Pe_{Dp}}{\pi x*}}\{1-|error|\}\right)\lambda* - |error| \quad \textbf{(B.22)}$$

Eq. (B.22) is a quadratic in terms of λ^* as follows:

$$0 = A\lambda*^2 + B\lambda* + C$$

$$\text{where: } A = \frac{x*}{Pe_{Dp}} - \frac{2x*}{Pe_{Dp}^2}\sqrt{\frac{Pe_{Dp}}{\pi x*}}(1 - |error|)$$
$$B = \frac{2x*}{Pe_{Dp}}\sqrt{\frac{Pe_{Dp}}{\pi x*}}(1 - |error|)$$
$$C = |error|$$

In this form with these coefficients, a solution for λ^* can be found.

APPENDIX C. EXPERIMENTAL RESULTS

In this appendix, data for the individual breakthrough experiments are shown in separate figures. These experiments are the salt tracer breakthroughs, the simple particle breakthroughs, and the coupled breakthroughs. For the simple breakthroughs, each figure is composed of three parts. Part (a) shows the measured experimental data for the entire experiment. Part (b) shows the linearized breakthrough with a least-squares fit. Part (c) shows the dimensionless breakthrough with a best-fit line. The development behind each of these parts of the figures was discussed in Chapter 5.

For the coupled breakthroughs, each experimental figure is composed of four parts. Part (a) shows the immediate breakthrough of both the particle and salt with both concentrations scaled similarly and the salt data inverted as necessary to match the particle breakthrough. Part (b) shows the dimensionless salt breakthrough with a best-fit line. Part (c) shows the measured experimental data for the entire experiment. Part (d) shows the particle breakthrough data versus the numerical model. As in the case of the simple breakthroughs, the development behind each of these parts of the figures was discussed in Chapter 5.

C.1 Salt Experiments

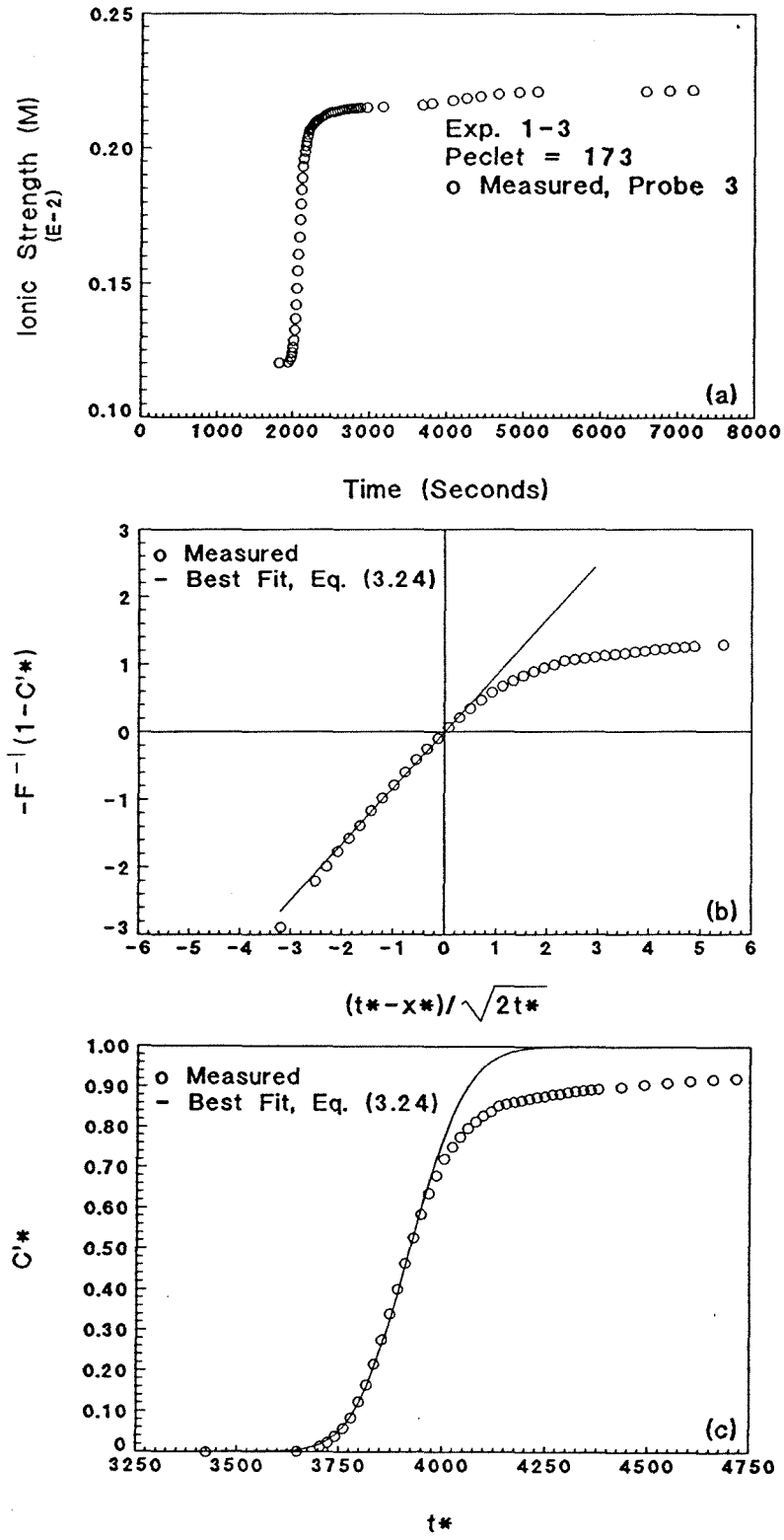

Fig. C.1: Exp. 1-3 forward breakthrough, conductivity probe 3, Pe = 174: (a) complete experimental data; (b) linearization with least-squares fit; and (c) breakthrough only with best-fit, Eq. (3.24).

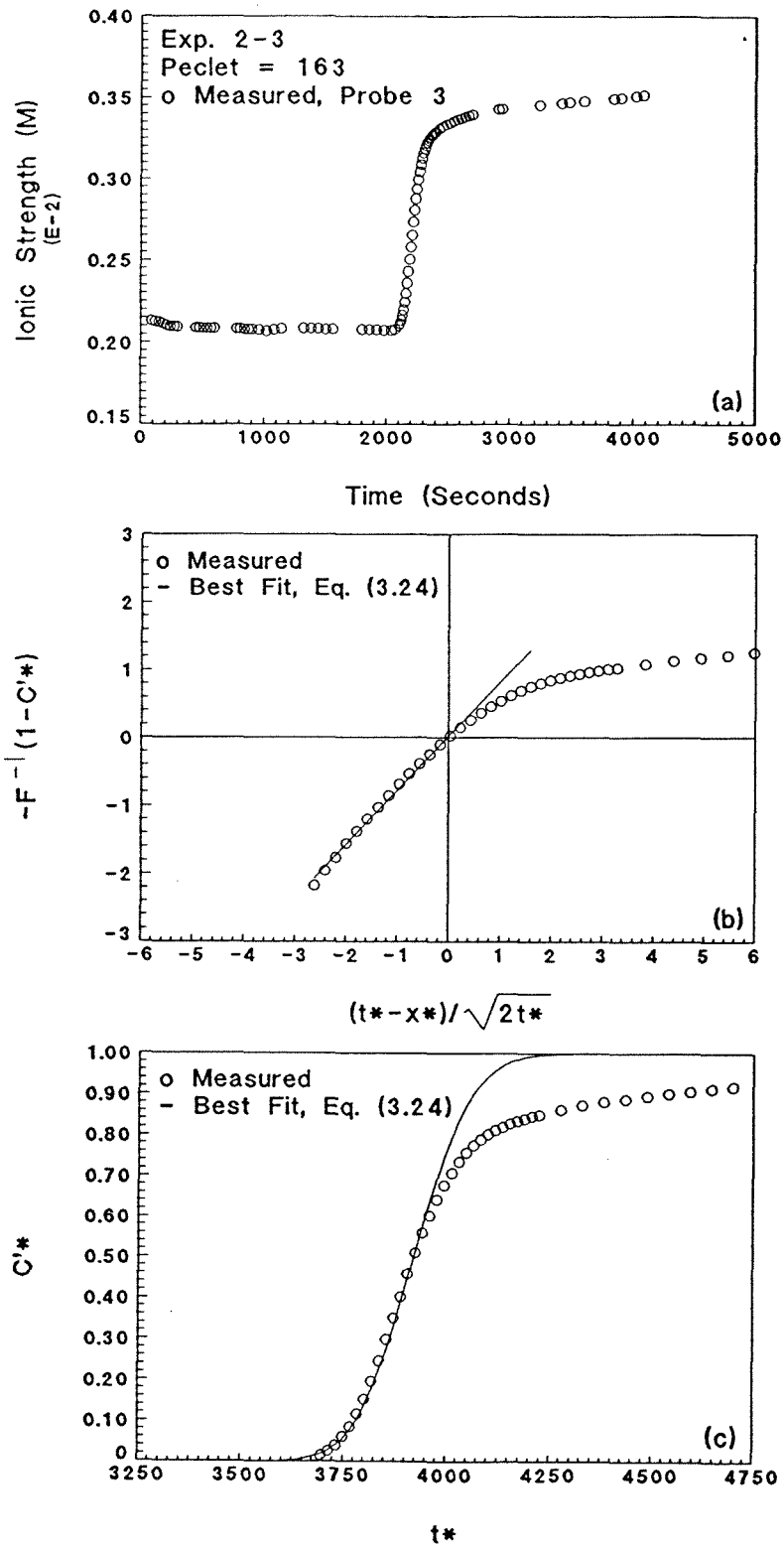

Fig. C.2: Exp. 2-3 forward breakthrough, conductivity probe 3, Pe = 163: (a) complete experimental data; (b) linearization with least-squares fit; and (c) breakthrough only with best-fit, Eq. (3.24).

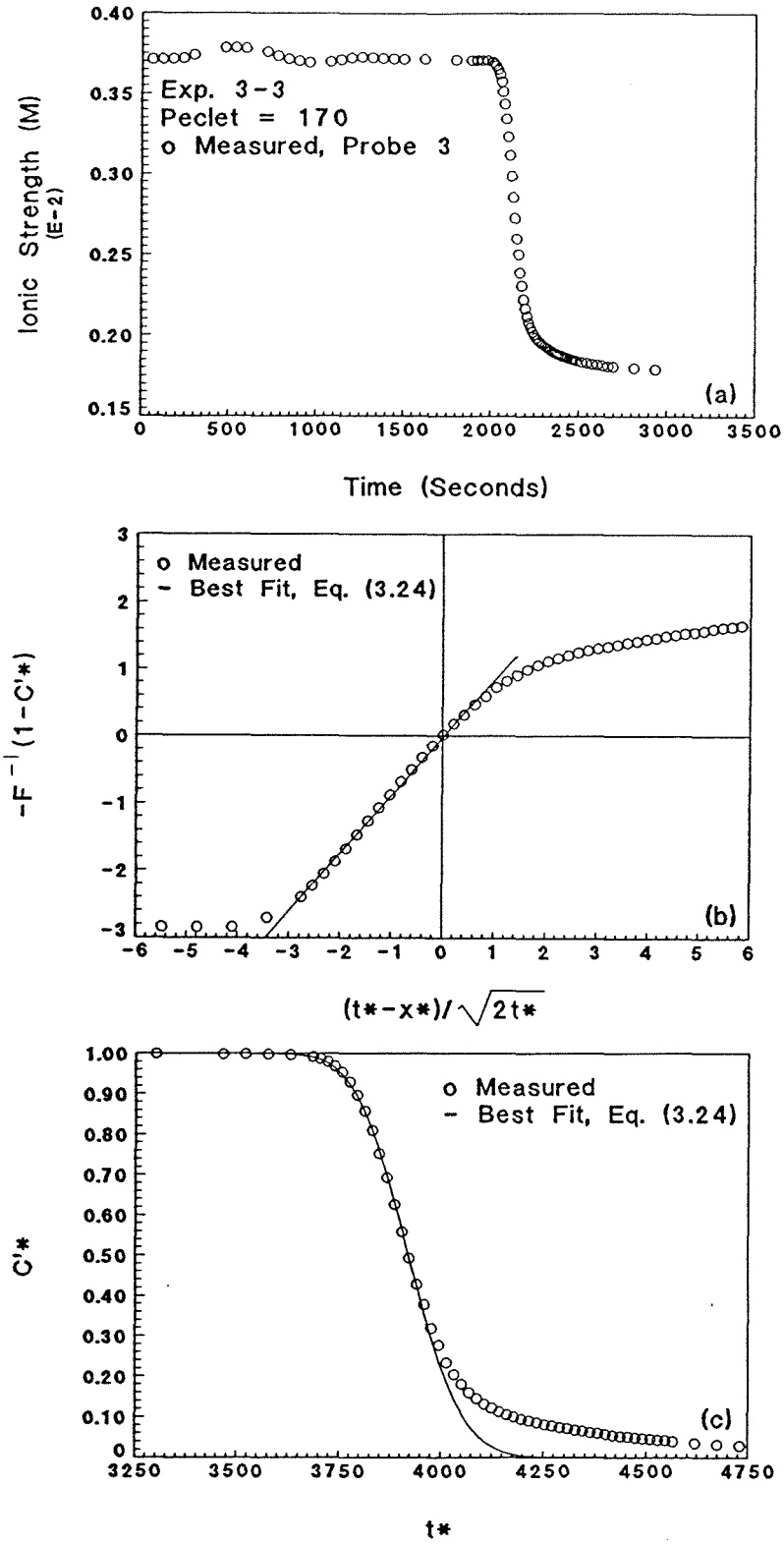

Fig. C.3: Exp 3-3 reverse breakthrough, conductivity probe 3, Pe = 170: (a) complete experimental data; (b) linearization with least-squares fit; and (c) breakthrough only with best-fit, Eq. (3.24).

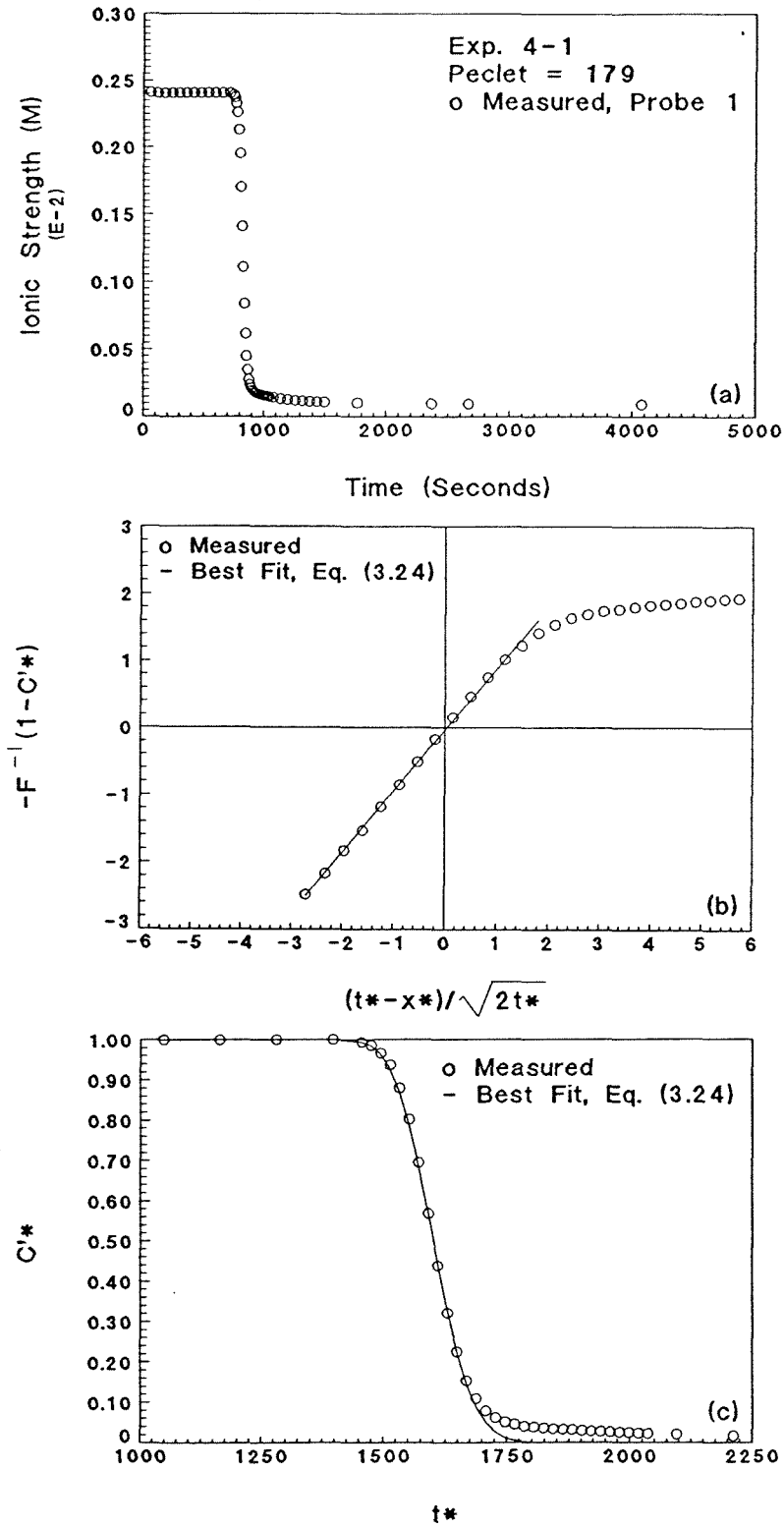

Fig. C.4: Exp. 4-1 reverse breakthrough, conductivity probe 1, Pe = 178: (a) complete experimental data; (b) linearization with least-squares fit; and (c) breakthrough only with best-fit, Eq. (3.24).

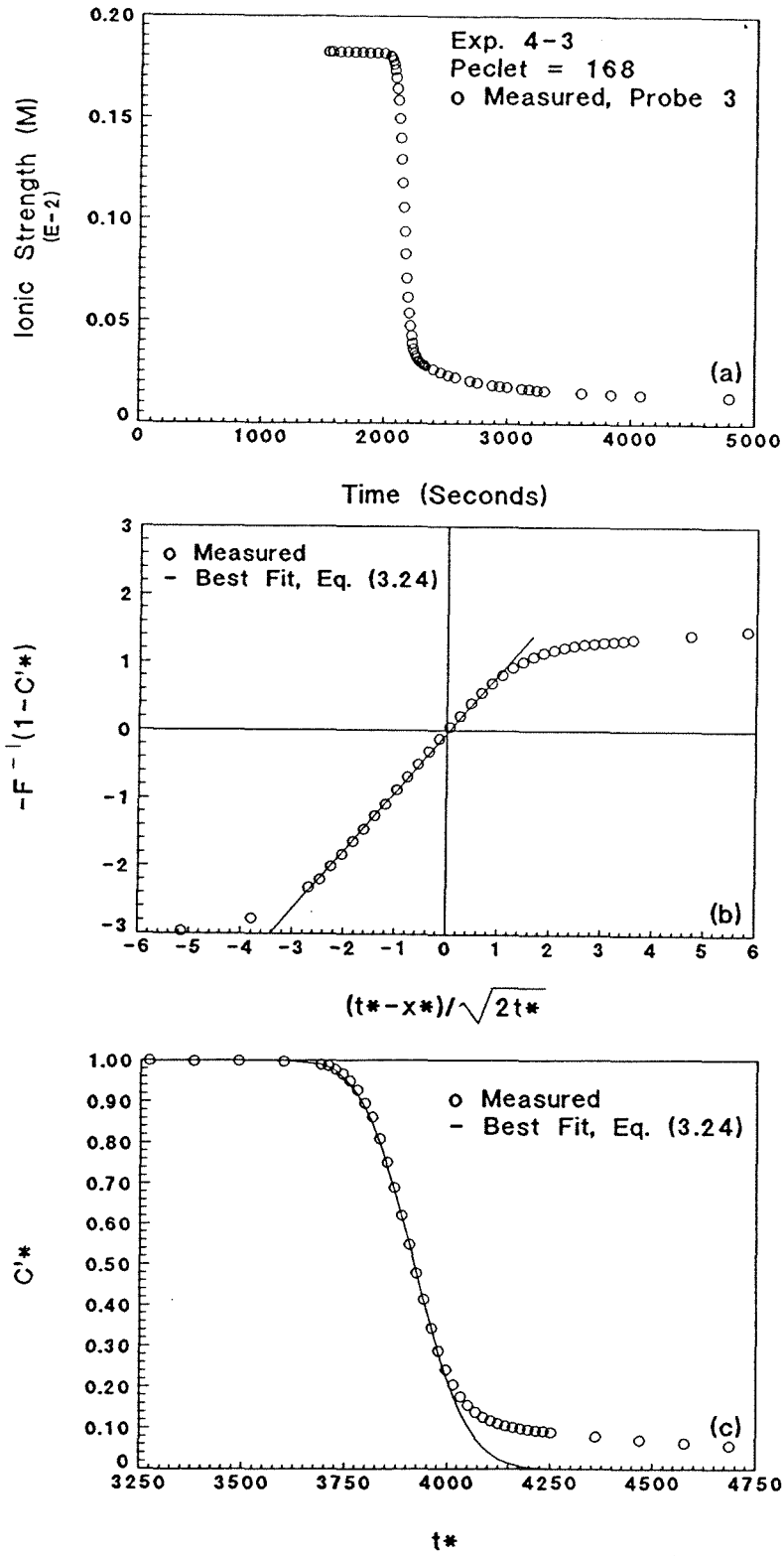

Fig. C.5: Exp. 4-3 reverse breakthrough, conductivity probe 3, Pe = 167: (a) complete experimental data; (b) linearization with least-squares fit; and (c) breakthrough only with best-fit, Eq. (3.24).

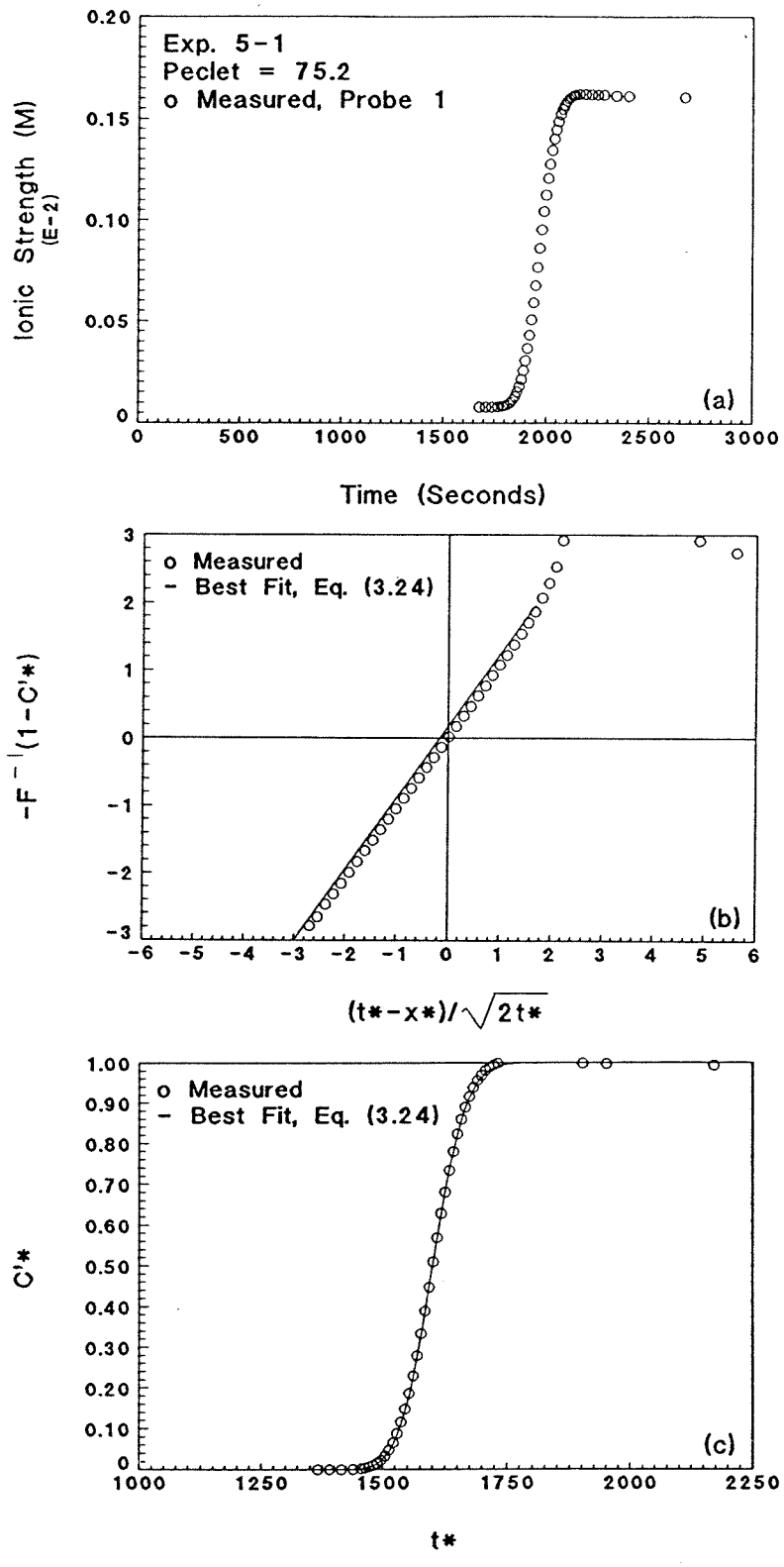

Fig. C.6: Exp. 5-1 forward breakthrough, conductivity probe 1, Pe = 75.5: (a) complete experimental data; (b) linearization with least-squares fit; and (c) breakthrough only with best-fit, Eq. (3.24).

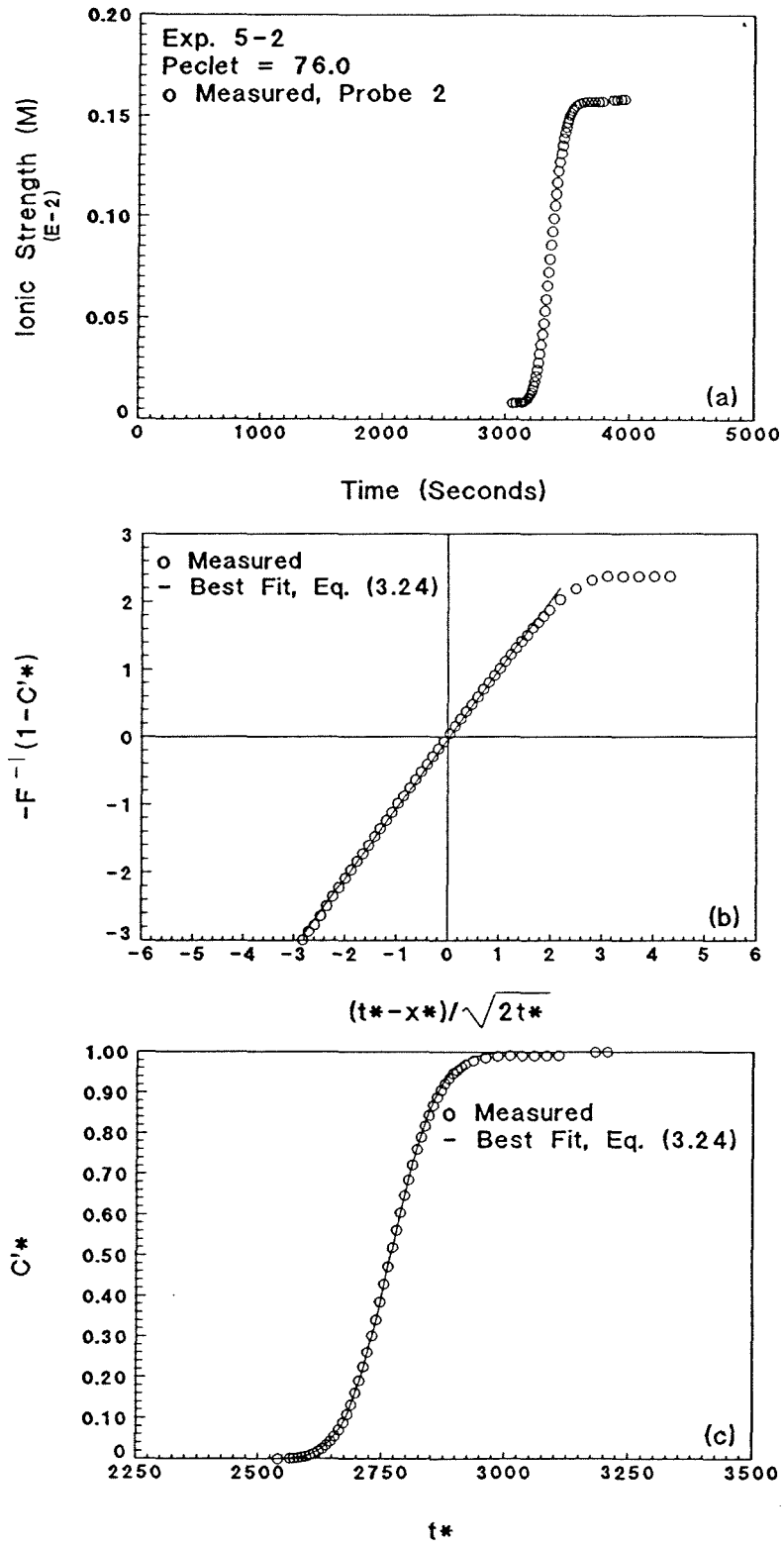

Fig. C.7: Exp. 5-2 forward breakthrough, conductivity probe 2, Pe = 76.3: (a) complete experimental data; (b) linearization with least-squares fit; and (c) breakthrough only with best-fit, Eq. (3.24).

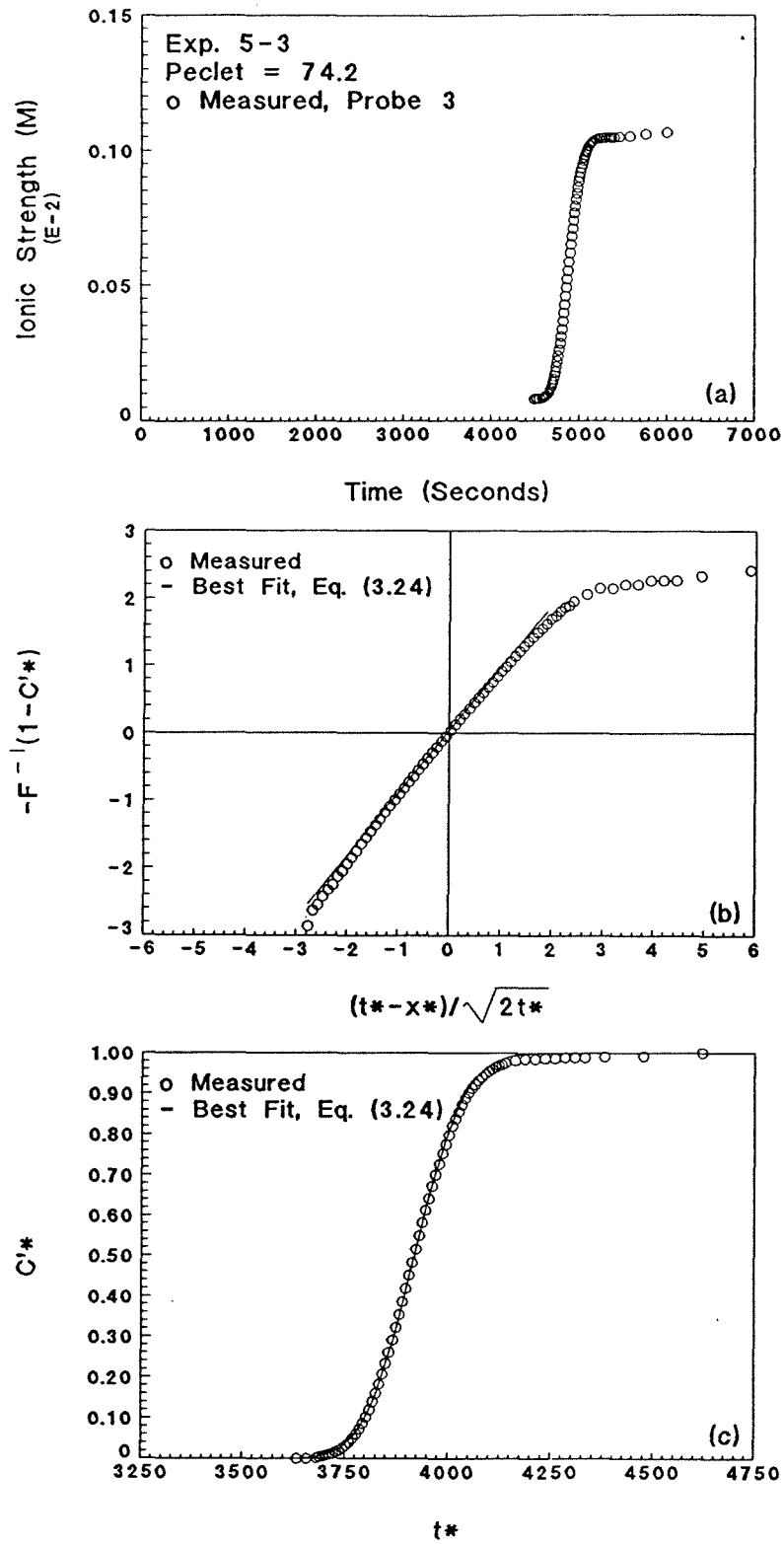

Fig. C.8: Exp. 5-3 forward breakthrough, conductivity probe 3, Pe = 74.6: (a) complete experimental data; (b) linearization with least-squares fit; and (c) breakthrough only with best-fit, Eq. (3.24).

C.2 1.0 micron Particle Experiments

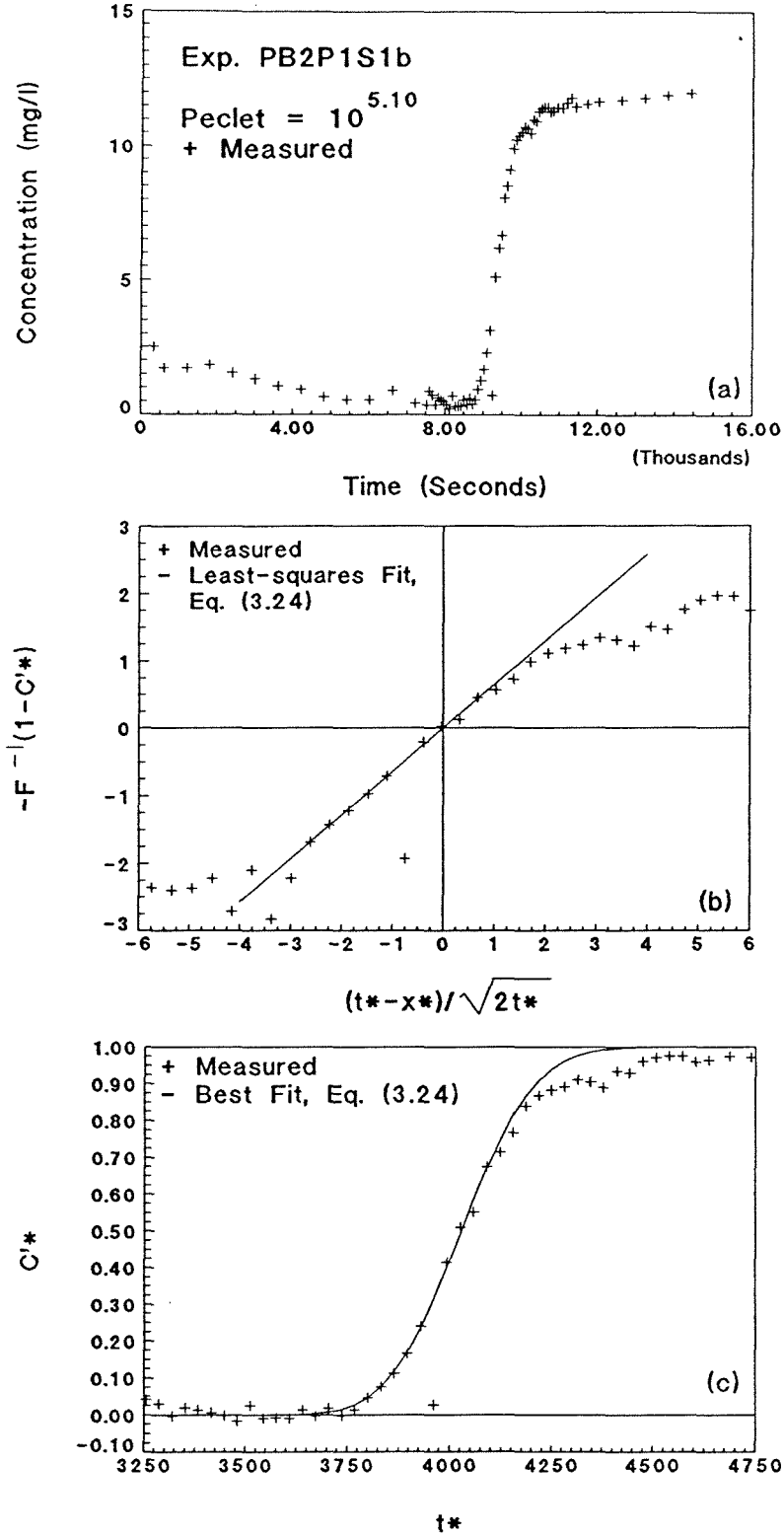

Fig. C.9: Exp. PB2P1S1b forward breakthrough, sample port 5, $Pe_p = 10^{5.10}$: (a) complete experimental data; (b) linearization with least-squares fit; and (c) breakthrough only with best-fit, Eq. (3.24).

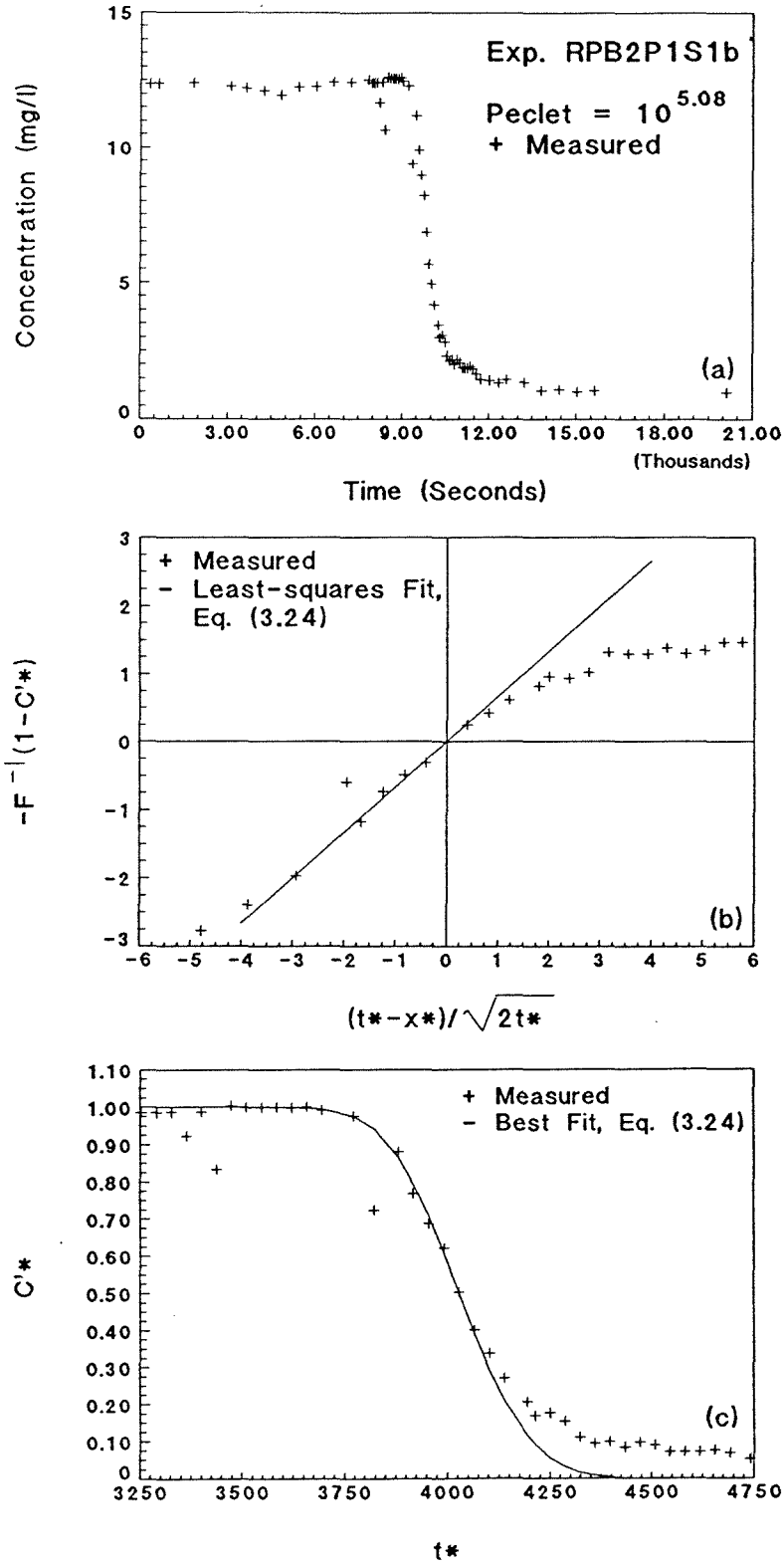

Fig. C.10: Exp. RPB2P1S1b reverse breakthrough, sample port 5, $Pe_p = 10^{5.08}$: (a) complete experimental data; (b) linearization with least-squares fit; and (c) breakthrough only with best-fit, Eq. (3.24).

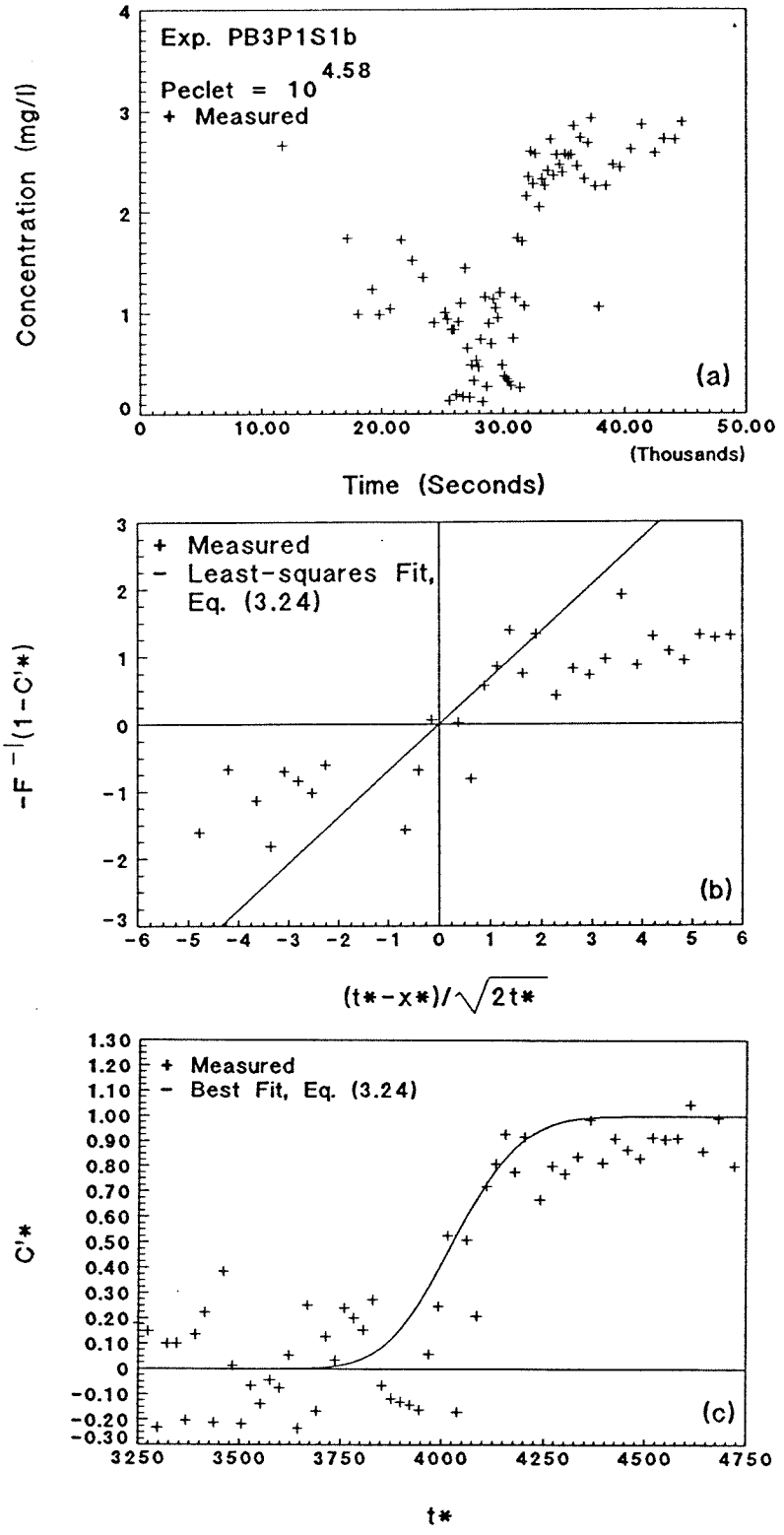

Fig. C.11: Exp. PB3P1S1b forward breakthrough, sample port 5, $Pe_p = 10^{4.58}$: (a) complete experimental data; (b) linearization with least-squares fit; and (c) breakthrough only with best-fit, Eq. (3.24).

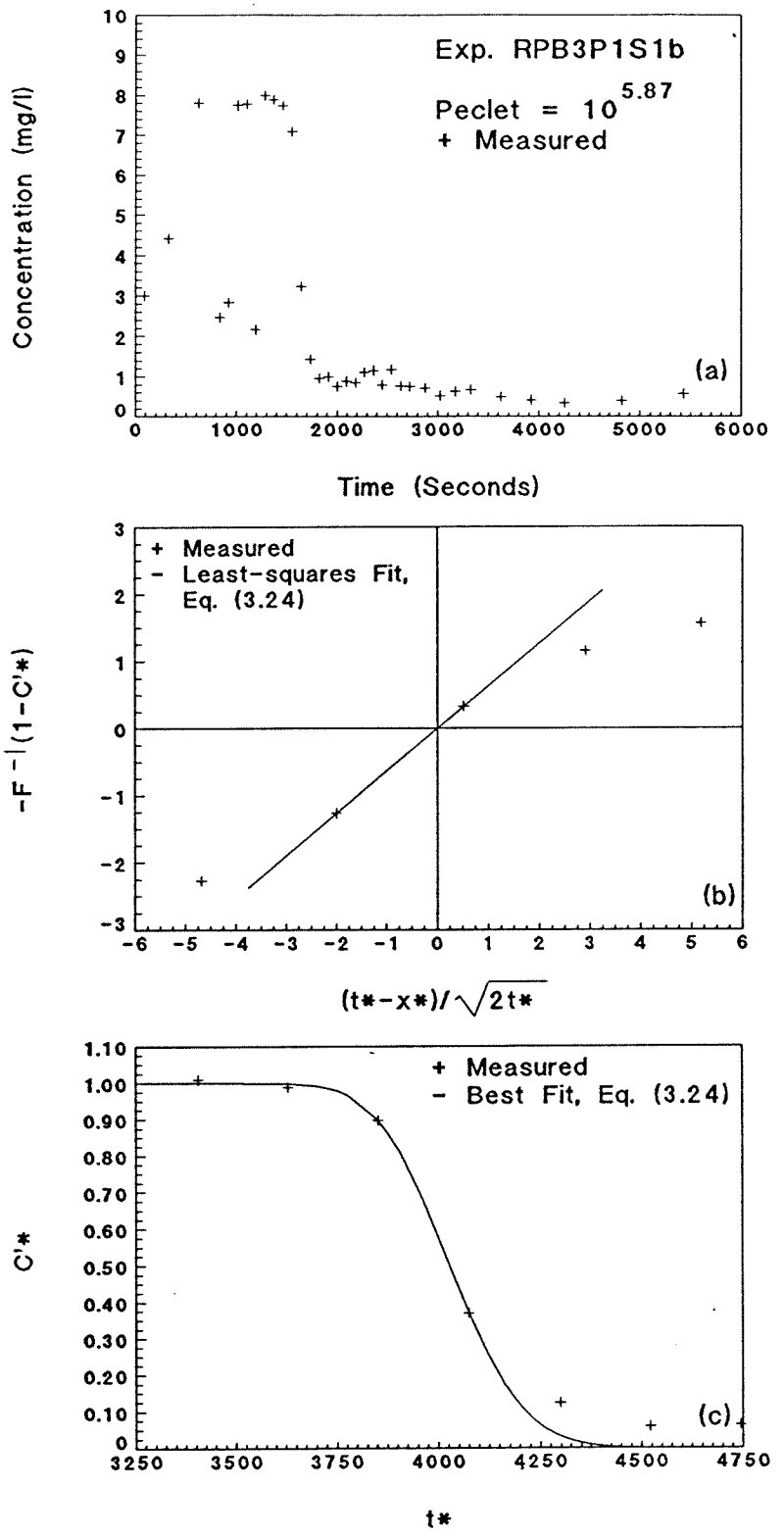

Fig. C.12: Exp. RPB3P1S1b reverse breakthrough, sample port 5, $Pe_p = 10^{5.87}$: (a) complete experimental data; (b) linearization with least-squares fit; and (c) breakthrough only with best-fit, Eq. (3.24).

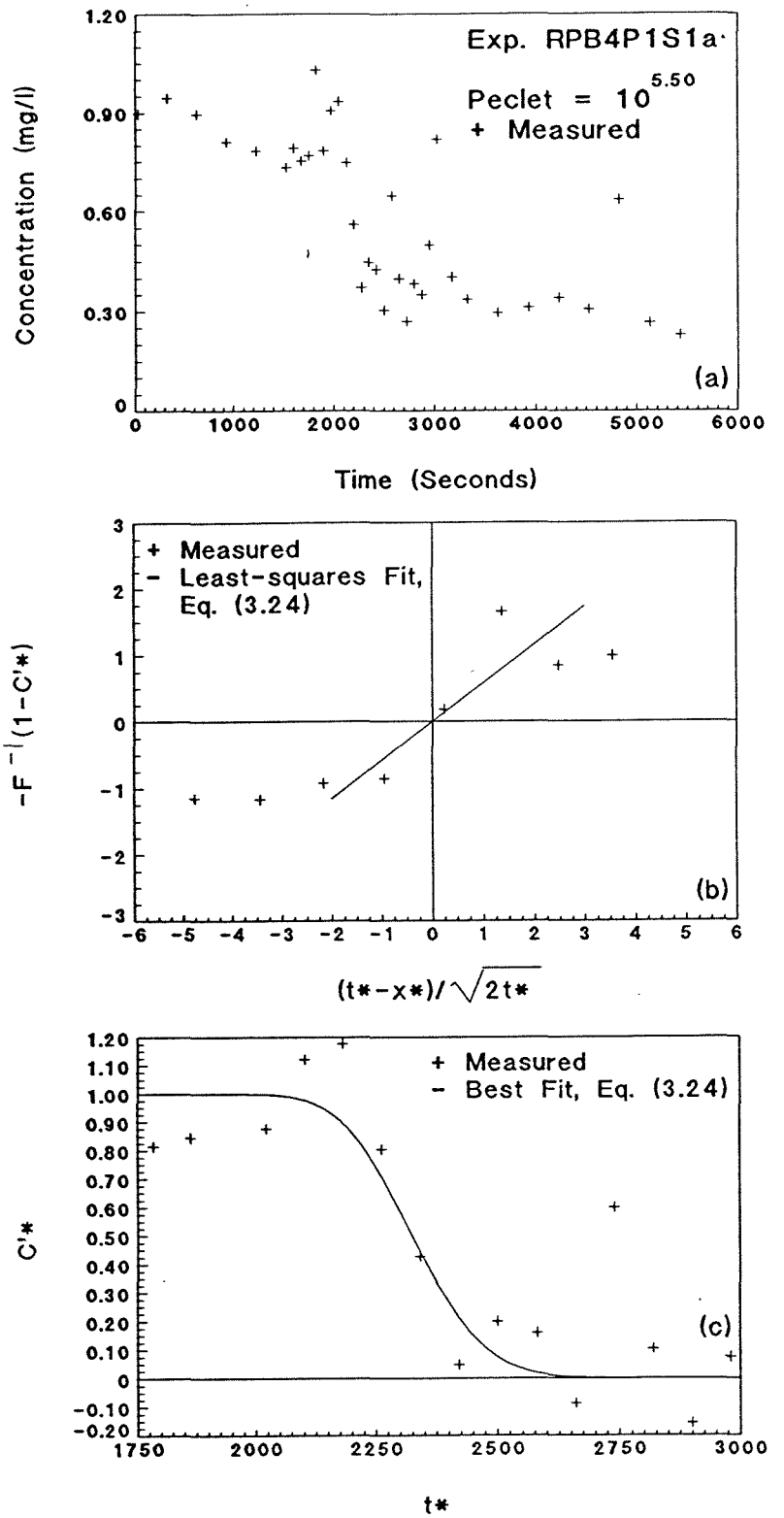

Fig. C.13: Exp. RPB4P1S1a reverse breakthrough, sample port 3, $Pe_p = 10^{5.50}$: (a) complete experimental data; (b) linearization with least-squares fit; and (c) breakthrough only with best-fit, Eq. (3.24).

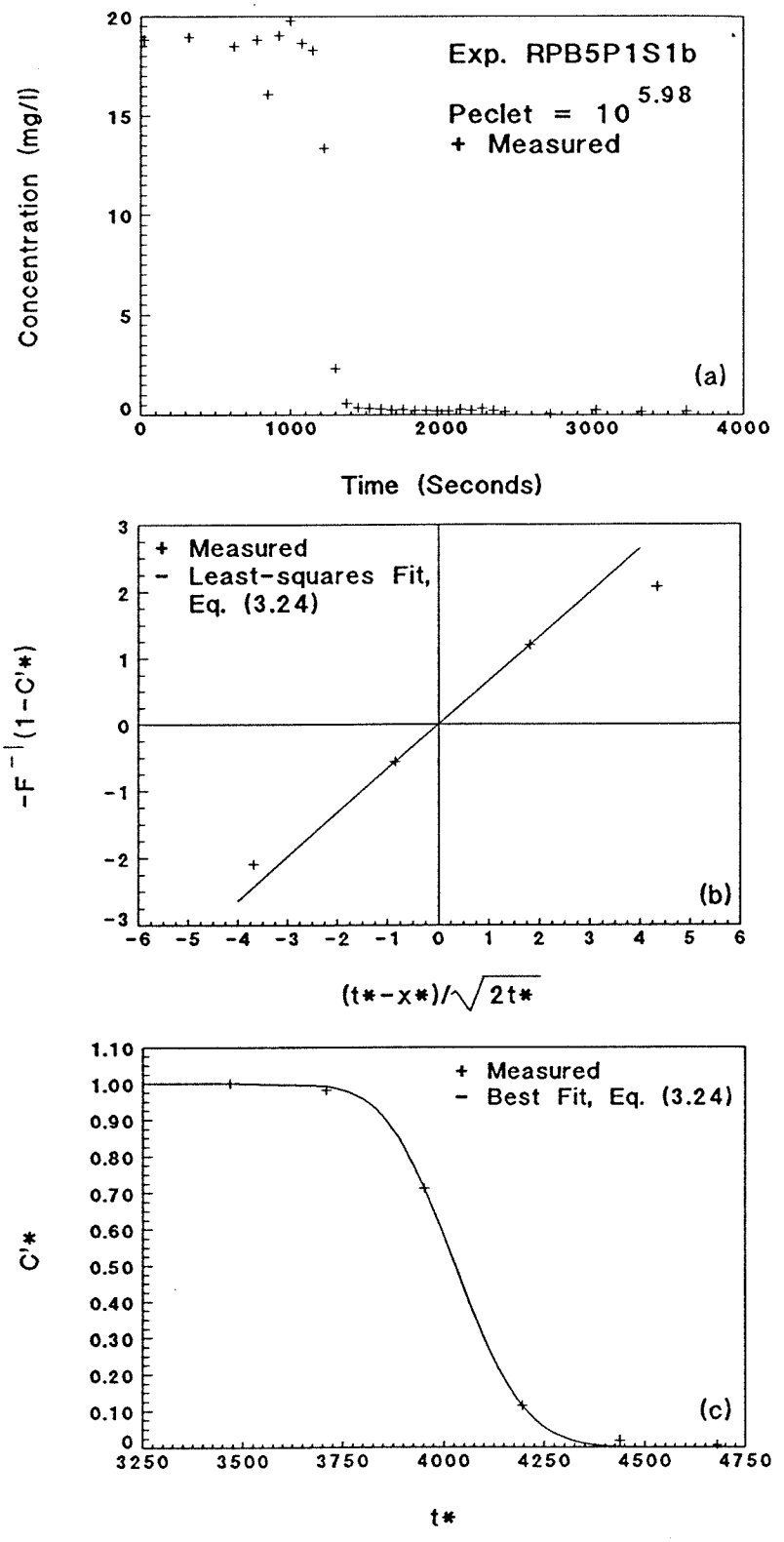

Fig. C.14: Exp. RPB5P1S1b reverse breakthrough, sample port 5, $Pe_p = 10^{5.98}$: (a) complete experimental data; (b) linearization with least-squares fit; and (c) breakthrough only with best-fit, Eq. (3.24).

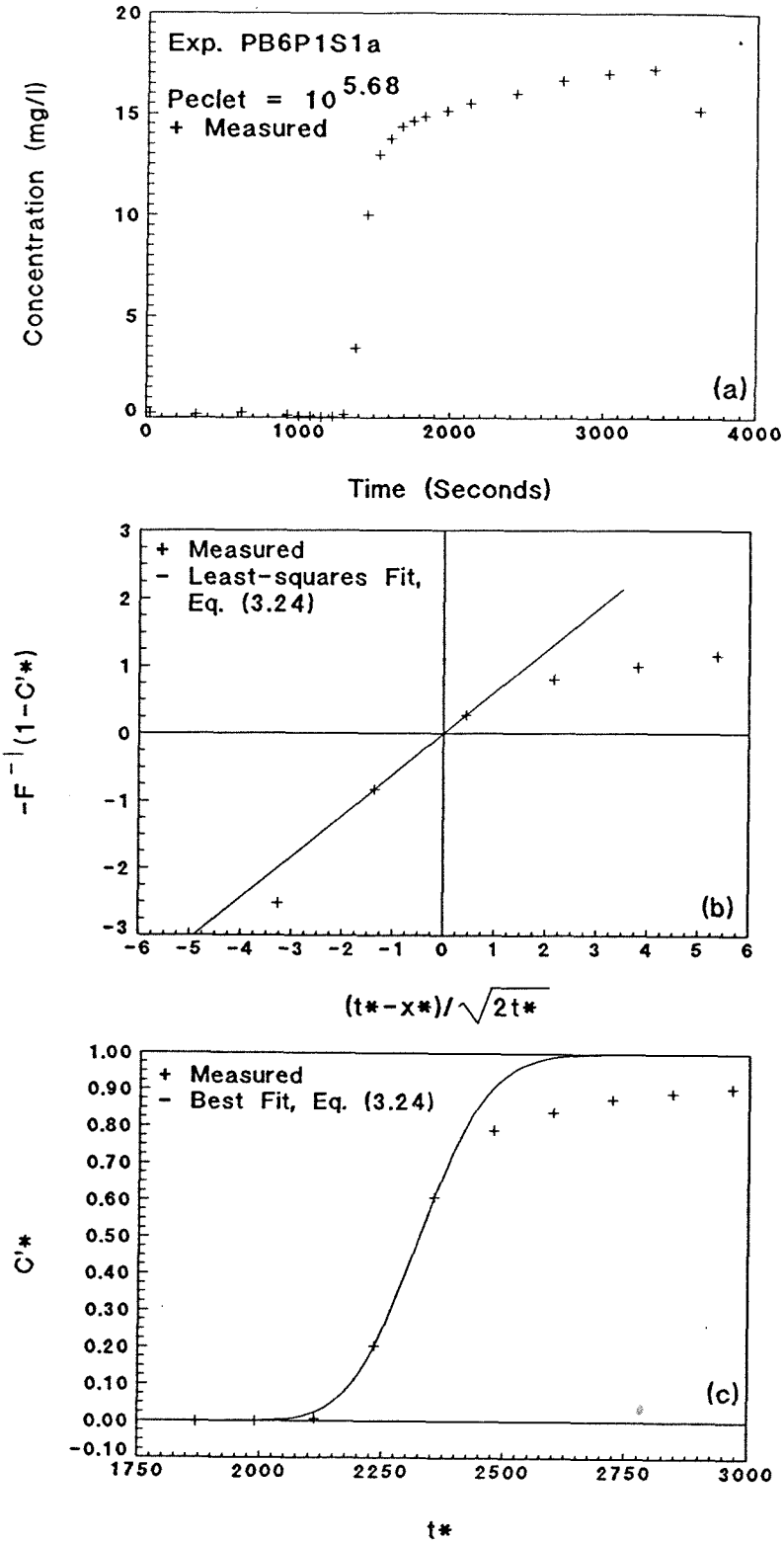

Fig. C.15: Exp. PB6P1S1a forward breakthrough, sample port 3, $Pe_p = 10^{5.68}$: (a) complete experimental data; (b) linearization with least-squares fit; and (c) breakthrough only with best-fit, Eq. (3.24).

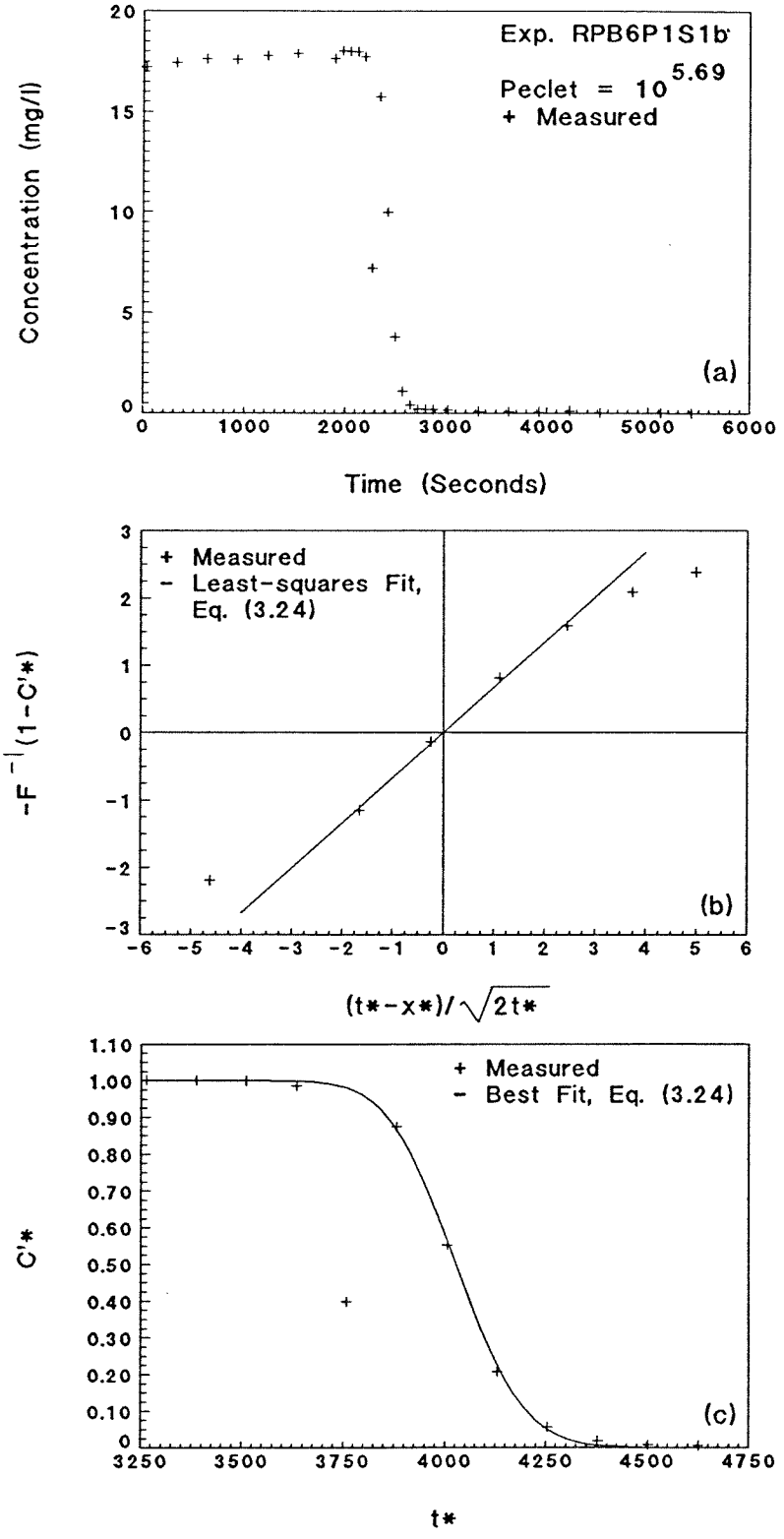

Fig. C.16: Exp. RPB6P1S1b reverse breakthrough, sample port 5, $Pe_p = 10^{5.69}$: (a) complete experimental data; (b) linearization with least-squares fit; and (c) breakthrough only with best-fit, Eq. (3.24).

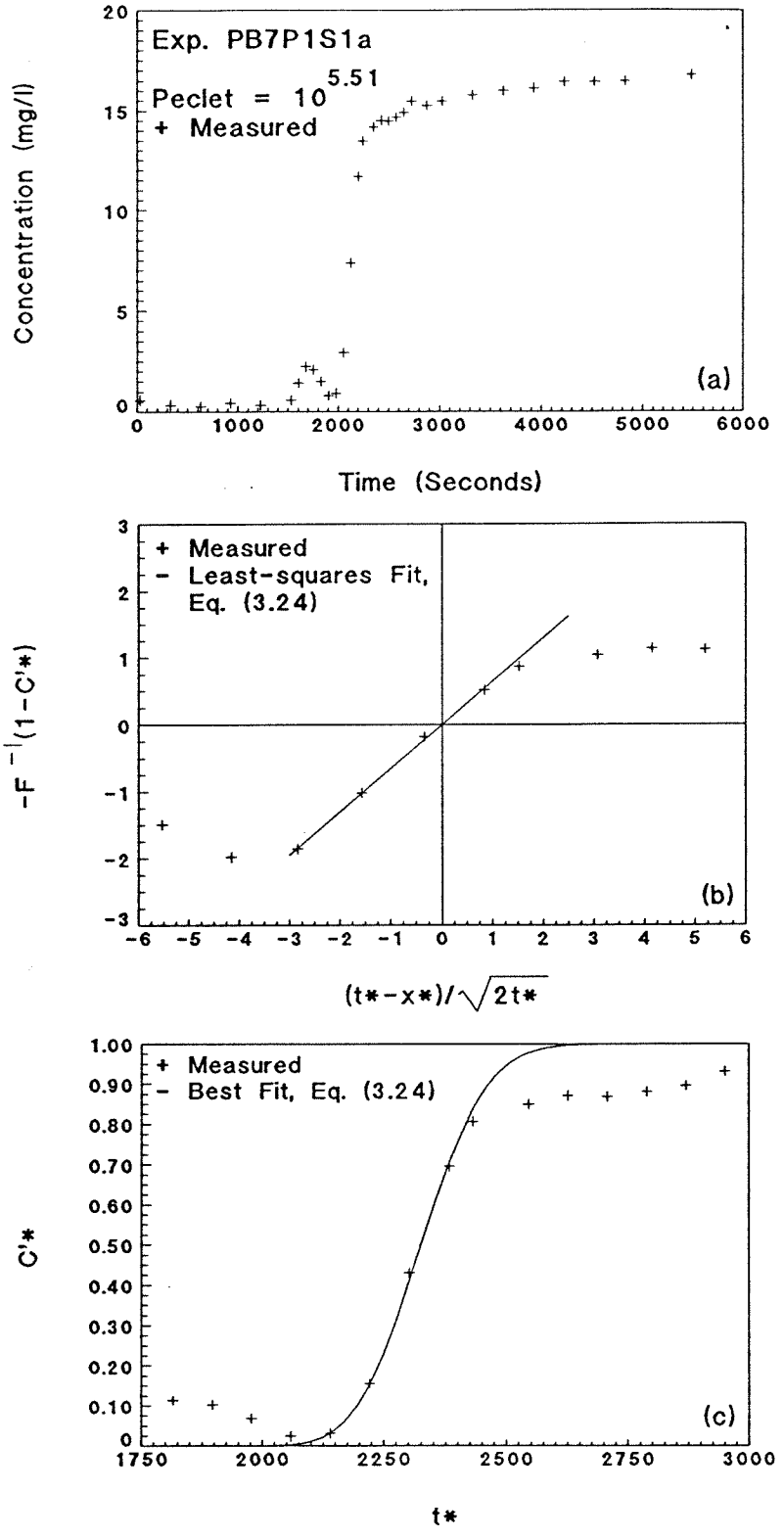

Fig. C.17: Exp. PB7P1S1a forward breakthrough, sample port 3, $Pe_p = 10^{5.51}$: (a) complete experimental data; (b) linearization with least-squares fit; and (c) breakthrough only with best-fit, Eq. (3.24).

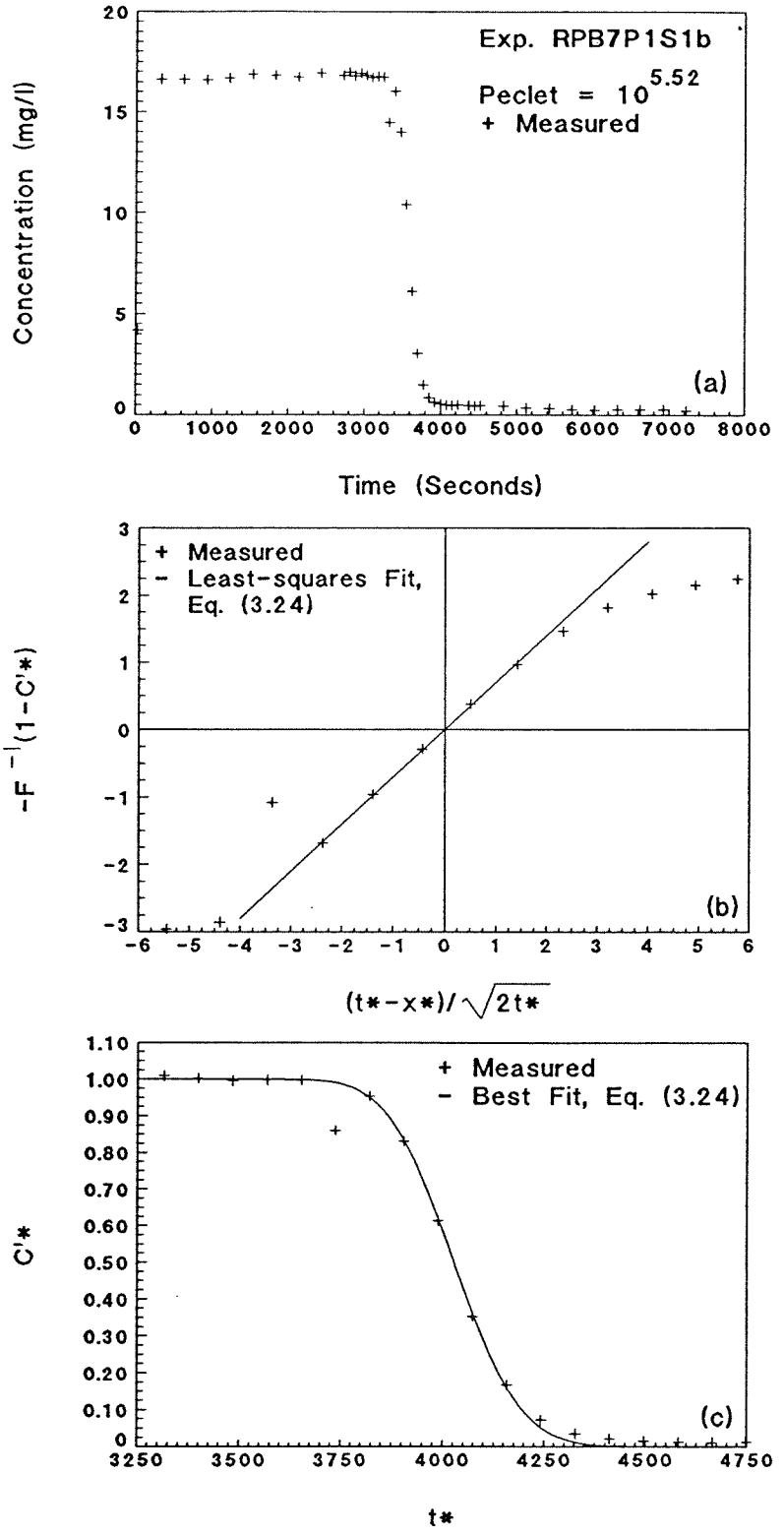

Fig. C.18: Exp. RPB7P1S1b reverse breakthrough, sample port 5, $Pe_p = 10^{5.52}$: (a) complete experimental data; (b) linearization with least-squares fit; and (c) breakthrough only with best-fit, Eq. (3.24).

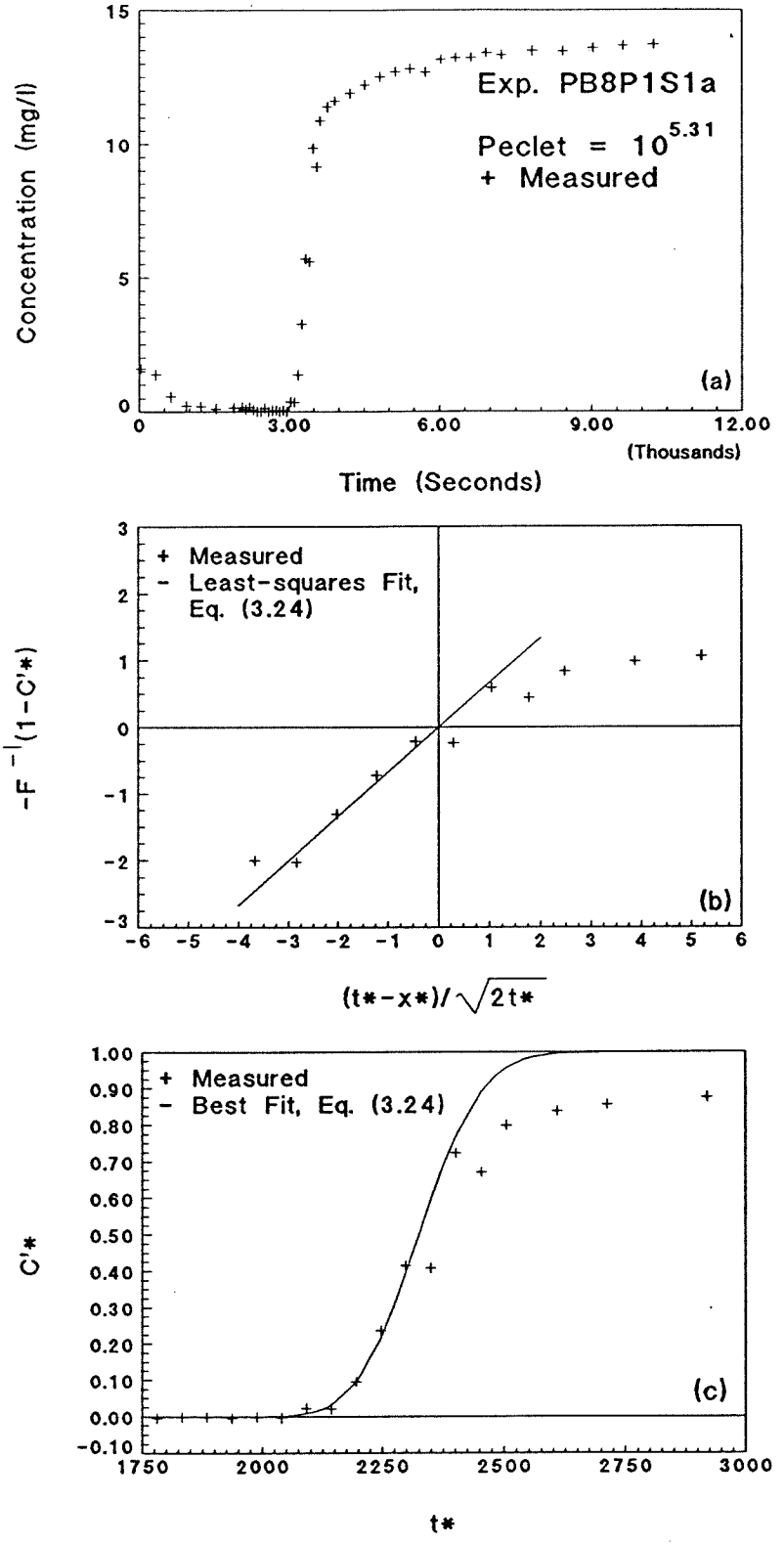

Fig. C.19: Exp. PB8P1S1a forward breakthrough, sample port 3, $Pe_p = 10^{5.31}$: (a) complete experimental data; (b) linearization with least-squares fit; and (c) breakthrough only with best-fit, Eq. (3.24).

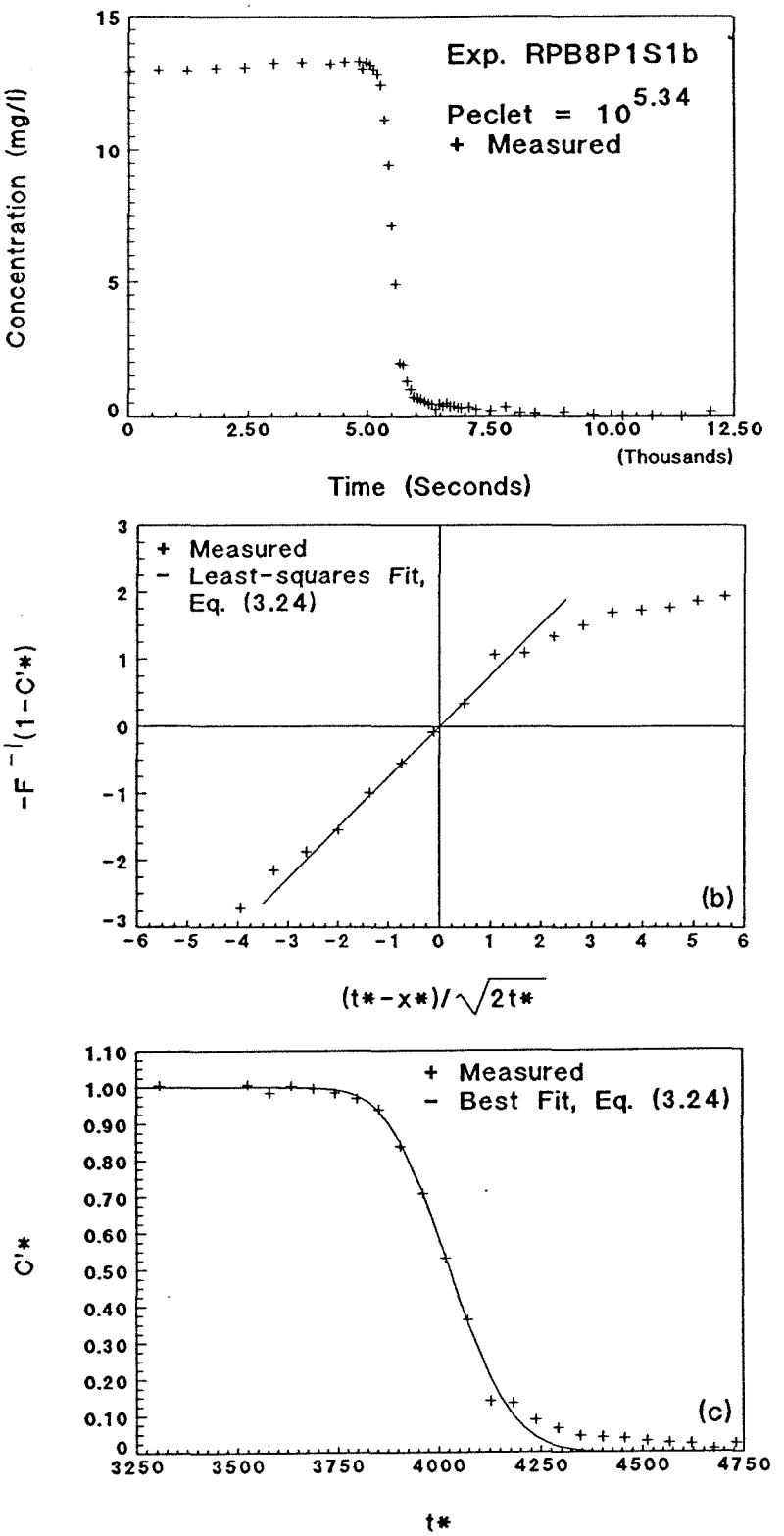

Fig. C.20: Exp. RPB8P1S1b reverse breakthrough, sample port 5, $Pe_p = 10^{5.34}$: (a) complete experimental data; (b) linearization with least-squares fit; and (c) breakthrough only with best-fit, Eq. (3.24).

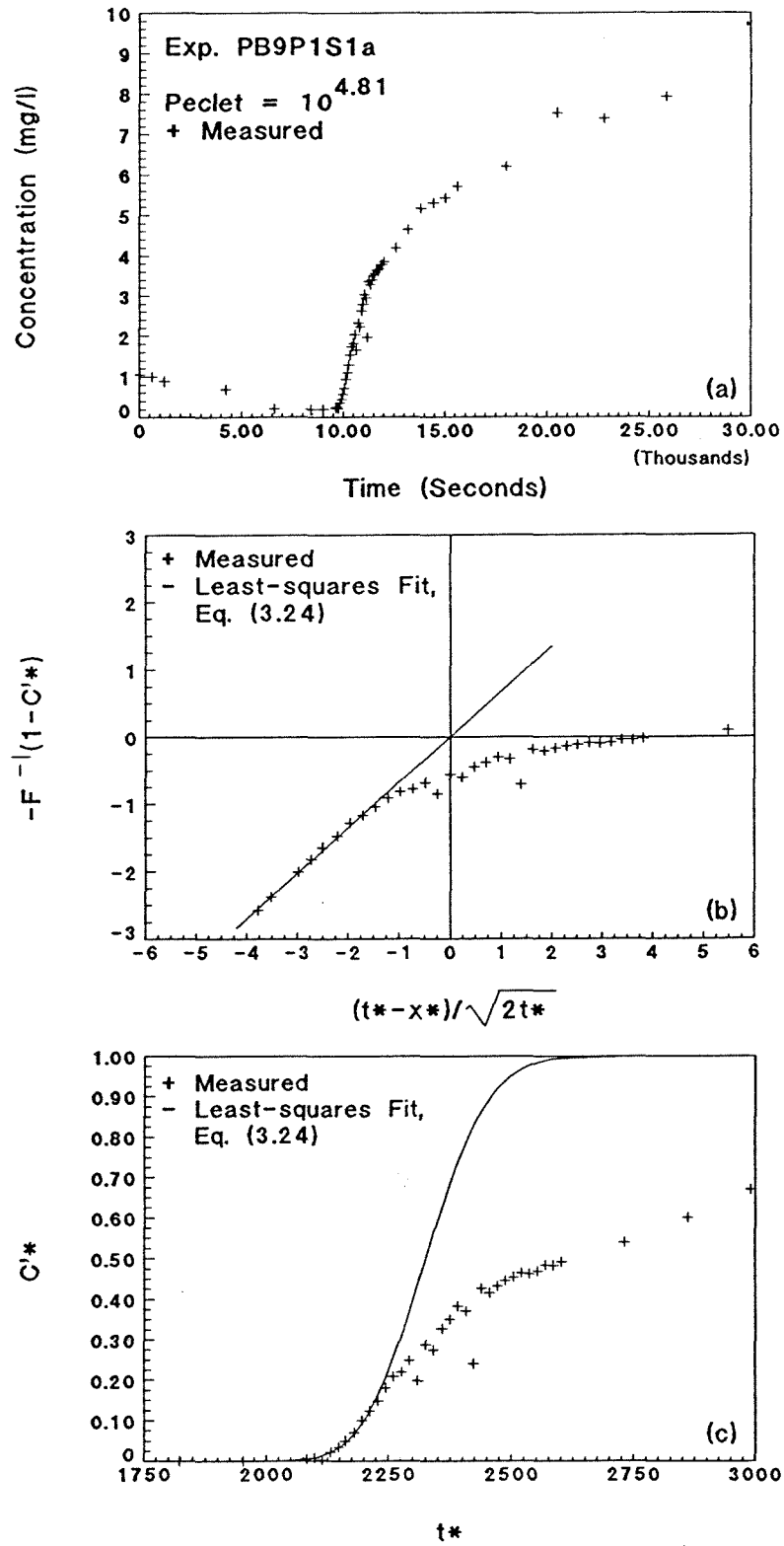

Fig. C.21: Exp. PB9P1S1a forward breakthrough, sample port 3, $Pe_p = 10^{4.81}$: (a) complete experimental data; (b) linearization with least-squares fit; and (c) breakthrough only with best-fit, Eq. (3.24).

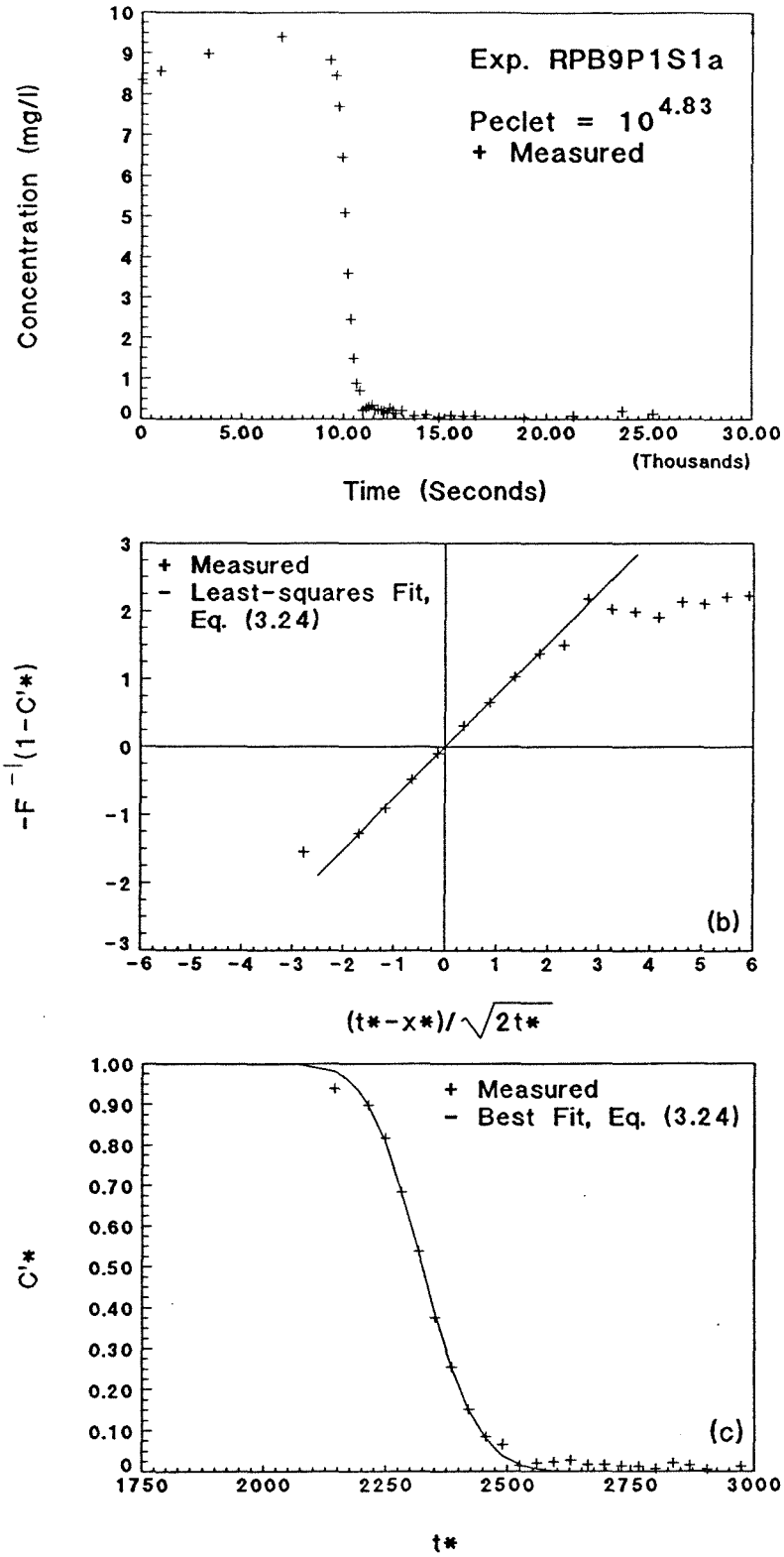

Fig. C.22: Exp. RPB9P1S1a reverse breakthrough, sample port 3, $Pe_p = 10^{4.83}$: (a) complete experimental data; (b) linearization with least-squares fit; and (c) breakthrough only with best-fit, Eq. (3.24).

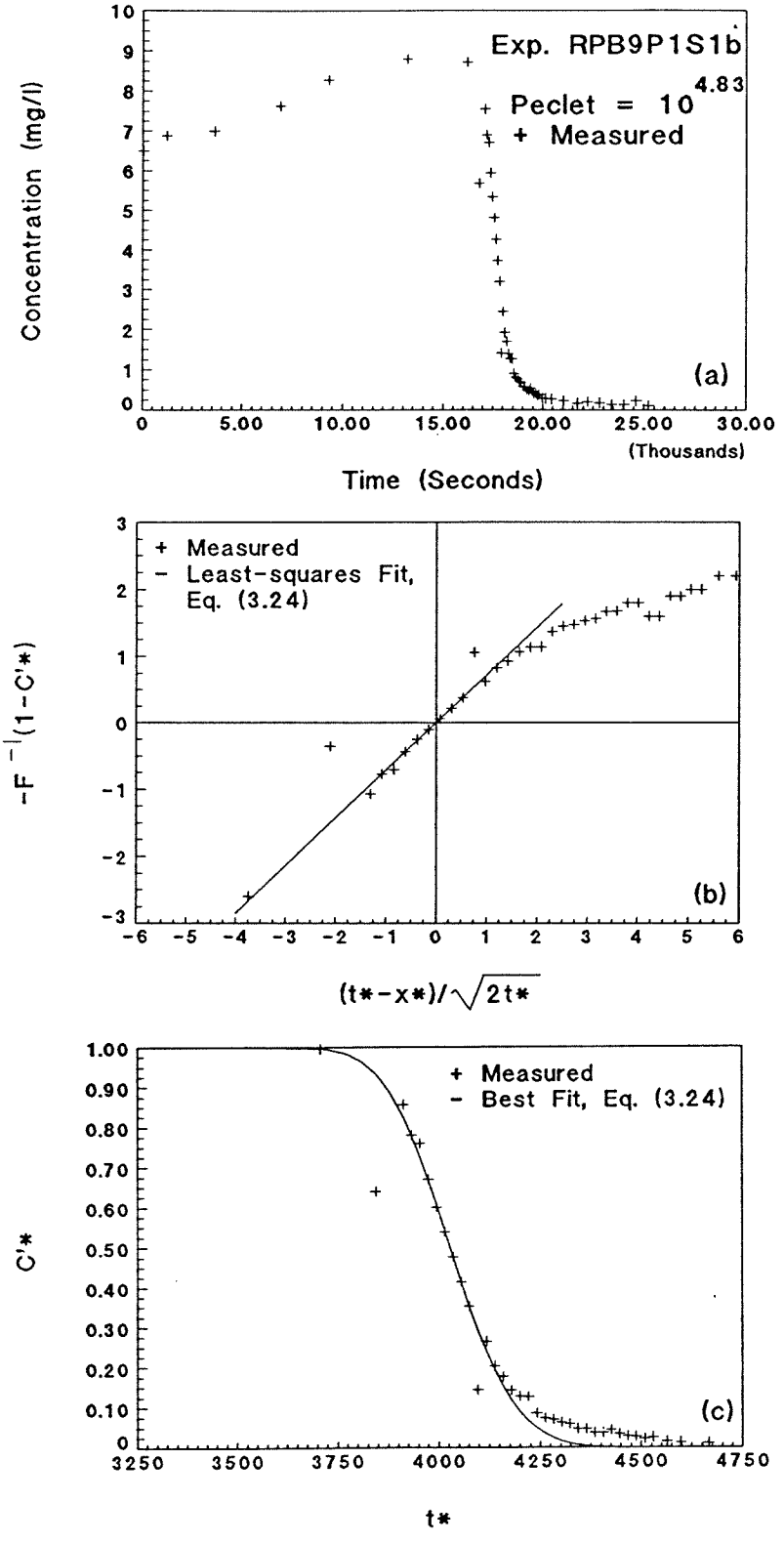

Fig. C.23: Exp. RPB9P1S1b reverse breakthrough, sample port 5, $Pe_p = 10^{4.83}$: (a) complete experimental data; (b) linearization with least-squares fit; and (c) breakthrough only with best-fit, Eq. (3.24).

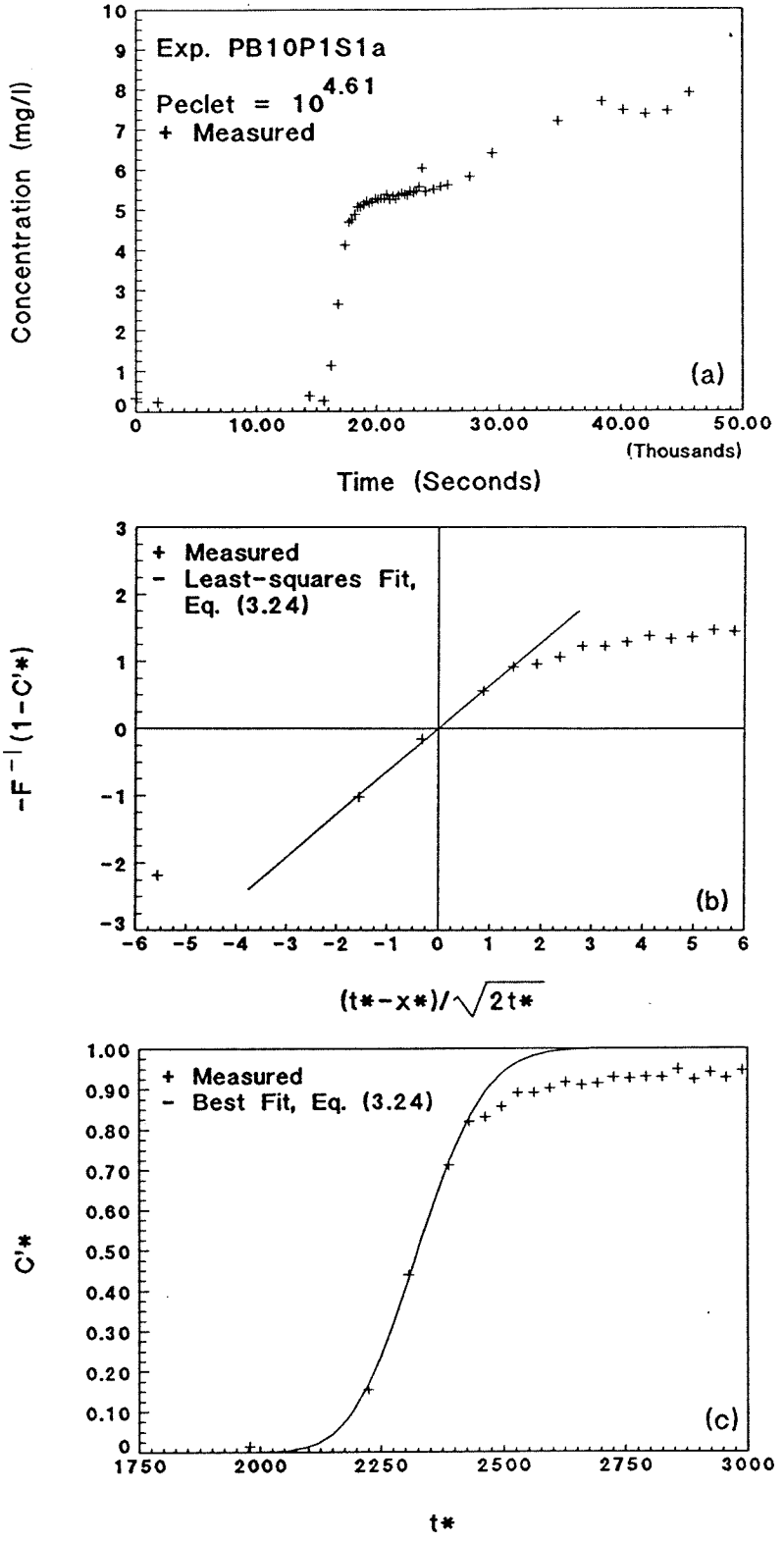

Fig. C.24: Exp. PB10P1S1a forward breakthrough, sample port 3, $Pe_p = 10^{4.61}$: (a) complete experimental data; (b) linearization with least-squares fit; and (c) breakthrough only with best-fit, Eq. (3.24).

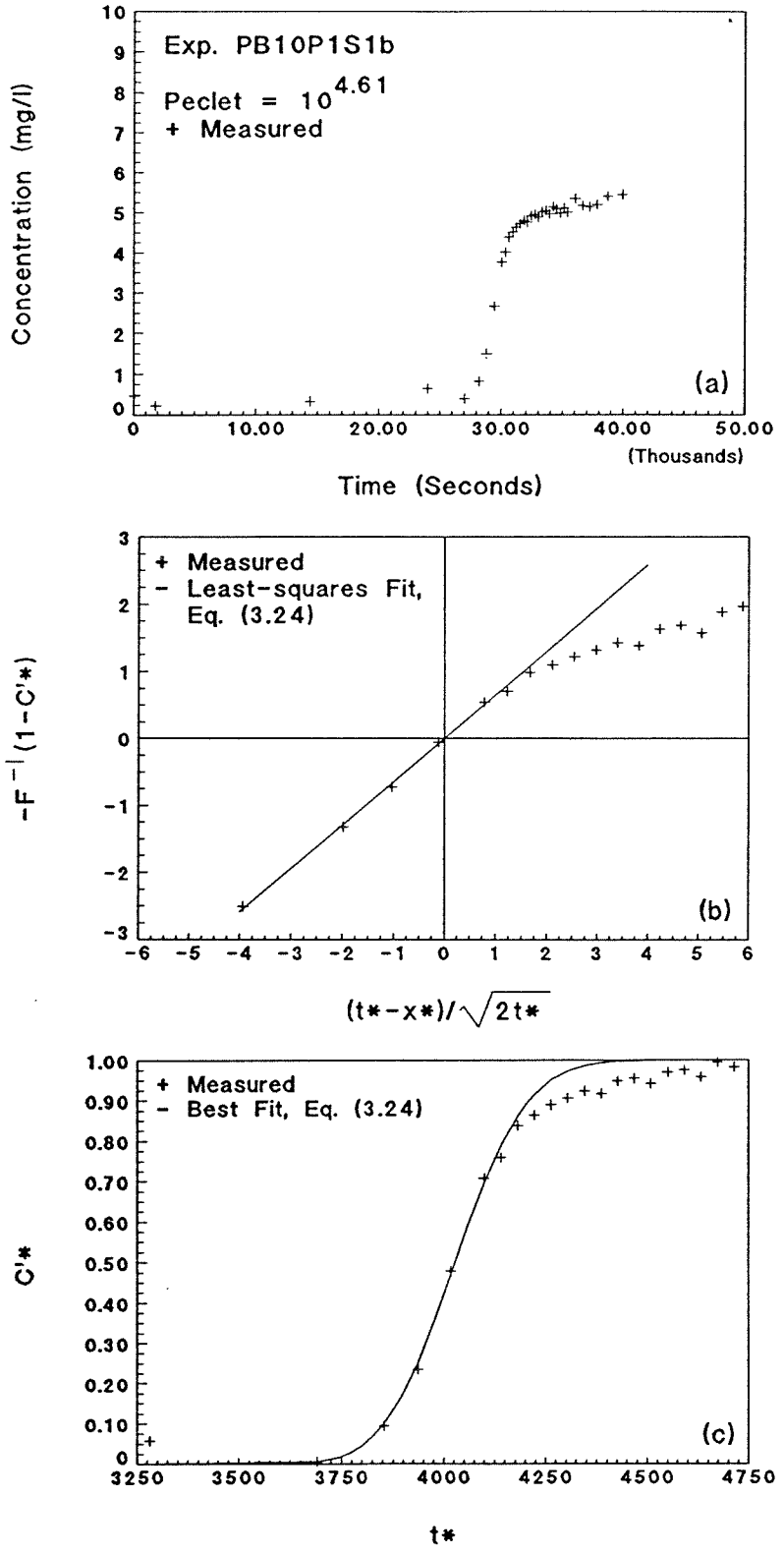

Fig. C.25: Exp. PB10P1S1b forward breakthrough, sample port 5, $Pe_p = 10^{4.61}$: (a) complete experimental data; (b) linearization with least-squares fit; and (c) breakthrough only with best-fit, Eq. (3.24).

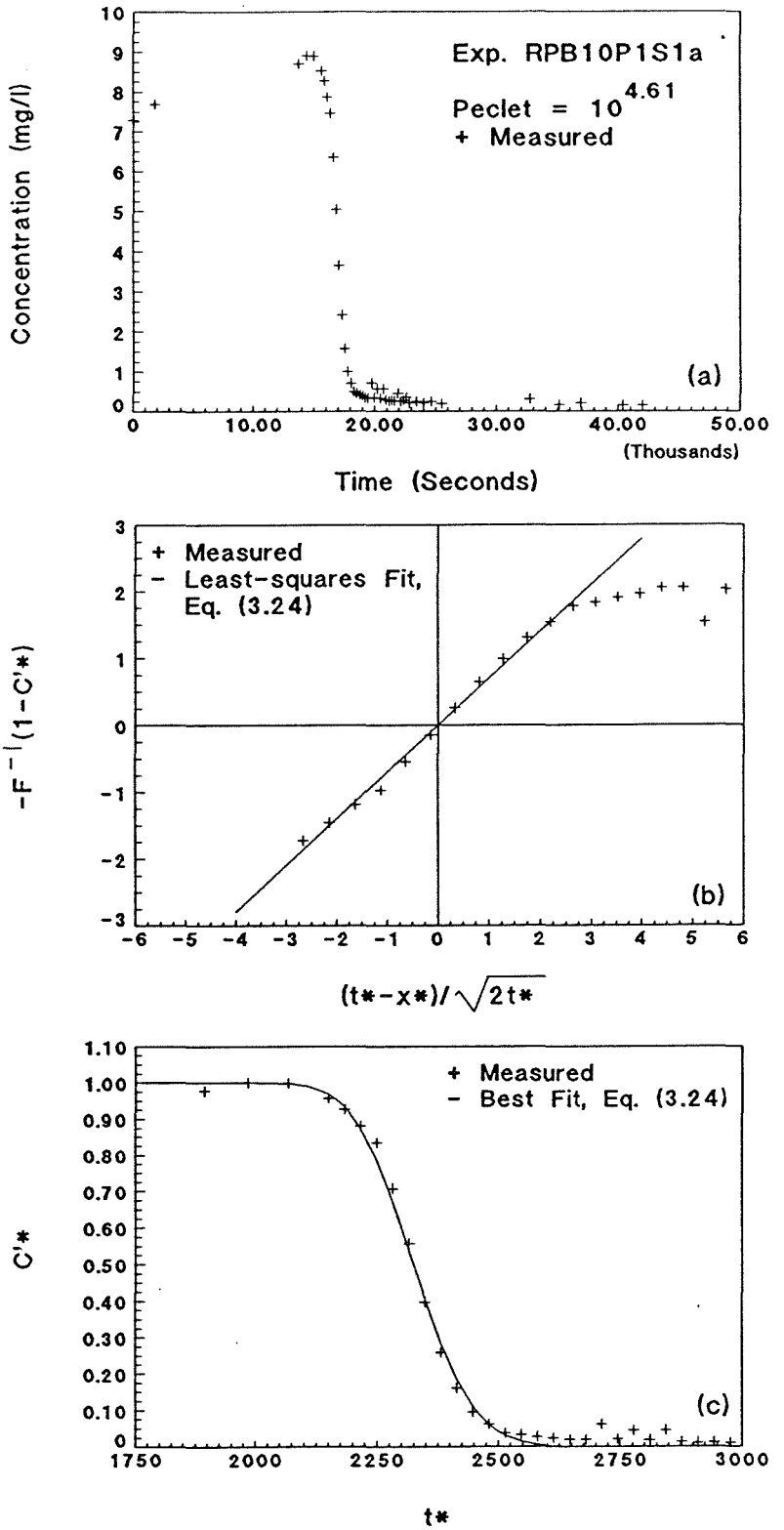

Fig. C.26: Exp. RPB10P1S1a reverse breakthrough, sample port 3, $Pe_p = 10^{4.61}$: (a) complete experimental data; (b) linearization with least-squares fit; and (c) breakthrough only with best-fit, Eq. (3.24).

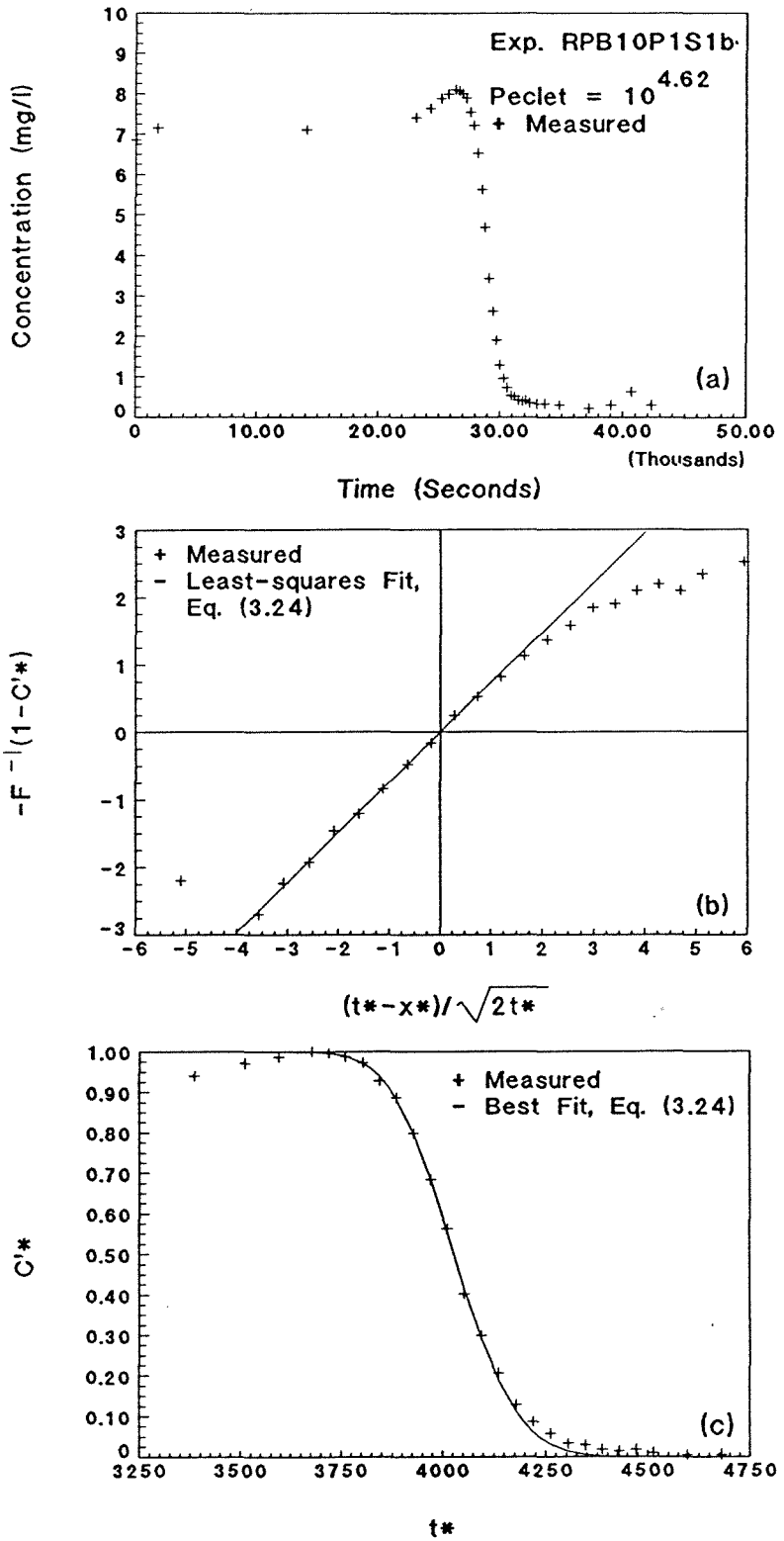

Fig. C.27: Exp. RPB10P1S1b reverse breakthrough, sample port 5, $Pe_p = 10^{4.62}$: (a) complete experimental data; (b) linearization with least-squares fit; and (c) breakthrough only with best-fit, Eq. (3.24).

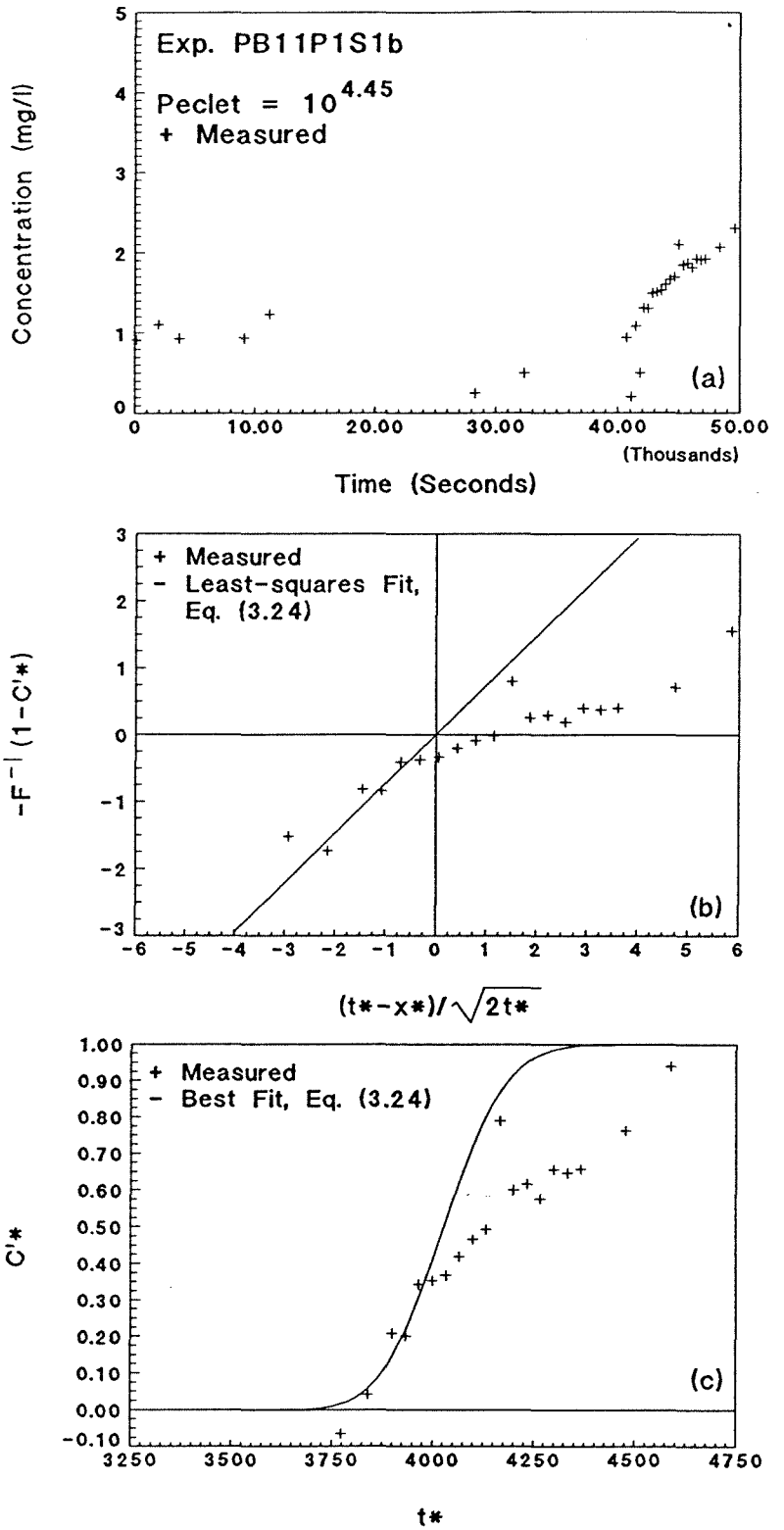

Fig. C.28: Exp. PB11P1S1b forward breakthrough, sample port 5, $Pe_p = 10^{4.44}$: (a) complete experimental data; (b) linearization with least-squares fit; and (c) breakthrough only with best-fit, Eq. (3.24).

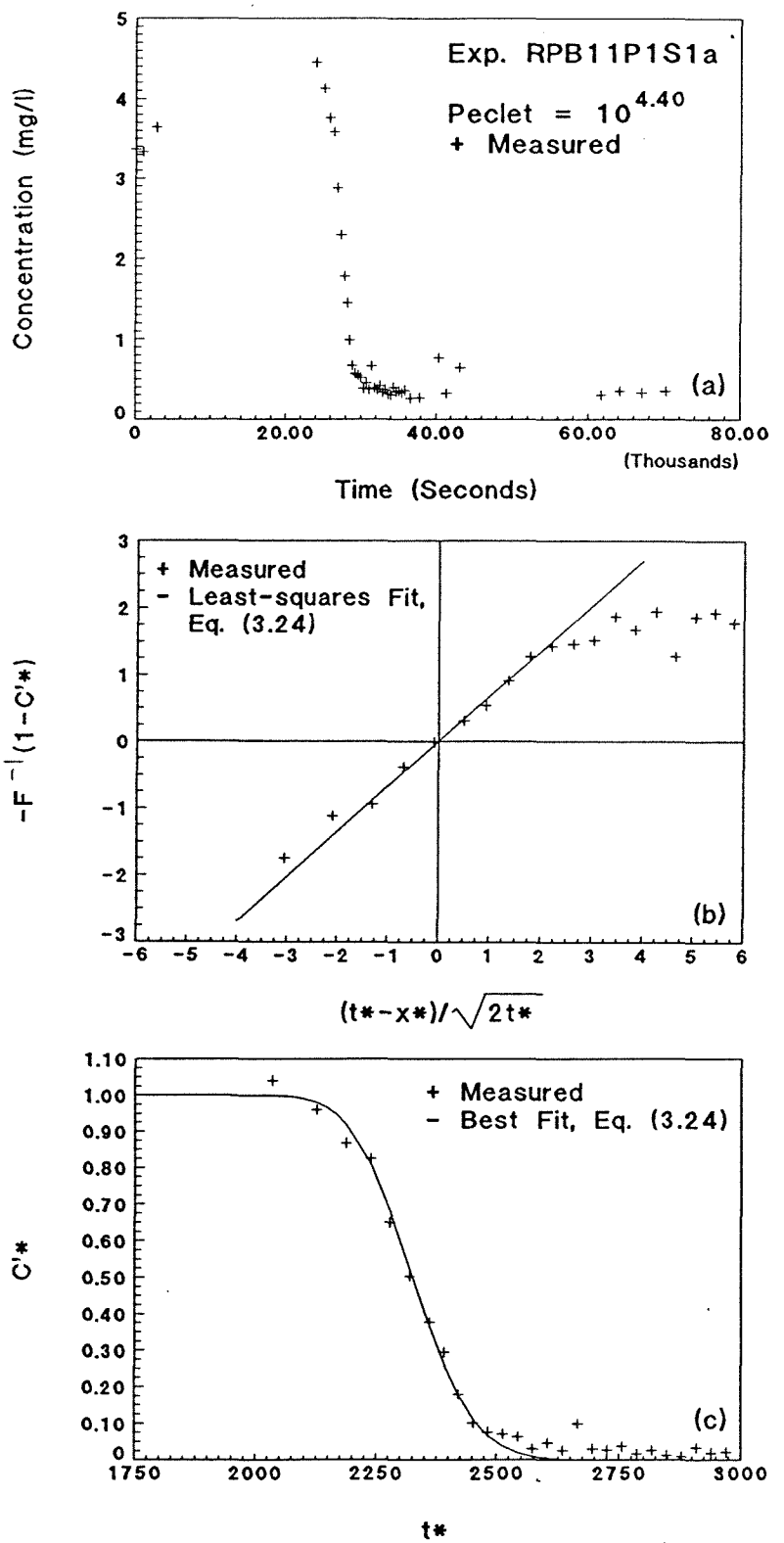

Fig. C.29: Exp. RPB11P1S1a reverse breakthrough, sample port 3, $Pe_p = 10^{4.40}$: (a) complete experimental data; (b) linearization with least-squares fit; and (c) breakthrough only with best-fit, Eq. (3.24).

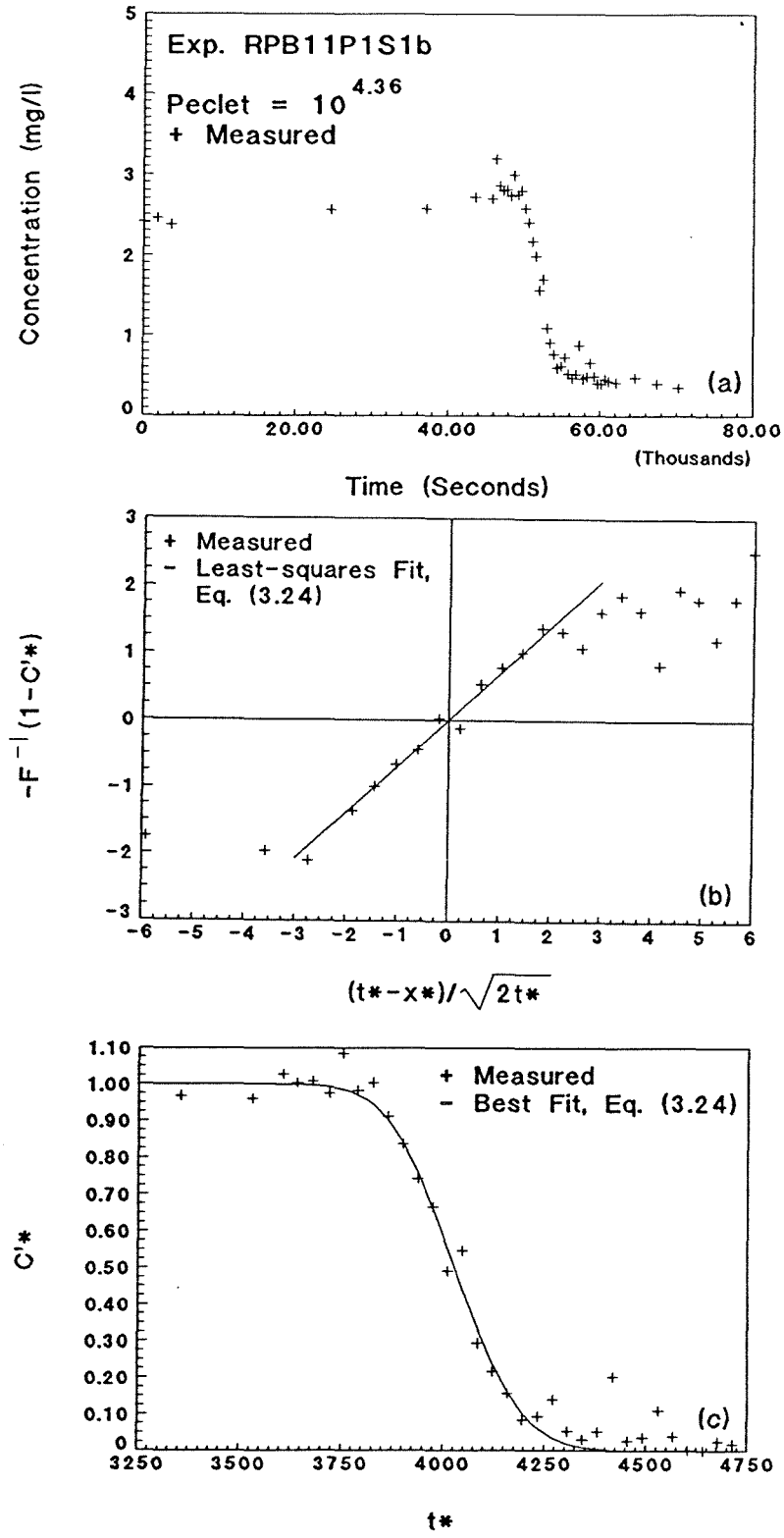

Fig. C.30: Exp. RPB11P1S1b reverse breakthrough, sample port 5, $Pe_p = 10^{4.36}$: (a) complete experimental data; (b) linearization with least-squares fit; and (c) breakthrough only with best-fit, Eq. (3.24).

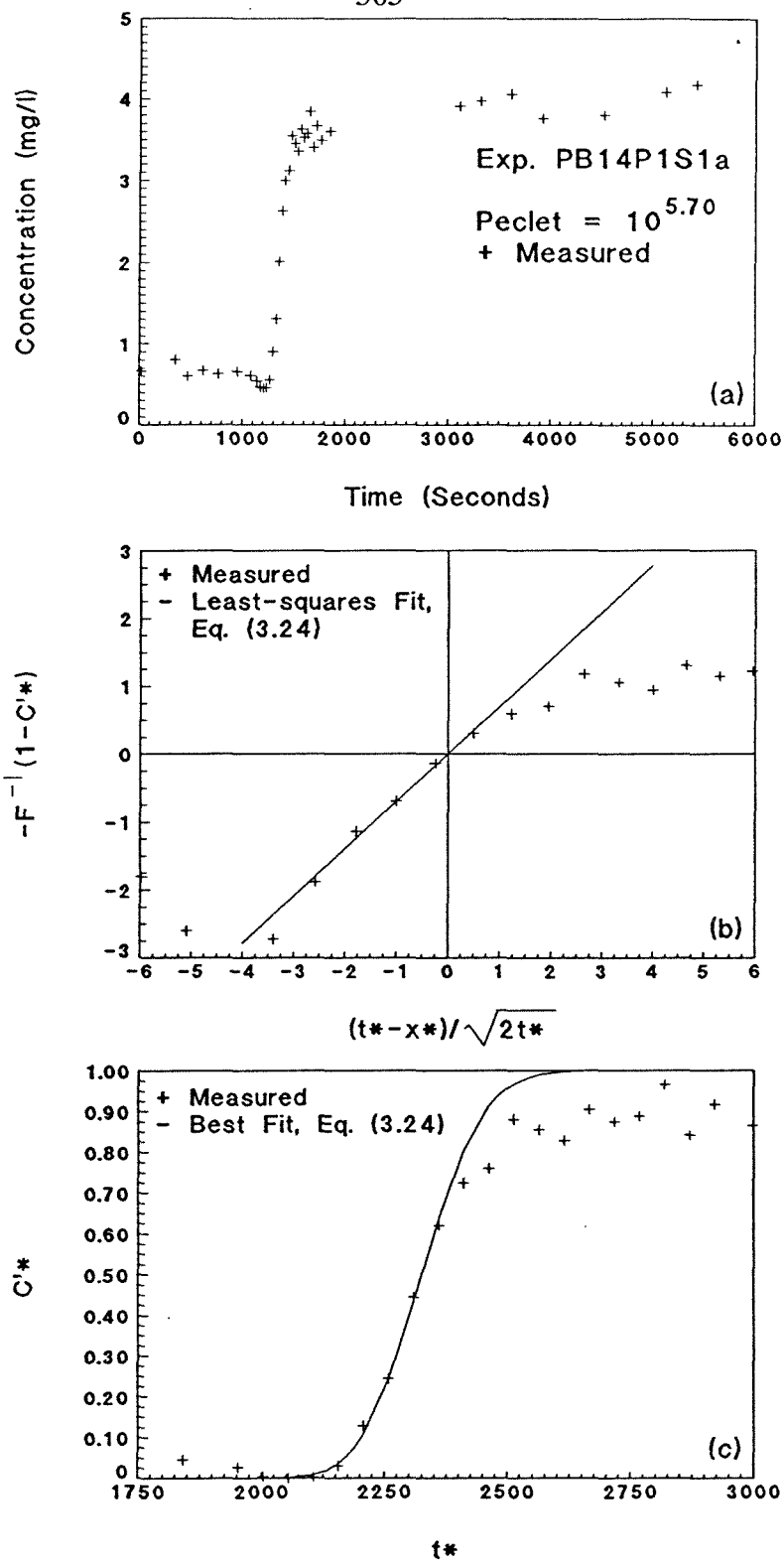

Fig. C.31: Exp. PB14P1S1a forward breakthrough, sample port 3, $Pe_p = 10^{5.70}$: (a) complete experimental data; (b) linearization with least-squares fit; and (c) breakthrough only with best-fit, Eq. (3.24).

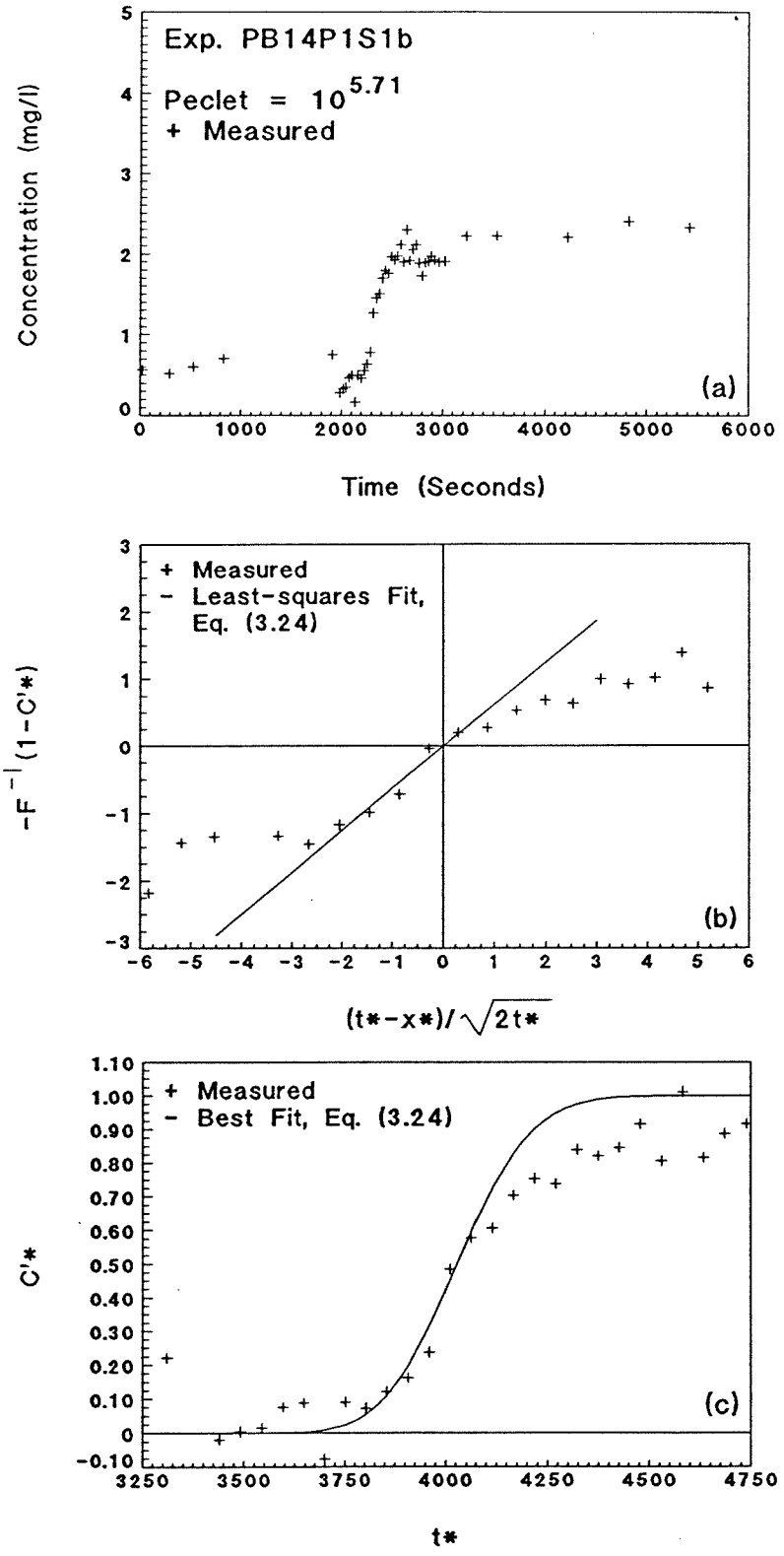

Fig. C.32: Exp. PB14P1S1b forward breakthrough, sample port 5, $Pe_p = 10^{5.71}$: (a) complete experimental data; (b) linearization with least-squares fit; and (c) breakthrough only with best-fit, Eq. (3.24).

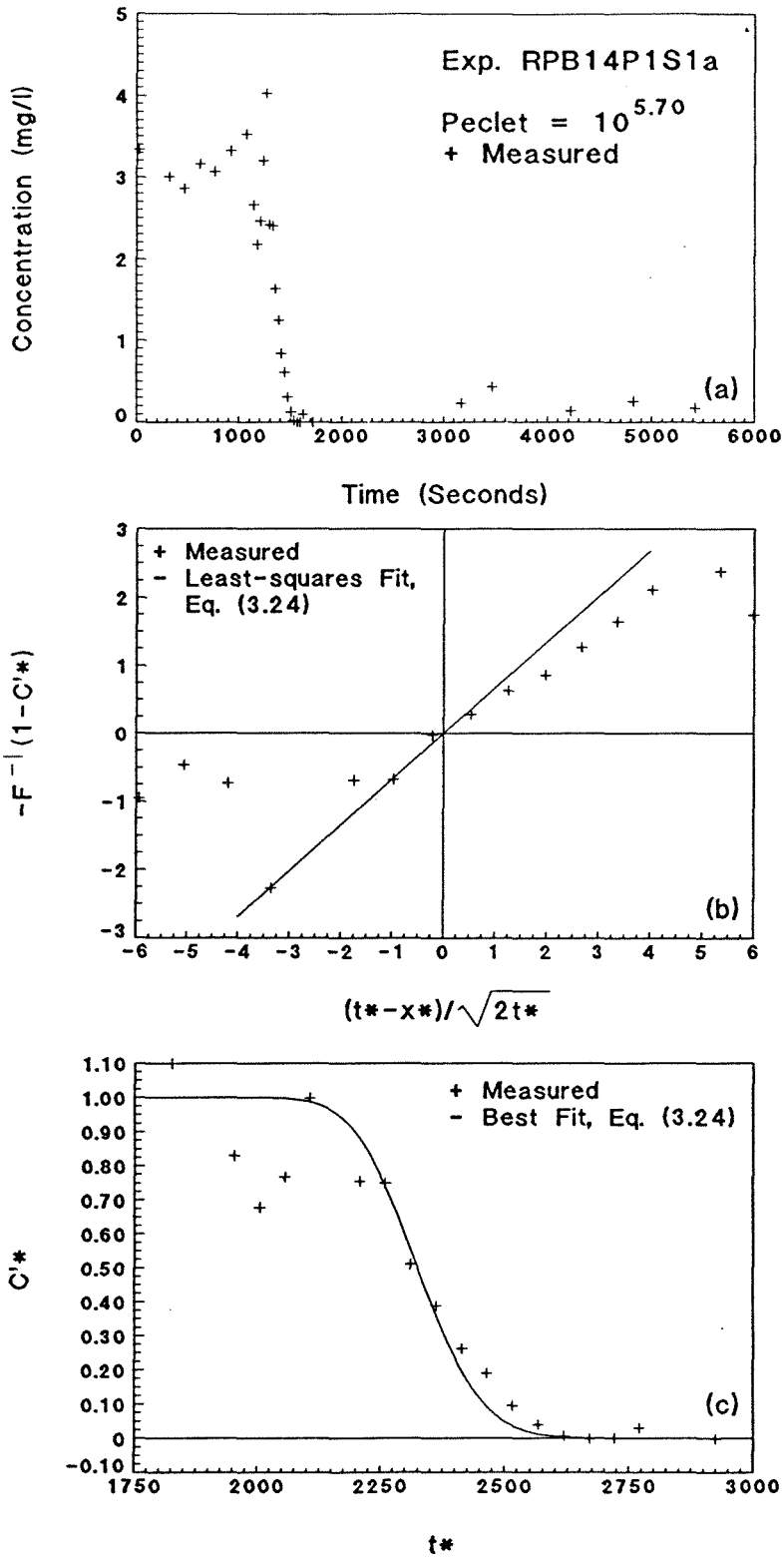

Fig. C.33: Exp. RPB14P1S1a reverse breakthrough, sample port 3, $Pe_p = 10^{5.70}$: (a) complete experimental data; (b) linearization with least-squares fit; and (c) breakthrough only with best-fit, Eq. (3.24).

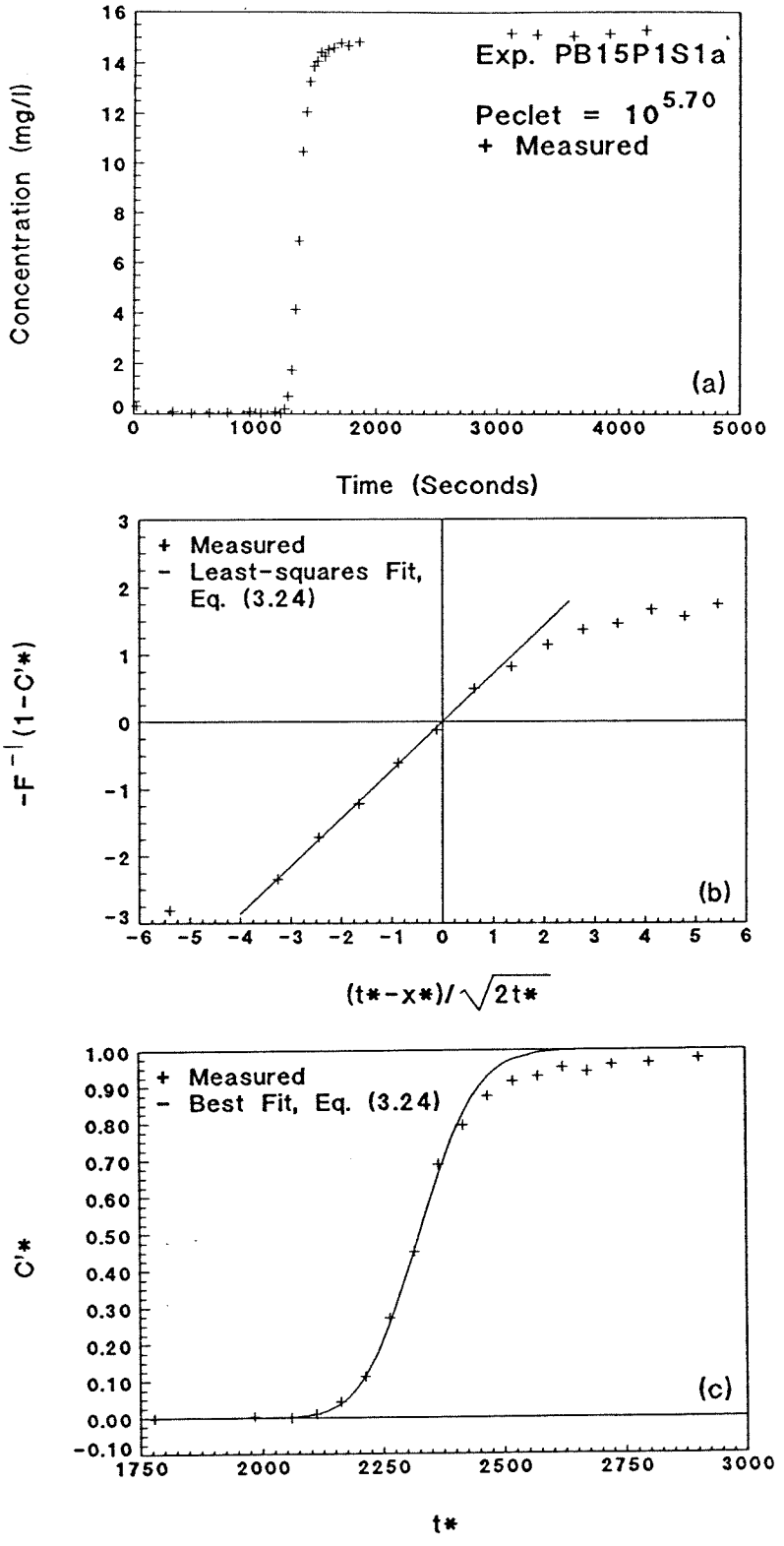

Fig. C.34: Exp. PB15P1S1a forward breakthrough, sample port 3, $Pe_p = 10^{5.70}$: (a) complete experimental data; (b) linearization with least-squares fit; and (c) breakthrough only with best-fit, Eq. (3.24).

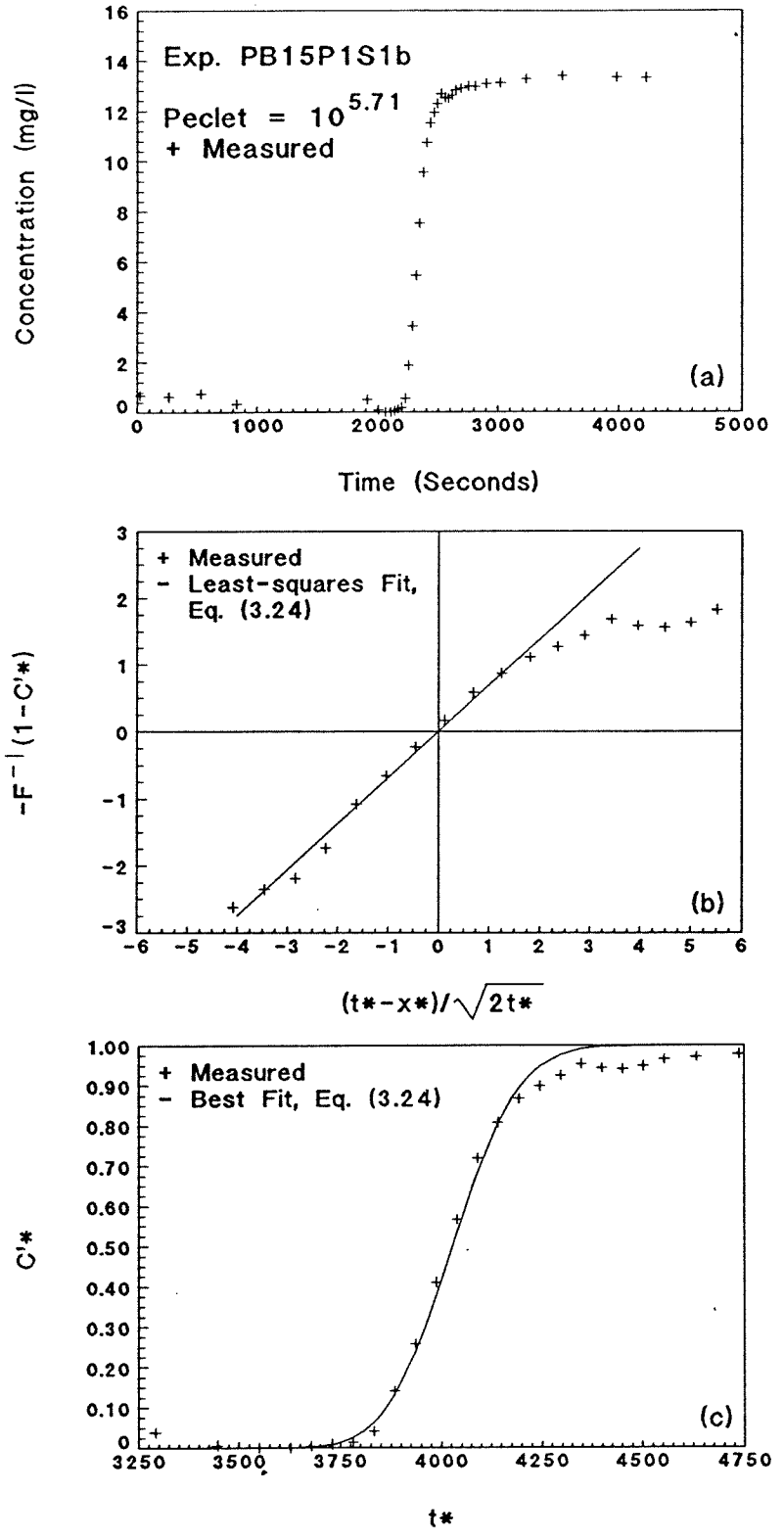

Fig. C.35: Exp. PB15P1S1b forward breakthrough, sample port 5, $Pe_p = 10^{5.71}$: (a) complete experimental data; (b) linearization with least-squares fit; and (c) breakthrough only with best-fit, Eq. (3.24).

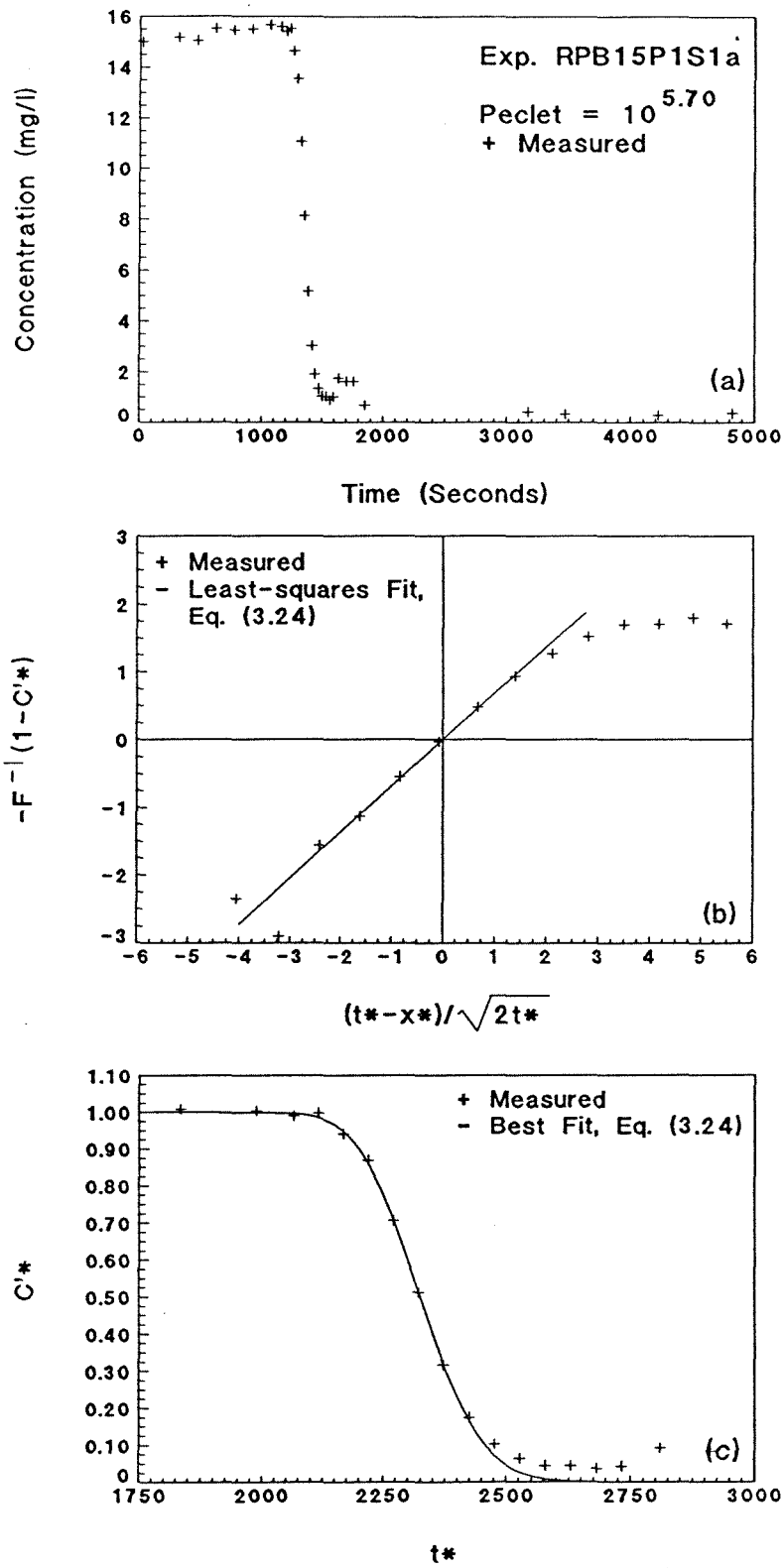

Fig. C.36: Exp. RPB15P1S1a reverse breakthrough, sample port 3, $Pe_p = 10^{5.70}$: (a) complete experimental data; (b) linearization with least-squares fit; and (c) breakthrough only with best-fit, Eq. (3.24).

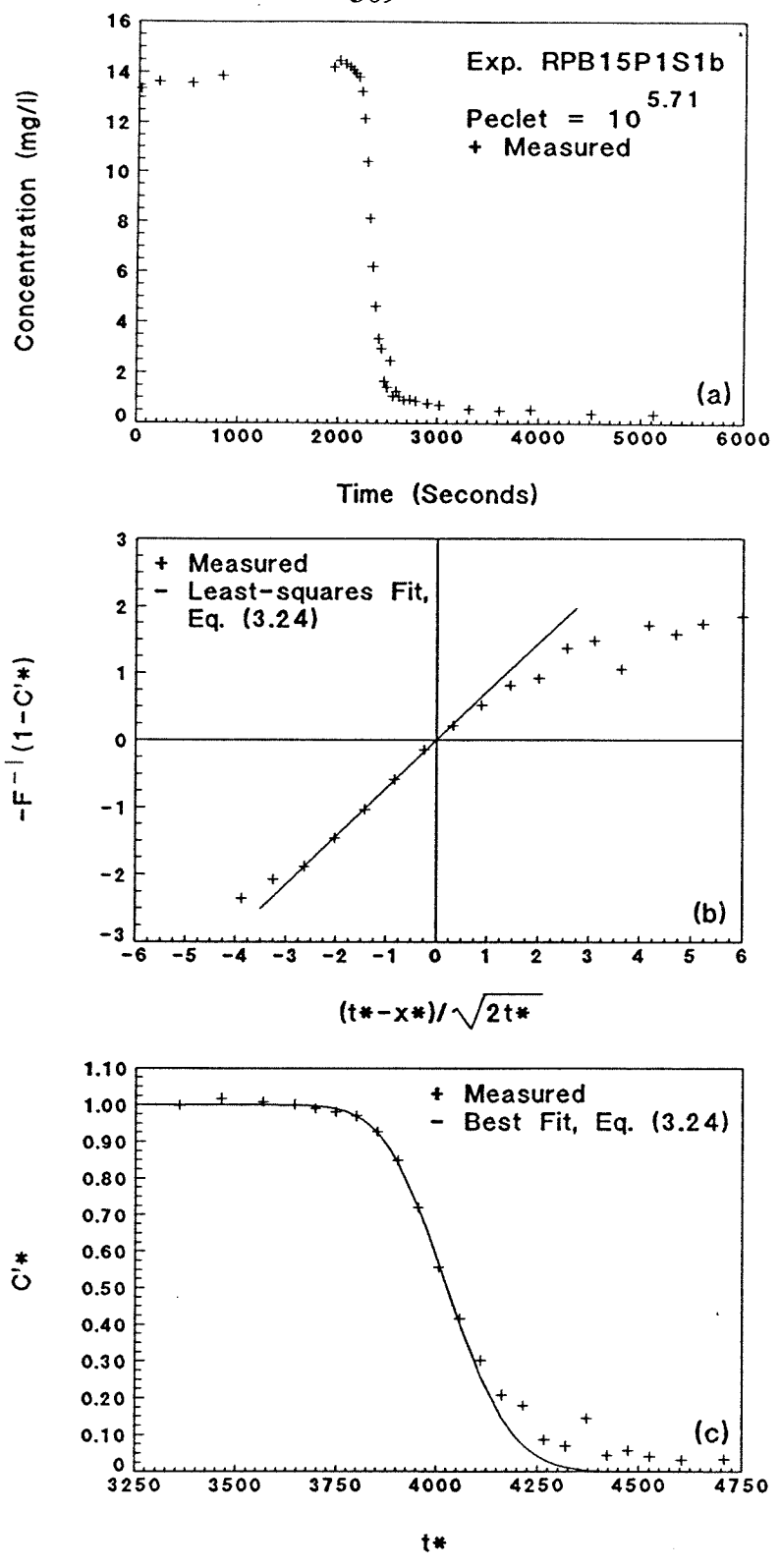

Fig. C.37: Exp. RPB15P1S1b reverse breakthrough, sample port 5, $Pe_p = 10^{5.71}$: (a) complete experimental data; (b) linearization with least-squares fit; and (c) breakthrough only with best-fit, Eq. (3.24).

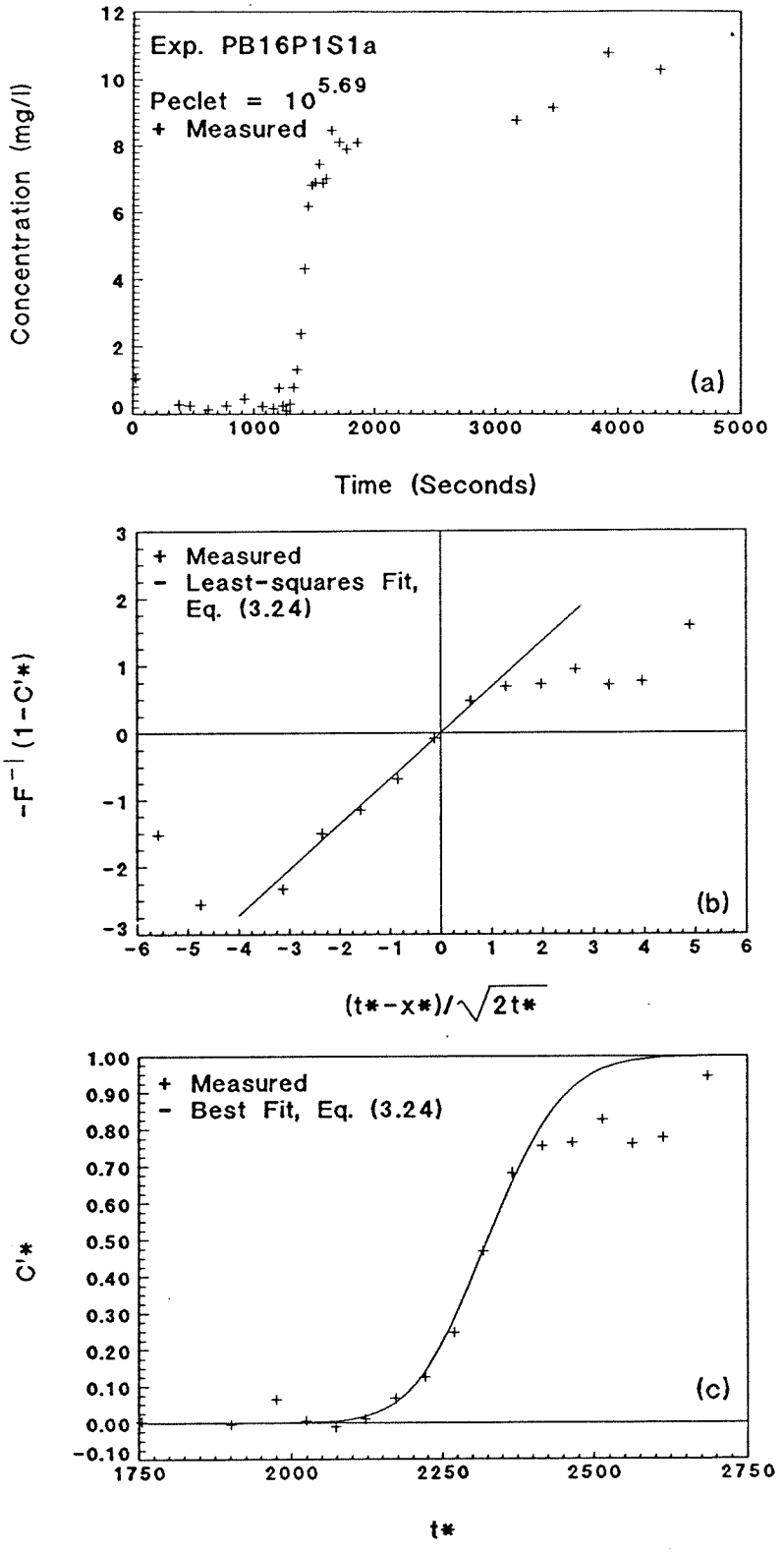

Fig. C.38: Exp. PB16P1S1a forward breakthrough, sample port 3, $Pe_p = 10^{5.69}$: (a) complete experimental data; (b) linearization with least-squares fit; and (c) breakthrough only with best-fit, Eq. (3.24).

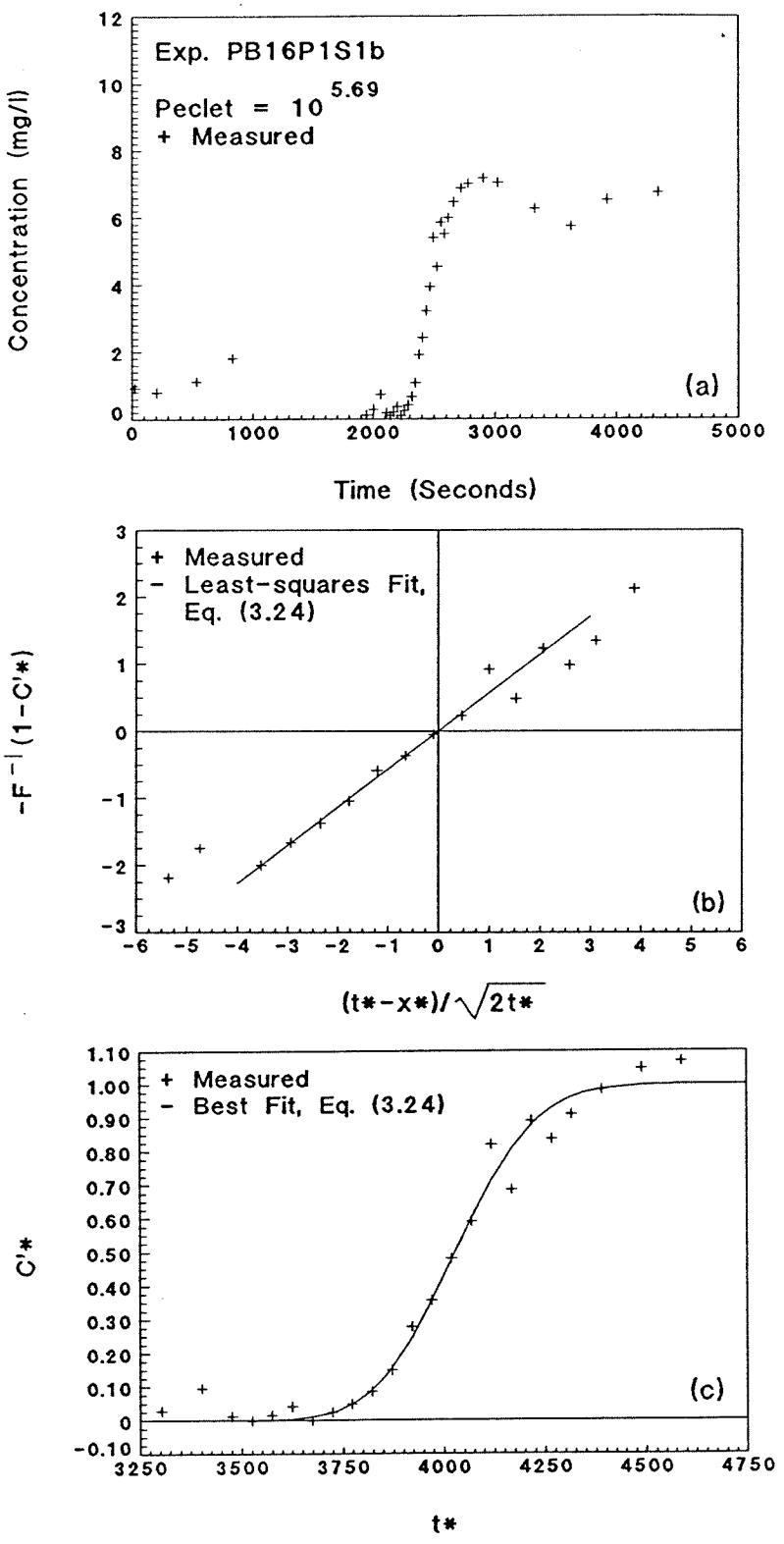

Fig. C.39: Exp. PB16P1S1b forward breakthrough, sample port 5, $Pe_p = 10^{5.70}$: (a) complete experimental data; (b) linearization with least-squares fit; and (c) breakthrough only with best-fit, Eq. (3.24).

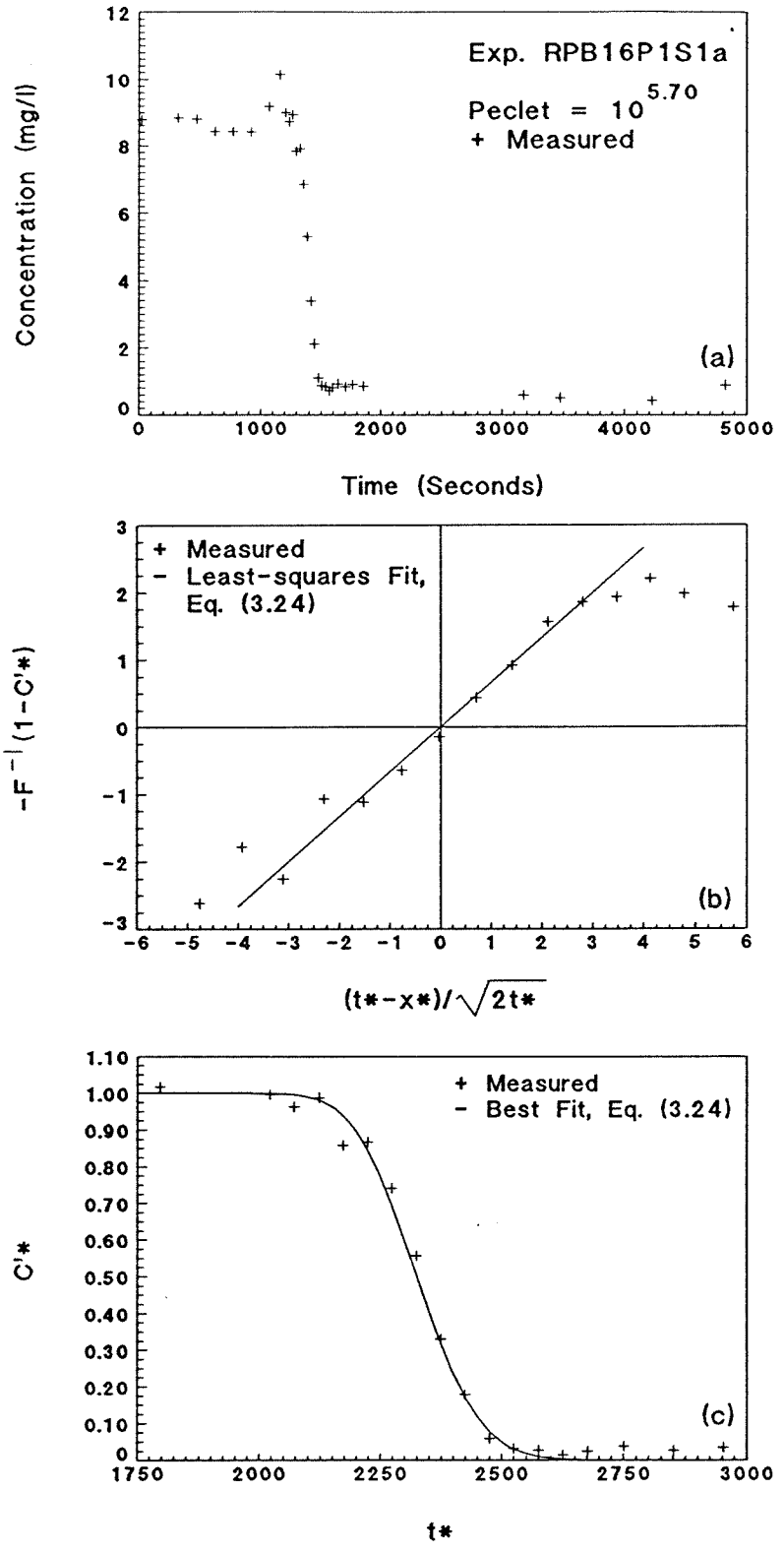

Fig. C.40: Exp. RPB16P1S1a reverse breakthrough, sample port 3, $Pe_p = 10^{5.70}$: (a) complete experimental data; (b) linearization with least-squares fit; and (c) breakthrough only with best-fit, Eq. (3.24).

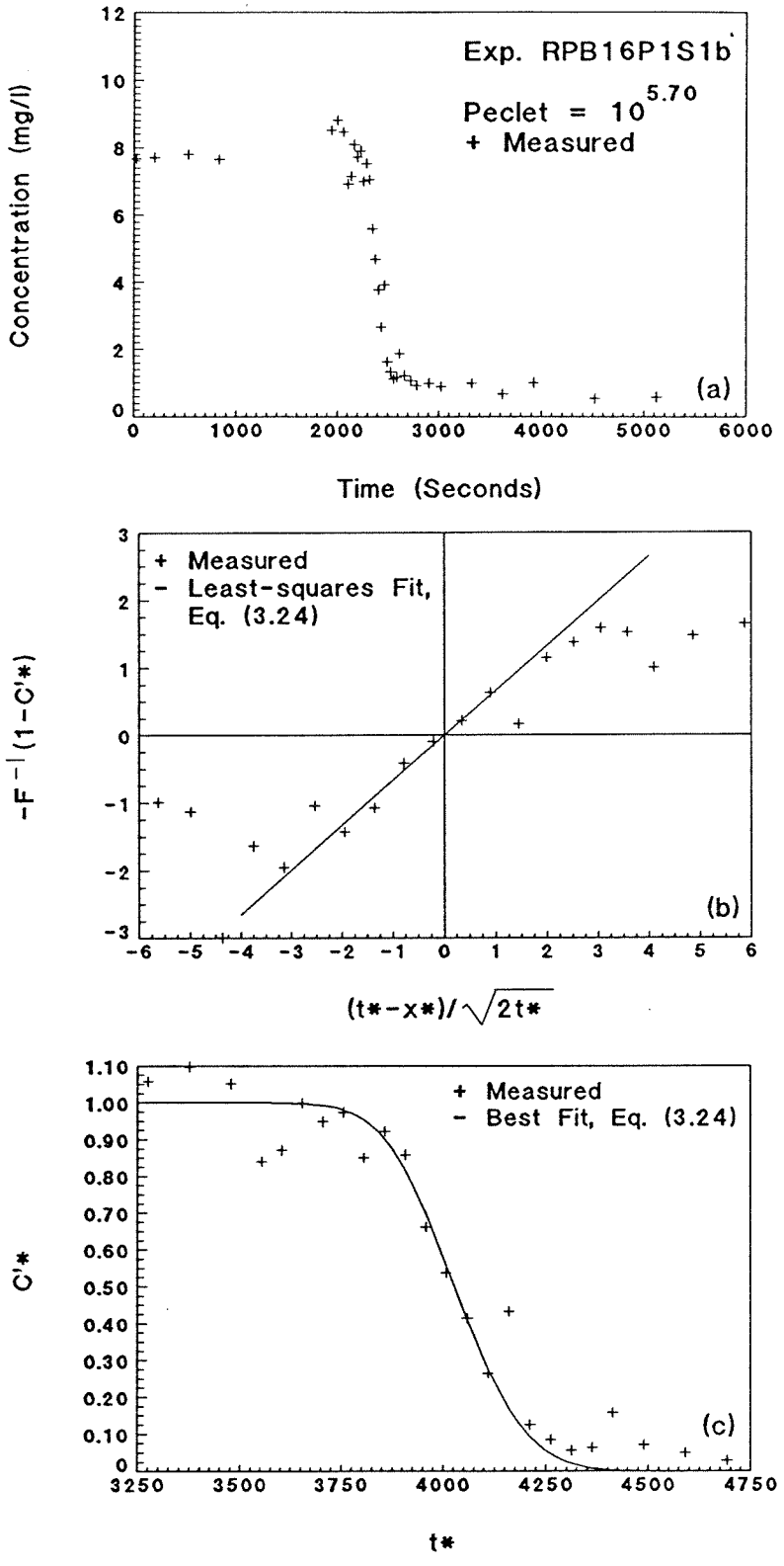

Fig. C.41: Exp. RPB16P1S1b reverse breakthrough, sample port 5, $Pe_p = 10^{5.70}$: (a) complete experimental data; (b) linearization with least-squares fit; and (c) breakthrough only with best-fit, Eq. (3.24).

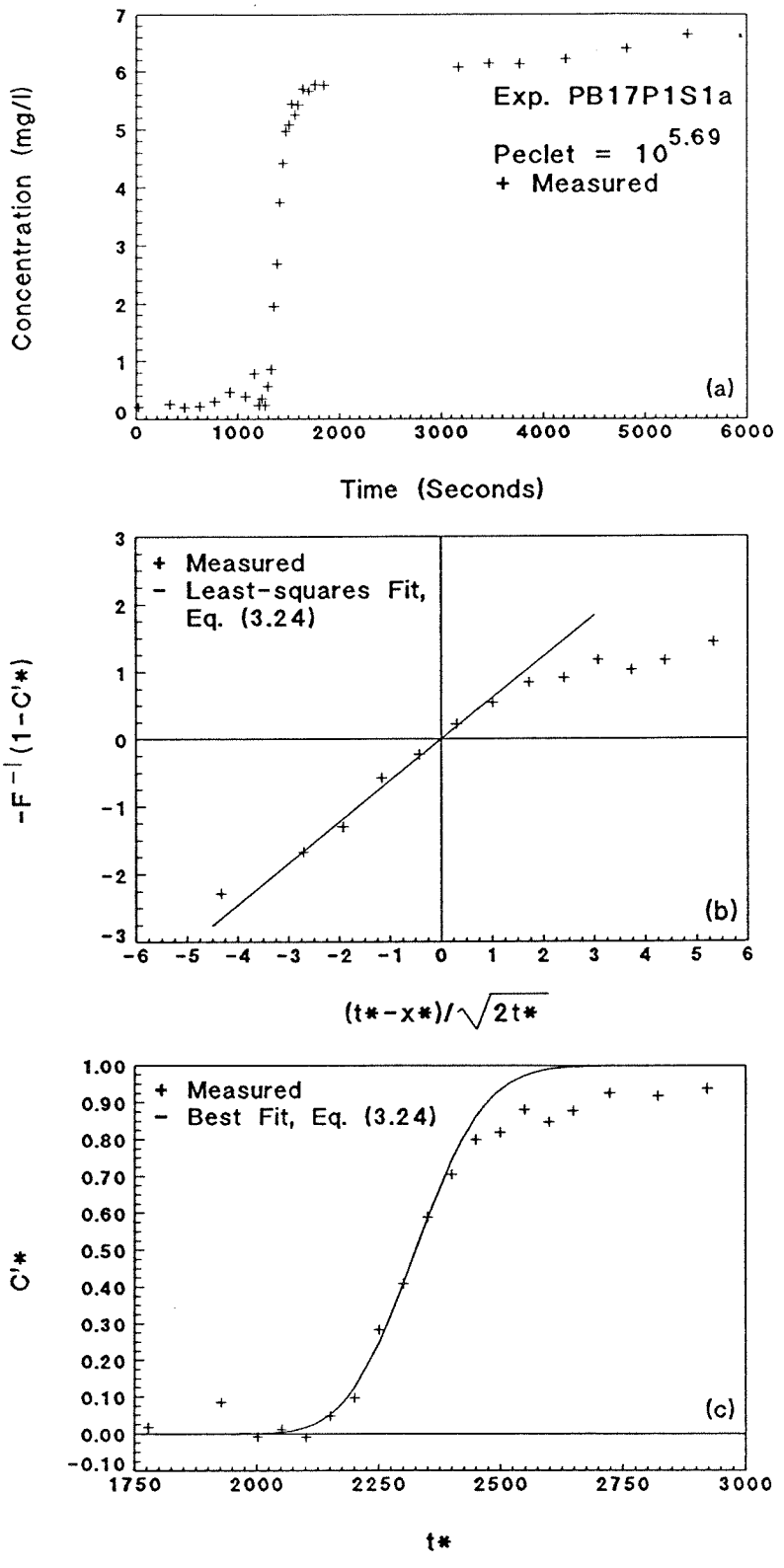

Fig. C.42: Exp. PB17P1S1a forward breakthrough, sample port 3, $Pe_p = 10^{5.69}$: (a) complete experimental data; (b) linearization with least-squares fit; and (c) breakthrough only with best-fit, Eq. (3.24).

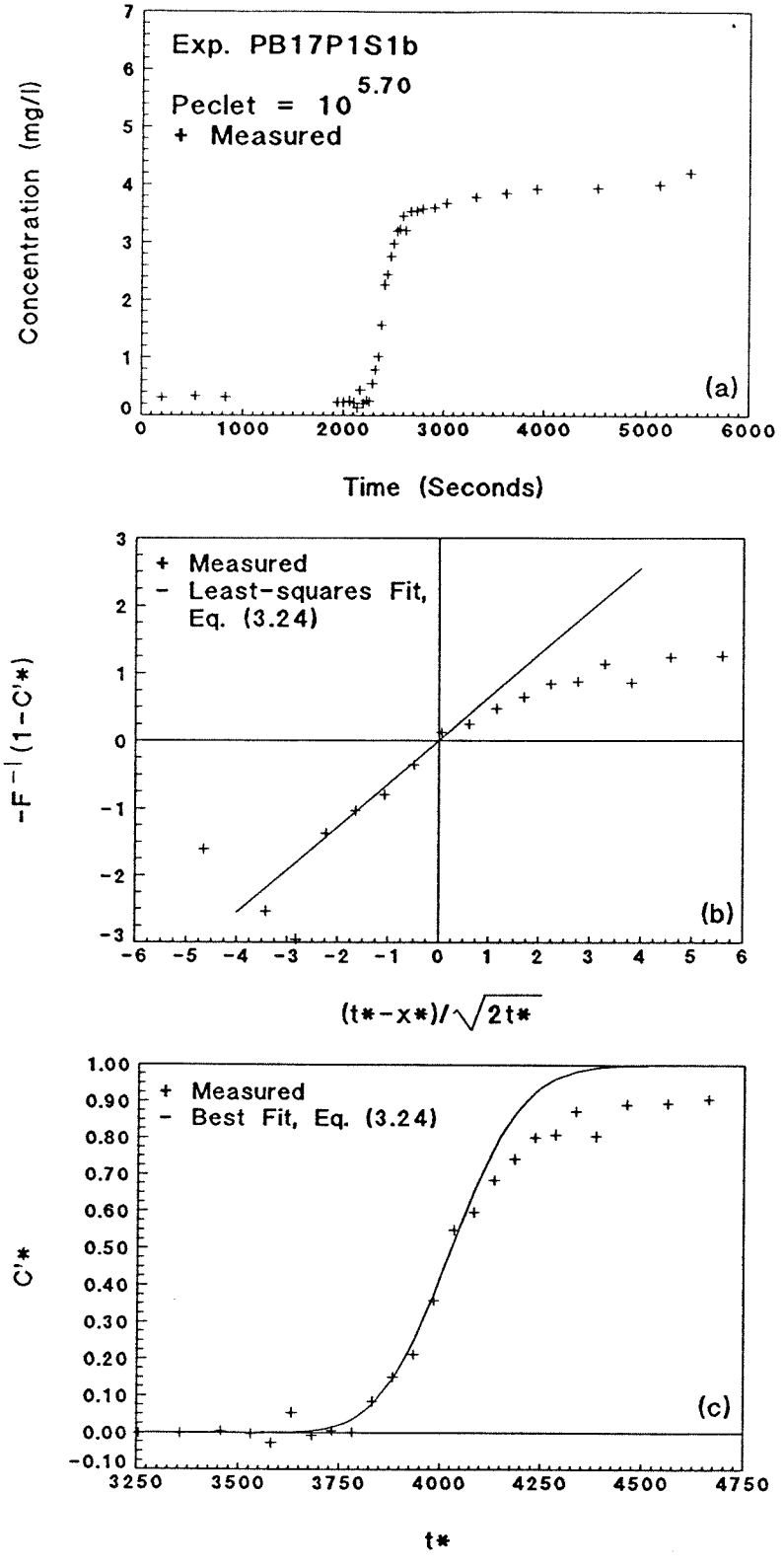

Fig. C.43: Exp. PB17P1S1b forward breakthrough, sample port 5, $Pe_p = 10^{5.70}$: (a) complete experimental data; (b) linearization with least-squares fit; and (c) breakthrough only with best-fit, Eq. (3.24).

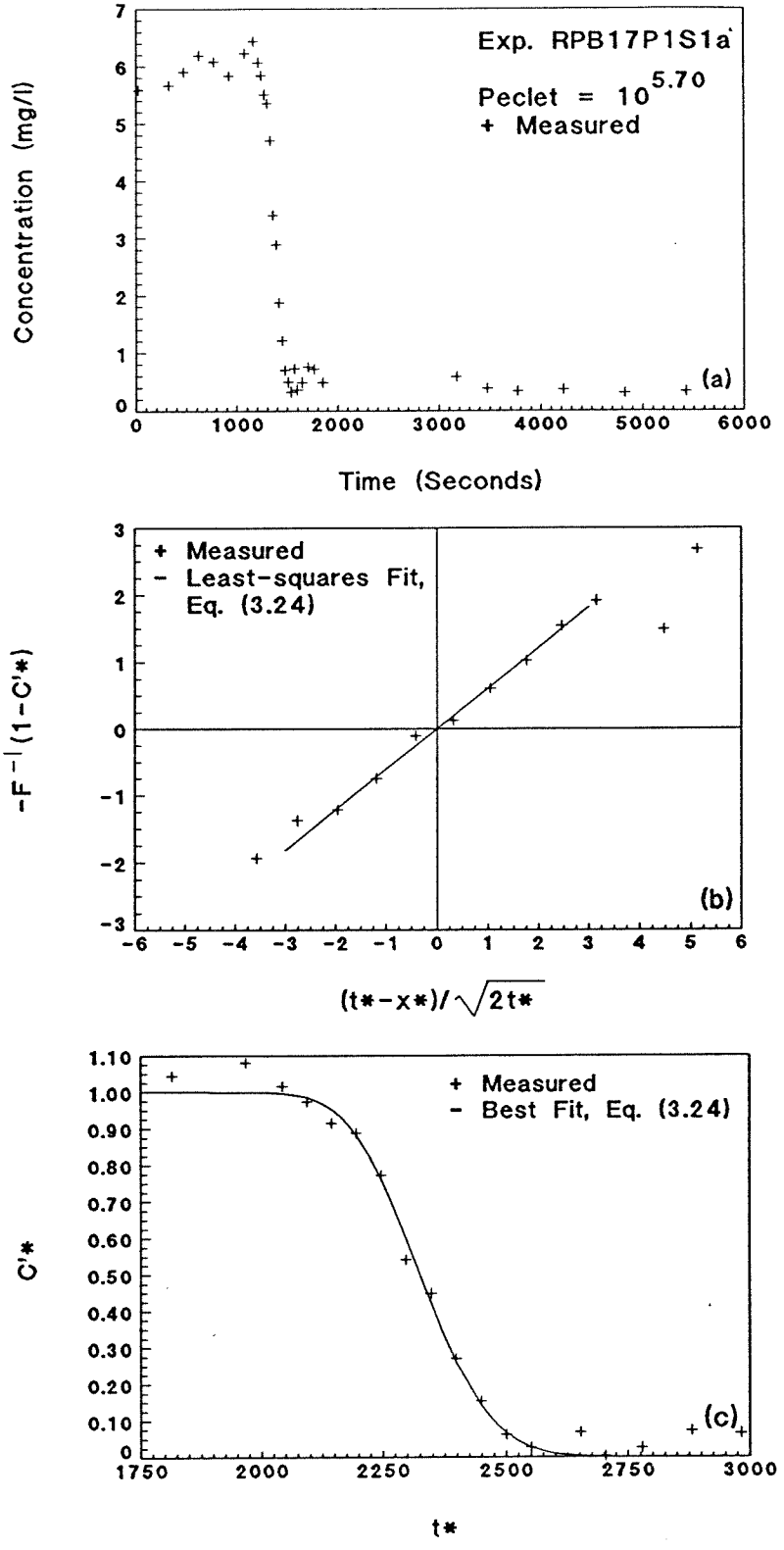

Fig. C.44: Exp. RPB17P1S1a reverse breakthrough, sample port 3, $Pe_p = 10^{5.70}$: (a) complete experimental data; (b) linearization with least-squares fit; and (c) breakthrough only with best-fit, Eq. (3.24).

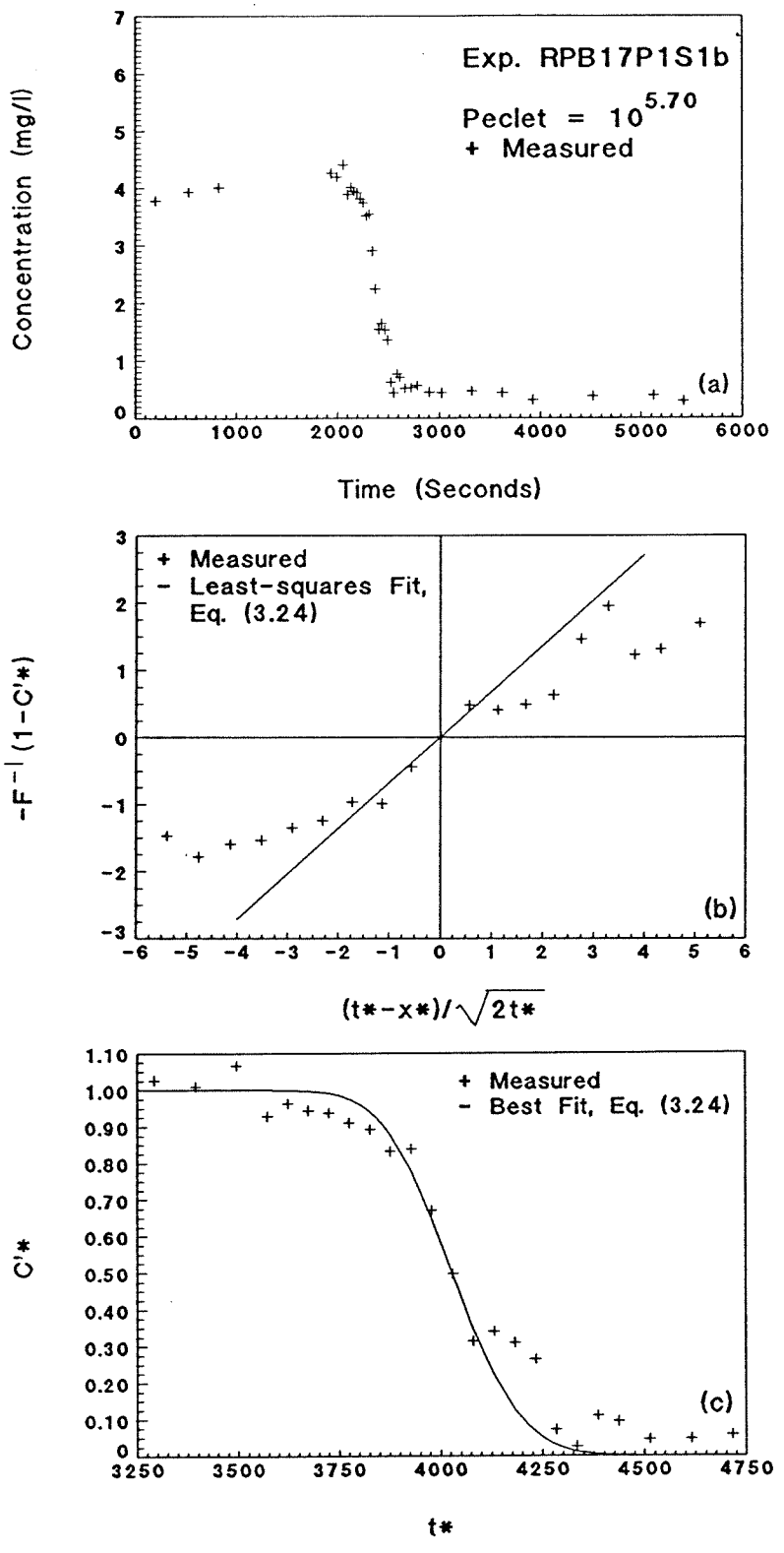

Fig. C.45: Exp. RPB17P1S1b reverse breakthrough, sample port 5, $Pe_p = 10^{5.70}$: (a) complete experimental data; (b) linearization with least-squares fit; and (c) breakthrough only with best-fit, Eq. (3.24).

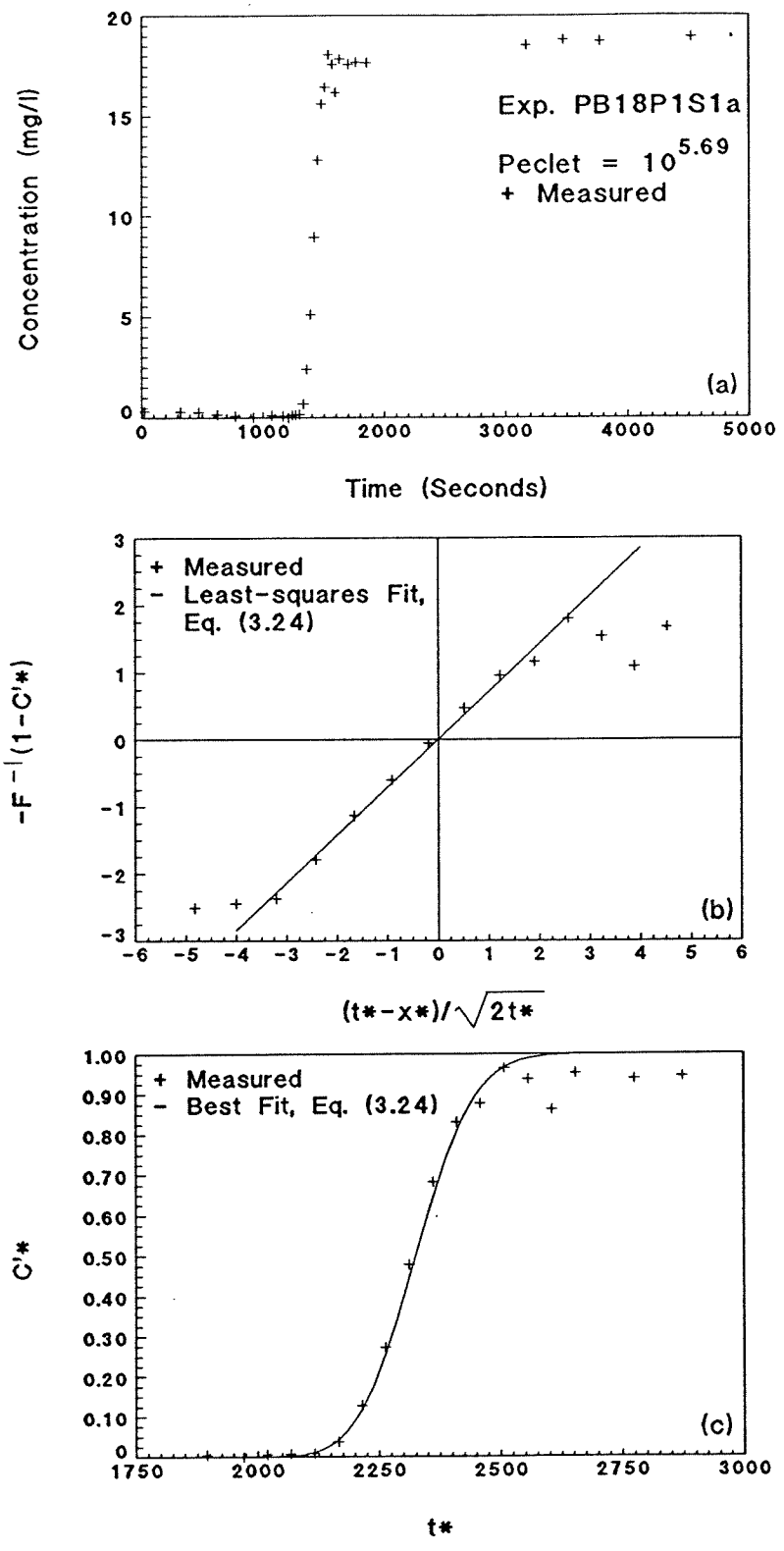

Fig. C.46: Exp. PB18P1S1a forward breakthrough, sample port 3, $Pe_p = 10^{5.68}$: (a) complete experimental data; (b) linearization with least-squares fit; and (c) breakthrough only with best-fit, Eq. (3.24).

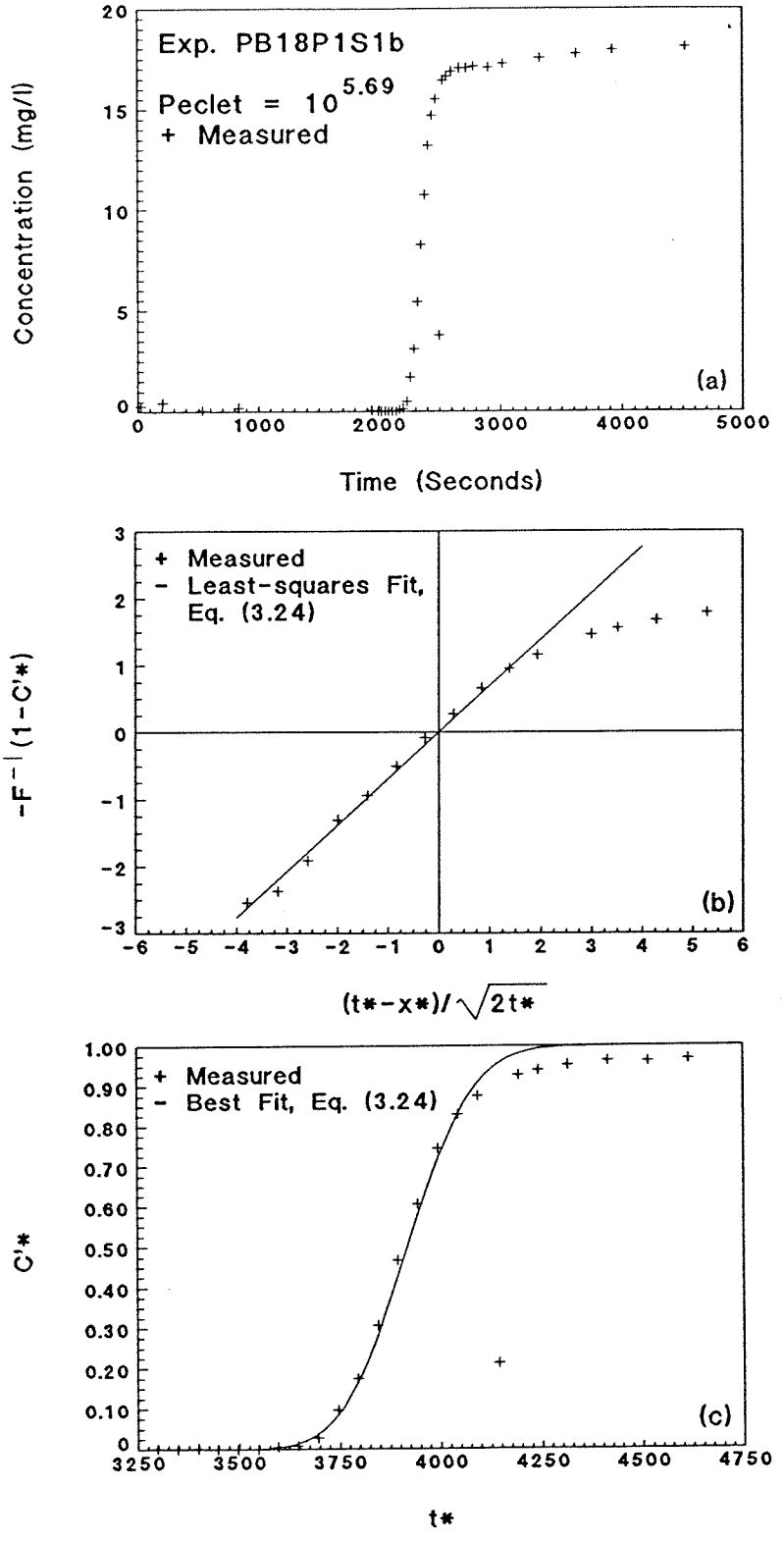

Fig. C.47: Exp. PB18P1S1b forward breakthrough, sample port 5, $Pe_p = 10^{5.69}$: (a) complete experimental data; (b) linearization with least-squares fit; and (c) breakthrough only with best-fit, Eq. (3.24).

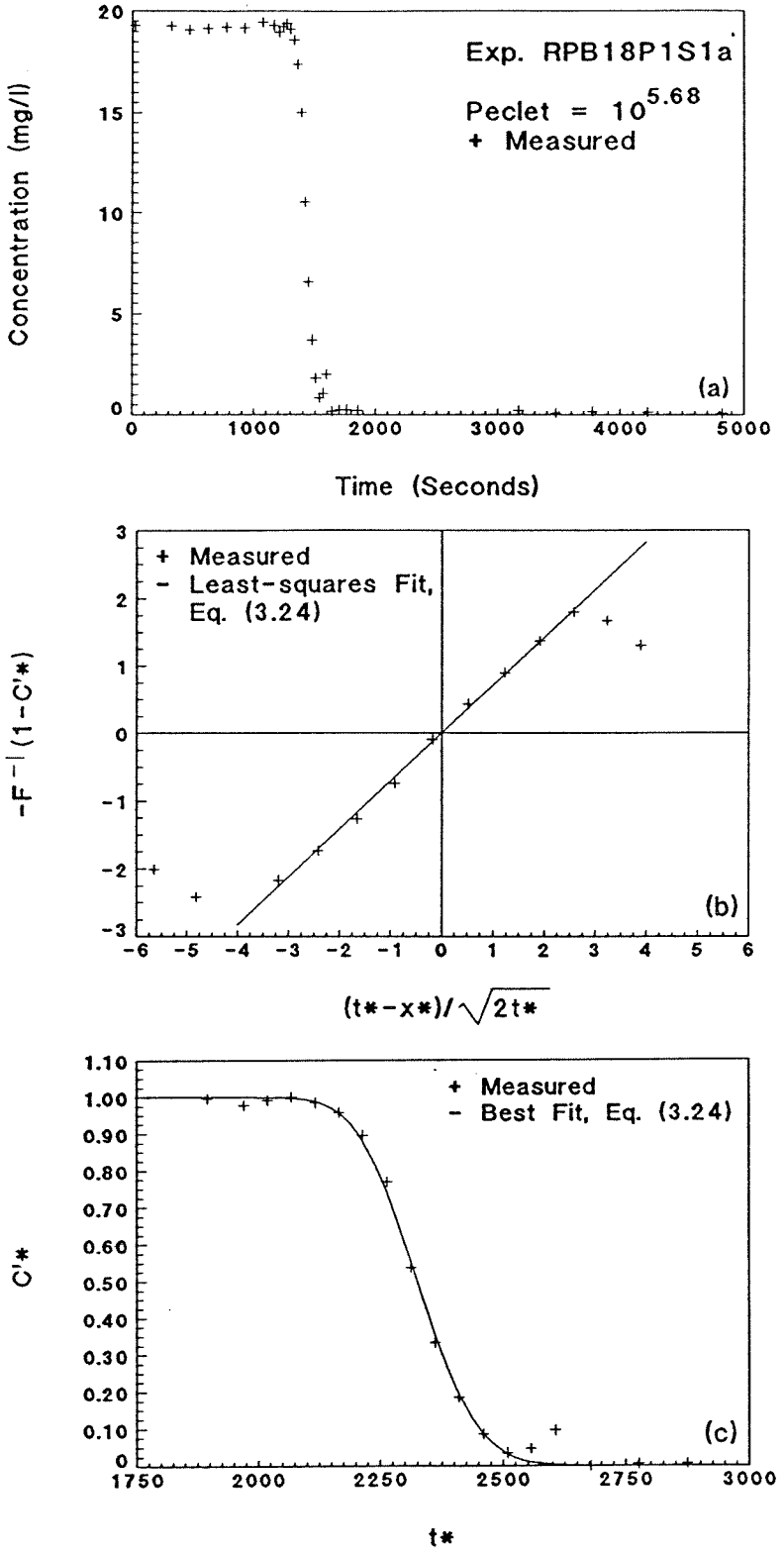

Fig. C.48: Exp. RPB18P1S1a reverse breakthrough, sample port 3, $Pe_p = 10^{5.68}$: (a) complete experimental data; (b) linearization with least-squares fit; and (c) breakthrough only with best-fit, Eq. (3.24).

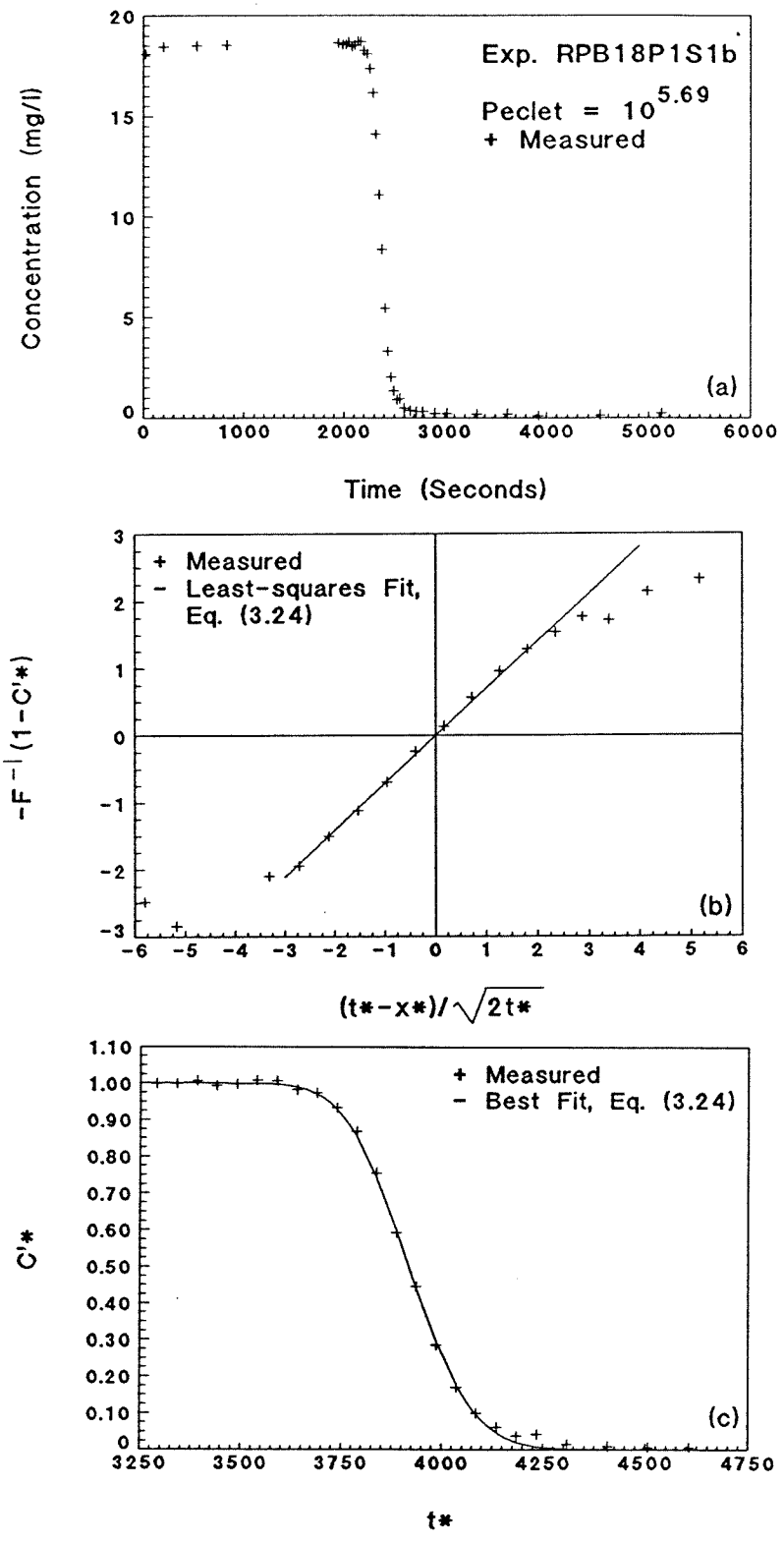

Fig. C.49: Exp. RPB18P1S1b reverse breakthrough, sample port 5, $Pe_p = 10^{5.69}$: (a) complete experimental data; (b) linearization with least-squares fit; and (c) breakthrough only with best-fit, Eq. (3.24).

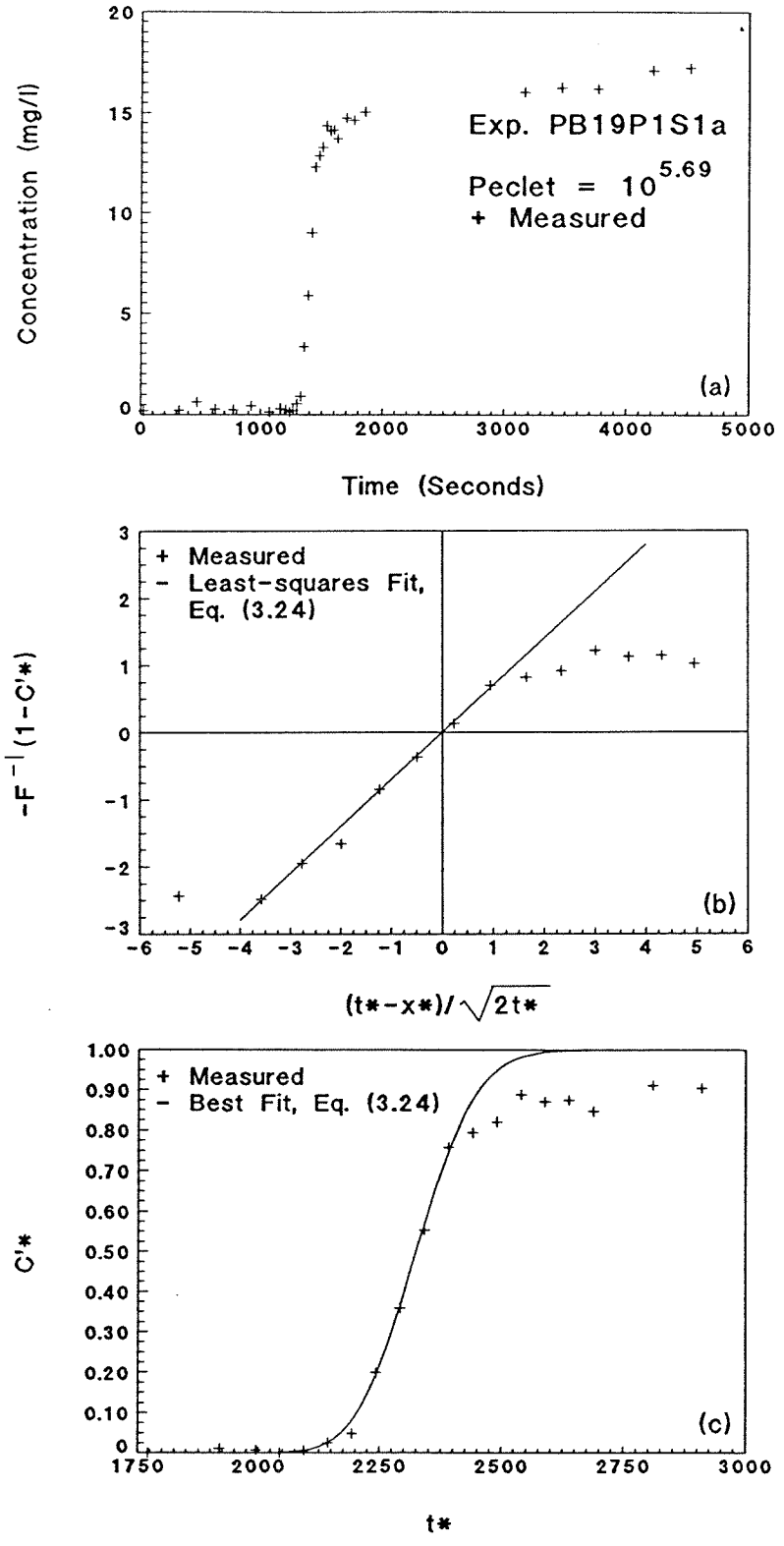

Fig. C.50: Exp. PB19P1S1a forward breakthrough, sample port 3, $Pe_p = 10^{5.69}$: (a) complete experimental data; (b) linearization with least-squares fit; and (c) breakthrough only with best-fit, Eq. (3.24).

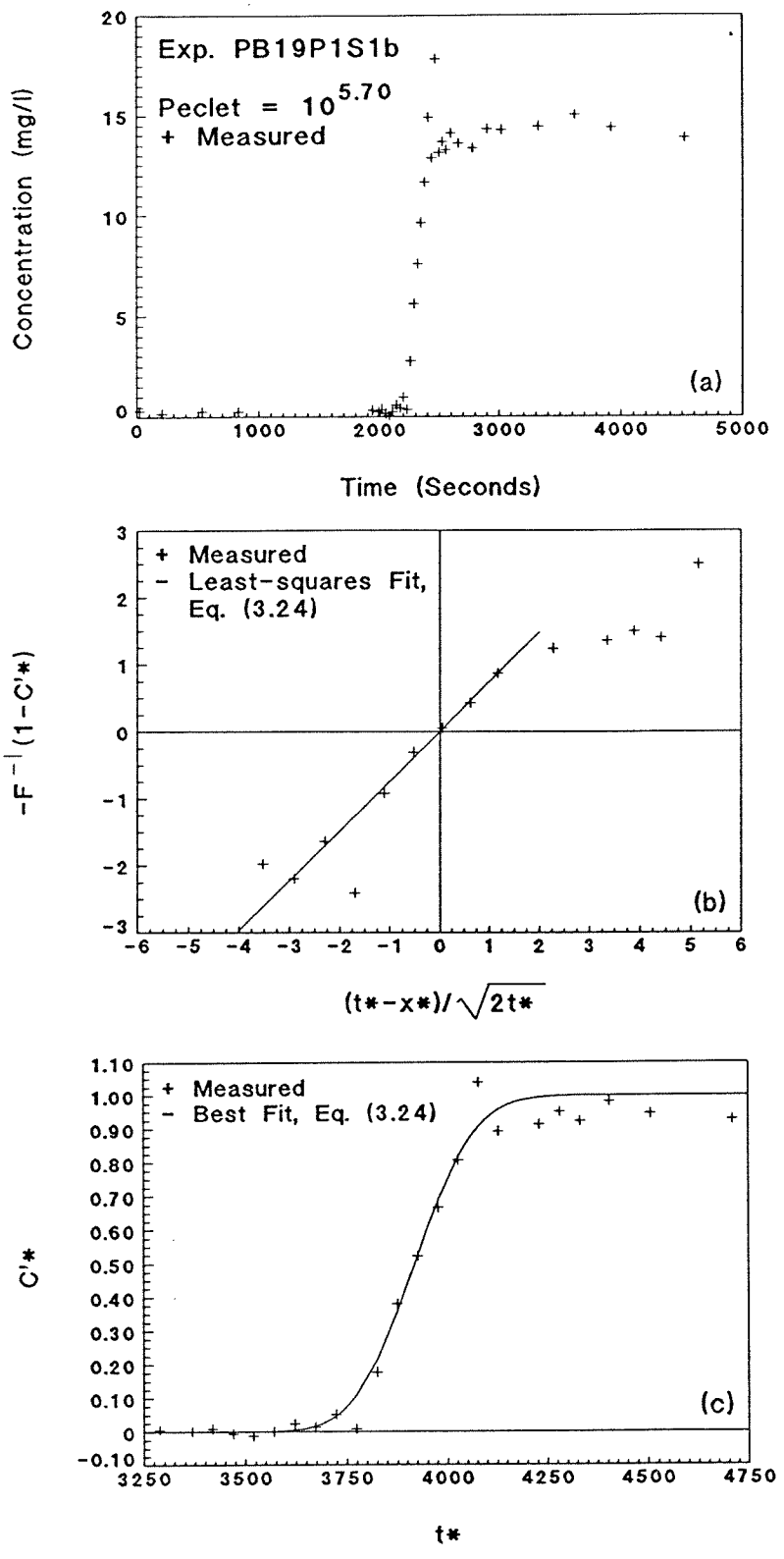

Fig. C.51: Exp. PB19P1S1b forward breakthrough, sample port 5, $Pe_p = 10^{5.70}$: (a) complete experimental data; (b) linearization with least-squares fit; and (c) breakthrough only with best-fit, Eq. (3.24).

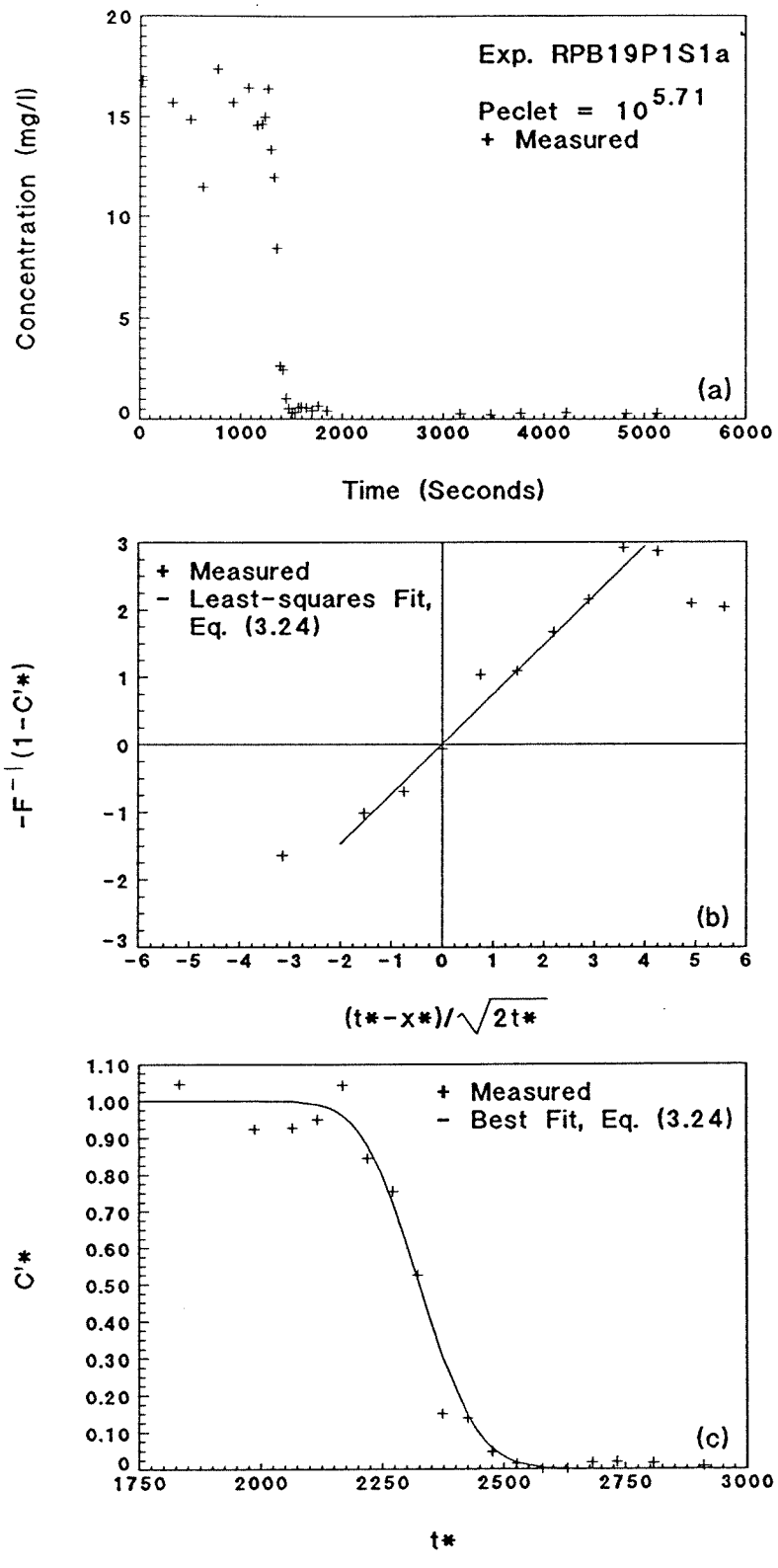

Fig. C.52: Exp. RPB19P1S1a reverse breakthrough, sample port 3, $Pe_p = 10^{5.71}$: (a) complete experimental data; (b) linearization with least-squares fit; and (c) breakthrough only with best-fit, Eq. (3.24).

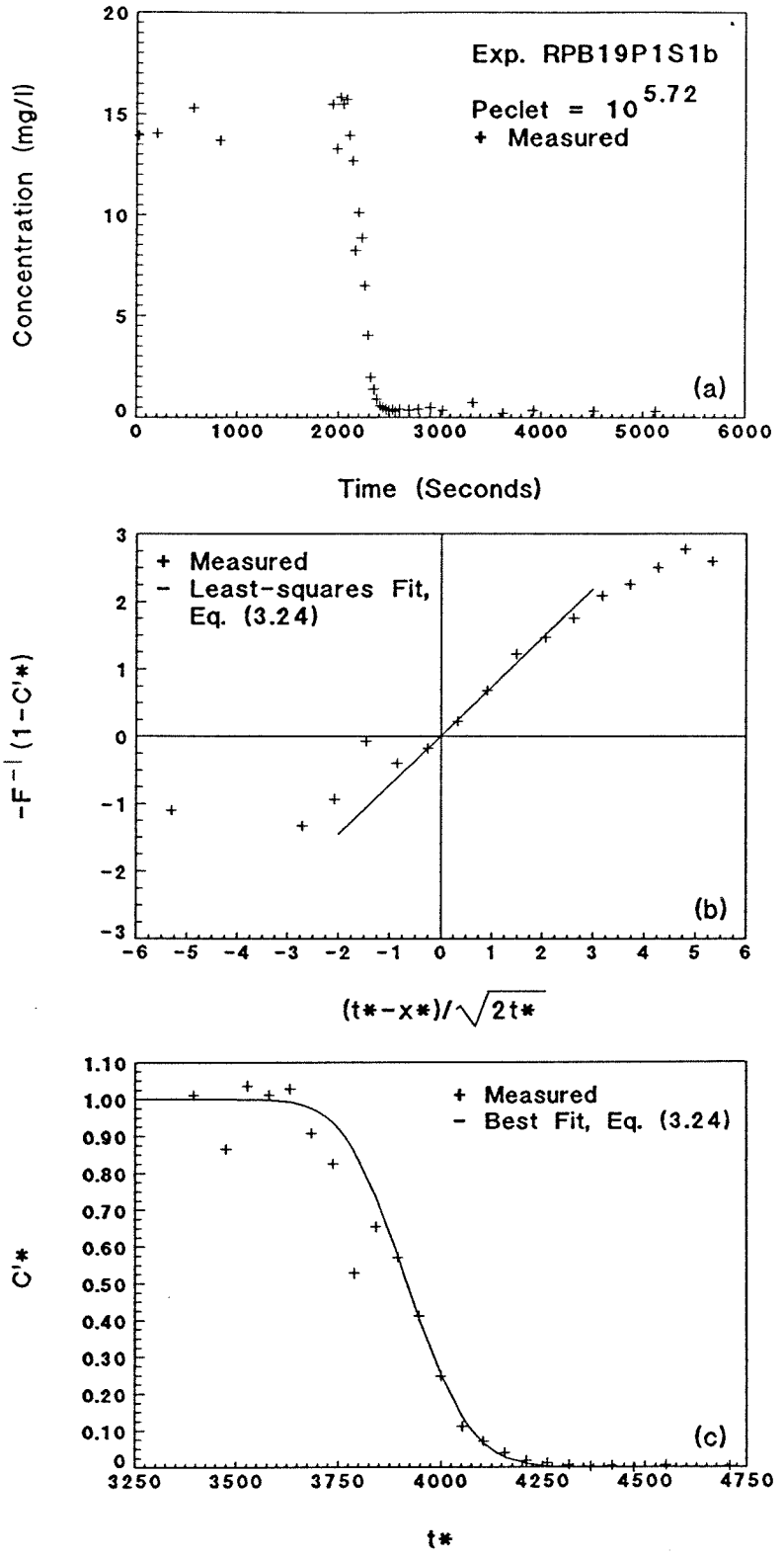

Fig. C.53: Exp. RPB19P1S1b reverse breakthrough, sample port 5, $Pe_p = 10^{5.72}$: (a) complete experimental data; (b) linearization with least-squares fit; and (c) breakthrough only with best-fit, Eq. (3.24).

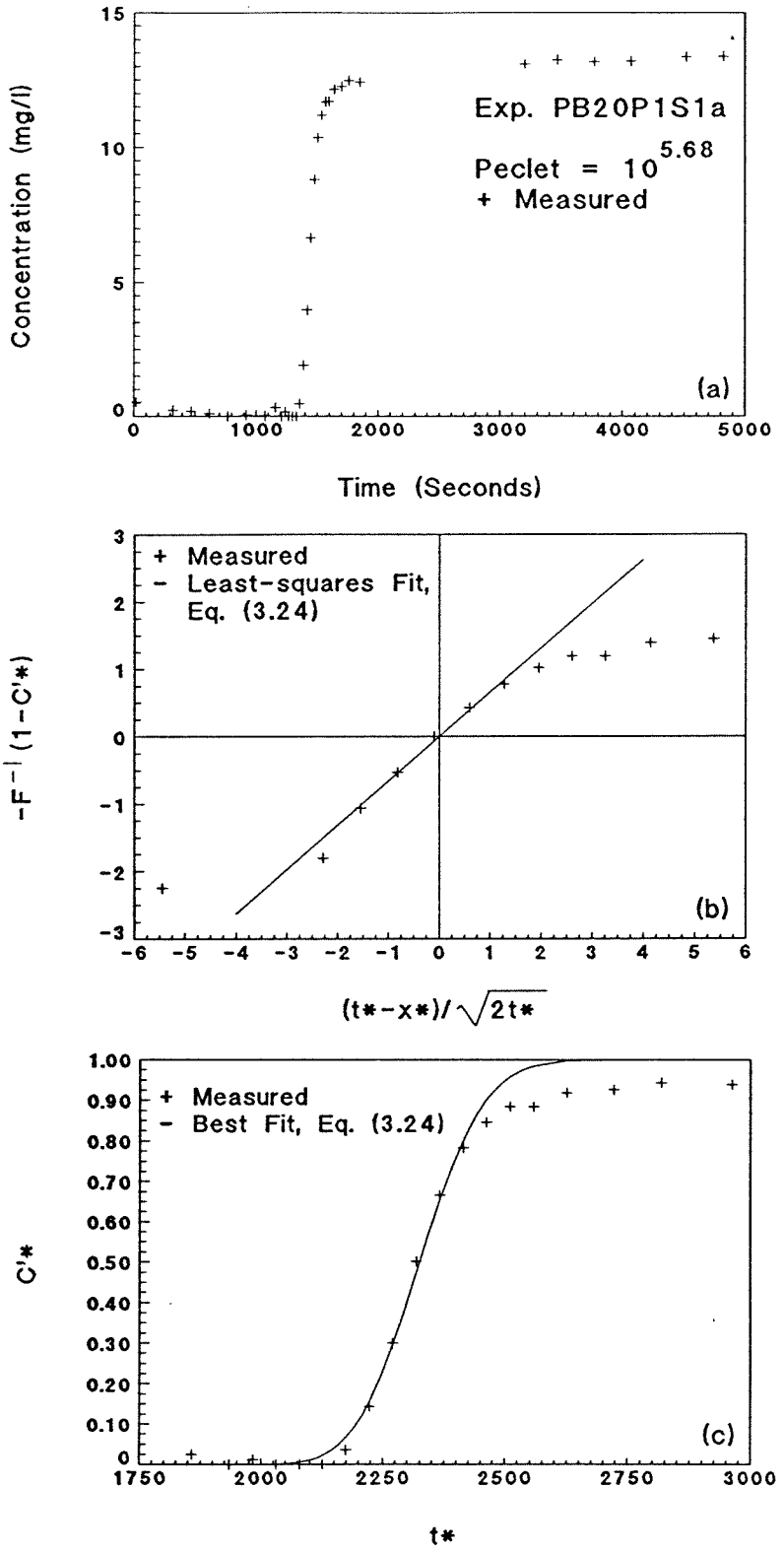

Fig. C.54: Exp. PB20P1S1a forward breakthrough, sample port 3, $Pe_p = 10^{5.68}$: (a) complete experimental data; (b) linearization with least-squares fit; and (c) breakthrough only with best-fit, Eq. (3.24).

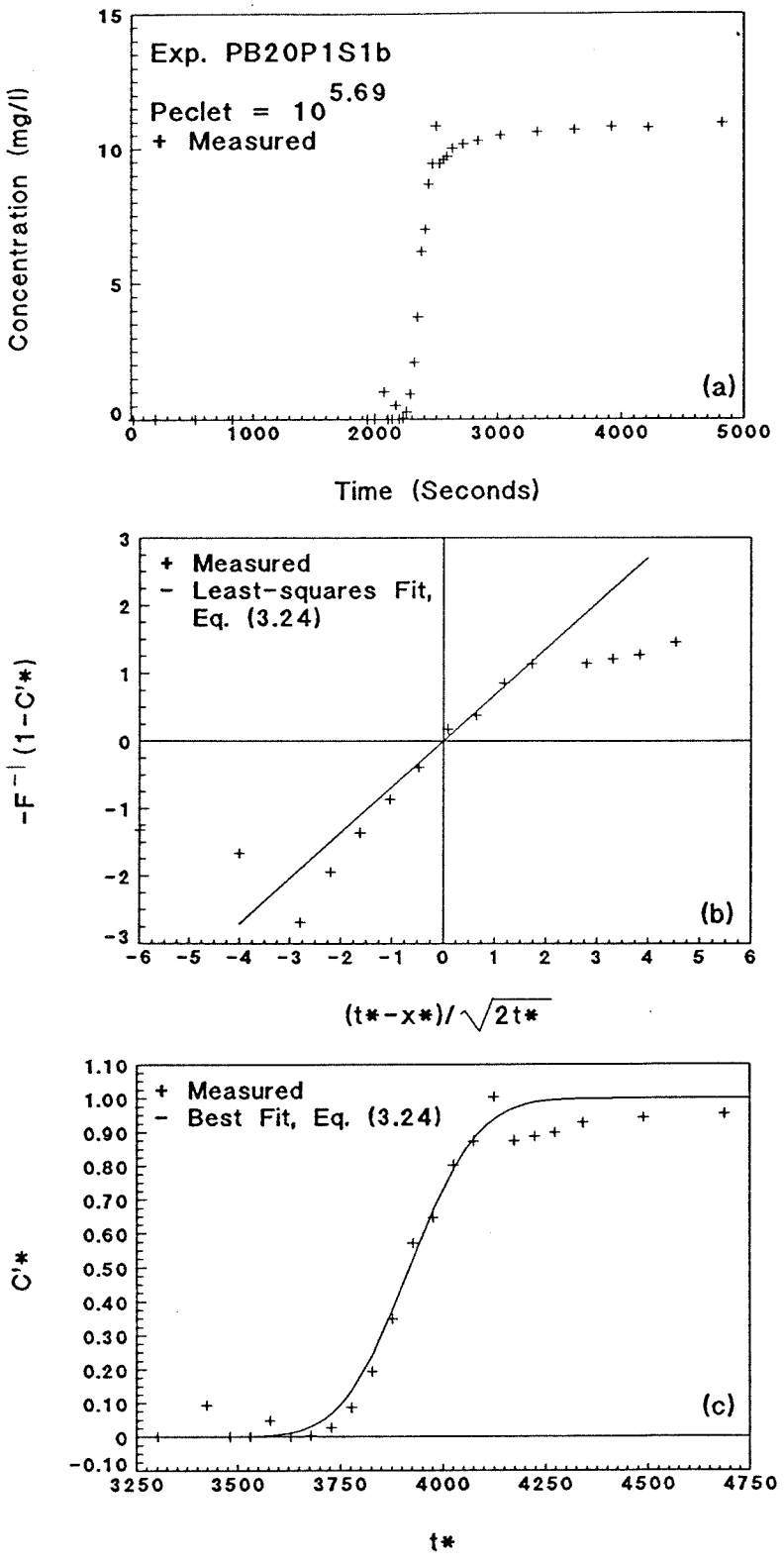

Fig. C.55: Exp. PB20P1S1b forward breakthrough, sample port 5, $Pe_p = 10^{5.69}$: (a) complete experimental data; (b) linearization with least-squares fit; and (c) breakthrough only with best-fit, Eq. (3.24).

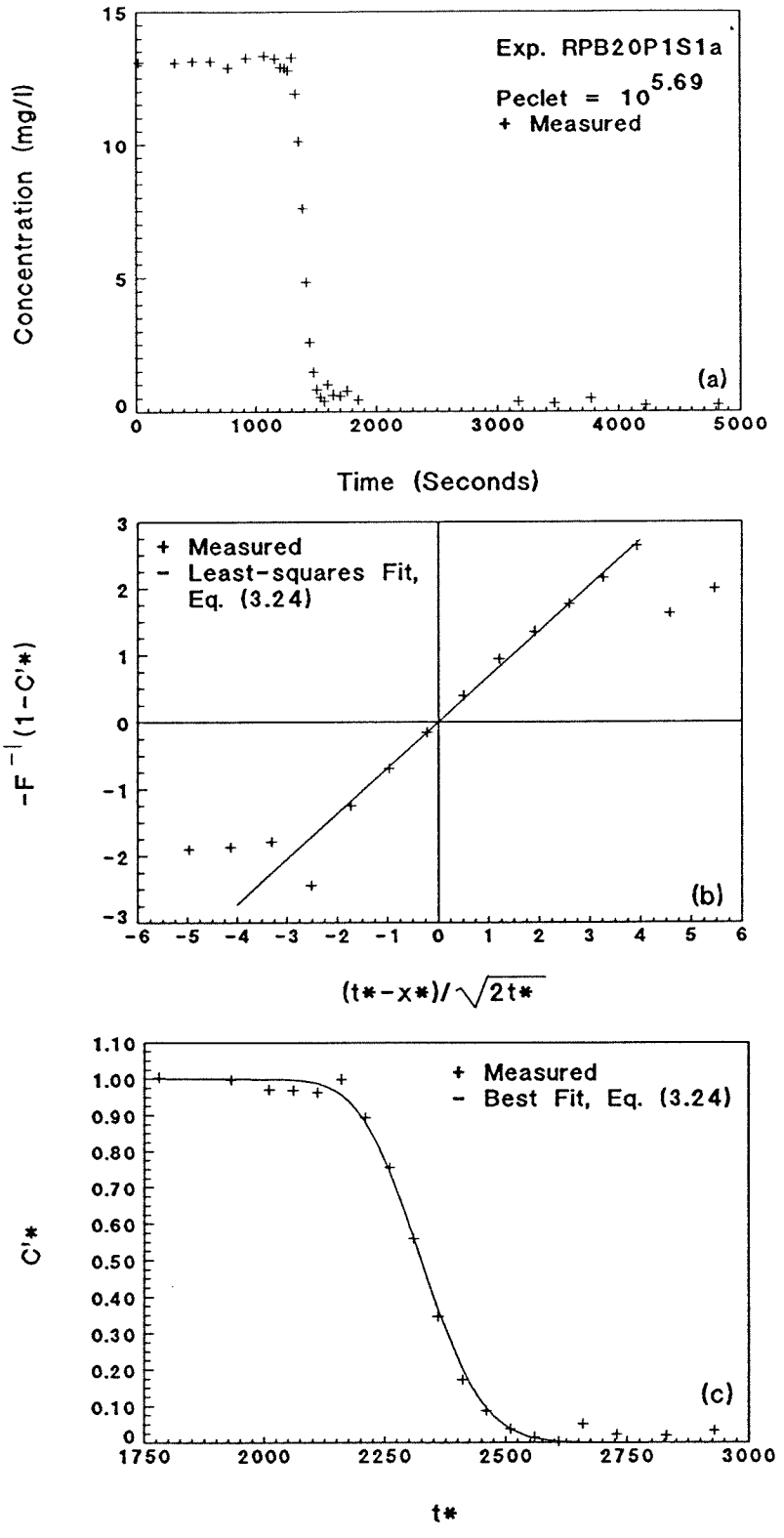

Fig. C.56: Exp. RPB20P1S1a reverse breakthrough, sample port 3, $Pe_p = 10^{5.69}$: (a) complete experimental data; (b) linearization with least-squares fit; and (c) breakthrough only with best-fit, Eq. (3.24).

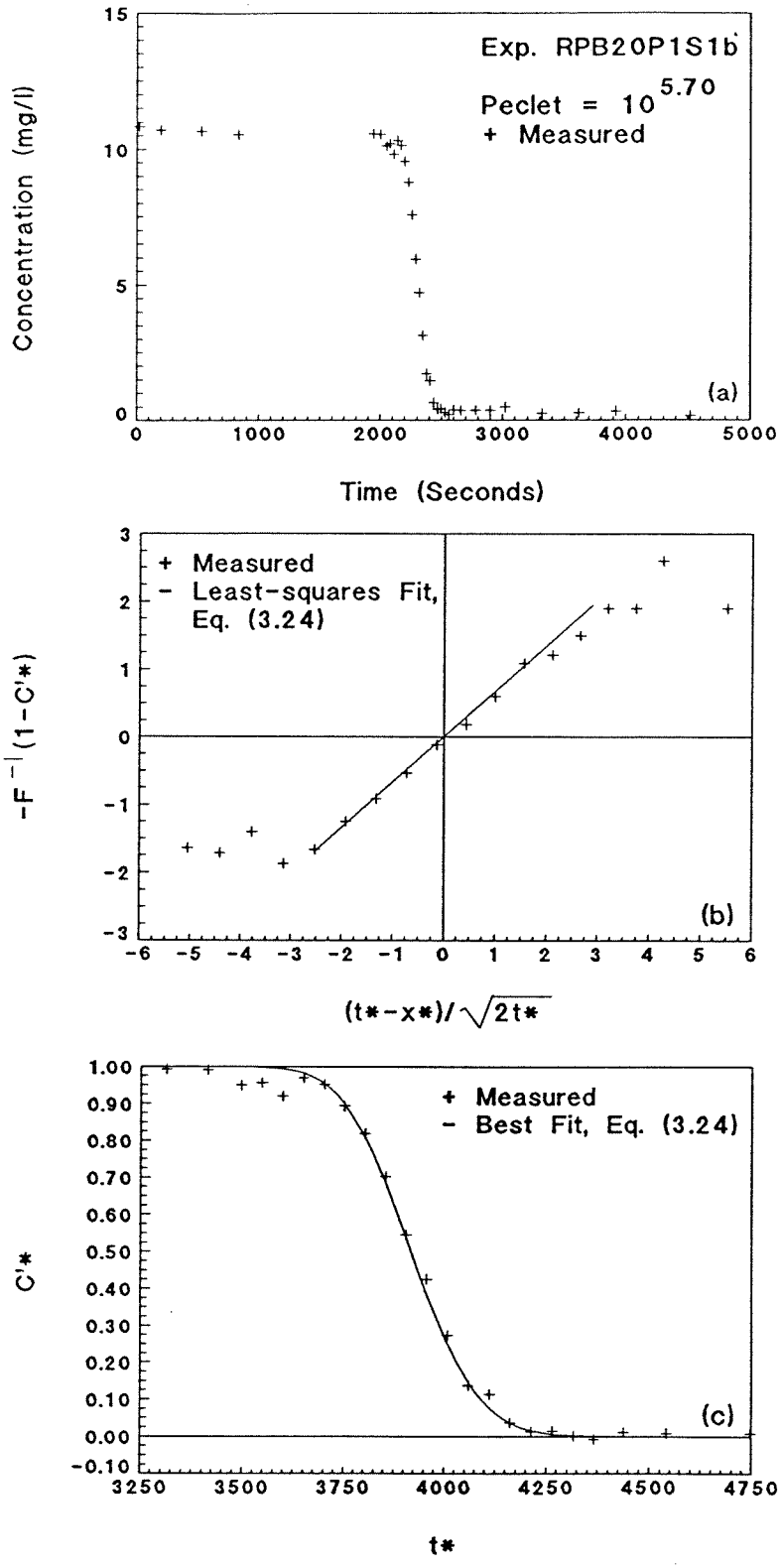

Fig. C.57: Exp. RPB20P1S1b reverse breakthrough, sample port 5, $Pe_p = 10^{5.70}$: (a) complete experimental data; (b) linearization with least-squares fit; and (c) breakthrough only with best-fit, Eq. (3.24).

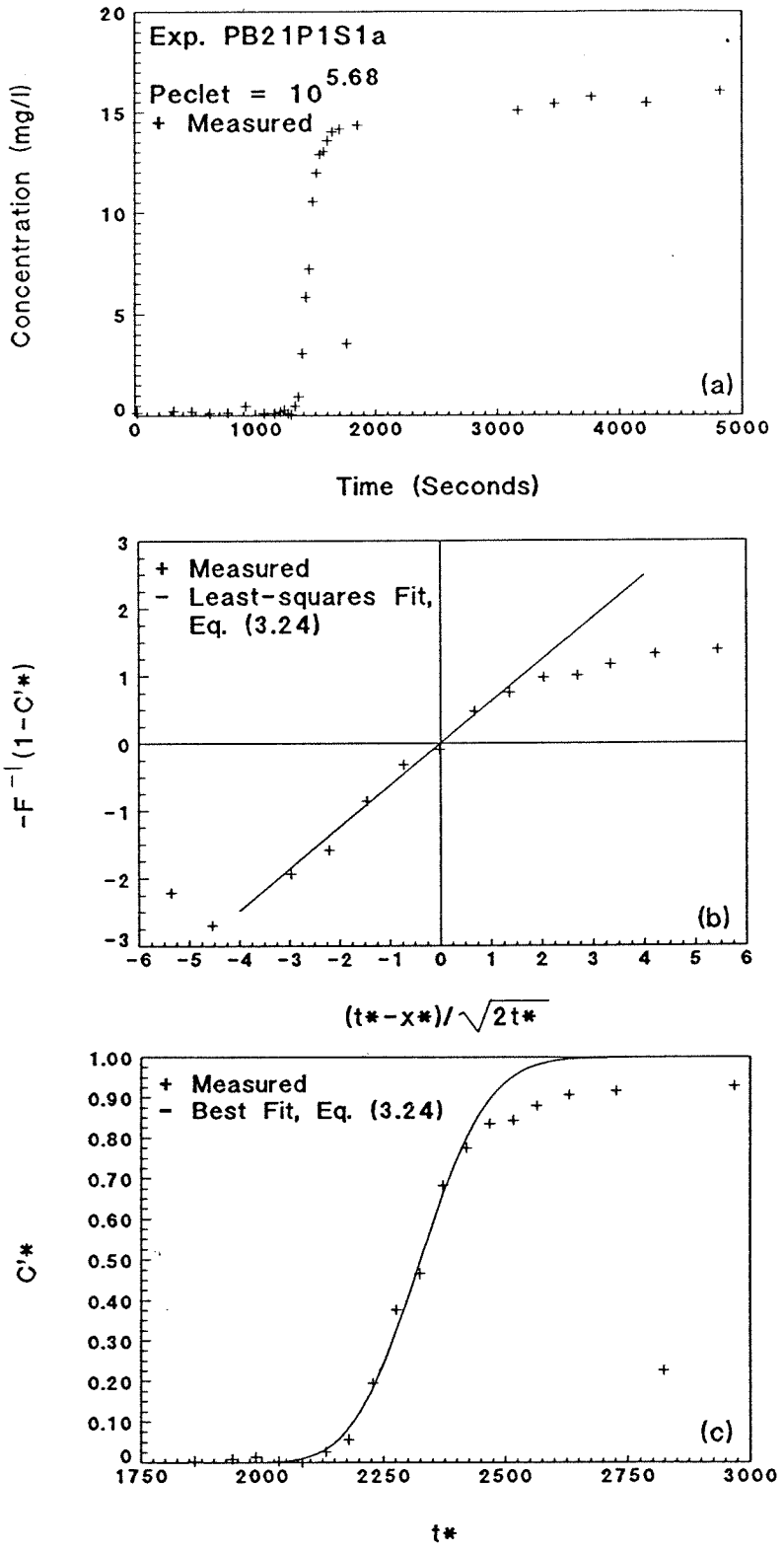

Fig. C.58: Exp. PB21P1S1a forward breakthrough, sample port 3, $Pe_p = 10^{5.68}$: (a) complete experimental data; (b) linearization with least-squares fit; and (c) breakthrough only with best-fit, Eq. (3.24).

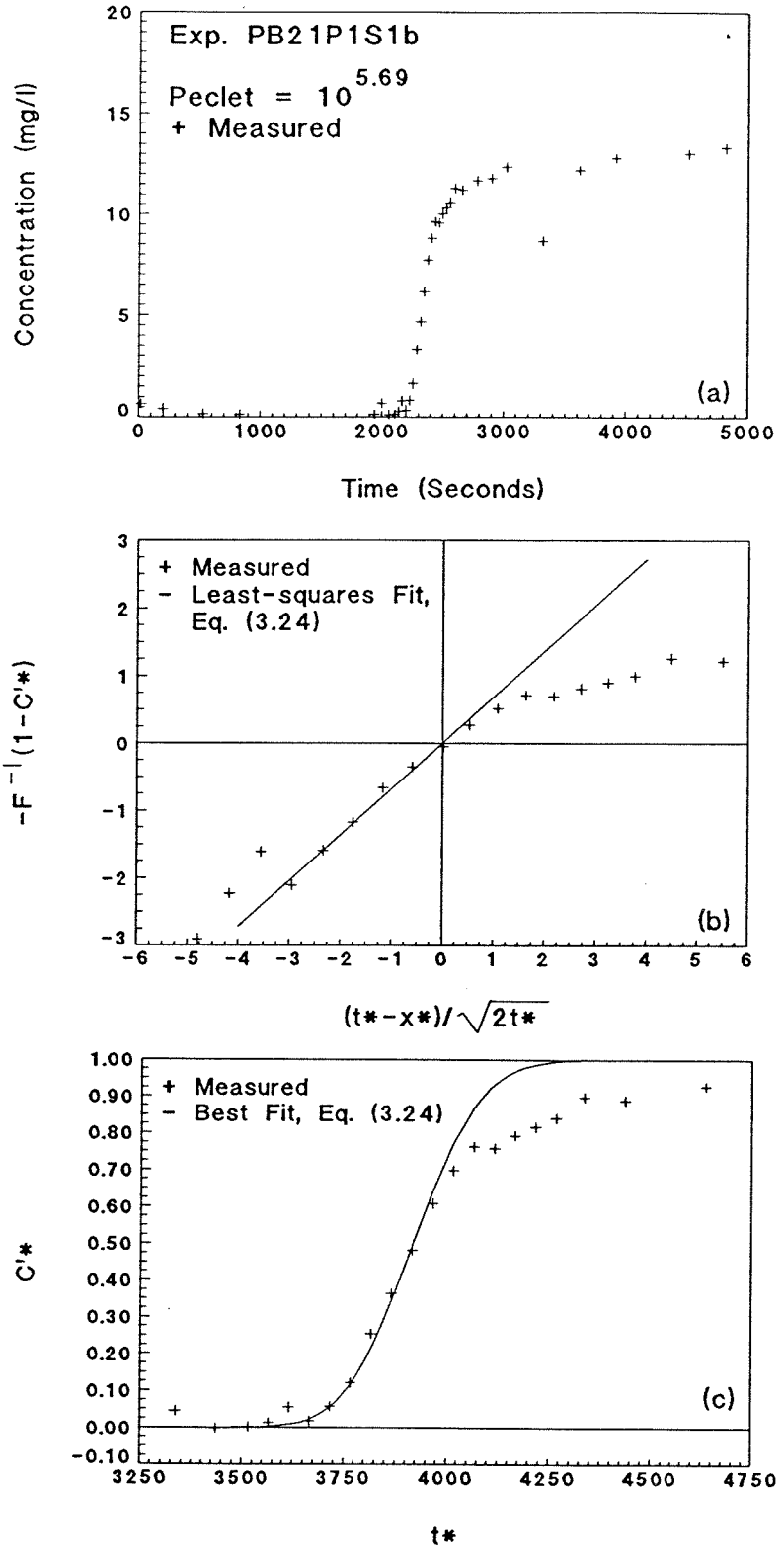

Fig. C.59: Exp. PB21P1S1b forward breakthrough, sample port 5, $Pe_p = 10^{5.69}$: (a) complete experimental data; (b) linearization with least-squares fit; and (c) breakthrough only with best-fit, Eq. (3.24).

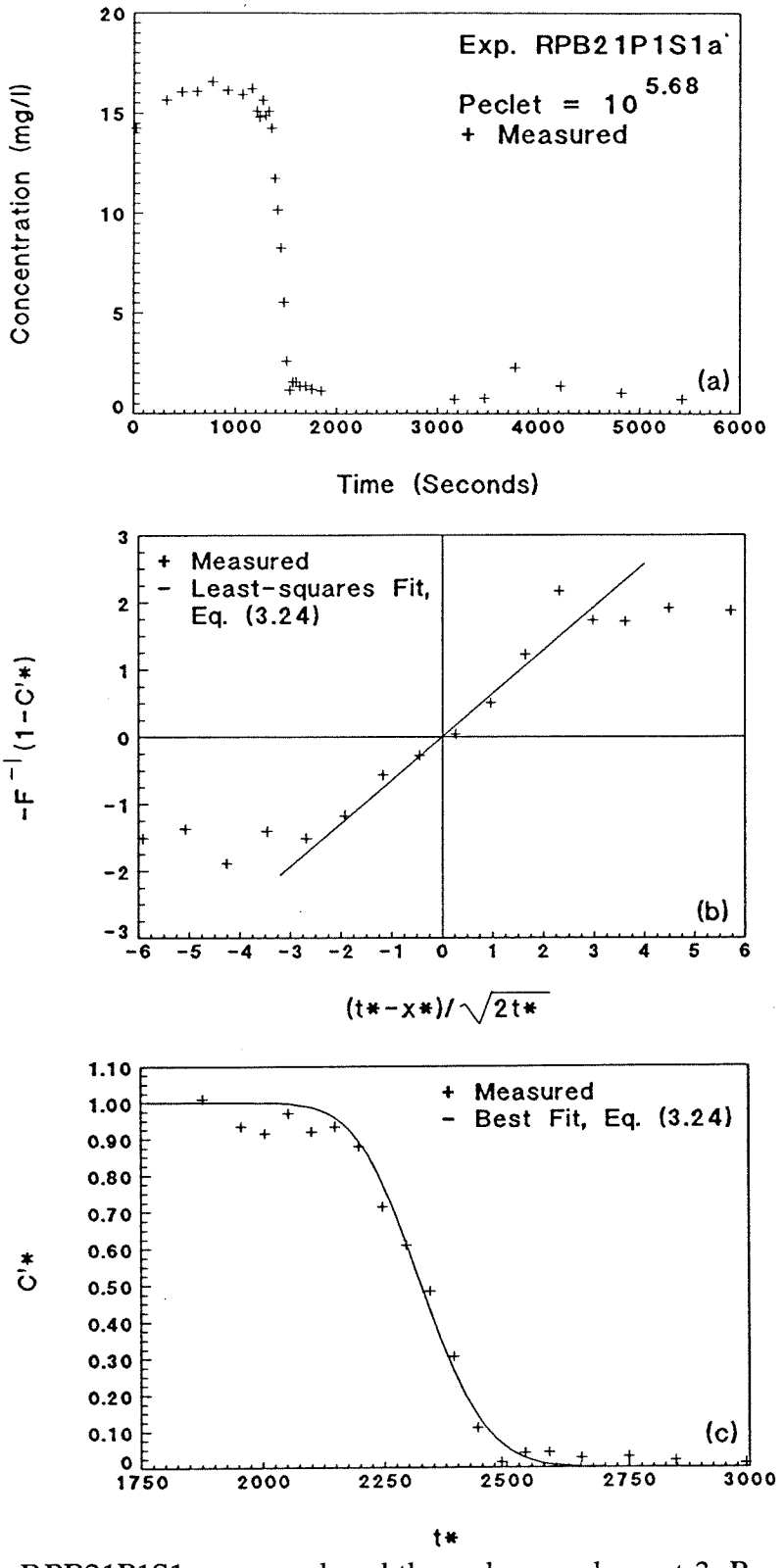

Fig. C.60: Exp. RPB21P1S1a reverse breakthrough, sample port 3, $Pe_p = 10^{5.68}$: (a) complete experimental data; (b) linearization with least-squares fit; and (c) breakthrough only with best-fit, Eq. (3.24).

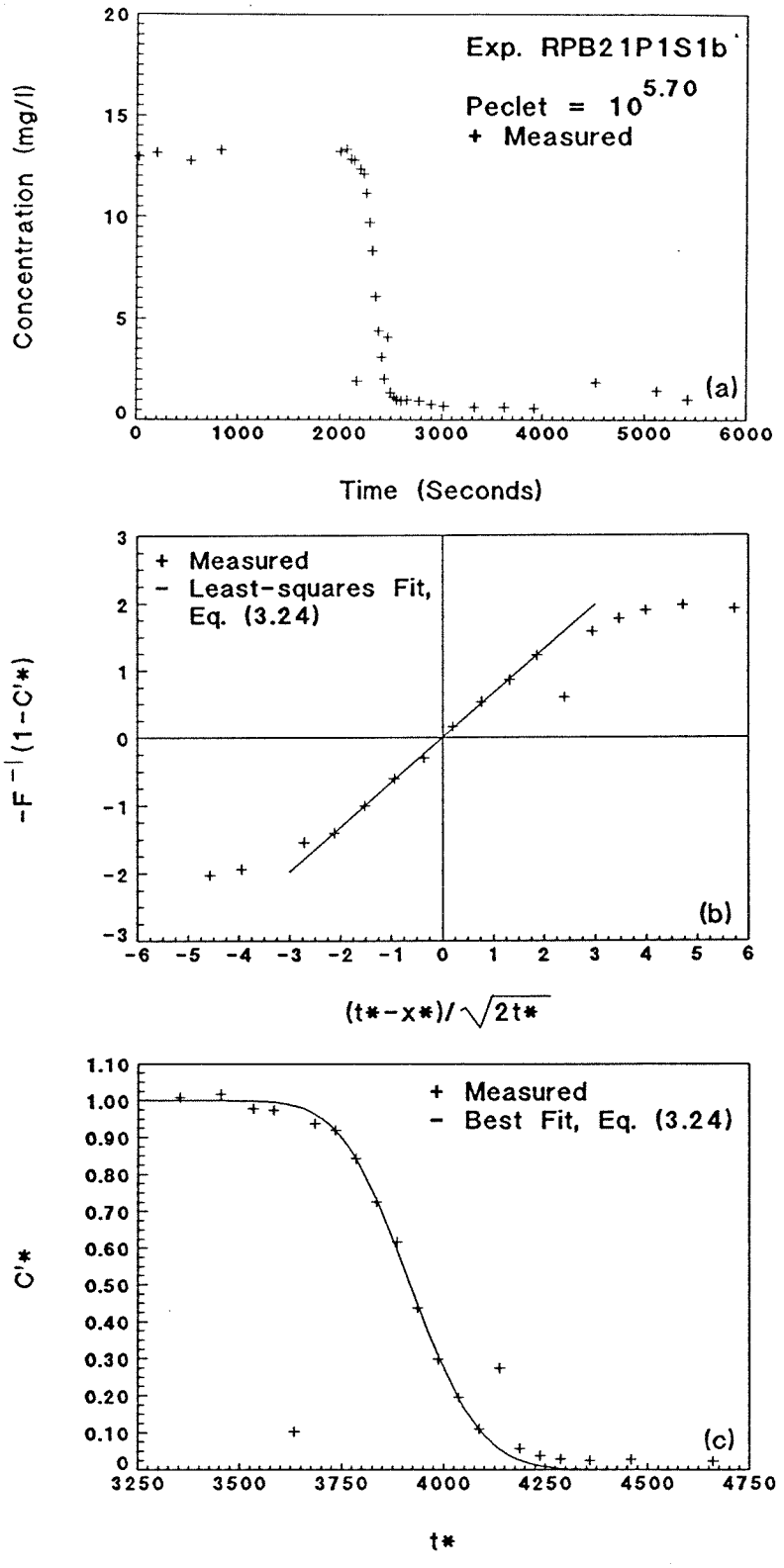

Fig. C.61: Exp. RPB21P1S1b reverse breakthrough, sample port 5, $Pe_p = 10^{5.70}$: (a) complete experimental data; (b) linearization with least-squares fit; and (c) breakthrough only with best-fit, Eq. (3.24).

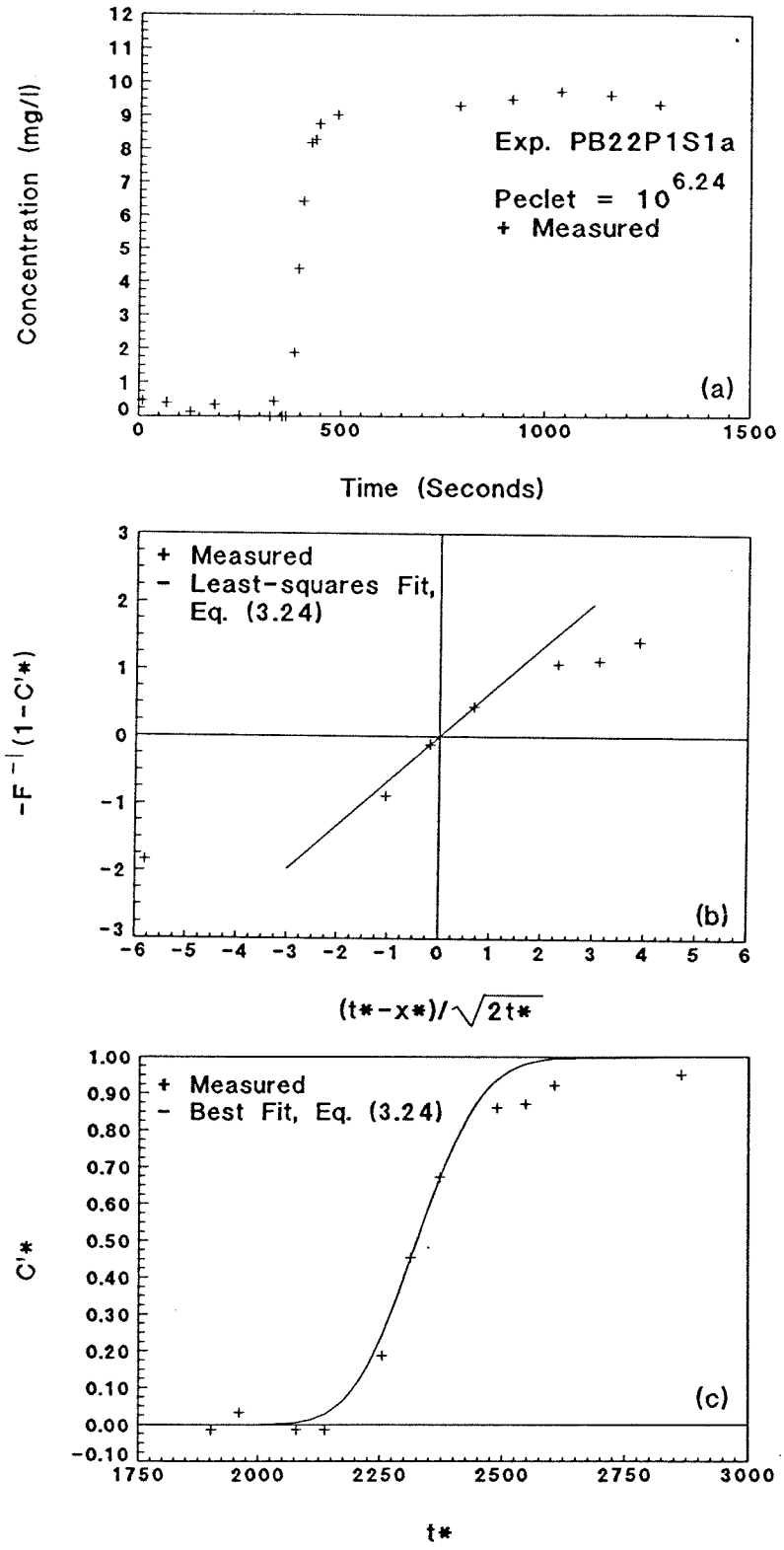

Fig. C.62: Exp. PB22P1S1a forward breakthrough, sample port 3, $Pe_p = 10^{6.24}$: (a) complete experimental data; (b) linearization with least-squares fit; and (c) breakthrough only with best-fit, Eq. (3.24).

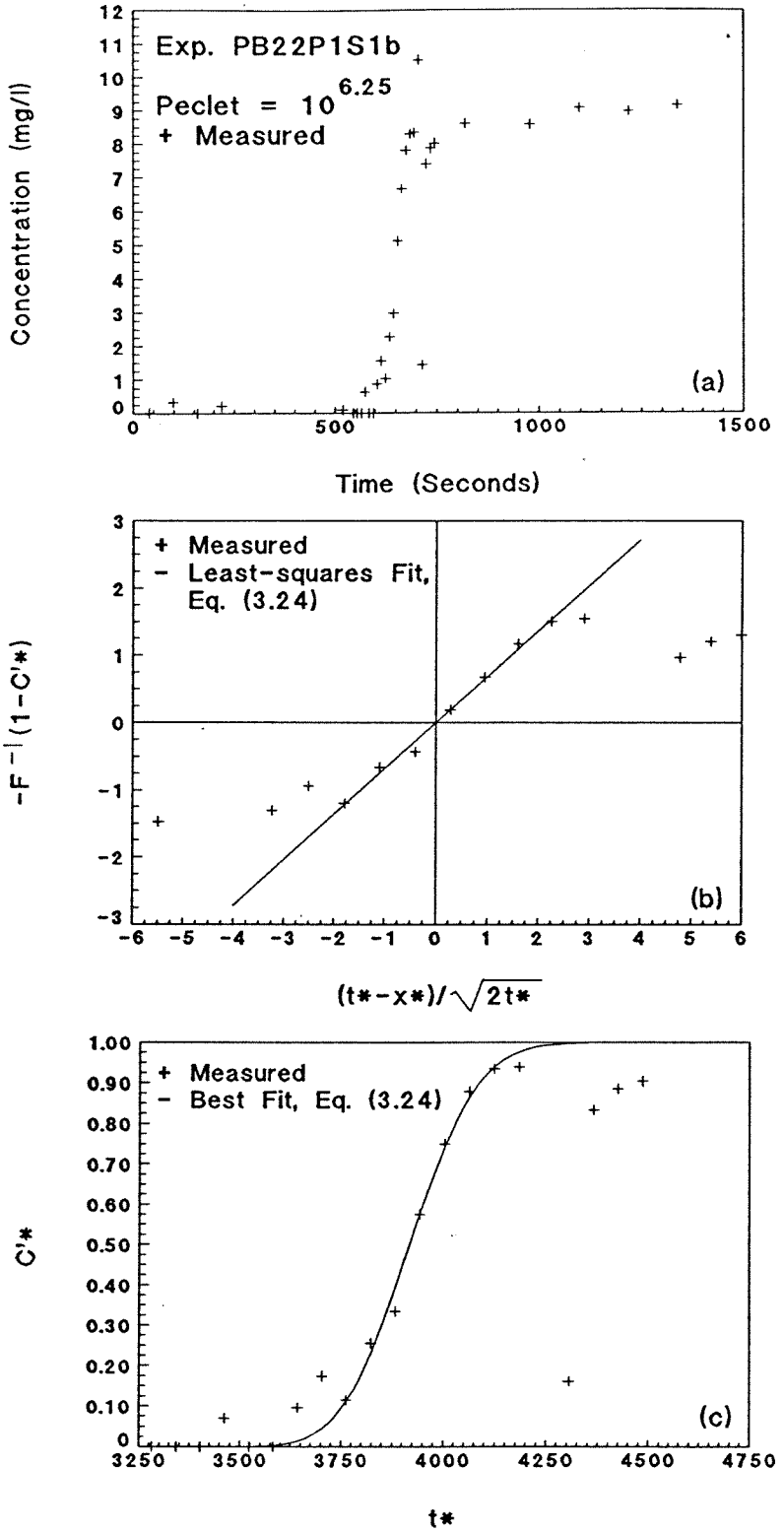

Fig. C.63: Exp. PB22P1S1b forward breakthrough, sample port 5, $Pe_p = 10^{6.25}$: (a) complete experimental data; (b) linearization with least-squares fit; and (c) breakthrough only with best-fit, Eq. (3.24).

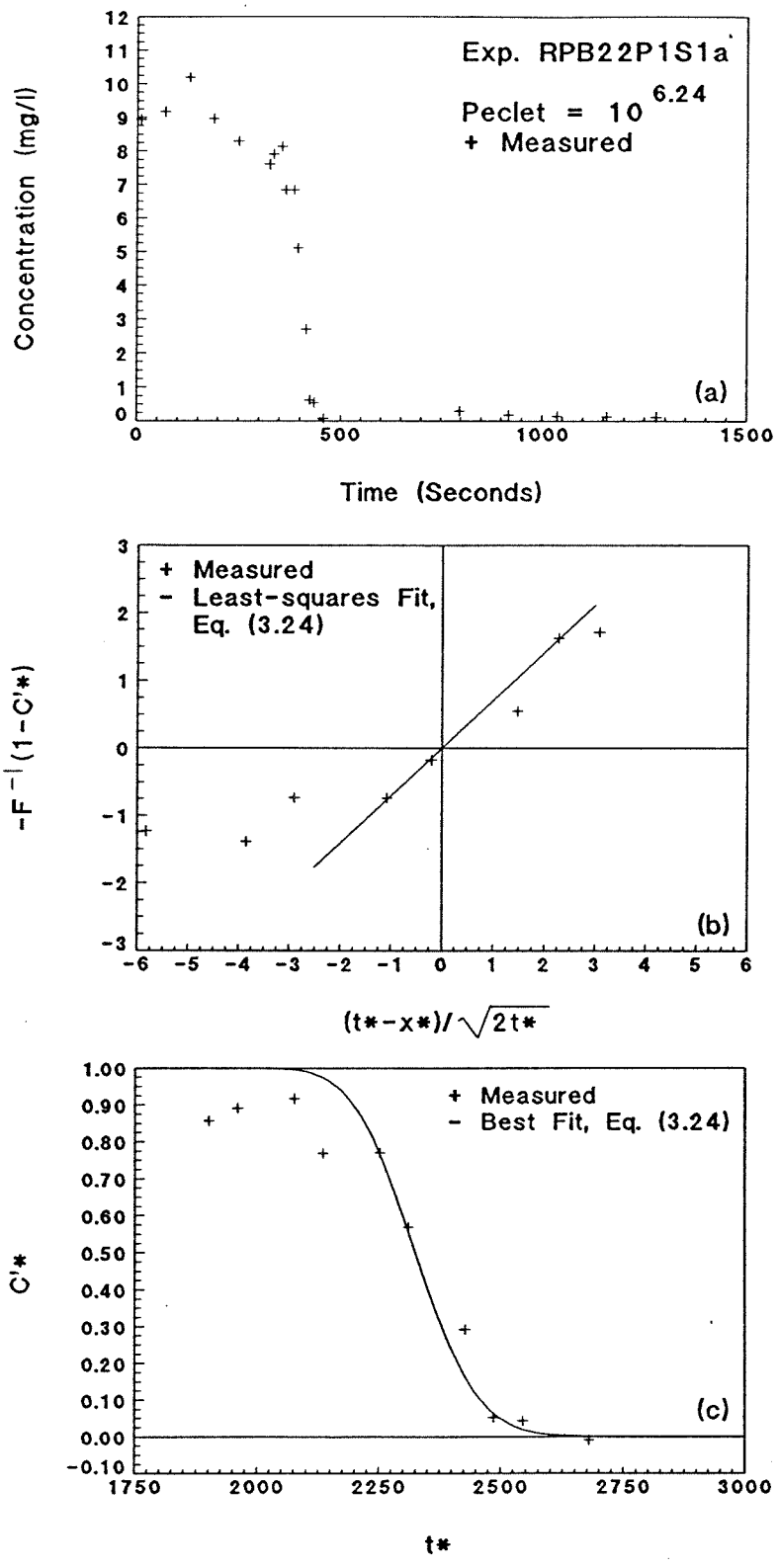

Fig. C.64: Exp. RPB22P1S1a reverse breakthrough, sample port 3, $Pe_p = 10^{6.24}$: (a) complete experimental data; (b) linearization with least-squares fit; and (c) breakthrough only with best-fit, Eq. (3.24).

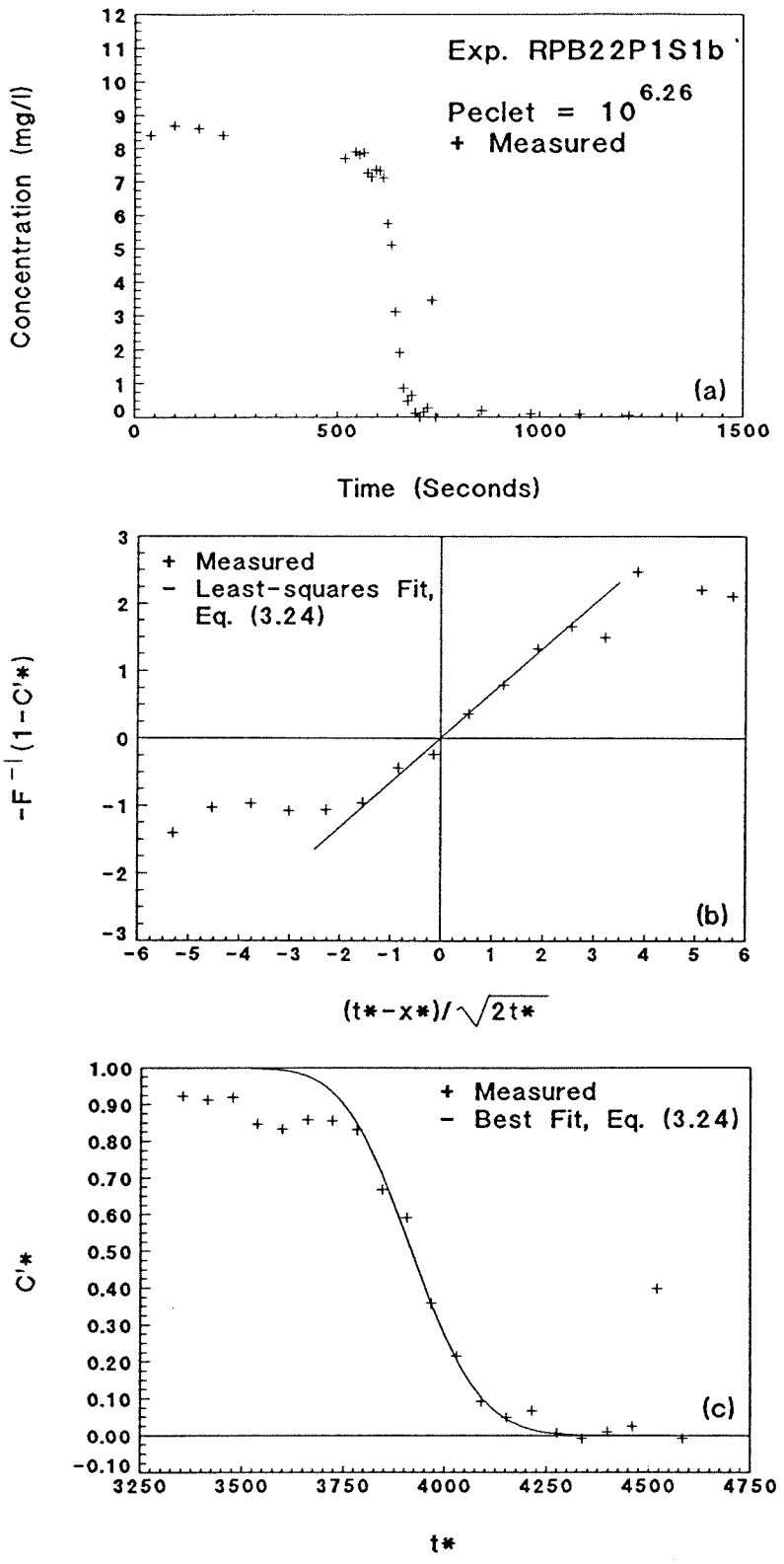

Fig. C.65: Exp. RPB22P1S1b reverse breakthrough, sample port 5, $Pe_p = 10^{6.26}$: (a) complete experimental data; (b) linearization with least-squares fit; and (c) breakthrough only with best-fit, Eq. (3.24).

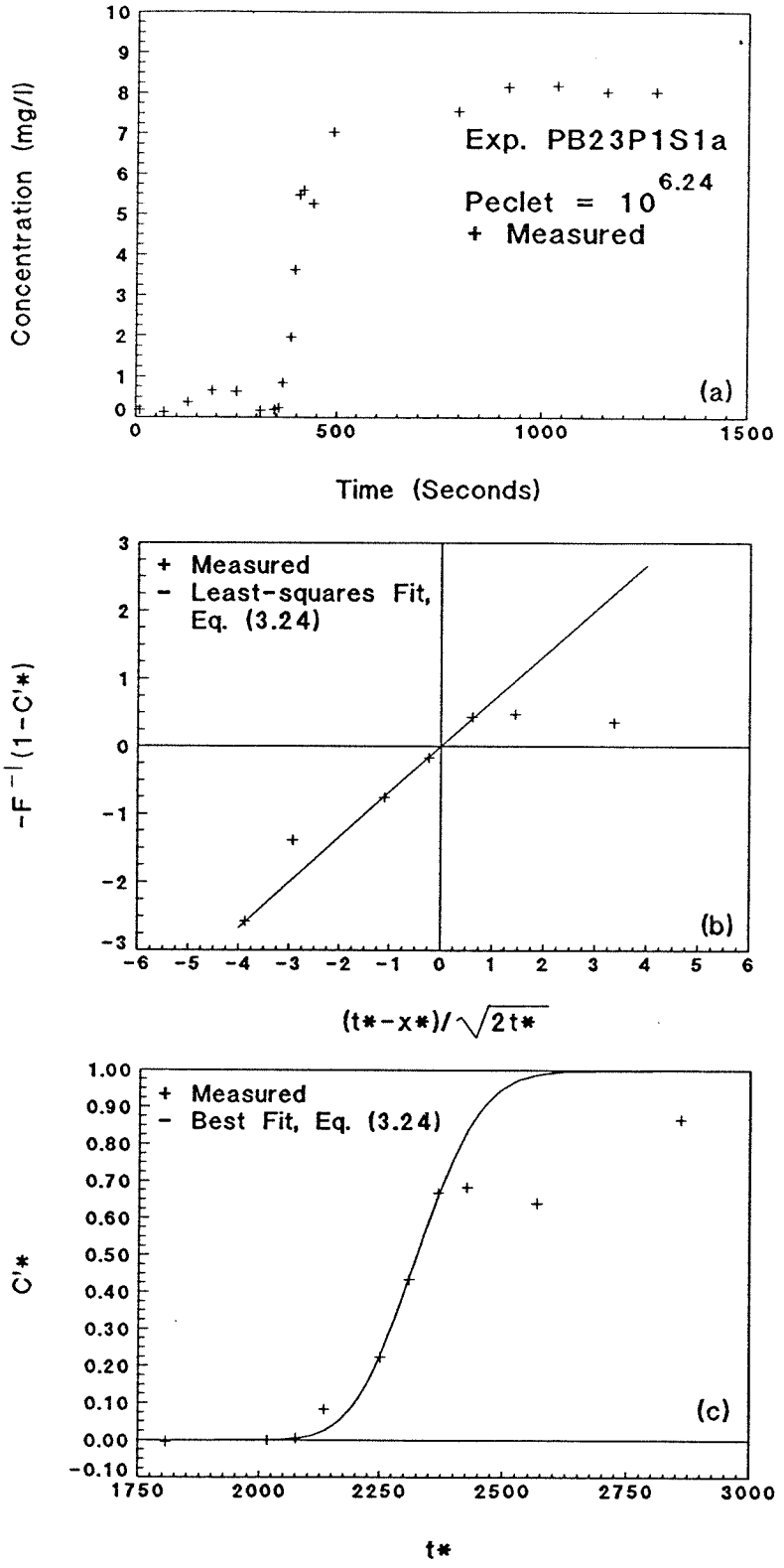

Fig. C.66: Exp. PB23P1S1a forward breakthrough, sample port 3, $Pe_p = 10^{6.24}$: (a) complete experimental data; (b) linearization with least-squares fit; and (c) breakthrough only with best-fit, Eq. (3.24).

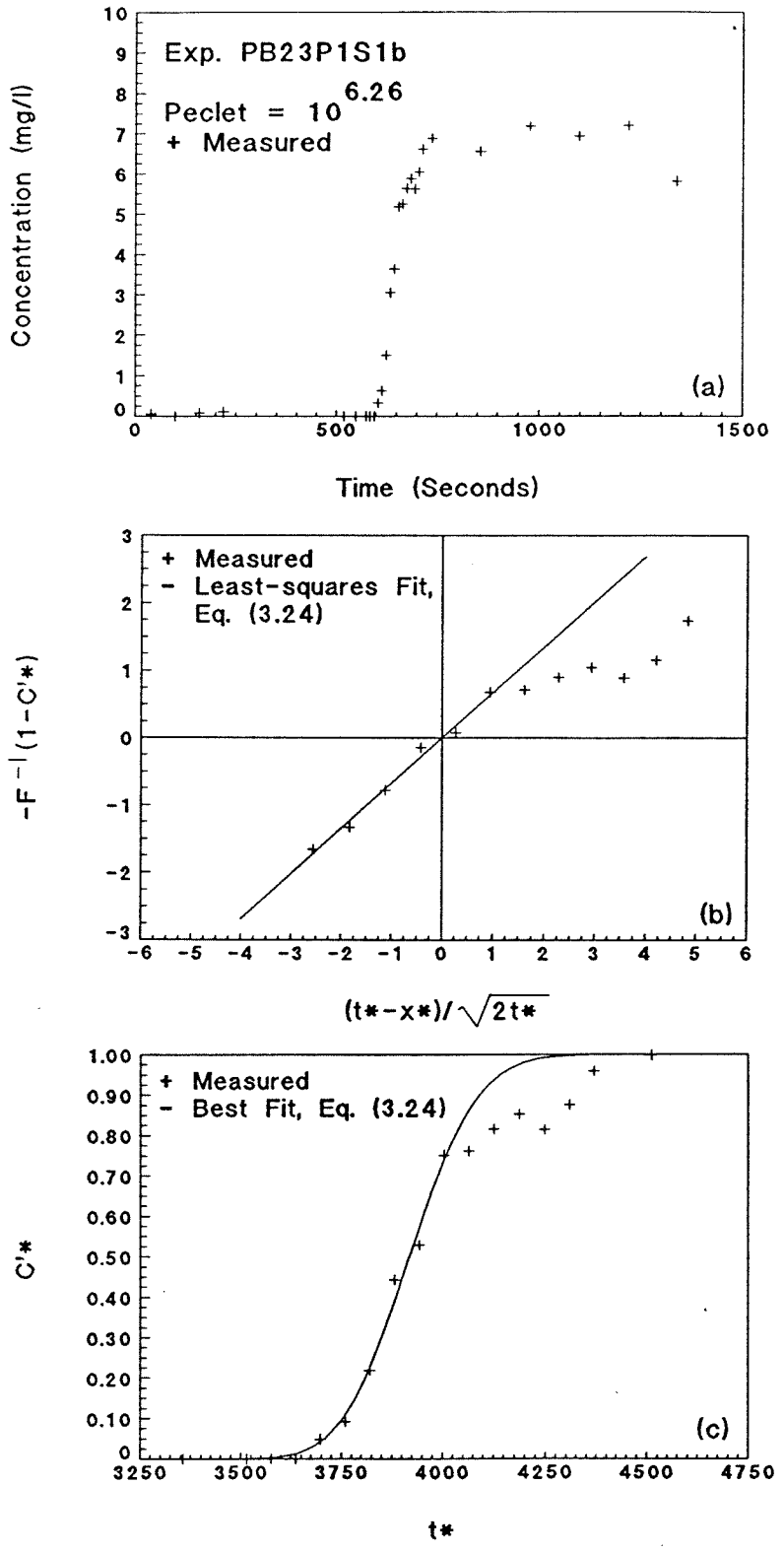

Fig. C.67: Exp. PB23P1S1b forward breakthrough, sample port 5, $Pe_p = 10^{6.26}$: (a) complete experimental data; (b) linearization with least-squares fit; and (c) breakthrough only with best-fit, Eq. (3.24).

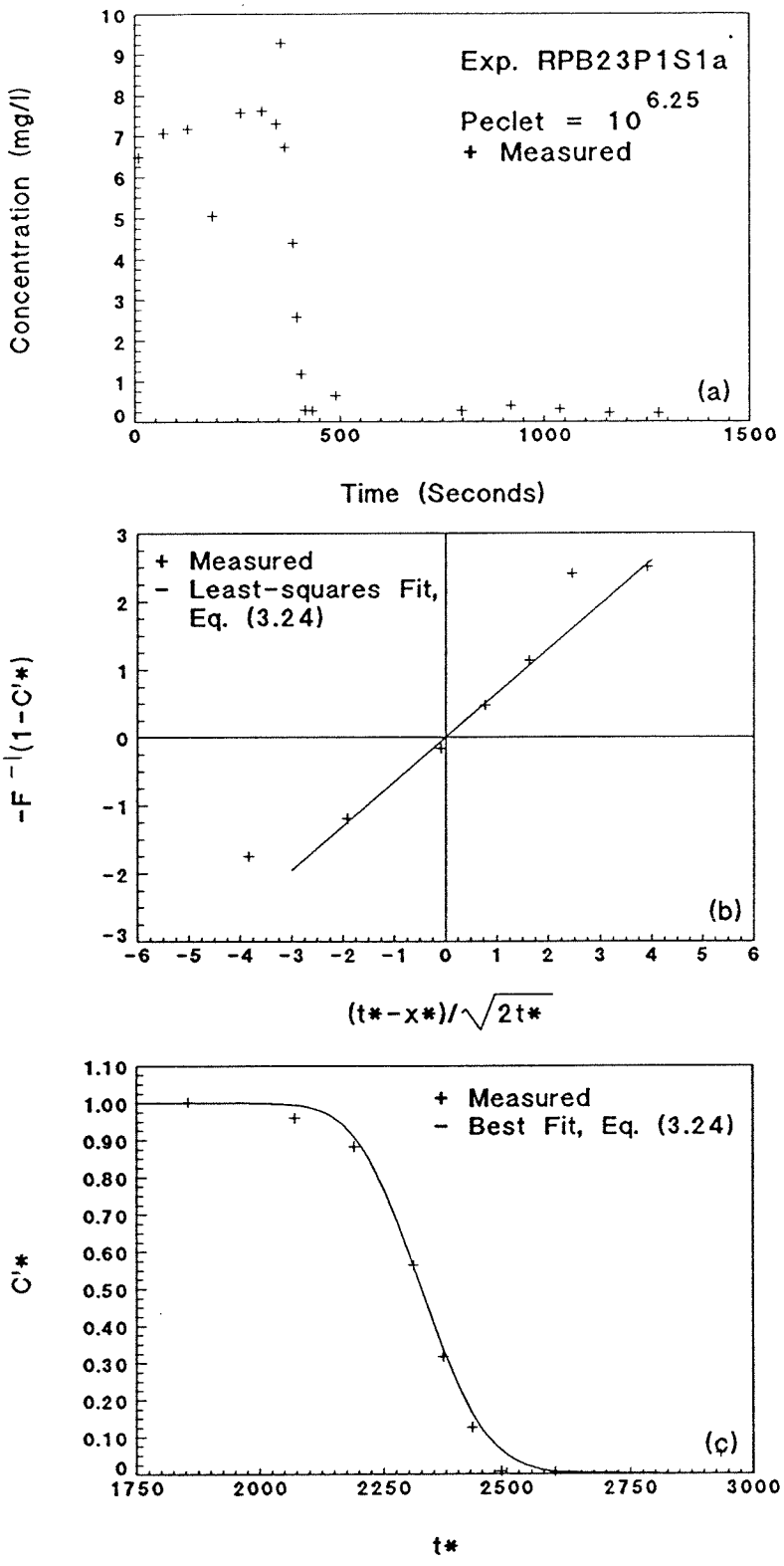

Fig. C.68: Exp. RPB23P1S1a reverse breakthrough, sample port 3, $Pe_p = 10^{6.25}$: (a) complete experimental data; (b) linearization with least-squares fit; and (c) breakthrough only with best-fit, Eq. (3.24).

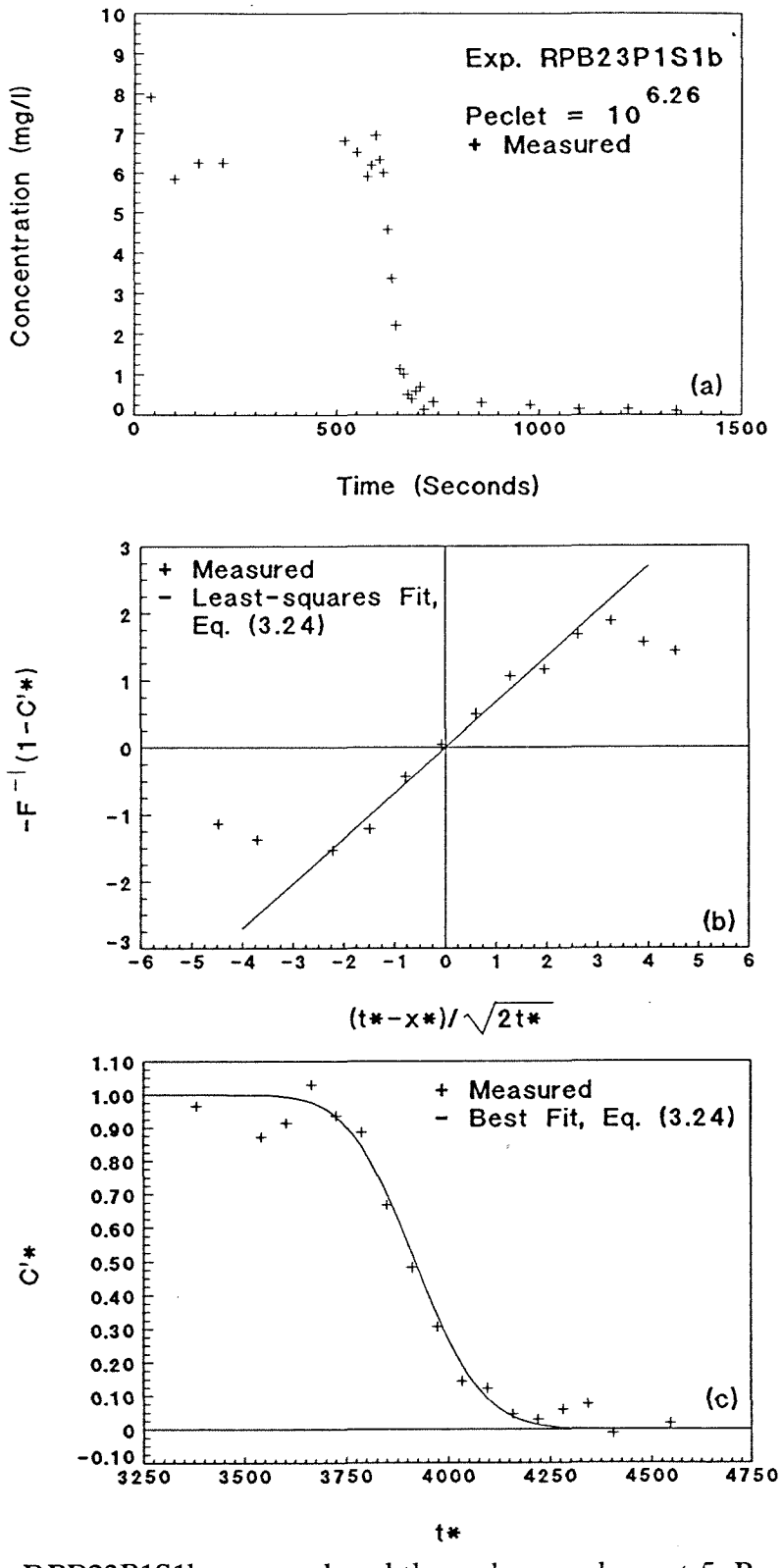

Fig. C.69: Exp. RPB23P1S1b reverse breakthrough, sample port 5, $Pe_p = 10^{6.26}$: (a) complete experimental data; (b) linearization with least-squares fit; and (c) breakthrough only with best-fit, Eq. (3.24).

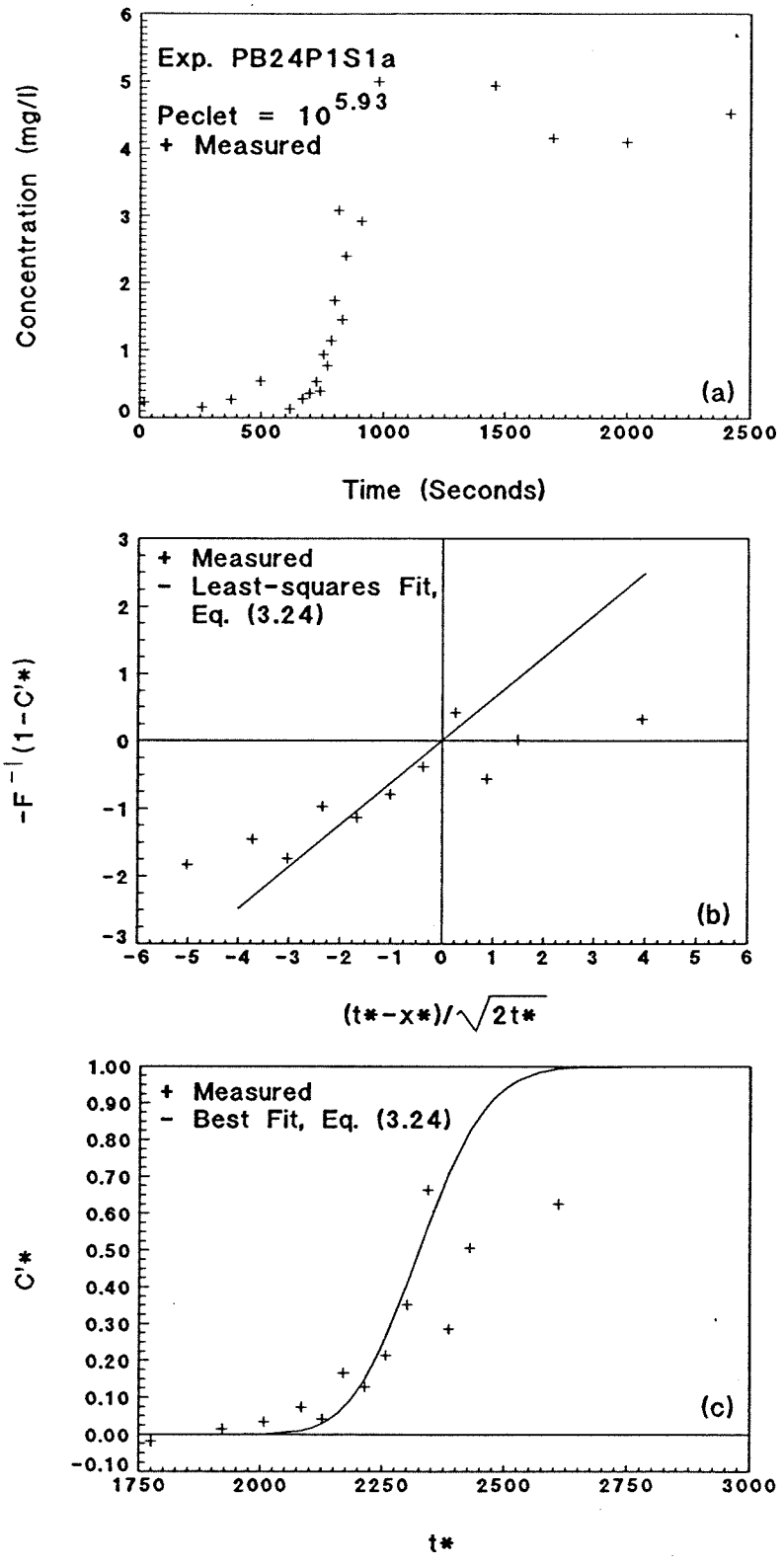

Fig. C.70: Exp. PB24P1S1a forward breakthrough, sample port 3, $Pe_p = 10^{5.93}$: (a) complete experimental data; (b) linearization with least-squares fit; and (c) breakthrough only with best-fit, Eq. (3.24).

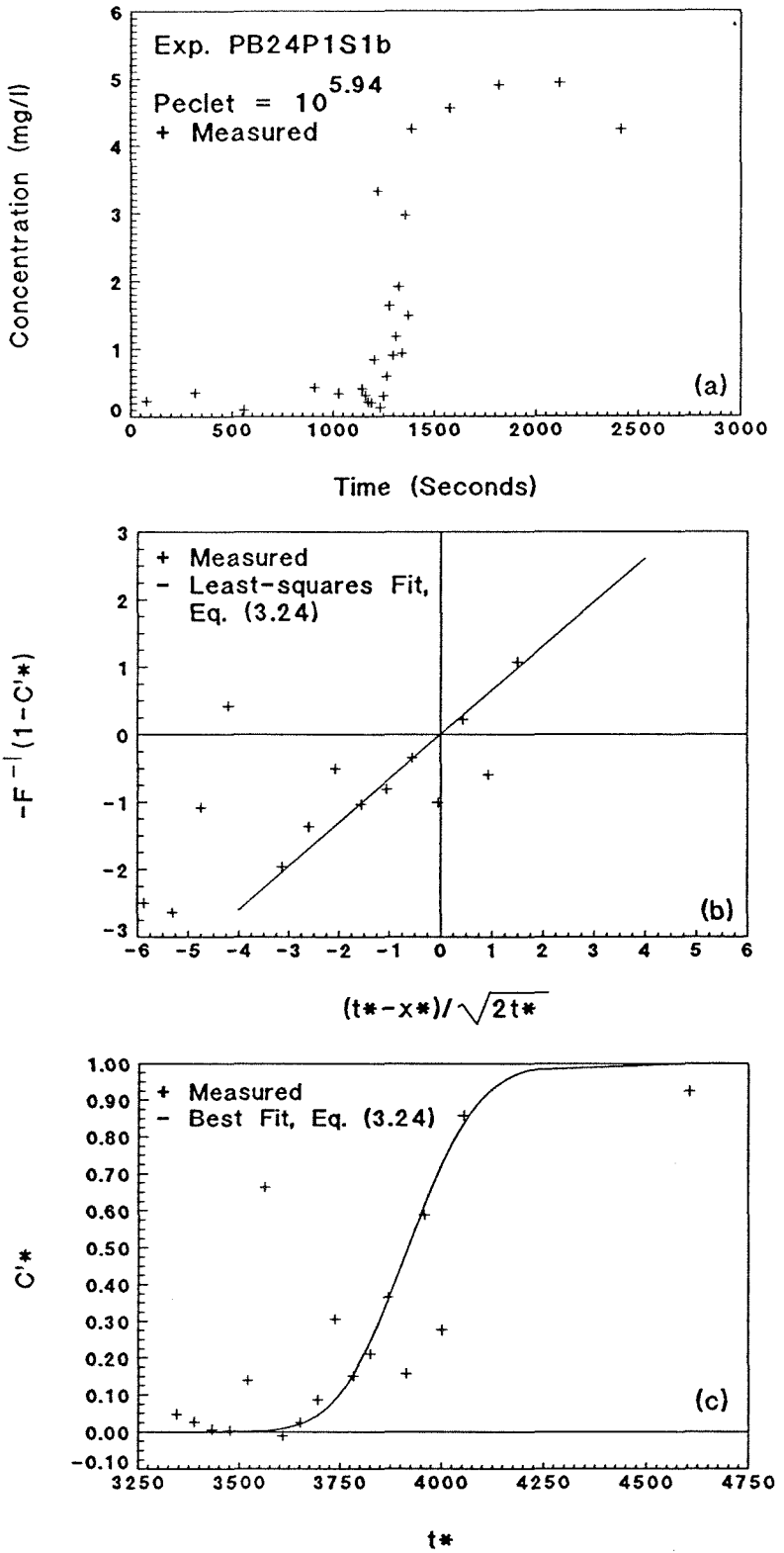

Fig. C.71: Exp. PB24P1S1b forward breakthrough, sample port 5, $Pe_p = 10^{5.94}$: (a) complete experimental data; (b) linearization with least-squares fit; and (c) breakthrough only with best-fit, Eq. (3.24).

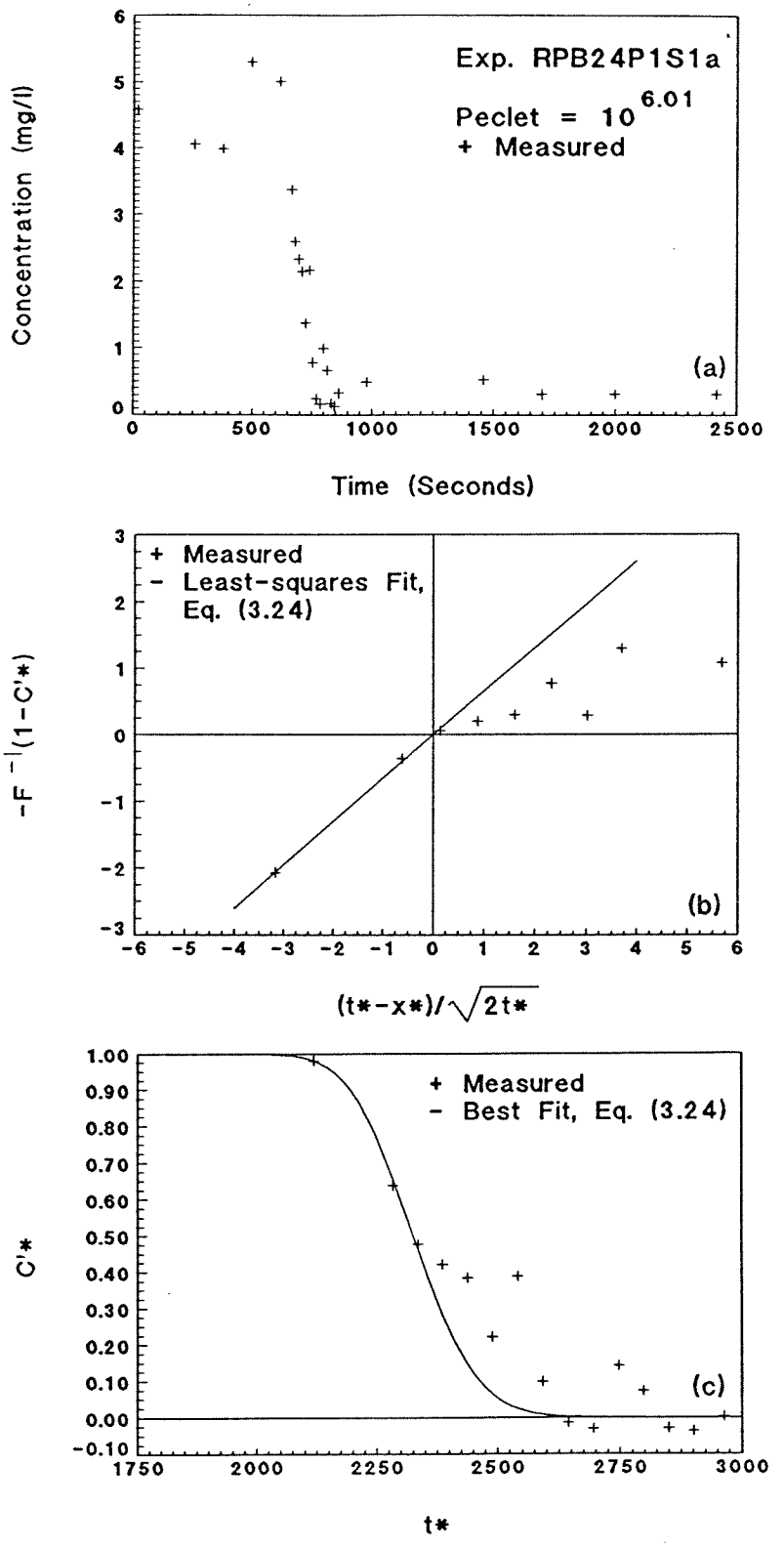

Fig. C.72: Exp. RPB24P1S1a reverse breakthrough, sample port 3, $Pe_p = 10^{6.01}$: (a) complete experimental data; (b) linearization with least-squares fit; and (c) breakthrough only with best-fit, Eq. (3.24).

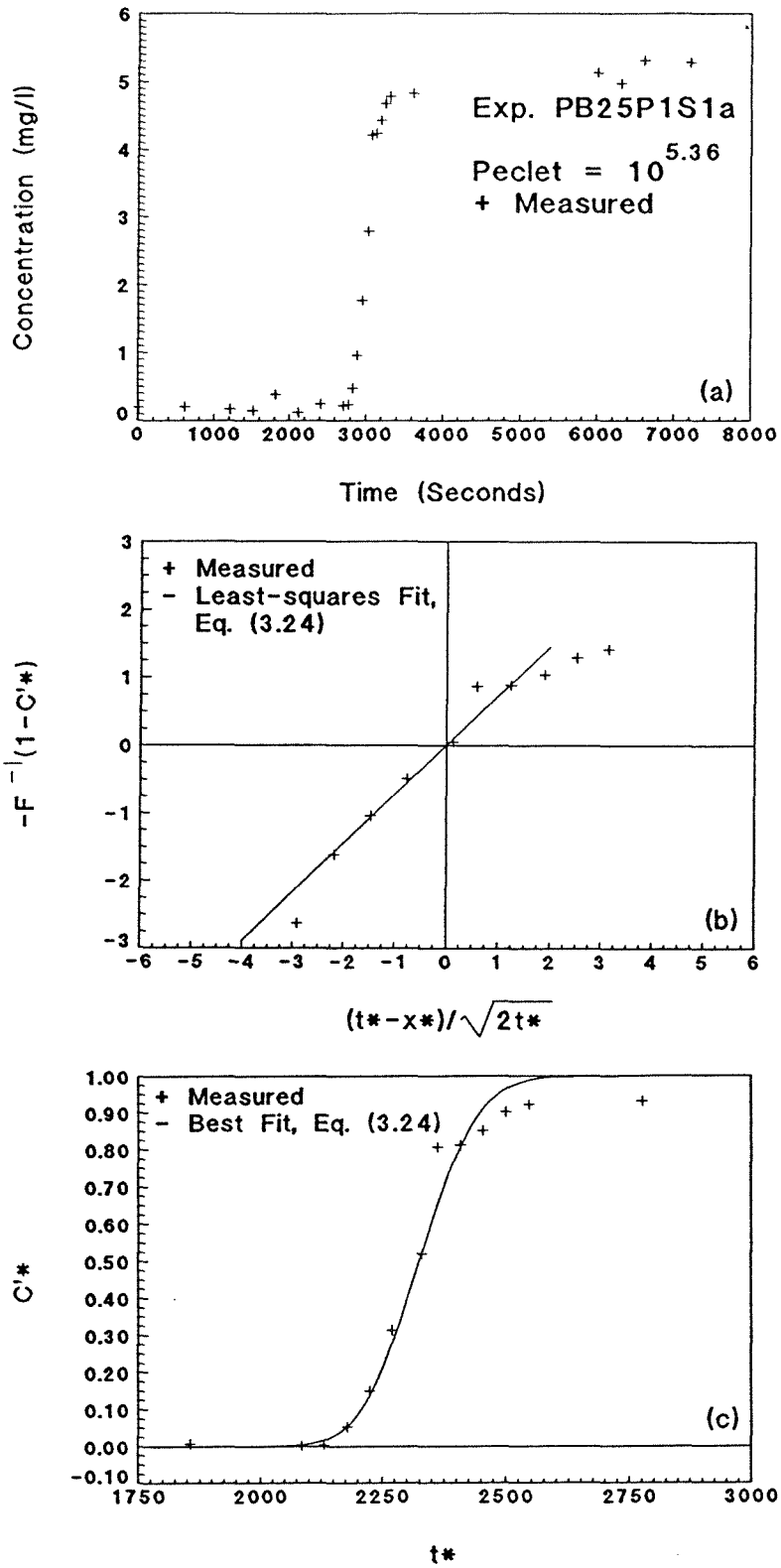

Fig. C.73: Exp. PB25P1S1a forward breakthrough, sample port 3, $Pe_p = 10^{5.36}$: (a) complete experimental data; (b) linearization with least-squares fit; and (c) breakthrough only with best-fit, Eq. (3.24).

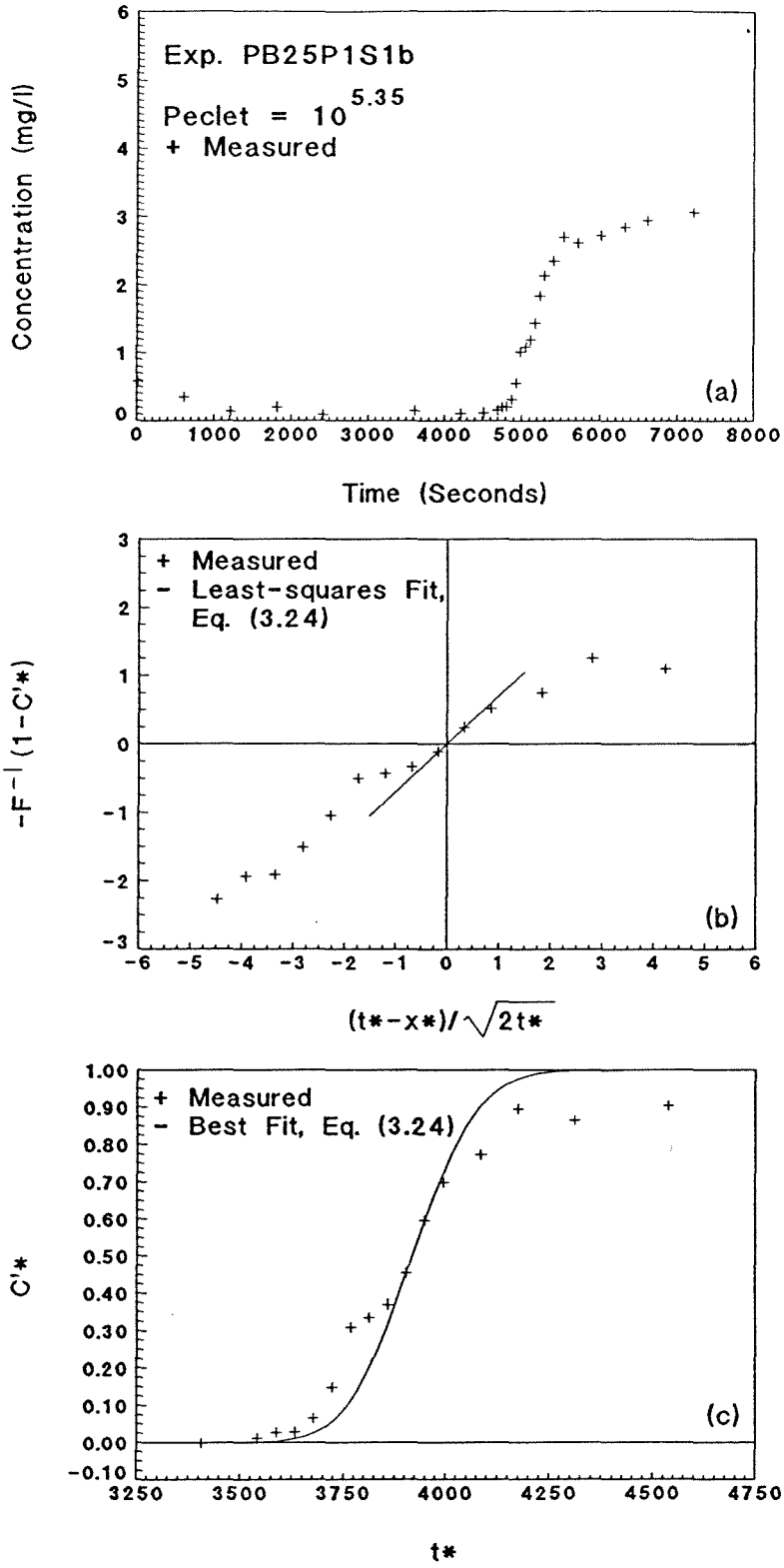

Fig. C.74: Exp. PB25P1S1b forward breakthrough, sample port 5, $Pe_p = 10^{5.35}$: (a) complete experimental data; (b) linearization with least-squares fit; and (c) breakthrough only with best-fit, Eq. (3.24).

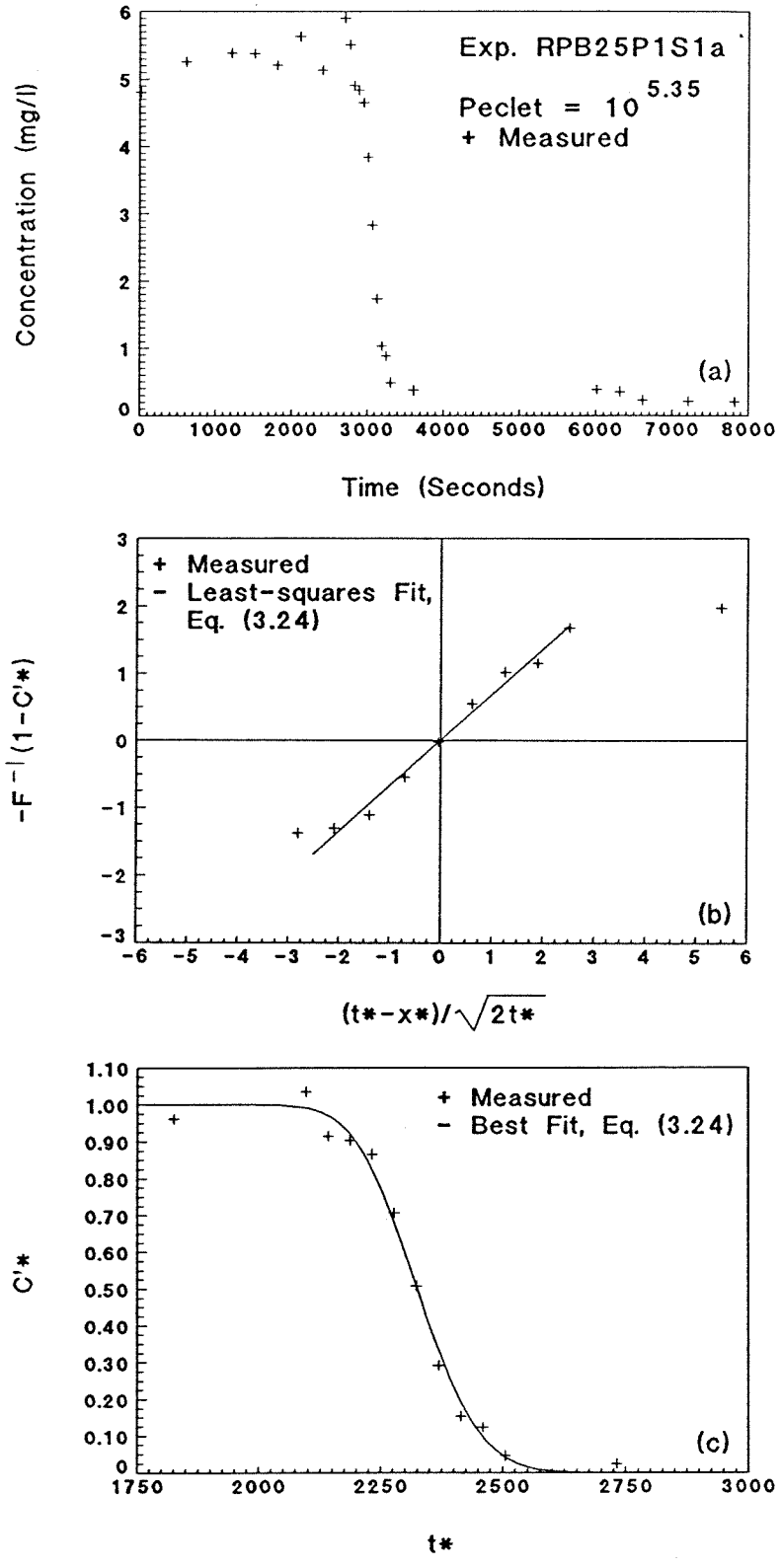

Fig. C.75: Exp. RPB25P1S1a reverse breakthrough, sample port 3, $Pe_p = 10^{5.35}$: (a) complete experimental data; (b) linearization with least-squares fit; and (c) breakthrough only with best-fit, Eq. (3.24).

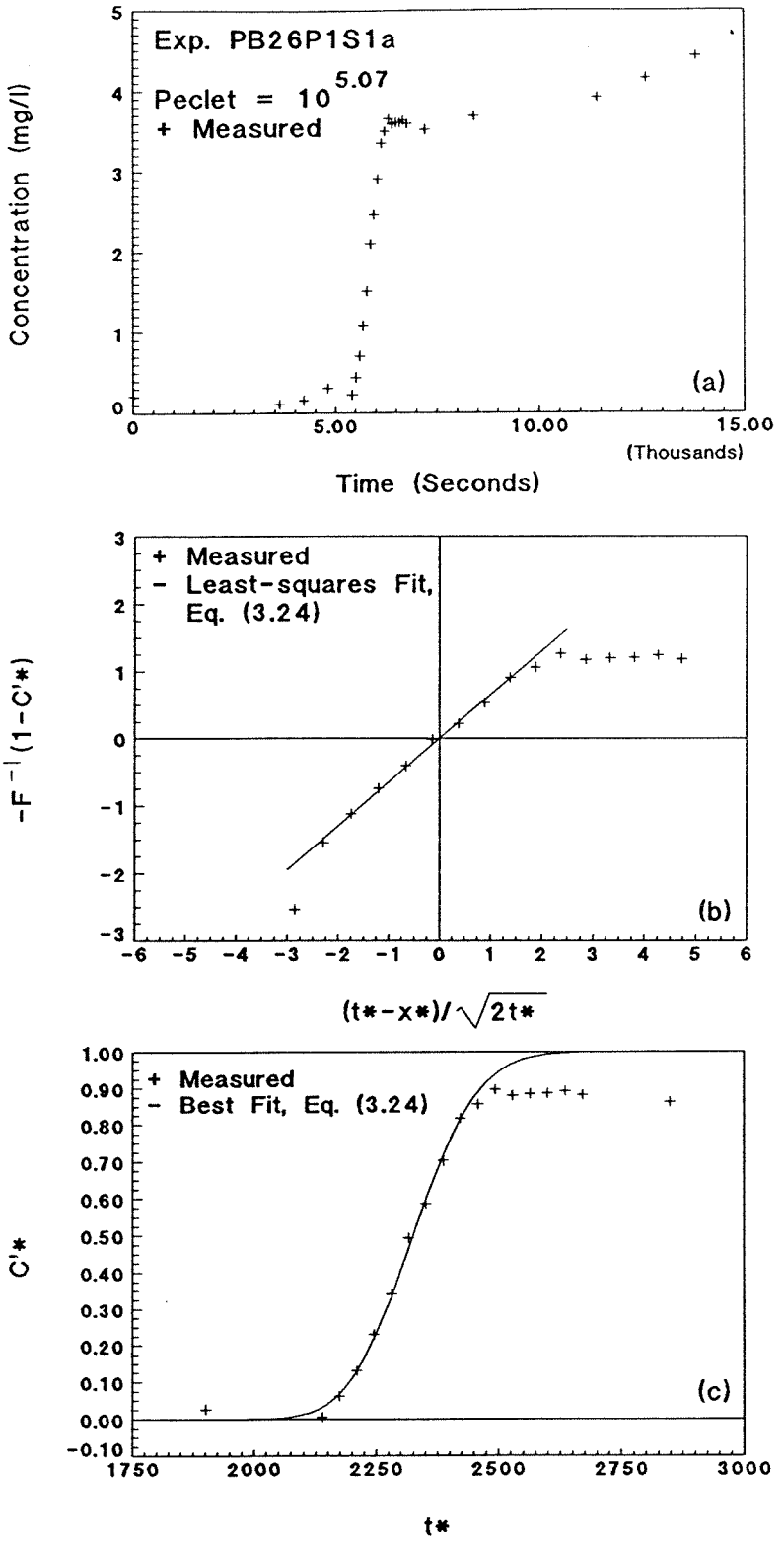

Fig. C.77: Exp. PB26P1S1a forward breakthrough, sample port 3, $Pe_p = 10^{5.07}$: (a) complete experimental data; (b) linearization with least-squares fit; and (c) breakthrough only with best-fit, Eq. (3.24).

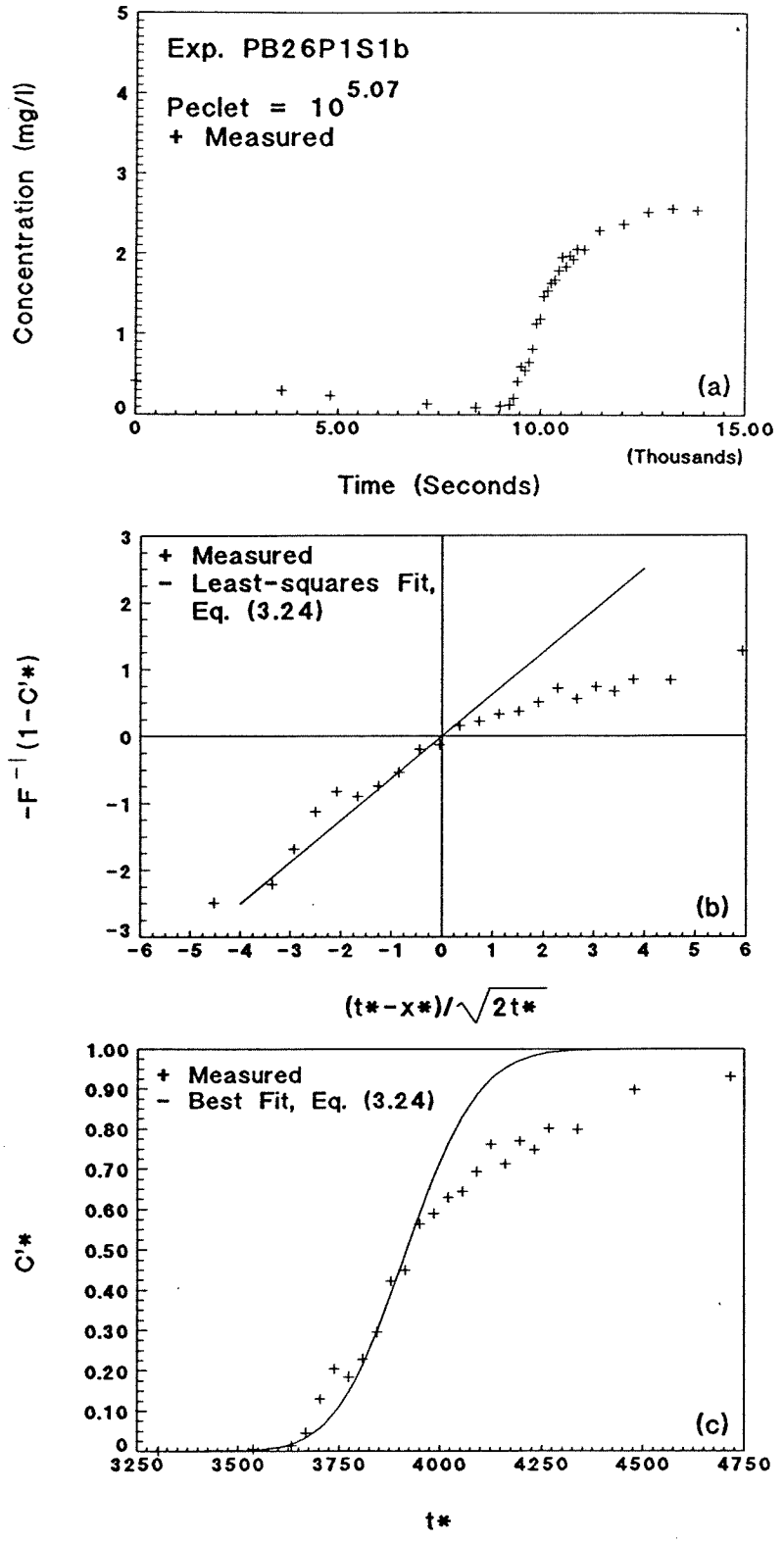

Fig. C.78: Exp. PB26P1S1b forward breakthrough, sample port 5, $Pe_p = 10^{5.07}$: (a) complete experimental data; (b) linearization with least-squares fit; and (c) breakthrough only with best-fit, Eq. (3.24).

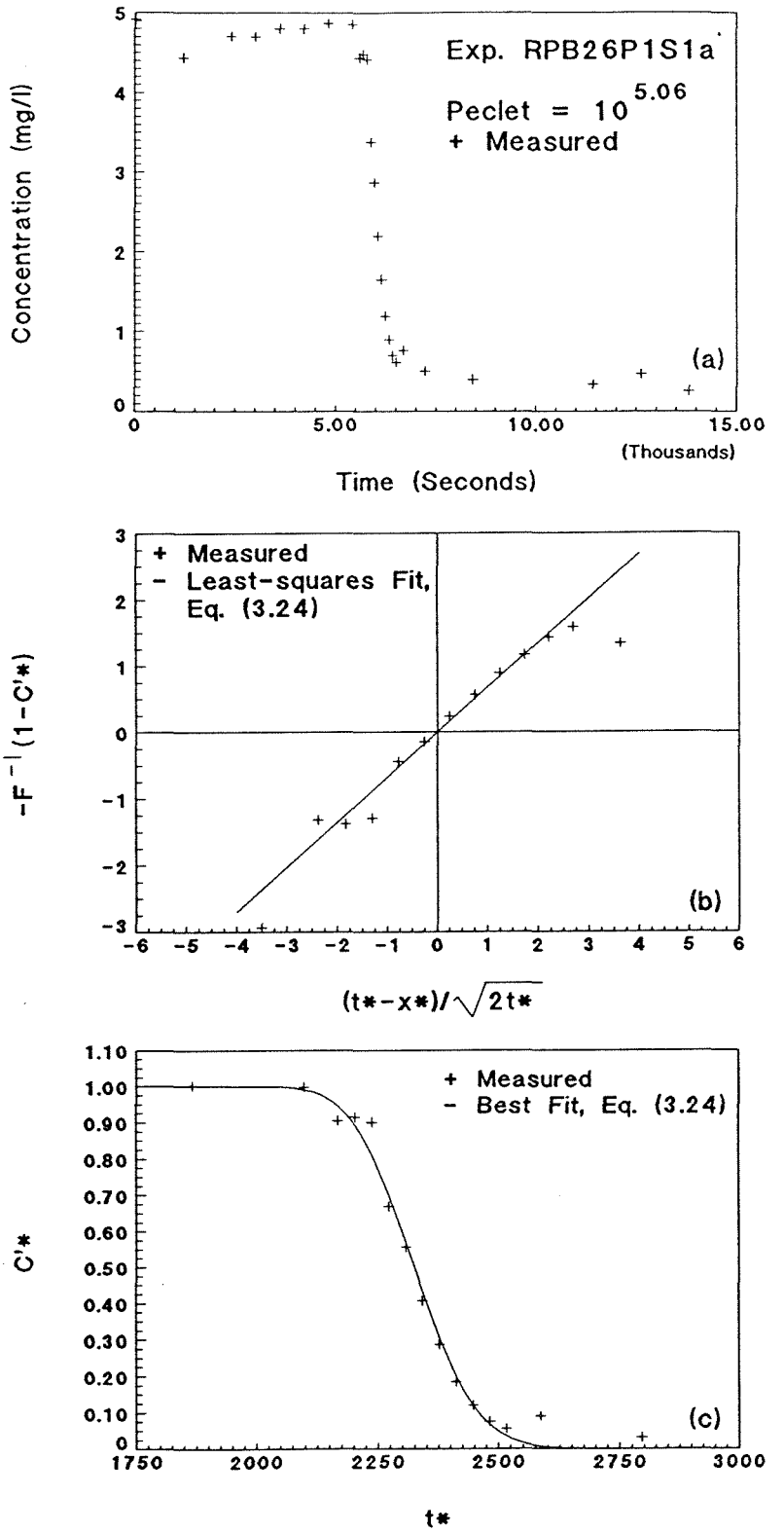

Fig. C.79: Exp. RPB26P1S1a reverse breakthrough, sample port 3, $Pe_p = 10^{5.06}$: (a) complete experimental data; (b) linearization with least-squares fit; and (c) breakthrough only with best-fit, Eq. (3.24).

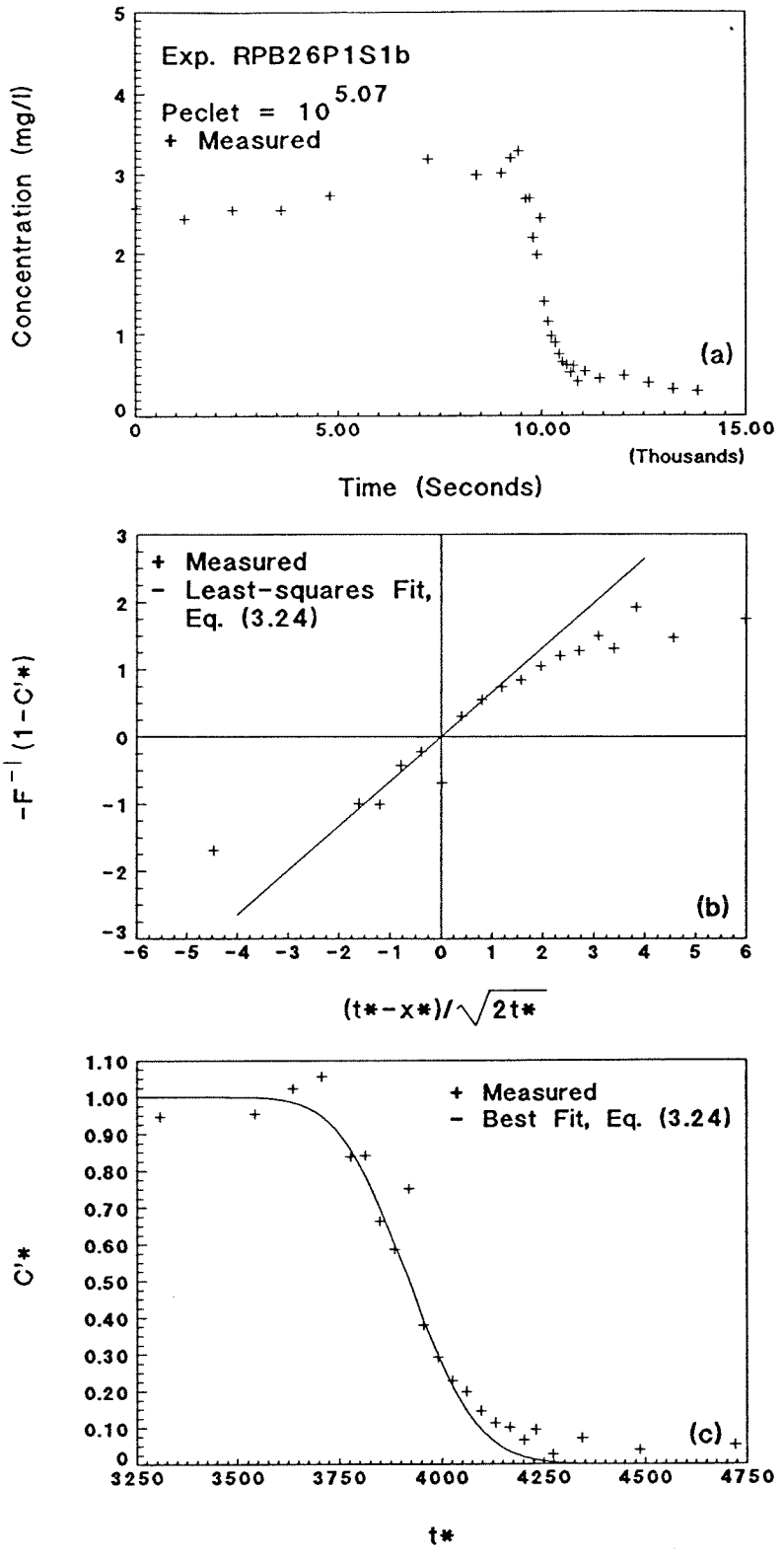

Fig. C.80: Exp. RPB26P1S1b reverse breakthrough, sample port 5, $Pe_p = 10^{5.07}$: (a) complete experimental data; (b) linearization with least-squares fit; and (c) breakthrough only with best-fit, Eq. (3.24).

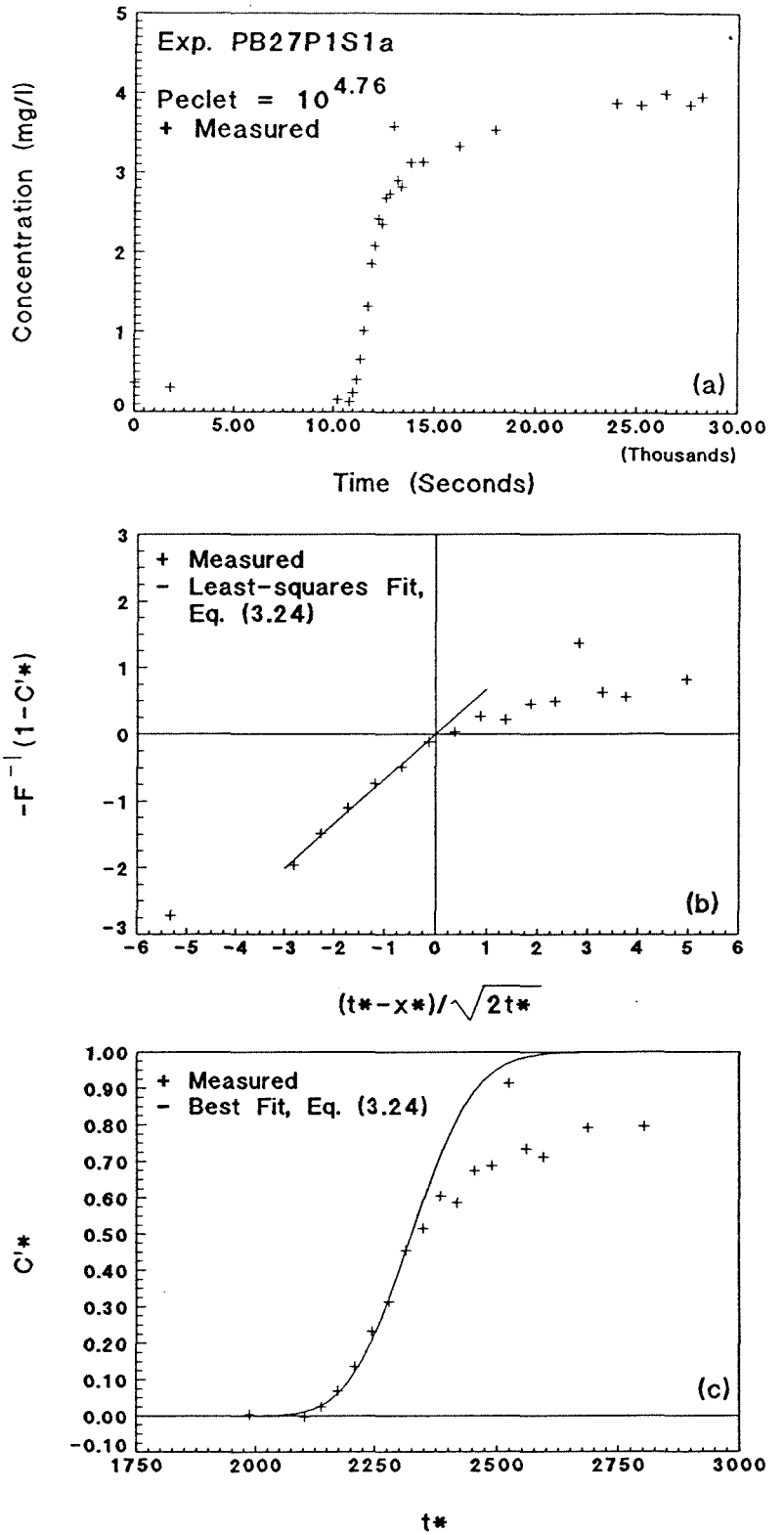

Fig. C.81: Exp. PB27P1S1a forward breakthrough, sample port 3, $Pe_p = 10^{4.76}$: (a) complete experimental data; (b) linearization with least-squares fit; and (c) breakthrough only with best-fit, Eq. (3.24).

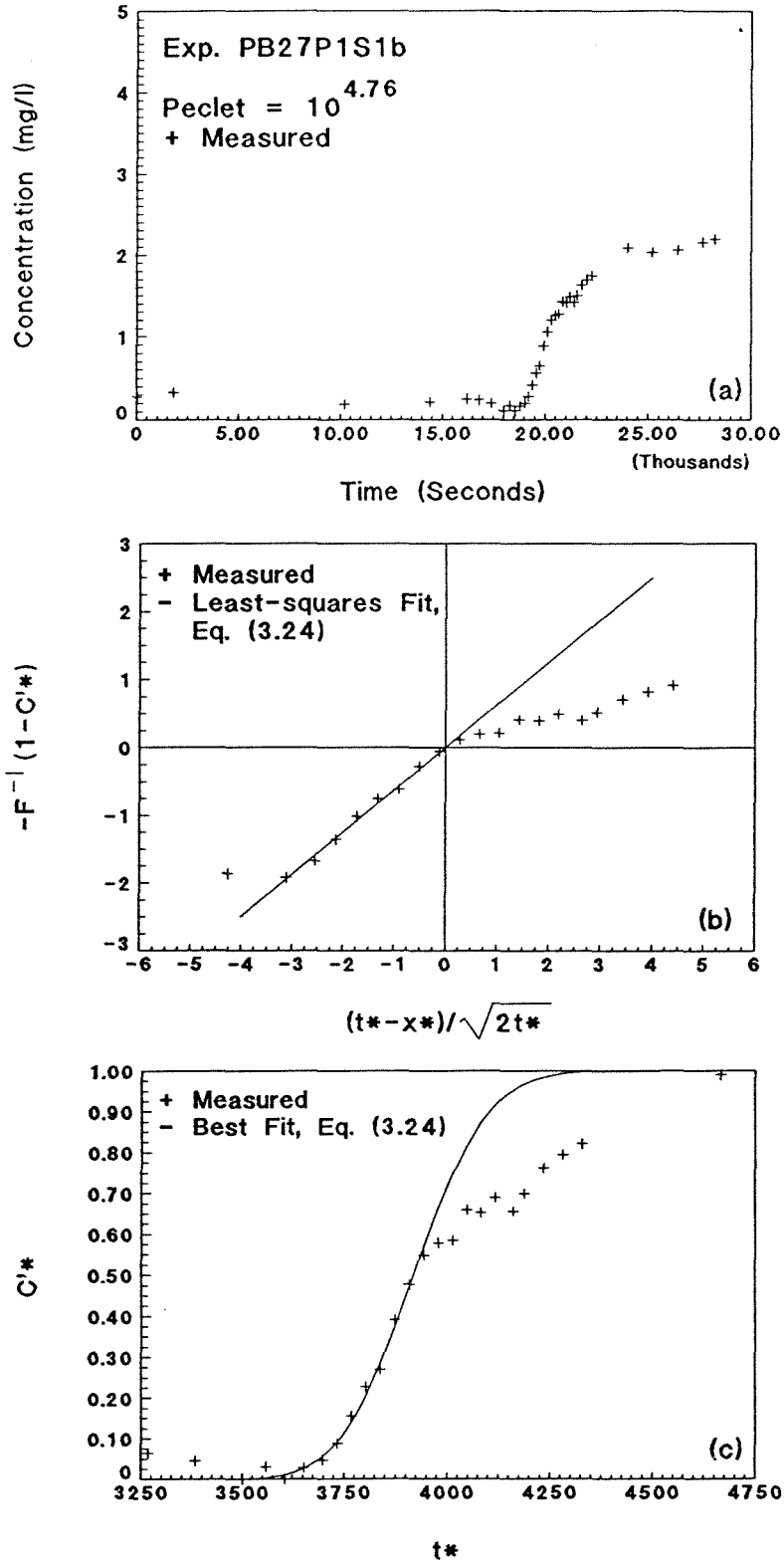

Fig. C.82: Exp. PB27P1S1b forward breakthrough, sample port 5, $Pe_p = 10^{4.76}$: (a) complete experimental data; (b) linearization with least-squares fit; and (c) breakthrough only with best-fit, Eq. (3.24).

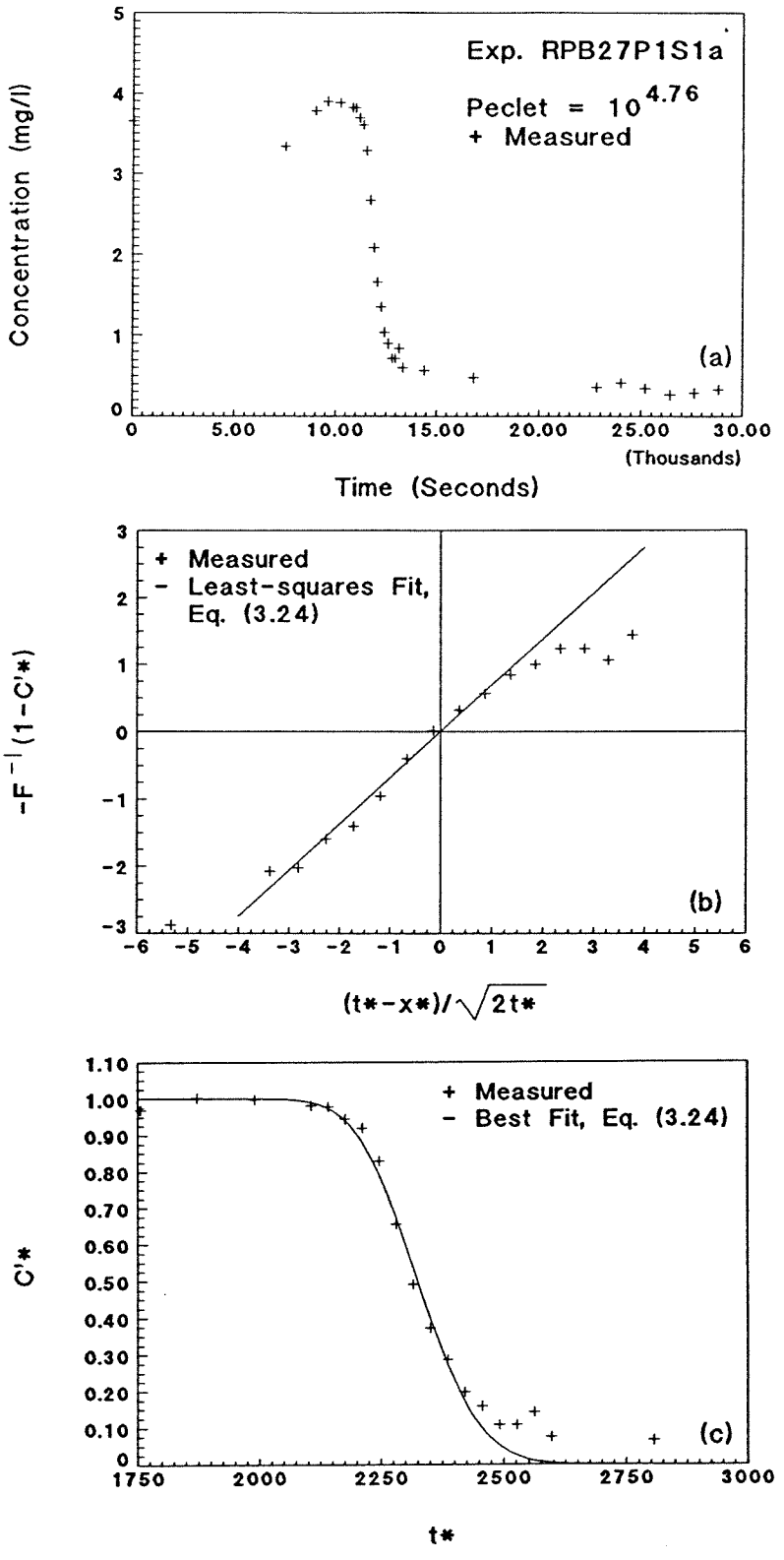

Fig. C.83: Exp. RPB27P1S1a reverse breakthrough, sample port 3, $Pe_p = 10^{4.76}$: (a) complete experimental data; (b) linearization with least-squares fit; and (c) breakthrough only with best-fit, Eq. (3.24).

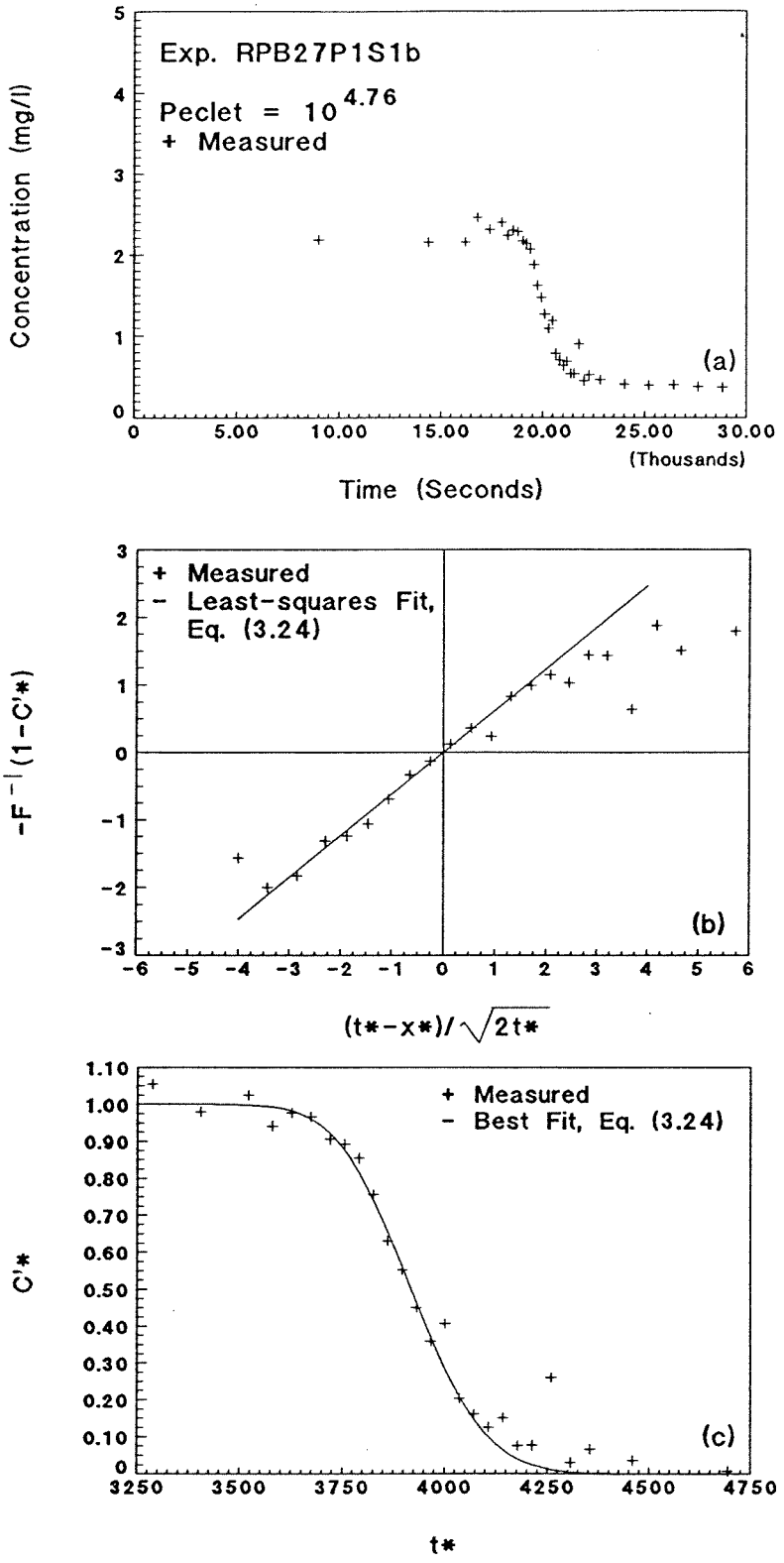

Fig. C.84: Exp. RPB27P1S1b reverse breakthrough, sample port 5, $Pe_p = 10^{4.76}$: (a) complete experimental data; (b) linearization with least-squares fit; and (c) breakthrough only with best-fit, Eq. (3.24).

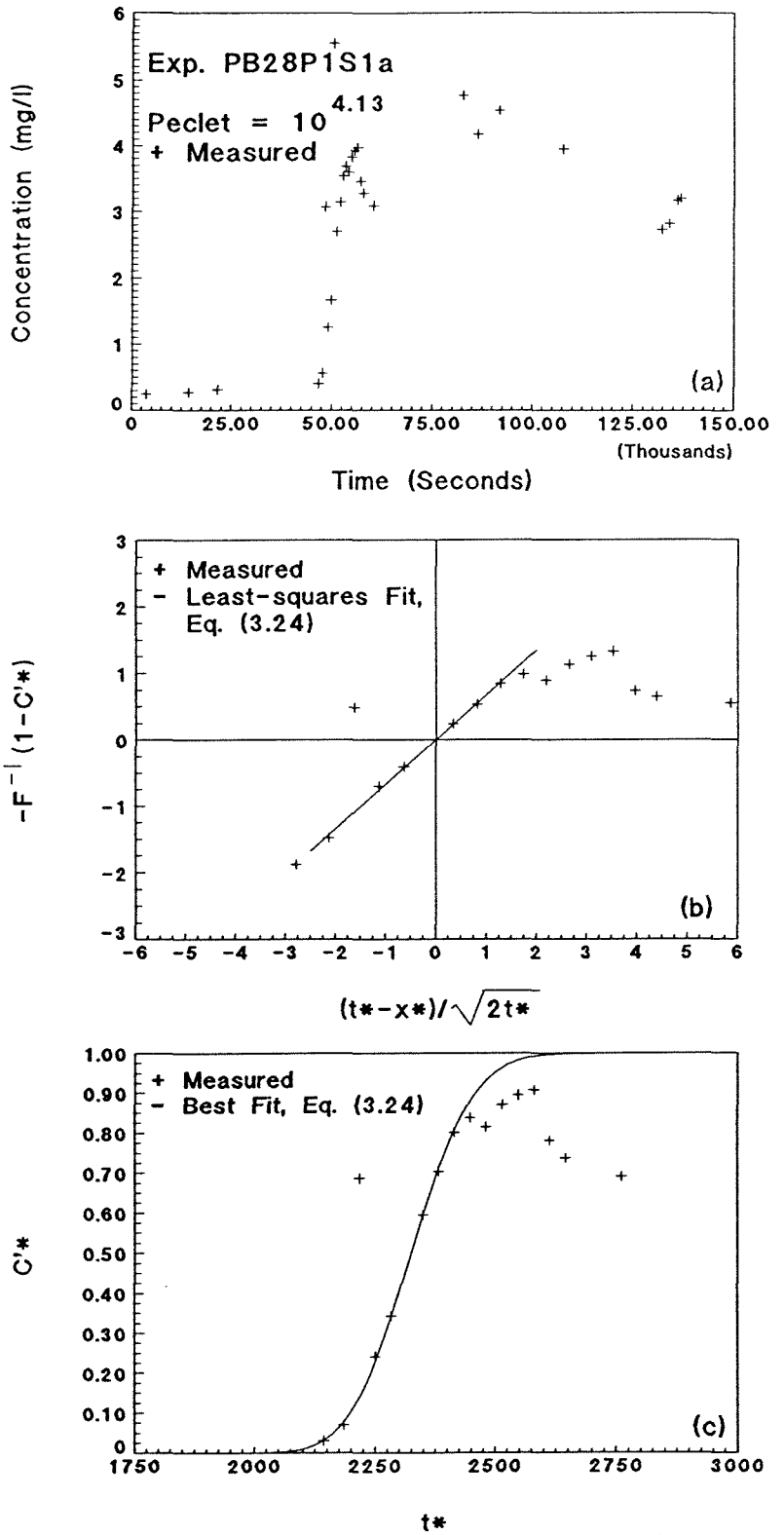

Fig. C.85: Exp. PB28P1S1a forward breakthrough, sample port 3, $Pe_p = 10^{4.13}$: (a) complete experimental data; (b) linearization with least-squares fit; and (c) breakthrough only with best-fit, Eq. (3.24).

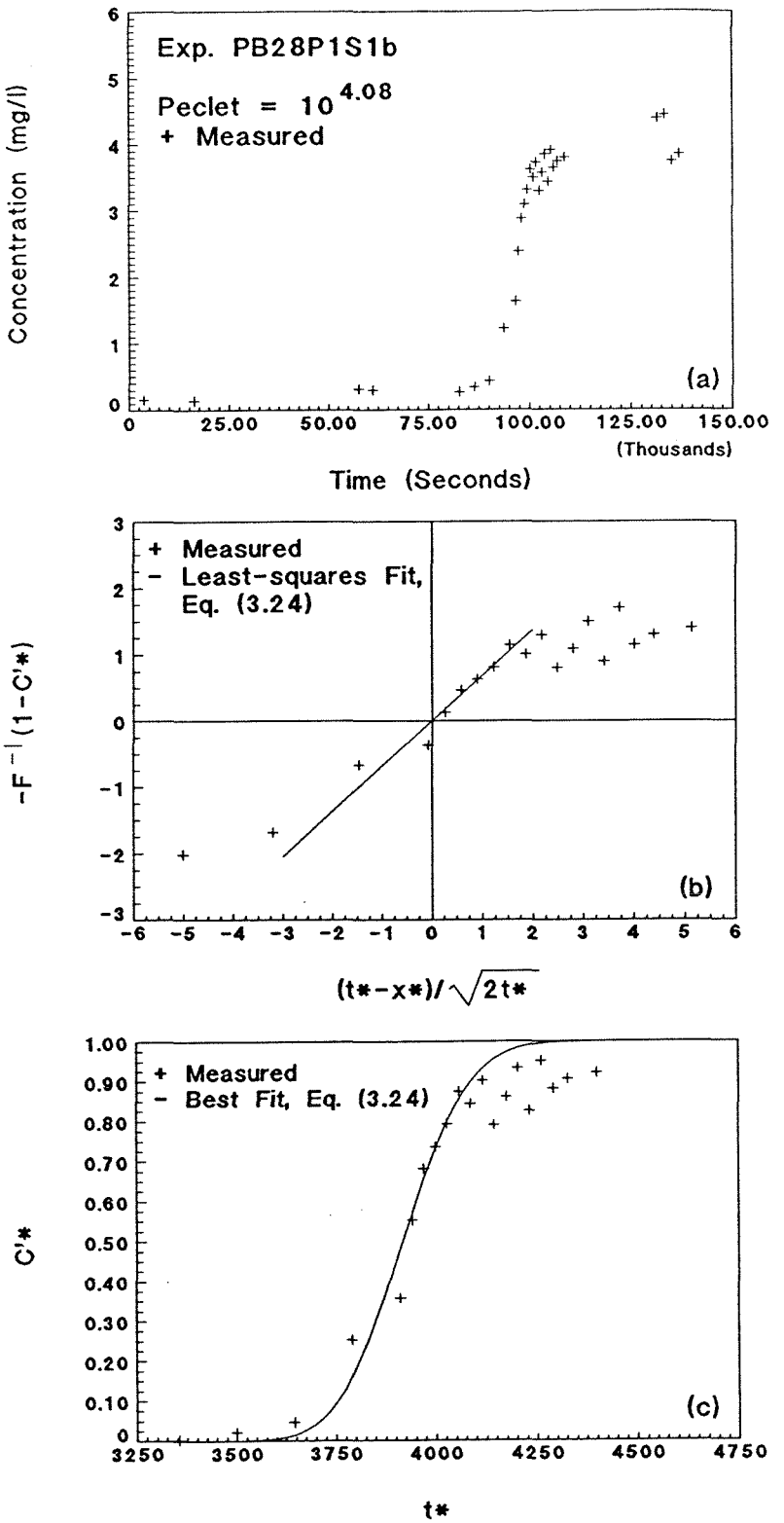

Fig. C.86: Exp. PB28P1S1b forward breakthrough, sample port 5, $Pe_p = 10^{4.08}$: (a) complete experimental data; (b) linearization with least-squares fit; and (c) breakthrough only with best-fit, Eq. (3.24).

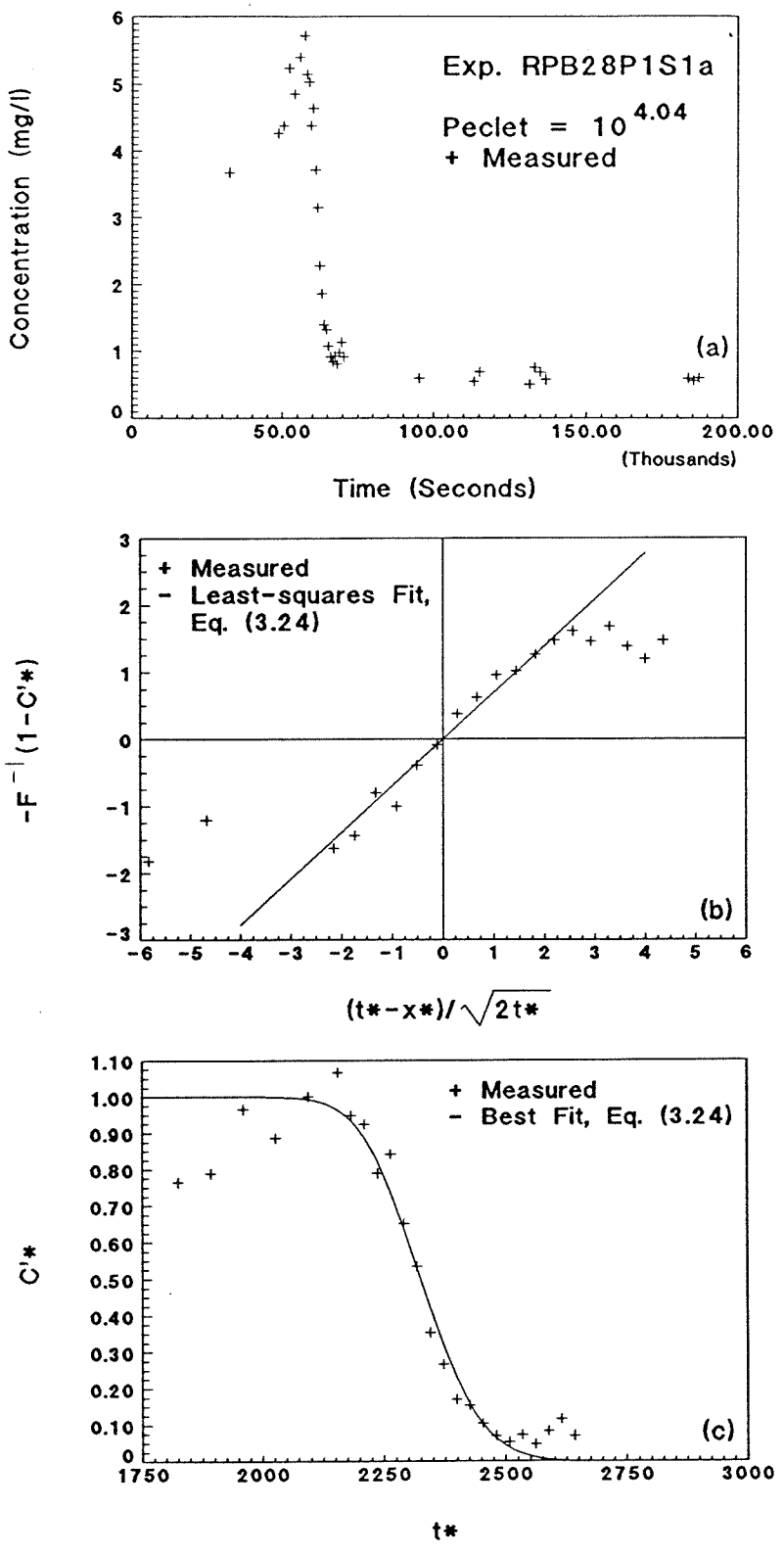

Fig. C.87: Exp. RPB28P1S1a reverse breakthrough, sample port 3, $Pe_p = 10^{4.05}$: (a) complete experimental data; (b) linearization with least-squares fit; and (c) breakthrough only with best-fit, Eq. (3.24).

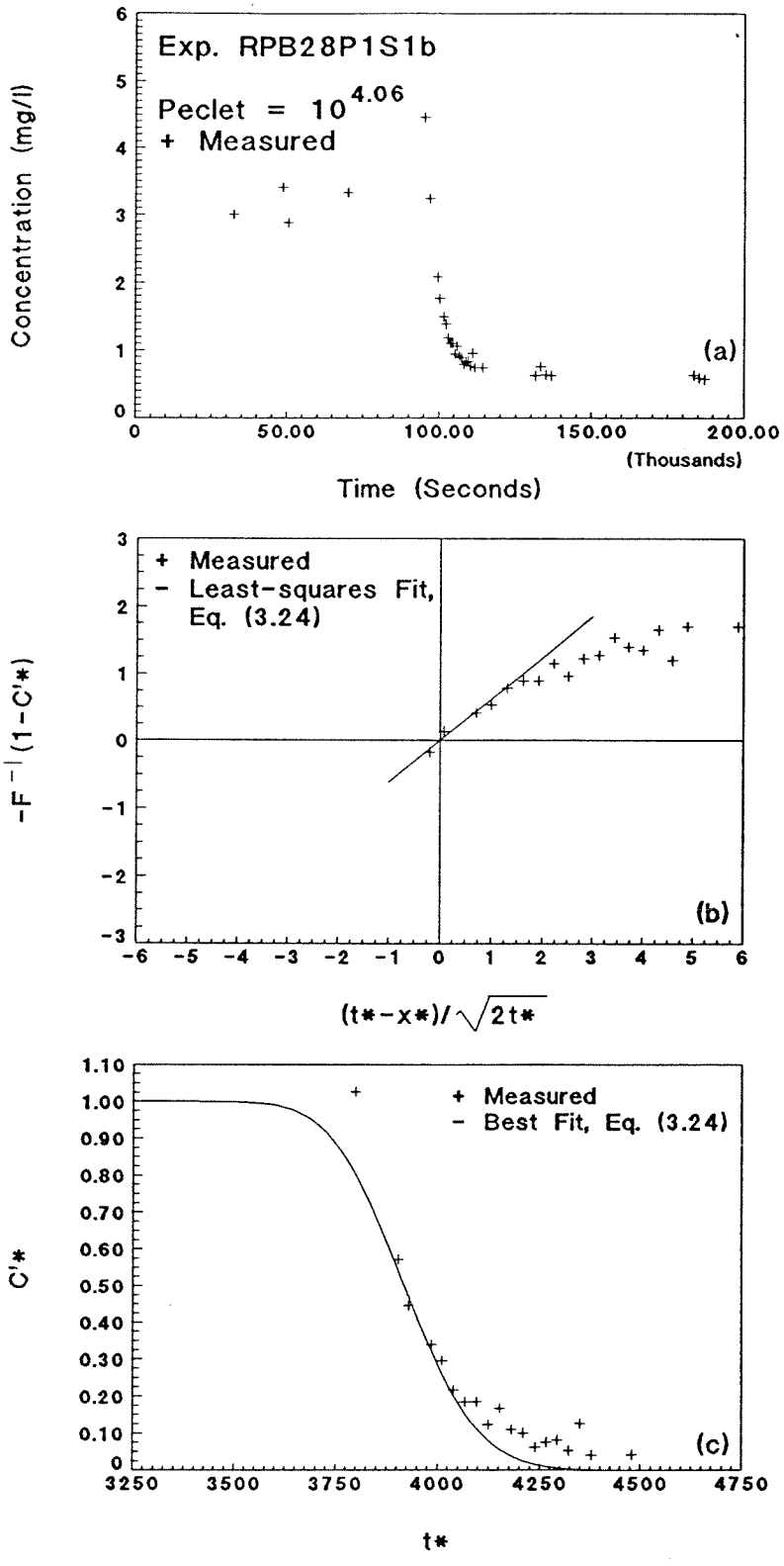

Fig. C.88: Exp. RPB28P1S1b reverse breakthrough, sample port 5, $Pe_p = 10^{4.06}$: (a) complete experimental data; (b) linearization with least-squares fit; and (c) breakthrough only with best-fit, Eq. (3.24).

C.3 2.8 micron Particle Experiments

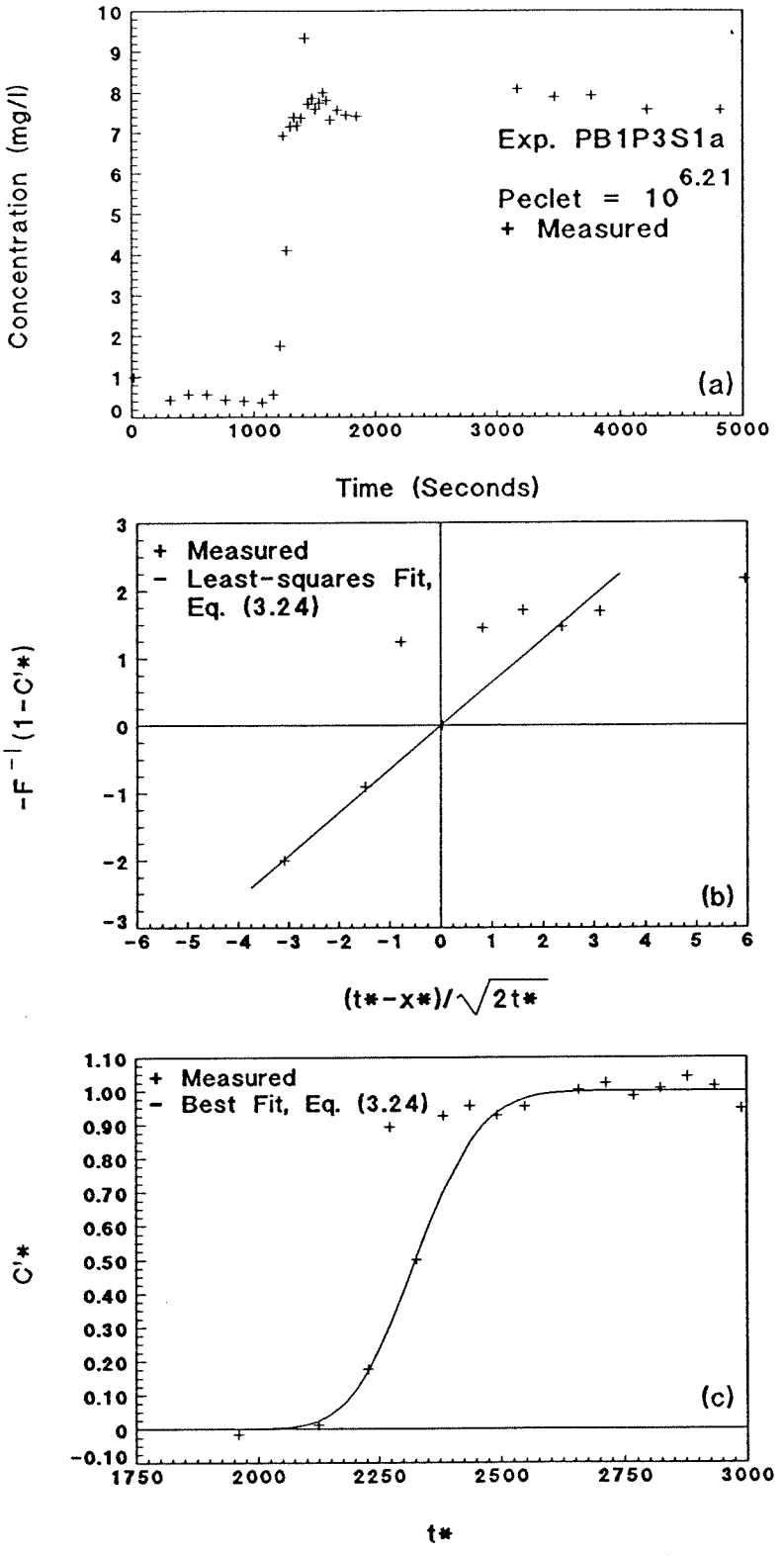

Fig. C.89: Exp. PB1P3S1a forward breakthrough, sample port 3, $Pe_p = 10^{6.18}$: (a) complete experimental data; (b) linearization with least-squares fit; and (c) breakthrough only with best-fit, Eq. (3.24).

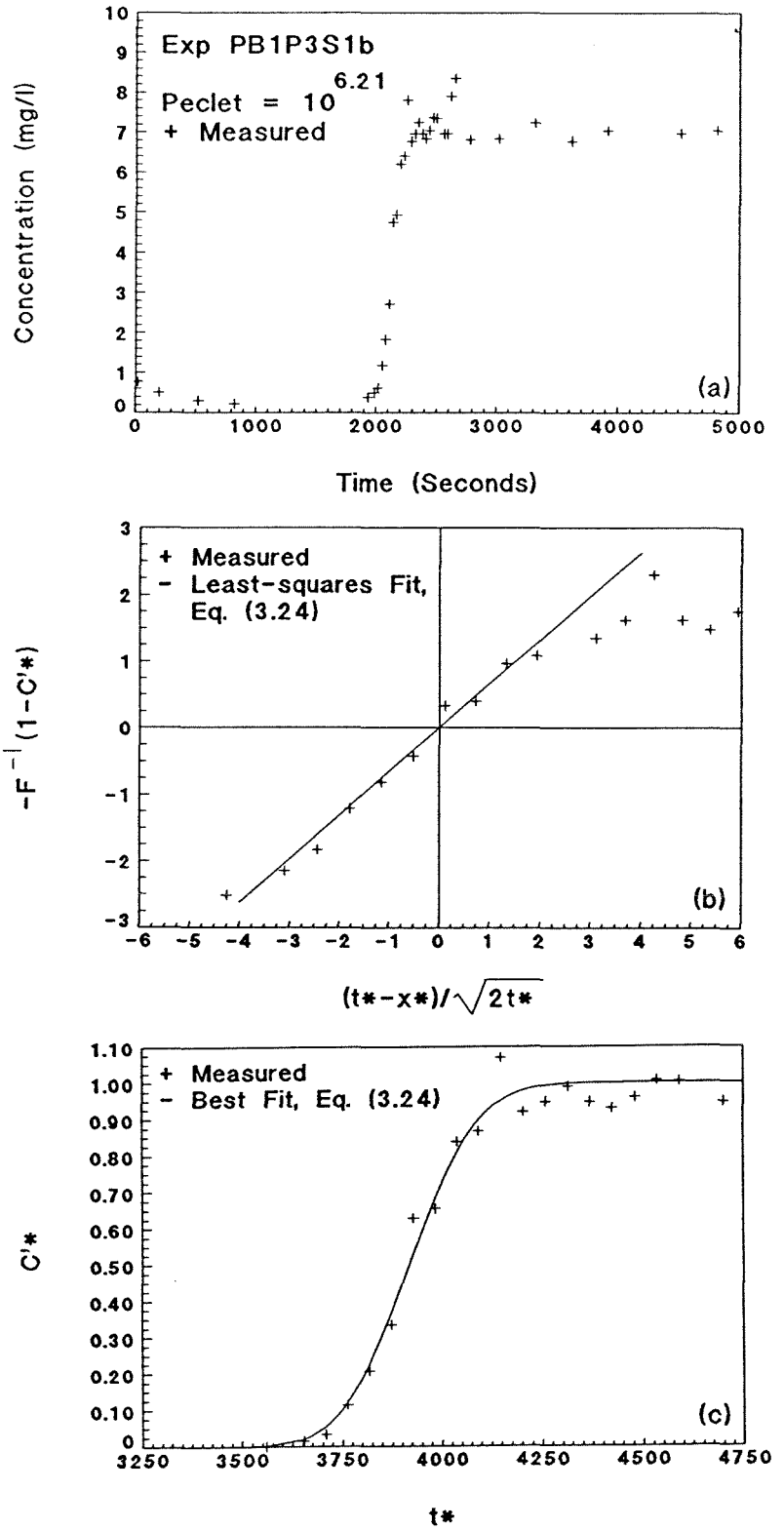

Fig. C.90: Exp. PB1P3S1b forward breakthrough, sample port 5, $Pe_p = 10^{6.18}$: (a) complete experimental data; (b) linearization with least-squares fit; and (c) breakthrough only with best-fit, Eq. (3.24).

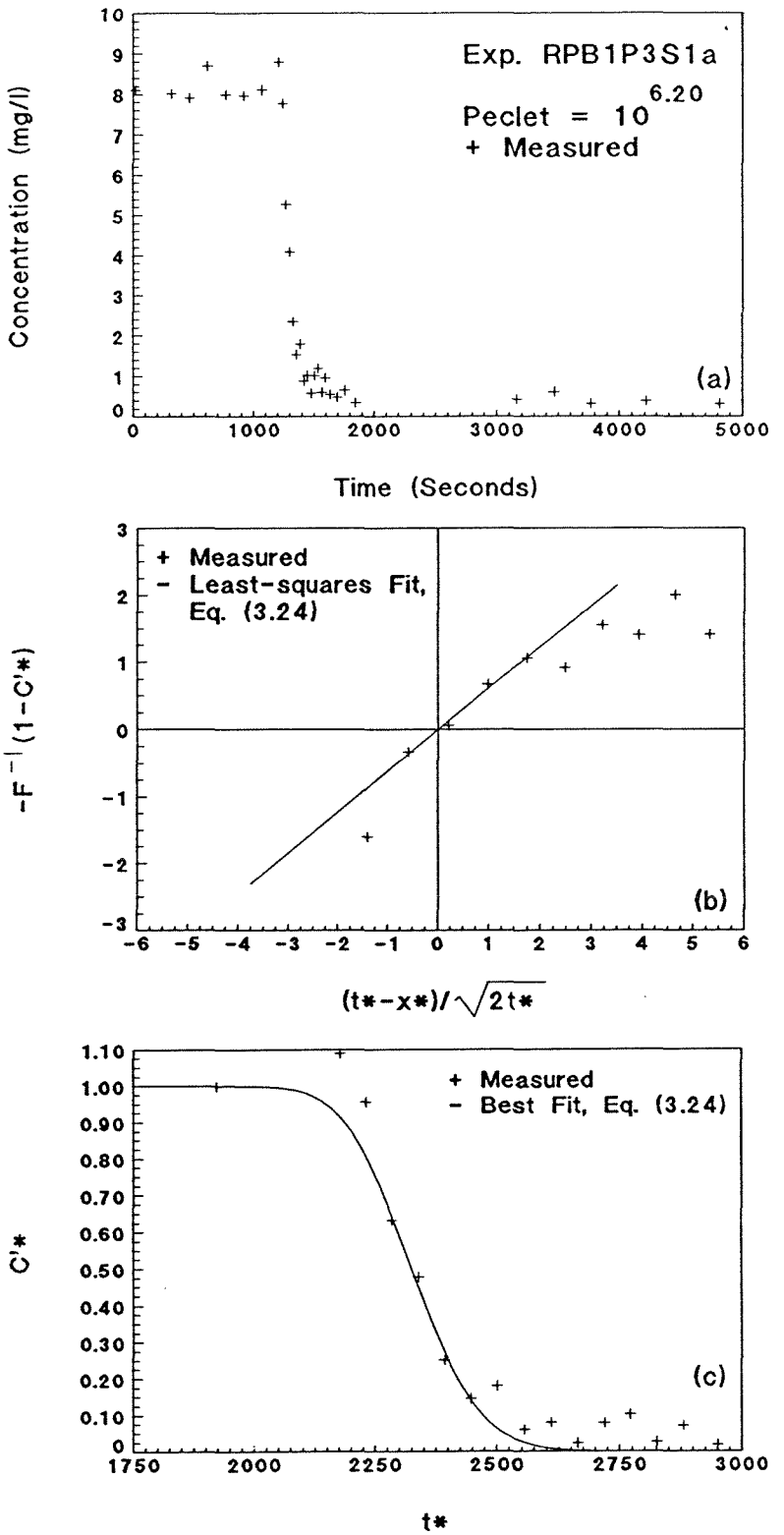

Fig. C.91: Exp. RPB1P3S1a reverse breakthrough, sample port 3, $Pe_p = 10^{6.18}$: (a) complete experimental data; (b) linearization with least-squares fit; and (c) breakthrough only with best-fit, Eq. (3.24).

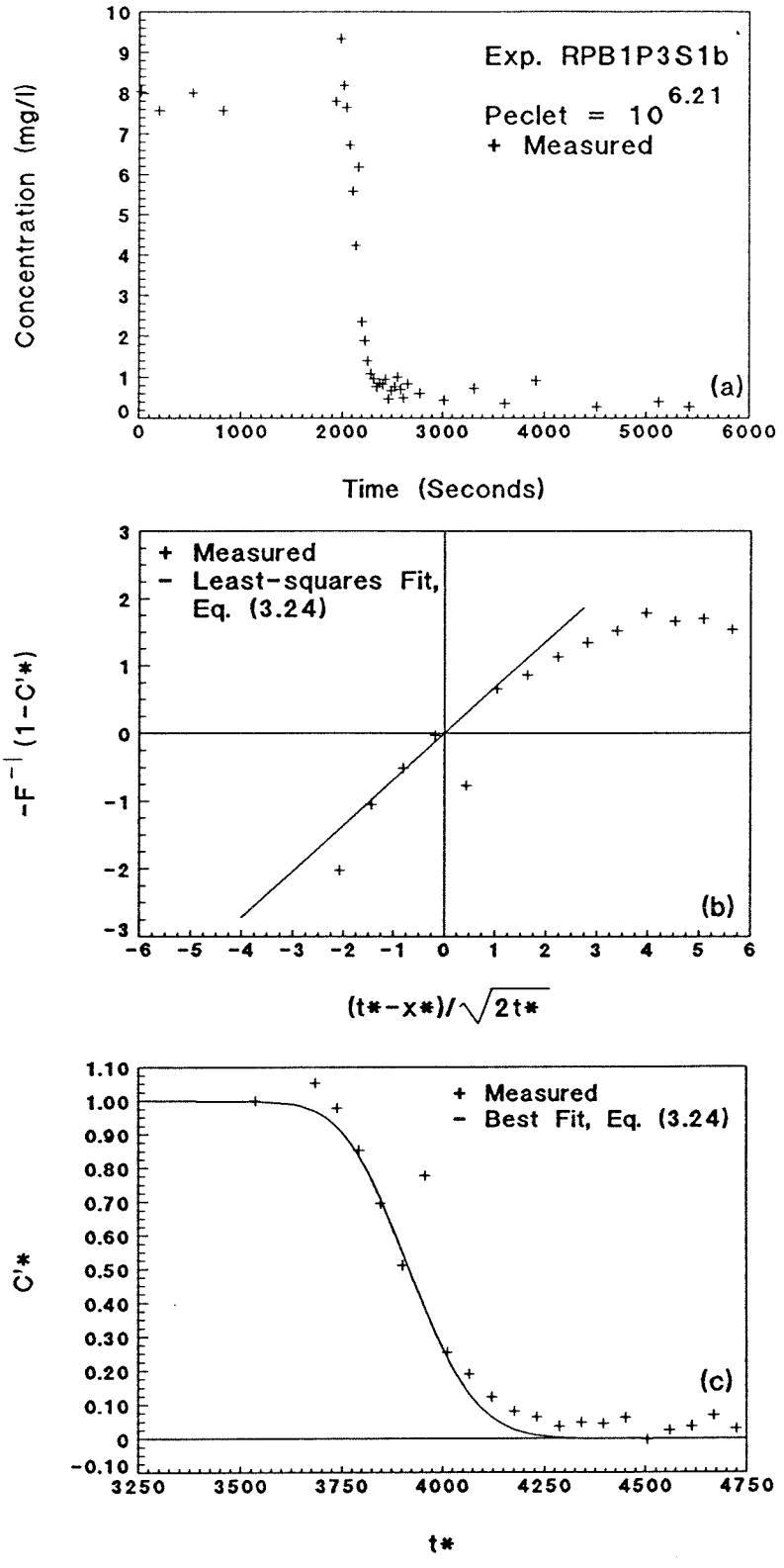

Fig. C.92: Exp. RPB1P3S1b reverse breakthrough, sample port 5, $Pe_p = 10^{6.18}$: (a) complete experimental data; (b) linearization with least-squares fit; and (c) breakthrough only with best-fit, Eq. (3.24).

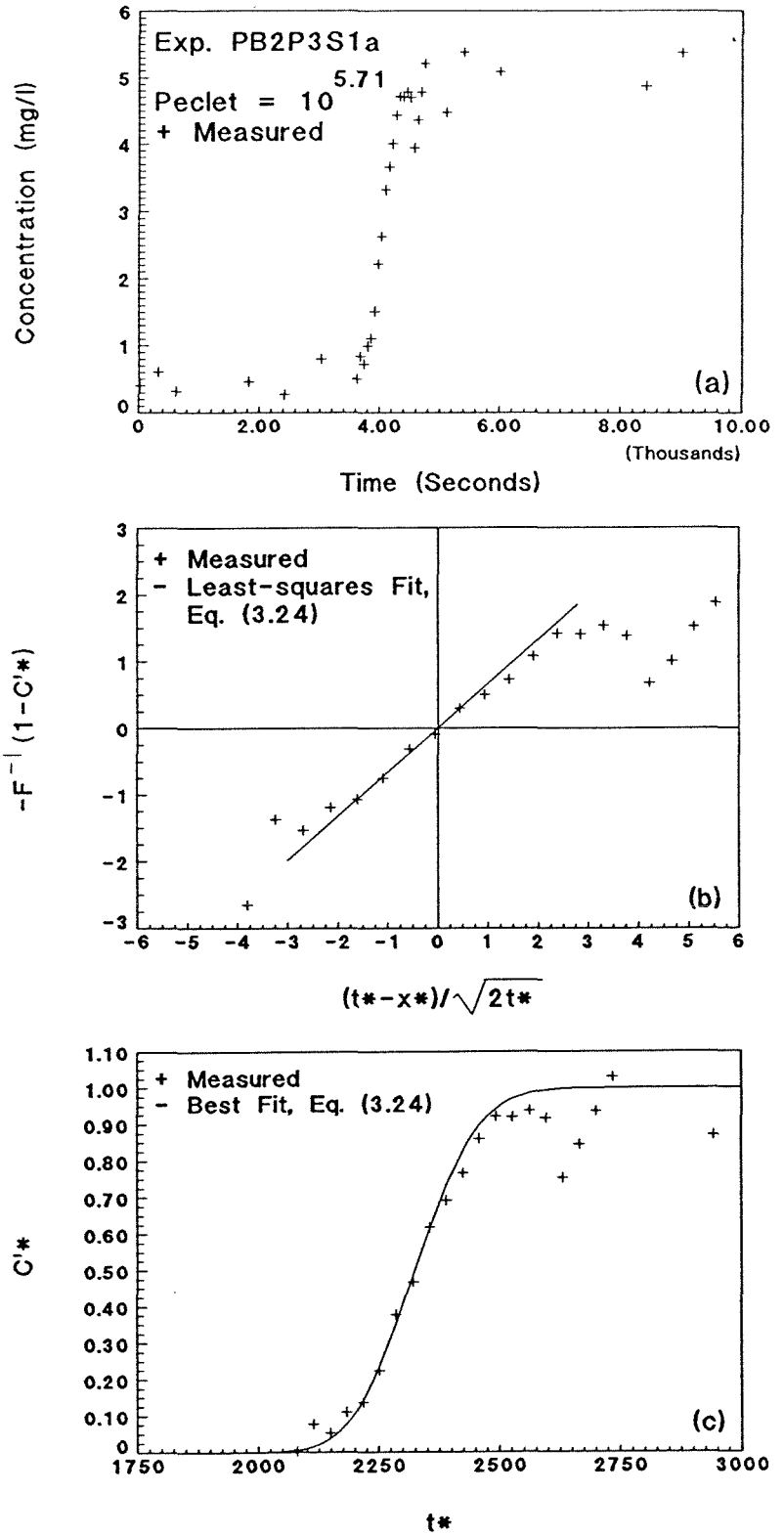

Fig. C.93: Exp. PB2P3S1a forward breakthrough, sample port 3, $Pe_p = 10^{5.68}$: (a) complete experimental data; (b) linearization with least-squares fit; and (c) breakthrough only with best-fit, Eq. (3.24).

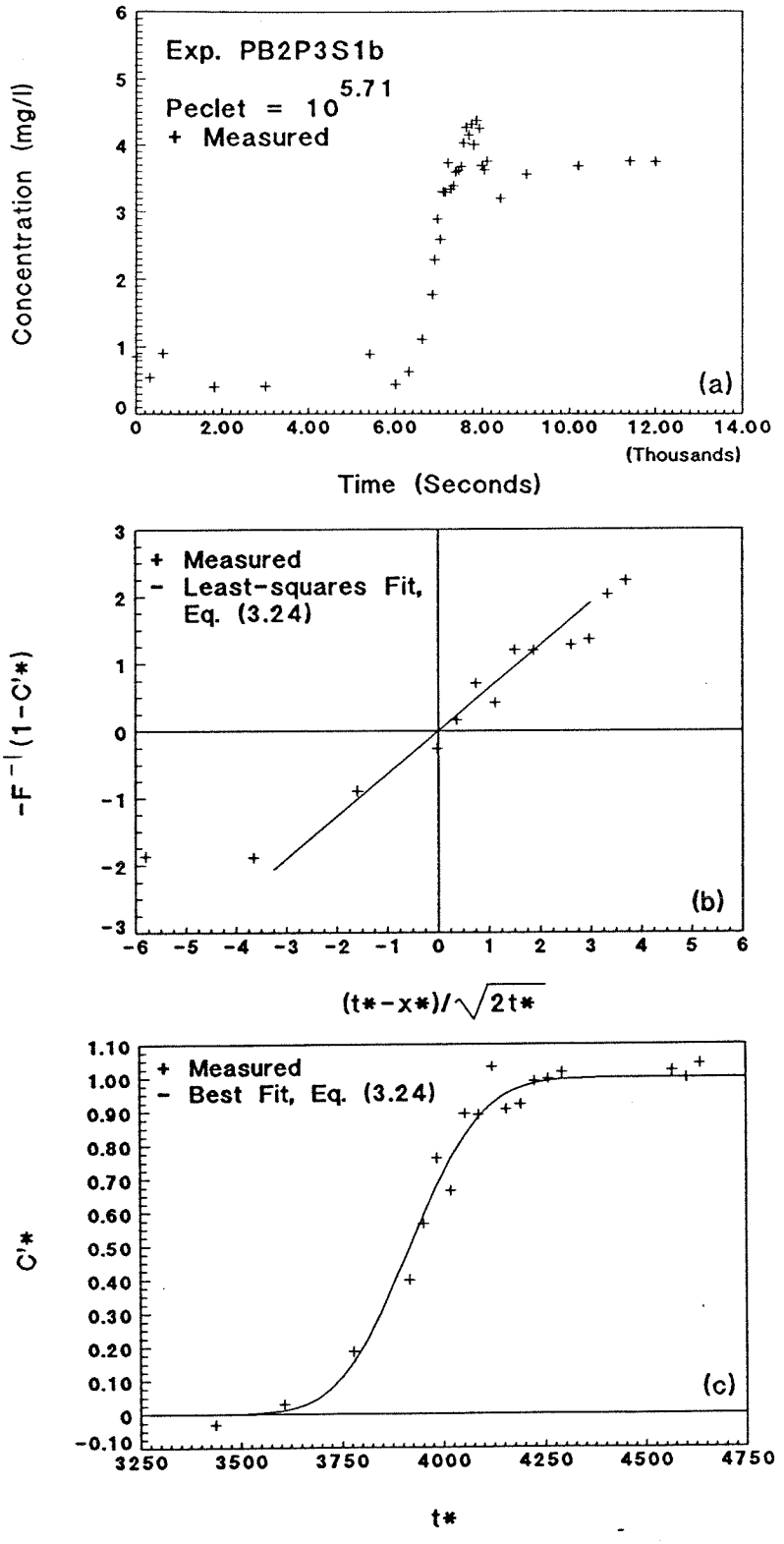

Fig. C.94: Exp. PB2P3S1b forward breakthrough, sample port 5, $Pe_p = 10^{5.68}$: (a) complete experimental data; (b) linearization with least-squares fit; and (c) breakthrough only with best-fit, Eq. (3.24).

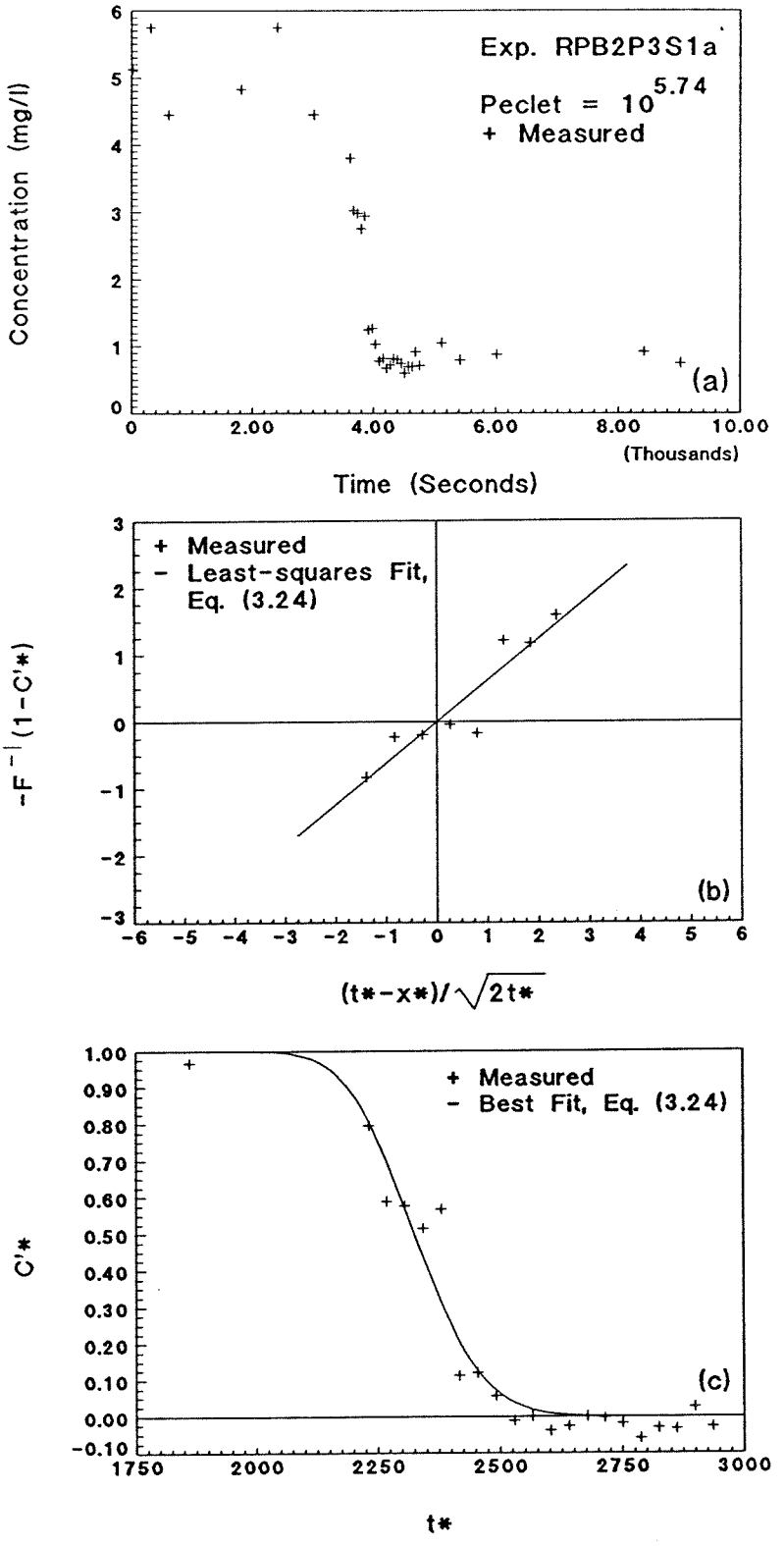

Fig. C.95: Exp. RPB2P3S1a reverse breakthrough, sample port 3, $Pe_p = 10^{5.71}$: (a) complete experimental data; (b) linearization with least-squares fit; and (c) breakthrough only with best-fit, Eq. (3.24).

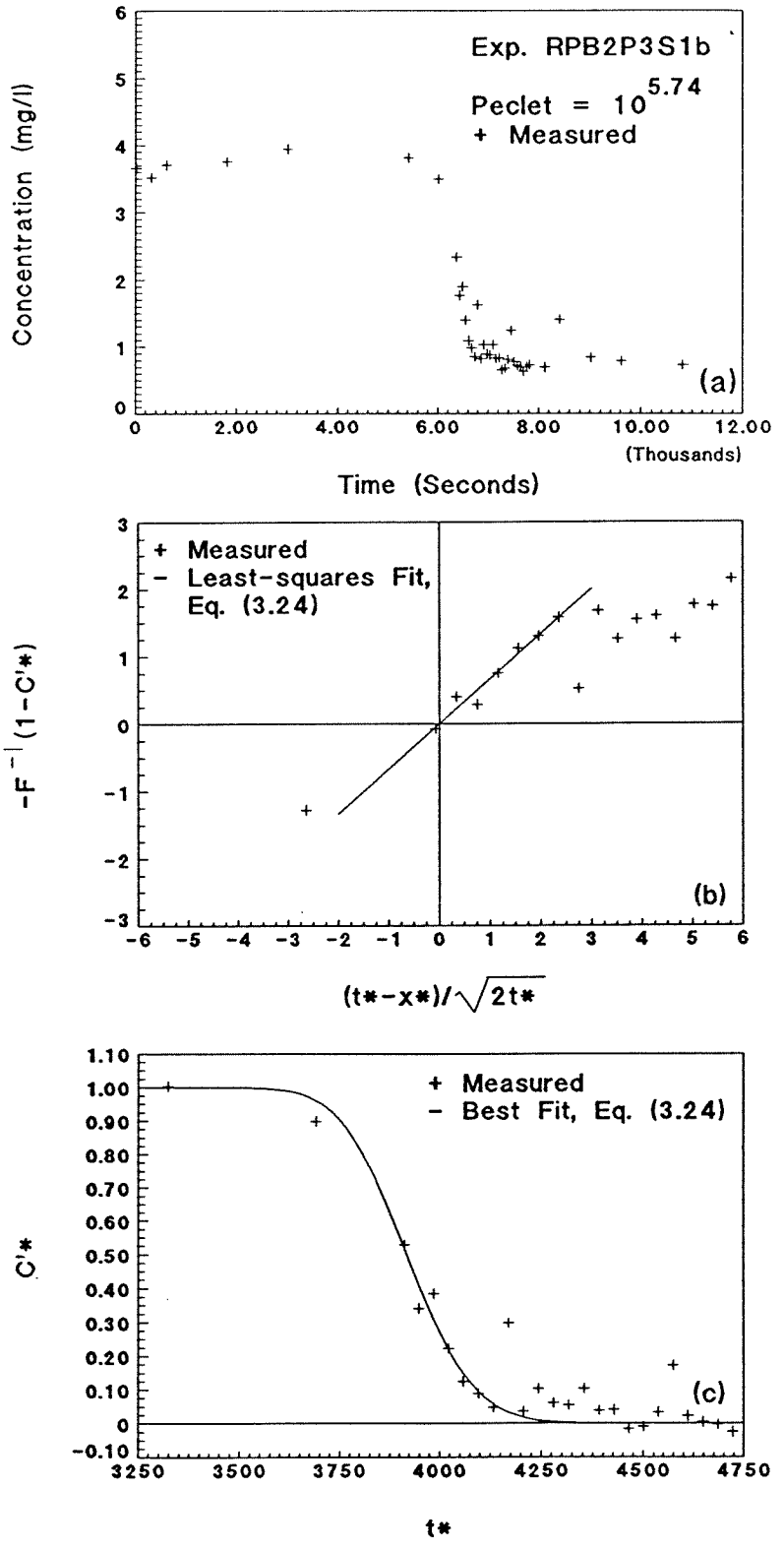

Fig. C.96: Exp. RPB2P3S1b reverse breakthrough, sample port 5, $Pe_p = 10^{5.71}$: (a) complete experimental data; (b) linearization with least-squares fit; and (c) breakthrough only with best-fit, Eq. (3.24).

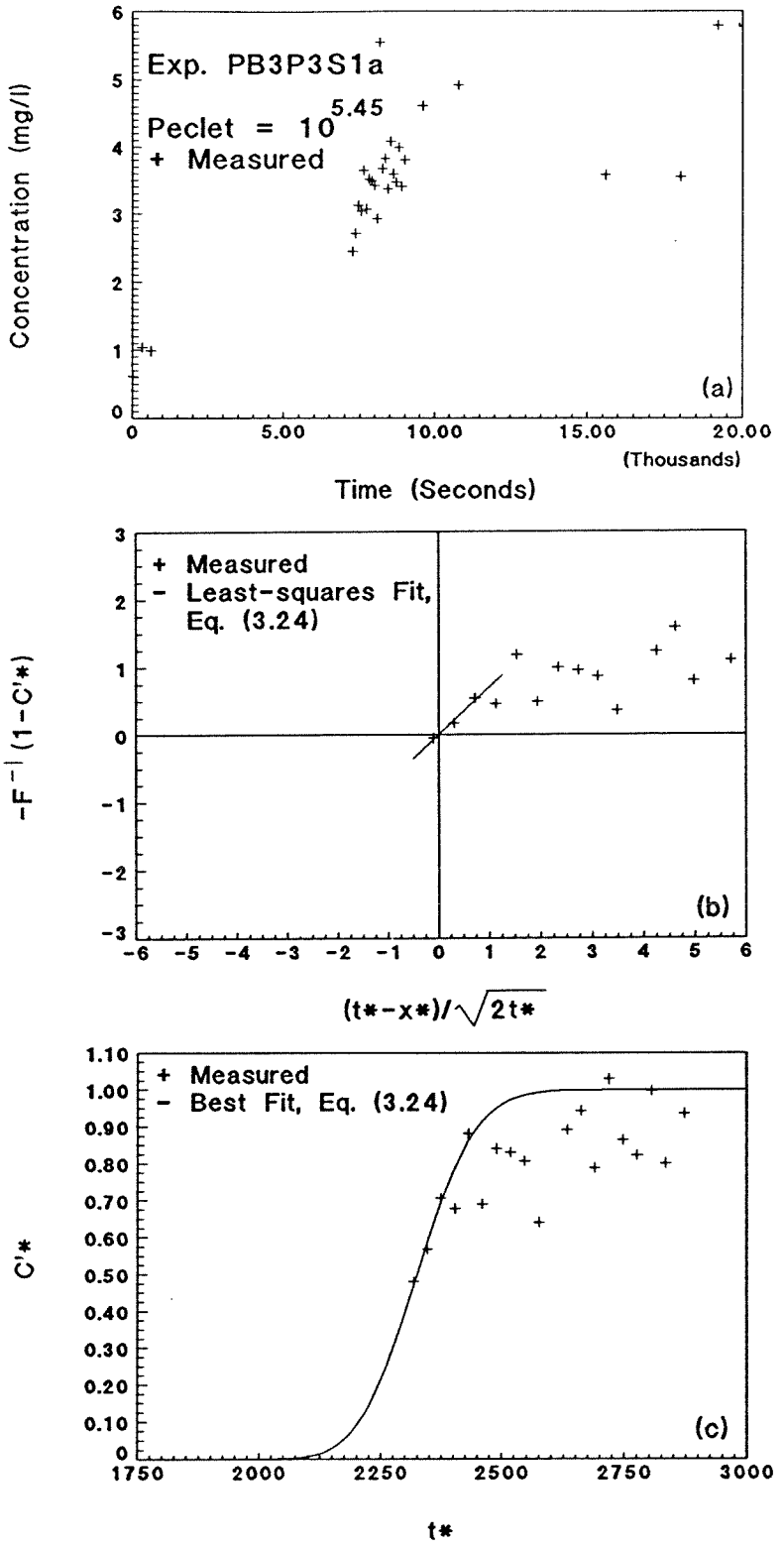

Fig. C.97: Exp. PB3P3S1a forward breakthrough, sample port 3, $Pe_p = 10^{5.42}$: (a) complete experimental data; (b) linearization with least-squares fit; and (c) breakthrough only with best-fit, Eq. (3.24).

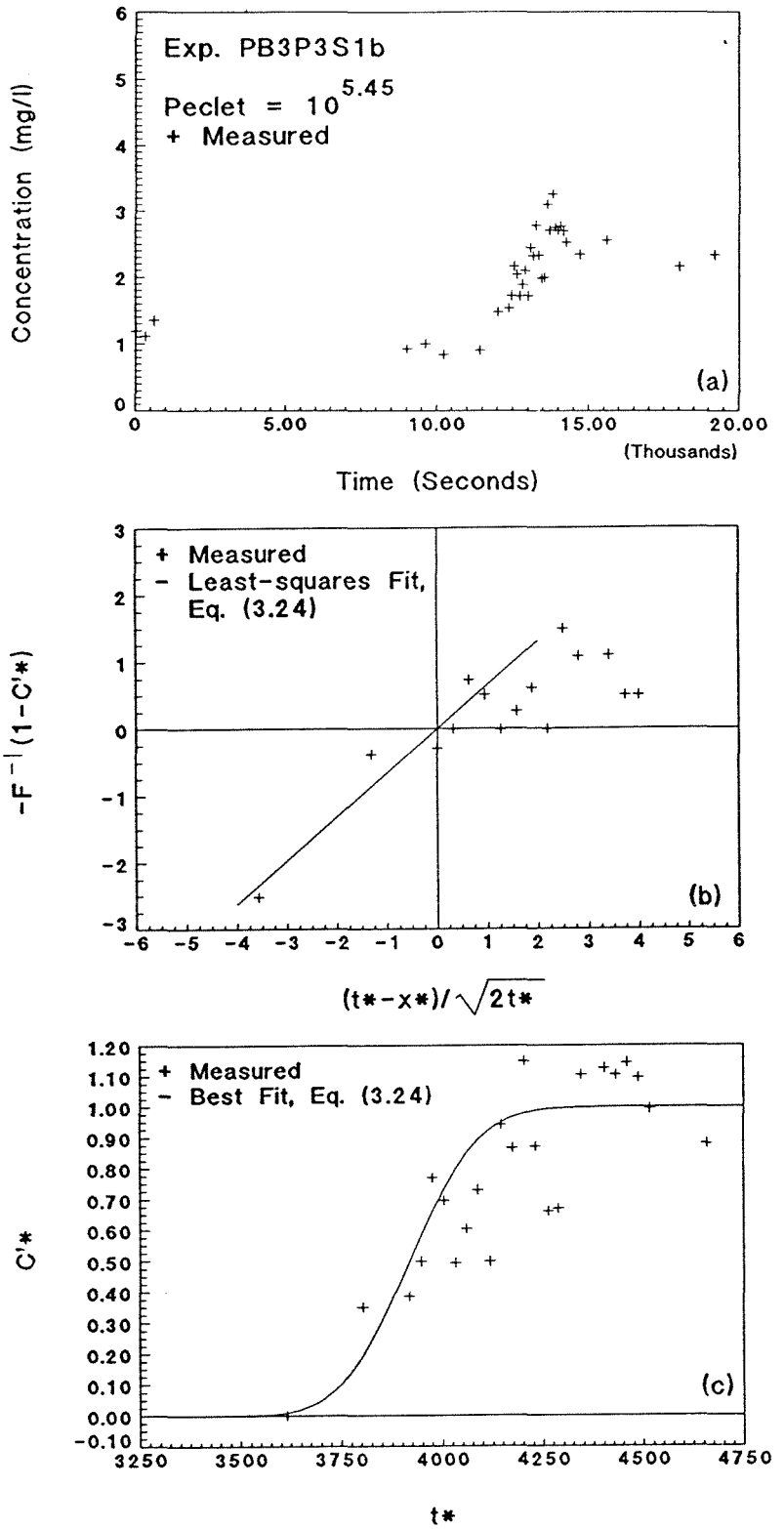

Fig. C.98: Exp. PB3P3S1b forward breakthrough, sample port 5, $Pe_p = 10^{5.42}$: (a) complete experimental data; (b) linearization with least-squares fit; and (c) breakthrough only with best-fit, Eq. (3.24).

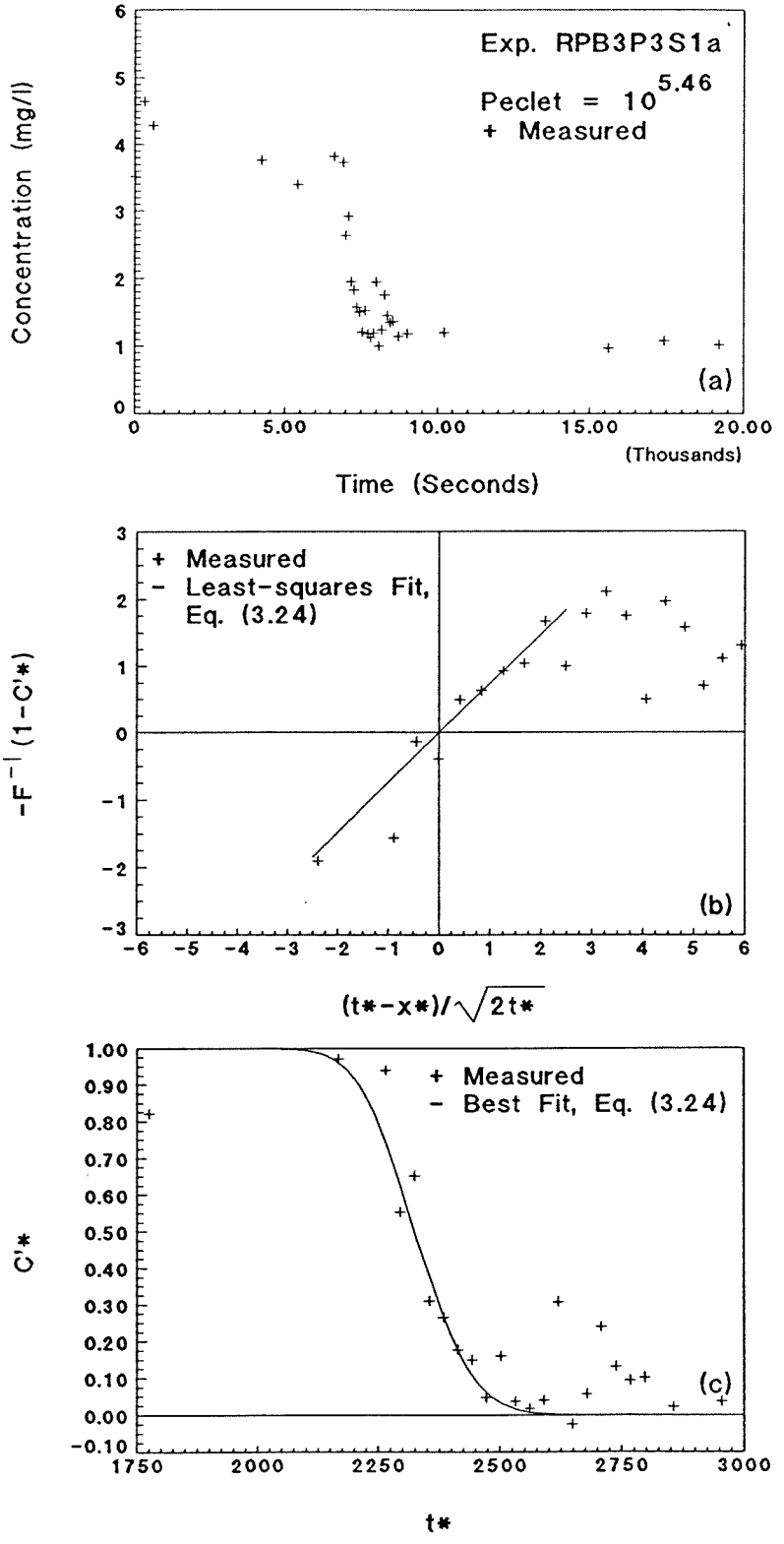

Fig. C.99: Exp. RPB3P3S1a reverse breakthrough, sample port 3, $Pe_p = 10^{5.44}$: (a) complete experimental data; (b) linearization with least-squares fit; and (c) breakthrough only with best-fit, Eq. (3.24).

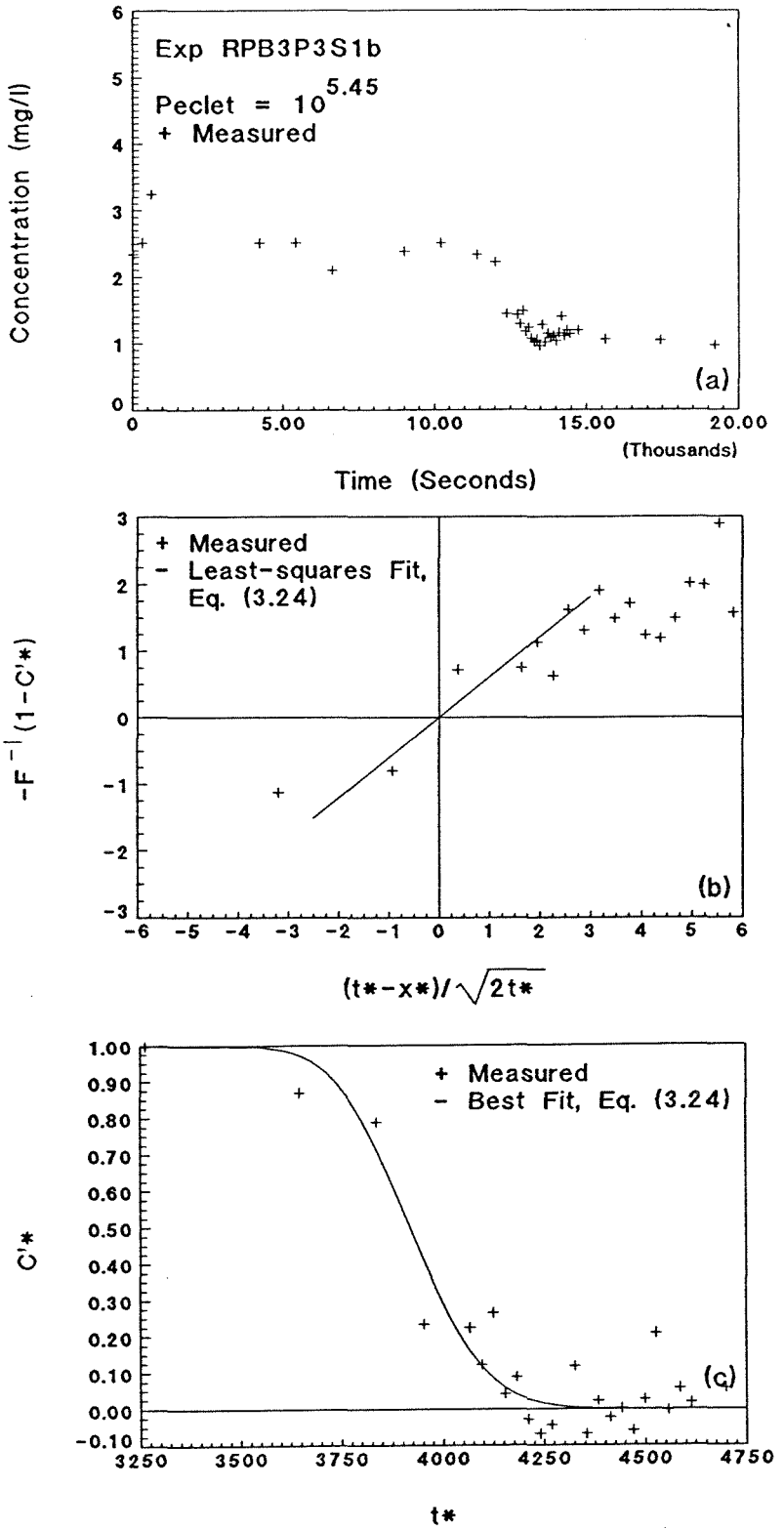

Fig. C.100: Exp. RPB3P3S1b reverse breakthrough, sample port 5, $Pe_p = 10^{5.42}$: (a) complete experimental data; (b) linearization with least-squares fit; and (c) breakthrough only with best-fit, Eq. (3.24).

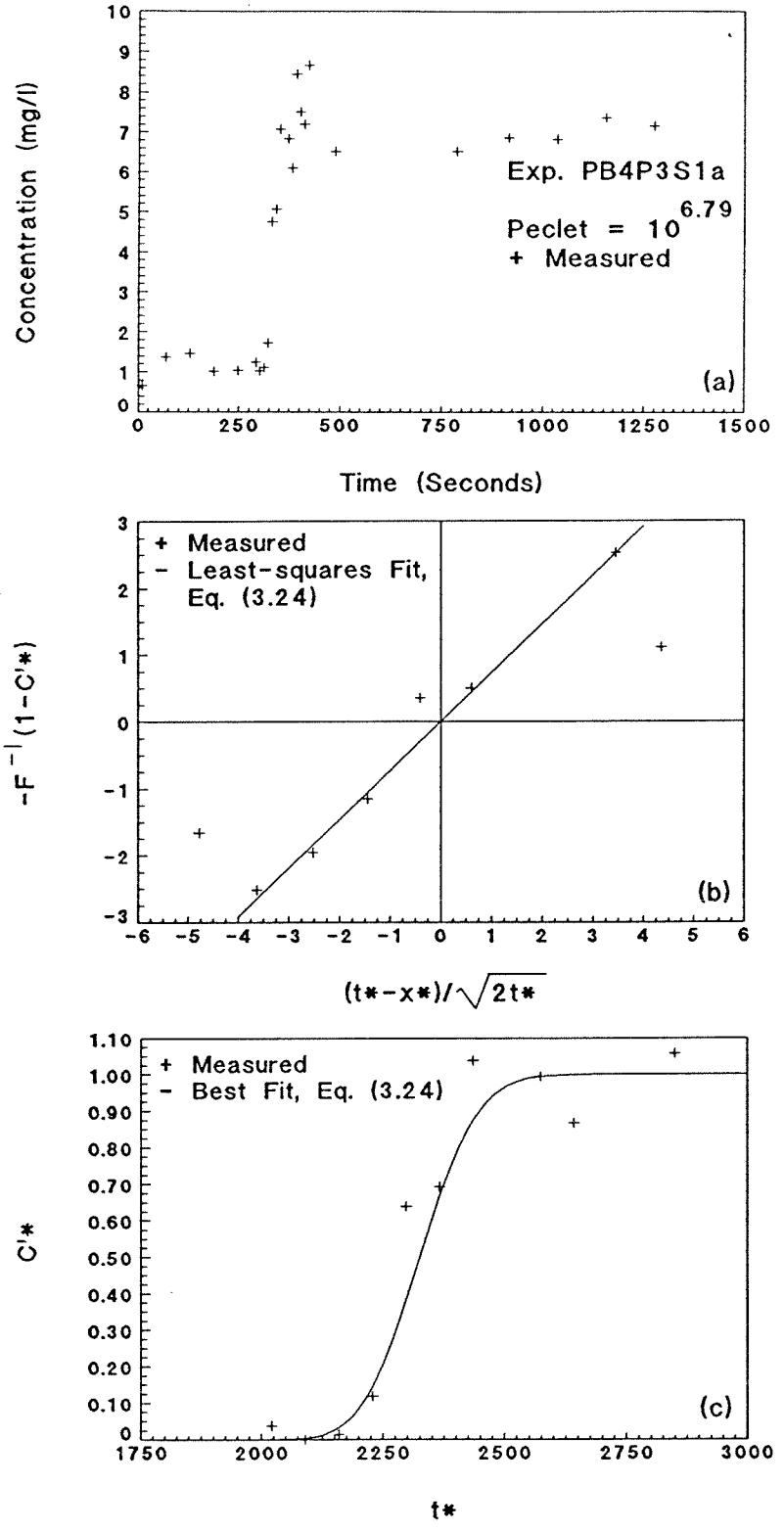

Fig. C.101: Exp. PB4P3S1a forward breakthrough, sample port 3, $Pe_p = 10^{6.76}$: (a) complete experimental data; (b) linearization with least-squares fit; and (c) breakthrough only with best-fit, Eq. (3.24).

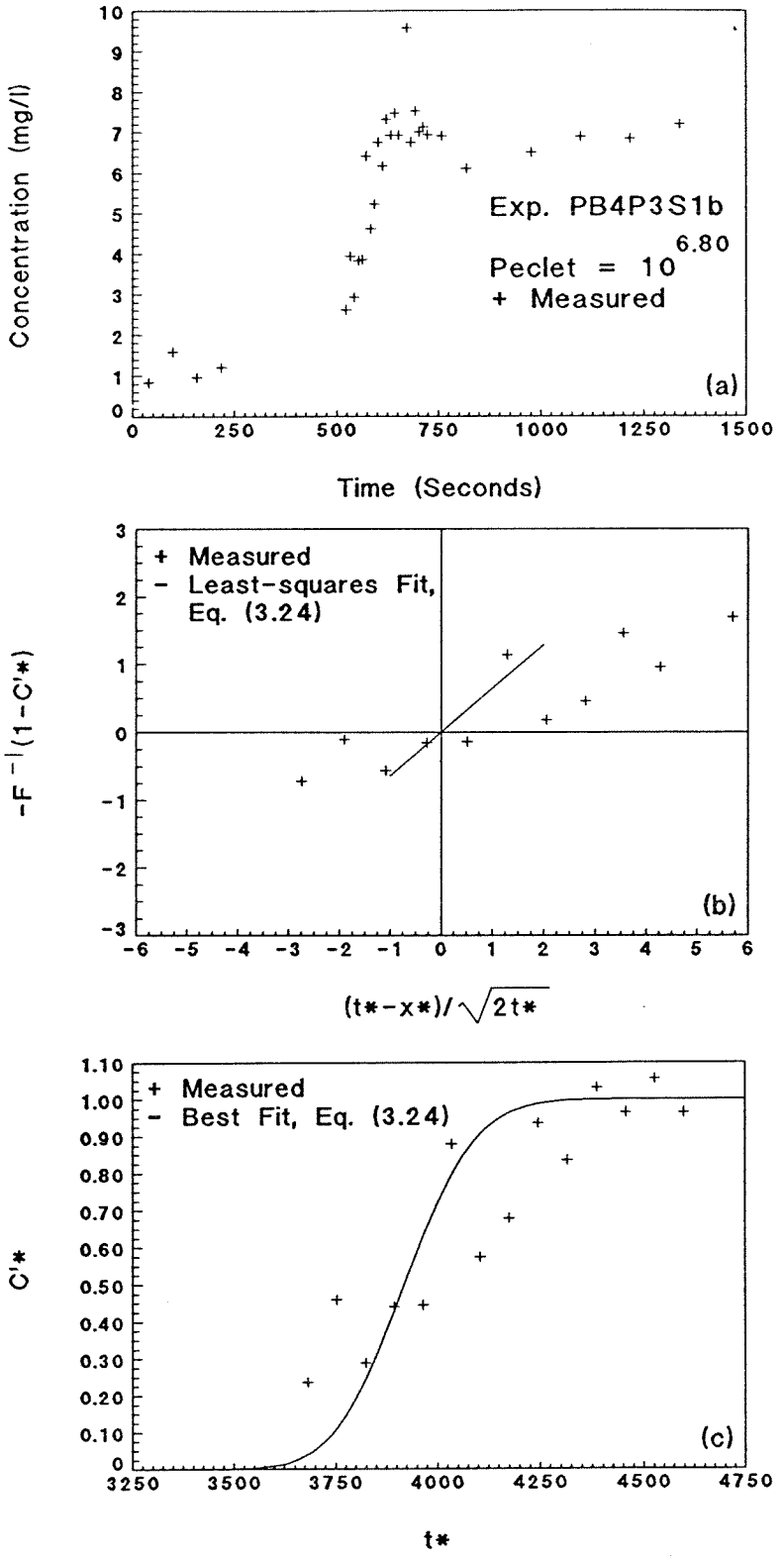

Fig. C.102: Exp. PB4P3S1b forward breakthrough, sample port 5, $Pe_p = 10^{6.77}$: (a) complete experimental data; (b) linearization with least-squares fit; and (c) breakthrough only with best-fit, Eq. (3.24).

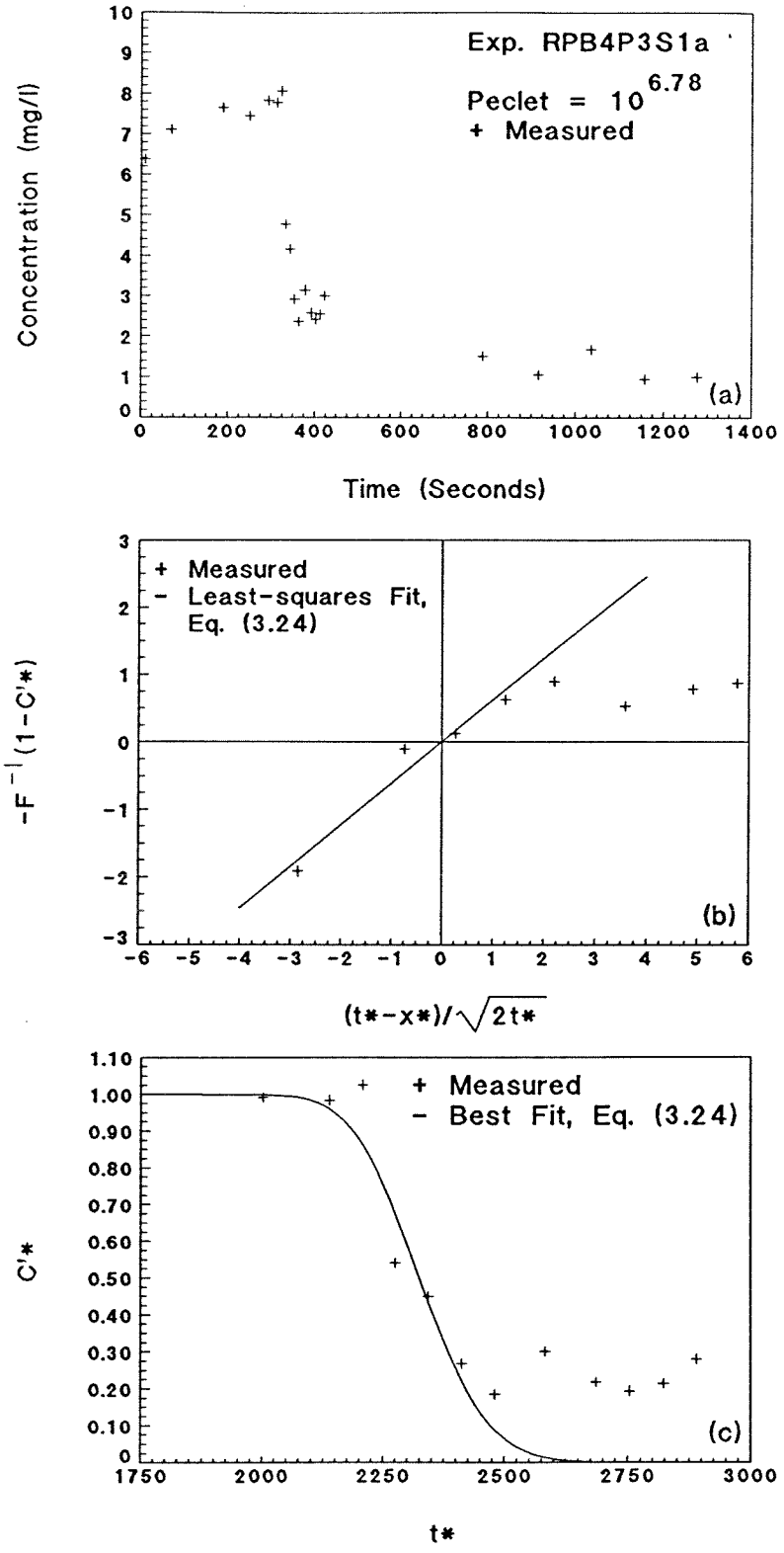

Fig. C.103: Exp. RPB4P3S1a reverse breakthrough, sample port 3, $Pe_p = 10^{6.75}$: (a) complete experimental data; (b) linearization with least-squares fit; and (c) breakthrough only with best-fit, Eq. (3.24).

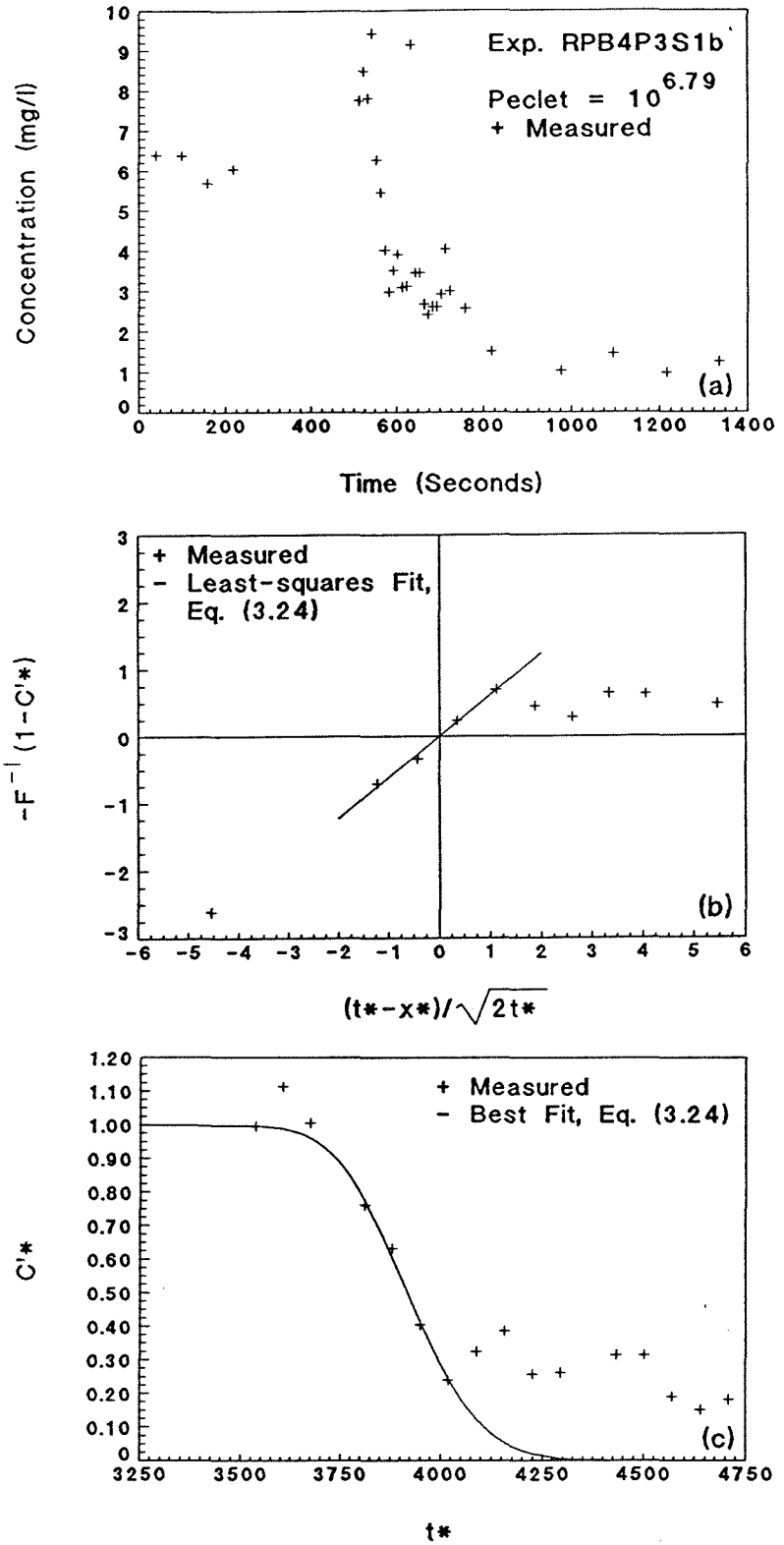

Fig. C.104: Exp. RPB4P3S1b reverse breakthrough, sample port 5, $Pe_p = 10^{6.76}$: (a) complete experimental data; (b) linearization with least-squares fit; and (c) breakthrough only with best-fit, Eq. (3.24).

C.4 0.1 micron Particle Experiments

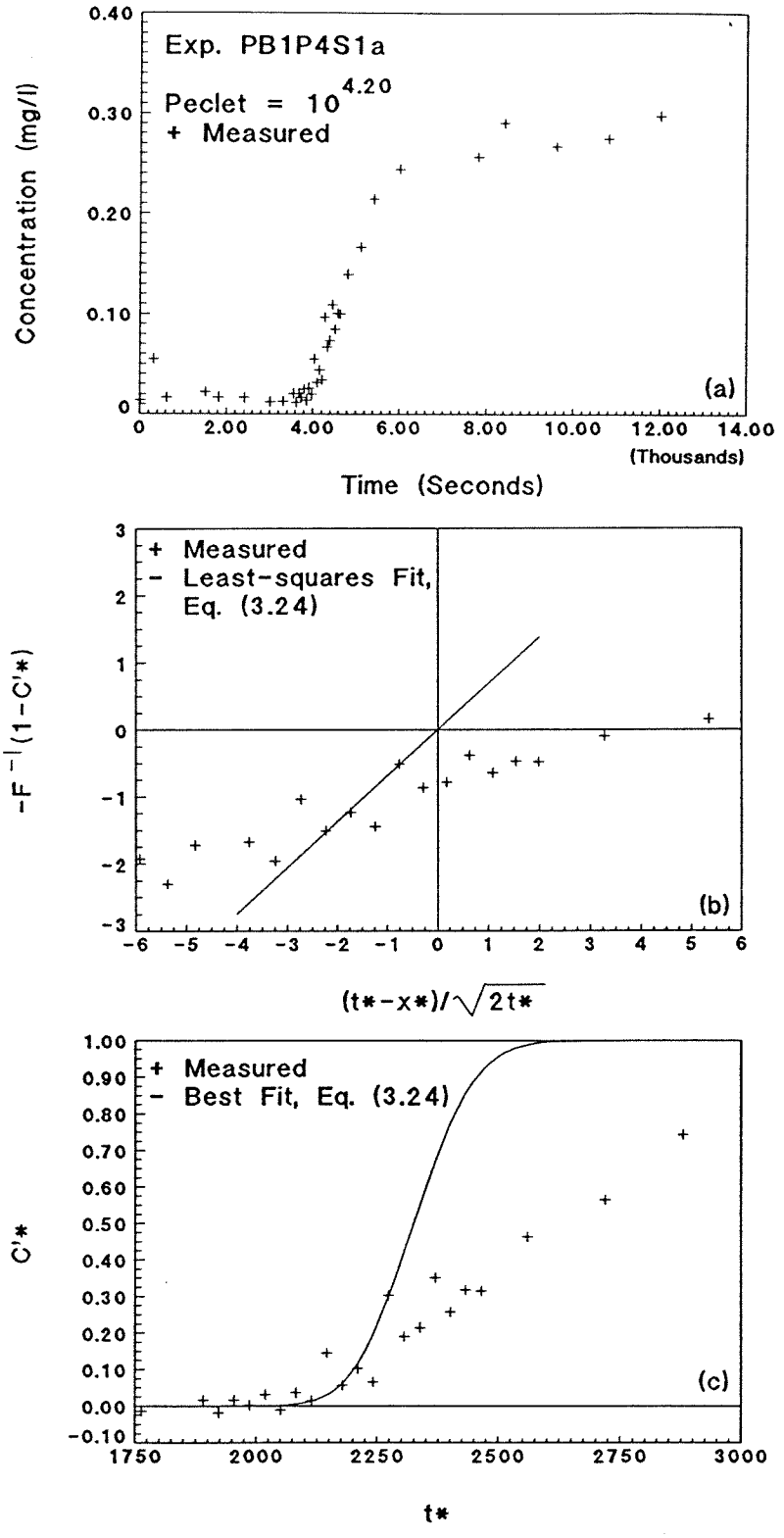

Fig. C.105: Exp. PB1P4S1a forward breakthrough, sample port 3, $Pe_p = 10^{4.20}$: (a) complete experimental data; (b) linearization with least-squares fit; and (c) breakthrough only with best-fit, Eq. (3.24).

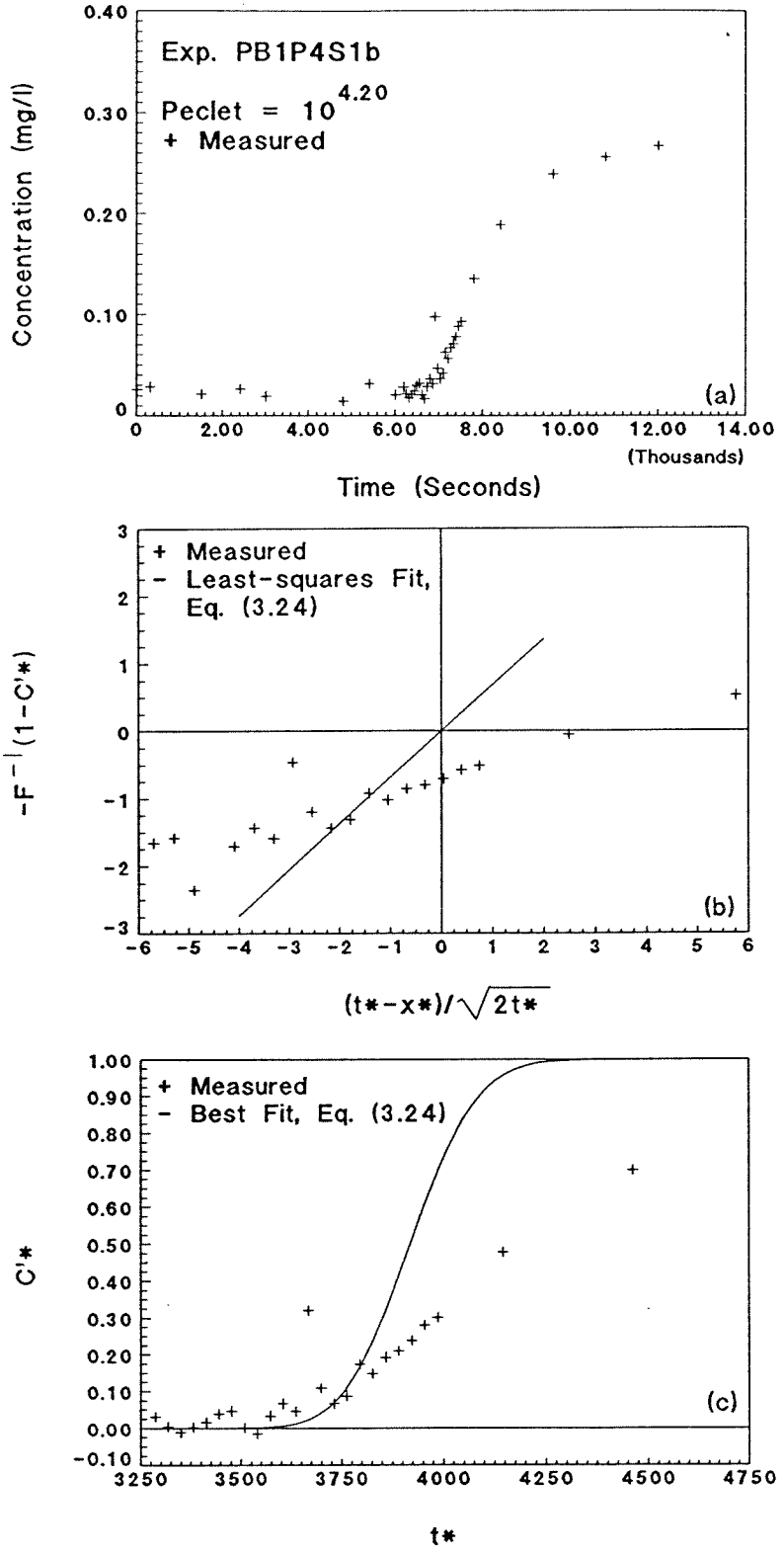

Fig. C.106: Exp. PB1P4S1b forward breakthrough, sample port 5, $Pe_p = 10^{4.20}$: (a) complete experimental data; (b) linearization with least-squares fit; and (c) breakthrough only with best-fit, Eq. (3.24).

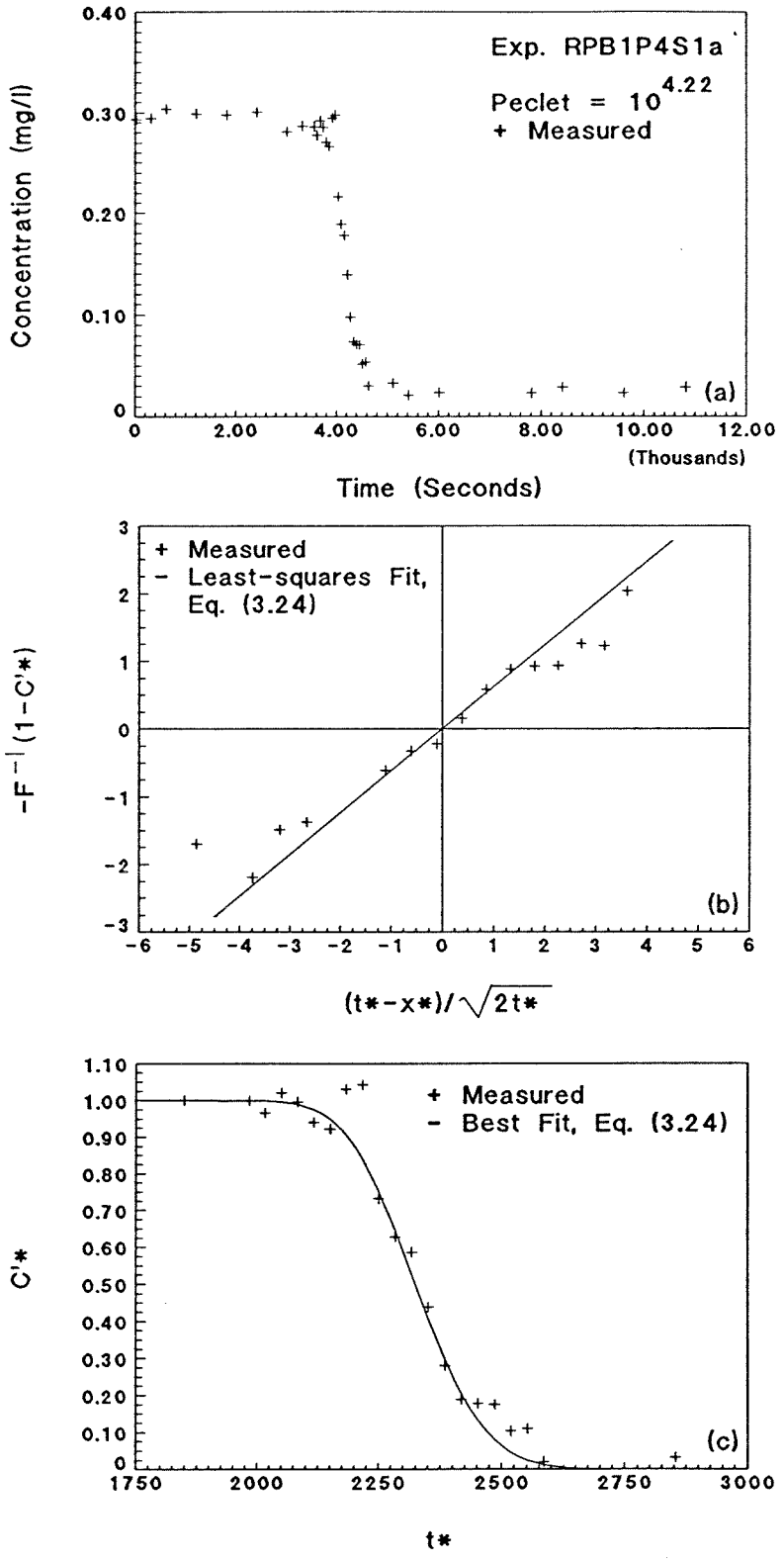

Fig. C.107: Exp. RPB1P4S1a reverse breakthrough, sample port 3, $Pe_p = 10^{4.22}$: (a) complete experimental data; (b) linearization with least-squares fit; and (c) breakthrough only with best-fit, Eq. (3.24).

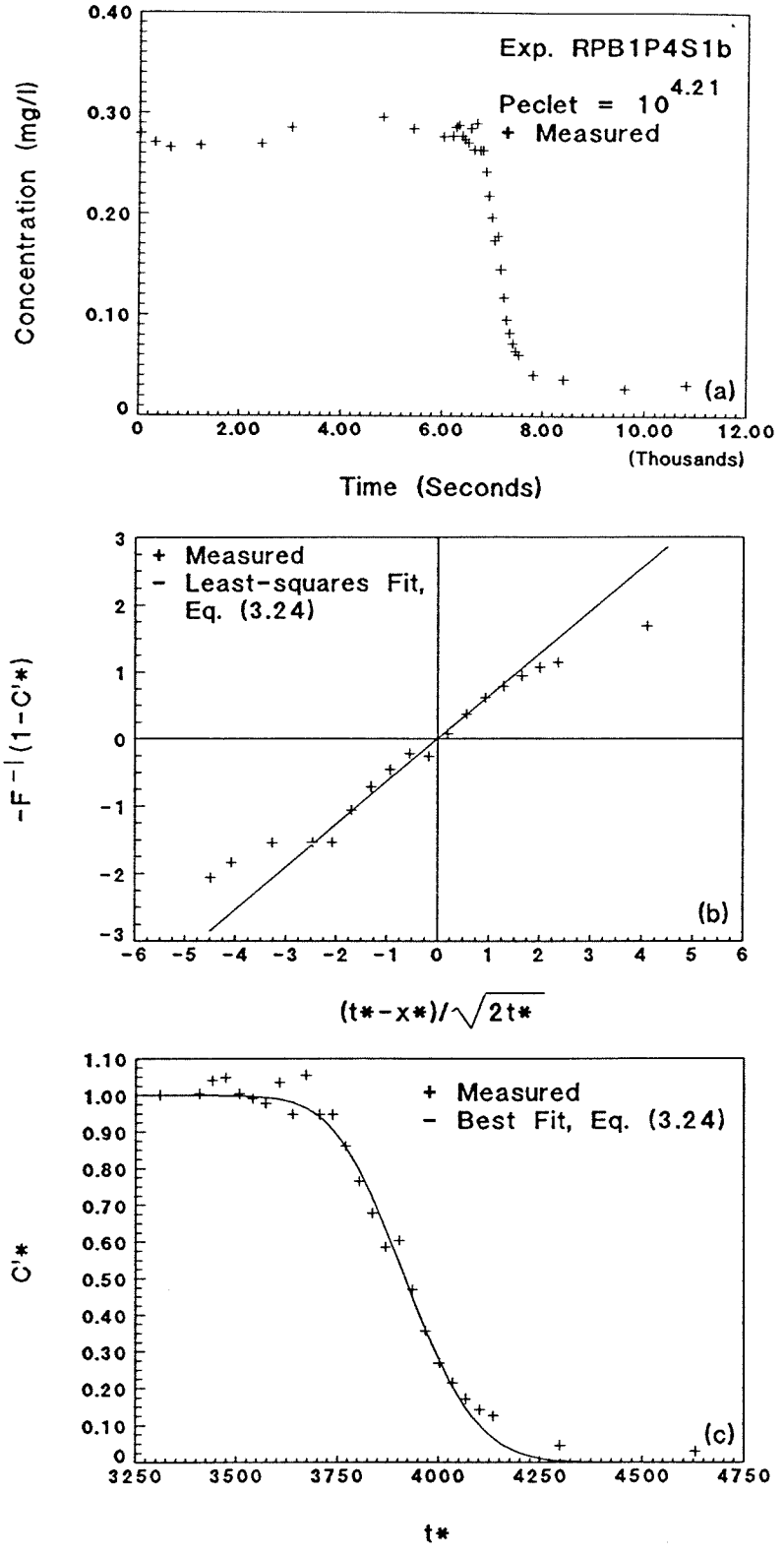

Fig. C.108: Exp. RPB1P4S1b reverse breakthrough, sample port 5, $Pe_p = 10^{4.21}$: (a) complete experimental data; (b) linearization with least-squares fit; and (c) breakthrough only with best-fit, Eq. (3.24).

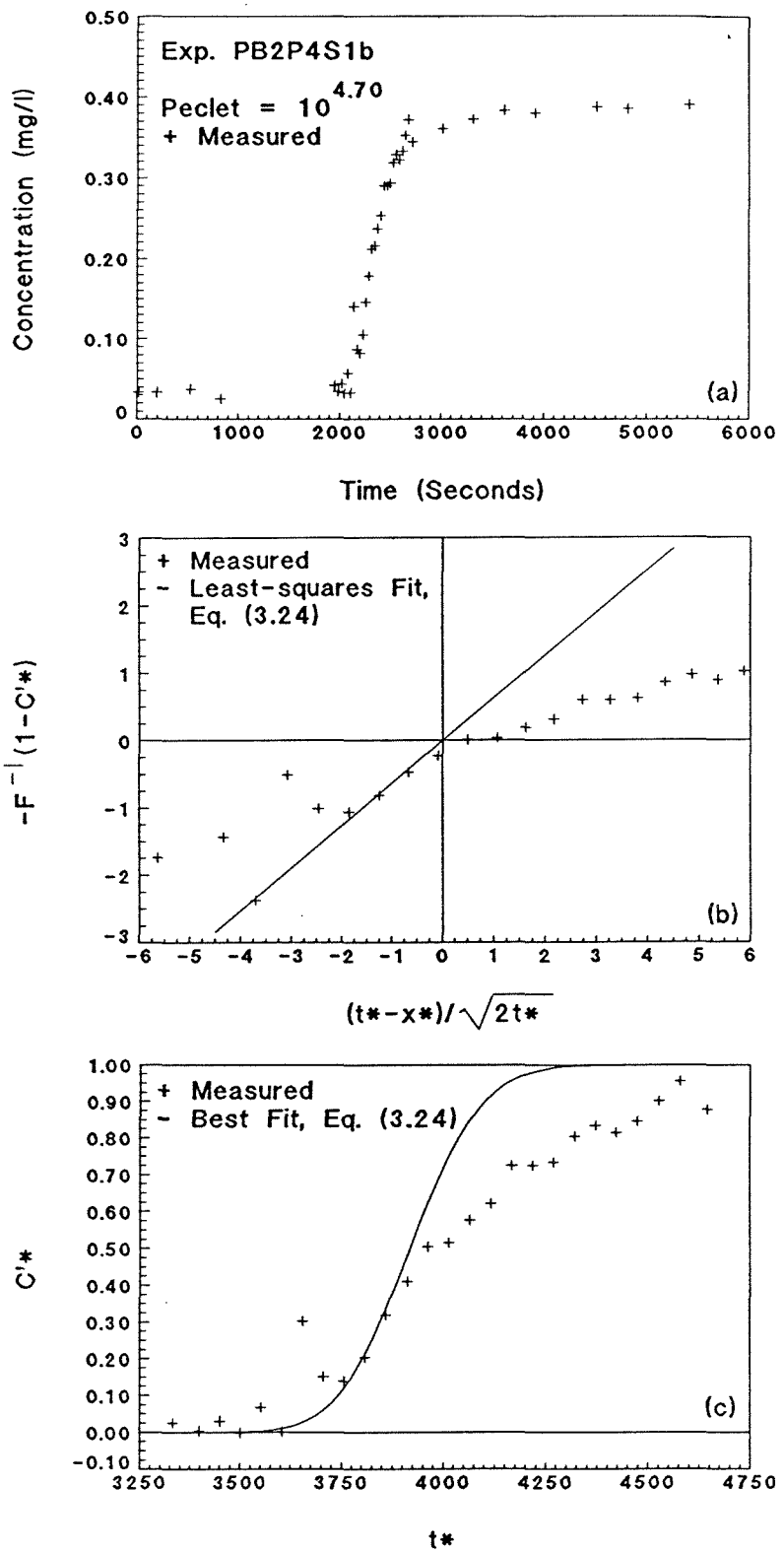

Fig. C.109: Exp. PB2P4S1b forward breakthrough, sample port 5, $Pe_p = 10^{4.70}$: (a) complete experimental data; (b) linearization with least-squares fit; and (c) breakthrough only with best-fit, Eq. (3.24).

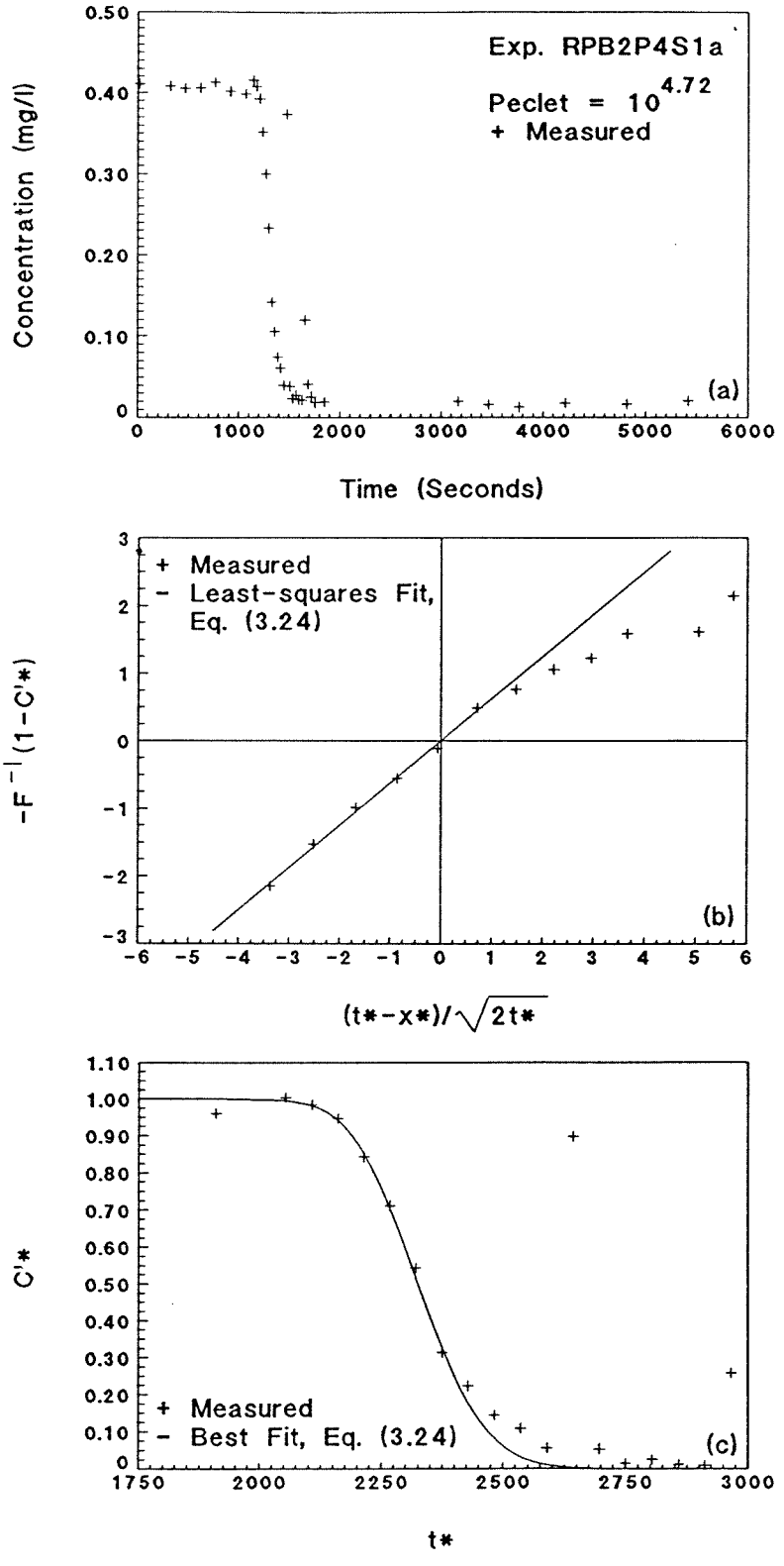

Fig. C.110: Exp. RPB2P4S1a reverse breakthrough, sample port 3, $Pe_p = 10^{4.72}$: (a) complete experimental data; (b) linearization with least-squares fit; and (c) breakthrough only with best-fit, Eq. (3.24).

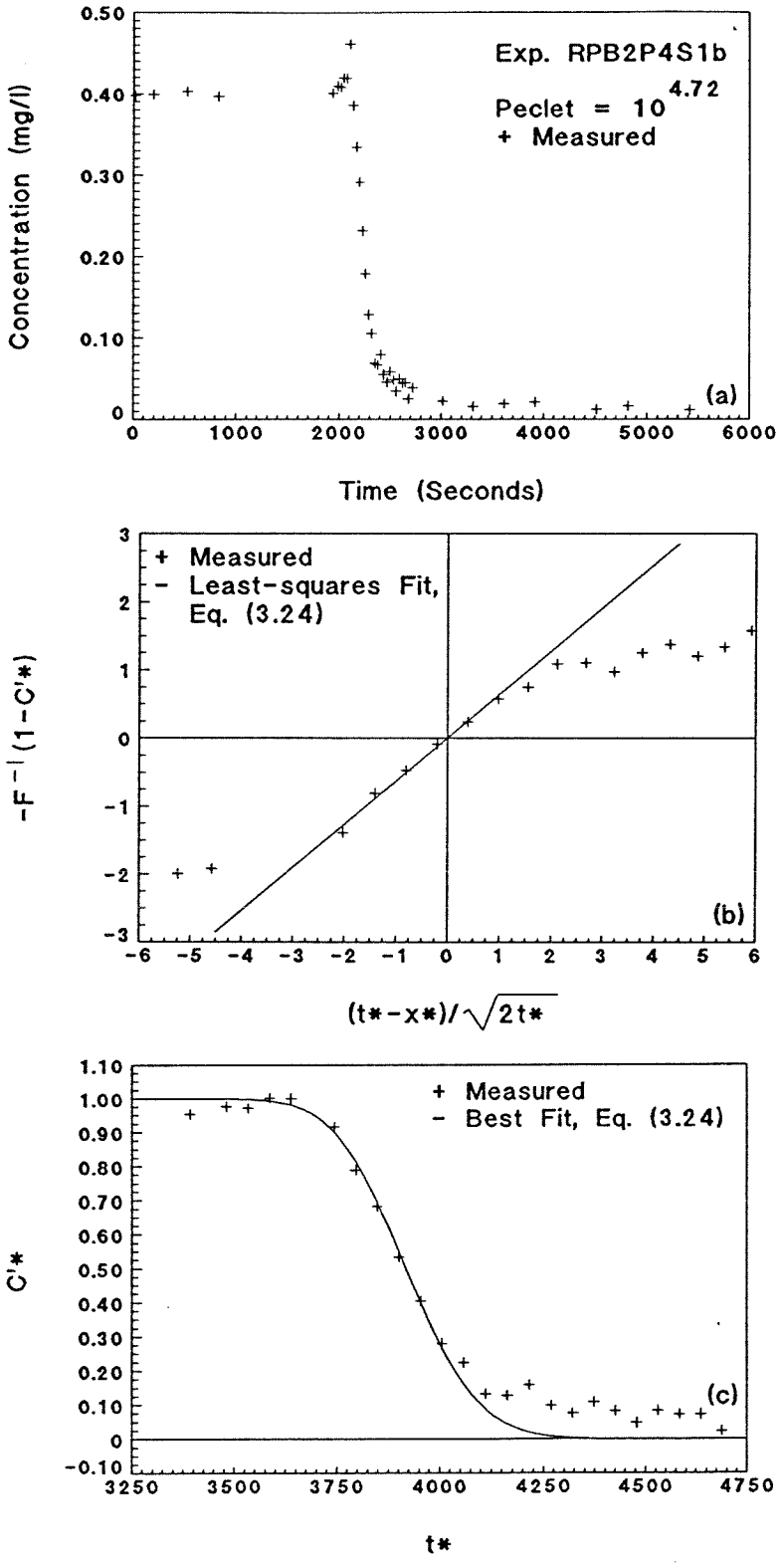

Fig. C.111: Exp. RPB2P4S1b reverse breakthrough, sample port 5, $Pe_p = 10^{4.72}$: (a) complete experimental data; (b) linearization with least-squares fit; and (c) breakthrough only with best-fit, Eq. (3.24).

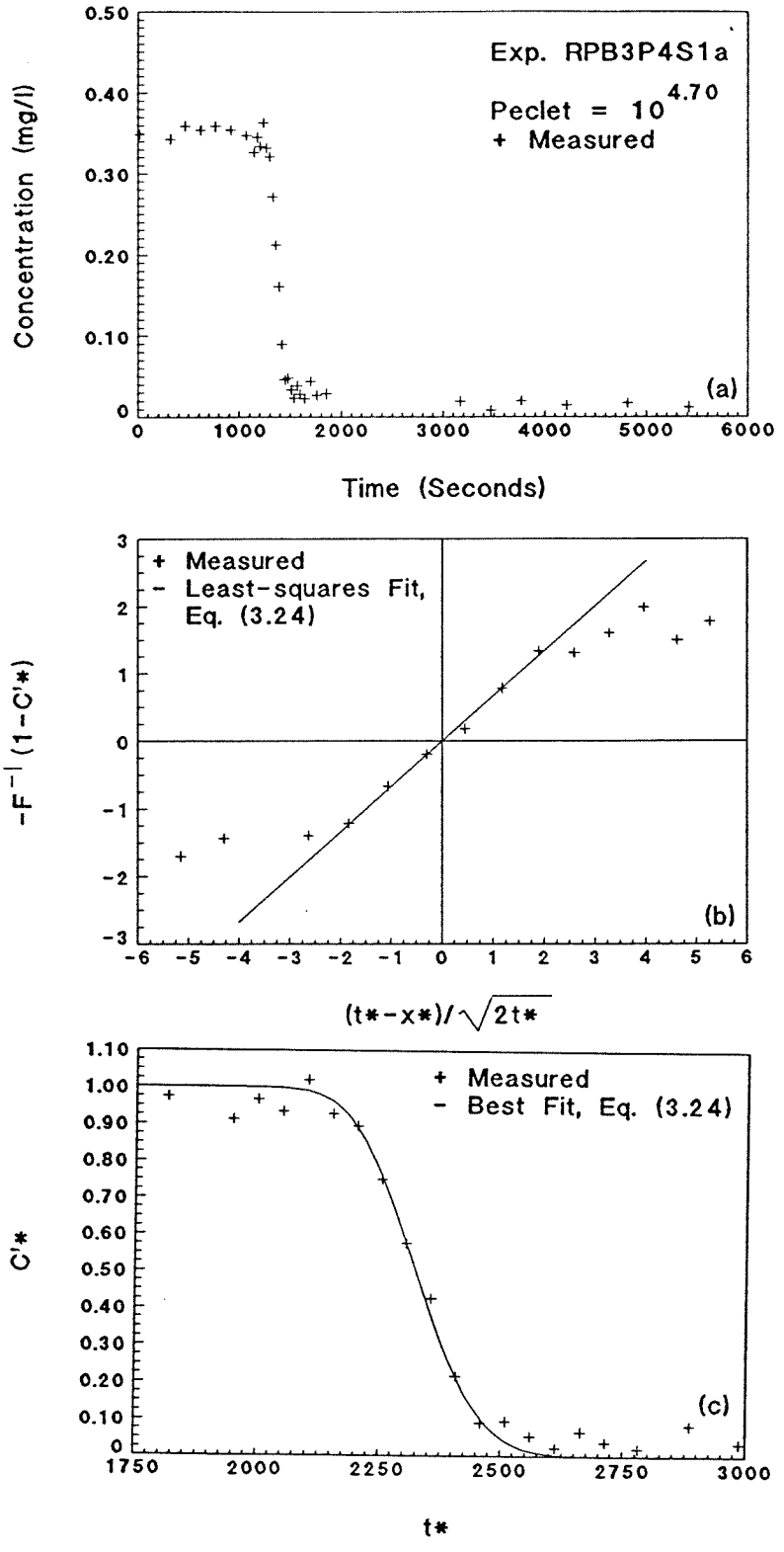

Fig. C.112: Exp. RPB3P4S1a reverse breakthrough, sample port 3, $Pe_p = 10^{4.70}$: (a) complete experimental data; (b) linearization with least-squares fit; and (c) breakthrough only with best-fit, Eq. (3.24).

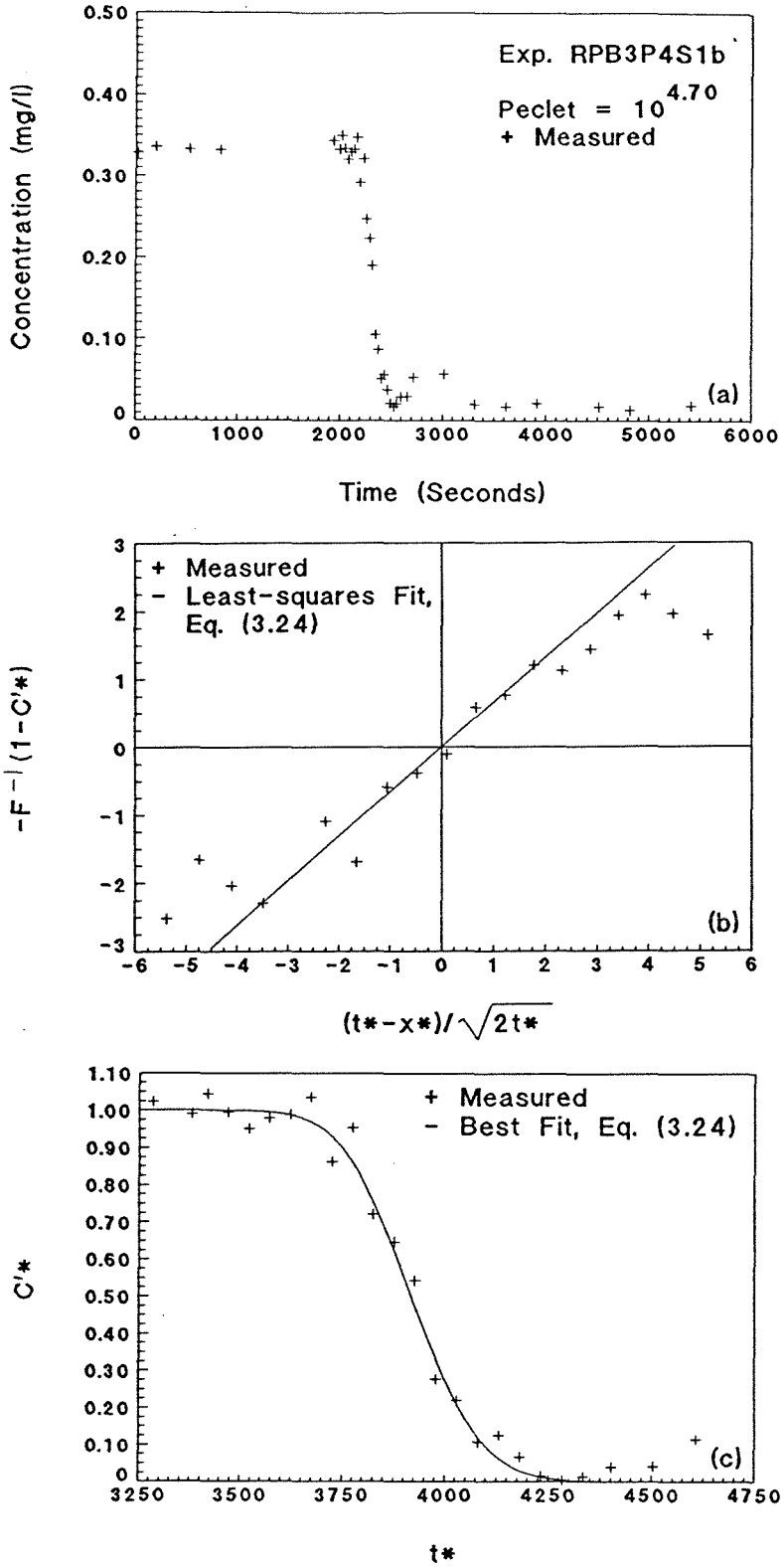

Fig. C.113: Exp. RPB3P4S1b reverse breakthrough curve, sample port 5, $Pe_p = 10^{4.70}$: (a) complete experimental data; (b) linearization with least-squares fit; and (c) breakthrough only with best-fit, Eq. (3.24).

C.5 Coupled Breakthrough Experiments

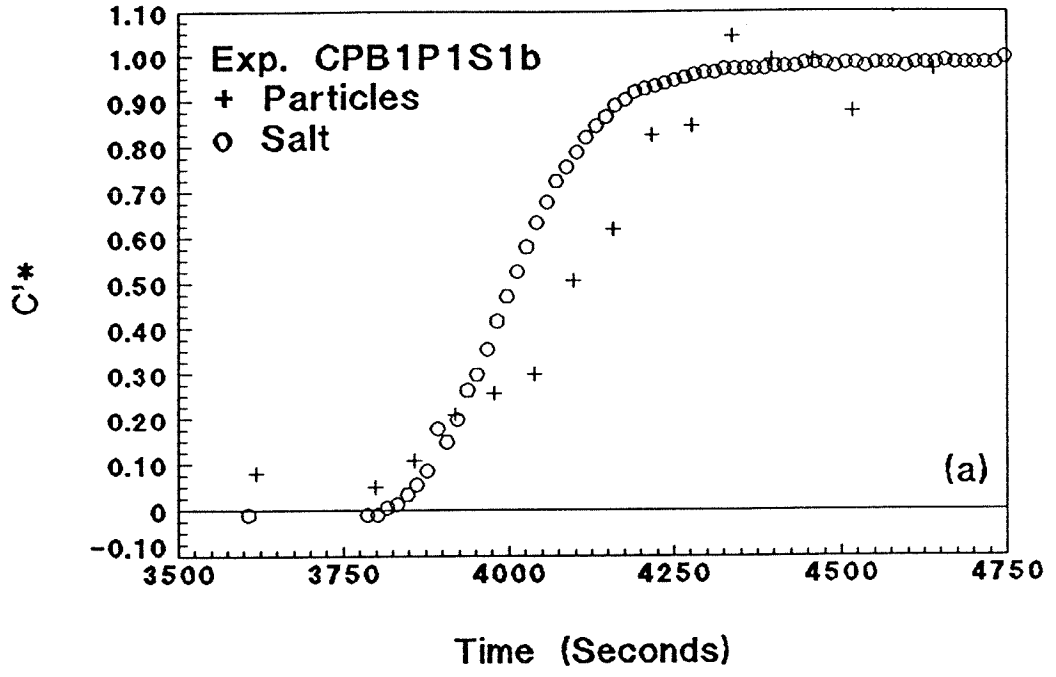

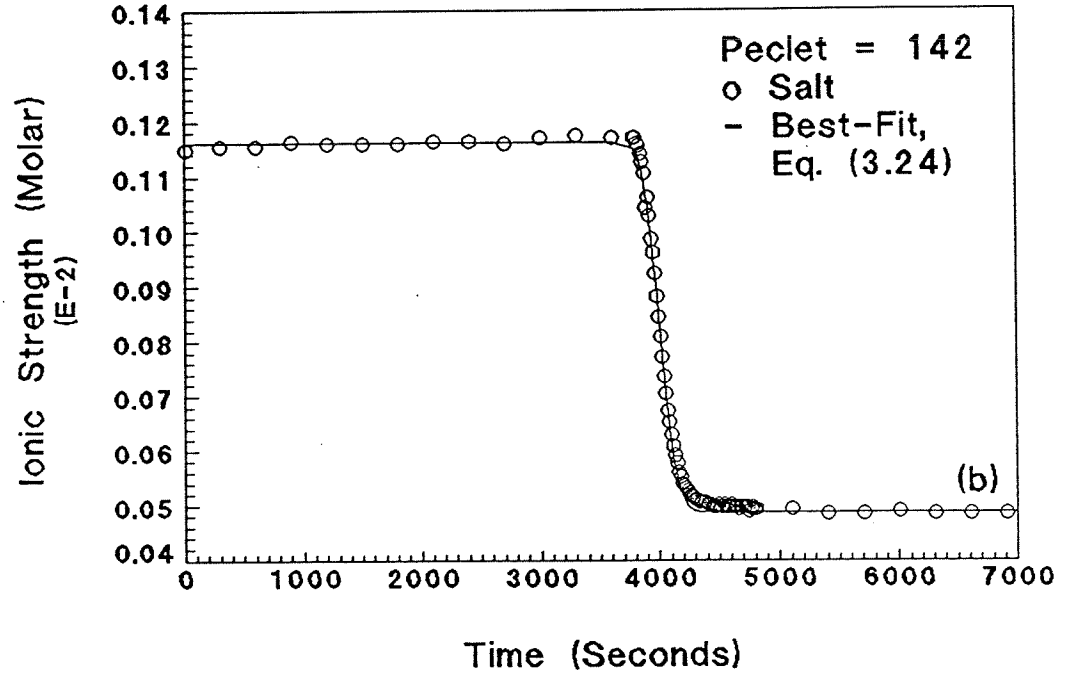

Fig. C.114: Exp. CPB1P1S1b coupled breakthrough, $Pe_p = 10^{5.45}$, Pe = 142, 1.0 micron particles: (a) particles and salt relative breakthroughs and (b) salt experimental data with best-fit, Eq. (3.24).

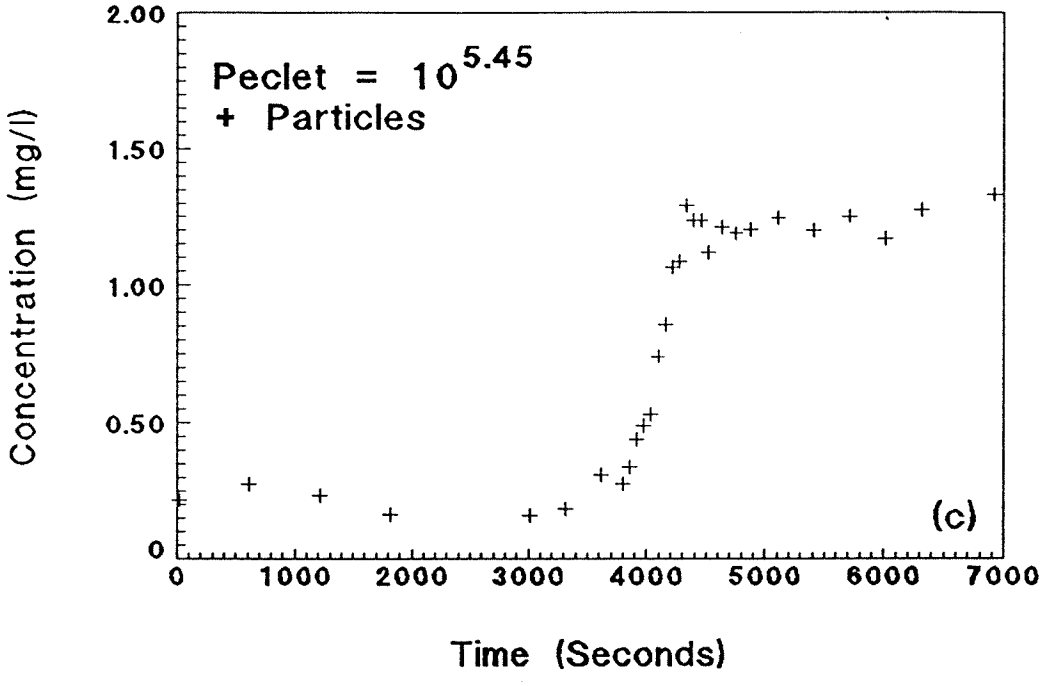

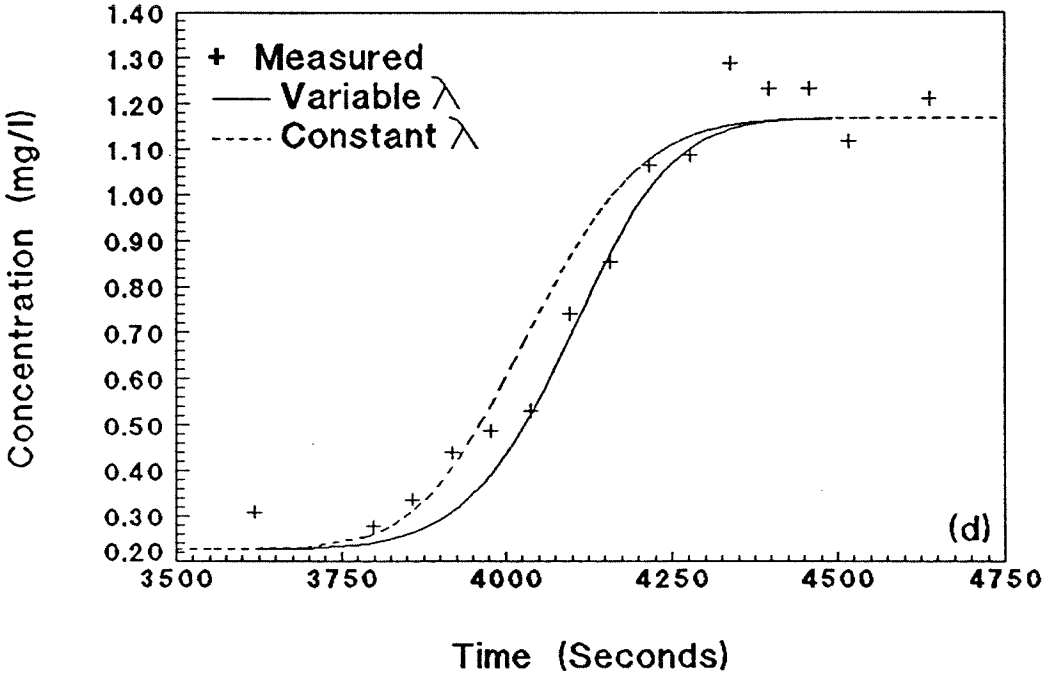

Fig. C.114(cont.): Exp. CPB1P1S1b coupled breakthrough, $Pe_p = 10^{5.45}$, Pe = 142, 1.0 micron particles: (c) particle breakthrough and (d) particle experimental data with best-fit, numerical model.

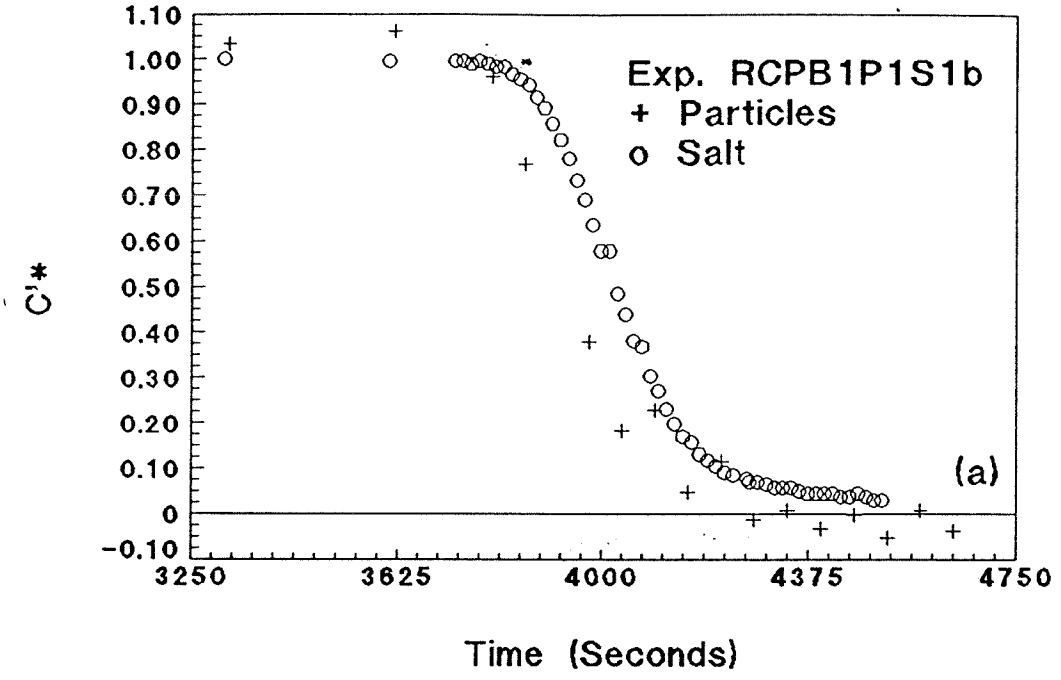

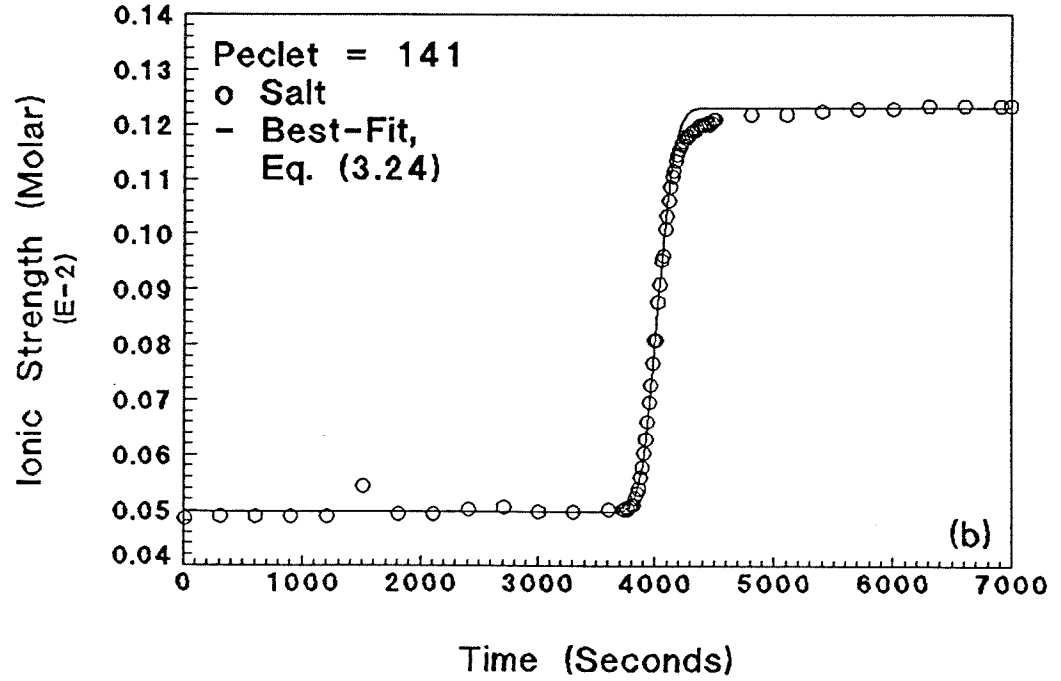

Fig. C.115: Exp. RCPB1P1S1b coupled breakthrough, $Pe_p = 10^{5.47}$, Pe = 141, 1.0 micron particles: (a) particles and salt relative breakthroughs and (b) salt experimental data with best-fit, Eq. (3.24).

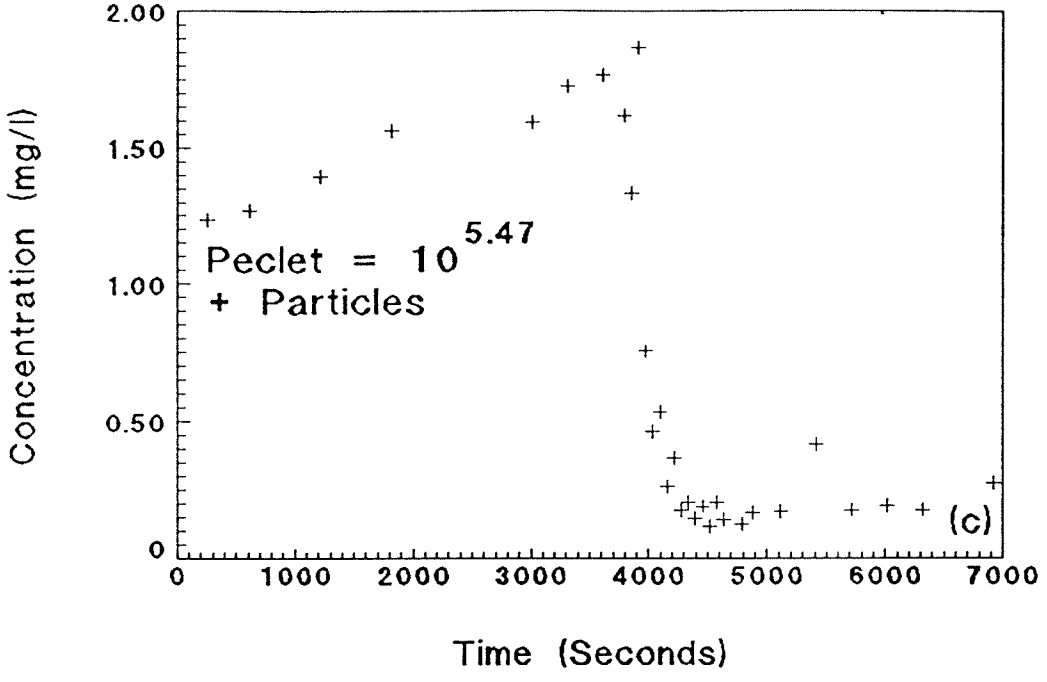

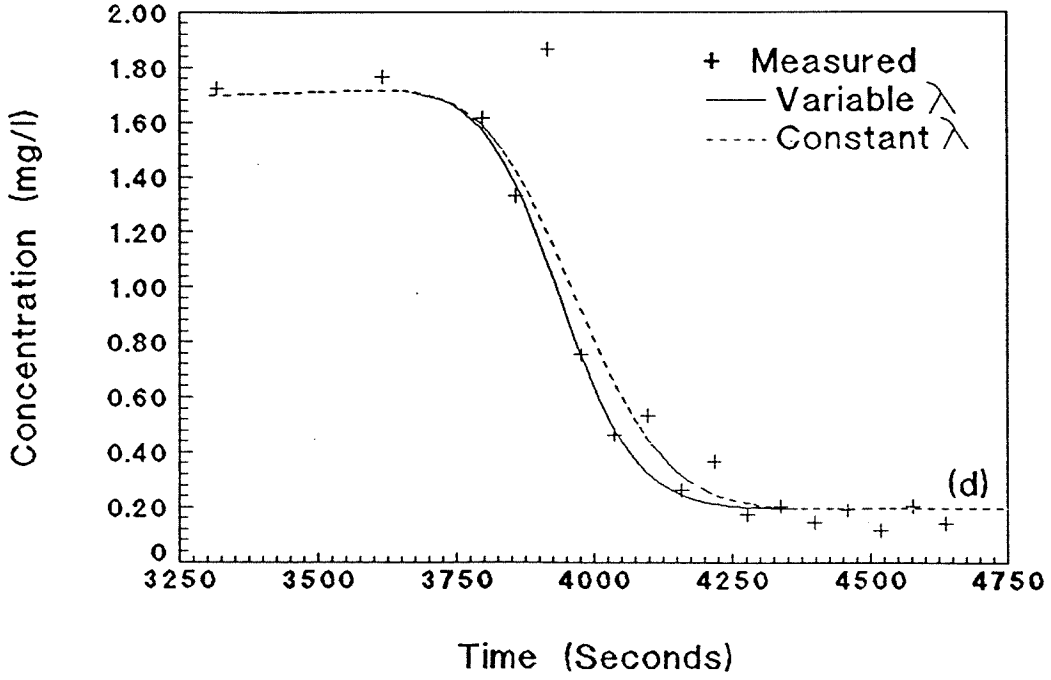

Fig. C.115(cont.): Exp. RCPB1P1S1b coupled breakthrough, $Pe_p = 10^{5.47}$, Pe = 141, 1.0 micron particles: (c) particle breakthrough and (d) particle experimental data with best-fit, numerical model.

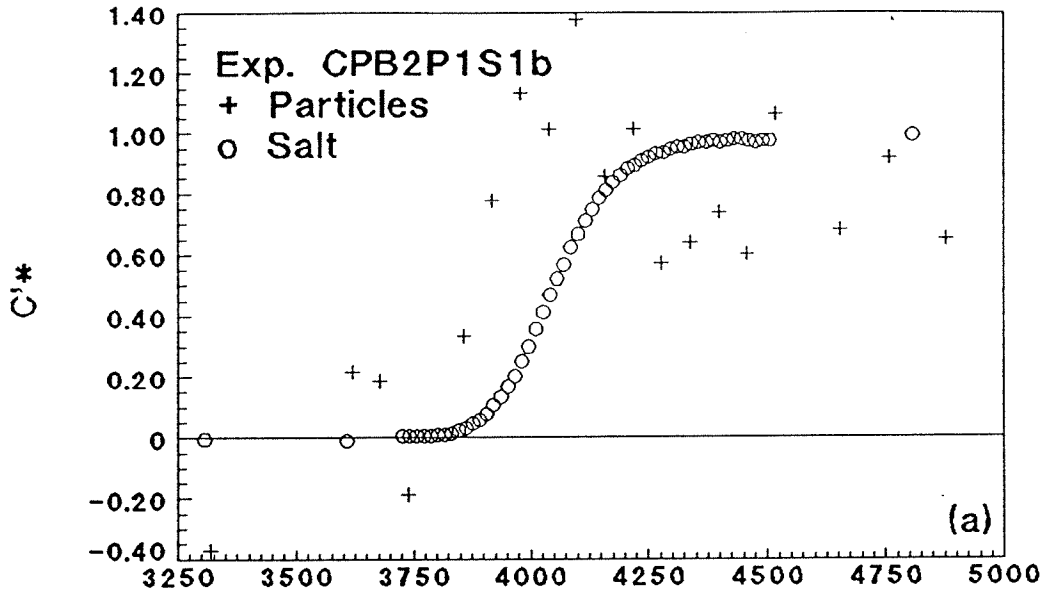

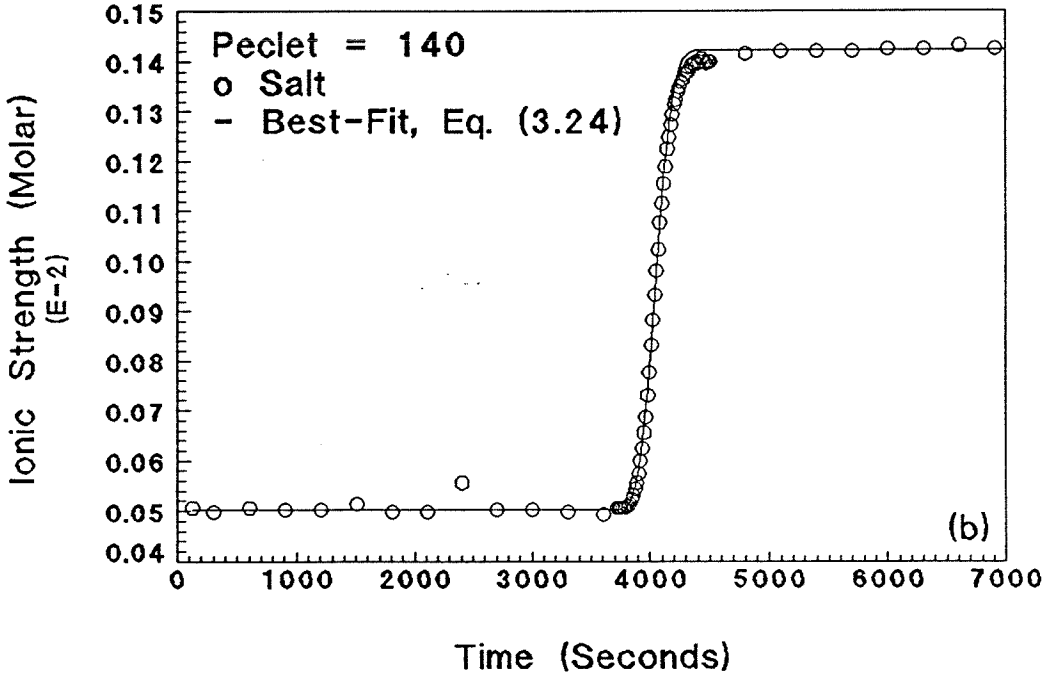

Fig. C.116: Exp. CPB2P1S1b coupled breakthrough, $Pe_p = 10^{5.48}$, Pe = 140, 1.0 micron particles: (a) particles and salt relative breakthroughs and (b) salt experimental data with best-fit, Eq. (3.24).

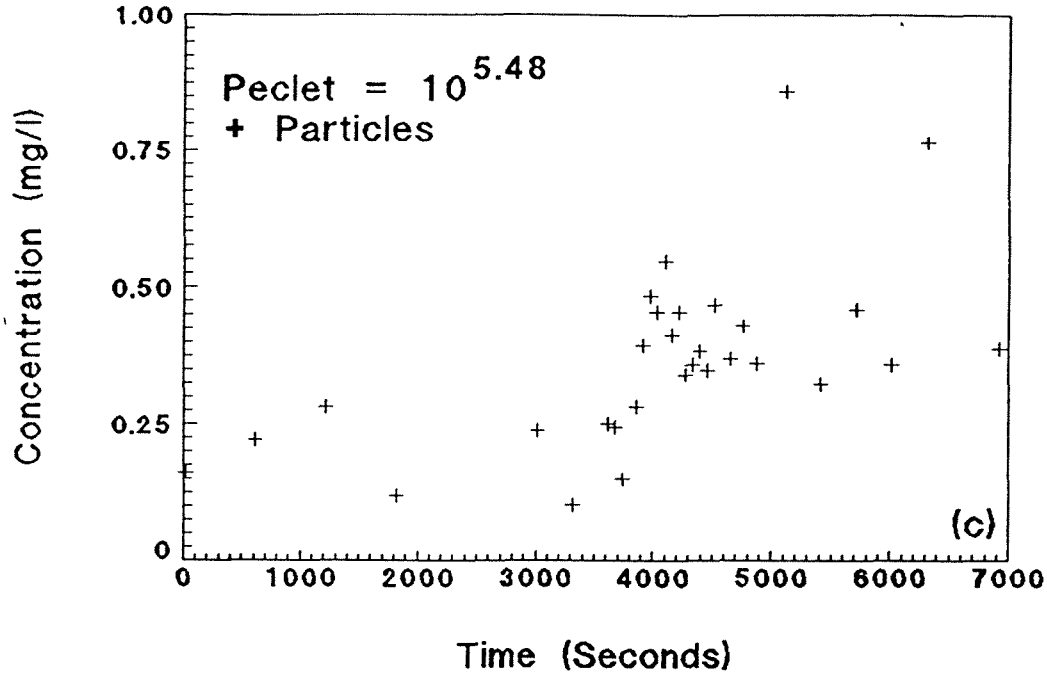

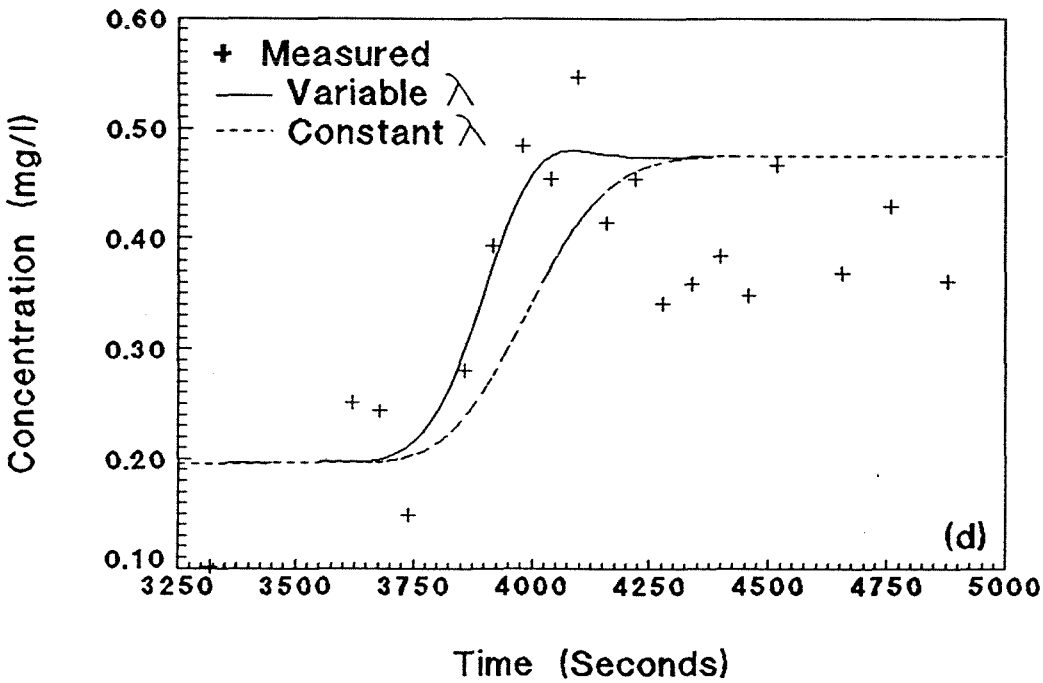

Fig. C.116(cont.): Exp. CPB2P1S1b coupled breakthrough, $Pe_p = 10^{5.48}$, Pe = 140, 1.0 micron particles: (c) particle breakthrough and (d) particle experimental data with best-fit, numerical model.

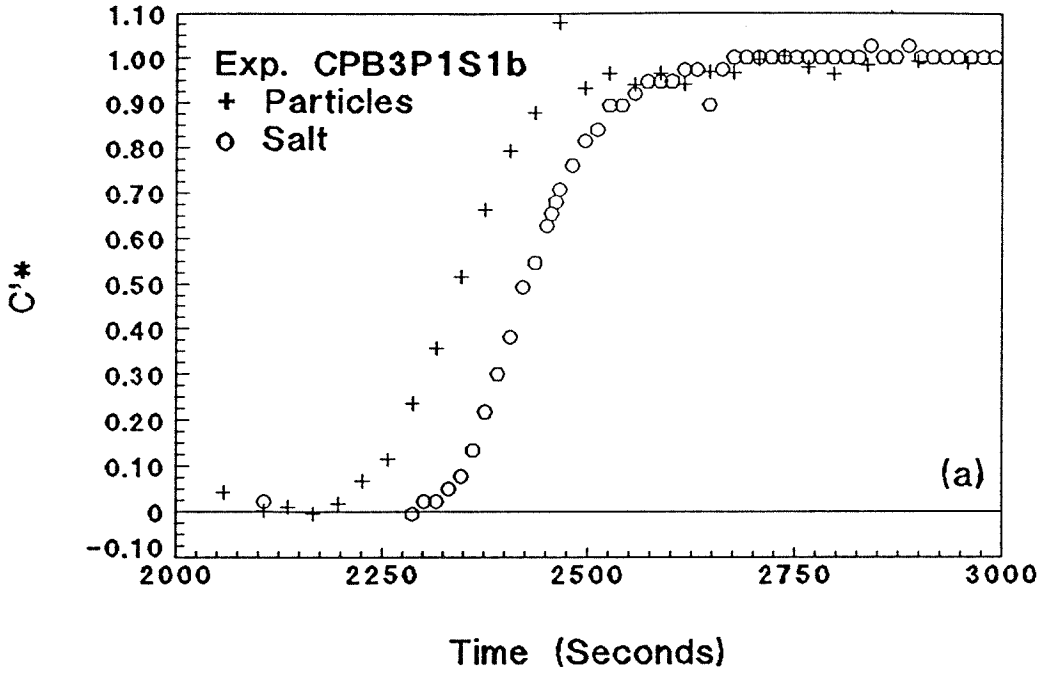

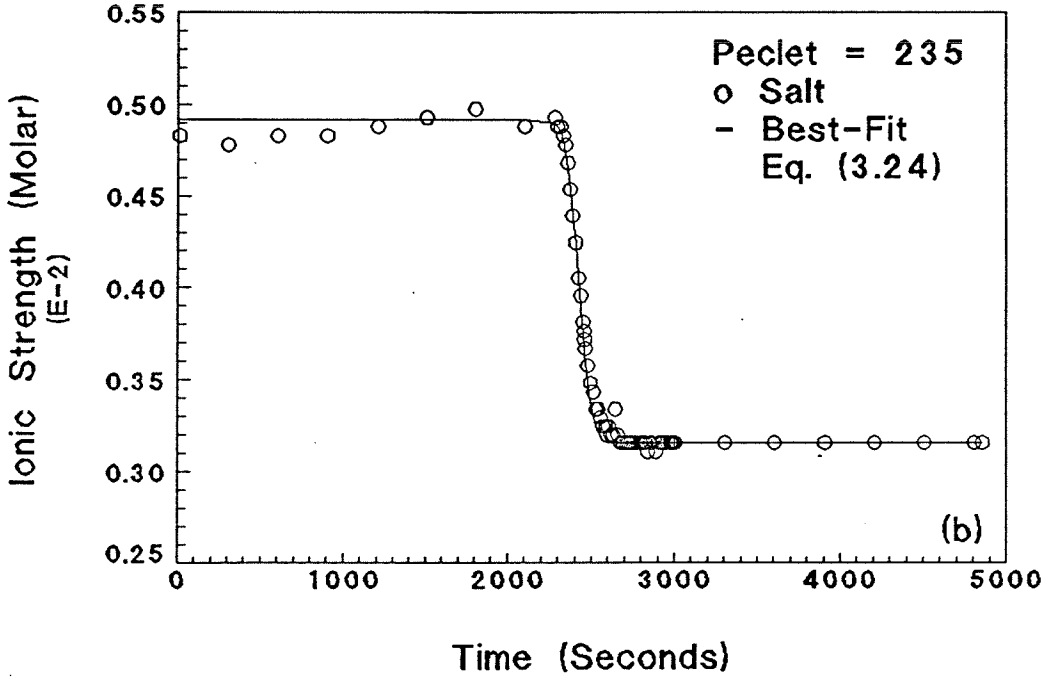

Fig. C.117: Exp. CPB3P1S1b coupled breakthrough, $Pe_p = 10^{5.70}$, Pe = 235, 1.0 micron particles: (a) particles and salt relative breakthroughs and (b) salt experimental data with best-fit, Eq. (3.24).

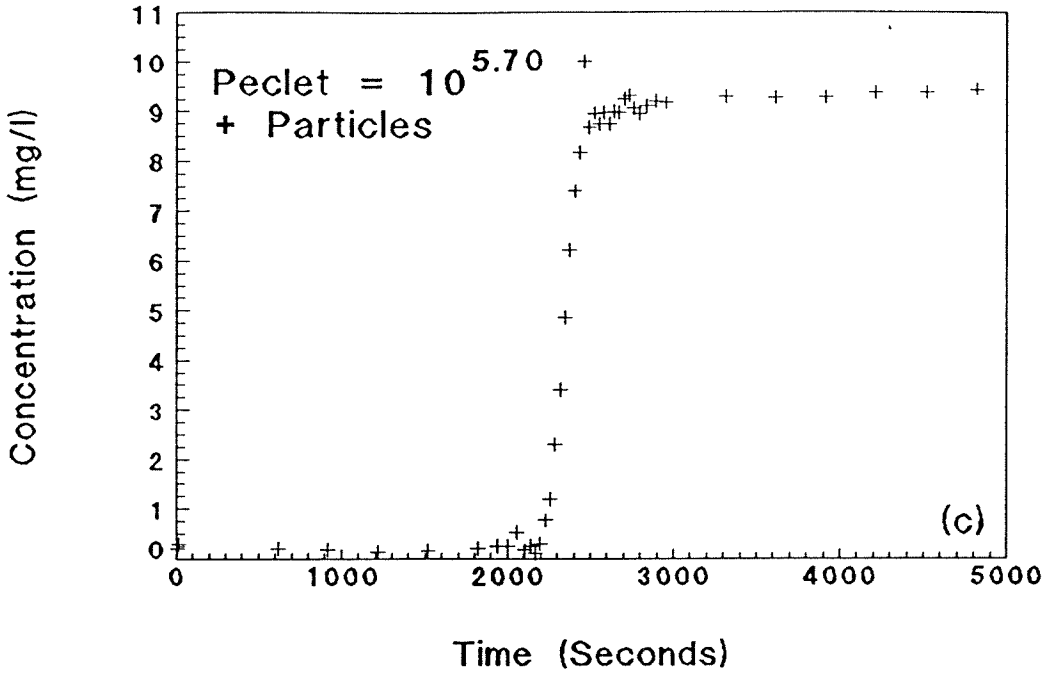

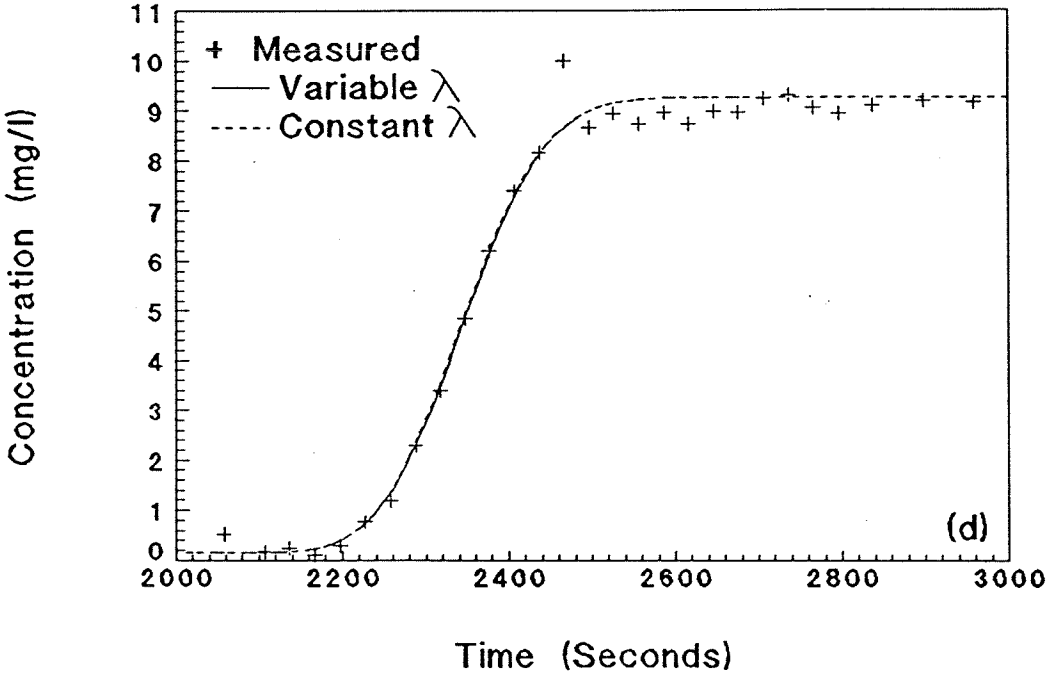

Fig. C.117(cont.): Exp. CPB3P1S1b coupled breakthrough, $Pe_p = 10^{5.70}$, Pe = 235, 1.0 micron particles: (c) particle breakthrough and (d) particle experimental data with best-fit, numerical model.

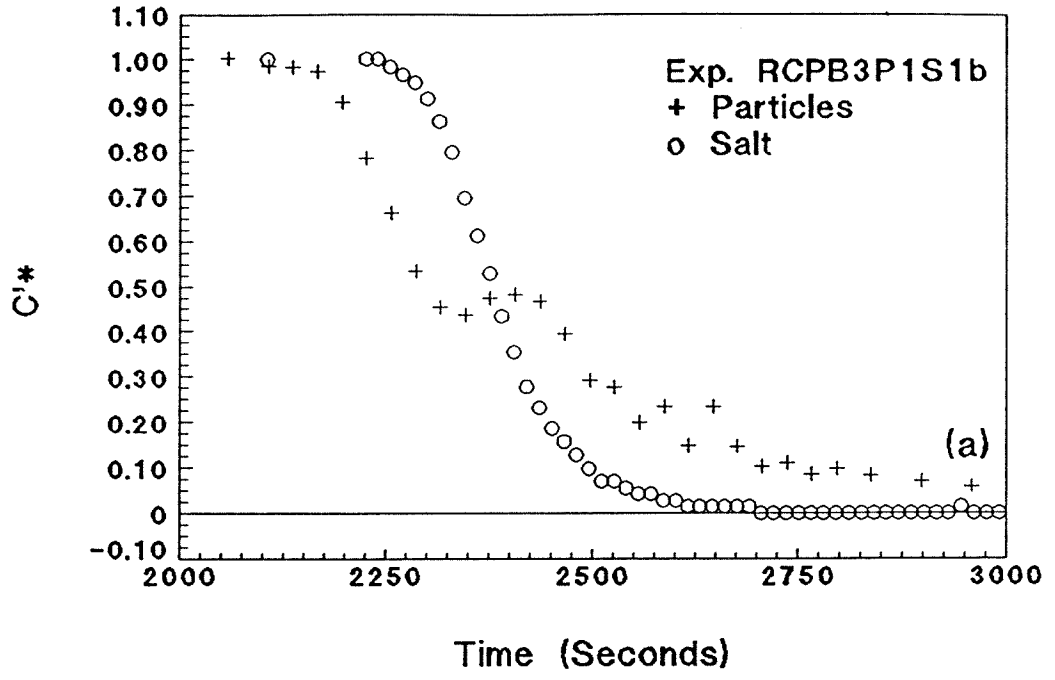

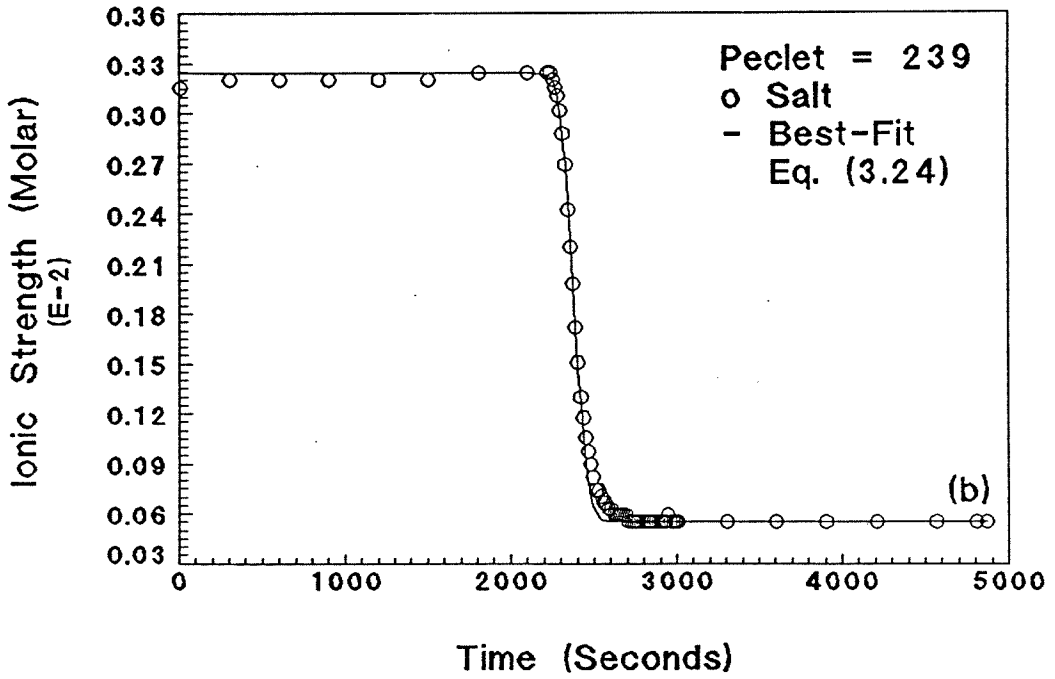

Fig. C.118: Exp. RCPB3P1S1b coupled breakthrough, $Pe_p = 10^{5.70}$, Pe = 239, 1.0 micron particles: (a) particles and salt relative breakthroughs and (b) salt experimental data with best-fit, Eq. (3.24).

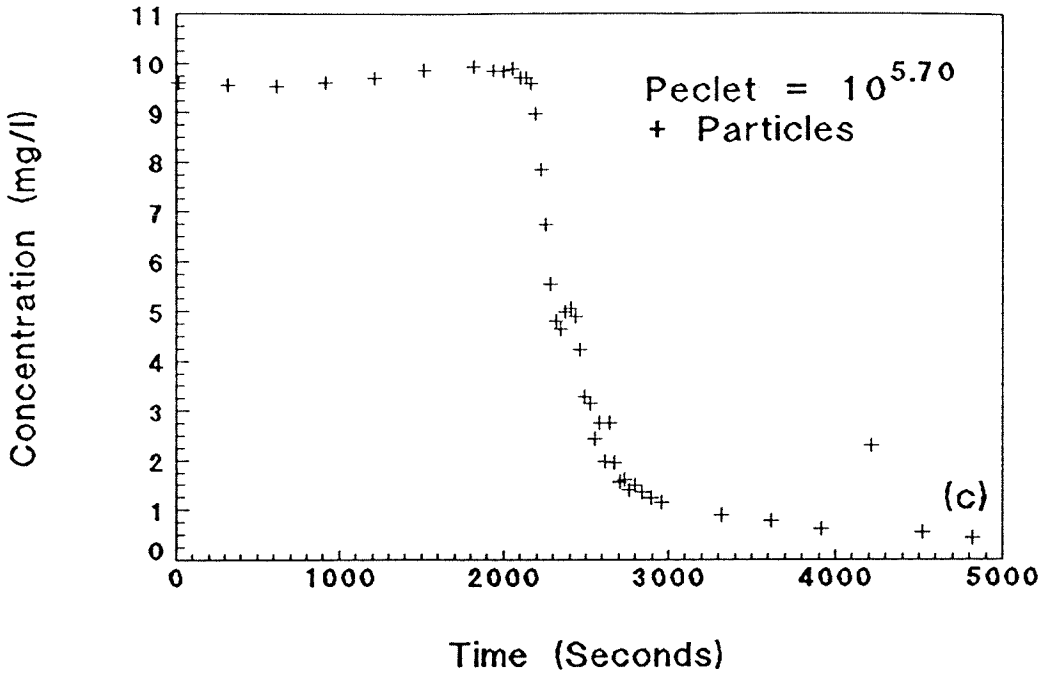

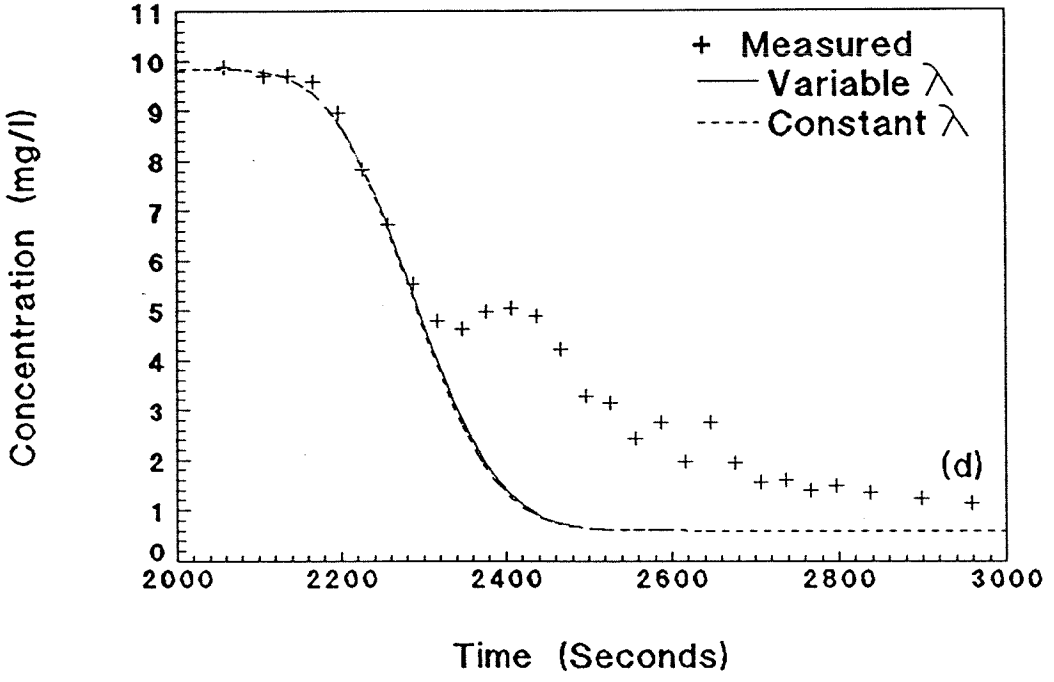

Fig. C.118(cont.): Exp. RCPB3P1S1b coupled breakthrough, $Pe_p = 10^{5.70}$, Pe = 239, 1.0 micron particles: (c) particle breakthrough and (d) particle experimental data with best-fit, numerical model.

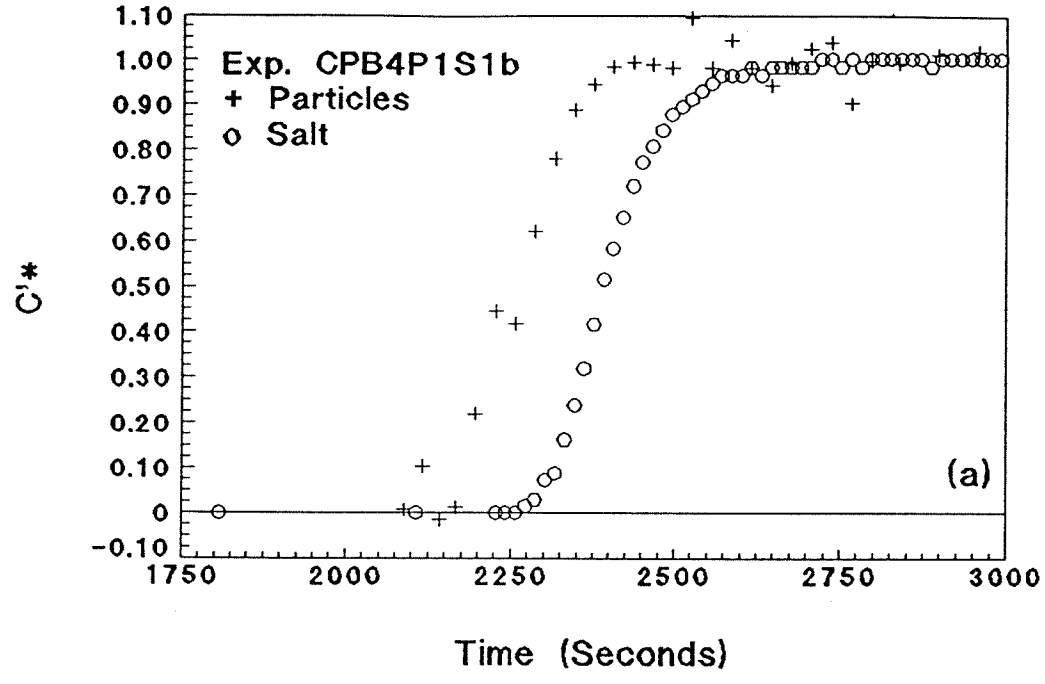

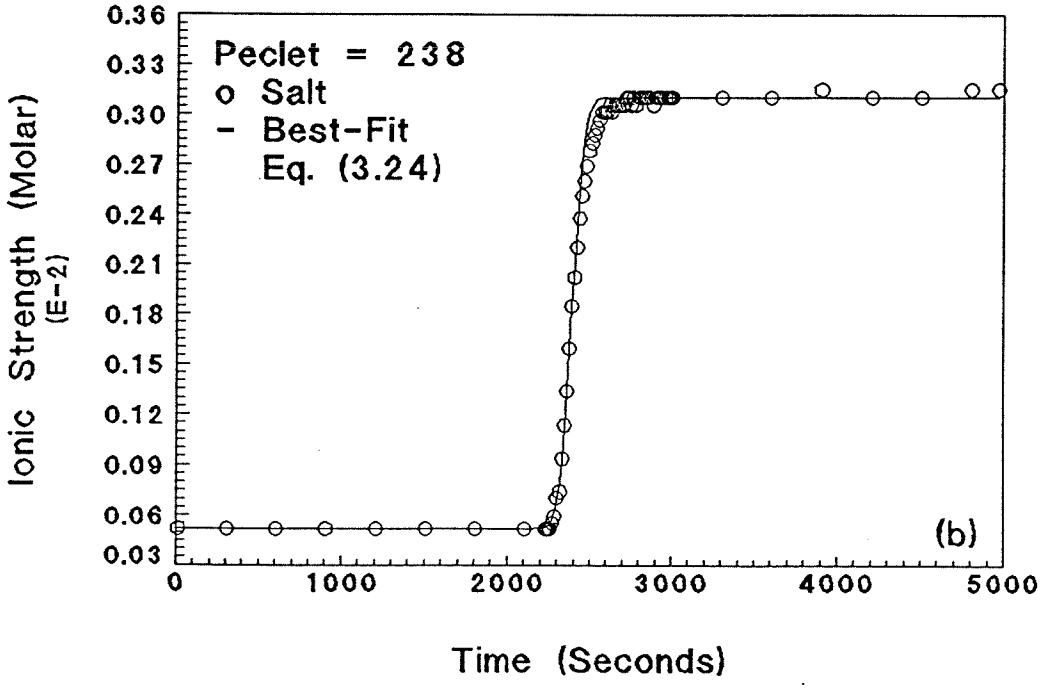

Fig. C.119: Exp. CPB4P1S1b coupled breakthrough, $Pe_p = 10^{5.71}$, Pe = 238, 1.0 micron particles: (a) particles and salt relative breakthroughs and (b) salt experimental data with best-fit, Eq. (3.24).

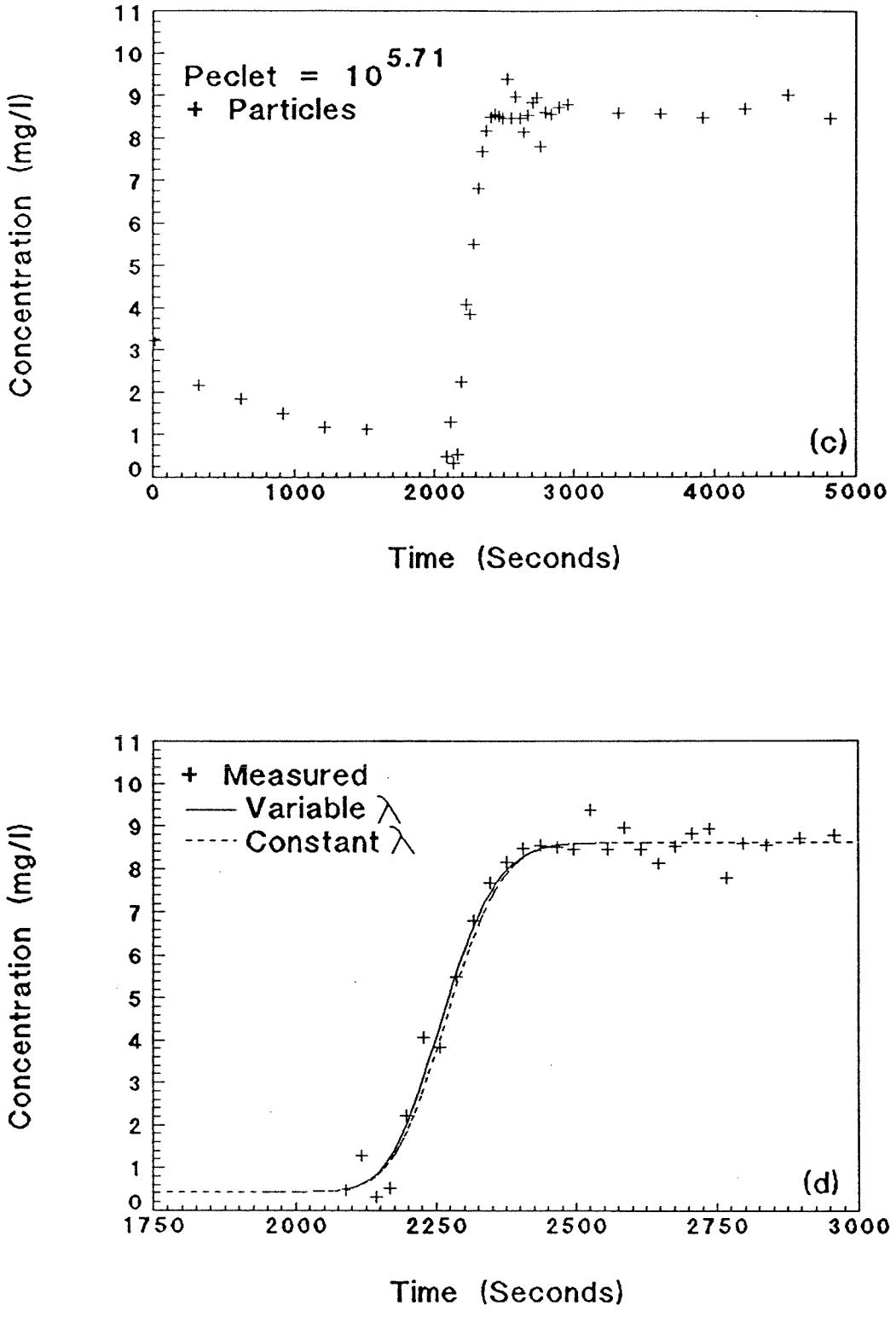

Fig. C.119(cont.): Exp. CPB4P1S1b coupled breakthrough, $Pe_p = 10^{5.71}$, Pe = 238, 1.0 micron particles: (c) particle breakthrough and (d) particle experimental data with best-fit, numerical model.

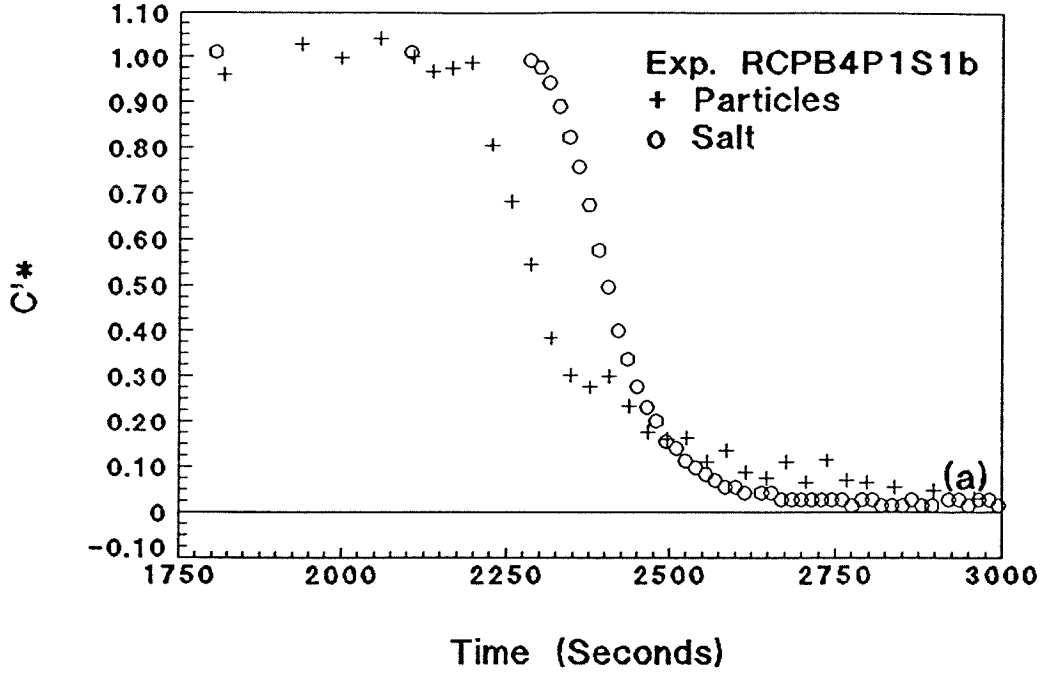

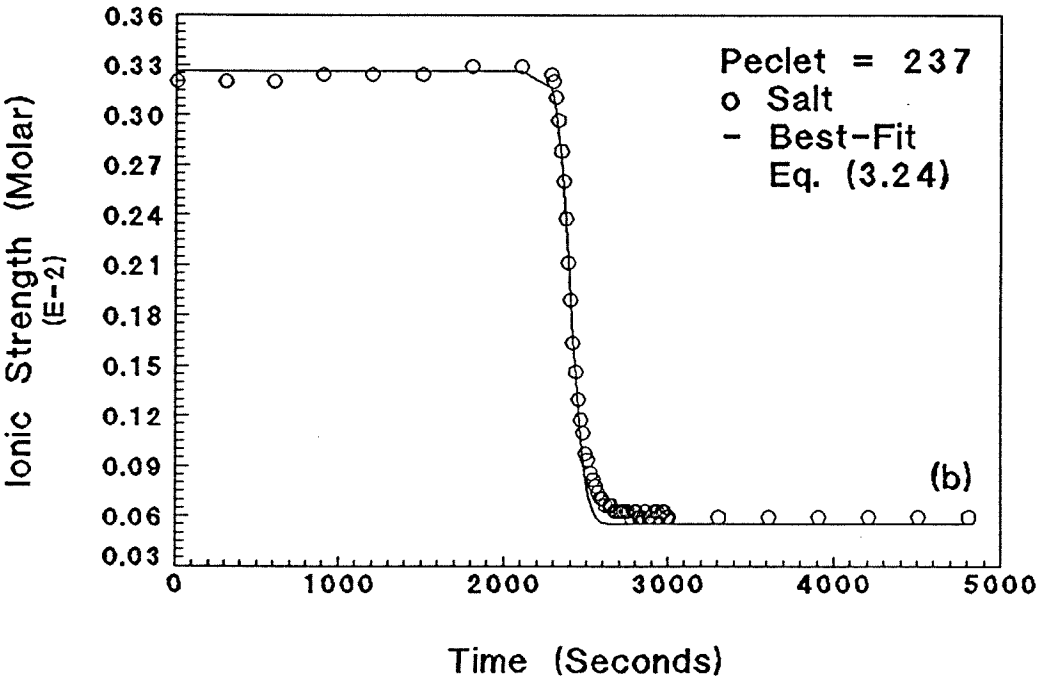

Fig. C.120: Exp. RCPB4P1S1b coupled breakthrough, $Pe_p = 10^{5.70}$, Pe = 237, 1.0 micron particles: (a) particles and salt relative breakthroughs and (b) salt experimental data with best-fit, Eq. (3.24).

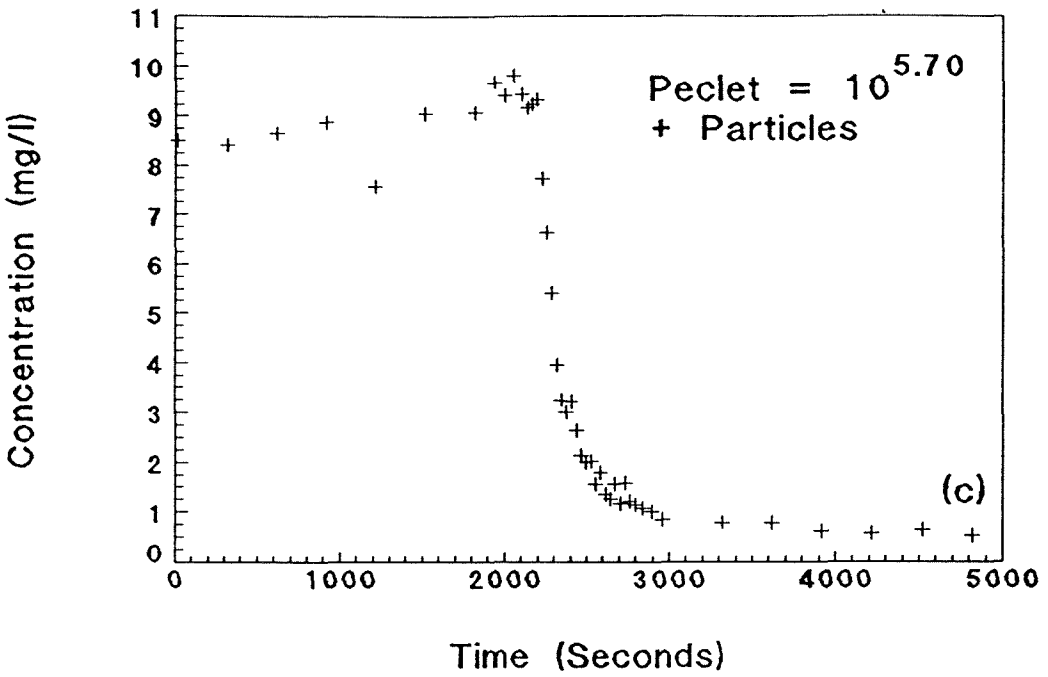

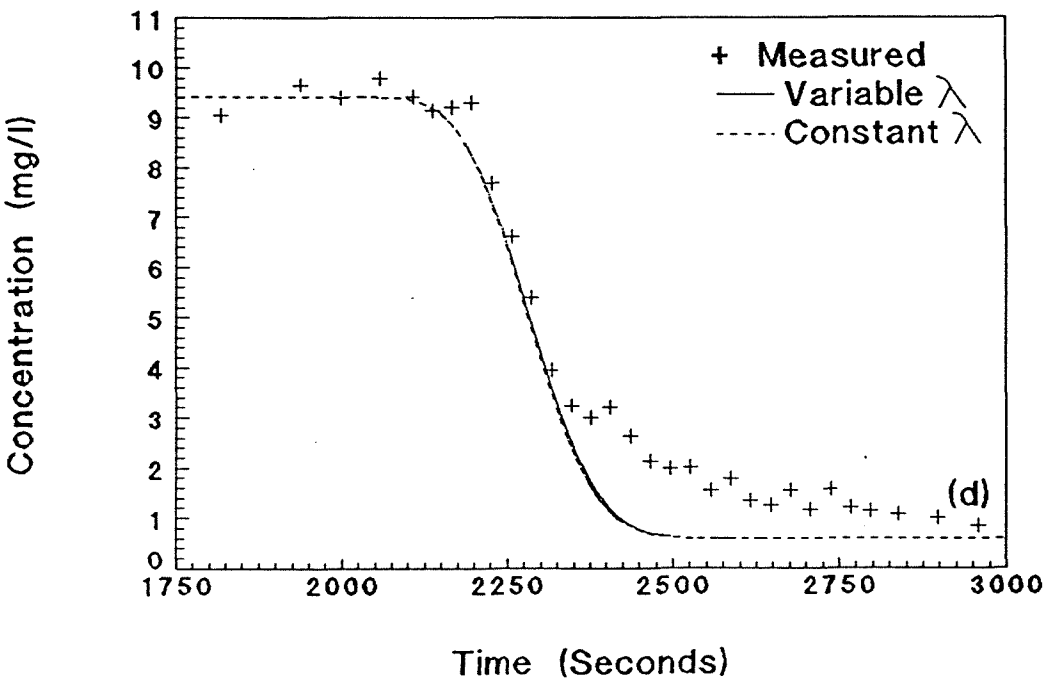

Fig. C.120(cont.): Exp. RCPB4P1S1b coupled breakthrough, $Pe_p = 10^{5.70}$, Pe = 237, 1.0 micron particles: (c) particle breakthrough and (d) particle experimental data with best-fit, numerical model.

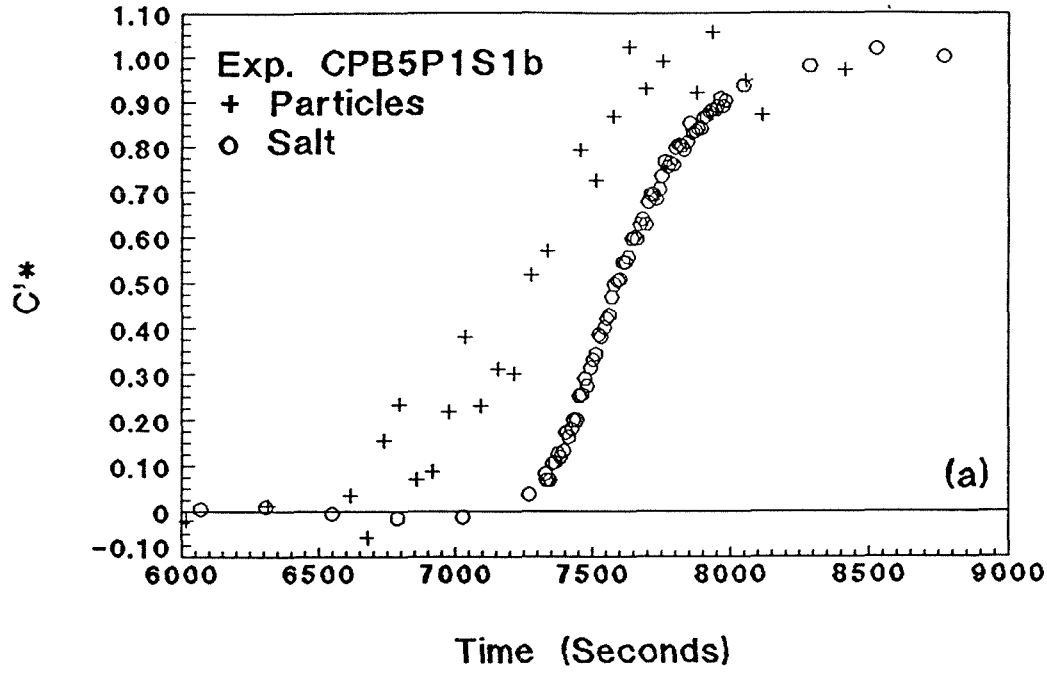

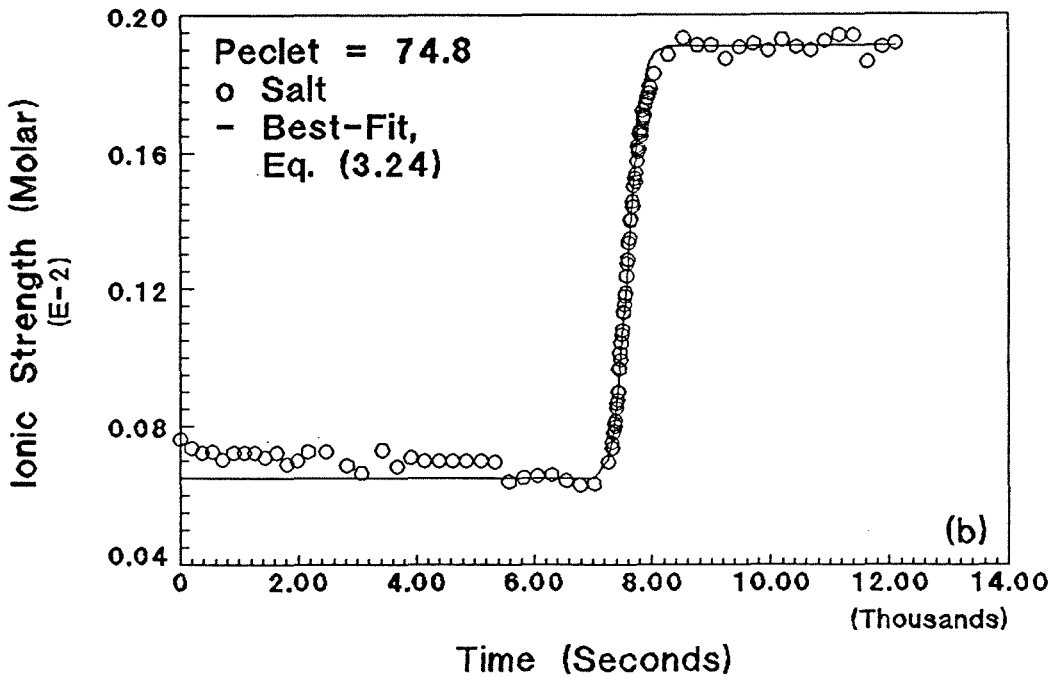

Fig. C.121: Exp. CPB5P1S1b coupled breakthrough, $Pe_p = 10^{5.20}$, Pe = 74.8, 1.0 micron particles: (a) particles and salt relative breakthroughs and (b) salt experimental data with best-fit, Eq. (3.24).

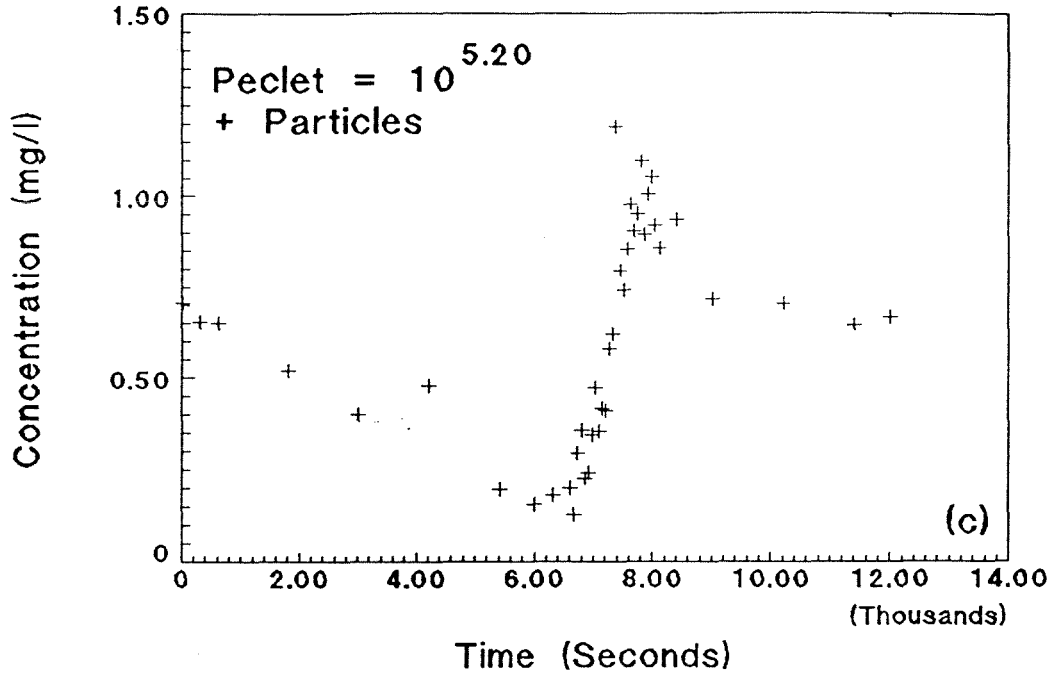

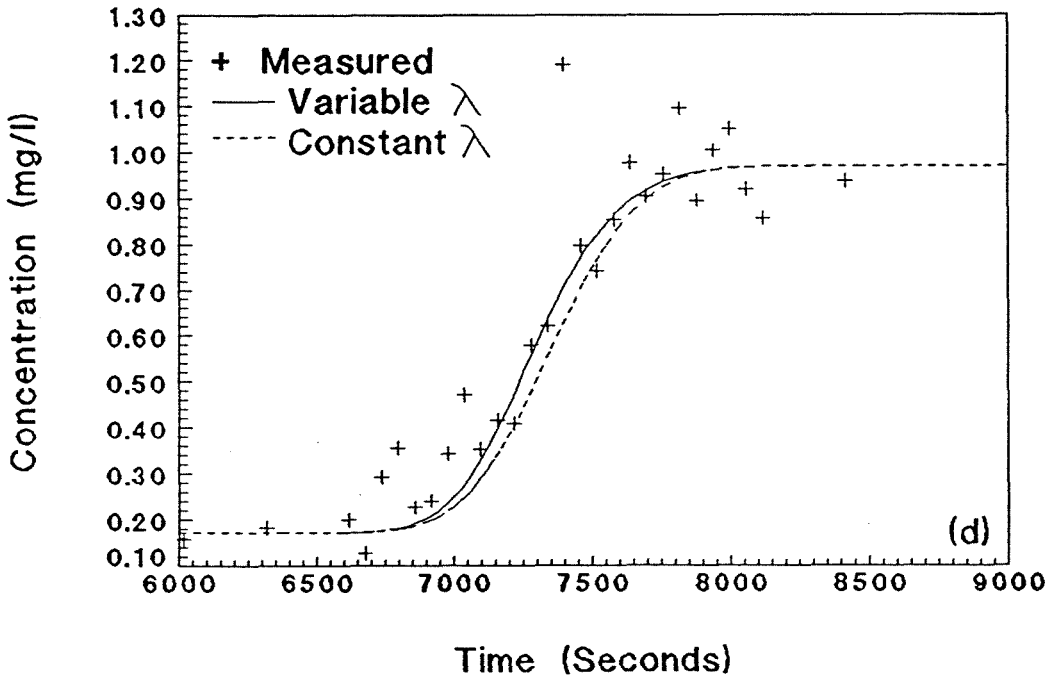

Fig. C.121(cont.): Exp. CPB5P1S1b coupled breakthrough, $Pe_p = 10^{5.20}$, Pe = 74.8, 1.0 micron particles: (c) particle breakthrough and (d) particle experimental data with best-fit, numerical model.

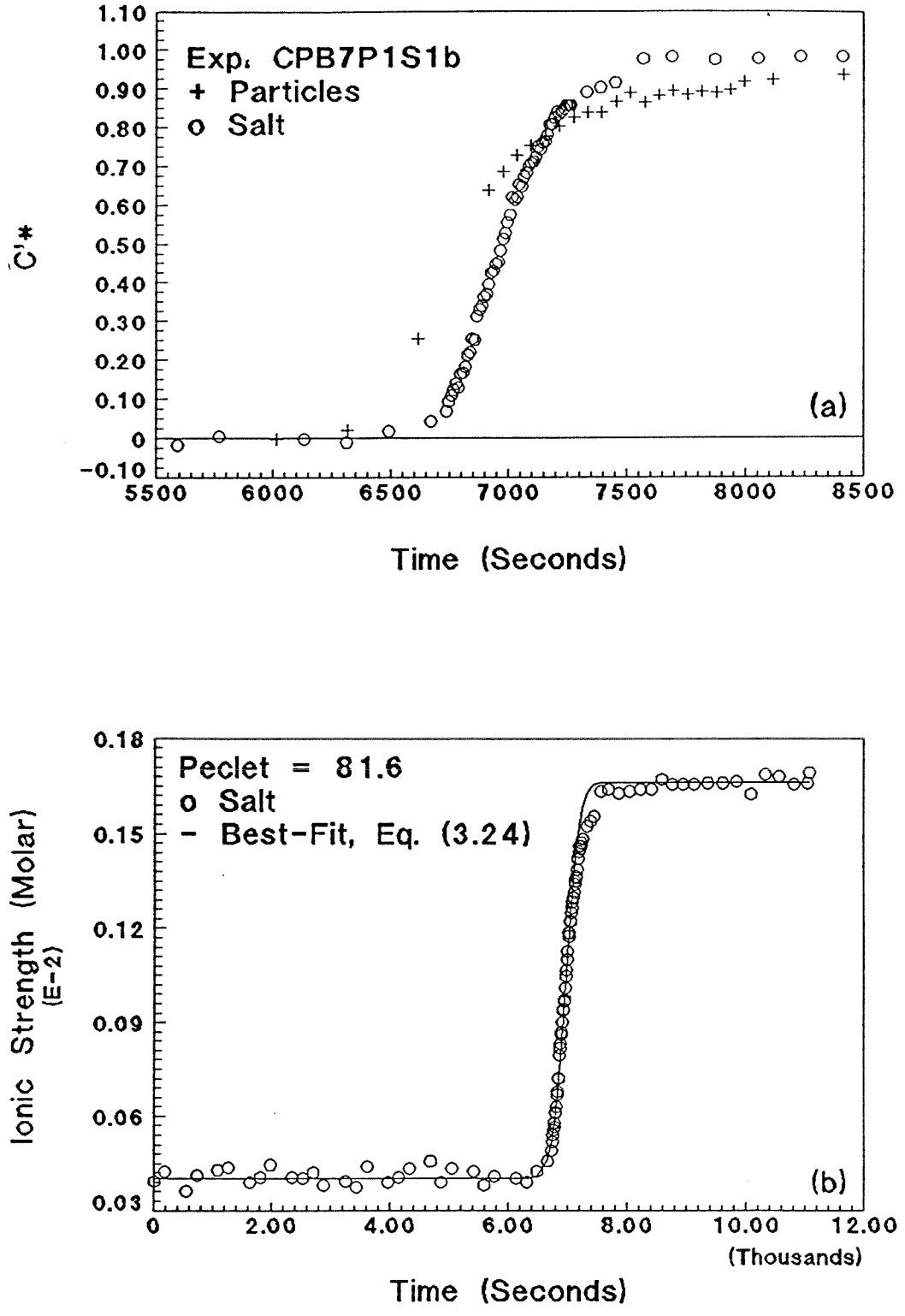

Fig. C.122: Exp. CPB7P1S1b coupled breakthrough, $Pe_p = 10^{5.23}$, Pe = 81.6, 1.0 micron particles: (a) particles and salt relative breakthroughs and (b) salt experimental data with best-fit, Eq. (3.24).

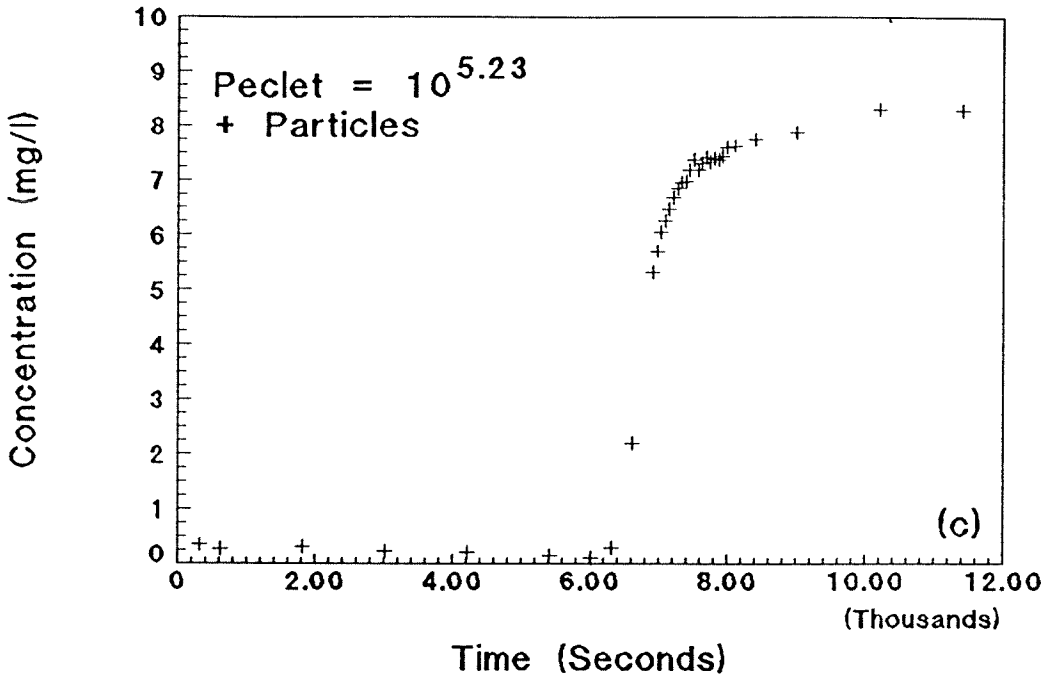

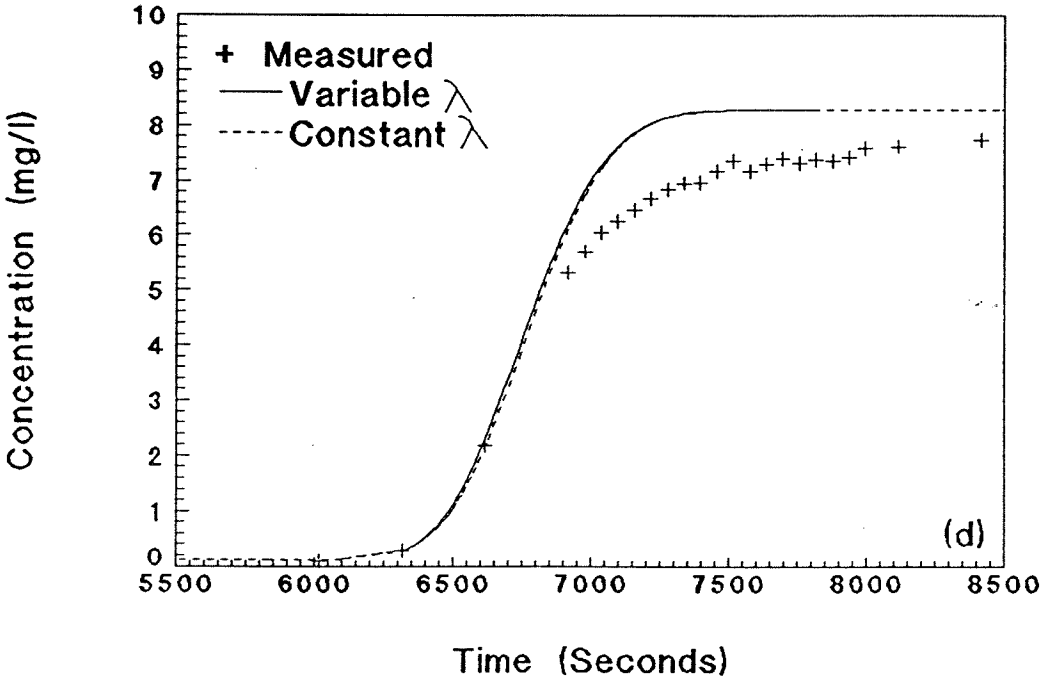

Fig. C.122(cont.): Exp. CPB7P1S1b coupled breakthrough, $Pe_p = 10^{5.23}$, Pe = 81.6, 1.0 micron particles: (c) particle breakthrough and (d) particle experimental data with best-fit, numerical model.

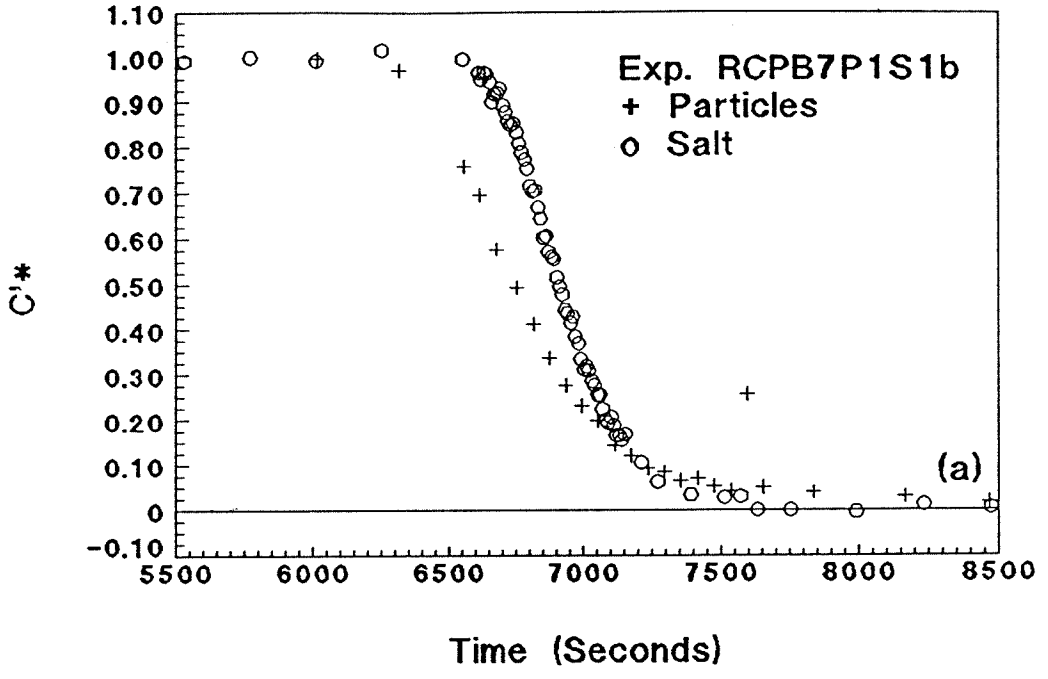

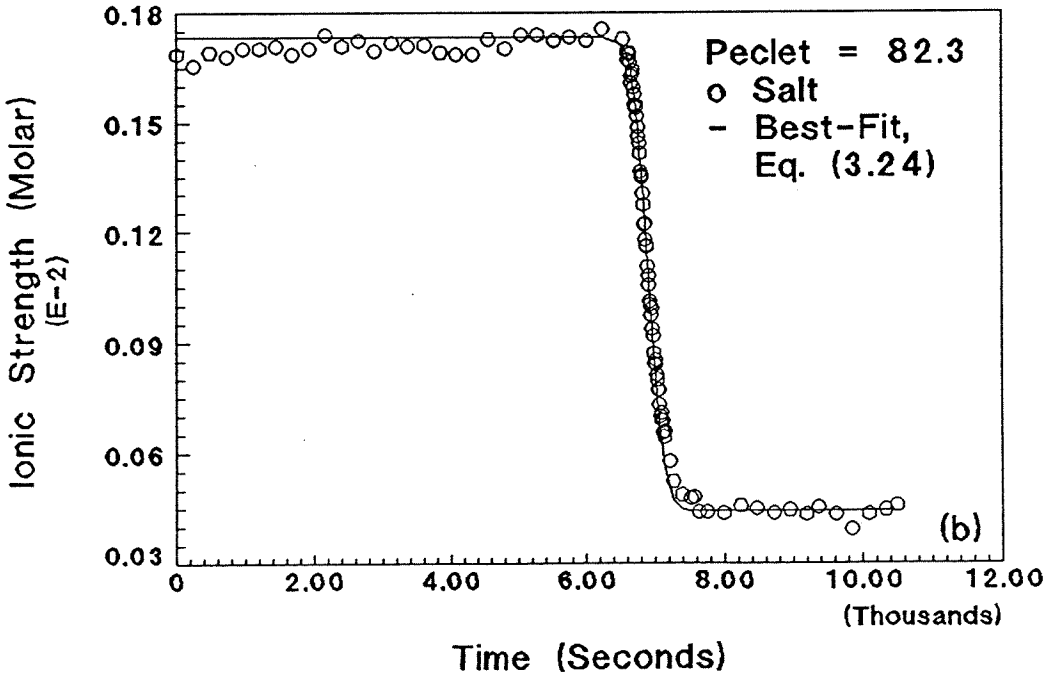

Fig. C.123: Exp. RCPB7P1S1b coupled breakthrough, $Pe_p = 10^{5.24}$, Pe = 82.3, 1.0 micron particles: (a) particles and salt relative breakthroughs and (b) salt experimental data with best-fit, Eq. (3.24).

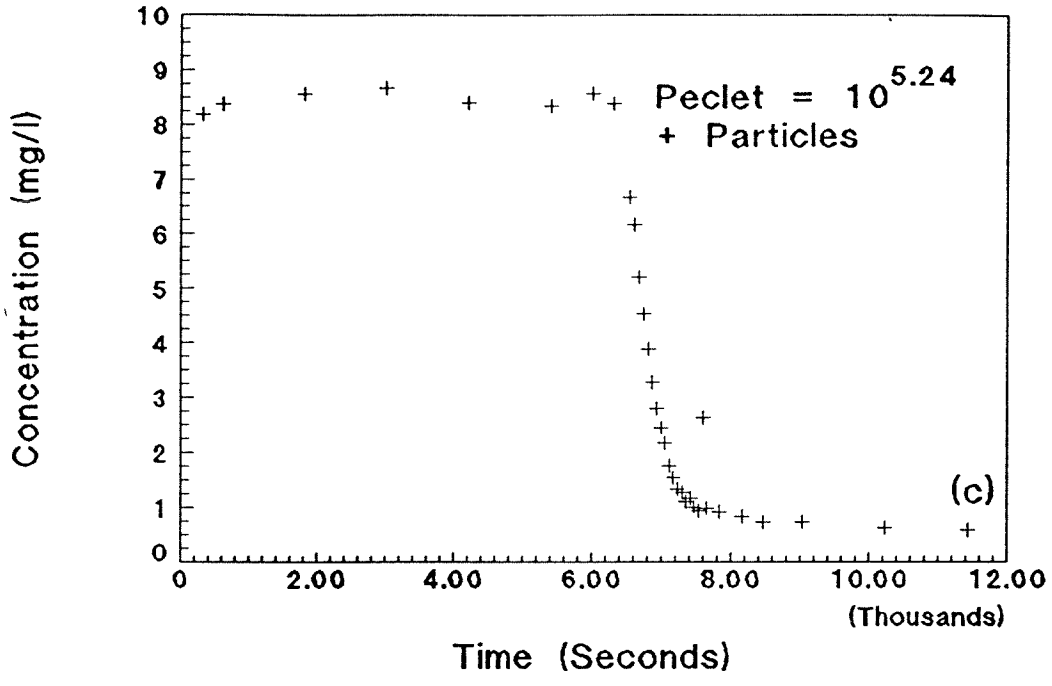

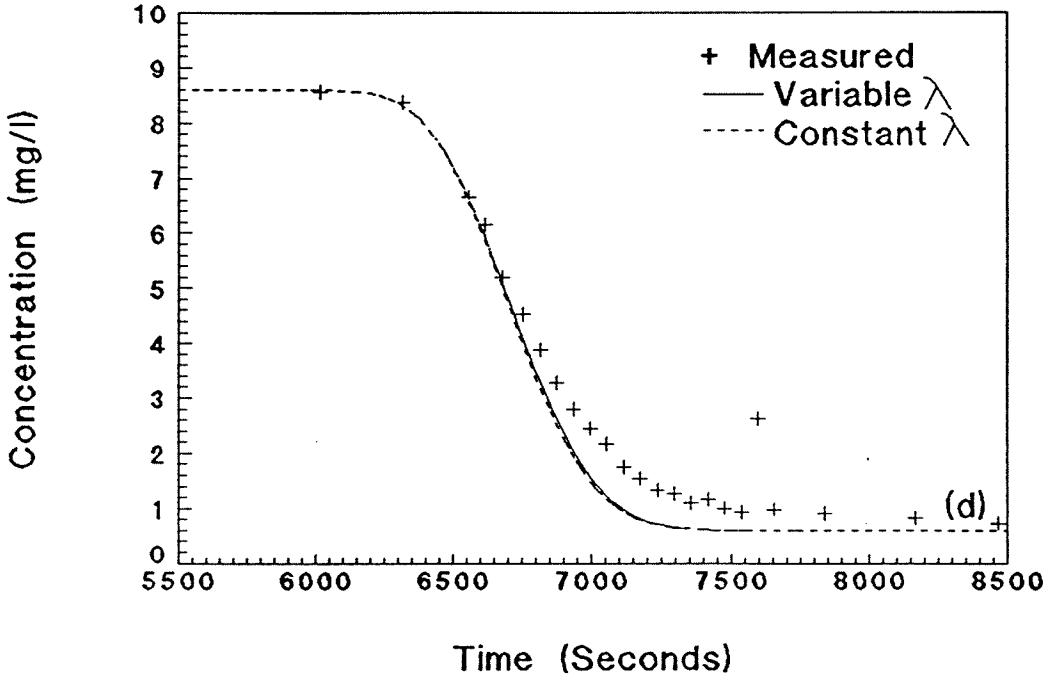

Fig. C.123(cont.): Exp. RCPB7P1S1b coupled breakthrough, $Pe_p = 10^{5.24}$, Pe = 82.3, 1.0 micron particles: (c) particle breakthrough and (d) particle experimental data with best-fit, numerical model.

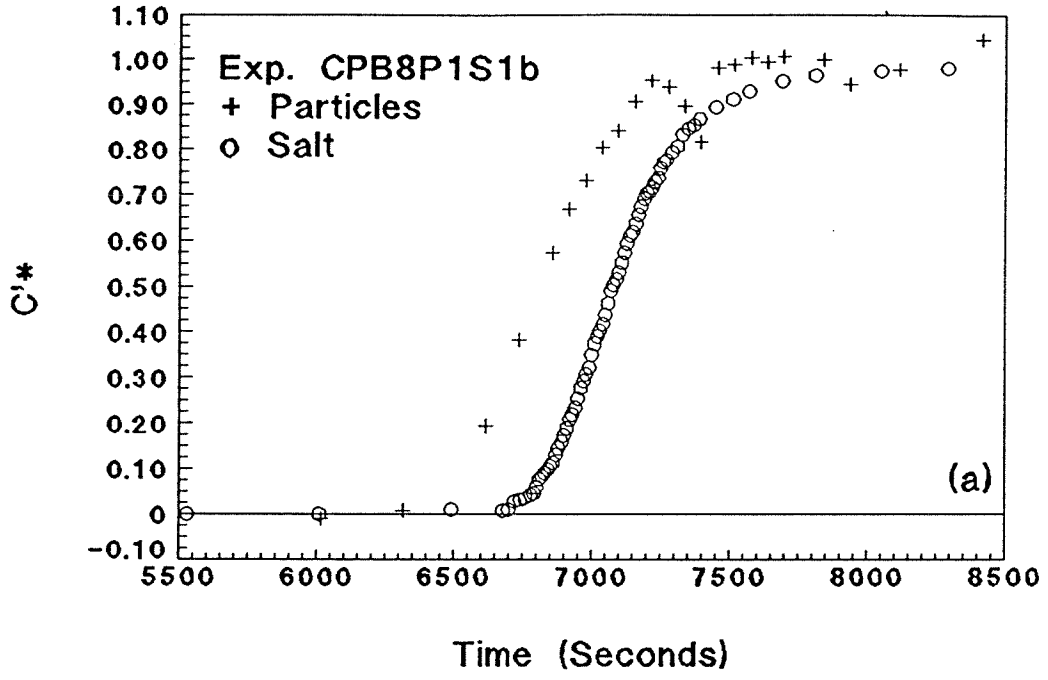

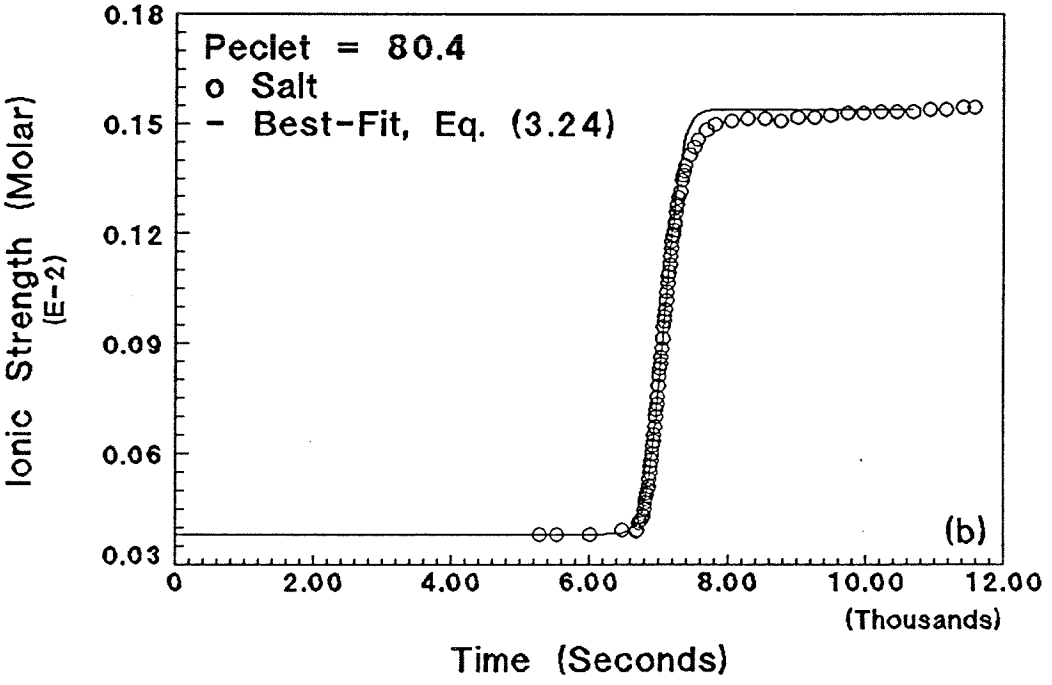

Fig. C.124: Exp. CPB8P1S1b coupled breakthrough, $Pe_p = 10^{5.23}$, Pe = 80.4, 1.0 micron particles: (a) particles and salt relative breakthroughs and (b) salt experimental data with best-fit, Eq. (3.24).

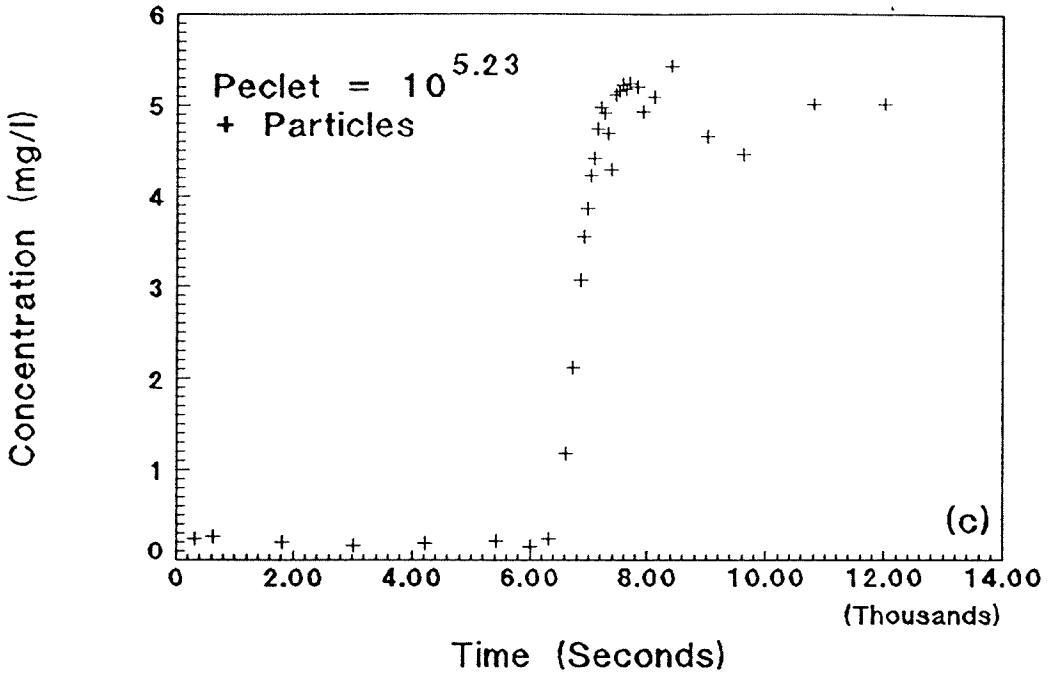

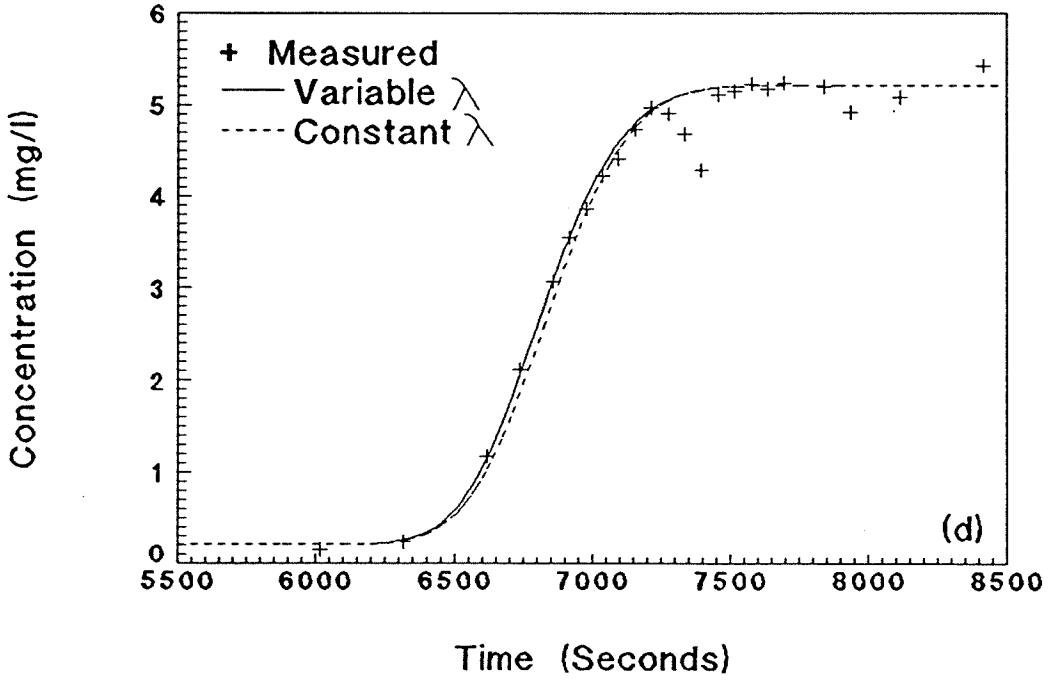

Fig. C.124(cont.): Exp. CPB8P1S1b coupled breakthrough, $Pe_p = 10^{5.23}$, Pe = 80.4, 1.0 micron particles: (c) particle breakthrough and (d) particle experimental data with best-fit, numerical model.

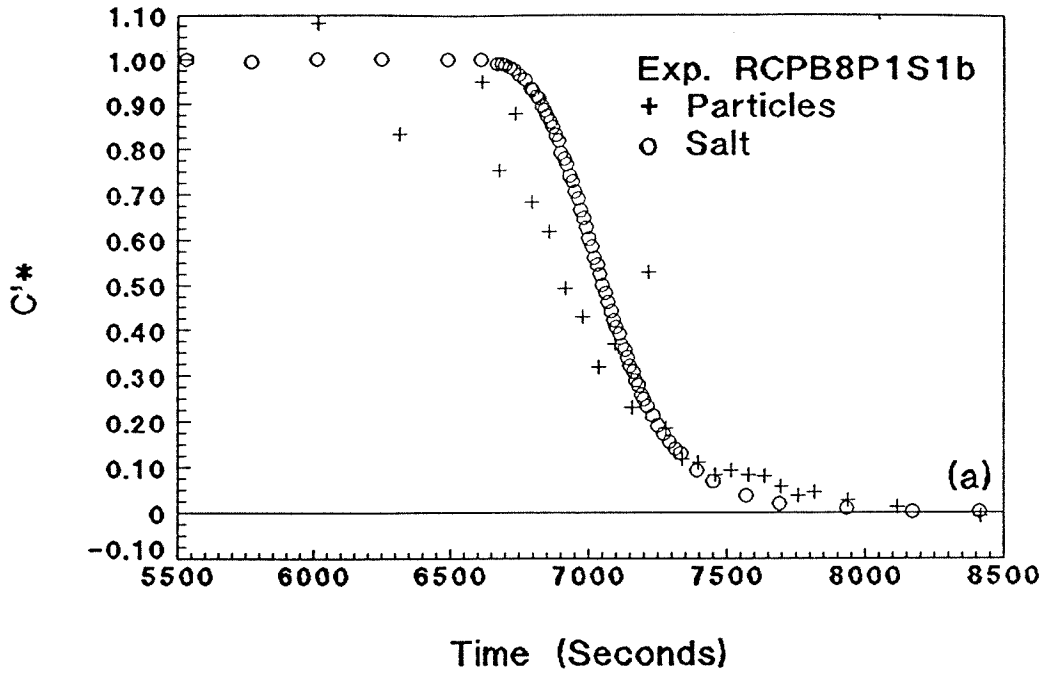

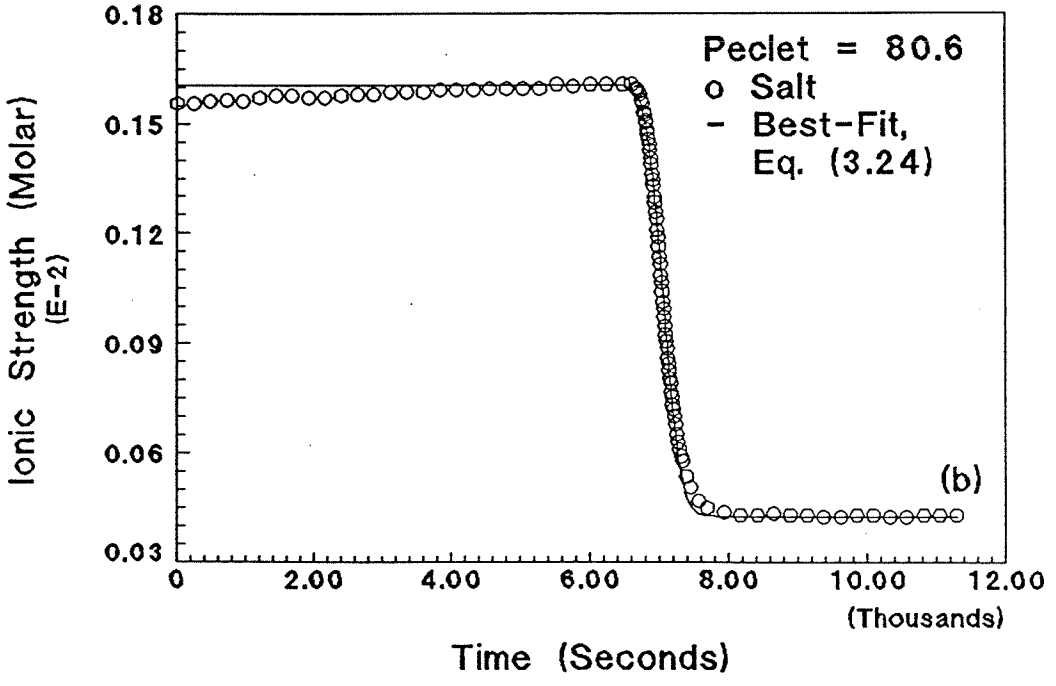

Fig. C.125: Exp. RCPB8P1S1b coupled breakthrough, $Pe_p = 10^{5.23}$, Pe = 80.6, 1.0 micron particles: (a) particles and salt relative breakthroughs and (b) salt experimental data with best-fit, Eq. (3.24).

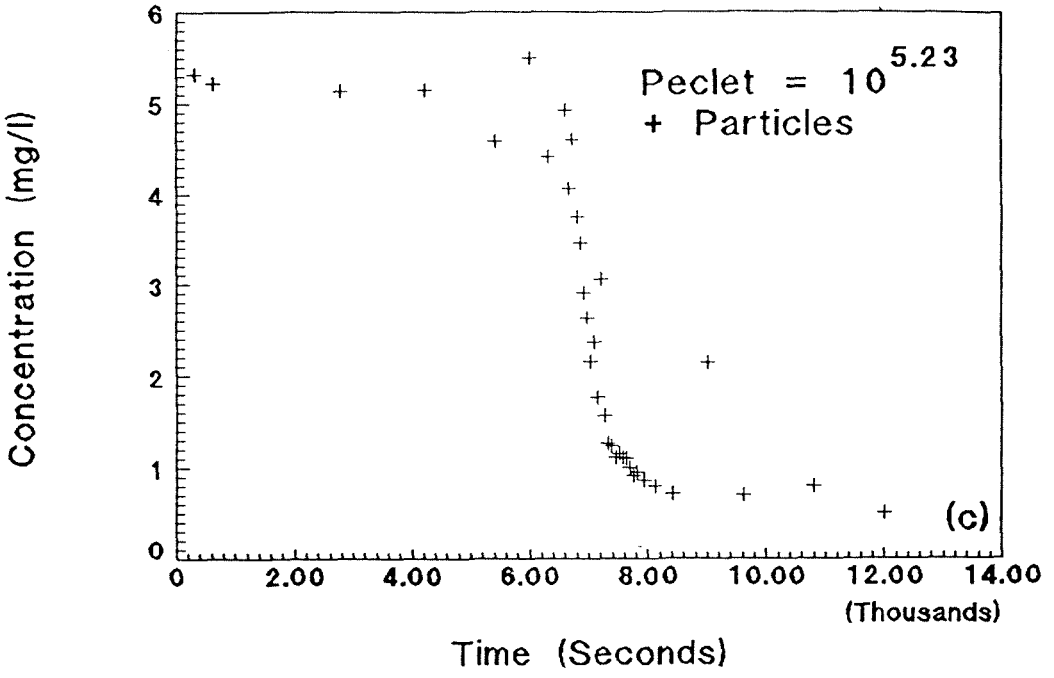

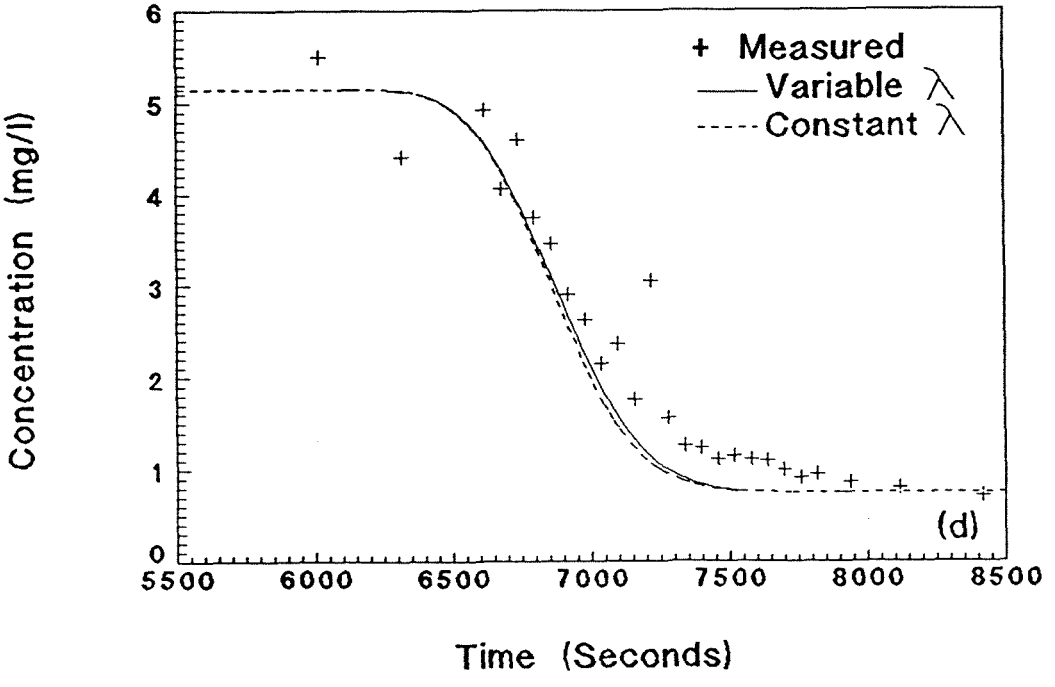

Fig. C.125(cont.): Exp. RCPB8P1S1b coupled breakthrough, $Pe_p = 10^{5.23}$, Pe = 80.6, 1.0 micron particles: (c) particle breakthrough and (d) particle experimental data with best-fit, numerical model.

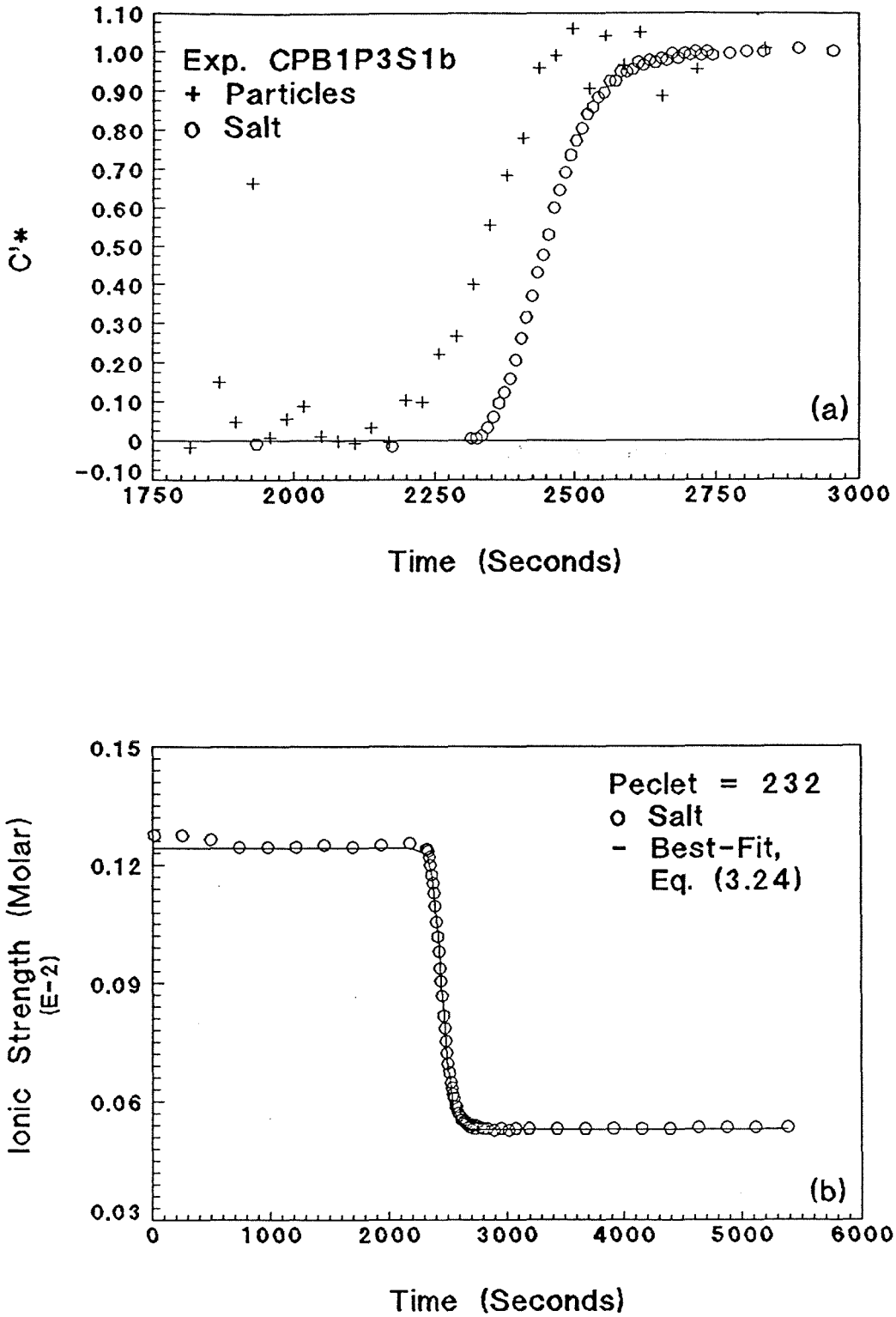

Fig. C.126: Exp. CPB1P3S1b coupled breakthrough, $Pe_p = 10^{6.14}$, Pe = 232, 2.8 micron particles: (a) particles and salt relative breakthroughs and (b) salt experimental data with best-fit, Eq. (3.24).

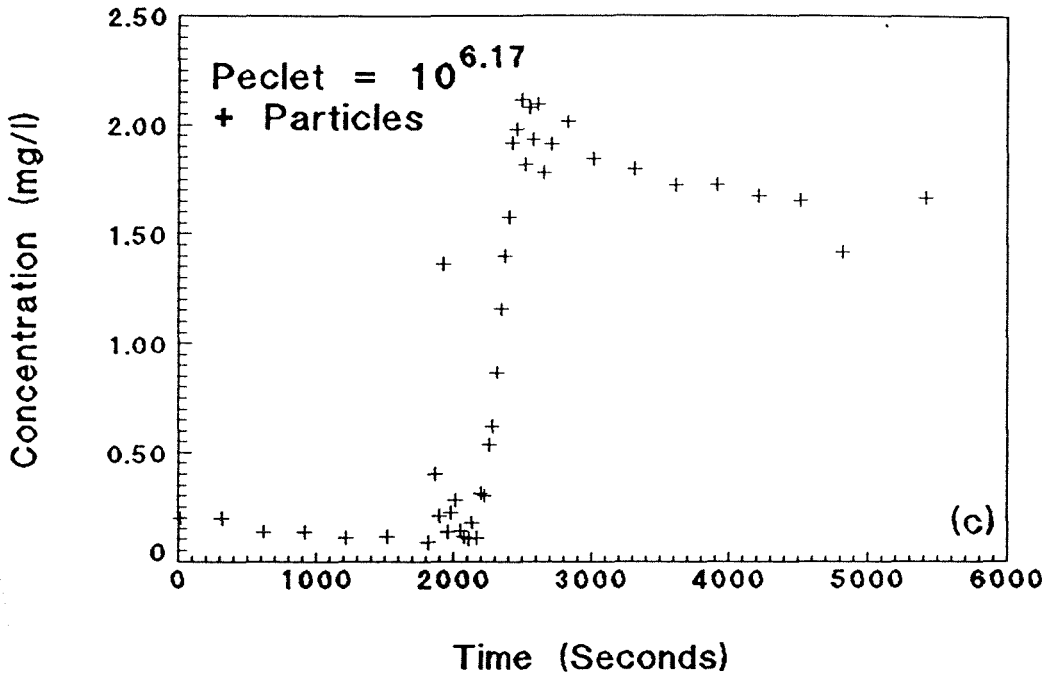

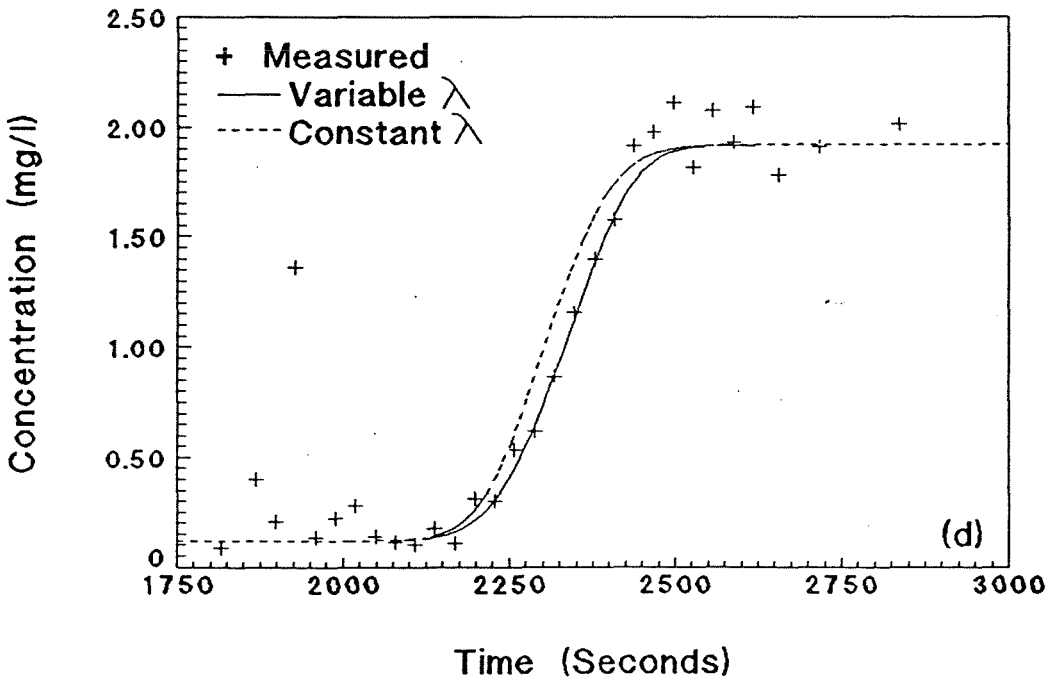

Fig. C.126(cont.): Exp. CPB1P3S1b coupled breakthrough, $Pe_p = 10^{6.14}$, Pe = 232, 2.8 micron particles: (c) particle breakthrough and (d) particle experimental data with best-fit, numerical model.

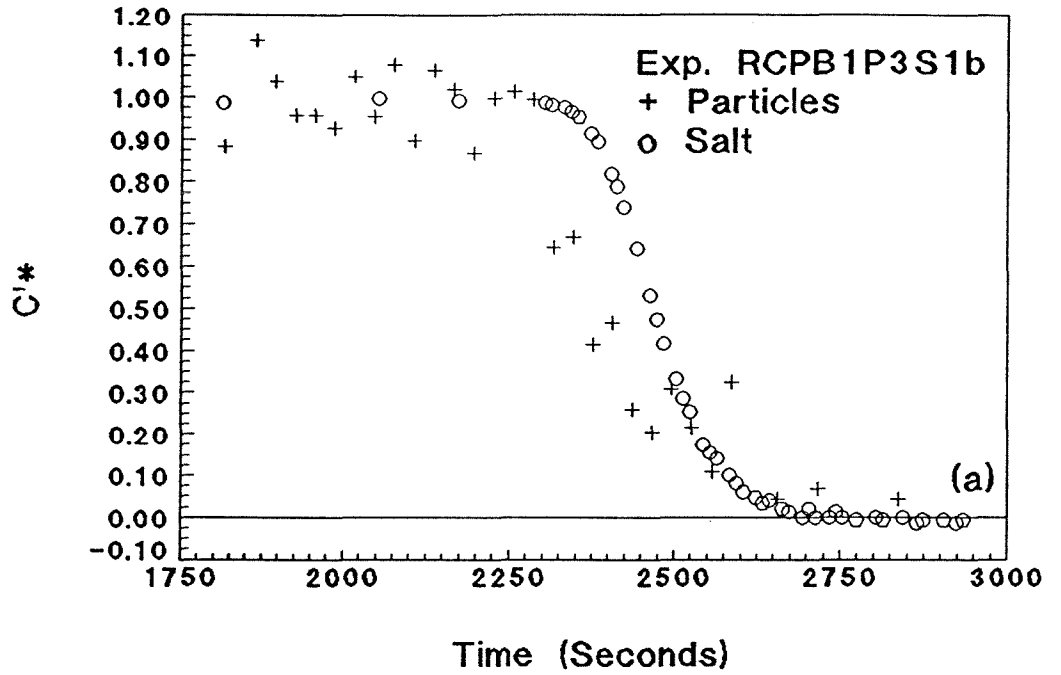

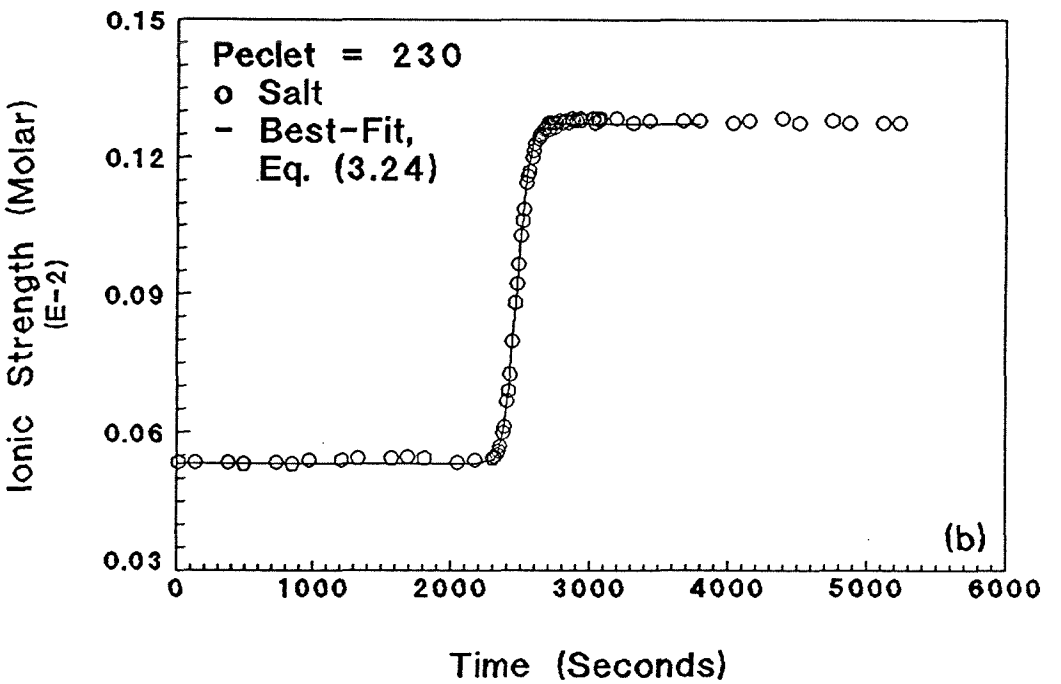

Fig. C.127: Exp. RCPB1P3S1b coupled breakthrough, $Pe_p = 10^{6.13}$, Pe = 230, 2.8 micron particles: (a) particles and salt relative breakthroughs and (b) salt experimental data with best-fit, Eq. (3.24).

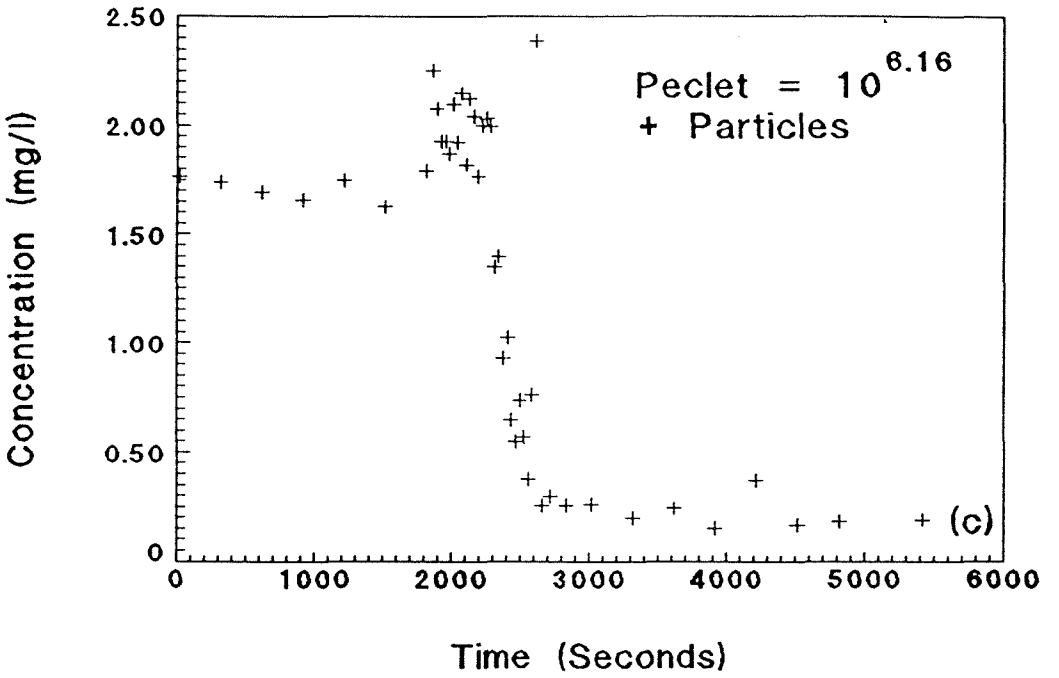

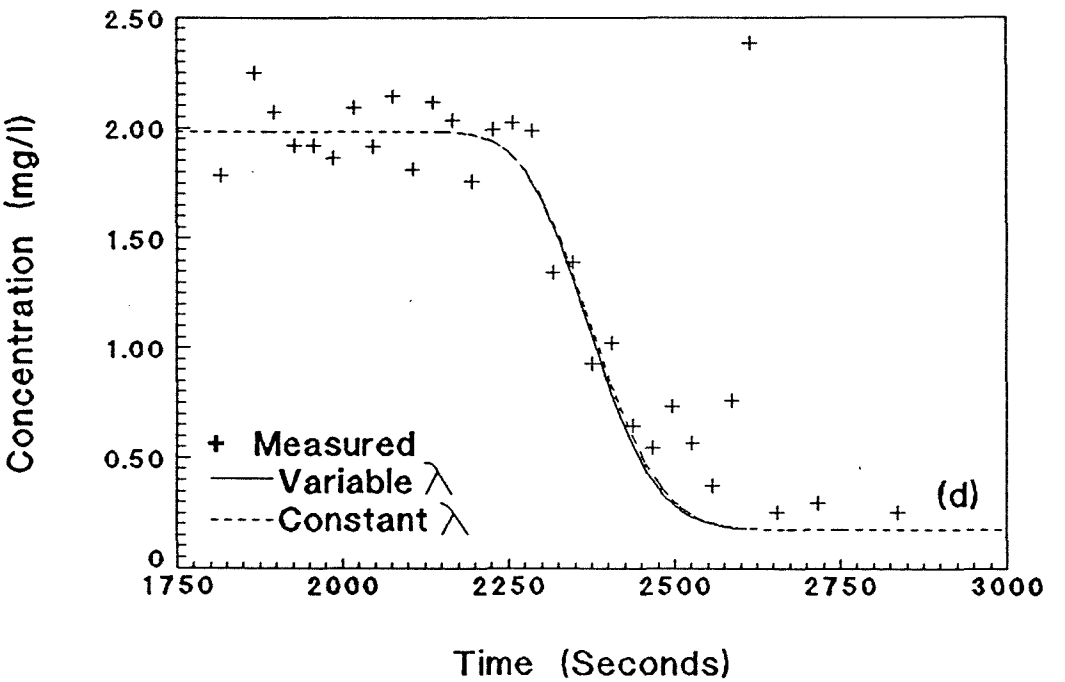

Fig. C.127(cont.): Exp. RCPB1P3S1b coupled breakthrough, $Pe_p = 10^{6.13}$, Pe = 230, 2.8 micron particles: (c) particle breakthrough and (d) particle experimental data with best-fit, numerical model.

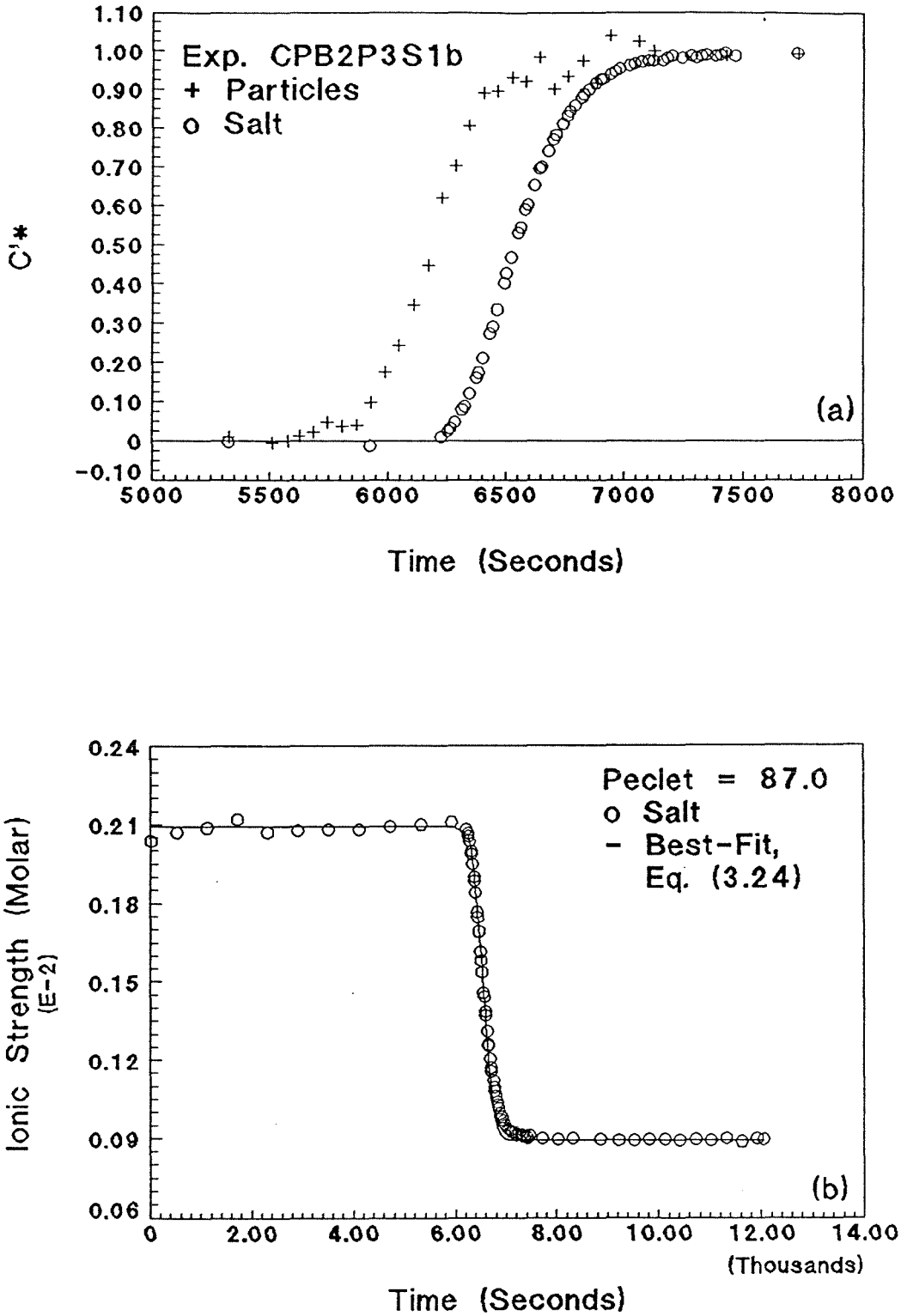

Fig. C.128: Exp. CPB2P3S1b coupled breakthrough, $Pe_p = 10^{5.72}$, Pe = 87.0, 2.8 micron particles: (a) particles and salt relative breakthroughs and (b) salt experimental data with best-fit, Eq. (3.24).

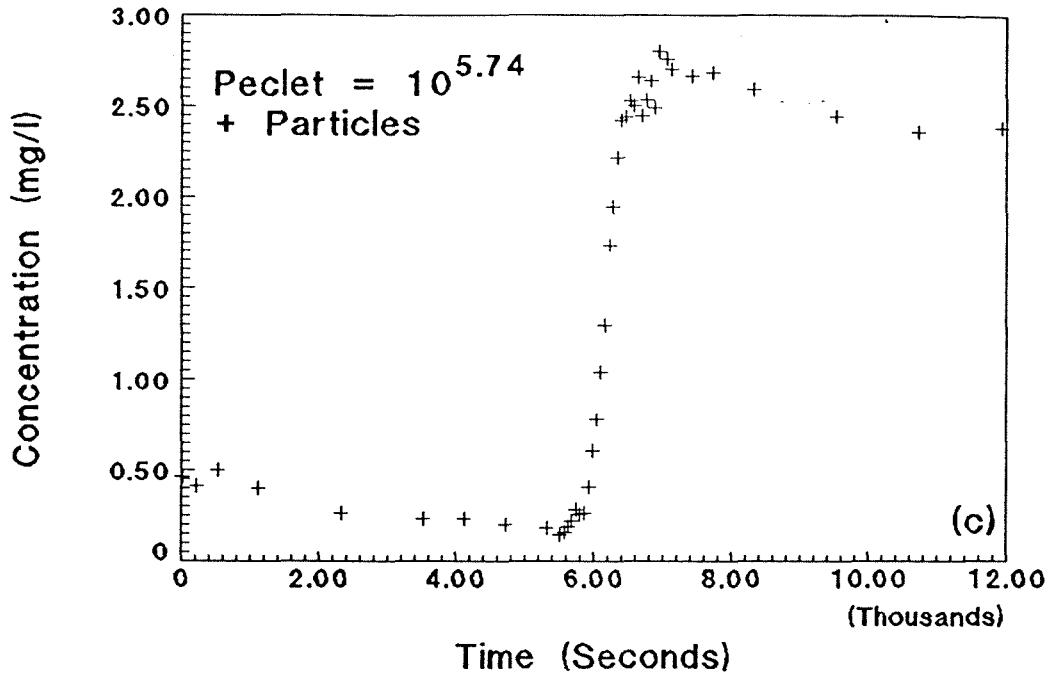

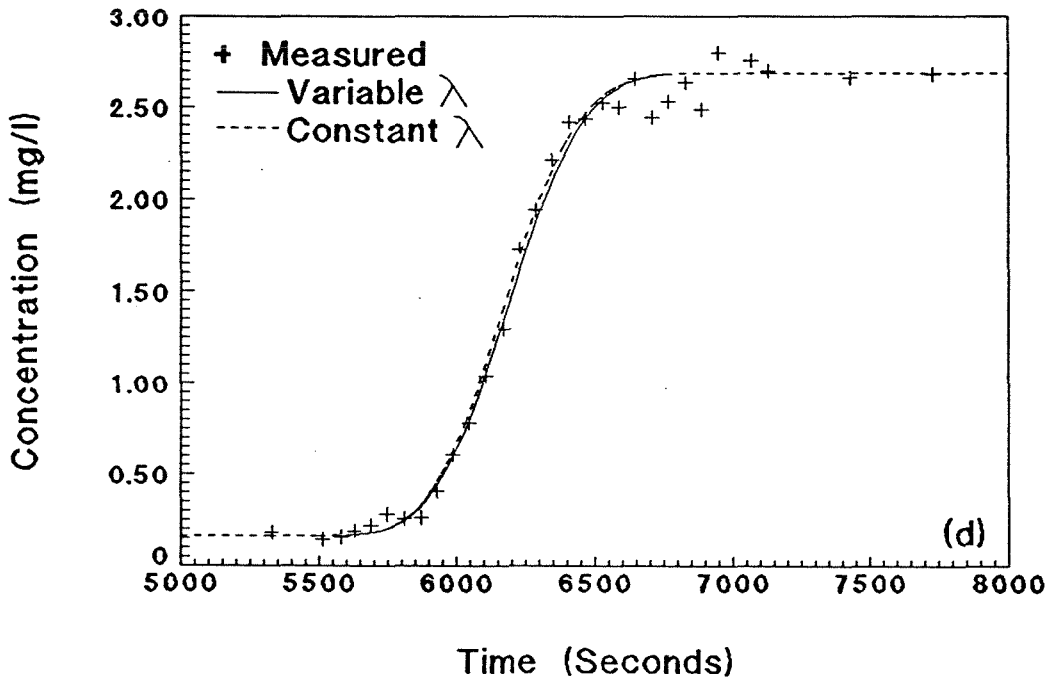

Fig. C.128(cont.): Exp. CPB2P3S1b coupled breakthrough, $Pe_p = 10^{5.72}$, Pe = 87.0, 2.8 micron particles: (c) particle breakthrough and (d) particle experimental data with best-fit, numerical model.

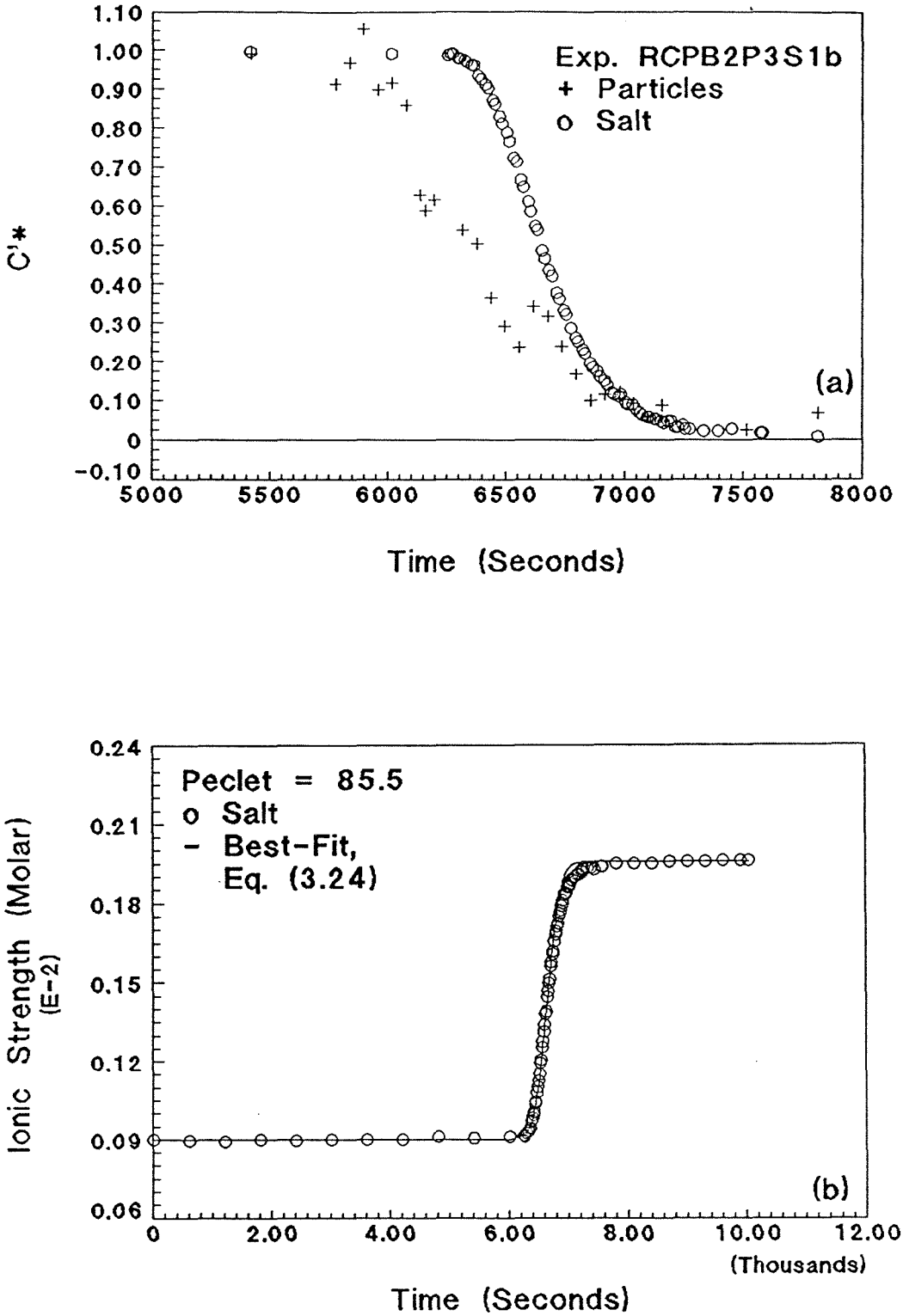

Fig. C.129: Exp. RCPB2P3S1b coupled breakthrough, $Pe_p = 10^{5.71}$, Pe = 85.5, 2.8 micron particles: (a) particles and salt relative breakthroughs and (b) salt experimental data with best-fit, Eq. (3.24).

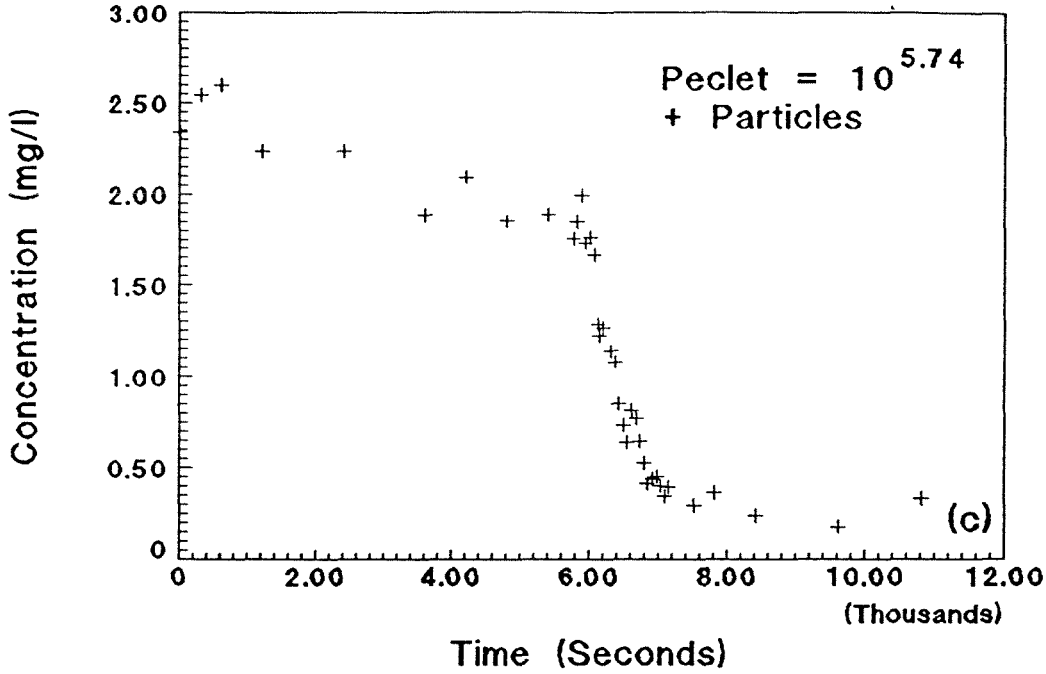

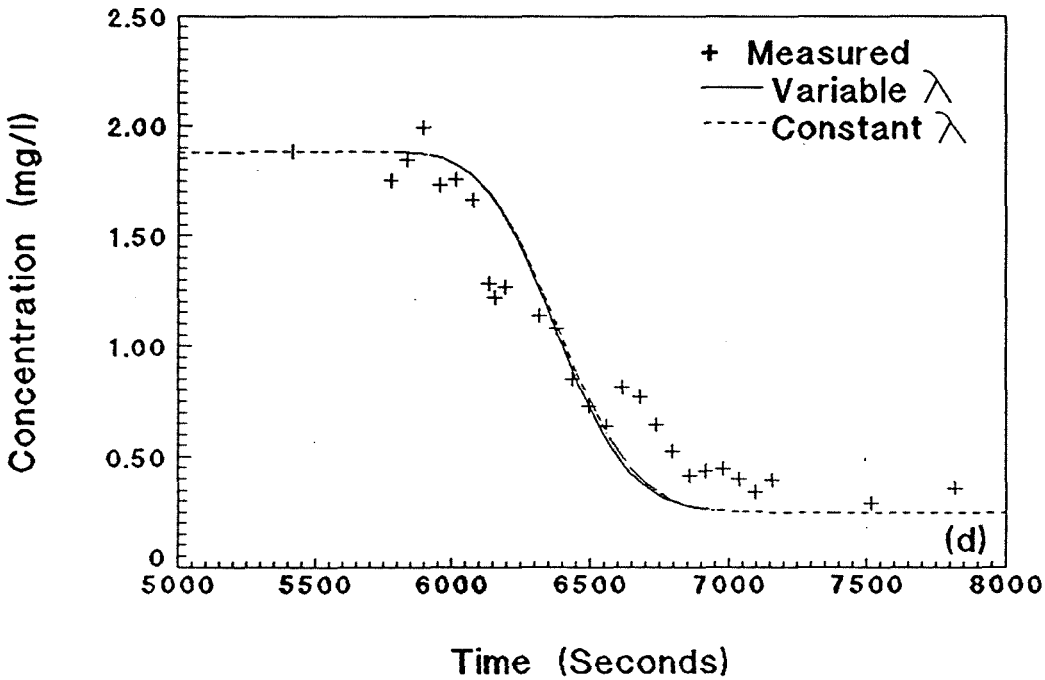

Fig. C.129(cont.): Exp. RCPB2P3S1b coupled breakthrough, $Pe_p = 10^{5.71}$, Pe = 85.5, 2.8 micron particles: (c) particle breakthrough and (d) particle experimental data with best-fit, numerical model.

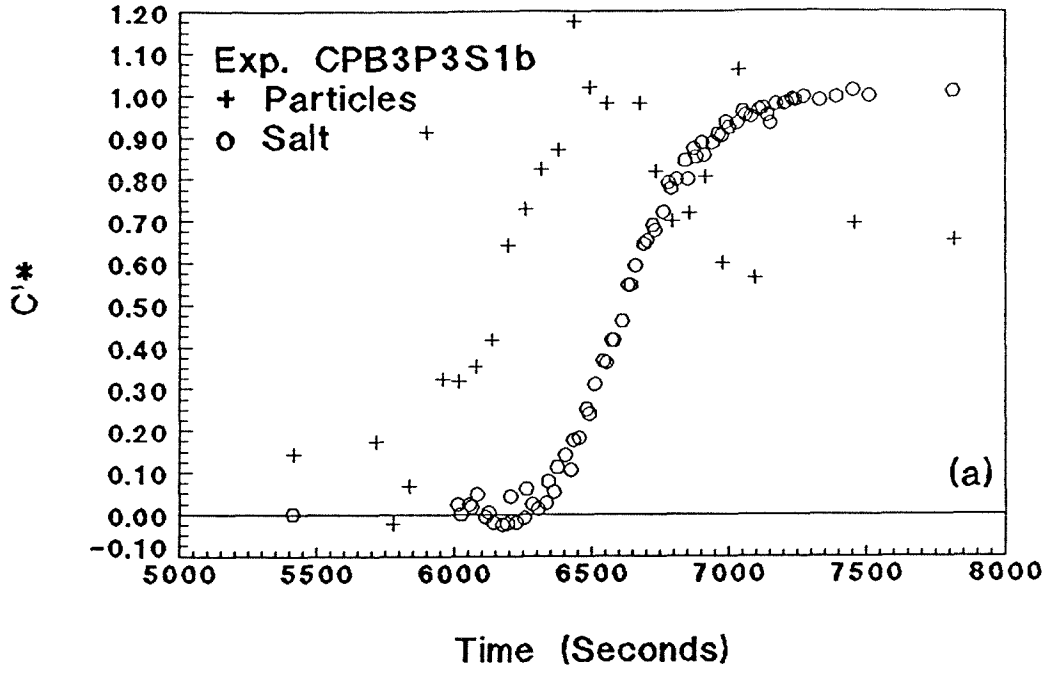

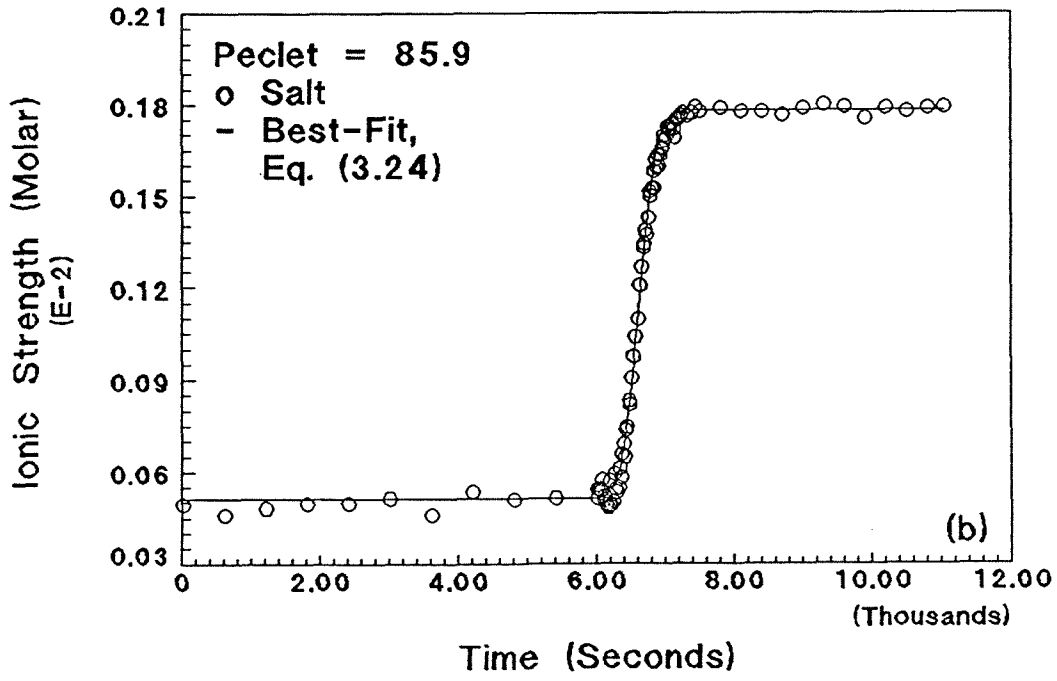

Fig. C.130: Exp. CPB3P3S1b coupled breakthrough, $Pe_p = 10^{5.72}$, Pe = 85.9, 2.8 micron particles: (a) particles and salt relative breakthroughs and (b) salt experimental data with best-fit, Eq. (3.24).

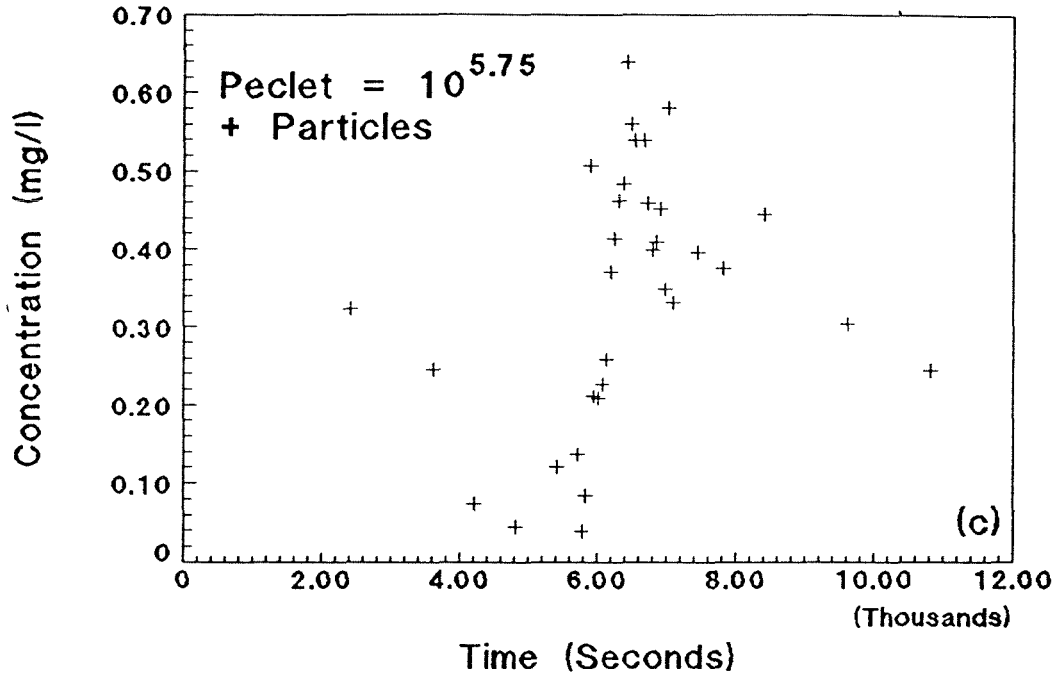

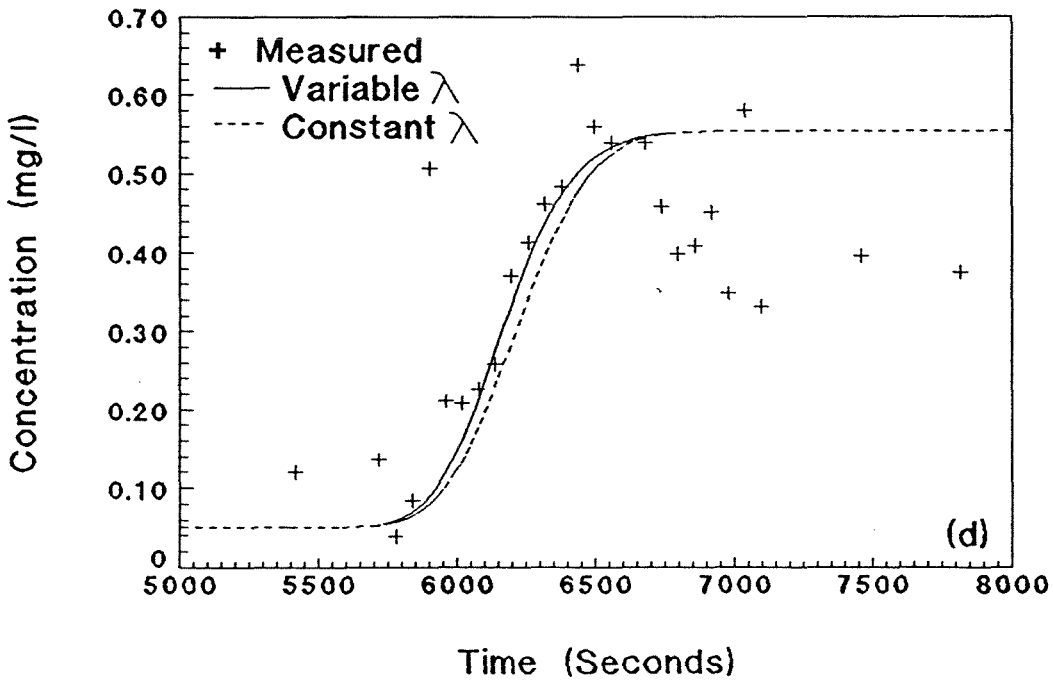

Fig. C.130(cont.): Exp. CPB3P3S1b coupled breakthrough, $Pe_p = 10^{5.72}$, Pe = 85.9, 2.8 micron particles: (c) particle breakthrough and (d) particle experimental data with best-fit, numerical model.

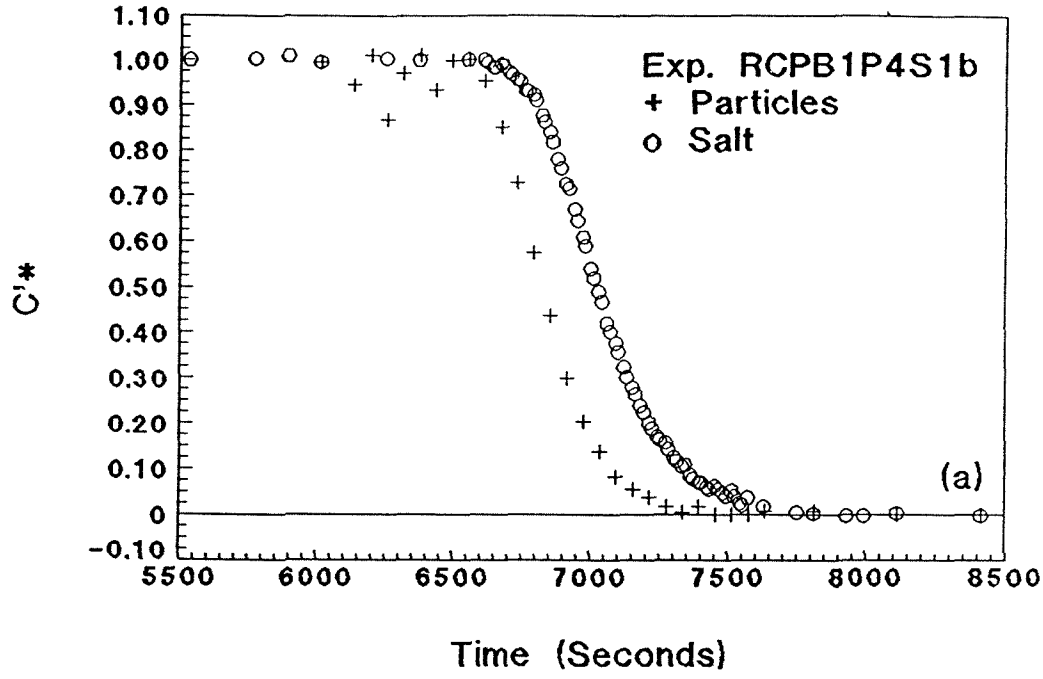

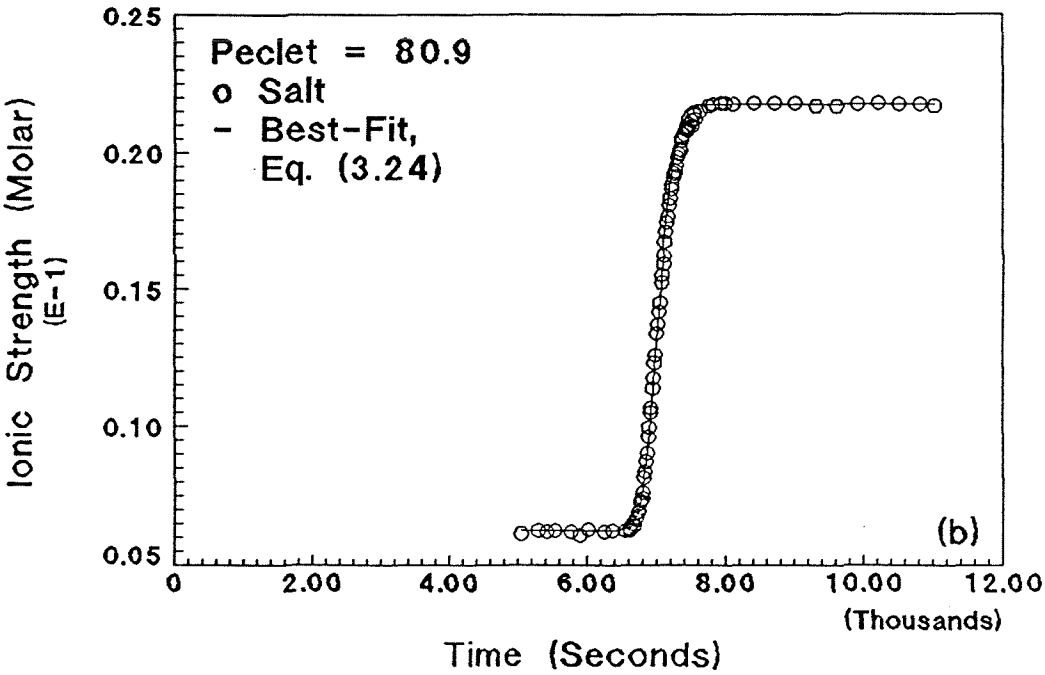

Fig. C.131: Exp. RCPB1P4S1b coupled breakthrough, $Pe_p = 10^{4.23}$, Pe = 80.9, 0.1 micron particles: (a) particles and salt relative breakthroughs and (b) salt experimental data with best-fit, Eq. (3.24).

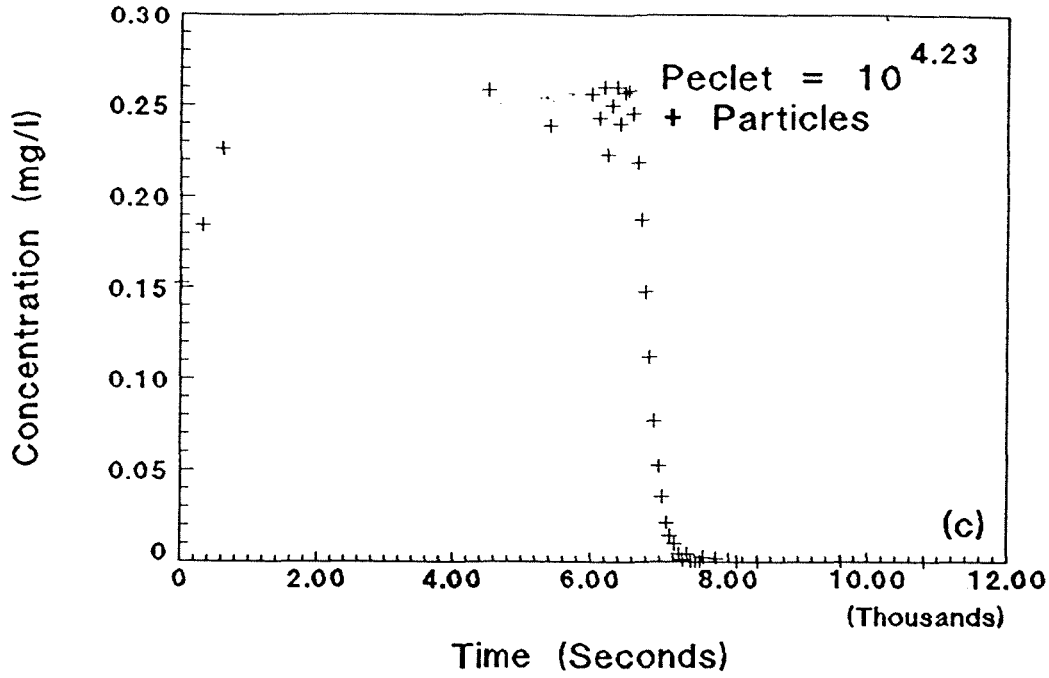

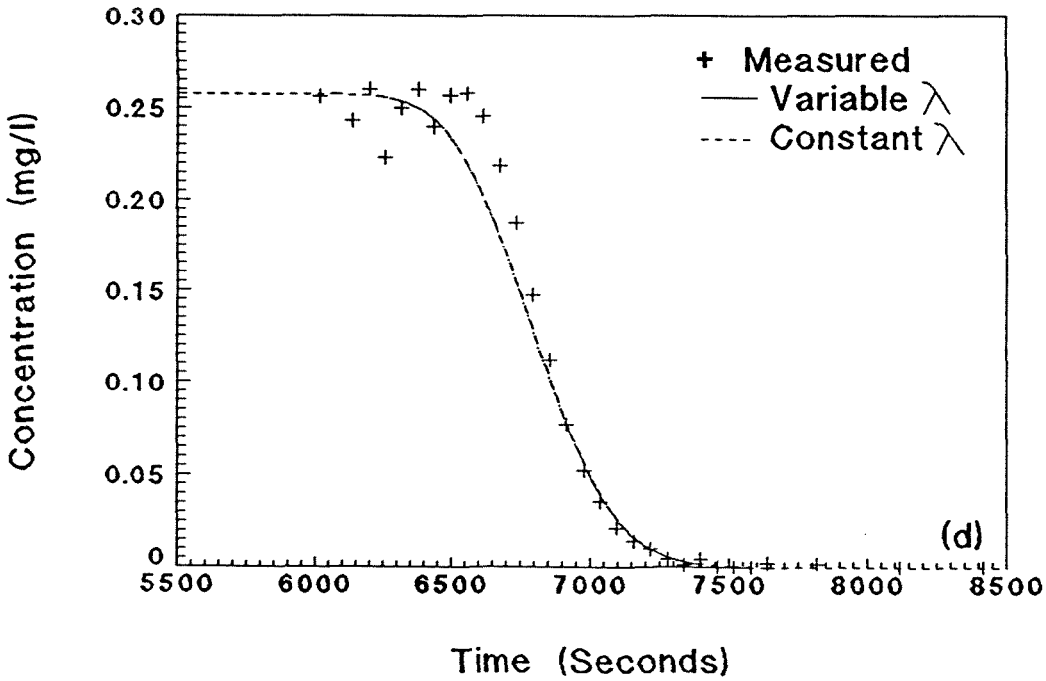

Fig. C.131(cont.): Exp. RCPB1P4S1b coupled breakthrough, $Pe_p = 10^{4.23}$, Pe = 80.9, 0.1 micron particles: (c) particle breakthrough and (d) particle experimental data with best-fit, numerical model.